

CRANFIELD UNIVERSITY

DJS BARRETT

Developments for the Calculation of Heavily Loaded Journal Bearings

SCHOOL OF ENGINEERING

EngD THESIS

CRANFIELD UNIVERSITY

SCHOOL OF ENGINEERING

DEPARTMENT OF POWER AND PROPULSION

EngD THESIS

Academic Years 2004-2009

DJS BARRETT

Developments for the Calculation of Heavily Loaded Journal Bearings

Academic Supervisor: Dr. J A Amaral Teixeira

Industrial Supervisor: Dr. I R W McLuckie

May 2010

This thesis is submitted in partial fulfilment of the requirements for the degree of
Engineering Doctorate

© Cranfield University, 2010. All rights reserved. No part of this publication may be
reproduced without the written permission of the copyright holder.

ABSTRACT

This thesis describes the development of an ElastoHydroDynamic (EHD) bearing calculation. The effect of body forces is shown to be important for highly loaded bearings in reciprocating internal combustion engines. Extension of the program to rotating machinery includes an examination of instability in the shaft bearings of a turbocharger. The development of a parameter to predict cavitation damage in a bearing is promising.

Several calculation results using the program are shown. These are engine main bearing and connecting rod big-end bearings and full floating bearings for a turbocharger. The calculations on the big-end bearing of a racing engine show why the designers were having difficulty understanding the correct location for the oil feed hole position. Effects of elastic deformation, thermal deformation and manufacturing/assembly deformation all have a significant effect on the extent of the oil film.

A novel calculation for a cavitation damage parameter is demonstrated successfully for a heavily loaded diesel engine bearing.

The importance of body forces on the oil film due to high accelerations on certain bearings is shown to be theoretically important but not yet demonstrated.

The program was written with the intention to be incorporated into the sponsoring company's range of engine design software. A part of that development process included carrying out calculations to demonstrate to customers and present papers at conferences. The results of some of these calculations have been included in this thesis.

Results of a study on the effect of crankshaft geometry on racing engine viscous friction losses were reported in a paper presented at the IDETC conference in Long Beach, 2005. This study used the first version of the software which only included Rigid Hydro Dynamics (RHD) at the time but was usable. Results of a study on stability of shaft motion in high speed turbocharger bearings were reported in a paper at the 8th International Turbocharger conference in London, 2006. At this time the program was

still only capable of RHD calculations but could now solve for multiple oil films simultaneously and sweep through the speed range. The studies on the effects of body forces and the development of a cavitation parameter will be presented in papers in the near future.

ACKNOWLEDGEMENTS

The author would like to thank his supervisors Dr. IRW McLuckie and Dr. J.A. Amaral Teixeira. Their patience and advice were much appreciated, especially at the inevitable points of stress.

The turbocharger results shown in the thesis were produced by work colleagues Drs. Edward Brooksbank and Boon Kai Teo using the software developed by the author for this project.

1.7	LAYOUT OF THESIS.....	22
CHAPTER 2.....		24
..... LITERATURE REVIEW		
.....		24
2.1	APPLICATIONS AND EXPERIMENTAL WORK.....	25
2.2	REYNOLD'S EQUATION AND SOLUTIONS.....	35
2.3	MASS CONSERVATION, BOUNDARY CONDITIONS AND CAVITATION.....	38
2.4	CONTACT AT ASPERITIES.....	45
2.5	GENERALISED MASS FLOW AT APERITIES.....	45
2.6	ELASTOHYDRODYNAMICS.....	47
2.7	THERMOELASTOHYDRODYNAMICS.....	49
2.8	FULL FLOATING BEARINGS.....	51
2.9	SOLUTION OF EQUATIONS.....	53
2.10	RHEOLOGY.....	53
2.11	BUSINESS RELATED TOPICS.....	54
2.12	OTHER TOPICS.....	56
2.13	CONCLUSIONS FROM THE LITERATURE SURVEY.....	58
2.13.1	CURRENT STATE OF KNOWLEDGE.....	58
CHAPTER 3.....		60
..... ANALYSIS METHODS		
.....		60
3.1	DERIVATION OF REYNOLD'S EQUATION.....	60
3.1.1	EXTENSION OF REYNOLD'S EQUATION FOR OIL FILM HISTORY.....	67
3.1.2	THE IMPORTANCE OF BODY FORCES.....	70

3.1.3	CAVITATION EROSION	76
3.1.4	FLOW FACTOR AND CONTACT.....	79
3.1.5	THERMOELASTOHYDRODYNAMICS.....	82
3.2	THE FINITE DIFFERENCE METHOD.....	82
3.3	THE FINITE ELEMENT METHOD.....	85
3.4	COUPLING THE METHODS.....	87
3.4.1	USING STIFFNESS AND MASS MATRICES	87
3.4.2	ADVANCED INTEGRATION AND ITERATIVE METHODS	88
3.5	ENGINE BEARING FORCES	89
3.5.1	ENGINE OPERATION.....	89
3.5.2	CALCULATION OF FORCES.....	89
3.6	TURBOCHARGER BEARING FORCES.....	93
CHAPTER 4.....		94
..... IMPLEMENTATION OF CALCULATION METHODS		
.....		94
4.1	RIGID HYDRO-DYNAMICS.....	94
4.2	MODIFICATIONS OF REYNOLD'S EQUATION.....	95
4.2.1	BODY FORCES.....	95
4.2.2	OIL FILM HISTORY.....	96
4.2.3	CAVITATION MODELLING.....	97
4.2.4	ASPERITY CONTACT AND FLOW FACTORS	98
4.2.5	LUBRICANT SUPPLY SYSTEM.....	98
4.3	STIFFNESS AND DAMPING	99
4.4	EXTENSION TO PISTON, RINGS AND OTHER PRODUCTS	101
4.5	ELASTO-HYDRO-DYNAMICS	102
4.6	CALCULATION OF ENGINE BEARING FORCES	105
4.7	CALCULATION OF TURBOCHARGER BEARING FORCES	106

CHAPTER 5.....	107
.....	
..... CALCULATION STUDIES	
.....	107
5.1 3 ENGINE FRICTION COMPARISON STUDY	107
5.2 V8 RACING ENGINE STUDY.....	107
5.3 TURBOCHARGER STUDY.....	108
5.4 REFINEMENT OF EHD CALCULATION METHODS USING TEST MODELS.....	109
5.4.1 ORBIT ENVELOPE METHODS	113
5.4.2 STABILITY OF EHD MODELS.....	114
5.4.3 DAMPING	118
5.5 ENGINE BEARING STUDIES	119
 CHAPTER 6.....	 121
.....	
..... RESULTS OF CALCULATIONS	
.....	121
6.1 3 ENGINE FRICTION COMPARISON STUDY	121
6.2 V8 RACING ENGINE STUDY.....	121
6.3 TURBOCHARGER STUDY.....	125
6.4 INVESTIGATION OF CALCULATION STABILITY	134
6.4.1 EFFECT OF DAMPING	134
6.4.2 RAYLEIGH DAMPING	135
6.4.3 FOURIER SMOOTHING OF BEARING SHAPE.....	136
6.5 DIESEL ENGINE MAIN BEARING RESULTS.....	139
6.6 DIESEL ENGINE BIG END BEARING RESULTS	141
6.7 RACING CONNECTING ROD BEARING STUDY	144
6.7.1 CIRCULAR BEARING	144
6.7.2 NON-CIRCULAR BEARING FEATURES AND EFFECTS OF ASSEMBLY	147

6.7.3	EFFECTS OF THERMAL LOADING	148
6.7.4	GENERAL PARAMETER STUDIES	163
6.8	CAVITATION DAMAGE PARAMETER	172
6.8.1	BASELINE CASE – DIESEL, RHD, 5000 RPM	174
6.8.2	DIESEL, RHD, PARTIAL GROOVES, 5000 RPM	190
6.8.3	GASOLINE, RHD, 5000 RPM	199
6.8.4	DIESEL, RHD, FASTER GAS PRESSURE RISE, 5000 RPM.....	208
6.8.5	DIESEL, RHD, 3000 RPM.....	217
6.8.6	DIESEL, RHD, 1000 RPM.....	225
6.8.7	DIESEL, EHD, 5000 RPM.....	233
6.8.8	DIESEL, EHD, PARTIAL GROOVES, 5000 RPM	245
 CHAPTER 7.....		 257
..... DISCUSSION OF RESULTS		
.....		257
7.1	GENERAL DISCUSSION OF RESULTS	257
7.2	RACING ENGINE BIG-END BEARING RESULTS	259
7.3	VERIFICATION OF FULL FLOATING BEARING RESULTS	260
7.4	CALCULATION OF CAVITATION PARAMETER.....	264
7.5	RELEVANCE OF THE PROJECT	271
 CHAPTER 8.....		 275
..... COMMERCIAL SIGNIFICANCE		
.....		275
8.1	INTRODUCTION.....	275
8.2	ENGINEERING PERSPECTIVE	278
8.3	IMPORTANCE OF THE PROJECT TO THE SPONSORING COMPANY AND INDUSTRY	280
8.3.1	SPONSORING COMPANY	280

8.3.2	INDUSTRY PERSPECTIVE	286
8.4	WORLDWIDE CONTEXT.....	291
8.4.1	POLITICAL	291
8.4.2	ECONOMIC.....	292
8.4.3	SOCIAL.....	292
8.4.4	TECHNICAL	293
8.5	FUTURE BUSINESS MODELS.....	294
8.6	MBA COURSE TOPICS	298
CHAPTER 9.....	299	
 CONCLUSIONS	
	299
9.1	ACHIEVEMENTS OF THE PROJECT.....	299
9.2	LESSONS FROM THE RESULTS	299
9.3	STATUS OF THE CURRENT WORK.....	300
9.4	INCORPORATION INTO AIES BUSINESS	301
REFERENCES	302	
APPENDIX A - EQUATIONS FOR SOLUTION OF REYNOLD’S EQUATION	319
APPENDIX B – FINITE ELEMENT STIFFNESS AND COMPLIANCE MATRIX	CONDENSATION	321
APPENDIX C - EQUATIONS FOR SOLUTION OF REYNOLD’S EQUATION	WITH OIL FILM HISTORY.....	324
APPENDIX D - ACCOUNTING AND FINANCE.....	326	

APPENDIX E - STRATEGY AND MANAGING INFORMATION SYSTEMS	328
APPENDIX F - MARKETING	331
APPENDIX G - ECONOMICS AND STRATEGIC DECISION SCIENCE	332
APPENDIX H EHD PROGRAM STRUCTURE.....	333

LIST OF FIGURES

Figure 1-1 Types of Tribological Contact	2
Figure 1-2 Lubrication Regimes	3
Figure 1-3 Operation of a Journal Bearing	5
Figure 1-4 Reynold's Equation Boundary Conditions	7
Figure 1-5 Elasto-Hydro-Dynamic Lubrication	8
Figure 1-6 Effect of Late Changes (Source Colin Mynott, 2005)	10
Figure 1-7 Hero Mountain – Payback Meadow (Source Dennis Nagy, 2005)	12
Figure 1-8 Finite Difference Mesh	15
Figure 1-9 EHD Procedure at Federal-Mogul (from McLuckie, Ma and Butler, 2000)	19
Figure 1-10 Connecting Rod (from Duffy,1994)	20
Figure 3-1 Thin oil film	63
Figure 3-2 Fluid flow in the x direction	64
Figure 3-3 Forces in the x direction on an infinitesimal control volume	65
Figure 3-4 Connecting rod small end bearing just before and after TDCF	71
Figure 3-5 Flow factors depend on film ratio and directionality of asperities	80
Figure 3-6 Contact pressure versus film thickness	81
Figure 3-7 Asperity contact at low oil film thickness ratio	81
Figure 3-8 Unwrapped Bearing	83
Figure 3-9 Finite Difference Mesh	84

Figure 3-10 Reynold's Equation Boundary Conditions	85
Figure 3-11 Connecting Rod (from Duffy,1994)	89
Figure 3-12 Slider-Crank Mechanism	90
Figure 3-13 Free Body Diagram	91
Figure 4-1 Automatically calculated bearing stiffness and damping coefficients (taken from McLuckie and Barrett (2007))	100
Figure 4-2 Piston and ring pressure distributions	101
Figure 4-3 Oil film pressure for different bearing housing stiffness	104
Figure 4-4 Oil film thickness at EHD contact	105
Figure 4-5 Finite Element models for matrix condensation	105
Figure 5-1 Typical Full Floating Bearing (Source McLuckie et al 2006)	108
Figure 5-2 X and Y force components (2.3 gmm unbalance at 20000 rev/min)	109
Figure 5-3 Finite Element models for matrix condensation	110
Figure 5-4 Typical Stiffness Array (Coarse Mesh)	110
Figure 5-5 Stiffness diagonal terms plotted around the circumference at four axial positions	111
Figure 5-6 Stiffness diagonal terms plotted on the unwrapped bearing surface	111
Figure 5-7 Inverse compliance diagonal terms plotted around the circumference at four axial positions	112
Figure 5-8 Inverse compliance diagonal terms plotted on the unwrapped bearing surface	112

Figure 5-9 RHD calculation and EHD by iterative method for big end bearing of high speed engine at 16200 rpm	113
Figure 5-10 Typical acceleration distribution on the mesh	114
Figure 5-11 Data transfer between dissimilar FE and FD meshes	115
Figure 5-12 Steps to coarsen FE mesh matrices	116
Figure 5-13 FE model symmetry	117
Figure 5-14 Effect of Rayleigh damping on different frequencies	119
Figure 5-15 EHD Meshes	119
Figure 6-1 Loads on Centre Main Bearing (Two Plane Crankshaft) (Source McLuckie & Barrett 2005b)	122
Figure 6-2 Loads on Centre Main Bearing (Single Plane Crankshaft) (Source McLuckie & Barrett 2005b)	122
Figure 6-3 Acceleration of Centre Main Journal (Two Plane Crankshaft) (Source McLuckie & Barrett 2005b)	123
Figure 6-4 Acceleration of Centre Main Journal (Single Plane Crankshaft) (Source McLuckie & Barrett 2005b)	123
Figure 6-5 Centre Main Bearing Results (Two Plane Crankshaft) (Source McLuckie & Barrett 2005b)	124
Figure 6-6 Centre Main Bearing Results (Single Plane Crankshaft) (Source McLuckie & Barrett 2005b)	124
Figure 6-7 Main Bearing Loads at 20000 rev/min (Source McLuckie & Barrett 2005b)	125
Figure 6-8 Friction Loss Comparison (Source McLuckie & Barrett 2005b)	125

Figure 6-9 Turbine end PGB journal orbit (0.023gmm unbalance, 4 micron Clearance & 4 bar oil supply pressure) at 3000, 5000, 20000 and 100000 rev/min	127
Figure 6-10 Turbine end PGB journal maximum eccentricity ratio versus speed with 4 – 16 micron clearance, 0.023 – 2.3gmm unbalance & 4 bar supply	127
Figure 6-11 Turbine end PGB journal maximum eccentricity ratio versus speed with 4 - 16 micron clearance, 0.023gmm – 2.3gmm unbalance and 0 bar oil supply	128
Figure 6-12 Turbine end FFB journal locus (0.23gmm, 2.5 micron inner/7 micron outer clearance, and supply pressure of 4 bar) at 1000, 3000, 30000 and 100000 rev/min	130
Figure 6-13 Turbine end FFB ring locus (2.3gmm, 2.5 micron inner/7 micron outer clearance, 4 bar) at 6000, 14000, 40000 and 100000 rev/min	131
Figure 6-14 Turbine end FFB journal (2.5/7 micron clearance, 0.023gmm – 2.3gmm unbalance, 4 bar) inner bearing eccentricity vs. speed	132
Figure 6-15 Turbine end FFB journal (2.5/7 micron clearance, 0.023gmm – 2.3gmm unbalance, 4 bar) outer bearing eccentricity vs. speed	132
Figure 6-16 Turbine end bearing PGB and FFB friction torque versus speed (varying unbalance, supply pressure and clearance)	133
Figure 6-17 Eccentricity ratios in X and Y direction for high speed engine	134
Figure 6-18 Restarted job - no damping	135
Figure 6-19 Restarted job – damping increasing from 50 to 10000 Nsm ⁻¹	135
Figure 6-20 Effect of increasing damping	136
Figure 6-21 Pressure distribution without smoothing	137
Figure 6-22 Oil film thickness distribution without smoothing	137
Figure 6-23 Pressure distribution - smoothed	138

Figure 6-24 Oil film thickness - smoothed	138
Figure 6-25 Simple test mesh for diesel engine main bearing	139
Figure 6-26 Comparison RHD and EHD journal orbits	140
Figure 6-27 Comparison RHD and EHD Maximum Oil Film Pressure	140
Figure 6-28 Comparison RHD and EHD Minimum Oil Film Thickness	141
Figure 6-29 Comparison RHD and EHD power loss	141
Figure 6-30 Diesel engine conrod big end bearing and housing	142
Figure 6-31 Comparison RHD and EHD journal orbits	142
Figure 6-32 Comparison RHD and EHD Maximum Oil Film Pressure	143
Figure 6-33 Comparison RHD and EHD Minimum Oil Film Thickness	143
Figure 6-34 Comparison RHD and EHD	143
Figure 6-35 High speed engine conrod big end bearing and housing	144
Figure 6-36 Comparison RHD (left) and EHD (right) journal orbits	145
Figure 6-37 Deformed shape near to Top Dead Centre Non-Firing	145
Figure 6-38 Comparison RHD and EHD Maximum Oil Film Pressure	146
Figure 6-39 Comparison RHD and EHD Min. Oil Film Thickness	146
Figure 6-40 Comparison RHD and EHD power loss	147
Figure 6-41 Measured assembled bearing profile	147
Figure 6-42 Curve fit to bearing profile	148
Figure 6-43 Bearing shape near TDC non-firing – EHD - non-circular bearing	148
Figure 6-44 Temperatures and deformations – constant flux	149

Figure 6-45 Temperatures and deformations – variable flux	150
Figure 6-46 Deformations due to bearing thermal loading	150
Figure 6-47 Typical bearing deformed shapes near to TDC non-firing – EHD circular bearing (left) versus thermally deformed bearing (right)	151
Figure 6-48 Effect of reducing constraint on conrod	152
Figure 6-49 Cumulative effect of increasing heat transfer to crankcase gases x4	153
Figure 6-50 Cumulative effect of increasing heat transfer to bearing surface x2 (from 5% to 10% of viscous power loss)	153
Figure 6-51 Effect of loosening constraint of the conrod model	154
Figure 6-52 Effect of increasing the heat transfer coefficient to the crankcase gas	154
Figure 6-53 Effect of increasing the heat transfer percentage to the bearing surface	155
Figure 6-54 Effect of extreme variation in material properties	156
Figure 6-55 Effect of material properties on deformation and temperature at the bearing surface	157
Figure 6-56 Average viscous torque	159
Figure 6-57 Percentage change of viscous torque	159
Figure 6-58 Thermo Elasto HydroDynamic calculation loop	160
Figure 6-59 Oil flow and viscous power loss	162
Figure 6-60 Temperature rise in the oil and average heat flux to bearing surface	162
Figure 6-61 Effect of mesh density - RHD	164
Figure 6-62 Effect of mesh density on pressure profile at 10 deg. crank angle(from top left – medium, fine, coarse)	164

Figure 6-63 Definition of oil hole position on big end bearing journal	165
Figure 6-64 Effect of oil hole position – RHD	166
Figure 6-65 Pressure distribution at 10 deg. crank angle – RHD (oil hole positions from top left – 30, 0, 60 deg.)	167
Figure 6-66 Effect of oil hole position on EHD models	168
Figure 6-67 Pressure distribution for different oil hole positions at 10 deg. crank angle – EHD (oil hole positions from top left – 30, 0, 60 deg.)	169
Figure 6-68 Effect of oil hole position – TEHD	170
Figure 6-69 Pressure distribution at 10 deg. crank angle – TEHD (oil hole positions from top left – 30, 0, 60 deg.)	170
Figure 6-70 Shaped bearing comparison of effects of oil hole position	171
Figure 6-71 Shaped bearing – effect of oil hole on pressure distribution at 10 degrees shaft angle for oil hole at 30 deg., 0 deg., 60 deg.	172
Figure 6-72 Diesel, RHD, 5000 rpm - Eccentricity	175
Figure 6-73 Diesel, RHD, 5000 rpm – Journal Orbit	175
Figure 6-74 Diesel, RHD, 5000 rpm - Velocity	176
Figure 6-75 Diesel, RHD, 5000 rpm - Velocity	176
Figure 6-76 Diesel, RHD, 5000 rpm – Peak Pressures	177
Figure 6-77 Diesel, RHD, 5000 rpm – Peak Pressure Snapshot	177
Figure 6-78 Diesel, RHD, 5000 rpm – Pressure Snapshot at 220 deg	178
Figure 6-79 Diesel, RHD, 5000 rpm – Pressure Snapshot at 380 deg	178
Figure 6-80 Diesel, RHD, 5000 rpm – Pressure Snapshot at 605 deg	179

Figure 6-81 Diesel, RHD, 5000 rpm – Peak Pressure Maxima Over Cycle	180
Figure 6-82 Diesel, RHD, 5000 rpm – Minimum Film Thicknesses	180
Figure 6-83 Diesel, RHD, 5000 rpm – Film Thickness Snapshot at Minimum	181
Figure 6-84 Diesel, RHD, 5000 rpm – Film Polar Plot at Minimum	181
Figure 6-85 Diesel, RHD, 5000 rpm – Film Thickness Minima Over Cycle	182
Figure 6-86 Diesel, RHD, 5000 rpm – Maximum Cavitation Velocity Over Cycle	183
Figure 6-87 Diesel, RHD, 5000 rpm – Cavitation Velocity Snapshot at Maximum	183
Figure 6-88 Diesel, RHD, 5000 rpm – Cavitation Velocity Snapshot at 55 deg	184
Figure 6-89 Diesel, RHD, 5000 rpm – Cavitation Velocity Snapshot at 310 deg	184
Figure 6-90 Diesel, RHD, 5000 rpm – Cavitation Velocity Snapshot at 445 deg	185
Figure 6-91 Diesel, RHD, 5000 rpm – Cavitation Velocity Maxima Over Cycle	185
Figure 6-92 Diesel, RHD, 5000 rpm – Minimum Pressure Gradient Over Cycle	186
Figure 6-93 Diesel, RHD, 5000 rpm – Snapshot of Pressure Gradient at Minimum in Cycle	187
Figure 6-94 Diesel, RHD, 5000 rpm – Pressure Gradient at 290 deg	187
Figure 6-95 Pressure Gradient Snapshot at 430 deg	188
Figure 6-96 Diesel, RHD, 5000 rpm – Pressure Gradient Minima Over Cycle	188
Figure 6-97 Diesel, RHD, 5000 rpm – Normalised Cavitation Damage Parameter	189
Figure 6-98 Diesel, Partial Grooves, RHD, 5000 rpm – Eccentricity	190
Figure 6-99 Diesel, Partial Grooves, RHD, 5000 rpm – Journal Orbit	191
Figure 6-100 Diesel, Partial Grooves, RHD, 5000 rpm – Journal Velocity	192

Figure 6-101 Diesel, Partial Grooves, RHD, 5000 rpm – Journal Velocity	192
Figure 6-102 Diesel, Partial Grooves, RHD, 5000 rpm – Peak Film Pressure Over Cycle	193
Figure 6-103 Diesel, Partial Grooves, RHD, 5000 rpm – Snapshot at Peak Pressure	193
Figure 6-104 Diesel, Partial Grooves, RHD, 5000 rpm – Peak Pressure Maxima Over Cycle	194
Figure 6-105 Diesel, Partial Grooves, RHD, 5000 rpm – Peak Cavitation Velocity Over Cycle	194
Figure 6-106 Diesel, Partial Grooves, RHD, 5000 rpm – Snapshot at Maximum Cavitation Velocity	195
Figure 6-107 Diesel, Partial Grooves, RHD, 5000 rpm – Cavitation Velocity Maxima Over Cycle	196
Figure 6-108 Diesel, Partial Grooves, RHD, 5000 rpm – Min. Pressure Gradient Over Cycle	196
Figure 6-109 Diesel, Partial Grooves, RHD, 5000 rpm – Snapshot of Pressure Gradient at Minimum	197
Figure 6-110 Diesel, Partial Grooves, RHD, 5000 rpm – Pressure Gradient Minima Over Cycle	198
Figure 6-111 Diesel, Partial Grooves, RHD, 5000 rpm – Normalised Cavitation Damage Parameter	199
Figure 6-112 Gasoline, RHD, 5000 rpm – Eccentricity	200
Figure 6-113 Gasoline, RHD, 5000 rpm – Journal Orbit	200
Figure 6-114 Gasoline, RHD, 5000 rpm – Journal Velocity	201
Figure 6-115 Gasoline, RHD, 5000 rpm – Journal Velocity	201

Figure 6-116 Gasoline, RHD, 5000 rpm – Peak Gas Pressure Over Cycle	202
Figure 6-117 Gasoline, RHD, 5000 rpm – Peak Pressure Snapshot	203
Figure 6-118 Gasoline, RHD, 5000 rpm – Peak Pressure Maxima Over Cycle	203
Figure 6-119 Gasoline, RHD, 5000 rpm – Maximum Cavitation Velocity Over Cycle	204
Figure 6-120 Cavitation Velocity Snapshot at Maximum	204
Figure 6-121 Cavitation Velocity Maxima Over Cycle	205
Figure 6-122 Gasoline, RHD, 5000 rpm – Minimum Pressure Gradient Over Cycle	205
Figure 6-123 Gasoline, RHD, 5000 rpm – Pressure Gradient Snapshot at Minimum	206
Figure 6-124 Gasoline, RHD, 5000 rpm – Pressure Gradient Minima Over Cycle	207
Figure 6-125 Gasoline, RHD, 5000 rpm – Normalised Cavitation Damage Parameter	207
Figure 6-126 Diesel, Fast Pressure Rise, RHD, 5000 rpm – Eccentricity	208
Figure 6-127 Diesel, Fast Pressure Rise, RHD, 5000 rpm – Journal Orbit	209
Figure 6-128 Diesel, Fast Pressure Rise, RHD, 5000 rpm – Journal Velocity	209
Figure 6-129 Diesel, Fast Pressure Rise, RHD, 5000 rpm – Journal Velocity	210
Figure 6-130 Diesel, Fast Pressure Rise, RHD, 5000 rpm – Peak Film Pressure Over Cycle	210
Figure 6-131 Diesel, Fast Pressure Rise, RHD, 5000 rpm – Peak Pressure Snapshot	211
Figure 6-132 Diesel, Fast Pressure Rise, RHD, 5000 rpm – Peak Pressure Maxima Over Cycle	212

Figure 6-133 Diesel, Fast Pressure Rise, RHD, 5000 rpm – Peak Cavitation Velocity Over Cycle	212
Figure 6-134 Diesel, Fast Pressure Rise, RHD, 5000 rpm – Cavitation Velocity Snapshot at Maximum	213
Figure 6-135 Diesel, Fast Pressure Rise, RHD, 5000 rpm – Cavitation Velocity Maxima Over Cycle	214
Figure 6-136 Diesel, Fast Pressure Rise, RHD, 5000 rpm – Minimum Pressure Gradient Over Cycle	214
Figure 6-137 Diesel, Fast Pres. Rise, RHD, 5000 rpm – Press. Grad. Snapshot at Minimum	215
Figure 6-138 Diesel, Fast Press. Rise, RHD, 5000 rpm – Press. Grad. Minima Over Cycle	216
Figure 6-139 Diesel, Fast Pressure Rise, RHD, 5000 rpm – Normalised Cavitation Damage Parameter	216
Figure 6-140 Diesel, RHD, 3000 rpm – Eccentricity	217
Figure 6-141 Diesel, RHD, 3000 rpm – Journal Orbit	218
Figure 6-142 Diesel, RHD, 3000 rpm – Journal Velocity	218
Figure 6-143 Diesel, RHD, 3000 rpm – Journal Velocity	219
Figure 6-144 Diesel, RHD, 3000 rpm – Peak Film Pressure Over Cycle	219
Figure 6-145 Diesel, RHD, 3000 rpm – Pressure Snapshot at Maximum	220
Figure 6-146 Diesel, RHD, 3000 rpm – Peak Pressure Maxima Over Cycle	221
Figure 6-147 Diesel, RHD, 3000 rpm – Maximum Cavitation Velocity Over Cycle	221
Figure 6-148 Diesel, RHD, 3000 rpm – Cavitation Velocity Snapshot at Maximum	222

Figure 6-149 Diesel, RHD, 3000 rpm – Cavitation Velocity Maxima Over Cycle	222
Figure 6-150 Diesel, RHD, 3000 rpm – Minimum Pressure Gradient Over Cycle	223
Figure 6-151 Diesel, RHD, 3000 rpm – Pressure Gradient Snapshot at Minimum	224
Figure 6-152 Diesel, RHD, 3000 rpm – Pressure Gradient Minima Over Cycle	224
Figure 6-153 Diesel, RHD, 3000 rpm – Normalised Cavitation Damage Parameter	225
Figure 6-154 Diesel, RHD, 1000 rpm – Eccentricity	226
Figure 6-155 Diesel, RHD, 1000 rpm – Journal Orbit	226
Figure 6-156 Diesel, RHD, 1000 rpm – Journal Velocity	227
Figure 6-157 Diesel, RHD, 1000 rpm – Journal Velocity	227
Figure 6-158 Diesel, RHD, 1000 rpm – Peak Film Pressure Over Cycle	228
Figure 6-159 Diesel, RHD, 1000 rpm – Film Pressure Snapshot at Maximum	228
Figure 6-160 Diesel, RHD, 1000 rpm – Peak Pressure Maxima Over Cycle	229
Figure 6-161 Diesel, RHD, 1000 rpm – Maximum Cavitation Velocity Over Cycle	229
Figure 6-162 Diesel, RHD, 1000 rpm – Cavitation Velocity Snapshot at Maximum	230
Figure 6-163 Diesel, RHD, 1000 rpm – Cavitation Velocity Maxima Over Cycle	231
Figure 6-164 Diesel, RHD, 1000 rpm – Minimum Pressure Gradient Over Cycle	231
Figure 6-165 Diesel, RHD, 1000 rpm – Pressure Gradient Snapshot at Minimum	232
Figure 6-166 Diesel, RHD, 1000 rpm – Pressure Gradient Minima Over Cycle	232
Figure 6-167 Diesel, RHD, 1000 rpm – Normalised Cavitation Damage Parameter	233
Figure 6-168 Diesel, EHD, 5000 rpm – Eccentricity	234
Figure 6-169 Diesel, EHD, 5000 rpm – Journal Orbit	234

Figure 6-170 Diesel, EHD, 5000 rpm – Journal Velocity	235
Figure 6-171 Diesel, EHD, 5000 rpm – Journal Velocity	235
Figure 6-172 Diesel, EHD, 5000 rpm – Peak Film Pressure Over Cycle	236
Figure 6-173 Diesel, EHD, 5000 rpm – Pressure Snapshot at Maximum	236
Figure 6-174 Diesel, EHD, 5000 rpm – Peak Pressure Maxima Over Cycle	237
Figure 6-175 Diesel, EHD, 5000 rpm – Minimum Film Thickness Over Cycle	237
Figure 6-176 Diesel, EHD, 5000 rpm – Film Thickness Snapshot at Minimum	238
Figure 6-177 Diesel, EHD, 5000 rpm – Film Shape at Minimum Film Thickness	238
Figure 6-178 Diesel, EHD, 5000 rpm – Film Snapshot at 55 deg	239
Figure 6-179 Diesel, EHD, 5000 rpm – Film Shape at 55 deg	239
Figure 6-180 Diesel, EHD, 5000 rpm – Film Thickness Minima Over Cycle	240
Figure 6-181 Diesel, EHD, 5000 rpm – Maximum Cavitation Velocity Over Cycle	241
Figure 6-182 Diesel, EHD, 5000 rpm – Cavitation Velocity Snapshot at Maximum	241
Figure 6-183 Diesel, EHD, 5000 rpm – Cavitation Velocity Maxima Over Cycle	242
Figure 6-184 Diesel, EHD, 5000 rpm – Minimum Pressure Gradient Over Cycle	242
Figure 6-185 Diesel, EHD, 5000 rpm – Pressure Gradient Snapshot at Minimum	243
Figure 6-186 Diesel, EHD, 5000 rpm – Pressure Gradient Minima Over Cycle	244
Figure 6-187 Diesel, EHD, 5000 rpm – Normalised Cavitation Damage Parameter	244
Figure 6-188 Diesel, partial grooves, EHD, 5000 rpm – Eccentricity	245
Figure 6-189 Diesel, partial grooves, EHD, 5000 rpm – Journal Orbit	246
Figure 6-190 Diesel, partial grooves, EHD, 5000 rpm – Journal Velocity	247

Figure 6-191 Diesel, partial grooves, EHD, 5000 rpm – Journal Velocity	247
Figure 6-192 Diesel, partial grooves, EHD, 5000 rpm – Peak Film Pressure Over Cycle	248
Figure 6-193 Diesel, partial grooves, EHD, 5000 rpm – Pressure Snapshot at Maximum	248
Figure 6-194 Diesel, partial grooves, EHD, 5000 rpm – Peak Pressure Maxima Over Cycle	249
Figure 6-195 Diesel, partial grooves, EHD, 5000 rpm – Minimum Film Thickness Over Cycle	250
Figure 6-196 Diesel, partial grooves, EHD, 5000 rpm – Film Thickness Snapshot at Minimum	250
Figure 6-197 Diesel, partial grooves, EHD, 5000 rpm – Film Thickness Minima Over Cycle	251
Figure 6-198 Diesel, partial grooves, EHD, 5000 rpm – Maximum Cavitation Velocity Over Cycle	252
Figure 6-199 Diesel, partial grooves, EHD, 5000 rpm – Cavitation Velocity Snapshot at Maximum	252
Figure 6-200 Diesel, partial grooves, EHD, 5000 rpm – Cavitation Velocity Maxima Over Cycle	253
Figure 6-201 Diesel, partial grooves, EHD, 5000 rpm – Minimum Pressure Gradient Over Cycle	253
Figure 6-202 Diesel, partial grooves, EHD, 5000 rpm – Pressure Gradient Snapshot at Minimum	254
Figure 6-203 Diesel, partial grooves, EHD, 5000 rpm – Pressure Gradient Minima Over Cycle	255

Figure 6-204 Diesel, partial grooves, EHD, 5000 rpm – Normalised Cavitation Damage Parameter	256
Figure 7-1 Waterfall bubble plot for turbine end PGB - 0.023 gmm unbalance, 4 microns, 4 bar supply pressure	261
Figure 7-2 Waterfall bubble plot for turbine end PGB - 2.3 gmm gross unbalance, 4 microns clearance, 4 bar supply pressure	262
Figure 7-3 Waterfall bubble plot for turbine end FFB - 0.23 gmm unbalance, 2.5/7 microns inner/outer clearance, 4 bar supply pressure	263
Figure 7-4 Waterfall bubble plot for turbine end FFB - 2.3 gmm gross unbalance, 2.5/7 microns inner/outer clearance, 4 bars supply pressure	264
Figure 7-5 Effect of Bearing on Cavitation Damage Parameter	265
Figure 7-6 Effect of Engine Speed on Cavitation Damage Parameter	266
Figure 7-7 Effect of Gas Pressure Curve on Cavitation Damage Parameter	267
Figure 7-8 Cavitation Damage Parameter	269
Figure 7-9 Typical Oil Flow Timing Cavitation (Forstner and Struwe, 2004)	269
Figure 7-10 Typical Vibration Cavitation (Forstner and Struwe, 2004)	270
Figure 7-11 Groove Cavitation (from Forstner and Struwe, 2004)	270
Figure 8-1 Effect of Delays (source Colin Mynott, 2005)	275
Figure 8-2 Effect of Late Changes (Source Colin Mynott, 2005)	276
Figure 8-3 Typical Wasted Time (Source Colin Mynott, 2005)	277
Figure 8-4 Risk vs. Time (Source Colin Mynott, 2005)	277
Figure 8-5 Perceived User Value vs. Perceived Price	284

Figure 8-6 Ansoff Strategic Development Matrix	286
Figure 8-7 Role of Knowledge in Systems	288
Figure 8-8 Importance of Correction Loops	289
Figure 8-9 Boston Matric	290
Figure 8-10 Initial Indicative Benefits Network	291
Figure 8-11 Porter’s Five Forces – Barriers to Entry	296
Figure 8-12 Demand Curve	297
Figure 9-1 Process Triangle	330

LIST OF TABLES

Table 1-1 Direct Cost versus Product Cost	12
Table 1-2 Advantages and Disadvantages Finite Difference Method (Based on table from Barrett - 2001).....	16
Table 1-3 Advantages and Disadvantages Finite Element Method.....	17
Table 1-4 Advantages/disadvantages - Transfer Matrix Method	18
Table 2-1 Review of EHD Programs - from Xu (1996a)	29
Table 2-2 Minimum Oil Film Thickness and Maximum Oil Film Pressure (from Poynton et al., 1998).....	31
Table 3-1 Typical Body Forces Relative to Terms in Reynold's Equation.....	72
Table 3-2 Typical Terms in Reynold's Equation.....	74
Table 6-1 Turbine end PGB sub-synchronous (half frequency) whirl onset speed.....	129
Table 6-2 Turbine end FFB sub-synchronous & synchronous whirl onset (varying unbalance, supply pressure and clearance).....	133
Table 6-3 Heat transfer sensitivity.....	151
Table 6-4 Material properties sensitivity study	156
Table 6-5 EHD test jobs	158
Table 6-6 EHD test job results	161
Table 6-7 Calculation List for Cavitation Damage Parameter	174
Table 7-1 Summary of Cavitation Damage Parameter Results.....	265

NOMENCLATURE

α	Damping coefficient
β	Damping coefficient
δ	Displacement
ϕ	Flow factor, conrod angle
λ	Oil film ratio
μ	Coefficient of friction
η	Absolute viscosity
θ	Fill ratio, crankshaft angle
ρ	Density
σ	RMS surface roughness
τ	Shear stress
ω	Rotational velocity
$\delta x, \delta y, \delta z$	Incremental positions in space
a	Acceleration
h	Film thickness as a function of x and y
i, j	Mesh position numbers in x and y direction
k	Constant of integration

p	Pressure as a function of x and y
t	Time
x,y,z	Positions in space
D	Damping coefficient
F	Force
L	Conrod length
M	Mass
OR	Offset between centre of action of cylinder gas pressure and the bore centre line
OP	Offset between piston centre of gravity and the bore centre line
OG	Offset between piston pin centre line and bore centre line
OC	Offset between crankshaft centre line and bore centre line
OGC	Offset between piston pin centre line and crankshaft centre line
R	Residual, radius, crankshaft radius
U, V, W	Velocities in x,y,z directions

ABBREVIATIONS

HD	HydroDynamic
RHD	Rigid HydroDynamic
EHD	ElastoHydroDynamic
TEHD	ThermoElastoHydroDynamic
FEM	Finite Element Method
FDM	Finite Difference Method
BEM	Boundary Element Method
TMM	Transfer Matrix Method
TDC	Top Dead Centre
TDCF	Top Dead Centre Firing
TDCNF	Top Dead Centre Non Firing
BDC	Bottom Dead Centre
PDM	Product Data Management
PLM	Product Lifecycle Management
CAD	Computer Aided Design
CAM	Computer Aided Manufacturing
CAE	Computer Aided Engineering
OEM	Original Equipment Manufacturer

CHAPTER 1

INTRODUCTION

1.1 HISTORICAL BACKGROUND

Various types of tribological interface have been known from ancient times where ever one part of a machine had to move relative to another while transmitting forces. Examples include the wheel, slider-crank mechanisms and gears. Although many devices can be operated without lubrication, it was soon discovered that applying lubricants such as greases or oil to the sliding surfaces reduces temperatures and wear, allowing operation for longer and/or at higher load and speed. Dowson (1998) gives a good overview of the history of tribology from the earliest times.

Many tribological contacts can be classified into lubricated or non-lubricated, conforming or non-conforming and also according to specific loading and sliding velocity. Lubricants can be liquid, greasy or solid. They can be applied to the contact continuously, occasionally or even just at the beginning of the machine's life. Fluids such as oil or even water can be supplied continuously from a reservoir or circulated by a pumped system. Easily sheared solids produced by wear processes can also be used as a lubricant. Non-conforming contacts are those where the contact area, in the absence of lubricant, would be relatively small, effectively a point or a line. Examples of non-conforming contact include cam to tappet, gear pairs and wheels on a hard surface. Conforming contacts are those where the shapes of the two components match each other approximately. In the absence of lubricant, the contact patch would be large. Examples include axle to wheel and the many bushes and plain journal bearings to be found in various machines. Different types of tribological contact are shown in Fig. 1.1. We can reduce the number of analysis variables by carrying out the calculation relative to the position of the contact point. This enables tribological calculations to be carried out in terms of:

- Local radii of curvature. The specific load and composite curvature $\frac{1}{R_1} + \frac{1}{R_2}$ determine whether the contact can be regarded as conforming or non-conforming. Large composite curvature implies non-conforming. Small curvature, often with one of the radii negative, implies a conforming contact.
- Material, surface and lubricant properties.
- Entrainment velocity = $(V_1+V_2)/2$ where V_1 and V_2 are the velocities of the contact point on the two interacting surfaces. A high entrainment velocity produces thick lubricant film to support the load and low viscous loss. A simple rolling contact has high entrainment velocity and zero sliding velocity.
- Sliding velocity = V_1-V_2 . A high sliding velocity produces high viscous loss. Combined with low or zero entrainment velocity it can produce high temperatures and wear rates.

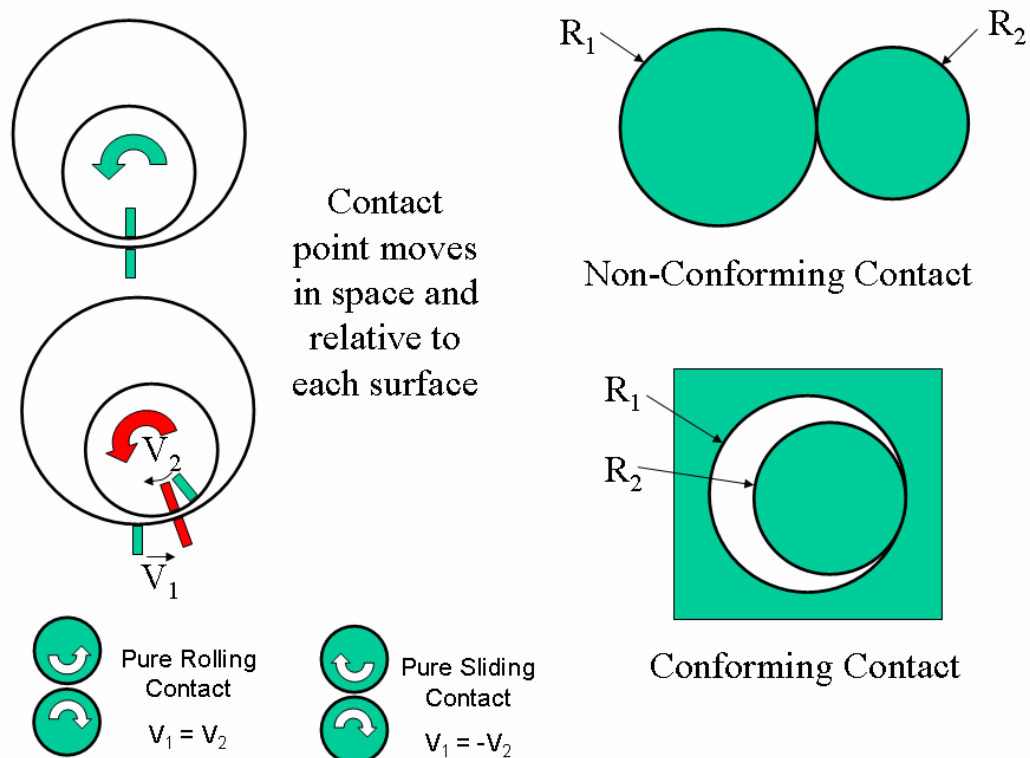


Figure 1-1 Types of Tribological Contact

The significance of specific loading and sliding velocity is that the product of these two (often known as the PV product) has the same dimensions as power. Indeed, the power dissipated in the contact is equal to the coefficient of friction multiplied by the PV product. In addition the combination of specific load and sliding velocity will cause a lubricated contact to behave in one of three regimes of lubrication, boundary, mixed or full lubrication. The general form of variation of coefficient of friction with the operating regime is shown in Fig. 1.2. This is the well known curve due to Stribeck (1902).

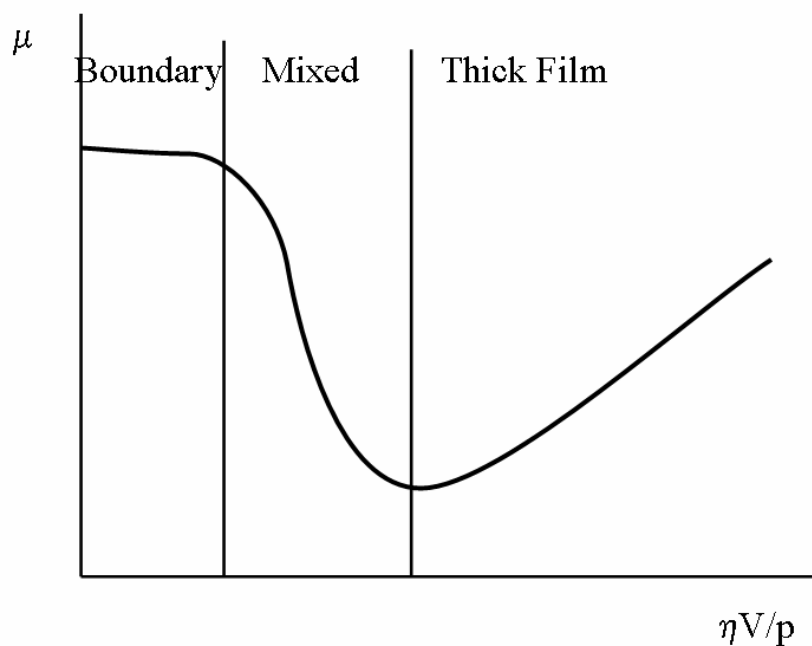


Figure 1-2 Lubrication Regimes

Increasing the fluid viscosity, entrainment velocity or reducing the specific load (average pressure) represented by the x axis increases the fluid film thickness. When the fluid film thickness is sufficiently high that it carries the entire operating load and there is no contact between the opposing asperities of the two surfaces the regime is known as thick film, full fluid or hydrodynamic lubrication. Wear rates and friction are low.

Reducing the fluid film thickness to a value comparable to the surface roughness of the opposing surfaces causes the asperities to contact and the load to be shared between the contact and the fluid film. This is known as mixed lubrication. The ratio of minimum fluid film thickness to composite surface roughness is known as the film ratio and represented by the symbol λ . At low values of film ratio, the load is carried predominantly by the asperities. This is known as boundary lubrication; the friction coefficient is high, approximately constant and determined by the properties of the two surfaces and any friction modifying additives in the lubricant. Wear rates are likely to be high in boundary lubrication.

Rolling element bearings appear at first sight to be a pure rolling non-conforming contact. Initially, they would appear to be relatively easy to understand through Hertzian contact analysis without the need for lubrication and should produce low friction losses. In reality, clearances, loads and inertia do cause significant sliding to take place but that is not the subject of this project.

Journal bearings appear to be more difficult to understand as there is no attempt to reduce the sliding motion between the two surfaces. Therefore it is necessary to understand the fluid flow of the lubricant between the interacting surfaces in the case of lubricated contact or the interaction between the surface asperities in the case of unlubricated contact. Journal bearings are the subject of this project. It was not until the late 19th and early 20th centuries that Tower (1883 and 1885), Reynolds (1886) and Sommerfeld (1904) provided understanding of the formation of pressure in a lubricant film in journal bearings. The pressure in the lubricant film increases due to a wedge action in the converging part of the oil film. In the diverging part of the space, the film ruptures and has close to zero pressure. Thus, the load carrying ability of a journal bearing is related to the eccentricity of the shaft within the bearing and the viscosity of the lubricant. This is illustrated in Fig. 1.3. Further detail of the work of Towers and Reynolds is described in Chapter Two.

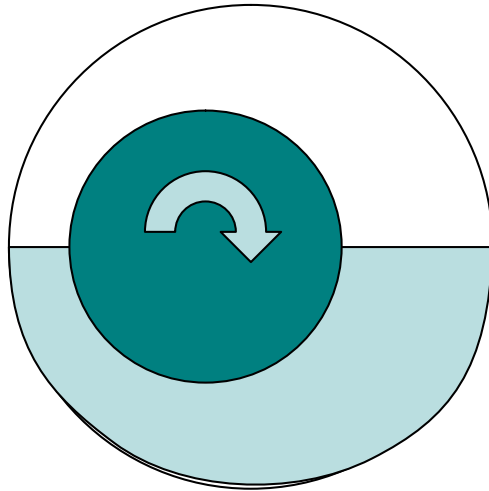


Figure 1-3 Operation of a Journal Bearing

Reynolds developed his famous Reynolds Equation to describe the pressure gradients in any shape of lubricant film in terms of the shape and the relative velocities of the bounding surfaces. More details of the derivation and solution of Reynolds Equation are given in Chapter Three.

Reynold's Equation shown in equation 1.1 has been taken from Halling (1989) and is a slightly simplified version for incompressible flow and constant fluid properties.

$$\frac{\partial}{\partial x} \left(h^3 \frac{\partial p}{\partial x} \right) + \frac{\partial}{\partial y} \left(h^3 \frac{\partial p}{\partial y} \right) = 6\eta(U_1 + U_2) \frac{\partial h}{\partial x} + 12\eta(V_2 - V_1) \quad 1-1$$

where:

- p Pressure as a function of x and y
- h Film thickness as a function of x and y
- x Dimension in direction of sliding
- y Dimension perpendicular to direction of sliding
- η Absolute viscosity

U_1 Velocity in x direction of lower surface

U_2 Velocity in x direction of upper surface

V_1 Velocity in z direction of lower surface

V_2 Velocity in z direction of upper surface

It can be seen that the equation is a partial differential equation and it is not easy to obtain pressures directly for an arbitrary film shape. Before the availability of powerful digital computers in the second half of the twentieth century it was found that it was possible to obtain solutions for particular approximations to real bearings.

Approximate solutions such as the Short Bearing Approximation (SBA) in which the bearing axial length is assumed to be small relative to the other dimensions were found to be useful, especially for steadily loaded bearings. The derivation of bearing stiffness and damping coefficients was also straight forward enabling the bearing stiffness to be built into the dynamic analysis of rotordynamic systems.

As computers started to become available, it became more practicable to solve Reynold's Equation numerically and provide solutions for many different shapes of bearing. Because of the limitations of computer power, these were generally still limited to steadily loaded bearings. By mapping the effect of velocity of the shaft across the clearance space at a large number of shaft eccentricities J. Booker developed the mobility method. This enabled shaft orbit calculations to be calculated relatively quickly for dynamically loaded bearings and this method continues to be used in the analysis of internal combustion engine bearings.

More powerful computers enabled a number of issues to be investigated by researchers seeking to understand discrepancies between predictions and real bearing behaviour. Jacobsen, Floberg and Olsson at Chalmers University investigated the conditions at film rupture on the trailing edge of the oil film. Methods such as the Short Bearing

Approximation assume that negative pressure cannot be carried by the oil film and therefore solves Reynold's Equation for the whole film but discards the negative pressure calculated in the diverging part of the film. More advanced methods track the oil fill ratio in the cavitated film back to the point of reformation, a method known as oil film history. These points are shown in Fig. 1.4 and analysed in mathematical detail in Chapter Three.

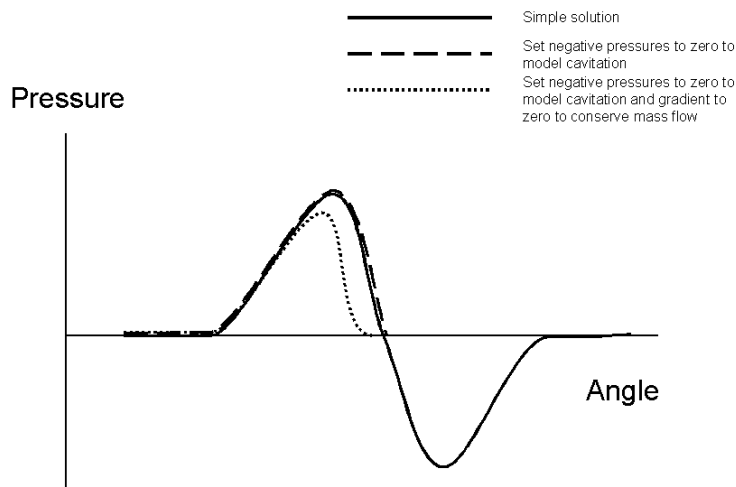


Figure 1-4 Reynold's Equation Boundary Conditions

Heavily loaded bearings were often found to produce calculated oil film thicknesses less than the surface roughness of the surfaces despite working satisfactorily in practice. This led to an interest in the load sharing between the asperities and the oil film as well as the effect of the asperities on the oil flow pattern. Structural deformation of the bearing and housing was easily shown to be significant compared to the bearing clearances at high loads. Conforming contacts are capable of giving a wrap-around effect as the bearing conforms to the shape of the shaft. The changed oil film shape to give a larger contact area leading to lower pressures and higher film thicknesses than were being calculated by methods that assumed rigid shaft and bearing. Coupling the

solution of Reynold's Equation to the solution of structural deformation is known as ElastoHydroDynamics (EHD). This is illustrated in Fig. 1.5.

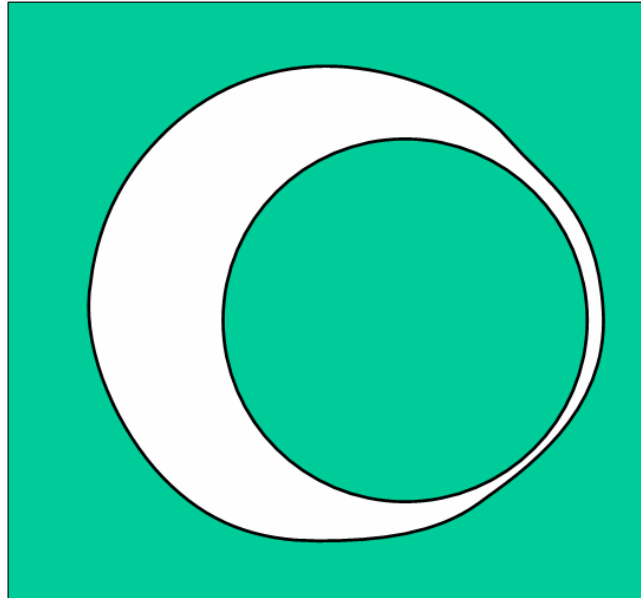


Figure 1-5 Elasto-Hydro-Dynamic Lubrication

The high oil film pressures are sufficient to deform the shape of the housing, leading to greater conformability and lower oil film pressure than a rigid housing.

Adding heat flow solutions and thermal deformation of the bearing is recognised as important for thrust bearings but has not been studied widely for journal bearings. This is despite the fact that it is easily shown to be a significant effect on the shape of the oil film.

The small end bearings of reciprocating internal combustion engines are subjected to high accelerations (up to approximately $8 \times 10^4 \text{ ms}^{-2}$ in Formula 1 racing engines). The two oil films on either side of the floating ring in Fully Floating Bearings are connected by oil holes that are also subject to high centrifugal accelerations. Commercially available bearing simulation programs are seldom used for these two applications.

Mesh based stress analysis by finite elements or boundary elements is well established for verifying the design integrity of engineering components. Elasto-hydrodynamic behaviour of bearings lead to a need to couple the finite difference solution of Reynold's Equation for the lubricant film to the finite element or boundary element calculated stiffness of the bearing structure. The extraction of reduced stiffness matrices from finite element models can be useful in achieving this coupling and is often available in commercial finite element packages such as ABAQUS or Nastran. It is not yet generally available from commercial boundary element programs. See Barrett (2001) for an initial study into the possibility of using the Boundary Element Method to generate reduced stiffness matrices.

Journal bearing manufacturing companies usually provide a comprehensive design and design analysis service to support their customers. They use several methods according to the industry, customer and stage in the design process. The simpler techniques are used at the concept design stage when little input data is available. The more complex methods require a larger amount of data which may require close interaction with the customer. Incorporating the more sophisticated techniques into the design process is often difficult for the end customer because of the time required to gather input data, create computer models and run them.

In the case of high speed rotating machinery rotordynamic calculations are often carried out using stiffness and damping coefficients to represent the bearings and the Transfer Matrix Method (TMM) to represent the shaft bending stiffness.

1.2 BUSINESS ASPECTS

Programs that solve Reynold's Equation have been written in engineering company R&D departments, consultancies and Universities for several decades now. Typical programs include the mass conservation effects researched by Jacobsen, Floberg and Olsson, flow modification due to the asperities and EHD effects. The source code for these programs is not generally available; the programs are available in executable form only. Generally the program executable is packaged with a Graphical User Interface and

available for a yearly rental charge that includes manuals, training and support. Companies offering such programs include Ricardo, AVL and Gamma Technologies.

Some of the manufacturers of large diesel engines have their own bearing analysis codes. Such large engines are very expensive to alter once they have been developed, so these manufacturers were the first to recognise the importance of getting their designs right at an early stage in the development process.

Many of the bearing manufacturing companies also have their own bearing analysis codes. The programs have often been developed in partnership with universities. They are used to provide development support to their customers during the machine development process, bearing selection (by size and material) and troubleshooting.

The role of simulations in mechanical engineering has increased steadily in recent decades. It is recognised that errors can be fixed much more cheaply at the design stage than once a product is in the market. This is illustrated in Fig. 1.6.

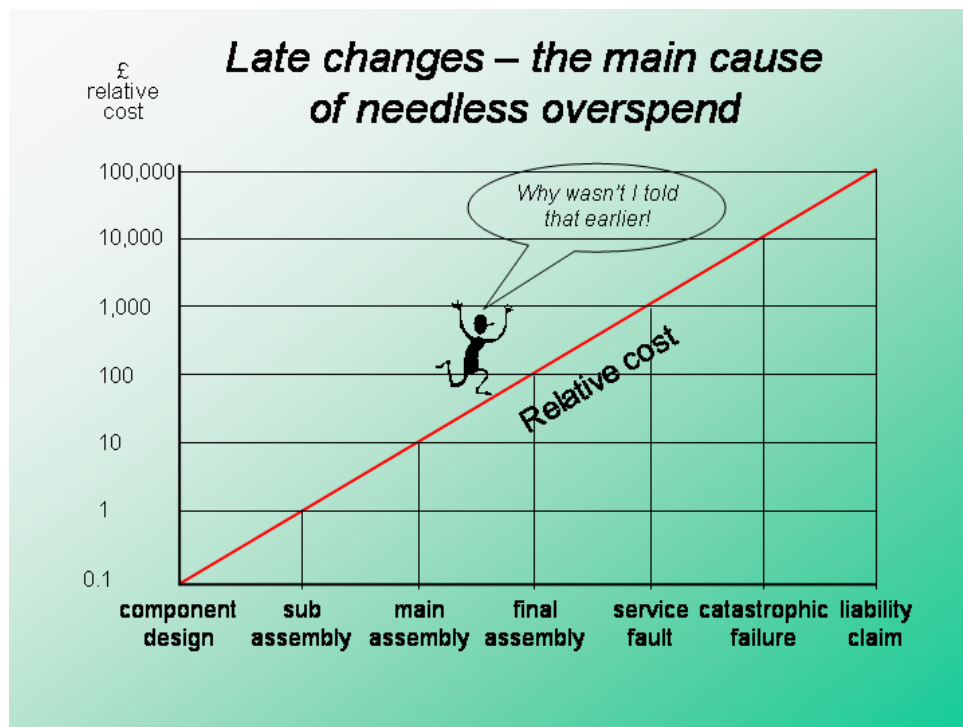


Figure 1-6 Effect of Late Changes (Source Colin Mynott, 2005)

There is a great deal of attention paid to Product Data Management (PDM) and other capabilities within Computer Aided Design (CAD) systems at present. The 2005 ASME/IDETC conference was attended by the author and included complete sessions on Design Theory and Methodology. Many of the papers appeared to examine individual cases without showing how these relate to the wider world or could be applied in the general case.

AIES Ltd. has general anecdotal evidence of dissatisfaction of management with current CAE procedures in companies. There is a desire to change the way things are being done because the current CAD/CAE vendors appear to have simply replaced one set of inefficient methods with another set that simply relies on even greater man power and computer power! Finding references that state the problem has proved rather more difficult. However, the author attended three keynote speeches by senior speakers at the ASME/IDETC conference in September 2005. All three speakers talked about these problems with different emphasis from their individual backgrounds. Unfortunately the keynote speeches were not included in the conference proceedings, so cannot be referenced directly. Therefore a summary of the most relevant speech is given here.

Dennis Nagy of CD-Adapco gave a one hour keynote speech at the ASME/IDETC conference (Nagy, 2005). This section is taken from hand written notes taken by the author during keynote speeches at the ASME/IDETC conference. His reference to hero mountain and payback meadow refers to the role of PhD level gurus on policy in the central R&D units of large Original Equipment Manufacturers. The Original Equipment Manufacturers (OEMs) are the large organisations at the end of the supply chain that supply the end product to consumers. They often have much more resources and understanding of their product than their suppliers. They specify software and methods for their high end 'heroic' CAE calculations. They also act as gatekeepers for these methods. This causes problems between the CAE engineers and the design engineers whose aim is to get the job done to the standard required for confidence in the suitability of their designs – that's use of CAE in 'payback meadow'. 1st tier suppliers often end up with the high end CAE systems under influence of the OEMs and the gurus although these may not be appropriate and they don't have their own gurus available to use them properly. Next tiers often just give up on CAE but there's a tier at

the ‘bottom’ of the chain that consists of small specialist consultancies that are competent in this technology.

Fig. 1.7 was used to illustrate what needs to happen to achieve the gains that are possible through correct use of CAE. Those engineers who use only the most basic methods must make the transition to using more effective methods without having to become specialists working at great detail.

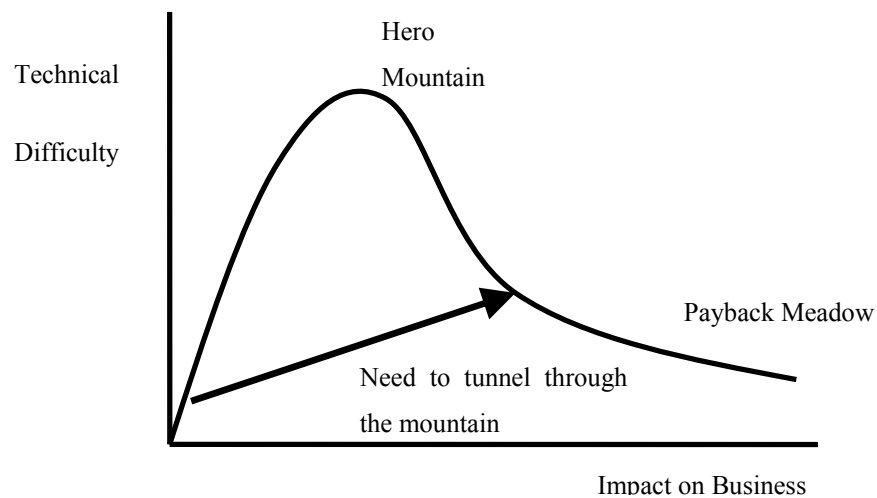


Figure 1-7 Hero Mountain – Payback Meadow (Source Dennis Nagy, 2005)

Another way of expressing the message of Fig. 1.7 was shown in Table 1.1:

Table 1-1 Direct Cost versus Product Cost

People/inputs	Direct Cost	Influence on product cost
Design	Low	High
Overhead	Low	High
Material	High	Low
Labour	High	Low

It has been stated that there needs to be a focus on change – tools and technologies to produce solutions which also implies that there will be problems and obstacles to overcome.

Simulation tends to lag behind design and innovation and be reactive. There is a need for a paradigm shift for it to become creative and proactive. The prize for achieving this will be that design engineers can develop products such as bearings and products that contain bearings with greater confidence that they will be correct at the design stage. The only way for simulation products to be part of such a shift is for them to be usable, accurate, fast and provide relevant results that can be interpreted by designers.

1.3 CALCULATION METHODS

1.3.1 THE FINITE DIFFERENCE METHOD

This section is based on Barrett (2001).

Specific pressure loading of bearings provides a simple method of assessing suitability of bearing dimensions for a particular load. It requires calculation of the loads in the system followed by division by the projected area of the bearing. The method is highly suitable for use at the initial design stage.

More advanced methods calculate the oil film thickness and pressure distribution within the oil film. Analytical solutions of Reynold's Equation have been published since the beginning of the 20th century. It is possible to use some of these techniques by hand but the advent of the digital computer made their use practicable.

The analytical solutions can only be obtained for relatively simple situations. It is a characteristic of differential equations that those that can be solved analytically can only be solved for simple bearing shapes and boundary conditions. Numerical techniques enable arbitrary bearing shapes and boundary conditions to be used but were cumbersome to use until digital computers became available. Using the pressure distribution from an analytical solution of Reynold's Equation to load a finite element model shows that engine bearing distortions are a similar magnitude to the clearances

that define the oil film shape. In cases of relatively large elastic deformations the analytical solutions are inaccurate because the shape of the oil film is no longer the same as that given by the undistorted shape of the shaft and bearing. Anecdotal evidence from bearing companies is that the stiffness of the surrounding structure can have a large influence on the performance of a bearing. Indeed, specified limits on specific loading allowed for the same bearing material in different types of application indicate that more sophisticated calculations are required for confidence in their accuracy.

Internal combustion engine companies have appreciated the limitations of analytical methods and adopted numerical solutions of Reynold's Equation. The bearings in these applications are heavily loaded and the loads vary with time. The finite difference method is one of the most popular methods for solving the fluid film equations. The oil film thickness is very much smaller than the other bearing dimensions. Therefore it is made an attribute at each nodal position in the mesh. The mesh must be orthogonal and aligned with the calculation axes. The system of equations at the mesh points is solved using a successive over relaxation technique to reduce calculation residuals to an acceptable value. This method is suitable for the nearly diagonal matrix involved. Some authors have used finite element techniques. The general nature of numerical solutions makes them suitable for non-circular bearing profiles produced deliberately or accidentally. This also means that they can be used for bearings that are deformed by the pressures that are produced in the oil film i.e. ElastoHydroDynamics (EHD). This requires an iterative solution because the oil film solution produces pressures that influence the bearing. The bearing stiffness then causes the oil film shape to change and that alters the pressure distribution.

Finite difference methods are simple to implement because they use nodes that lie in lines of constant x or y . The differential expressions of the problem can be re-written as a difference table using $\delta x_{i-1/2} = x_i - x_{i-1}$, $\delta_2 x_i = \delta x_{i+1/2} - \delta x_{i-1/2}$ etc. In the case of journal bearings the mesh is cylindrical in form and the local x , y co-ordinates are the cylindrical polar circumferential and axial co-ordinates in real space. The mesh has no dimension in the direction of film thickness because film thickness is an attribute at

each node. See Fig. 1-8. Chapter 3 includes a complete explanation of the finite difference method.

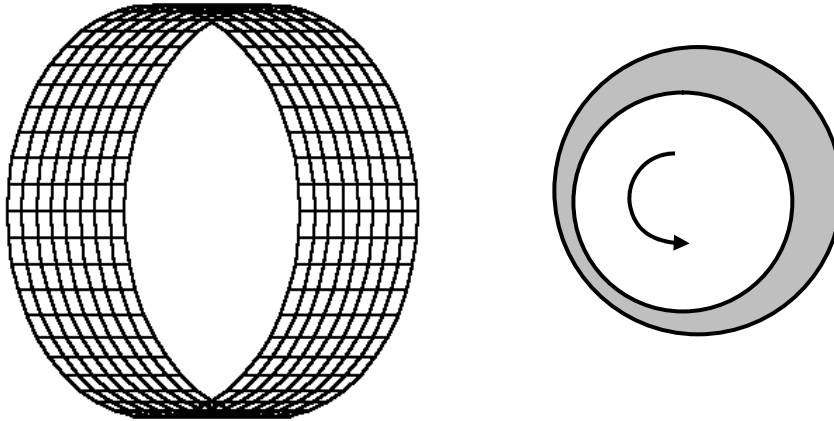


Figure 1-8 Finite Difference Mesh

Solution of Reynold's Equation on a Finite Difference mesh is started by assuming an initial pressure distribution, differentiating it using the difference table and calculating the residual at each node in terms of the adjacent nodes. The values are adjusted iteratively around the mesh until some convergence condition for the residuals is met.

The advantages and disadvantages of the finite difference method are summarised in Table 1.2.

Table 1-2 Advantages and Disadvantages Finite Difference Method (Based on table from Barrett - 2001)

Advantages	Disadvantages
<ul style="list-style-type: none"> • Simple to implement • Easy to mesh for simple geometries • Popular method for hydro-dynamic calculations with many references available • In-house, university and commercial codes available 	<ul style="list-style-type: none"> • More difficult to mesh for complex geometries - orthogonal mesh can't follow geometry exactly • Difficult to apply boundary conditions at inclined edges • Needs fine mesh for accuracy

1.3.2 THE FINITE ELEMENT METHOD

This section is based on Barrett (2001).

The finite element method is the most popular method world-wide for solving thermal and structural equations on complex shaped parts. The main reason for the popularity is its versatility. The use of piecewise discretisation of the solution domain and the mapping of elements from cartesian space into an intrinsic element space mean that highly complex problems can be solved with relatively simple mathematics. General purpose programs are available commercially. The overall procedure can be summarised:

- Discretise the problem domain
- Element stiffness matrices calculated using shape functions and transformation from orthogonal element space to cartesian space
- Overall problem stiffness matrix assembled from element stiffness matrices
- Solution obtained after applying boundary conditions

The method is very popular and its advantages and disadvantages can be listed as:

Table 1-3 Advantages and Disadvantages Finite Element Method

Advantages	Disadvantages
<ul style="list-style-type: none"> • Very versatile • Can deal with complex geometries • Can deal with complex boundary conditions • Can deal with non-linearities if required 	<ul style="list-style-type: none"> • Difficult to mesh for complex 3D geometries <ul style="list-style-type: none"> • Serious because of person-time vs. CPU time issue • Can be relatively inaccurate <ul style="list-style-type: none"> • Skill required • Checking of results

1.3.3 THE TRANSFER MATRIX METHOD

The transfer matrix method is used in rotor dynamics calculations. It combines different physical quantities in the same arrays. Column arrays are used to represent data at the points and multi-column arrays the connections between the points. It is possible to calculate natural frequencies and/or forced response behaviour of beam structures. The matrices representing the problem can be multiplied through re-using the matrices as the calculation progresses. This is efficient computationally due to the lack of simultaneous equation solution required in FEM and in terms of computer memory due to re-use of the same matrices during the calculation.

The Transfer Matrix Method has been overlooked in recent times due to the ready availability of computers. However, it is still used for rotating machinery calculations. Its relevance can be understood by reference to the business issues in Chapters 1 and 8.

It is a method that does not rely on detailed definition of the geometry and is therefore easily used at the concept phase of product development.

AIES Ltd. regard the Transfer Matrix Method as a useful tool to include in its bearing calculation capability.

The advantages and disadvantages can be summarised as:

Table 1-4 Advantages/disadvantages - Transfer Matrix Method

Advantages	Disadvantages
<ul style="list-style-type: none"> • No meshes required • Computationally efficient – suitable for use with a calculator • Clear what the analyst has done! 	<ul style="list-style-type: none"> • Not well known outside rotordynamics • Not easy to automatically abstract geometry from a CAD model

The approach of AIES to integrating geometry and mesh also allows them to assign other engineering attributes to the geometry. This can include transfer matrix attributes. Therefore, the Transfer Matrix Method is important for AIES’s bearing analysis techniques. There will also be advantages in combining it with the Finite Element Method, for example, where excitation into the shaft system comes from more complex shaped components such as blades.

1.4 COUPLING CALCULATION METHODS

Rigid HydroDynamic (RHD) calculations only require basic bearing geometry data, load and oil properties to provide the solution of the oil film pressures. ElastoHydroDynamic (EHD) calculations are useful for heavily loaded bearings as explained in section 1.3.1. EHD calculations require the hydrodynamic calculation to be coupled to the structural calculation, which requires much more data, in particular the distributed stiffness of the structure. A typical EHD coupled procedure is shown in Fig. 1.9, in this case using the ABAQUS finite element program for the structural solution and AVL Excite program for the hydrodynamic solution and coupling.

Bearing EHD analysis at Federal-Mogul.

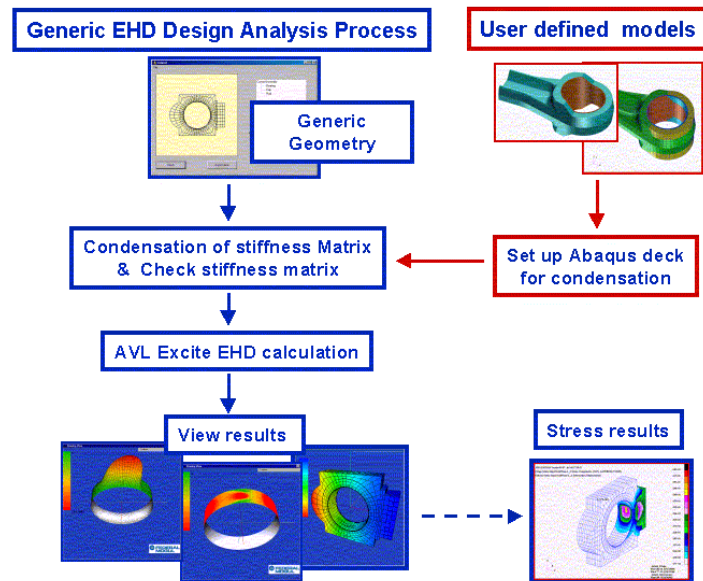


Figure 1-9 EHD Procedure at Federal-Mogul (from McLuckie, Ma and Butler, 2000)

In this case the finite element mesh of the bearing and surrounding structure is produced using a commercially available meshing program. The speed of mesh generation tends to be a bottleneck in the process and can be increased by using mesh templates. The finite element program data deck includes instructions for the ABAQUS finite element program to calculate reduced stiffness and mass matrices at the bearing surface. The reduced matrices are written to a file.

For the example shown of connecting rod bearings calculation of the forces in the con-rod is carried out over the engine cycle within AVL Excite. Bearing dimensions and oil properties are supplied as data to the program.

The economies of producing this sort of analysis code mean that many companies choose to use commercially available programs such as AVL Excite

The finite difference solution of Reynold's Equation produces output as pressures at nodes. Nodal forces are calculated using the areas of the element faces. The finite element mesh must match the finite difference mesh at the join.

1.5 FORCES ON BEARINGS

This study concentrated on the forces acting on the bearings of reciprocating internal combustion engines and of rotating machinery such as turbochargers.

Fig. 1.10 shows the layout of a single cylinder from a reciprocating internal combustion engine. The pistons and piston rings can also be regarded as bearings but with an axial rather than rotational motion. They are amenable to similar analysis to the rotating bearings at the two ends of the connecting rod and the crankshaft main bearings.

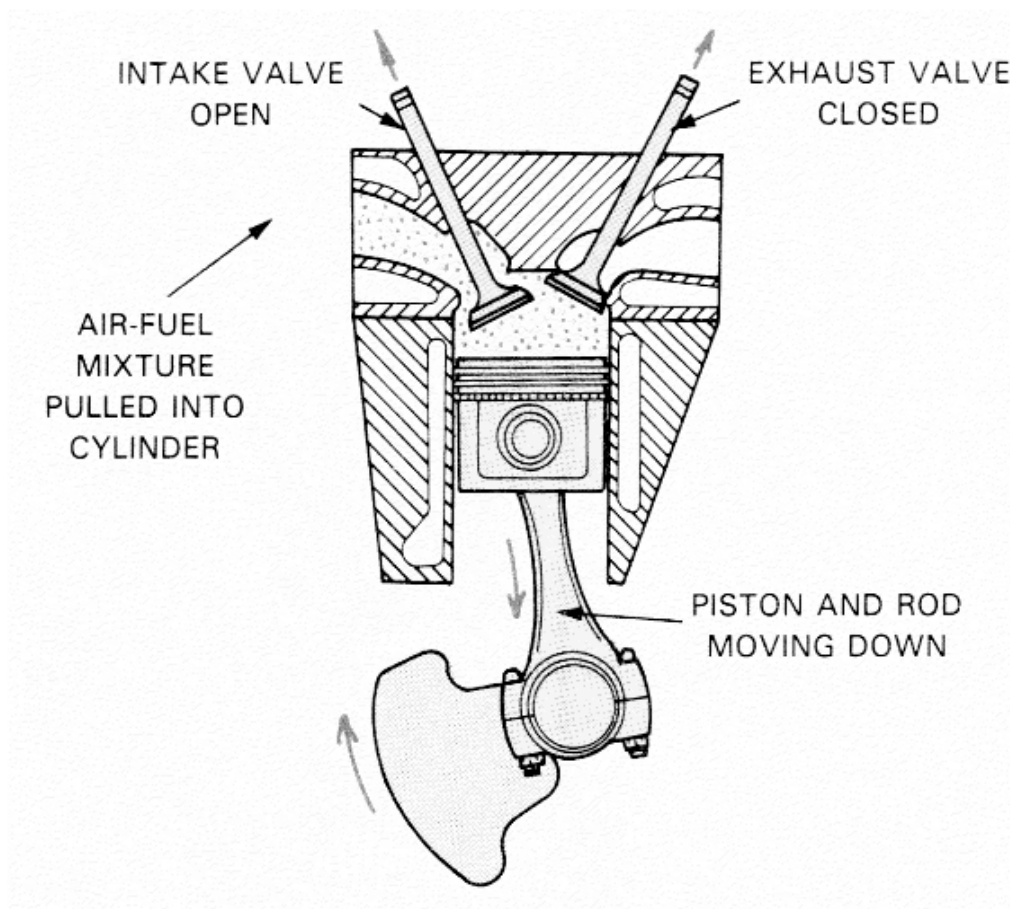


Figure 1-10 Connecting Rod (from Duffy,1994)

Due to the slow rotational speed of such engines relative to the natural frequencies of the components, analysis of the bearing loads is generally carried out quasi-statically. Resolving forces in orthogonal directions enables the forces on the bearings to be calculated. This is shown in Barrett (2001) and Chapter 3.

The forces from the individual connecting rods can then be resolved on the engine crankshaft to produce the loads on the engine main bearings. Various methods can be used to distribute the loads between the main bearings. The most sophisticated method is to couple the bearing solutions with the structural solution for the crankshaft. If it is wished to calculate the forces separately from the bearing solution some approximation must be accepted. The current program used at AIES Ltd. And developed by the author assumes no transfer of bending moments through the shaft at each bearing location. This reduces the problem to a statically determinate one and the loads are calculated by moments. More sophisticated methods include the moment-area method and Clapeyron's Theorem. These methods will be incorporated into AIES's shaft loading program in the future.

Rotating machinery such as turbochargers and electrical generators might appear to be much simpler to analyse because the gravitational load acting on the bearings is easy to calculate by taking moments. However such devices rotate at high speeds, often near or sometimes even above the first natural frequency in bending of the shaft system. The out of balance forces are usually significant relative to the gravitational load. The rigid body motion of the shaft system on the bearings may also have natural frequencies within the operating range due to the finite stiffness of the bearings.

The current turbocharger bearing force program at AIES Ltd. assumes a rigid shaft supported on two bearings. Loads applied to the shaft are resolved horizontally and vertically. Moments are taken to calculate the bearing reactions. The loads are also sorted into order along the length to calculate shear forces and bending moments acting on the shaft.

The loads that can be applied at present are gravity loading, out of balance centrifugal loading at user specified locations and harmonic loading to represent aerodynamic loads, also at user specified locations.

1.6 OBJECTIVES

The objectives of the project were

- Implement a general finite difference bearing solver
 - a. Capable of forming the basis for multi-bearing, fully floating bearing, piston, piston ring and tappet solvers
 - b. Including the features of current commercially available solvers such as mass conservation, asperity contact and EHD
- Incorporate physical effects that have not been included in bearing analysis programs by other researchers
 - a. TEHD effects
 - b. Add the effect of body forces on the oil film
- Place the program into the business context
 - a. Integrate the software into a commercially available design program
 - b. Assess the program in the business context of both the sponsoring company and its customers
 - c. Propose the direction of future work within the business context

1.7 LAYOUT OF THESIS

The thesis layout is split into separate chapters covering the major topics.

- Chapter One is a simple introduction to the project with little technical detail.
- Chapter Two is the literature survey. Many references were found relating to EHD, asperity contact, mass conservation and cavitation. There was nothing on oil film body forces in journal bearings.

- Chapter Three describes the analysis methods in detail
- Chapter Four describes the implementation of the algorithms
- Chapter Five shows the calculation studies. These start with initial studies carried out with early versions of the program, including verification against classical solutions. The studies then go on to the final parametric studies showing the effects of body forces
- Chapter Six shows the results of the calculations
- Chapter Seven discusses the results
- Chapter Eight places the study into the business context
- Chapter Nine is the Conclusion
- References and Appendices are provided at the end

CHAPTER 2

LITERATURE REVIEW

A literature review was started early in the project. Many references were found to be very focussed on applications engineering using commercially available bearing codes. These are interesting as they often show the effect of design changes and, in a few cases, are accompanied by measurements. In most cases, these sorts of papers include basic theory only and it may be difficult to know the exact theoretical basis for the calculations. These references are discussed early in the literature review. The review then moves on to the theoretical basis of bearing codes. Papers that deal with pistons, thrust bearings and other tribological devices are included where there is information that is relevant to journal bearings.

In general, thin oil films are analysed using Finite Difference (FD) solutions of Reynolds Equation. The FD solutions use a 2D mesh with oil film thickness as a property at each node point. This is possible because the oil film thickness is much smaller than the other dimensions of the bearing.

The commercial availability of Computational Fluid Dynamics (CFD) programs offering Finite Volume (FV) solution of the Navier Stokes equations is well known. These programs are now used in many engineering companies on a routine basis. Currently, these programs can only be used in 2D or 3D. For a CFD calculation of a bearing fluid film with calculation points through the film thickness it would be necessary to carry out calculations in 3D. The thin films, typically 1 to 50 μm , combined with aspect ratio requirements for the Finite Volume mesh cause excessive number of nodes for CFD calculation. The increasing power of computers according to Moore's Law may make CFD solutions important in the future, so this subject is discussed briefly in the literature survey and the thesis.

2.1 APPLICATIONS AND EXPERIMENTAL WORK

Many papers report only the use of software and/or measurement techniques to investigate tribological issues in pistons or journal bearings. In those papers that consider software it is effectively regarded as an experimental tool perhaps with a summary of the underlying principles. They are reported here because they contain important information about the context for using hydrodynamic calculations. They also show which calculation features are important.

Measurements and solution of Reynolds Equation for plain journal bearings has been a regular topic in the engineering journals for many years. Tower (1883 and 1885) performed experiments measuring the pressure generated in a bearing under load. His discovery that the pressure varied by location and the peak pressure was considerably higher than the mean pressure, calculated from the load and projected area, was the starting point for the theoretical work of Reynolds (1886), Sommerfeld (1904) and other workers since that time.

Since those early days, papers about bearing calculations are often clearly split between theoretical works dealing with solution of Reynold's Equation, adding new features etc. and papers that often feature some theory but concentrate on applications studies. Typical applications work including measurements from the automotive bearings industry is shown by Conway-Jones, Jones and Kendrick (1983).

Ramos, Jimenez and Martinez, (1999) is typical of application papers presented at conferences hosted by the suppliers of commercially available software, in this case Ricardo PISDYN. The authors concentrate on the use of the software in the piston development process. The use of such software enables alternative piston skirt profile designs to be evaluated prior to prototype manufacture and testing. They use the results of EHD calculations to select the best profile based on minimising the amount of asperity contact occurring in regions where the fluid film thickness is less than the composite surface roughness of the surfaces. The two profile designs were tested in engines and the wear patterns shown to correspond to the areas of asperity contact in the simulations. The lack of wear modelling and lack of measurements of oil film thickness mean that the correlation claimed in the paper is rather uncertain. Photographs of the

worn piston skirts are shown. The wear patterns are slightly different to each other but do appear to correspond approximately to the analysis results. Istenes (1999) found similar observed correlation between asperity contact pressure and wear rate. This paper also compared kinetic energy loss at movement events against perceived engine noise. Neither paper features any theory nor any measurements other than wear profiles. In both cases the effects of bore distortion were not considered nor variation of piston skirt shape from position to position in the engine. That could be responsible for the variations in wear patterns measured on individual pistons. In both papers, the effects of temperature distribution on piston shape and skirt stiffness were taken into account for an EHD calculation. Ricardo's PISDYN program outputs asperity contact pressure to aid wear rate ranking. There would appear to be no wear modelling itself, according to these papers.

Kageyama et al. (2000) erroneously state that there have been few examples of the theoretical calculation of piston skirt contact pressures and deformations at the date of publication. They take an experimental approach to obtaining the compliance matrix of the piston skirt and compensation of the shape due to cylinder pressure and temperature distribution. Verification of rig measurements was obtained by gap transducers and thermocouples in the piston of a running engine. The authors correlate piston side force with strain gauge measurements and then use gap transducers and strain gauges in the running engine to calculate the piston skirt deformations and pressure distribution.

Aoyama, Suzuki, Atsushi, Takashi, Ozasa, Kato and Ito (2005) investigated the occurrence of high frequency noise in a diesel engine at particular speed and load. They observed that the noisy engine also had cavitation damage on the main bearing from which the noise appeared to emanate. They used an ElastoHydroDynamic (EHD) program and measurements to confirm that the noise was associated with rapid motion of the main bearing journal across the clearance space. They also proposed and tested a solution. There are no details of the EHD calculation method except to state that mass conserving boundary conditions are used with fill ratio calculated in the cavitated region.

The importance of this paper lies in the details of the use of the EHD calculation. They found that the noise was a short duration high frequency event at main bearing no. 7 at

the peak cylinder pressure on cylinder no. 5. The noise event was non-periodic, later associated with variations in the cylinder pressure from cycle to cycle. The investigation of the cause of cavitation damage is highly relevant to this thesis but may also indicate a shortcoming in the EHD solution used by the authors. They calculated the coupled bearing stiffness and damping coefficients from the EHD solution through the engine cycle. They then used these to calculate bearing instability by eigenvalue calculation with the equivalent mass matrix for the bearing journal. This showed that bearing instability occurred at the angle of noise generation. Thus the authors were able to show that cavitation generated noise is likely to arise when there is

- Rapid fluctuation of cylinder pressure
- Instability of the main journal
- Existence of high degree of cavitation in the bearing

producing a short duration vibration of the main journal in the radial direction and noise. Variation of parameters confirmed the findings, noise only occurring when all three conditions were met simultaneously. A test rig was built and this showed that noise arose when the collapse of the cavitation reached the edge of the bearing and thus the atmosphere. Altering the journal using holes, micro-grooves etc. failed to make a significant difference. A solution was found by applying circular grooves near the edge of the bearing, filled with oil. This prevented the cavitation collapse region reaching the edge of the bearing. The solution was confirmed by engine tests. No explanation is given for the effectiveness of the grooves other than the cavitation region not reaching the atmosphere. The implication that the noise emanates from the edge of the bearing contradicts the earlier part of the paper in which the noise is correlated with vibration of the cylinder block measured with accelerometers. It seems more likely that the prevention of the cavitation reaching the edge of the bearing makes the oil film stiffer, thus changing the natural frequency of the system at that point in the cycle.

This work may show a limitation in the EHD solution in that it was not able to predict the instability. That was done externally to the EHD program using the stiffness of the oil film. A solution that solves the equations of motion including the mass matrix for the

journal should predict instability as it happens within the engine cycle. However, the use of damping and numerical integration time step control could easily cause such short duration, high frequency events to be missed. A significant finding of this paper is also the unperiodic nature of the instability event due to cycle to cycle variation in the combustion. Most analysis of bearings in internal combustion engines is performed using a single cycle combustion pressure curve. This means that the prediction of cavitation and noise effects in bearings is not straight forward.

The following references are mainly focussed on applications or measurement work but also include sufficient theory to understand the theoretical basis of the work without much detail.

van der Tempel, Moes and Bosma (1985) use a 2 step Newton-Raphson approach to iterate to an equilibrium journal position for a rigid journal and flexible connecting rod structure. The equations of motion include the mass and acceleration terms although the masses are simply equally distributed over the active nodes. Some of the detail of the equations used may be useful to incorporate into the work of this project as good stability is claimed. The solution is for a plain stress finite element model and SBA (Short Bearing Approximation) formulation of Reynold's Equation. Comparison with and without nodal masses shows that the masses are significant. Comparison with Fantino et al. (1983) is made; he used a smaller number of cubic finite elements and ignored the mass terms. The difference in results is significant and should be a warning to all researchers!

Torii, Nakakubo and Nakada (1992) is again typical of many papers in this area. They look at the effect of elastic deformations and initial bearing shape on the behaviour of a connecting rod bearing. They find that both are significant, in particular, misalignment of the cap to the connecting rod.

Xu (1996a) gives a general over view of methods being used by different researchers in the field of EHD. Table 2.1 is taken from the paper. Lubrication theory 'Short' means that a parabolic distribution of pressure is assumed axially on the bearing. The solution technique refers to the solution for the bearing position and the solution for Reynold's Equation.

Table 2-1 Review of EHD Programs - from Xu (1996a)

Program Source	Lubrication Theory	Elastic Model	Inertial Effects	Solution Technique
Fantina, Godet & Frene (1983)	Short	2D	No	Forward Iterative, FD
Oh & Goenka (1985)	Finite	3D	No	Newton-Raphson, FE
Goenka & Oh (1986)	Short	3D	No	Newton-Raphson, FE
McIvor & Fenner (1989)	Finite	3D	No	Newton-Raphson, FE
Xu & Smith (1990)	Finite	2D	No	Newton-Raphson, FD
Van der Temple, Moes & Bosma (1985)	Short	2D	No	Newton-Raphson, FD
Aithen & McCallion (1991)	Short	2D	Yes	Newton-Raphson, FE
Kumar, Goenka & Booker (1990)	Finite	Mode shapes	No	-
Bonneau, Guines, Frene & Toplosky (1995)	Finite	3D	Yes	Newton-Raphson, FE
Krasser, Laback, Loibnegger & Pribsch (1994)	Finite	3D	No	Forward Iterative & Newton-Raphson, FD

What is clear from the table is that researchers have attempted to model EHD effects in bearings with greater fidelity as increased computer power has become available. This has led to full finite difference or finite element solutions of Reynold's Equation on the bearing face capable of including feed holes and grooves. Few programs have included inertia effects of the structure at the date of the paper (1996). The paper goes on to show the differences in results between RHD and EHD calculations. These include large differences in maximum oil film pressure and minimum oil film thickness as well as

interesting differences in their distribution on the bearing surface. The effects include double pressure peaks due to the pinching or wrap-around effect under extreme loads and edge loading due to the pressure distribution being concentrated towards the bearing centre line. These effects are related to practical problems with photographs of wear markings on bearings and confirm the importance of EHD calculations. An interesting aspect of the paper is to relate the pressure distribution on the bearing surface to the different types of cracks that appear on bearings by using the pressure distribution to load a finite element model of the bearing. Radial cracks from the bearing surface near the centre line of the bearing are associated with high normal stresses due to the film pressure. Circumferential/radial cracks originating at the bearing lining and backing interface are associated with high shear stresses near to the edge of the bearing.

Xu (1996b) is a study of the differences between the EHD calculations of bearing behaviour in an engine compared to the same bearing in a test rig. The test rig only applies load in a single direction and has a much stiffer housing than the real bearing housing. The results show that the rig is no longer suitable for assessing the bearings of modern engines that operate at high speeds and with significant elastic deformations. However, some similarity of results could be obtained by using a realistic bearing housing rather than the standard housing of the rig.

Hellinger, Raffel and Rainer (1997) give no theory whatsoever but show the use of AVL's commercially available software in the simulation of gear noise. The paper is useful in showing the relationship between finite element calculation on a structure, in this case a gearbox casing, and the calculation of the behaviour of the system.

The paper by Poynton, Xu, Wang and Warriner (1998) is typical of many papers in this subject area, describing the improvement of the design of the big end connecting rod bearing of the Mirrlees Blackstone MB430 engine. This engine supplies the small end bearing with oil from a groove in the big end bearing. The bearing had already been improved by changes to the design of the groove and the position of the journal oil feed hole, leading to reduced wear rates. Running the proprietary EHD program 'SABRE-EHL', it was possible to calculate the oil film pressures and thickness and understand why the second groove design was better.

Table 2-2 Minimum Oil Film Thickness and Maximum Oil Film Pressure (from Poynton et al., 1998)

	Initial Design	Improved Design
Min. Oil Film Thickness	3.36 μm @ 35° Bearing Angle, 260° Crank Angle	5.03 μm @ 35° Bearing Angle, 259° Crank Angle
Max. Oil Film Pressure	119 MPa @ 356° Bearing Angle, 19° Crank Angle	117 MPa @ 3.8° Bearing Angle, 13° Crank Angle

The paper gives only very basic details of the theory. An interesting feature of the program used is that it includes variation of the viscosity with pressure using the Barus viscosity-pressure relationship $\eta = \eta_0 e^{\alpha p}$ where α is the pressure-viscosity coefficient. The journal position was calculated using a Newton-Raphson technique. The deformation of the bearing surface was calculated using a reduced compliance matrix.

Okamoto, Hanahashi, Katagiri (1999) also give a little theory and concentrate on an application of the EHD program. They start with a review of trends in maximum cylinder pressures (heading towards 20 MPa) and specific loadings on connecting rod bearings (heading towards 100 MPa) of 7 to 9 litre displacement diesel engines. They examine the effect of increasing the cylinder pressure on an engine and the effect of changing the bearing axial length on maximum oil film pressure, minimum oil film thickness and average power loss. The authors find that the minimum oil film thickness is only slightly reduced by increasing the maximum cylinder pressure because, on this engine, the minimum oil film thickness occurs at a part of the cycle dominated by inertia loads. The maximum oil film pressure and average power loss increase as would be expected. The reduction of bearing length increases maximum oil film pressure and reduces minimum oil film thickness as expected. However, the reduction in power loss due to lower area only arises for a moderate change. Larger changes cause the power loss to increase due to the higher shear rate of the oil film.

Okamoto, Kitahara, Ushijima, Aoyama, Xu and Jones (2000) use EHD to study the effects of bearing wear in a bearing test rig. They show that bearing wear starts at the edges due to the concave deformation in the axial direction of the bearing under

pressure loading. In the case of relatively lightly loaded bearings, the worn shape then causes the pressure distribution to change giving a higher peak pressure in the centre of the bearing, leading to any crack initiation to start at the centre. For highly loaded bearings, the combination of higher pressure and pressure gradient near the edge causes crack initiation there before the wear process can redistribute the pressure.

Ma, McLuckie, Poynton and Garner (2001) study the effect of structure elasticity and oil pressure-viscosity effect on the oil film thickness and oil film pressure of the connecting rod big end bearing of the Mirrlees Blackstone MB430 engine. They used the commercially available EHD program 'EXCITE' which uses the reduced stiffness and mass matrices for the structural stiffness effects. They conclude that the stiffness effects are significant, in particular the prediction of minimum oil film thickness at the edge of the bearing.

Offner, Krasser, Laback and Priebisch (2001) describe the equations of motion used when applying EHD solution to the piston and liner. This case differs from a journal bearing, not only in terms of the directions of sliding, but also in having to interpolate profiles on both bodies including deformation effects. They comment on the issues of interpolating measured data for piston skirt and liner shape. They use Newmark's method for time integration. They show the effects of parameter variations on the calculations for a small single cylinder engine running at 3000 rev/min, including piston ovality, clearance and entry oil film thickness.

Yu and Sawicki (2002) compare the results of using the mobility method with a mass conserving numerical method for the Rigid HydroDynamic (RHD) analysis of a reciprocating compressor bearing. They review the theory including Elrod's method for implementing Jacobsen, Floberg and Olsson's boundary conditions using continuous variation of fluid density. They also describe the mobility method. They describe a modified Thomas method for solving the discretised Reynold's Equation and claim good solution times. This project uses the successive over relaxation method and it may be useful to compare with the method in this paper. Unsurprisingly, the authors find that the mobility method runs very much faster than their numerical method (10s vs. 30h. on a Pentium 266MHz computer!). It also significantly underestimates the eccentricity ratio.

Ma, Offner, Loibnegger, Pribsch and McLuckie (2003) start by summarising methods of bearing calculation. The rapid methods are often approximate and insufficiently accurate whereas rigorous methods can take many hours to run. The authors describe the combination of Short Bearing Approximation (SBA) and Long Bearing Approximation (LBA) from Hirani et al. (1999). Journal misalignment is modelled by approximating the bearing in two halves. EHD is modelled by applying the pressures from the combined SBA/LBA model to the structural model. The exact details are not given. The new modelling method is then compared with a full EHD model for a big end bearing, a main bearing and a coupled main bearing system for rigid and elastic housings. The accuracy of the new method is somewhat mixed, assessed for minimum oil film thickness, peak oil film pressure and orbits but is very much faster (factor 10 – 100 typically).

Brajdic-Mitidieri, Gosman, Ioannides and Spikes (2005) use an open source CFD program (FOAM) to examine the effect of pocket features on the performance of a slider pad bearing. The reason for using a CFD program implementing a solution of the full Navier-Stokes Equations is that the limitation of Reynold's Equation when dealing with situations where the fluid inertia, turbulent flow, mixed phases etc. are significant. The effect of pockets is that the fluid flow is in the film thickness direction at the pocket, which violates the assumptions in the derivation of Reynold's Equation. The effect of the pocket is to reduce the local shear stress more than the reduction of load carrying capacity. This gives a lower coefficient of friction. The effect is large at low convergence ratios which produce cavitation at the entrance to the pocket. A 2D solution was used in a code that allows large aspect ratio cells. The validity of the CFD solution was checked against a Reynold's solution for a simple slider bearing geometry at different mesh densities, many of the tests being within 1%. The dimensions of the model and the mesh densities used indicate that CFD may be a usable tool for bearing studies. The authors finish the paper with a 3D study but with no indication of number of cells or run times. Although the paper demonstrates that CFD is usable for thin hydrodynamic films, the studies were steady state rigid hydrodynamic. Time varying, elastohydrodynamic studies would require much more computer time.

Weimar (2002) uses laser measurement techniques to examine the oil film thickness as do Dhunput et al. (2007) with a particular interest in the cavitation behaviour in the divergent film.

McLuckie and Barrett (2005a) used the first RHD version of the software developed for this project to examine the effect of crankshaft layout on the loads and viscous losses in the main bearings of

Mehenny, Taylor, Jones and Xu (1997) examine the effects of imperfect shape of engine crankpins. They noted that the departure from perfect circular form of machined crankpins often exceeds the RHD calculated film thickness for a perfect crankpin and bearing. Their theoretical model was RHD with oil film history cavitation model. They found that the effect of including the imperfections was significant on oil film thickness and oil film pressure.

Liu, Zhang and Zheng (2008) used a 1D approach to the thermal modelling.

Meili, Zhiming, Xiaoyang, Wen, Kai and Sun (2008) carried out experiments using parallel plates to measure cavitation effects and correlate with a new cavitation theoretical model of Sun et al.(2008). They found significant tensile stresses could arise briefly in the fluid. The development of the cavitated region did not always agree well with the theoretical model and appeared to depend on nucleation by entrained air bubbles. The size of the bubbles appeared to be important.

Miao, Chang and Chen (2008) use CFD to examine the flow of lubricant in a bearing with herringbone grooves. Such studies show that the ability of CFD is now becoming usable for bearing studies despite the very thin films. The advantages of CFD software include the ability to handle heat generation, two phase flow etc. However, this study was carried out at fixed eccentricity ratios, probably due to slow speed of calculation?

Ozasa (2008) used an EHD model with generalised mass flow, mass conservation and pressure-viscosity effect to study the effect of surface roughness with different directional characteristics on the friction losses in a big end bearing. He found the pressure-viscosity coefficient to be important as well as the directionality of the surface roughness.

Sun and Gui (2007) study the effect of interaction of bearing oil film with the calculation of crankshaft fillet stress. They use a beam element representation to model the crankshaft stiffness and then use the oil film pressures as boundary conditions onto a 3D crankshaft FE model. The hydrodynamic solution is RHD. They find large effect of the oil film stiffness on crankshaft fillet stress.

The paper by Suzuki et al. (2008) is in Japanese so only the abstract and figures were studied. They used an EHD model and compared two methods to reduce the oil flow – reduce the oil supply pressure or change the bearing shape.

Skjoedt, Butts, Assanis and Bohac (2008) is purely an experimental study. They measure engine friction in a Ford Duratech V6 engine and look at the effect of viscosity and friction modifiers. Unsurprisingly, as engines have components that work in hydrodynamic and boundary lubrication regimes, they find significant effect on the friction. They give details of the experimental technique as accurate measurement of engine friction sufficient to reliably detect small changes is notoriously difficult.

2.2 REYNOLD'S EQUATION AND SOLUTIONS

Reynolds (1886) was the first person to develop the theory that explained the experimental measurements of Tower (1883 and 1885). The equation that he developed is named after him! He obtained exact analytical solutions for simple slider bearings and approximate analytical solution for the infinitely wide journal bearing (i.e. flow in 1-D only). Sommerfeld (1904) obtained an exact solution for infinite journal bearings. Michell (1905) solved Reynold's Equation for a finite width journal bearing generating an infinite series for the pressure at any point on the bearing.

Early solutions of Reynold's Equation were analytical. In order for the expressions to be integrated, various assumptions were made. These included parabolic pressure distribution axially (Short Bearing Approximation), infinite extent axially (Long Bearing Approximation), Sommerfeld's Boundary Condition ($p = 0$ at $\theta = 0, \pi$) etc. The solutions gave different answers and could only be used for perfectly circular bearings with no features such as holes or partial grooves. However, they were accurate enough

for many design purposes and computation was easy enough in the days before digital computers were readily available.

Christopherson (1941), Cameron and Wood (1949) and Cameron (1949) cover the mathematics for circular journal bearings. Until this time, only analytical solutions for infinite bearings had been available. The authors used the relaxation method due to Southwell (1946) to also generate pressure profiles and attitude/eccentricity ratio curves for finite bearings of different diameter to length ratios.

Lloyd and McCallion (1968) include an investigation of the effect of the over-relaxation factor on the speed of convergence. They produced an equation to calculate the optimum relaxation factor.

$$relax = 2 \times \left(\frac{1 - \sqrt{1 - \mu^2}}{\mu^2} \right) \text{ where } \mu = 1 - \frac{\frac{\pi^2}{2} \left(4 + \left(\frac{\pi D}{L} \right)^2 \right)}{m_x^2 + \left(\frac{\pi m_y D}{L} \right)^2} \quad 2-1$$

Examination of the equation for typical L/D ratios and mesh sizes and the author's experience on this project suggests that values of over-relaxation factor around 1.5 suffice for the majority of cases. The option to use Lloyd and McCallion's equation to set the over-relaxation factor has been included in the software developed for this project.

Wilcock (1974) and Reinhardt and Lund (1975) examine the occurrence of turbulent flow in journal bearings. Turbulence can most easily be dealt with by increasing the viscosity to represent its effect and the authors show the modification to Reynold's Equation that they use. The Reynold's No. for higher speed bearings can exceed the value at which turbulence is seen. This becomes even more likely where low viscosity fluids are used such as water, process fluids, liquid metals etc. The results of this work have not been incorporated into the program written for this project but it may be useful to do so in the future.

Reason and Narang (1982) discuss the problems of numerical solutions (computer time, large data input and output) and the need for higher accuracy in analytical solutions.

Many approximate analytical solutions have been produced over the years including Sommerfeld (1904), Frankel (1946), Dubois and Ocvirk (1955) and Smalley et al. (1966). The difference in maximum pressure and other parameters produced by the different solutions can be a factor greater than two. The authors develop an analytical method based on combining expressions for Short Bearing Approximation (SBA) and Long Bearing Approximation (LBA) that gives reasonable accuracy for steadily loaded journal bearings with simple analytical expressions that could be stored on a programmable calculator. The paper has not been studied in great detail here but may reward study later when finding ways to increase computing speed of the EHD calculations presented in this thesis.

Reason and Siew (1982 and 1985) studied the effect of flow of the lubricant at a porous surface on Reynold's Equation. They used the method proposed by Rouleau and Steiner (1974) to add the extra flow terms into Reynold's Equation including the slip velocity at the boundary due to the pore mouths. The method of Lloyd and McCallion (1968) was used for numerical solution for steady state bearings and they produced graphs of output parameters versus permeability of the surface.

Lin (1997) modifies Reynold's Equation to take account of the non-Newtonian behaviour of lubricants with additives or suspended particles. He finds a significant beneficial effect on the predicted performance of a squeeze film damper.

Taylor (1999) looked at the inclusion of shear thinning into the Short Bearing Approximation approximate analytical solution for journal bearings. Many Reynold's Equation researchers have included pressure-viscosity effect using Barus' Equation ($\eta = \eta_0 e^{-\alpha p}$ where α is the pressure-viscosity coefficient) into numerical solutions. The paper describes the incorporation of the Cross Equation ($\eta = \eta_\infty + \frac{\eta_0 - \eta_\infty}{1 + |\dot{\gamma}/\dot{\gamma}_c|^m}$) into the

Short Bearing Approximation. The paper shows results for three different oils at three different temperatures for an automotive connecting rod big end bearing. It concludes that the shear thinning behaviour of the oil is important to take into account for bearing studies.

McLuckie (1990) studies the instability of a shaft on gas bearings. The influence of the 'O' ring seals is significant.

Brunetiere and Tournier (2007) examine the effects of fluid inertia on the flow in hydrostatic seals. They find that the error from neglecting these terms is significant in the case of a misaligned seal.

Wang and Khonsari (2008a and b) develop classical style equations but incorporate Jakobsen-Floberg-Olson boundary conditions and use curve fitting. This gives them a rapid calculation of the oil film to use for calculation of unstable operation of a rigid shaft on two journal bearings. They study the effect of boundary condition assumption, steady state eccentricity ratio, oil feed pressure and oil feed position on the instability threshold speed.

Xia, Qiao, Zheng and Zhang (2009) also take the approach of reducing Reynold's Equation to a more manageable form in order to be able to carry out rotordynamic calculations in unstable operating regimes. They give a comprehensive listing of the mathematics.

2.3 MASS CONSERVATION, BOUNDARY CONDITIONS AND CAVITATION

Jacobson and Floberg (1957) noted that even early researchers such as Sommerfeld (1904) had expressed concern that the cavitation of the oil film had not been considered correctly. Solutions of Reynold's Equation for simple circular journal bearings with steady loading had always assumed that the oil film pressure was zero at the point of maximum oil film thickness and then positive for π radians to the point of minimum film thickness. The other half of the bearing would be assumed to have zero pressure although Reynold's Equation actually produces a symmetrical pressure distribution with negative pressures in the region of diverging oil flow. Without the assumption of zero pressure where Reynold's Equation predicts negative pressure, circular journal bearings would carry almost no load. In reality, the oil film cavitates and forms separate streamers when the pressure goes below the vapour pressure as the film shape starts to

diverge. The flow of oil in the cavitated region is lower than predicted by a solution of Reynold's Equation and therefore the start of positive pressure as the film shape starts to converge again is not at the point of maximum oil film thickness but slightly further around the bearing, affecting the whole pressure distribution.

Jacobson and Floberg used the example of a simple circular journal bearing and used a Finite Difference formulation with relaxation of the pressure distribution to solve Reynold's Equation. They calculated the start and finish position of the cavitated region iteratively using boundary conditions for continuity of mass flow for the behaviour of the film at the entry and exit to the cavitated region.

The 1st Leeds-Lyon Symposium in 1974 was on 'Cavitation and Related Phenomena in Lubrication'. Papers cover a range of subjects not all directly related to behaviour of thin oil films in journal bearings. The first paper (Swales, 1974) provides a general overview of cavitation phenomena from an experimental point of view. He categorises the following types

- Travelling – bubbles travelling with the fluid, expanding, contracting, collapsing, re-opening. Noise of collapse gives a characteristic singing noise and damage if collapse is near a solid boundary
- Fixed – stable cavity where flow detaches from the boundary. Can be unstable with travelling cavities detaching from an oscillating fixed cavity associated with a back-filling jet
- Vortex – Less serious – caused by local reduction in pressure at vortex cores e.g. propeller tips
- Vibratory – small oscillations causing pressures below the vapour pressure in te fluid. Similar to boiling but short duration prevents bubble growth

Cavity contents include the gaseous phase of the fluid and gases that were dissolved in the fluid. Dissolved gases are generally a small proportion of the cavity contents but affect bubble formation and collapse.

Thin film cavities are often stable and gas filled rather than vaporous – may be fed from the atmosphere at the edges. Types classified as

- Separation – open, ventilated
- Ligament – closed, spanning the gap, gaseous
- Bubble

Swales states that cavitation damage often indicates vaporous cavitation especially where events don't give time for gas to diffuse out. Vaporous cavitation often produces a characteristic high frequency noise.

Timperley (1974) discusses tensile properties of liquids. He admits that theoretical knowledge of the subject is poor. There are strong influences from nucleation which varies strongly with the fluid, the nucleation material and even electrical effects. The effect is also strongly time dependent and even history dependent.

Dowson and Taylor (1974) provide a comprehensive look at the subject specifically regarding cavitation in journal bearings and referencing the previous work of Gumbel (1914), Swift(1931) and Stieber (1933). They state that gaseous cavitation is most commonly associated with journal bearings and that vaporous cavitation, causing damage, is associated with hydraulic machinery. They review the development of theory for the conditions at film rupture. Simply ignoring the negative pressures in a full Reynold's Equation solution is known as the Gumbel or half-Sommerfeld solution and is often sufficiently accurate. Consideration of flow continuity at film rupture gives rise to the Swift-Stieber – pressure gradient zero at the trailing edge. However, flow separation and surface tension effects can give rise to a negative pressure region at the point of cavitation. It may be worthwhile to study this paper in more detail to see if it is possible to incorporate the effects into the program written for this project. This will have to be done after this project.

Ettles (1974) discusses cavitation in response to the previous papers. He states that most theoretical and experimental approaches involve gaseous cavitation but that vaporous cavitation is the more relevant problem. The contradiction is due to the difference

between static experiments and theory and the dynamic nature of many problems. Collapse of gaseous bubbles is proposed to be time dependent and therefore unlikely to be damaging. Growth and collapse of vaporous bubbles is a phase change and thermodynamic but can occur very suddenly at a given combination of temperature and pressure. Bubble generation takes place from nucleating features – existing micro-bubbles, solid particles or surface asperities. He proposes that these aspects have received insufficient attention.

Elrod and Adams (1974) show that previous work by Jakobsen and Floberg has been appropriate to analytical solutions and somewhat clumsy in dealing with the cavitation interface. They point out that Reynold's Equation can be expressed with variable density giving a single equation that applies in full film and cavitated region. What is different between the two regions is which variables are constant or zero.

Floberg (1974) deals with the question of tensile strength of the oil. He also states that this is only important in lightly loaded bearings. This may explain why commercial automotive bearing programs do not take account of this effect.

There are many other interesting papers in the proceedings of the 1st Leeds-Lyon Symposium on Tribology, despite it being more than 30 years ago. Examples include Dyson (1974) on air entrainment into hydrodynamic contacts, Savage (1974) on cavity instability among many others.

Elrod (1981) expands on the 1974 paper with details of the algorithm for using variable density to model full film and cavitated region.

Dowson, Taylor and Miranda (1985a and b) describe an implementation of Elrod and Adams's method for steadily loaded bearings with grooves. They also carried out experiments using a test rig with glass bushes. They were able to measure eccentricity ratio, side leakage rate and see the film ruptures and reformation locations through the glass bushes. The agreement between calculation and experiment is impressive but the film boundaries are not as close as the other parameters. The authors discuss the discrepancy in terms of the lack of account for tensile loads in the film at rupture.

Brewe and Jacobson (1987) also use Elrod's method but to look at the effect of vibration on the formation of cavitated region and the hysteresis effect on the load carrying capability. They cite the previous experimental work of Jacobson and Hamrock (1983) but it doesn't appear that they make any direct comparisons.

Brewe, Ball and Khonsari (1990) provide a large review of research activities on cavitation in a 65 page NASA technical report.

Kumar (1991), Kumar and Booker (1991) and Shi (2002) develop Finite Element approaches to solving for mass conservation in the fluid film in preference to the Finite Difference approach.

Wang, Wang and Lin (2003) develop a calculation for a combined thrust bearing and journal bearing and use it to investigate the effects of viscosity, misalignment and oil feed position. They find that misalignment increases the load carrying capacity, the position of oil feed is significant and that using a mass conserving algorithm is important when the two regions are coupled.

The paper by Forstner and Struwe (2004) is interesting because it relates the oil film cavitation behaviour to the appearance of cavitation damage in journal bearings. Bearing surfaces are damaged by the generation and immediate collapse of small gas bubbles as the oil film cavitates. They state that useful work understanding detail of cavitation has been carried out by researchers using CFD, especially in fields such as pump wheels, turbine blades, propellers and valves. Understanding cavitation in bearings remains a problem due to the difficulty of applying CFD models with such detail to thin oil films and under large time varying loads. Bearing programs that solve Reynold's Equation including mass conservation are only able to calculate pressure distribution in the filled region, oil fill ratio in the cavitated region and oil film thickness. The authors examine the factors that give rise to cavitation damage. Different bearing materials resist the effects of cavitation erosion to different extents but do not eliminate the root cause.

Certain types of cavitation damage appear around the edges of bearing features due to insufficient rounding or chamfering affecting the flow at the sudden section change and

producing turbulent flow. These types of turbulence are usually dealt with simply by attention to detail design around grooves, tangs and crush relief. More severe and intractable cavitation damage tends to occur due to pressure fluctuations from mis-timed oil feed events and vibration loading from the engine.

One of the factors mentioned by Forstner and Struwe was the change of fuel type for a pre-existing engine. This is a common topic these days due to environmental concerns. Gasoline powered engines may be converted to run on Liquid Petroleum Gas (LPG), methanol or ethanol. Diesel powered engines may be converted to run on a number of alternative fuels but one of the main conversions is to Compressed Natural Gas (CNG). CNG has a much higher octane rating than gasoline. Although it is suitable for spark ignition, a higher compression ratio is needed to take full advantage of the potential greater efficiency. The higher compression ratio of diesel engines and their greater structural strength makes conversion of diesel engines to CNG attractive. Semin and Rosli (2009) describe such a conversion comparing gas pressure curves. It appears that, generally, the peak gas pressure is lower for CNG compared to the original diesel engine. However, at certain running conditions, the rate of increase of gas pressure may be higher. Could this be the cause of a greater propensity for cavitation damage to arise in these engines?

Yuan et al. (2007) also look at the effect of the lubrication system on cavitation in engine bearings. They use a CFD approach to examine the aeration of the oil being fed to the bearings.

Other topics also arise in cavitation studies, for example http://ricardo.com/Documents/IA/Software/SCAEpdfs/SoftwareCAE_Q2_2009.pdf (2009) which shows the use of Ricardo's piston dynamics software in the examination of cavitation on the water side of cylinder liners. This is a common problem on diesel engines because the high cylinder pressures combined with heavy, stiff pistons gives rise to large impact forces against the liner. The water on the other side of the liner is close to boiling temperature. The high saturated vapour pressure at these temperatures means that vibration

Ausas, Ragot, Leiva, Jai, Bayada, and Buscaglia (2007) compare results from a classical Reynold's non-mass conserving model and an Elrod and Adams mass conserving model. They find that the non-conserving model is adequate for smooth bearing surface and has the advantage of computational efficiency. For a bearing with a textured surface they find that the difference in results between the two models is much higher.

Feng et al. (2008) investigate cavitation assumptions in Reynold's Equation solution and their effect on the unbalance response for a static indeterminate rotordynamic system. They find that the cavitation assumptions have a large effect.

Jang and Khonsari (2008) develop non-mass conserving and mass conserving algorithms for use in squeeze film and rotational situations. They compare their model with experiments and conclude that there is reasonable agreement.

Pan, Kim and Rencis (2008) propose an alternative cavitation theory to that of Floberg, Elrod and Adams. They take the view that the behaviour in the cavitated region has been over simplified and that there are adhered films. The paper is difficult to read – it is rather terse. Its use of 1D examples for comparison with Elrod and Adams may not be completely valid in this author's opinion because 1D Finite Difference solutions of Reynold's Equation have inadequate control of boundary conditions. That criticism may not be valid and more study of this paper may be useful. In any case, criticism of one aspect of the comparisons that the authors make does not necessarily invalidate their approach. As with other refinements of Reynold's, Gumbel's and Sommerfeld's original work, it is always worth remembering that the improvement of accuracy may be fairly small compared to other sources of inaccuracy that affect all simulation work.

Schweizer (2008) use a finite element approach to solving Reynold's Equation with Reynold's boundary condition. They are able to map onto a mesh that follows the film cavitation boundary precisely and claim good computational efficiency and stability.

Sun et al. (2008) include the effect of tensile forces in their model which is applied to a parallel plate oscillatory squeeze film bearing. The tensile forces are modelled using meniscus with contact angle and surface tension as well as tensile pressure within the fluid related to nucleation size for bubble formation.

Ausas, Jai and Buscaglia, G.C. (2009) implement the Elrod and Adams mass conserving hydrodynamic solution with a Newmark integration method for solution of equations of motion. The solution includes iterative aspects and they include a pseudo-code listing in the paper which may be worth further examination.

2.4 CONTACT AT ASPERITIES

Effects on the hydrodynamic calculation of very thin oil films of the same order of magnitude as the composite surface roughness of the two surfaces are important. The standard formulation assumes smooth surfaces. The surface roughness has two effects. Firstly the opposing asperities start to make contact at a nominal approach distance of some small multiple of the composite surface roughness value of the surfaces. They carry a proportion of the load on the bearing leaving the rest to be carried by the wedge action of the oil film. The paper by Greenwood and Tripp (1971) gives polynomial expressions for the stiffness of asperity contact. They use Hertzian contact theory to examine the effect of large numbers of idealised asperities on opposing sides of nominally flat surfaces being brought together. Halling and Nuri (1985) also look into this issue. The importance of this work is that it enables contact load sharing for mixed lubrication regime to be calculated simply from the film thickness to surface roughness ratio.

For general reference on contact calculations with a very large number of references, Guzelby (1992) is a good starting point. Landenberger (1995 and 1998) and Landenberger and El-Zafrany (1996) look into the use of the Boundary Element Method (BEM) for contact problems. This may be useful in the future for investigating contact between real world non-idealised asperities but that is going outside the requirements of this project at this time.

2.5 GENERALISED MASS FLOW AT ASPERITIES

In addition to the effect of load sharing between the asperities and the oil film, the oil flow is affected because the oil must flow between the peaks of the asperities. Several papers study this subject in order to modify Reynold's Equation.

Patir (1978) and Patir and Cheng (1978) consider the effect of asperities from the fluid flow point of view. As the mean film thickness approaches the composite surface roughness of the two surfaces part of the load is carried by contact of the asperities. This starts to become significant for film ratios below about 3 because of the statistical nature of surface roughness. In addition, the fluid flow is affected because a significant proportion of the fluid is having to flow between the asperities. In the derivation of Reynold's Equation it is assumed that the surfaces are smooth and that is adequate for thick films. The authors build on the work of Tseng and Saibel (1967), Christensen and Tonder (1973), Rhow and Elrod(1974) and Chow and Cheng (1976) who all looked at very specific surface roughness problems. The authors developed a method to calculate the flow coupling between the x and y directions using a finite difference solution and ran it for a number of film ratios to obtain functions to modify Reynold's Equation. It was the work of Peklenik (1968) on surface characterisation that enabled them to extend this to roughness with directional characteristics. At the date of writing this thesis, this modification to Reynold's Equation, known as generalised mass flow, has not been incorporated but will be in the future.

Elrod (1979) uses Patir and Cheng's work to examine the effect and also discusses the limits of roughness wavelength for using Patir and Cheng's method. Wavelength below about 5 times the surface roughness implies that the fluid flow should be modelled directly.

Tripp (1983) and Wu and Zheng (1989) also build on the work of Patir and Cheng, concentrating on methods to calculate the flow factors that are used to modify Reynold's Equation.

The methods due to Jacobson and Floberg (1957), Olsson (1965), Greenwood and Tripp (1971), Patir (1978) and Patir and Cheng (1978) is used by many authors up to the present day such as Lang (1997), Sahlin et al. (2007a and b), Ma (2007), Ozasa (2006), Rao and Sawicki (2004, 2005), Martin (2008), Tønder (2008) and Bobach, Bartel and Deters (2008).

Cupillard, Glavatskih and Cervantes (2008) use CFD to look at the performance of bearings with dimpled surface. Features sufficiently deep to give effects in the film thickness are clearly beyond the capability of Reynold's Equation which assumes constant pressure through the film thickness. The authors found that the optimum dimple dimensions and position depends on the operating conditions.

Turaga, Sekhar and Majumdar (1999) use stiffness and damping coefficients derived from rough surface bearing models to examine the effect on a rotordynamic calculation.

2.6 ELASTOHYDRODYNAMICS

One of the earliest references on numerical solution for ElastoHydroDynamics is that due to Biswas and Snidle (1977) and Evans and Snidle (1978). They used the Boundary Element Method (BEM) for the structural solution and Finite Difference Method (FDM) for solving Reynold's Equation. The situation was a sphere loaded against a flat surface.

An early example of an EHD solution applied to connecting rod big-end bearings is Oh and Goenka (1985). They use a time varying quasi-static analysis using a compliance matrix at the bearing surface. They use a Newton-Raphson method to iterate to the journal position.

Evans and Johnson (1986a) look at the effect of the high pressures implied by EHD deformations to study changes in the regime of rheological behaviour. They have four regimes: Newtonian linear viscoelastic, non-linear viscous (Eyring), non-linear viscoelastic and elastic-plastic. In the elastic-plastic phase, the fluid flows at a constant shear stress independent of the shear stress. EHD behaviour is generally associated with high specific loading so it seems sensible to build in more advanced rheological models.

McIvor and Fenner (1989) use the Finite Element method for both the Reynold's Equation solution and the structural equations. It is a quasi-static solution using the Newton-Raphson method for iteration at each step. The authors realised that a great deal of computational effort is expended reformulating matrices and obtained a large increase in computational efficiency by not carrying out these reformulations at every step.

Xu and Smith (1990) use the FDM for the fluid film and FEM for the structural equations with the Newton-Raphson method for iteration. An interesting aspect of this paper is the use of a 2D FE model of the bearing housing.

Sun and Lin (1992) used the Finite Element Method for the Reynold's Equation solution with the Boundary Element Method for the structural equations.

Ai and Cheng (1993) take a very unusual approach for a method that's optimised for surfaces that have surface waviness. Only surface roughness within intermediate wavelengths is suitable. They iterate to a solution using superposition of pressure distributions.

Sharda, Chandrawat and Bahl (1993) used the Finite Element Method for the Reynold's Equation solution and the structural equations. They examined the effect of misalignment. A rigid misaligned bearing gives lower minimum film thickness and so reduces the load capacity of the bearing. Flexibility allows the bearing to conform and increases the minimum film thickness compared to the rigid misaligned bearing. The improvement of stability margin for rotordynamic situations of misaligning the bearings is reduced by flexibility.

Kohno, Takahashi and Saki (1994) use the Finite Element Method for the hydrodynamic solution and the Boundary Element Method for the structural solution.

Most of the EHD studies reported up to the mid 1990s have been static; they have used only the stiffness matrix of the structure. Dynamic studies have been shown by Knoll, Schoenen and Wilhelm (1997) among several others. Such studies use the mass matrix of the structure and the methods are suitable if excitation frequencies approach or exceed the first natural frequency of the structure.

Bahai and Xu (1997) use an EHD analysis with Newton-Raphson iteration to apply pressures to an elastic-plastic Fourier element model. The purpose of doing this is to study the generation of residual stresses and the possibility of cracks.

Ozasa, Noda and Konomi (1997) compare analyses of an RHD model with EHD and EHD with oil holes and structural body forces. The program uses Finite Difference

solution for Reynold's Equation and Newton-Raphson for iteration of the solution at each time step.

Lahmar, Haddad and Nicolas (1998) use a conventional Finite Difference approach for the fluid film solution and an under-relaxation iterative approach for the elastic deformations. They use a method involving complex Kolosov-Muskhelishvili potentials, whatever they are!

Kudish, Kelley and Mikrut (1999) show a formulation of EHD for a situation of two conformal cylinders. They use a perturbation series for the pressure and seem to have a problem with arbitrary initial conditions that this author has failed to understand!

Boedo and Booker (2000) describe an EHD modelling technique using superposition of natural modes for the elastic deformation.

Using the Boundary Element Method coupled to the Finite Difference Method has not been used by many authors. Barrett, El-Zafrany and McLuckie (2002) investigated the possibility using a 2D model with verification against a commercial Finite Element code for the structural deformations. Their conclusion was that the BEM provides a more accurate solution for the same surface mesh density compared to FEM and that it would be easy to extend the method to 3D models. The great advantage of BE models is that they require far less user time on mesh generation. As computers become more powerful, this factor becomes more important. The BEM has fallen out of favour as automatic tetrahedral mesh generators have become available for Finite Element meshing, especially in CAD programs. However McLuckie, Ma and Butler (2000) showed that tetrahedral elements are very poor for use in EHD calculations. This is because the parabolic shape functions are unsuitable for contact and/or coupling to FDM, the stiffness matrix is often lacking in smoothness and they are simply too inaccurate and inefficient.

2.7 THERMOELASTOHYDRODYNAMICS

Rodkiewicz and Yang (1995) developed a ThermoElasticHydroDynamic (TEHD) analysis technique for fixed pad sliding thrust bearings using the Boundary Element

Method (BEM) for heat transfer in the pad, Finite Element Method for deformations, Finite Difference Method (FDM) for fluid film solution. Iteration is carried out using the Newton-Raphson method.

Shi and Wang (1997) and Wang, Shi and Lee (1997) report a TEHD solution for journal bearings using FEM, FDM and influence functions for temperature and deformation. The overall solution is iterative and they use it to look at heavily loaded bearings and the heat generated by asperity contact in mixed lubrication regime.

Ma and Taylor (1999) investigated the TEHD behaviour of statically loaded bearings of different shapes. The hydrodynamic equations were solved using the Finite Difference Method. The heat generation was calculated using the 2D energy equation on the bearing centre line only. The authors investigated a large number of bearing geometries and varied shaft speed at different loads.

Gandjalikhan Nassab and Maneshian (2007) use CFD to carry out a THD calculation on a finite length journal bearing.

Zengeya, Gadala and Segal (2007) use a Finite Element Method to carry out a THD calculation on a journal bearing.

Hartinger, Gosman, Ioannides and Spikes (2008) use the Finite Volume Method (FVM) in the openFOAM open source CFD program to investigate the TEHD behaviour of rollers in a rolling element bearing.

Durany, Pereira and Varas (2008) use the Finite Element Method for Reynold's Equation solution, cell-vertex volume method for the energy equation and dual reciprocity Boundary Element Method for temperature distribution in the bush.

Shyu, Jeng and Li (2008) use the Legendre collocation method with bulk-flow model for THD calculations in journal bearings.

van Ostayen and van Beek (2009) use the Finite Element Method to carry out THD calculations on lemon shaped bearings and propose design changes.

2.8 FULL FLOATING BEARINGS

General information on the application of full floating bearings is sometimes available at the launch of new products. An example is Hirata, Akita, Arnold and Ohkita (1992) regarding the introduction of a new turbocharger. Such papers are quite widespread and their purpose has more to do with marketing and displaying technology than providing a contribution to technical knowledge. They tend to be of little use to a project such as this but include cross sections that show the design features and general proportions being used

Shaw and Nussdorfer (1947) showed experimental techniques to produce charts for designing full floating bearings. General information is also available in the text book by Shaw and Mack (1949).

Wilcock (1983), MacInnes and Johnston (1982), Trippett and Li (1984) and Trippett (1986) report various experiments and calculations and the discrepancies between them. It is proposed that thermal effects are important when trying to predict the ring rotational velocity.

Wilcock (1983) refers to his previous work, Wilcock (1980), on thrust bearings on the role of dividers in increasing the load carrying efficiency of bearings, defined as the ratio of power loss to load carried. The thrust bearing work had shown that the load carrying efficiency is independent of the viscosity of the lubricant as power loss and load are both proportional to viscosity. One effect of this finding was that the load carrying efficiency is not affected by turbulence which can be considered as an increase in viscosity. However, using the well known Petrov assumption that power loss can be approximated by a simple calculation of shear with the journal central in the bearing, it is shown that power loss in a full floating bearing can be 0.40 times the power loss in the equivalent single film bearing for turbulent flow only. The reason is that the effective turbulent velocity is the laminar velocity multiplied by $Re^{0.657}$ and $Re = \rho U h / \mu$. However, this ignores the effect of the ring on the load capacity of the bearing. Wilcock goes on to show that similar power reductions can be obtained for a range of different flow conditions and bearing geometries and typical equilibrium ring speeds are

from 0.33 to 0.45 of shaft speed. In the discussion section, R.J. Trippett points out that lower ring speeds are often found due to thermal effects and this would reduce the power loss advantage. The real advantage of floating ring bearings is the effect on stability.

Orcutt and Ng (1968) and Tanaka and Hori (1972) compare the theoretical and measured behaviour of full floating bearings.

Rohde and Ezzat (1980) investigate the possibility to use full floating bearings for both connecting rod and main bearings in reciprocating piston engines. They conclude that it is feasible to use them because the minimum film thicknesses are acceptable and friction losses would be reduced.

Li and Rohde (1981) investigate the effect of Short Bearing Approximation versus finite bearing theory using the impedance method. They solve the equations of motion and examine the non-linear behaviour of the bearings.

Anisimov and Anisimova (1999) have investigated the calculation of full floating bearings using finite difference solutions of Reynolds Equation. They have included a thermal balance calculation.

Full floating bearing applications at lower speeds have also been reported. Mokhtar, El-Butch and Ibrahim (2005) proposed using such bearings for engine crankshafts. Noda, Nozawa, Yamamoto and Yamada (1995) treated a piston pin as an example of a full floating bearing.

Holt, San Andrés, Sahay, Tang, Rue and Gjika (2003) showed experimental data on turbocharger full floating bearing instability. They varied lubricant temperature and pressure and measured the effect on casing accelerations over the operating speed range. They found that the onset of instability was affected by pressure but not by temperature and that the amplitude of the instability was also affected.

A follow-up paper by San Andrés and Kerth (2004) also showed these experimental results and reported that it is necessary to include a thermal model for its effect on clearances and oil viscosity to get accurate model predictions.

McLuckie, Barrett and Teo (2006) reported the modelling of unstable behaviour of plain and full floating bearings for a dynamic rigid shaft system using RHD calculation and solution of the equations of motion. The development of the program was carried out under this EngD project and full results are shown in Chapter 6 of this thesis.

2.9 SOLUTION OF EQUATIONS

Bajer (2000 & 2002) gives an overview with equations of various numerical integration procedures. The integration methods used for the program in this project are the Runge-Kutta-Cash-Karp, Bulirsch-Stoer and Newmark-Beta. The first two methods are for first order differential equations. Using them for second order differential equations introduces a phase delay between acceleration and velocity that can lead to instability. Bajer covers the principles and equations for a number of methods that are suitable for the second order differential equations such as equations of motion. The methods include Newmark, Bossak, Hilber-Hughes-Taylor, Park-Housner, Trujillo and the space-time element method. It would seem well worthwhile to provide some of these methods in the hydrodynamic solver of this project. The programming has started but testing and results will be too late for inclusion in this thesis.

Gear and Kevrekidis (2003) describe a method for integration of difficult numerical equations for situations where it is only convenient to calculate the differential function at positive time steps. That may make it suitable for use on this project where carrying out the Finite Difference relaxation calculation is more efficient if carried out at consistently advancing time steps. This is because the pressure distribution at each time step is used to seed the pressure distribution at the next time step. No attempt has been made at the time of writing this thesis to implement Gear and Kevrekidis's method.

2.10 RHEOLOGY

Bair and Winer (1979) measure the shear properties of three lubricants at temperature and pressure. These properties are important for determining the maximum traction that can be achieved in elastohydrodynamic contacts. These properties are especially relevant for CVT transmissions and not generally taken into account for low friction

systems such as bearings. The paper by Evans and Johnson (1986) complements the Bair and Winer paper because it covers the experimental techniques available as well as giving an overview of the properties.

Chamnirasart, Al-Sharif, Rajagopal and Szeri (1993) investigate the properties of bubbly oil. They review the early work by Einstein (1906) on the effect of two phase systems on viscosity which was extended by Taylor (1932) and Hayward (1961) leading to the viscosity correction

$$\mu = \mu_1(1+1.5\phi) \qquad 2-2$$

after simplification and confirmation by Hayward's experiments where ϕ is the volume ratio of the bubbles. They go on to examine the effect on hydrodynamic theory and check their results against the experiments of Braun and Hendricks (1981). Although the authors claim good qualitative agreement the calculated and measured axial pressure distributions appear to be significantly different at certain angular positions.

Mokhiamer, Crosby and El-Gamal (1999) studied the influence of non-Newtonian lubricant properties, specifically the couple stress term that arises with long chain organic molecule additives. They modify Reynold's Equation and compare results for an EHD test case. They find that there is significant benefit – increased load carrying capacity, reduced friction and reduced side leakage.

Castle and Bovington use a high frequency reciprocating rig to study the effect of a range of friction modifiers under EHD conditions in the boundary and full film regimes. The effect of the friction modifiers was found to be significant even under full film conditions.

2.11 BUSINESS RELATED TOPICS

Mynott (2005) provided the author with copies of his slides from a presentation on the business benefits of simulation. His presentation emphasised the importance of introducing new products on time and keeping errors from the later stages of the development process. Failure to do that has a disproportionate effect on the costs. The

highest costs are incurred by warranty claims and product withdrawals etc. and the topic is described in more detail in Chapter 8.

Nagy (2005) gave a keynote speech at the IDETC conference in Long Beach talking about the role of high end simulations and the inability of many companies to make good use of simulation. The topic is described in more detail in Chapter 1.

McLuckie and Barrett (2005b) and McLuckie (2003) describe the need for rapid generation of simulation models. Their method is to use geometrical objects that already have mesh associated with them to build models without the need for a separate meshing task.

Prusha (2005) gave a keynote speech at the IDETC conference on early phase design for complex systems at JPL. His view is that issues of model fidelity and concurrent engineering are predominantly people management issues rather than being about software. The issue of costs of errors in design can be very severe when building mission vehicles for space. The contents of his speech are relayed in Chapter 8.

Nacsa et al (2005) give an overview of the techniques now being used to capture business knowledge. They point out that commercially available product data management (PDM) tools are not being taken up by small and medium enterprises (SMEs). It appears from their paper that it is possible to capture various aspects of process knowledge. Much of the knowledge about a product concerns its manufacture and might appear not to be related to design and design analysis activities.

This must be regarded as outside the scope of this project. However it is relevant because the aim of AIES's software is to capture product knowledge within the CAE process. Much of the cost of a product is determined at the design stage. There are many ways of expressing this. One way is by plotting risk against project spend as shown by Mynott (2005)

McBeath (2010) describes potentially revolutionary changes to the business model for simulation programs. He describes the business model and technical capabilities of the FOAM open source CFD program. This is expanded in Chapter 8.

2.12 OTHER TOPICS

Some other topics are listed here where they provide some relevant background information that could feed into understanding the behaviour of journal bearings.

The paper by Ting and Mayer (1974) is interesting despite not being about journal bearings or about Reynold's Equation. It uses a simple classical expression for the oil film thickness between a piston ring and liner. What is really interesting about the paper is that it combines the calculation of forces, gas flow through the ring pack, elastic behaviour of piston rings, hydrodynamic calculation and uses Archard's wear formula to map the locations of wear on a cylinder liner. The program developed for this EngD project has also been adapted by this author's colleagues for piston skirt and piston ring calculations. The methods in Ting and Mayer's paper are being incorporated in that work. Lechtape-Grueter (1995) also developed a piston ring calculation procedure. Felter (2008) uses a mesh-free method for solving the fluid film equations.

Tao, Duan and Yang (2004) and Pinkus and Lund (1981) look at the body forces in the fluid film for thrust bearings. These were the only sources found for body forces in the fluid film and applied only to thrust bearings.

Boedo (1995) looks at the influence of the structural body forces, effectively another term pre-loading the bearing shape prior to application of the oil film pressures. These terms may be significant in many cases and should be incorporated into this project at a future date. Note that these forces should not be confused with the body forces acting on the lubricant film.

Miller (1996) describes theory of software that is used for simulating hydraulic systems including bearing oil supply systems. The 1-D calculations tend to be more efficient than 3D CFD calculations. Additionally, the geometry is simpler to describe and therefore appropriate for use early in the design process. This and similar software could be integrated into bearing simulation codes.

Brewe (1988 and 1989) continue their previous work correlating calculations with the measurements of Jacobsen and Hamrock on squeeze film dampers.

White and Chan (1992) use a Finite Element solution for Reynold's Equation in 1D to develop a tilting pad journal bearing code. Tilting pads are useful for high speed shafts to avoid instability. They assess stiffness and damping of the bearing against frequency and bearing pre-load. Bearing pre-load is important for stability in high speed rotating machinery because low static load leads to low stiffness.

Yang, San Andres and Childs (1993) and San Andres, Yang and Childs (1993) develop a THD procedure for cryogenic seals. An interesting aspect of the results of calculations is that there can be sufficient increase in temperature in the fluid to affect the properties.

RHD and EHD studies have been carried out on components other than plain bearings and could provide useful information. The dissertation by Lang (1997) is on the subject of piston skirt hydrodynamics. He includes the solution of the equations of motion of the piston by numerical integration.

Kecskemethy (2005) gave a presentation at the IDETC conference. He regards Object Oriented methods as very important for the development of analysis systems that can be altered quickly to deal with new situations. He specialises in Multi-Body Dynamic (MBD) systems. The presentation is not in the conference proceedings but this author has a copy.

Gurr, Lloyd and Rulfs (2008) examine the performance of stern tube bearings on a ship. Manoeuvring gives rise to forces on the bearing that vary in direction and give rise to changes in the oil film thickness.

Estupiñan and Santos (2009) use analytical solutions of Reynold's Equation (combination of Short Bearing and Long Bearing Approximations) combined with multi-body dynamics to calculate results for the bearings in a reciprocating compressor.

Wang, Tsai and Cha (2009) use parallel processing to carry out design optimisation to maximise the load capacity of a slider bearing THD calculation. They use a Dividing Rectangle method on a compute cluster and give details of the issues to obtain efficient parallel processing.

Wang and Su (2009) study the cavitation behaviour of diesel fuel flowing through injector nozzles. The cavitation plays a fundamental role in breaking up the flow of fuel into droplets.

2.13 CONCLUSIONS FROM THE LITERATURE SURVEY

2.13.1 CURRENT STATE OF KNOWLEDGE

It is clear that elasto-hydrodynamic modelling including the effects of film history, heat generation, asperity contact, shear thinning and pressure viscosity effects have been investigated over several years. Some of these effects are available in commercially produced software. These effects are highly relevant to the subject of this project, heavily loaded lubricated contacts.

Certain important effects have not been investigated adequately in the literature reviewed so far. These include the coupling of analyses between bearing surfaces such as the two sides of full floating bearings and/or integration with shaft dynamics. The effects of body forces on the fluid flow are thought to be important to the behaviour of full floating bearings. It leads to starvation of the oil film in the axial direction for the inner film.

The slow rotation speed combined with very high accelerations (several thousand g) would also seem to indicate that reciprocating machine small end bearings also need the inclusion of body forces. Indeed it would seem likely that the body forces would be the main forces acting on the oil film and this will be investigated.

The asperity contact and flow factors are important to enable accurate modelling of highly loaded thin oil film contacts. These will be incorporated into the current models in the near future.

CFD calculations have been reported by several authors in recent years. Generally these are useful in situations where the assumptions in Reynold's Equation don't apply such as significant variation in film thickness leading to non-uniform pressure through the thickness and velocity components normal to the surfaces. Other situations are heat flow

and detailed modelling of cavity formation. Lack of computer power combined with the large number of cells required by the extreme model aspect ratio is almost certainly restricting use to static cases at present. Therefore Finite Difference solutions of Reynold's Equation are likely to be popular for some years yet.

CHAPTER 3

ANALYSIS METHODS

3.1 DERIVATION OF REYNOLD'S EQUATION

Reynold's Equation can be derived from consideration of the laminar flow of a fluid through an infinitesimal control volume. The following assumptions are made:

- The fluid is incompressible
- The fluid is Newtonian –
 - shear stress proportional to shear strain rate
- Fluid properties are constant
- Inertia effects are insignificant relative to viscous effects
- The fluid film has a small thickness relative to other dimensions
- Pressure constant through the thickness
- Laminar flow only – parallel to the sliding direction
- No slip at the bounding surfaces nor other surface effects
- No body forces

The other way to derive the equation is by simplifying the Navier-Stokes Equations by applying these assumptions.

The equation is written in a 2D form because the pressure is assumed to be constant through the thickness. The oil film thickness is small compared to the other dimensions and therefore a property at each location in 2D space.

The following version is taken from Halling (1989). It adds incompressible flow and constant oil viscosity and density to the preceding assumptions. A full derivation follows and the reader can readily work out differing versions of the equation without these assumptions.

$$\frac{\partial}{\partial x} \left(h^3 \frac{\partial p}{\partial x} \right) + \frac{\partial}{\partial y} \left(h^3 \frac{\partial p}{\partial y} \right) = 6\eta(U_1 + U_2) \frac{\partial h}{\partial x} + 12\eta(V_2 - V_1) \quad 3-1$$

where:

- p Pressure as a function of x and y
- h Film thickness as a function of x and y
- x Dimension in direction of sliding
- y Dimension perpendicular to direction of sliding
- η Absolute viscosity
- U_1 Velocity in x direction of lower surface
- U_2 Velocity in x direction of upper surface
- V_1 Velocity in z direction of lower surface
- V_2 Velocity in z direction of upper surface

In the case of journal bearings the 2D mesh is wrapped around the bearing so the sliding and squeeze velocity vary around the bearing for the journal moving in a single direction.

Thus Reynold's Equation becomes:

$$\frac{\partial}{\partial x} \left(h^3 \frac{\partial p}{\partial x} \right) + \frac{\partial}{\partial y} \left(h^3 \frac{\partial p}{\partial y} \right) = 6\eta U \frac{\partial h}{\partial x} + 12\eta V \quad 3-2$$

where:

$$V = V_z \cos\left(\frac{x}{R}\right) + V_{x'} \sin\left(\frac{x}{R}\right) \quad 3-3$$

$$U = \omega R + V_z' \sin\left(\frac{x}{R}\right) + V_{x'} \cos\left(\frac{x}{R}\right) \quad 3-4$$

x = circumferential dimension

y = axial dimension

V_z' = velocity of shaft downwards

$V_{x'}$ = transverse velocity of shaft

R = radius of shaft

ω = rotational velocity of shaft (constant)

The full derivation follows:

The local axis directions used are shown in Fig.3.1. The corresponding velocities are u , v , w . Note that the film thickness h can vary with x and z but also with time due to the movement of the bounding surfaces.

Thin oil film

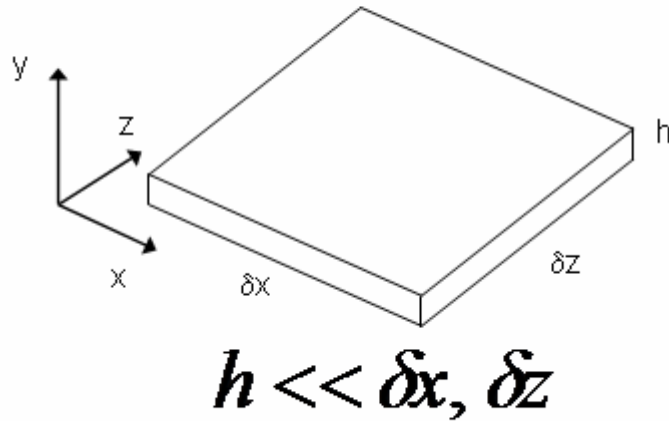


Figure 3-1 Thin oil film

Fluid flow in a plane of constant z is shown in Figure 3.2. The flow profile on the right hand side of the figure is made up of a combination of linear variation from the bottom to top surface (Couette flow due to relative sliding of the surfaces) and a parabolic variation (Poisuille flow due to pressure gradient). This is easily understood by the fact that there are no additional forces acting on the fluid apart from the surface tractions in Couette flow but that there is a constant additional force acting on each layer of fluid in Poisseuille flow. The equations are derived below.

Flow in x direction

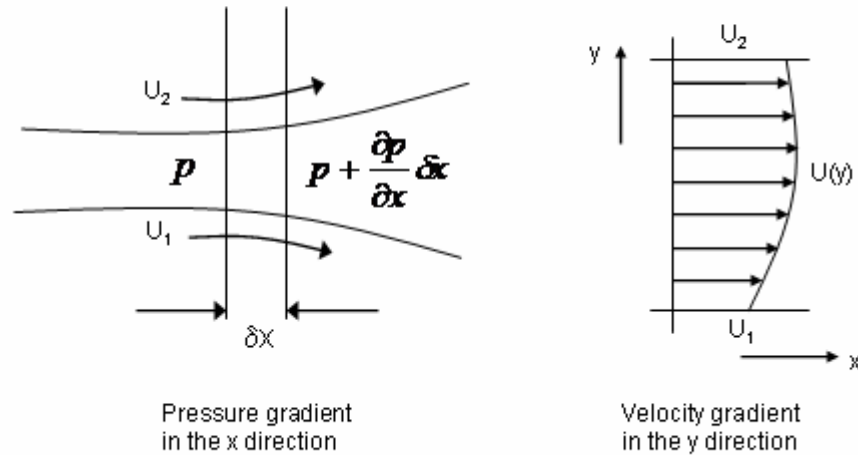


Figure 3-2 Fluid flow in the x direction

Flow rate in the x direction per unit depth in the z direction $q_x = \int_0^h U(y) dy$ 3-5

And similarly in the z direction per unit depth in the x direction $q_z = \int_0^h W(y) dy$ 3-6

For a Newtonian fluid, the shear stress in the fluid film is given by

$$\tau_{xz} = \eta \frac{\partial u}{\partial y} \text{ and } \tau_{xy} = \eta \frac{\partial w}{\partial y} \quad 3-7$$

The forces on an infinitesimal control volume are shown in Fig. 3.3, including body force due to acceleration of the bearing. Only the forces in the x direction are shown. The forces in the z direction are similar. Similar figures can be found in many text books on bearings including Pinkus (1990), p.81. Note that the body force on the fluid volume has been included in the following derivation. It is not included in standard texts on this subject and the author cannot find evidence of other researchers including it for journal bearing studies. Some thrust bearing derivations do include it as a constant radial value only.

Forces on control volume

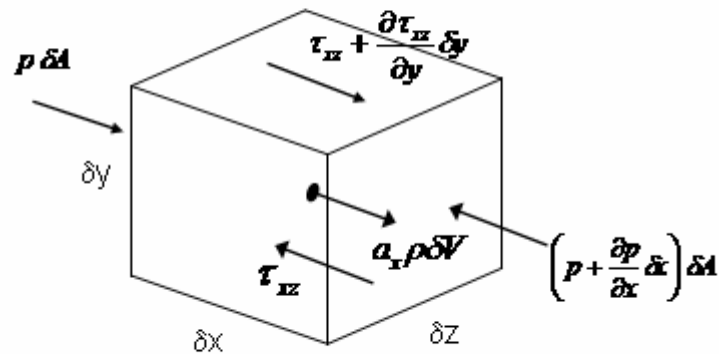


Figure 3-3 Forces in the x direction on an infinitesimal control volume

Resolving the forces in the x direction and including variation in the z direction

$$\frac{\partial p}{\partial x} \delta x \delta y \delta z = \frac{\partial \tau_{xz}}{\partial y} \delta y \delta x \delta z - a_x \rho \delta x \delta y \delta z \quad 3-8$$

$$\frac{\partial p}{\partial x} = \frac{\partial}{\partial y} \left(\eta \frac{\partial u}{\partial y} \right) - a_x \rho \quad 3-9$$

Integrating twice enables us to get the velocity profile – note that dp/dx is considered to be constant in the y direction.

$$\frac{\partial u}{\partial y} = \left(\frac{\partial p}{\partial x} + a_x \rho \right) \frac{y}{\eta} + k_1 \quad 3-10$$

$$u = \left(\frac{\partial p}{\partial x} + a_x \rho \right) \frac{y^2}{2\eta} + k_1 y + k_2 \quad 3-11$$

Using the velocities at the boundaries of the film U_1 at $y = 0$ and U_2 at $y = h$ leads to

$$u = U_1 + (U_2 - U_1)\frac{y}{h} + \frac{1}{2\eta}\left(\frac{\partial p}{\partial x} + a_x\rho\right)\left[\left(y - \frac{h}{2}\right)^2 - \frac{h^2}{4}\right] \quad 3-12$$

Integrating across the film to get the oil flow rate will enable us to use oil flow continuity to solve the equations

$$q_x = \int_0^h u \, dy \quad 3-13$$

$$q_x = \frac{(U_2 + U_1)}{2}h - \frac{h^3}{12\eta}\left(\frac{\partial p}{\partial x} + a_x\rho\right) \quad 3-14$$

Flow continuity with no motion of the top and bottom surfaces would require the flow rate in the x direction to be unchanging. In dynamic bearing calculations, the top and bottom surfaces can move with velocities V_1 and V_2 .

$$\frac{\partial h}{\partial t} = V_2 - V_1 \text{ and flow continuity requires } \frac{\partial q_x}{\partial x} + \frac{\partial h}{\partial t} = 0 \quad 3-15$$

Therefore

$$\frac{\partial}{\partial x}\left(\frac{h^3}{\eta}\left(\frac{\partial p}{\partial x} + a_x\rho\right)\right) = 6(U_2 + U_1)\frac{\partial h}{\partial x} + 12\frac{\partial h}{\partial t} \quad 3-16$$

which is Reynold's Equation for flow in one direction.

Adding flow in the z direction extends the equation simply to

$$\frac{\partial}{\partial x}\left(\frac{h^3}{\eta}\left(\frac{\partial p}{\partial x} + a_x\rho\right)\right) + \frac{\partial}{\partial z}\left(\frac{h^3}{\eta}\left(\frac{\partial p}{\partial z} + a_z\rho\right)\right) = 6(U_2 + U_1)\frac{\partial h}{\partial x} + 6(W_2 + W_1)\frac{\partial h}{\partial z} + 12\frac{\partial h}{\partial t}$$

3-17

Which is Reynold's Equation for sliding velocity in x and z directions and body forces in x and z directions.

Reducing a_x to zero produces the well known form of Reynold's Equation derived in text books such as Cameron (1983).

3.1.1 EXTENSION OF REYNOLD'S EQUATION FOR OIL FILM HISTORY

Reynolds Equation is not valid in the cavitation region of the bearing. Use of Reynold's Equation as it stands would produce large negative pressures in the diverging oil film and produce bearings with little or no load carrying capacity. In reality, the oil film ruptures in this region and produces approximately zero oil film pressure. A common way of dealing with this is simply to set pressure to zero whenever Reynold's Equation produces a negative value. This is known as the Gumbal or Half-Sommerfeld Boundary Condition and is often regarded as sufficiently accurate (Bannister, 2001). However, it over predicts the quantity of oil available where the wedge action re-forms the oil film. The work of Olson, Jakobsen and Floberg included the calculation of the oil flow in the cavitated region. They used a density (or oil fill ratio) parameter in the Reynolds Equation. It is essential that this method is included in the RHD and EHD Finite Difference solvers in order to calculate cavitation damage parameters and take account of limited oil supply from feed holes. Tracking the proportion of oil at the mesh points in the cavitated region also enables a more accurate solution to be obtained at the reforming of the wedge action. Inclusion of body forces and oil feed system characteristics will cause oil starvation at parts of the load cycle.

The equations from the preceding section can be repeated with variable density. Approaches taken by other workers e.g. Elrod (1981) and others such as Sahlin et al. (2007) assume continuous variation of density. This is appropriate when dealing with aerated oil but the approach adopted for this project so far is that of Jacobsen, Floberg (1957) and Olsson (1965). This assumes a discontinuity of density at oil film rupture. The use of an oil fill ratio θ with actual density = $\rho\theta$ where ρ is a single density value throughout the positive pressure region is more suitable for the numerical solution if there is not a smooth variation of density with pressure.

Now the equations of the previous section become:

Flow rate in the x direction per unit depth in the z direction $q_x = \int_0^h U(y) dy$ 3-18

And similarly in the z direction per unit depth in the x direction $q_z = \int_0^h W(y) dy$ 3-19

For a Newtonian fluid, the shear stress in the fluid film is given by

$$\tau_{xz} = \theta\eta \frac{\partial u}{\partial y} \text{ and } \tau_{xy} = \theta\eta \frac{\partial w}{\partial y} \quad 3-20$$

Resolving the forces in the x direction and including variation in the z direction

$$\frac{\partial p}{\partial x} \delta x \delta y \delta z = \frac{\partial \tau_{xz}}{\partial y} \delta y \delta x \delta z - a_x \theta \rho \delta x \delta y \delta z \quad 3-21$$

$$\frac{\partial p}{\partial x} = \frac{\partial}{\partial y} \left(\theta\eta \frac{\partial u}{\partial y} \right) - a_x \theta \rho \quad 3-22$$

Integrating twice enables us to get the velocity profile – note that dp/dx is considered to be constant in the y direction.

$$\frac{\partial u}{\partial y} = \left(\frac{\partial p}{\partial x} + a_x \theta \rho \right) \frac{y}{\theta\eta} + k_1 \quad 3-23$$

$$u = \left(\frac{\partial p}{\partial x} + a_x \theta \rho \right) \frac{y^2}{2\theta\eta} + k_1 y + k_2 \quad 3-24$$

Using the velocities at the boundaries of the film U_1 at $y = 0$ and U_2 at $y = h$ leads to

$$u = U_1 + (U_2 - U_1) \frac{y}{h} + \frac{1}{2\theta\eta} \left(\frac{\partial p}{\partial x} + a_x \theta \rho \right) \left[\left(y - \frac{h}{2} \right)^2 - \frac{h^2}{4} \right] \quad 3-25$$

Integrating across the film to get the oil flow rate will enable us to use oil flow continuity to solve the equations

$$q_x = \int_0^h u \, dy \quad 3-26$$

$$q_x = \frac{(U_2 + U_1)}{2} h - \frac{h^3}{12\theta\eta} \left(\frac{\partial p}{\partial x} + a_x \theta \rho \right) \quad 3-27$$

Flow continuity with the top and bottom surfaces moving with velocities V_1 and V_2 is now a mass flow continuity instead of volume flow because the fill ratio is not constant.

$\frac{\partial h}{\partial t} = V_2 - V_1$ and mass flow continuity from a control volume with moveable top and

bottom surfaces requires $\frac{\partial(\theta\rho q_x)}{\partial x} + \frac{\partial(\theta\rho h)}{\partial t} = 0$ 3-28

As ρ is constant $\frac{\partial(\theta q_x)}{\partial x} + \frac{\partial(\theta h)}{\partial t} = 0$ 3-29

Therefore

$$\frac{\partial}{\partial x} \left(\frac{h^3}{\eta} \left(\frac{\partial p}{\partial x} + a_x \theta \rho \right) \right) = 6(U_2 + U_1) \frac{\partial(\theta h)}{\partial x} + 12 \frac{\partial(\theta h)}{\partial t} \quad 3-30$$

Adding flow in the z direction extends the equation simply to

$$\frac{\partial}{\partial x} \left(\frac{h^3}{\eta} \left(\frac{\partial p}{\partial x} + a_x \theta \rho \right) \right) + \frac{\partial}{\partial z} \left(\frac{h^3}{\eta} \left(\frac{\partial p}{\partial z} + a_z \theta \rho \right) \right) = 6(U_2 + U_1) \frac{\partial(\theta h)}{\partial x} + 6(W_2 + W_1) \frac{\partial(\theta h)}{\partial z} + 12 \frac{\partial(\theta h)}{\partial t} \quad 3-31$$

The equation from the work of Jacobson and Floberg (1957), Olsson (1965) and Elrod (1981) is shown below (equation 3.32) and lacks the body force terms.

$$\frac{\partial}{\partial x} \left(\frac{1}{12\eta} \theta \cdot h^3 \cdot \frac{\partial P}{\partial x} \right) + \frac{\partial}{\partial z} \left(\frac{1}{12\eta} \theta \cdot h^3 \cdot \frac{\partial P}{\partial z} \right) = \left(\frac{u_1 + u_2}{2} \right) \cdot \frac{\partial(\theta \cdot h)}{\partial x} + \frac{\partial(\theta \cdot h)}{\partial t} \quad 3-32$$

It also has an extra oil fill ratio term and this discrepancy can be explained by the author assuming that breaking of the film into striations would reduce the effective viscosity (equation 3.20) whereas other workers may have assumed no effect. There will be no

effect on solution of the equations because q will only be assumed to have a value less than one where $p = dp/dx = 0$. This means that the difference in the equations disappears in the two regions ($\theta = 1, \theta < 1$). However, the difference does cause the calculated viscous force in the cavitated region to differ.

Oil mass flow is proportional to the pressure gradient. Conserving mass flow at the trailing end of the oil film means that both the pressure and pressure gradient must be zero (Eqn. 3.33).

$$\frac{\partial P}{\partial x_n} = 0 \quad 3-33$$

This is the Jacobsen, Floberg and Olsson (JFO) boundary condition. Mass conservation over the whole bearing requires that

$$\nabla \cdot (\rho \cdot v) + \frac{\partial \rho}{\partial t} = 0 \quad 3-34$$

Cranfield theses by Hyett (1983) and Pedder(1983) include detail on the calculation algorithm. The changes to the finite difference equations have been worked out (Appendix C) and the method has been incorporated into the bearing program. The reader may note that the solution can be split into two regions. Where the oil fill ratio is equal to one and pressure is positive, the equation reduces to the original form of Reynold's equation and the successive over relaxation method can be used. Similarly where the oil fill ratio is less than one and the film pressure is now zero rather than negative, the successive over relaxation method can be used but the oil fill ratio is the parameter being relaxed instead of the film pressure. However, the boundary between the two regions cannot be dealt with in this way and the extra equations for mass flow conservation are required to solve the problem.

3.1.2 THE IMPORTANCE OF BODY FORCES

The body force terms were included in the Reynold's Equation derivation above. It is worth judging the likely magnitude of the effect on terms within the equation before

running test cases. Simple cases can be used to judge the effect for typical FFB ring rotation speed (30000 rev/min) and racing engine small end accelerations (80000 m s⁻²).

The accelerations at the small end bearings on high speed gasoline powered engines can exceed 80000 m/s². The situation for the small end bearing lubricated by a feed hole in the connecting rod is shown in the following figures. The left hand side of Fig, 3.4 shows the situation just before the Top Dead Centre position and the application of combustion pressure. The right hand side shows the situation just after the application of combustion pressure sufficiently high to overcome the inertia forces of the piston.

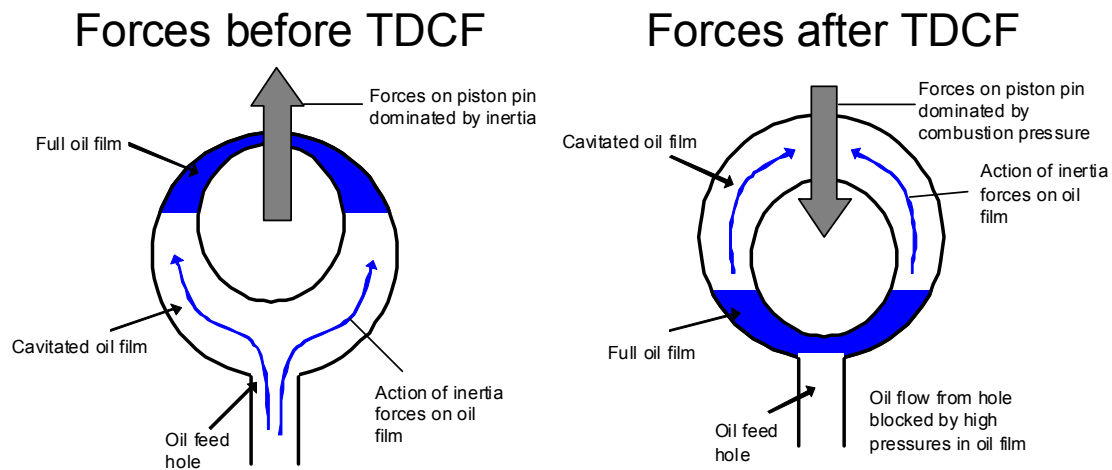


Figure 3-4 Connecting rod small end bearing just before and after TDCF

The version of Reynold's Equation including body forces is explained in Section 6. For an infinite bearing with flow in the x direction only, this version of Reynold's Equation can be reduced to

$$\frac{\partial}{\partial x} \left(\frac{h^3}{\eta} \left(\frac{\partial p}{\partial x} + a_x \rho \right) \right) = 6(U_2 + U_1) \frac{\partial h}{\partial x} + 12 \frac{\partial h}{\partial t} \quad 3-35$$

Assuming oil with constant density of 890 kg/m³ and viscosity of .01 Ns/m² and very simplistic calculations of gradients from typical pressure of 100MPa and typical dimensions gives the following values for the innermost expressions on the left hand side. The four bearings are typical dimensions for big end and small end bearings for a small diesel engine and a high speed engine.

Table 3-1 Typical Body Forces Relative to Terms in Reynold's Equation

	Brg 1	Brg 2	Brg 3	Brg 4
Bearing diameter	0.05	0.025	0.035	0.02
Shaft speed (rpm)	4000	400	16000	1600
Film thickness h	2.00E-05	1.00E-05	1.00E-05	5.00E-06
Surface Velocity U	10.47	0.52	29.32	1.68
dh/dx	4.00E-04	4.00E-04	2.86E-04	2.50E-04
dh/dt	8.38E-03	4.19E-04	1.68E-02	8.38E-04
dp/dx	4.00E+09	8.00E+09	5.71E+09	1.00E+10
a_x	1.50E+04	1.50E+04	1.00E+05	1.00E+05
da_x/dx	6.00E+05	1.20E+06	5.71E+06	1.00E+07
$a_x \times \rho$	1.34E+07	1.34E+07	8.90E+07	8.90E+07
d^2p/dx^2	8.00E+10	3.20E+11	1.63E+11	5.00E+11
Ratio $\frac{a_x \rho}{\frac{\partial p}{\partial x}}$	0.0033375	0.00166875	0.015575	0.0089

It can be seen that the body force terms are significantly less than the pressure gradient terms. The highest ratio being for the high speed engine at around 1%. However, these figures are for the large pressure gradients that occur near to maximum pressure. The ratio would be very much higher away from this zone.

The left hand side of the Reynold's Equation can be expanded (assuming constant viscosity) to give:

$$\frac{\partial p}{\partial x} 3h^2 \frac{\partial h}{\partial x} + h^3 \frac{\partial^2 p}{\partial x^2} + \rho h^3 \frac{\partial a_x}{\partial x} + \rho a_x 3h^2 \frac{\partial h}{\partial x} = 6(U_2 + U_1)\eta \frac{\partial h}{\partial x} + 12\eta \frac{\partial h}{\partial t} \quad 3-36$$

Again using the typical values of Table 3.1, each of these terms can be calculated:

Table 3-2 Typical Terms in Reynold's Equation

	Brg 1	Brg 2	Brg 3	Brg 4
Term 1: $\frac{\partial p}{\partial x} 3h^2 \frac{\partial h}{\partial x}$	1.92E-03	9.60E-04	4.90E-04	1.88E-04
Term 2: $h^3 \frac{\partial^2 p}{\partial x^2}$	6.40E-04	3.20E-04	1.63E-04	6.25E-05
Term 3: $\rho h^3 \frac{\partial a_x}{\partial x}$	4.27E-06	1.07E-06	5.09E-06	1.11E-06
Term 4: $\rho a_x 3h^2 \frac{\partial h}{\partial x}$	6.41E-06	1.60E-06	7.63E-06	1.67E-06
Term 5: $6(U_2 + U_1)\eta \frac{\partial h}{\partial x}$	2.51E-04	1.26E-05	5.03E-04	2.51E-05
Term 6: $12\eta \frac{\partial h}{\partial t}$	1.01E-03	5.03E-05	2.01E-03	1.01E-04

Again, the body force terms can be seen to be around 1% of the other terms for the high speed engine and the ratio would increase significantly in regions of lower pressure gradient (terms 1 and 2). However, note the very high potential for dominance by the squeeze film terms (Term 6). Therefore, we can probably conclude that the body forces would have a significant influence away from the high pressure regions and at low squeeze motion.

The feeding of oil into the cavitated region and the interrupted nature of the oil supply (especially to the small end bearing) are thought to be significant factors in high speed engine bearings. Therefore, these figures do support the need to include body forces in the equations. Comparison of full elastohydrodynamic bearing calculations with and without the body forces will be performed.

In the cavitated region dp/dx is zero, meaning that the left hand side of Reynold's equation would be dominated entirely by the body forces. To judge the effect of the body forces in this region, it should be remembered that the use of Reynold's Equation with half-Sommerfeld boundary condition means that Reynold's Equation does not apply in the cavitated region. It is necessary to use the expression due to Jacobson and Floberg (1957).

$$\frac{\partial}{\partial x} \left(\frac{\theta h^3}{\eta} \left(\frac{\partial p}{\partial x} + a_x \rho \right) \right) = 6(U_2 + U_1) \frac{\partial \theta h}{\partial x} + 12 \frac{\partial \theta h}{\partial t} \quad 3-37$$

Where θ is the oil fill ratio between zero and one. The fill ratio is assumed to be equal to one in areas with positive pressure value. The minimum pressure is zero and, in this region cavitation is modelled by $\theta < 1$. In the cavitated region Reynold's Equation (1D) reduces to

$$\frac{\partial}{\partial x} \left(\frac{\theta h^3}{\eta} a_x \rho \right) = 6(U_2 + U_1) \frac{\partial \theta h}{\partial x} + 12 \frac{\partial \theta h}{\partial t} \quad 3-38$$

Of course, the body forces now totally dominate the left hand side of the equation!

The left hand side of the Reynold's Equation can be expanded (assuming constant viscosity) to give:

$$\begin{aligned} & \theta \left(\frac{\partial p}{\partial x} 3h^2 \frac{\partial h}{\partial x} + h^3 \frac{\partial^2 p}{\partial x^2} + \rho h^3 \frac{\partial a_x}{\partial x} + \rho a_x 3h^2 \frac{\partial h}{\partial x} \right) + \frac{\partial \theta}{\partial x} h^3 \left(\frac{\partial p}{\partial x} + a_x \rho \right) \\ & = 6(U_2 + U_1) \eta \left(\theta \frac{\partial h}{\partial x} + h \frac{\partial \theta}{\partial x} \right) + 12 \eta \left(\theta \frac{\partial h}{\partial t} + h \frac{\partial \theta}{\partial t} \right) \end{aligned} \quad 3-39$$

Again, in the cavitated region this reduces to

$$\theta \left(\rho h^3 \frac{\partial a_x}{\partial x} + \rho a_x 3h^2 \frac{\partial h}{\partial x} \right) + \frac{\partial \theta}{\partial x} h^3 a_x \rho = 6(U_2 + U_1) \eta \left(\theta \frac{\partial h}{\partial x} + h \frac{\partial \theta}{\partial x} \right) + 12 \eta \left(\theta \frac{\partial h}{\partial t} + h \frac{\partial \theta}{\partial t} \right) \quad 3-40$$

The situation for full floating bearings on turbochargers is a little different. Ignoring excitations due to unbalance and instability, there would be no variation of the body

forces around the bearing, although note that this does not cause term 4 to disappear. The reason is that the equations include an interaction between the film thickness and the body force terms. Working through the calculation above gives very similar results to the other bearings but term 3 becomes zero.

Perhaps of more interest for these bearings is the influence of centrifugal load on the pressure differential across the feed hole between the two films. Assuming a ring diameter of 15mm and rotation speed of 5000 rad/s gives a centrifugal acceleration of 200000 m/s^2 . A ring thickness of 3 mm gives a pressure differential of around 0.55MPa simply by calculating the centrifugal force on the mass of oil in the oil hole. That is not a large pressure relative to the maximum oil film pressures that could be expected but is higher than the pressure delivered by typical automotive oil pumps and could be expected to have a significant effect on delivery of oil into cavitated regions of the outer oil film.

3.1.3 CAVITATION EROSION

The reason for including oil film history is not simply the desire for more accurate modelling in the presence of limited oil supply but the ability to assess the possibility of cavitation erosion damage in the bearing. Forstner and Struwe (2004) have used oil film history calculation in the study of damage in a connecting rod big end bearing. They reviewed the types of cavitation damage seen in internal combustion engine bearings and their probable causes

- Flow cavitation at groove edges due to rapid flow associated with shape of groove edge or rapid deformation changes
- Cavitation due to pressure waves and flow reversal – may be associated with poor oil flow timing from feed holes and appears as localised crescent shaped damage
- Cavitation due to vibrations appears as random spots of erosion
- Cavitation due to turbulence may occur near to crush relief and tang features that disturb the flow that is assumed to be laminar

They developed three criteria for examining the Elasto Hydrodynamic plots of oil film pressure, thickness and fill ratio

- High pressure must not be next to low fill ratio region

- High pressure must not be intersected by oil supply holes
- Rapid suction of oil from a hole or groove into an empty or expanding gap has to be avoided

No single parameter was developed to predict cavitation damage probability although it would seem possible to develop something in terms of flow velocities and this will be examined in the following paragraphs. The results of an EHD analysis were examined by Forstner and Struwe using their three criteria above and appeared to correlate well with patterns of damage in a connecting rod bearing. They recommend EHD plus analysis of oil feed through the supply system. Note that connecting rod bearings are usually fed from partial grooves in the main bearings leading to uneven oil flow and pressures.

The oil passages feeding the oil film are important. A simplified approach to assessing the timing of the opening and closing of the feed holes as they pass into and out of the partial grooves in the main bearings is shown in Forstner and Struwe (2004).

Cavitation bubbles arise when the oil pressure reduces. In the case of a mythical fluid with no aeration and zero saturated vapour pressure, cavitation would only arise when the solution of Reynold's Equation gives below zero pressure. Mathematical ways of dealing with this situation are dealt with elsewhere in this thesis. The solutions adopted in the program written for this project include the half-Sommerfeld method and the Reynold's boundary condition with oil film history (Jacobsen-Floberg-Olsen). In the future, it may be useful to implement a method with continuous variation of fluid density (Elrod etc.) but that has not been done here.

In reality, the oil has a saturated vapour pressure (albeit very low for standard lubricating oils at typical engine temperatures) and may have considerable levels of aeration. In internal combustion engines, there is often a considerable level of contamination by fuel. In the case of gasoline engines, the fuel is very volatile and will contribute an ability to generate vapour bubbles. Diesel fuel is rather less volatile but that means that it is even less likely to be able to escape from the lubricating oil by evaporation within the engine sump. As an engine is used, the level of contamination of

the lubricating oil tends to increase. This includes water, carbon and other combustion breakdown products as well as the fuel.

Note that Swales (1974) states 'By analogy with the water situation, vaporous cavitation and hence cavitation damage is only likely in situations where there is insufficient time for air to diffuse out of the oil'. In other words he is saying that cavitation bubbles and damage are associated with vapour bubble formation rather than diffused gases, such as air, forming bubbles in high speed situations. It would seem that some experimental work to examine the effect of aeration on cavitation bubble formation for different time constants would be useful. The effect of other contaminants, affecting the saturated vapour pressure, would also be important.

It is stated that cavitation damage in bearings is associated with pressure waves from bubble collapse rather than directly from bubble formation. However, this is not necessarily something that occurs mainly at pressure increase and/or oil film reformation from a cavitated region. It would seem more likely that cavitation damage arises at pressure reduction and/or film separation when the bubbles form and collapse in the disturbed flow or collapse when they collide with bounding surfaces. It is noticeable that, in free boundary situations such as propeller tips, cavitation damage is associated with bubble formation.

University tribology departments sometimes use large Perspex models to demonstrate fluid film separation in journal bearings. It would be useful to be able to see the fluid flow in small real high speed journal bearings subjected to dynamic loading. Dhunput, Teodorescu and Arcoumanis (2007) used laser optical methods to look at cavitation in the diverging film of piston ring to liner contact, indicating that further experimental research may be possible.

It was decided that a limitation of many commercially available programs, including that used by Forstner and Struwe, is that they do not give an indication of the likelihood of incurring cavitation damage without a great deal of manual and generally qualitative more than quantitative post-processing. There is a need to relate the results of the calculation to the likelihood of cavitation damage. Ultimately this will need more study

to include the detailed physics, fluid properties including surface tension and saturated vapour pressure and the bearing surface fatigue properties.

The main influences on the generation of cavitation bubbles are likely to be low pressure, high negative rate of change of pressure and high separation velocity of the surfaces. High negative rate of change of pressure tends to occur at the trailing edge of the oil film where the pressure drops to zero in any case. Rate of pressure change dp/dt has units of force/(area x time). Velocity has units of length/time. Multiplying the two results together gives units of force/(length x time²). This can be converted to power units, force x length / time, by dividing by the shaft speed in deg/s and by multiplying by the bearing area $\pi D/L$. This calculation was written into the program and results shown and discussed later.

3.1.4 FLOW FACTOR AND CONTACT

For thin films that arise on heavy loading of bearings the film thickness may be comparable to the surface roughness. It is possible to modify Reynold's Equation to take account of the changed flow resistance as the oil film becomes so thin that significant proportion of the flow is between the asperities of the rough surfaces. Lang (1997) shows the modelling of this, based on the work of Patir and Cheng (1978), Elrod (1979) and Tripp (1983) among others. Wu and Zheng (1989) appear to have taken a slightly simpler approach.

The modification of Reynold's Equation can be represented as:

$$\frac{\partial}{\partial x_i} \left[\phi_{ij}^p \frac{\bar{h}^3}{12\eta} \frac{\partial \bar{p}}{\partial x_j} \right] = \frac{1}{2}(U_2 + U_1) \frac{\partial \bar{h}}{\partial x_i} + \frac{1}{2}(U_2 - U_1) \sigma \sigma^\Delta \frac{\partial \phi_{ij}^s}{\partial x_j} + \frac{\partial \bar{h}}{\partial t} \quad 3-41$$

where σ is a composite surface roughness parameter and the ϕ s are flow factors obtained from the surface roughness and directional parameters. Note that the terms in Reynold's Equation are no longer independent: there is coupling of the flows in the two directions.

Patir's original work constructed several models of oil films with different arrangements of asperities including orientations. For each distribution of idealised asperities on

opposing surfaces he constructed about 10 models of varying alignments between them. He ran a Reynolds Equation solver for each of the film shapes and tabulated the flows in the two perpendicular directions. The coefficients depend on the ratio of film thickness to composite asperity height and on a directionality parameter (Fig. 3.5).

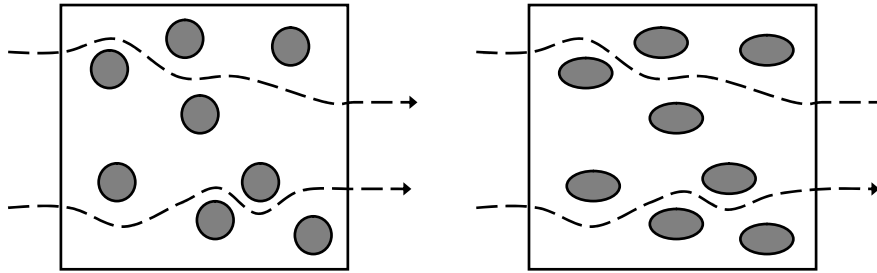


Figure 3-5 Flow factors depend on film ratio and directionality of asperities

Patir and Cheng (1978) have a table of coefficients for calculating the ϕ s for different film thickness ratios. The directionality parameter is simply a length to width ratio of the asperity shape.

So far, the EHD program has seldom caused problems due to negative film thickness. The RHD program has a Hertz contact based contact stiffness that is activated when the eccentricity ratio exceeds a critical value. This routine is disabled for EHD calculations because the eccentricity ratio often exceeds 1 by a considerable amount. It would help to ensure stable operation of the program and general robustness to include a node by node contact algorithm based on local film thickness. This problem was solved by Greenwood and Tripp (1971) who generated a curve of contact stiffness versus ratio of film thickness to surface roughness (lambda ratio). See Fig. 3.6.

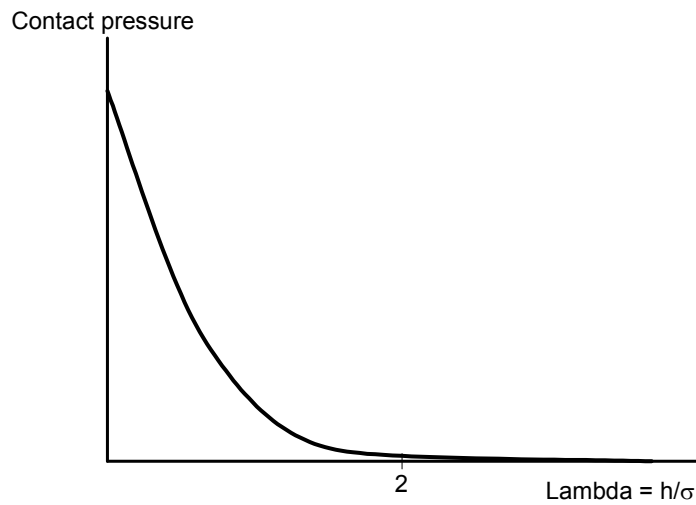


Figure 3-6 Contact pressure versus film thickness

Greenwood and Tripp examined a large number of different asperity height distributions and found that these tend not to affect the standard assumption that the contact area is simply proportional to the nominal contact pressure.

The contact pressure is the nominal normal pressure between the asperities and adds to the oil film pressure in supporting the motion of the bearing journal (Fig. 3.7).

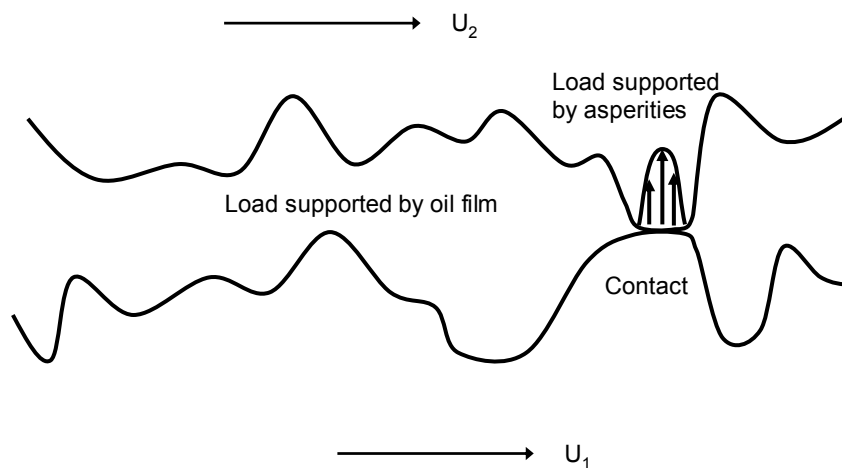


Figure 3-7 Asperity contact at low oil film thickness ratio

Due to the statistical nature of surface roughness parameters there is still significant load carrying by the asperities at a lambda ratio (equal to film thickness divided by

surface roughness) well above 1.0. In fact the assumption of Gaussian distribution of asperity heights means that there is no point at which the contact pressure goes to zero. For practical purposes, it becomes negligible for lambda ratios above 4.0.

Such a progressive curve of contact pressure versus oil film ratio would not only give a very stable operation of the program at small oil film thickness. It would also give a significantly more accurate calculation and enable power loss for a mixed lubrication regime to be calculated more accurately using a sliding contact boundary coefficient of friction for that part of the normal load carried by asperity contact. The boundary coefficient of friction is already used in the RHD calculations.

The hydrodynamic models will be updated to incorporate the flow factors and contact models. It is expected that this will improve calculation stability still further for highly loaded models as well as improve accuracy.

3.1.5 THERMOELASTOHYDRODYNAMICS

Work on this project in 2007 showed that there is a need to incorporate the capability to carry out thermal deformation calculations within the bearing oil film calculation. The implementation of a ThermoElastoHydroDynamic solver should be relatively straightforward to implement as an additional loop around the current EHD calculation. However, extraction of a reduced thermal conductivity matrix from finite element models may be more difficult as this appears not to be supported in the ABAQUS finite element program. However, code to carry out the condensation is available from the author's MSc project (Barrett, 2001). It may be possible to implement this as a user routine within ABAQUS.

3.2 THE FINITE DIFFERENCE METHOD

Solution by successive over relaxation of residuals is one of the most common methods of solving Reynold's Equation. It requires the calculation of the residual at each point in the mesh.

$$\bar{p}_{ij} = \bar{p}(p_{i-1}, p_{i+1}, p_{j-1}, p_{j+1})$$

$$R_{ij} = p_{ij} - \bar{p}_{ij}$$
3-42

The new values are then calculated by:

$$p_{ij} = p_{ij} - R_{ij} \times \alpha$$
3-43

Where α is an over-relaxation factor that is found by experiment to give a faster convergence. Lloyd and McCallion (1968) studied the optimum over-relaxation factor to use: 1.5 is generally a reasonable value.

See Appendix B for details of the finite difference calculation.

It is important to set appropriate boundary condition issues in the Reynold's Equation solutions. The nodes at the two circumferential ends of the mesh are tied together. That takes care of the 'unwrapping' of the mesh. See Fig. 3.8 and 3.9.

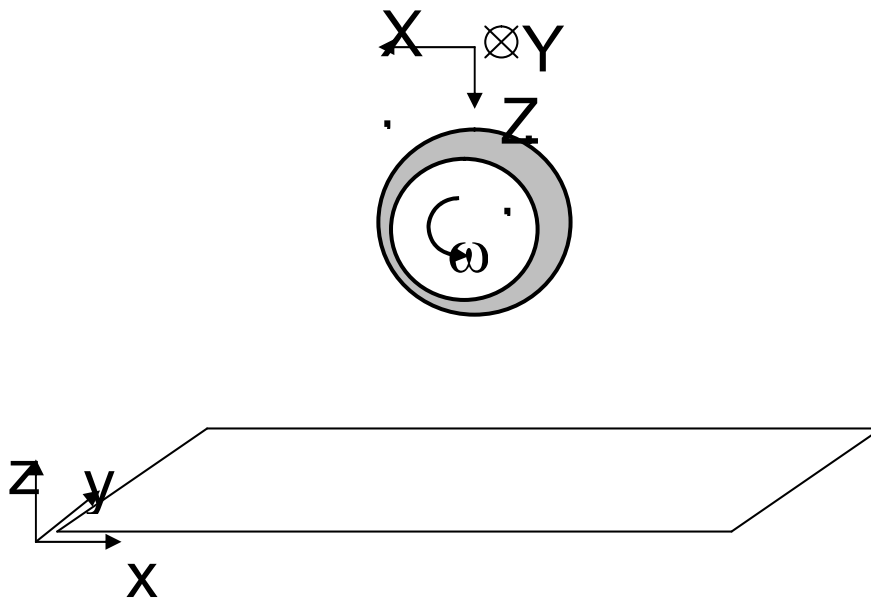


Figure 3-8 Unwrapped Bearing

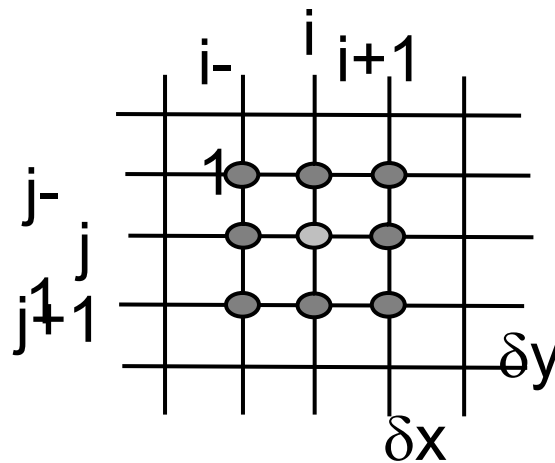


Figure 3-9 Finite Difference Mesh

Secondly, the pressures at the edges, oil feed holes and any grooves must be set. The relaxation method will automatically respect the boundary conditions by simply ensuring that relaxation is not applied to any node with a boundary condition attached. Reynold's Equation produces positive pressures in regions where the oil film is converging and negative pressures where it is diverging. Certain types of thrust bearing with a single wedge shaped film are not affected but journal bearings have both converging and diverging films at all times. The relaxation solution described so far would produce a symmetrical film pressure distribution shown in Fig. 3.10, known as the full Sommerfeld solution. The large negative pressures cannot be sustained in a real bearing and the oil film cavitates or separates into streamers. Reynold's equation does not apply in this region. Consideration of continuity of mass flow shows that the correct procedure is to set all negative pressures to zero and the gradient of pressure to zero at the trailing edge of the film (Reynold's boundary condition). Analytical solutions are generally full Sommerfeld solution but all negative pressures set to zero after the calculation without changing the gradient (Half Sommerfeld solution). Half Sommerfeld solutions are also commonly used for numerical calculations. These curves are all shown in Fig. 3.10.

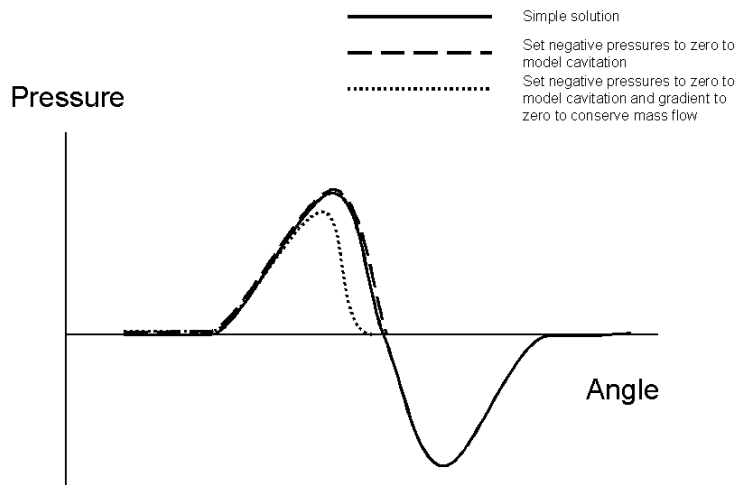


Figure 3-10 Reynold's Equation Boundary Conditions

The point at which the pressure curve passes through zero for the Reynold's boundary condition is not the same as for the half-Sommerfeld condition.

The RHD model by itself can be used to solve for pressures and oil flows in a bearing at fixed eccentricity ratio and velocity. However, for static force input, an iterative solution is required or, for forced response calculations, the equations of motion must be solved.

$$M_j \ddot{x}_j = F_{RHD}(x_j, \dot{x}_j) + F_{external}(t) - D \dot{x}_j - K x_j \quad 3-44$$

3.3 THE FINITE ELEMENT METHOD

The Finite Element Method is now so well known and commercial programs readily available that it is not usually necessary to write programs. Theory of the method is also readily accessible from standard text books such as Zienkiewicz and Taylor (2000). The

commercially available program ABAQUS was used in this project to produce reduced stiffness and mass matrices for ElastoHydroDynamic (EHD) calculations.

The method implemented in commercial finite element programs can be summarised:

- Discretise the calculation domain into elements joined to each other at nodes. Displacements and forces at the nodes are the variables being solved
- Generate a matrix [B] relating strain to nodal displacements by differentiation of shape functions that relate the values of parameters within the elements to the nodal values
- Generate Jacobian matrix [J] relating volumes in real space to volumes in unit element space
- Use principle of least work, generalise Hooke's law (matrix [D]) and the Gauss-Legendre method of integration using look-up tables to generate element stiffness matrices relating nodal forces and displacements for each element $\{F_e\} = [K_e]\{\delta_e\}$ where F is a force vector at the nodes on the element, δ is the corresponding displacement vector and K is the stiffness matrix relating them.
- The elements can then be assembled by simple addition into an overall stiffness matrix relating all the nodal forces and displacements in the model: $\{F\} = [K]\{\delta\}$ which can be manipulated to solve for the unknown forces and displacements in terms of the known forces and displacements.

Commercially available programs such as ABAQUS provide a user interface to enable geometry to be discretised into elements, load and constrain the model, run the calculation and examine the results. Most applications engineers using finite element programs do not have a detailed understanding of the underlying calculations.

3.4 COUPLING THE METHODS

3.4.1 USING STIFFNESS AND MASS MATRICES

EHD calculations require that the pressure from the FD solution of Reynolds Equation is used to modify the oil film shape. In turn, the modified film shape changes the pressures. Iterative solutions are possible for static cases. In this case, with continuously varying bearing load, the equations of motion at each node on the surface of the bearing are solved.

$$M_n \ddot{x}_n = F_{HD}(x_n, \dot{x}_n) - D \dot{x}_n - K x_n \quad 3-45$$

The terms in the equation apply only at the finite element nodes on the bearing surface. They are not simply the terms from the system mass and stiffness matrices of the model because the rest of the model has an influence through the matrices. The matrices must be reduced to the active nodes on the bearing surface by the following method, which is shown for the stiffness matrix only. The extraction of the reduced mass matrix is identical.

The system of equations is easily sub-divided into equations involving nodes at constraints, nodes with forces applied and nodes of interest on the bearing surface (active nodes) the nodes of interest:

$$\begin{Bmatrix} F_1 \\ F_2 \\ F_3 \end{Bmatrix} = \begin{bmatrix} K_{11} & K_{12} & K_{13} \\ K_{21} & K_{22} & K_{23} \\ K_{31} & K_{32} & K_{33} \end{bmatrix} \begin{Bmatrix} \delta_1 \\ \delta_2 \\ \delta_3 \end{Bmatrix} \quad 3-46$$

The sub-divided stiffness matrix is easily manipulated into the reduced stiffness matrix

$$\{F_1\} = [K^*] \{\delta_1\} + C(\{\delta_2\}, \{F_3\}) \quad 3-47$$

Where F_1 and δ_1 represent the forces and displacements on the bearing surface. ABAQUS is able to carry out this matrix extraction automatically. However, note the right hand term which is a pre-load term, not available from ABAQUS. The mass

matrix extraction is identical and ABAQUS stores the matrices in a file with the ‘.mtx’ extension in lower triangular form.

3.4.2 ADVANCED INTEGRATION AND ITERATIVE METHODS

Equation 3.39 can be solved using any of a number of integration methods to obtain the displacements at each node in terms of the acceleration and velocity at the previous time step. The Runge-Kutta-Cash-Karp, Bulirsch-Stoer and Newmark-Beta methods have been implemented. The Newmark-Beta method has only been implemented for calculation of the journal locus at present. The other two methods were implemented using code from the Numerical Recipes in Fortran, Press et al. (1992).

The experiments reported briefly in Chapter 6 on an iterative approach to solving the equations of motion were inconclusive and will be pursued further.

A search for more advanced integration methods found an interesting summary paper (Bajer, 2000 and 2002). It is clear that adapting advanced high order integration methods for first order differential equations such as Runge-Kutta-Cash-Karp and Bulirsch-Stoer or Predictor-Corrector methods can give stability problems. The reason is that the velocity must be calculated before the position can be calculated. This introduces a single step phase shift in the response that can produce overshooting of the solution or oscillation.

The Newmark-Beta method is a well known method to solve second order differential equations and is a simplification of the well known Hilber-Hughes-Taylor method. Other similar methods include the Bossak method and all three shown in Bajer (2002).

Further simplifications of the Hilber-Hughes-Taylor methods due to Trujillo and Park-Housner are stated to be very efficient and unconditionally stable but make simplifications to the mass matrix. That may be especially relevant for bearing calculations in which the forcing frequency is well below the natural frequency of the bearing structure. These calculations will be insensitive to the mass but the mass has an important influence on the calculation step size. It may enable low speed calculations to be much more efficient. A problem with the current code is that the program run times increase as the shaft rotational speed reduces.

Extension of the Newmark-Beta programming from working with the RHD solver to also working with the EHD solver has started. All EHD calculations so far have been performed using the Bulirsch-Stoer method. Some further investigation of integration and iteration methods will take place and coding of the Bossak and Hilber-Hughes-Taylor methods has started.

3.5 ENGINE BEARING FORCES

3.5.1 ENGINE OPERATION

Connecting rod bearings in reciprocating piston internal combustion engines have highly loaded journal bearings at both ends. See Fig. 3.11 taken from Duffy (1994).

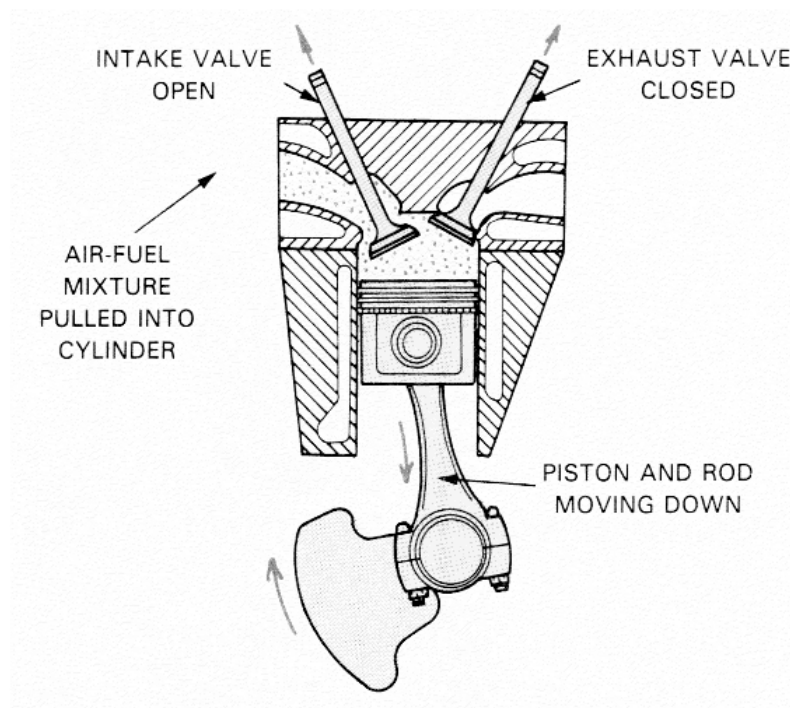


Figure 3-11 Connecting Rod (from Duffy,1994)

3.5.2 CALCULATION OF FORCES

The connecting rod forces can be calculated using a free body diagram. Data required for an engine include masses, geometry and a cylinder gas pressure curve.

Fig. 3.12 shows the basic geometry of a slider crank mechanism where:

R Crank radius ($=\frac{1}{2}$ stroke)

L Con-rod length (between bearing centre lines)

OGC Offset of the piston pin centre line from the crankshaft centre line in the 'thrust' direction

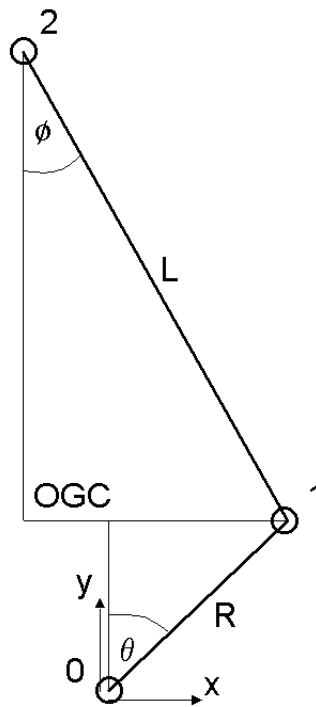


Figure 3-12 Slider-Crank Mechanism

The crankshaft is assumed to rotate at constant speed in a clockwise direction. The current crankshaft angle is θ . The con-rod angle is ϕ .

Fig. 3.13 shows the free body diagrams for the crank, rod, piston pin and piston.

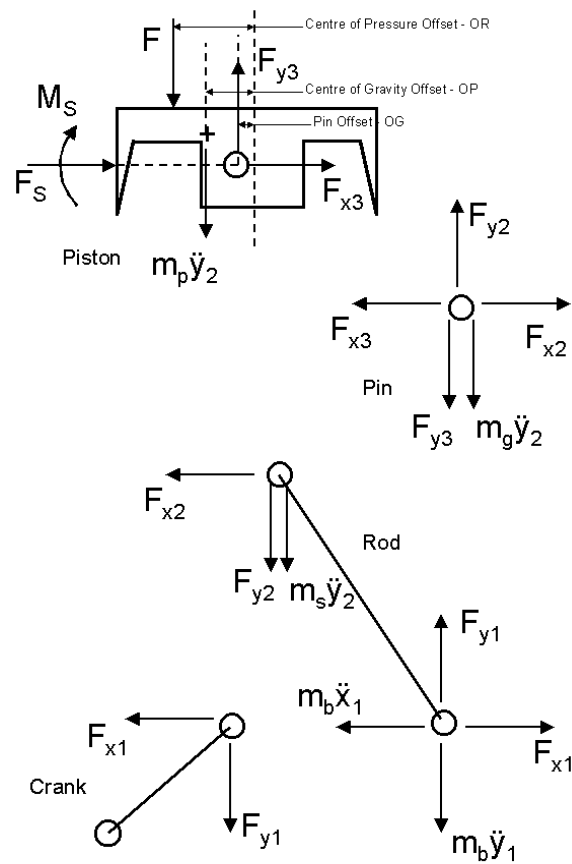


Figure 3-13 Free Body Diagram

The positive horizontal and vertical forces at each joint are the forces applied to the upper component by the lower component.

The con-rod has been approximated by two masses at the small-end and big-end centre lines giving the same position of centre of gravity. This does not give the same rotary inertia as the real con-rod but the error can be shown to be very small for real con-rods.

The data shown in Fig.3.13 are:

θ Crankshaft angle

ϕ Con-rod angle

F_{xn}	Force on component n+1 due to component n in the x direction
F_{yn}	Force on component n+1 due to component n in the y direction
m_b	Mass of con-rod at the big end
m_s	Mass of con-rod at the small end
m_p	Mass of piston
x''_n	Acceleration at joint n in x direction
\ddot{y}_n	Acceleration at joint n in the y direction
F	Gas pressure force on the piston crown
F_s	Piston side force at the height of the pin
M_s	Piston side moment to move side force up or down (height of action = M_s/F_s)
OR	Offset of centre of action of gas pressure from bore centre line
OP	Offset of piston centre of gravity from bore centre line
OG	Offset of piston pin centre line from bore centre line

where $n = 1, 2$ or 3 at the crank to rod, rod to pin and pin to piston joints.

Note that OGC from Fig. 3.12 = OG - OC where OC = offset of crank centre line from bore centre line.

Details of the calculation of the forces in the slider crank mechanism are shown in Barrett (2001).

The forces from the individual connecting rods can then be resolved on the engine crankshaft to produce the loads on the engine main bearings. Various methods can be used to distribute the loads between the main bearings. The most sophisticated method is to couple the bearing solutions with the structural solution for the crankshaft. If it is wished to calculate the forces separately from the bearing solution some approximation

must be accepted. The current program used at AIES Ltd. assumes no transfer of bending moments through the shaft at each bearing location. This reduces the problem to a statically determinate one and the loads are calculated by moments. More sophisticated methods include the moment-area method and Clapeyron's Theorem. These methods will be incorporated into AIES's shaft loading program in the near future.

3.6 TURBOCHARGER BEARING FORCES

The current turbocharger bearing force program at AIES Ltd. assumes a rigid shaft supported on two bearings. Loads applied to the shaft are resolved horizontally and vertically. Moments are taken to calculate the bearing reactions. The loads are also sorted into order along the length to calculate shear forces and bending moments acting on the shaft.

The loads that can be applied at present are gravity loading, out of balance centrifugal loading at user specified locations and harmonic loading to represent aerodynamic loads, also at user specified locations.

CHAPTER 4

IMPLEMENTATION OF CALCULATION METHODS

4.1 RIGID HYDRO-DYNAMICS

The finite difference method was implemented as a very straightforward numerical differentiation based on the mesh dimensions. If higher order terms are required they are obtained by building up the differences based on the values of the next lower order terms. Quite simply:

$$\frac{dy}{dx} \approx \frac{\Delta y}{\Delta x} \quad \text{and} \quad \frac{d^2y}{dx^2} \approx \Delta \left(\frac{\Delta y}{\Delta x} \right) / \Delta x \quad \text{etc.} \quad 4-1$$

$$\text{and } \Delta x_{i-1/2} = x_i - x_{i-1}, \Delta_2 x_i = x_{i+1/2} - x_{i-1/2} \quad \text{etc.} \quad 4-2$$

Appendix A shows the Reynold's equation solution using the finite difference method and over relaxation.

The RHD solution gives force for given journal position within the bearing. Using force as input requires that the position of the journal is computed indirectly. The MSc thesis by the author (Barrett, 2001) used a 2D Newton-Raphson approach to iterate to a solution. The current RHD program gives a choice of that iteration method or numerical integration from the imbalance of forces (applied force minus oil film force at the previous step) to integrate to velocity and position. The methods implemented were the Bulirsch-Stoer, Runge-Kutta-Cash-Karp and the Newmark Beta methods. The methods work well for high speed bearings with solution times sometimes less than one minute but can be slow at the lower rotation speeds. This may be due to the small magnitude of the inertia forces compared to the other forces.

The program automatically applies prescribed pressures to any nodes specified by the user and maintains these through the relaxation calculation.

A contact algorithm was implemented based on a linear spring stiffness and limitation of bearing eccentricity based on the composite surface roughness of the journal and bearing surfaces. See Appendix. For very highly loaded bearings the eccentricities calculated can become large, leading to numerical problems. In reality, partial contact would result in asperities carrying part of the load and limiting the eccentricity making this modification to the method realistic as well as expedient.

4.2 MODIFICATIONS OF REYNOLD'S EQUATION

4.2.1 BODY FORCES

The accelerations at the connecting rod bearings were added to the output from the bearing forces program and to the input to the bearing program.

In the cavitated region dp/dx is zero, meaning that the left hand side of Reynold's equation would be dominated entirely by the body forces. To judge the effect of the body forces in this region, it should be remembered that the use of Reynold's Equation with half-Sommerfeld boundary condition means that Reynold's Equation does not apply in the cavitated region. It is necessary to use the expression due to Jacobson and Floberg (1957).

$$\frac{\partial}{\partial x} \left(\frac{\theta h^3}{\eta} \left(\frac{\partial p}{\partial x} + a_x \rho \right) \right) = 6(U_2 + U_1) \frac{\partial \theta h}{\partial x} + 12 \frac{\partial \theta h}{\partial t} \quad 4-3$$

Where θ is the oil fill ratio between zero and one. The fill ratio is assumed to be equal to one in areas with positive pressure value. The minimum pressure is zero and, in this region cavitation is modelled by $\theta < 1$. In the cavitated region Reynold's Equation (1D) reduces to

$$\frac{\partial}{\partial x} \left(\frac{\theta h^3}{\eta} a_x \rho \right) = 6(U_2 + U_1) \frac{\partial \theta h}{\partial x} + 12 \frac{\partial \theta h}{\partial t} \quad 4-4$$

Of course, the body forces now totally dominate the left hand side of the equation!

4.2.2 OIL FILM HISTORY

Oil film history, or mass conservation has been investigated by other workers in this field. Although not innovative, it is essential that it be included in the solvers for this project. Reynold's Equation is not valid in the cavitation region of the bearing. The Sommerfeld boundary condition is the simplest way to model the cavitated region by solving Reynold's Equation for the whole bearing but setting the resultant pressure to zero wherever the solution produces a negative pressure. This over predicts the quantity of oil in the cavitated region and available oil where the wedge action re-forms the oil film but the accuracy is often regarded as adequate for lightly loaded bearings. Tracking the proportion of oil at the mesh points in the cavitated region enables a more accurate solution to be obtained. This is important for this project because one of the effects of body forces will be to cause oil starvation at parts of the load cycle.

A modified version of Reynolds Equation to include the fill ratio at each mesh point is used

$$\frac{\partial}{\partial x} \left(\frac{1}{12\eta} \theta \cdot h^3 \cdot \frac{\partial P}{\partial x} \right) + \frac{\partial}{\partial z} \left(\frac{1}{12\eta} \theta \cdot h^3 \cdot \frac{\partial P}{\partial z} \right) = \left(\frac{u_1 + u_2}{2} \right) \cdot \frac{\partial(\theta \cdot h)}{\partial x} + \frac{\partial(\theta \cdot h)}{\partial t} \quad 4-5$$

Originally due to Jacobsen and Floberg (1957). θ is the oil fill ratio with value between 0 and 1.

Conserving mass flow at the trailing end of the oil film means that Reynold's Boundary Condition should be used. Reynold's Equation shows that mass flow is proportional to the pressure gradient. As the condition at the edge of the oil film is one of constant mass flow the pressure gradient must also be zero in addition to the pressure being zero:

$$\frac{\partial P}{\partial x_n} = 0 \quad 4-6$$

This is the Jacobsen, Floberg and Olsson (JFO) boundary condition. Mass conservation over the whole bearing requires that

$$\nabla \cdot (\rho \cdot v) + \frac{\partial \rho}{\partial t} = 0 \quad 4-7$$

See Jacobson and Floberg (1957) and Olsson (1965).

The changes to Reynold's Equation are shown in Appendix C.

4.2.3 CAVITATION MODELLING

Oil film history models the oil flow in the cavitated region of the bearing by incorporating the fill ratio into Reynolds Equation as shown above. Damage can be caused to the bearing by the cavitation and reformation processes. Forstner and Struwe (2004) have used oil film history calculation in the study of damage in a connecting rod big end bearing.

Forstner and Struwe reviewed the types of cavitation damage seen in internal combustion engine bearings and their probable causes, explained in the previous chapter.

Commercially available bearing simulation programs are limited in that they make no attempt to calculate parameters that might be useful to a designer. Therefore it was decided to make a start at building in the calculation of a cavitation parameter.

The previous chapter discussed the generation of a cavitation parameter. The calculation was incorporated into the hydrodynamic program.

There is no calculation of dp/dt or $dp/d\theta$ in the solution of Reynold's Equation so it was calculated by taking the difference in pressure at each node from one calculation step to the next. It was found that the results can be very unsmooth. The length of each calculation step is variable within the programmed integration techniques, Runge-Kutta-

Cash-Karp, Bulirsch-Stoer and Newmark-Beta, and can be very small. This will tend to exaggerate any lack of smoothness in the results, which is a characteristic of differentiation in any case. Therefore, the results shown in chapter 6 are based on differentiation over the print interval (5 degrees of shaft rotation in this case) using straightforward $\delta p/\delta\theta$. More sophisticated methods of numerical differentiation may be desirable in the future.

The cavitation damage parameter is calculated by multiplying the cavitation velocity (dh/dt taken directly from the values in the Reynold's Equation solution) and the negative rate of change of pressure relative to shaft angle $-\delta p/\delta\theta$. As only positive dh/dt and negative $\delta p/\delta\theta$ contribute to cavitation damage, negative dh/dt and positive $\delta p/\delta\theta$ are ignored when calculating the cavitation damage parameter.

The cavitation damage parameter is calculated by the program at each results print angle. The values are calculated at each node.

4.2.4 ASPERITY CONTACT AND FLOW FACTORS

High forces lead to small oil film thickness, less than the composite surface roughness of the journal and bearing surfaces. The current model incorporates a linear contact algorithm based on the Hertz contact stiffness. Greenwood and Tripp (1971) developed polynomial expressions for the relationship between force and deflection for contacting surfaces in terms of the surface roughness. These expressions should be incorporated into the solver which currently uses linear contact stiffness.

Another effect of the surfaces approaching each other to give film thickness of the same order as the composite surface roughness is that the oil flow is not correctly modelled by Reynolds Equation. As with oil film history, it is possible to modify Reynolds Equation with flow factors that take the increased flow resistance into account.

4.2.5 LUBRICANT SUPPLY SYSTEM

Section 4.2.1 discussed body forces within Reynolds Equation. Another effect of high body forces is to modify the conditions in the oil supply system. Programs are available

commercially that can calculate pressures and flows in pipe networks under acceleration loadings. However, they do not have interfaces to bearing solvers. The problem is to couple the effect of accelerations on the lubricant supply with the body forces and oil film history effects in the bearing.

It will be necessary to write a 1-D oil flow program that incorporates body forces and multi-phase flow (due to cavitation). This will need to be coupled with the bearing solver which currently only recognises pressure boundary conditions. It will need to be able to work with fill ratio and flow rate boundary conditions.

The modifications to incorporate the oil supply system will also be part of the requirement to connect the two sides of the Full Floating Bearing. The calculations shown in section 7 assumed an oil supply groove on each side of the bearing. Real FFBs have oil holes connecting the two sides with the oil supply being to the bearing housing side only.

4.3 STIFFNESS AND DAMPING

Most rotor-dynamics calculations carry out a natural frequency calculation or a time marching calculation of the structural equations. These are usually solved using the Transfer Matrix Method with the bearings abstracted to stiffness and damping values. This works especially well for rotary machinery in which the static loading is large relative to the dynamic loading. Many people use the Short Bearing Approximation (SBA). This method assumes a parabolic pressure distribution axially in the bearing. It is only accurate for moderate eccentricity ratios, below about 0.6, and cannot model partial grooves.

There is a need for RHD and even EHD models to be used to produce stiffness and damping curves. The bearing program was developed to do this by calculating the change in load due to small perturbations in the eccentricity ratio in x and y directions about the loaded equilibrium position.

$$\begin{Bmatrix} \delta F_x \\ \delta F_y \end{Bmatrix} = \begin{bmatrix} K_{11} & K_{12} \\ K_{21} & K_{22} \end{bmatrix} \begin{Bmatrix} \delta x \\ \delta y \end{Bmatrix} \quad 4-8$$

$$[K] = \begin{bmatrix} \frac{\partial F_x}{\partial x} & \frac{\partial F_x}{\partial y} \\ \frac{\partial F_y}{\partial x} & \frac{\partial F_y}{\partial y} \end{bmatrix} \quad 4-9$$

The following figures show stiffness and damping coefficients for an example bearing. Childs (1993), Vance (1988) and Bannister (2000) show similar curves calculated analytically. The advantage of calculating them using numerical models is that higher eccentricity ratios (typical of more heavily loaded bearings) and more complex geometry such as partial grooves can be dealt with more accurately. The method can be used to design bearings and use the eight coefficients in a dynamic system model.

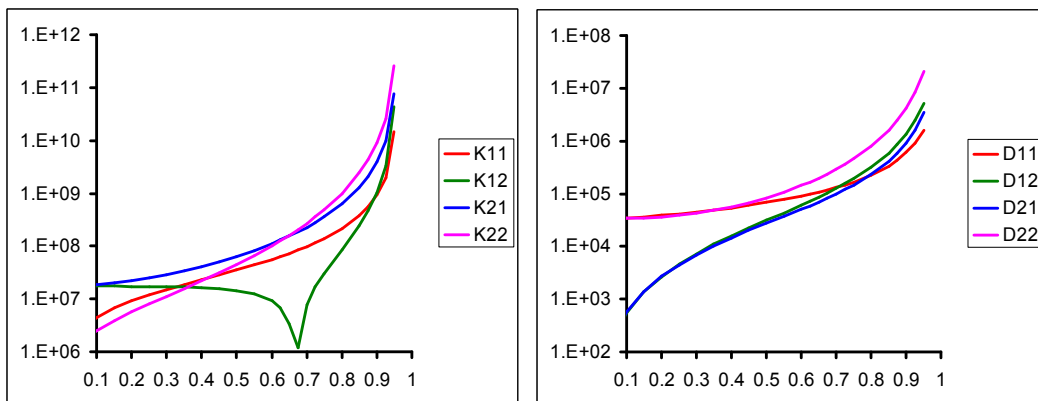


Figure 4-1 Automatically calculated bearing stiffness and damping coefficients (taken from McLuckie and Barrett (2007))

These curves and curves for other bearing geometries have been checked against the curves in the references (for the same L/D ratio) and found to agree extremely closely at small eccentricity ratios (below about 0.6) and depart at increasing ratios. Note that the coefficients have been transformed into the load frame of reference. This is normal for rotordynamic calculations with large gravity load.

4.4 EXTENSION TO PISTON, RINGS AND OTHER PRODUCTS

The journal bearing programs were written by the author. Work colleague Dr. BoonKai Teo extended the programs to carry out calculations for pistons and piston rings. Reynold's Equation remains the same as for a journal bearing but the calculation of position and velocity is different because the sliding velocity is now in line with the cylinder axis.

The equations of motion are also a little different because any axial offset between the centre of pressure and the gudgeon pin centre line causes the piston to tilt. The equation for transverse motion across the liner clearance space is similar to the journal bearing but with only one component

$$M \ddot{x} = F_{RHD}(x, \dot{x}, \theta, \dot{\theta}) + F_{external}(t) - D \dot{x} - K x \quad 4-10$$

and the tilt motion

$$I \ddot{\theta} = M_{RHD}(x, \dot{x}, \theta, \dot{\theta}) + M_{external}(t) - D \dot{\theta} - K \theta \quad 4-11$$

where the external forces and moments are calculated from the rigid body analysis of a perfect slider-crank mechanism. The hydrodynamic moment is the product of the hydrodynamic force and the difference in axial position between the centre of hydrodynamic force and the gudgeon pin centre line.

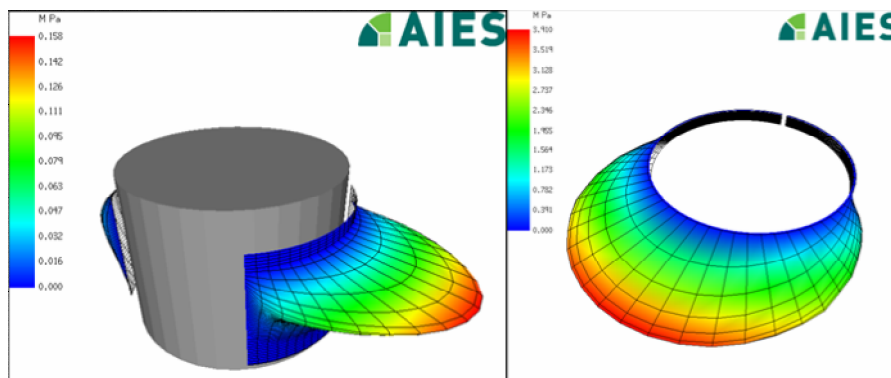


Figure 4-2 Piston and ring pressure distributions

The piston ring program will be extended to an EHD solution by the author in the future. Such a 3D solution for piston rings is not currently available in the market place and it can be expected to generate considerable interest.

A version of the program has also been adapted by a work colleague at AIES Ltd. for fixed pad thrust bearing calculations.

4.5 ELASTO-HYDRO-DYNAMICS

High pressure lubricated contacts distort sufficiently to affect the shape of the oil film and hence the pressure distribution. It is easily shown that a typical pressure distribution from an RHD calculation applied to a finite element model of bearing and housing can produce deformations of higher magnitude than the oil film clearance values that had been assumed to be constant.

An ElastoHydroDynamic (EHD) calculation that recognises the interaction between oil film solution and structural deformation requires simultaneous solution of the structural and fluid flow equations. A start was made at implementing such a procedure in 2D by Barrett (2001). Reynolds Equation with oil film history terms

$$\frac{\partial}{\partial x} \left(\frac{1}{12\eta} \theta \cdot h^3 \cdot \frac{\partial P}{\partial x} \right) + \frac{\partial}{\partial z} \left(\frac{1}{12\eta} \theta \cdot h^3 \cdot \frac{\partial P}{\partial z} \right) = \left(\frac{u_1 + u_2}{2} \right) \cdot \frac{\partial(\theta \cdot h)}{\partial x} + \frac{\partial(\theta \cdot h)}{\partial t} \quad 4-12$$

is coupled to the equations of motion for the journal

$$M_j \cdot \ddot{x}_j = F_{RHD}(x_j, \dot{x}_j) + F_{external}(t) - D \cdot \dot{x}_j - K \cdot x_j \quad 4-13$$

and the system of equations of motion of bearing housing node points

$$M_n \cdot \ddot{x}_n = F_{HD}(x_n, \dot{x}_n) - D \cdot \dot{x}_n - K \cdot x_n \quad 4-14$$

through the pressure (P) and oil film thickness (h) terms. The equations of motion now constitute a large system of equations including the journal centre motion and the motion of all of the active nodes on the bearing surface..

The current Rigid HydroDynamic (RHD) solution includes this coupling already but the movements at all nodes are the same (i.e. u and x are the same). The coupling between the structural and fluid flow equations takes place at the nodes. Finite elements with linear shape functions are used as these have consistent corner force directions. See Landenberger (1995 and 1998) for discussion of higher order elements for contact and similar situations.

Commercially available finite element programs often include a facility to write user subroutines. In principle, it would be possible to write the hydrodynamic solution as such a routine and run the entire EHD calculation in the finite element program. This is not practicable because of the long computer run times that would arise. The program would solve for the deformations and stress at every node point in the structure at every calculation step. The non-linear part of the calculation is the oil film. Therefore it is more efficient to extract a reduced stiffness and mass matrix applying just to the active nodes on the bearing surface from the finite element model and use it in the hydrodynamic program.

The assembled stiffness matrix for the structure can be partitioned into active nodes (to be retained), free nodes (no constraint) and constrained nodes. Appendix B shows how the matrix can be reduced to the active nodes. This is very useful for Multi Body Dynamics, contact studies and tribological studies where the overhead of solving matrix equations is very large. Some commercially available Finite Element programs provide this capability as standard.

For dynamic calculations it is desirable to include the mass matrix. This can be reduced in a similar way but most commercially available programs use the Guyan reduction method which is better at capturing the natural modes of vibration of the structure with lower numbers of degrees of freedom. See standard Finite Element references.

Once the reduced matrices have been obtained, the following equation is solved, similar to eqn. (2), but now the number of nodes is larger.

$$M_n \ddot{x}_n = F_{HD}(x_n, \dot{x}_n) - D \dot{x}_n - K x_n \quad 4-15$$

The RHD program of year 1 was extended to EHD in year 2.

Figure 4.3 shows the EHD behavior of a journal bearing at increasing flexibility of the housing. Note how the initial increase in flexibility spreads the load but further increase causes two distinct pressure peaks as the sides of the bearing housing deform.

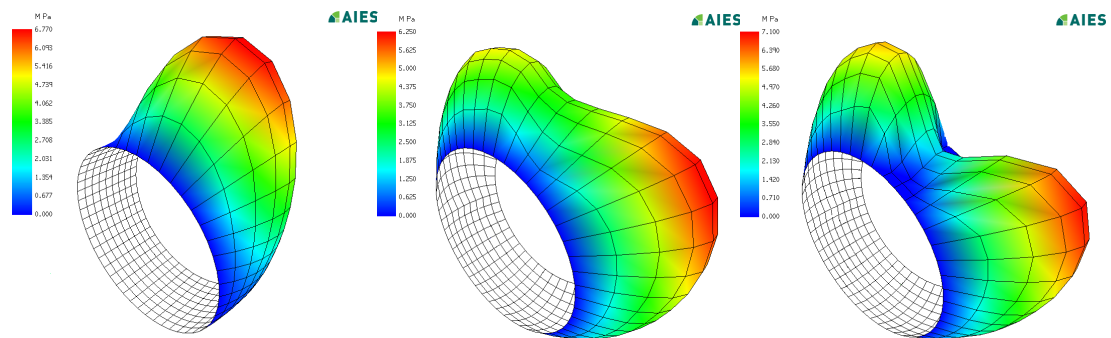


Figure 4-3 Oil film pressure for different bearing housing stiffness

This behaviour is well known and gives a basic confirmation of correct program operation. Further checks have compared pressure distribution against deflection between these calculations and the original finite element models.

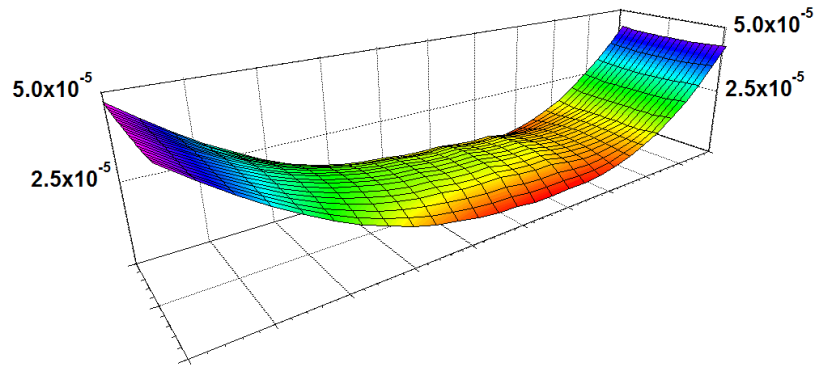


Figure 4-4 Oil film thickness at EHD contact

Figure 4.4 above shows the typical tendency of heavily loaded bearing oil film thickness to be a minimum at the edges of the bearing due to deformation under oil film pressure. Again, this behaviour at EHD contacts is well known.

Tests are continuing using the stiffness and mass matrices from the ABAQUS finite element models shown in Fig. 4.5 representing a connecting rod big end and a main bearing.

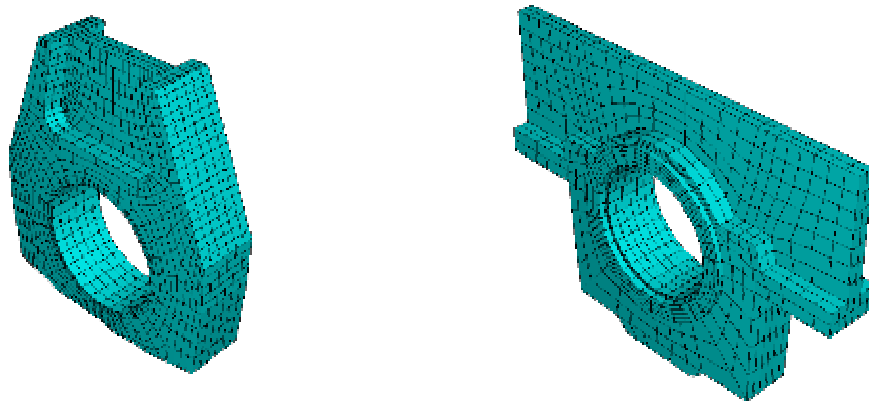


Figure 4-5 Finite Element models for matrix condensation

4.6 CALCULATION OF ENGINE BEARING FORCES

Section 3.5.2 shows the method used to calculate connecting rod forces. This was implemented in a Fortran program. The loads at each connecting rod big end were

resolved and moments calculated to obtain the loads on the engine main crankshaft bearings. This program, also in Fortran, uses the assumption that no bending moments are carried by the shaft at each main bearing position. This simplifies the calculation to a statically determinate problem. While this technique is common in the automotive industry, it is intended to calculate the bearing loads correctly in the future. Other approximate methods such as the moment-area method or Clapeyron's method may also be tried.

4.7 CALCULATION OF TURBOCHARGER BEARING FORCES

Chapter 3 describes the method of calculating the turbocharger bearing forces. This was implemented in a Fortran program. The program takes the mass, centre of gravity position and out of balance mass-radius products to calculate the bearing reactions and shaft bending moments versus speed.

The program includes the ability to apply additional forces in the form of Fourier coefficients. This is intended to enable studies of the excitation due to blade aerodynamic effects in the future.

Currently, the calculations are simple static resolving of forces and moments. It is intended to modify the program to carry out dynamic calculations in the future. This will be essential for machines running near or above the first bending frequency of the shaft.

CHAPTER 5

CALCULATION STUDIES

5.1 3 ENGINE FRICTION COMPARISON STUDY

Three current production reciprocating piston engines were studied for a customer. The confidential nature of this study means that the reference (McLuckie & Barrett, 2005a) is not in the public domain. The advantage of working with a customer was that they were able to supply real data, including test results.

Calculations were carried out for the crankshaft main bearings, connecting rod big and small end bearings, piston to piston pin bearings, camshaft bearings, the non-conforming contact between cam lobes and followers (by EHL calculation for a nominal line contact) plus the valve guides and various seals. The calculations were carried out for several speeds with and without cylinder pressure to simulate the standard motor industry ‘strip-down’ friction test.

5.2 V8 RACING ENGINE STUDY

The change in regulations in Formula 1 motor racing for the 2006 season included a change from engines with a V10 cylinder layout and 3 litres swept displacement to a V8 layout and 2.4 litre displacement. Conventional V8 engines for road use feature a crankshaft layout in which the crankpins are arranged in two planes. This is done to achieve a better balance of the reciprocating forces thus reducing vibration. Racing V8 engines often use a single plane crankshaft similar to that used in in-line 4 cylinder engines. The purpose is to give a stronger crankshaft and more equal distribution of gas flows in the exhaust systems on each side of the engine. However, some categories of V8 racing engine also use two plane crankshafts. The pressure to use motor sport to test green solutions makes the effect of design decisions on friction losses important so it was decided to investigate the effect of crankshaft layout on friction.

5.3 TURBOCHARGER STUDY

The next job tested the Full Floating Bearing (FFB) calculation capability. These bearings are used on turbocharger bearings. The developers of turbochargers don't usually use calculation programs but test a new turbocharger on a gas stand. Very small clearances are required to maintain stability over the speed range. Full Floating Bearings have an intermediate rotating ring. This effectively gives two bearings operating at a lower relative speed than the equivalent single bearing.

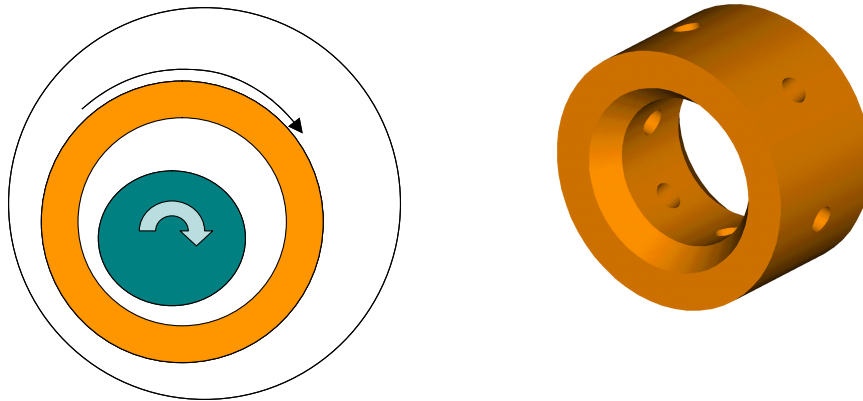


Figure 5-1 Typical Full Floating Bearing (Source McLuckie et al 2006)

Loads were calculated for typical turbocharger dimensions based on a real turbocharger. Different levels of unbalance loads were calculated from BS (6861-1) grade G1.0, G10 and G100 representing very accurate balance to gross unbalance. These values correspond to 0.023 to 2.3 g mm. Typical high speed turbo machinery is balanced to Grade 2.5.

The equations of motion for the shaft and the ring must be solved simultaneously with the two oil films. The RHD Reynold's Equation solution was modified to handle multiple oil films. The two equations of motion to be solved were

$$M_j \ddot{x}_j = F_{RHD}(x_j, \dot{x}_j) + F_{external}(t) - D \dot{x}_j - K x_j \quad 5-1$$

$$M_r \ddot{x}_r = F_{RHD}(x_r, \dot{x}_r) - F_{RHD}(x_j, \dot{x}_j) - D \dot{x}_r - K x_r \quad 5-2$$

Figure 5.2 shows typical force components at 20000 rev/min. The unbalance sinusoidal load increases with the square of the rotational velocity and quickly becomes orders of magnitude larger than the constant gravity load at higher speeds.

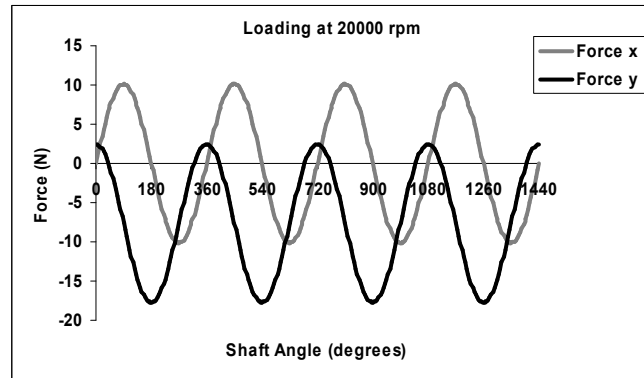


Figure 5-2 X and Y force components (2.3 gmm unbalance at 20000 rev/min)

Load cases were run for the turbine end bearing at a range of speeds from 1000 to 100000 rev/min. The unbalance was varied from 0.023 to 2.3 gmm and oil supply pressure from 0 bar to 4 bar.

5.4 REFINEMENT OF EHD CALCULATION METHODS USING TEST MODELS

The stiffness and mass matrices from the ABAQUS finite element models shown in Fig. 5.3 have been used for ElastoHydroDynamic calculations. They are connecting rod big ends for a high speed engine and small diesel engine and main bearing of the small diesel engine. Initial runs of the EHD program were found to be long and unreliable. These models were used to investigate the reasons and find solutions.

Fig. 5.4 shows the radial terms in the stiffness matrix for a much coarser mesh of one of the models. Note the negative terms away from the diagonal, sometimes within one node position. This can affect calculation stability and the investigation of this is shown

in a later section. It is not easy to distinguish the stiffness of the different regions of the bearing.

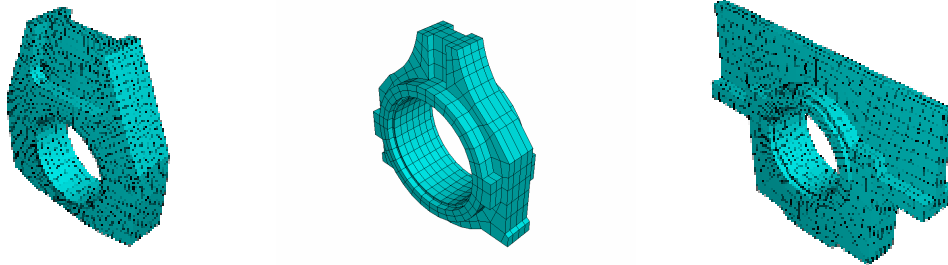


Figure 5-3 Finite Element models for matrix condensation

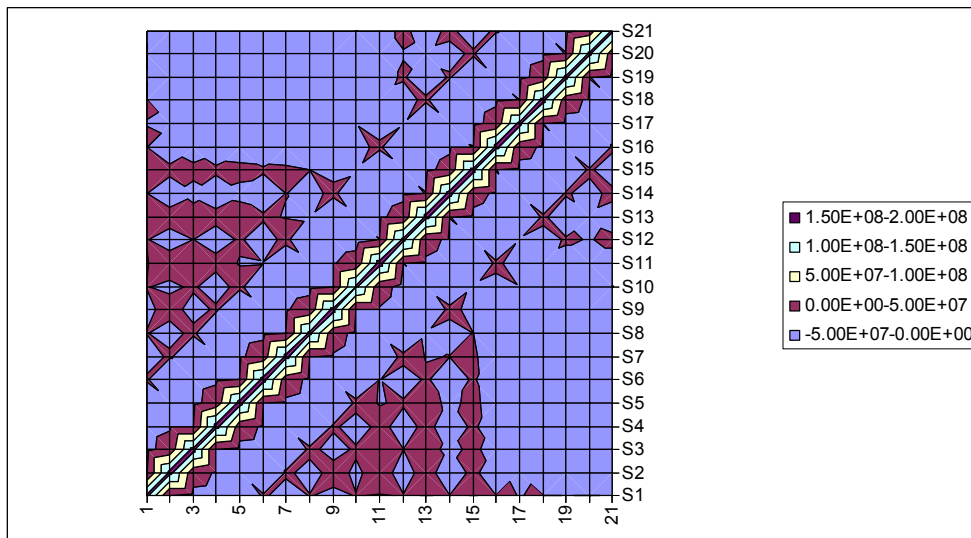


Figure 5-4 Typical Stiffness Array (Coarse Mesh)

The numbers on the x and y axes are the node numbers. The mesh was a 7 x 3 mesh with nodes numbered consecutively in the axial direction followed by the nodes at the next circumferential location.

Fig. 5.5 and 5.6 plot the radial stiffness diagonal terms around the bearing. The stiffness variation is not strong because the stiffness matrix is based on zero deflection at adjacent nodes. This makes stiffness matrix terms as indicative of mesh density variations as structural stiffness variations and these plots are not very useful.

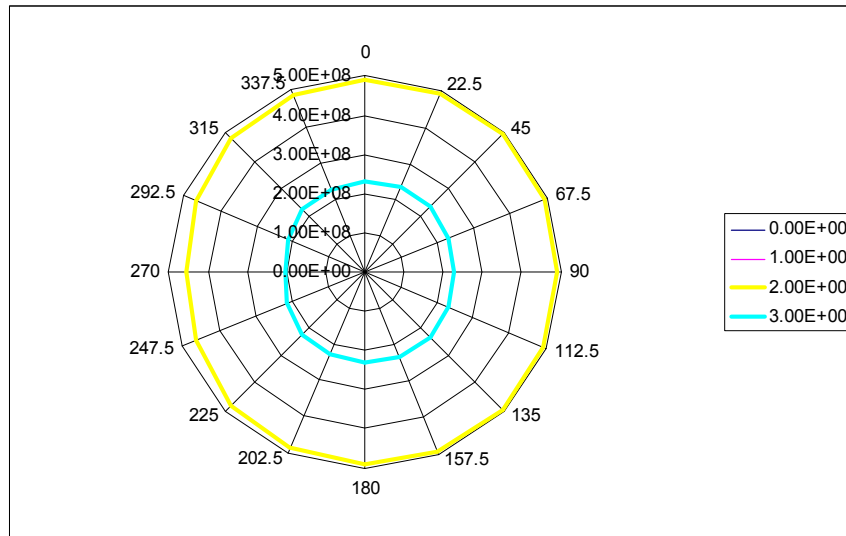


Figure 5-5 Stiffness diagonal terms plotted around the circumference at four axial positions

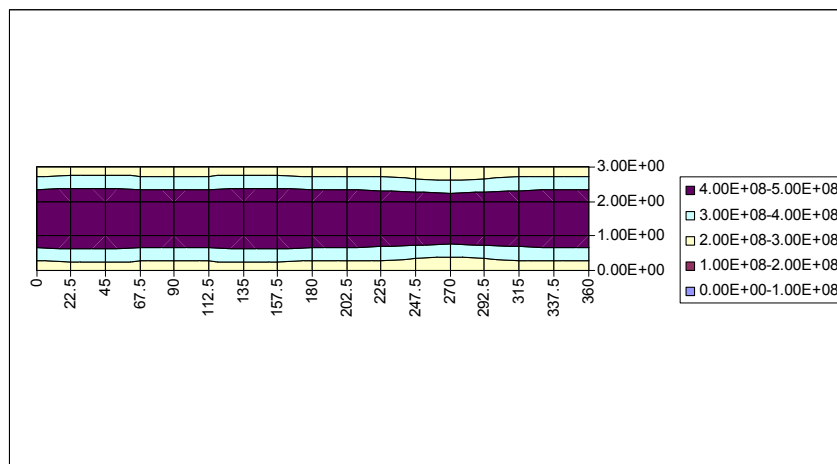


Figure 5-6 Stiffness diagonal terms plotted on the unwrapped bearing surface

Fig. 5.7 and 5.8 give a better representation of the local stiffness by calculating it from the compliance matrix (inverse of the stiffness matrix) and then taking the reciprocal of the diagonal value to give a stiffness value with no constraint on the adjacent nodes. Note that the model is constrained elsewhere on the mesh. The orientation of the model is that 90 degrees on the angular axis lies in the upwards direction. It is clear that the model is most flexible in the direction of the bearing cap as would be expected.

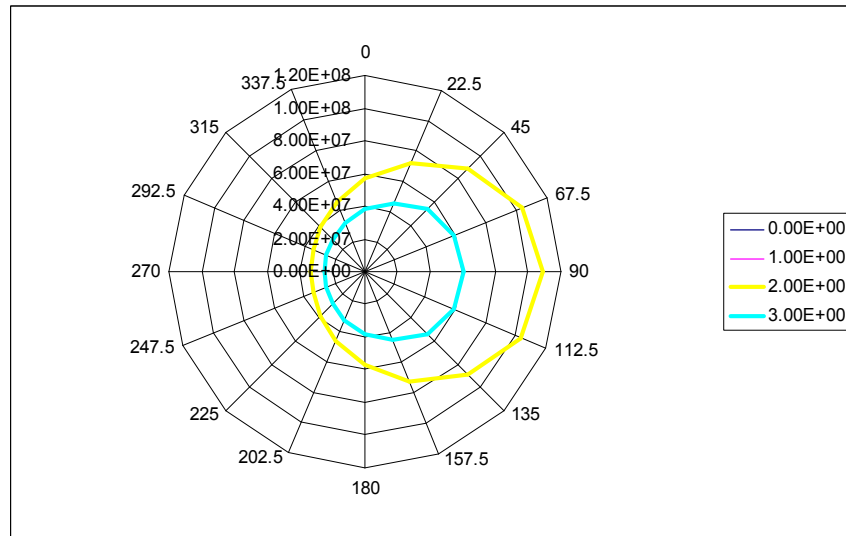


Figure 5-7 Inverse compliance diagonal terms plotted around the circumference at four axial positions

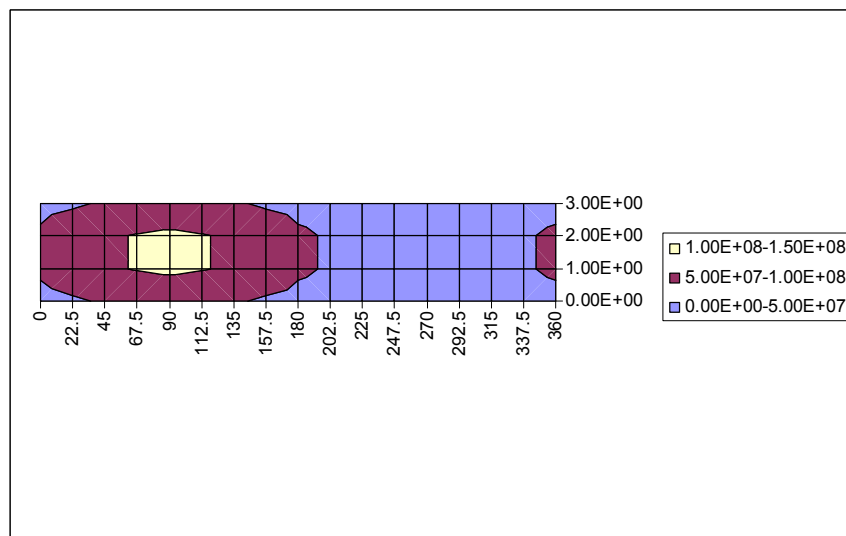


Figure 5-8 Inverse compliance diagonal terms plotted on the unwrapped bearing surface

Also note that the bearing is stiffer at the axial mid-plane than at the edges. These plots are very useful to show the stiffness variation around the bearing structure and could be used to assess the structure prior to carrying out EHD calculations as well as to explain the bearing behaviour when describing the EHD calculation results.

5.4.1 ORBIT ENVELOPE METHODS

A start was made on ideas for improving the calculation time for the ElastoHydroDynamic calculations by using an iterative approach.

Fig. 5.9 shows some initial results for the big end bearing of the high speed engine. The left hand plot shows the bearing orbit for an RHD calculation. The right hand plot shows the bearing orbit for the same bearing using EHD.

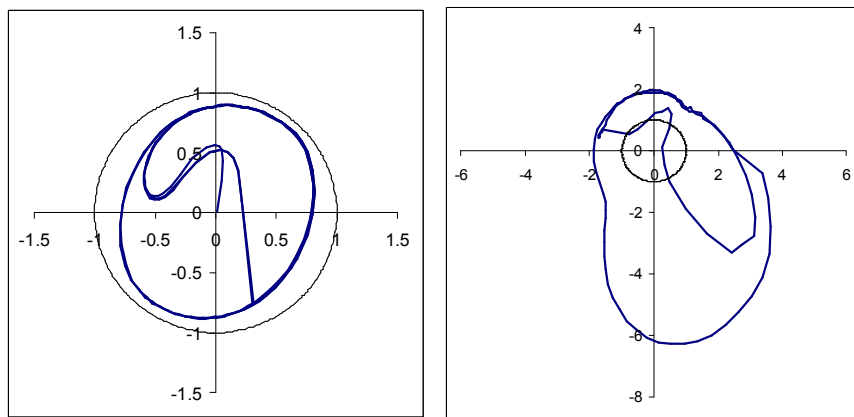


Figure 5-9 RHD calculation and EHD by iterative method for big end bearing of high speed engine at 16200 rpm

Note the very high eccentricity ratios for the EHD calculation which was expected for this very highly loaded bearing. Further work on this method was suspended when checking the results showed an error in the calculation of bearing deformation. The error was responsible for causing unreliability in the numerical integration approach that had been used until this point. Making the numerical integration robust was then pursued for the rest of the project and is shown in the following sections along with various investigations.

The iterative approach showed great promise and its development will be continued. Part of the motivation is to reduce the number of arithmetical operations caused by small time steps in the integration approach. The potential gain is to greatly reduce the time required to carry out EHD calculations.

5.4.2 STABILITY OF EHD MODELS

Although EHD results were shown in the second year report, it was then found to be impossible to guarantee successful program operation in all cases. Calculations at high shaft rotation frequencies were found to be especially problematic. This prompted investigations into the effect of adding damping to the equations of motion. There is also some tendency for deflection at one node on the finite element model to produce an opposite motion at the adjacent nodes. That is simply an illustration of the inaccuracy of finite element models at dealing with force or deflection distributions that are finer or similar in dimension to the mesh size. It was found that using a finer oil film Finite Difference mesh than the structural Finite Element mesh was especially important for improving calculation stability.

Different Mesh Densities FD/FE

Using a finer Finite Difference mesh to the Finite Element mesh enabled the pressure from each node of the oil film calculation to be spread over several structural nodes. Also, the change of oil film thickness at each oil film node could be interpolated from the structural node deflections. This reduced the tendency to produce ‘hour glass’ deflection modes, illustrated in one of the test cases in Fig. 5.10.

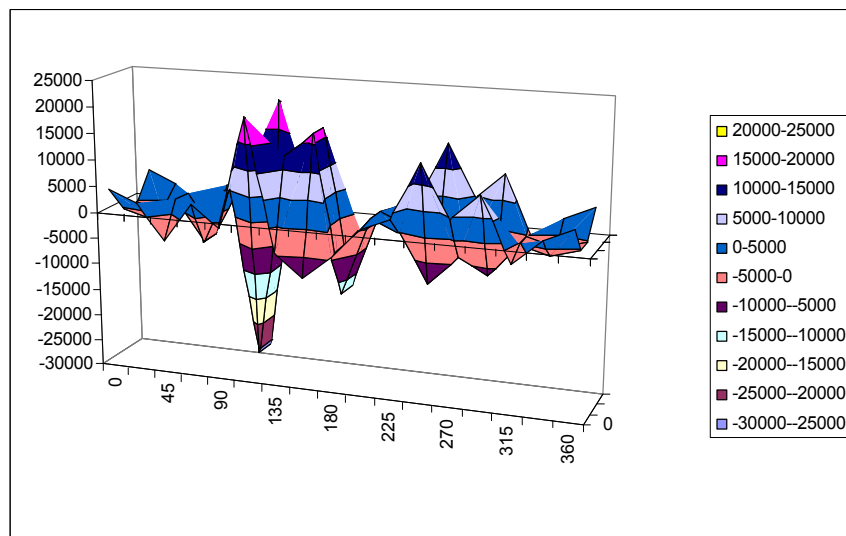


Figure 5-10 Typical acceleration distribution on the mesh

The acceleration at each node is often very different to the acceleration at the adjacent nodes, in many cases even being the opposite sign. The example shown was a distribution of radial accelerations on the surface of a bearing at a single time step.

Fig. 5.11 shows a ratio of 3:1 between the FD mesh and FE mesh which was found to be successful.

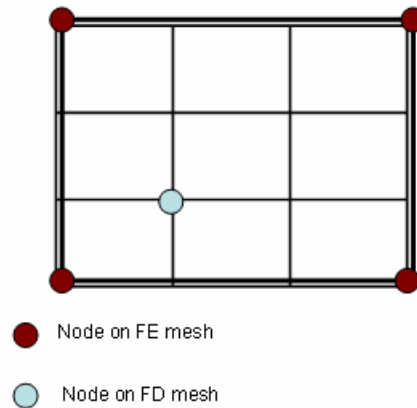


Figure 5-11 Data transfer between dissimilar FE and FD meshes

The deflections and pressures were simply interpolated between the two meshes.

In the case of coarse models this also required a capability to coarsen the reduced mass and stiffness matrices. A reason for this is the difficulty of producing good quality meshes without highly distorted elements with low number of nodes on the bearing surface. Therefore, it may be preferable to reduce the stiffness and mass matrices on the bearing surface to the mesh density required than create a very coarse finite element model. These equations are shown here.

$$\begin{Bmatrix} F_1 \\ F_2 \\ F_3 \\ F_4 \end{Bmatrix} = \begin{bmatrix} K_{11} & K_{12} & K_{13} & K_{14} \\ K_{21} & K_{22} & K_{23} & K_{24} \\ K_{31} & K_{32} & K_{33} & K_{34} \\ K_{41} & K_{42} & K_{43} & K_{44} \end{bmatrix} \begin{Bmatrix} \delta_1 \\ \delta_2 \\ \delta_3 \\ \delta_4 \end{Bmatrix} \quad 5-3$$

Where subscripts 1 & 3 = nodes to be retained either side of the nodes to be eliminated, 2 = nodes to be eliminated between the retained nodes, 4 = nodes not involved

Step 1 eliminates the displacements at the nodes to be removed by constraining them to the average displacement of the adjacent nodes - $\delta_2 = \frac{1}{2}(\delta_1 + \delta_3)$ leading to

$$\begin{Bmatrix} F_1 \\ F_2 \\ F_3 \\ F_4 \end{Bmatrix} = \begin{bmatrix} K_{11}^* & K_{13}^* & K_{14}^* \\ K_{21}^* & K_{23}^* & K_{24}^* \\ K_{31}^* & K_{33}^* & K_{34}^* \\ K_{41}^* & K_{43}^* & K_{44}^* \end{bmatrix} \begin{Bmatrix} \delta_1 \\ \delta_3 \\ \delta_4 \end{Bmatrix} \quad 5-4$$

where $K_{nm}^* = K_{nm} + \frac{1}{2}K_{n2}$, $n=1$ to 4 , $m = 1, 3$

Step 2 eliminates force at the nodes to be removed by distributing to the adjacent nodes - $F_1 = F_1 + \frac{1}{2}F_2$ and $F_3 = F_3 + \frac{1}{2}F_2$ leading to

$$\begin{Bmatrix} F_1 \\ F_3 \\ F_4 \end{Bmatrix} = \begin{bmatrix} K_{11}^{**} & K_{13}^{**} & K_{14}^{**} \\ K_{31}^{**} & K_{33}^{**} & K_{34}^{**} \\ K_{41}^* & K_{43}^* & K_{44} \end{bmatrix} \begin{Bmatrix} \delta_1 \\ \delta_3 \\ \delta_4 \end{Bmatrix} \quad 5-5$$

where $K_{nm}^{**} = K_{nm}^* + \frac{1}{2}K_{2m}^*$, $n=1,3$, $m=1,3,4$

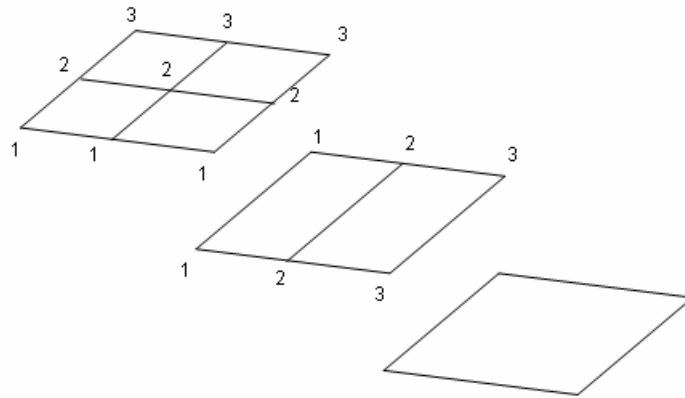


Figure 5-12 Steps to coarsen FE mesh matrices

The steps above are carried out to coarsen the mesh in one direction, then the other as illustrated in Fig.5.12.

Mesh symmetrisation

The RHD solver was already able to detect symmetry of the bearing boundary conditions (including grooves and oil holes) about the centre line and perform the Successive Over Relaxation solution of Reynold's Equation on half of the mesh. EHD calculations take much longer, hours instead of minutes for a full internal combustion engine cycle. Therefore, a routine was written to detect symmetry from the terms in the stiffness and mass matrix diagonals and automatically reduce the matrices. This is more complex for the FE model than for the FD model because the matrices are fully populated.

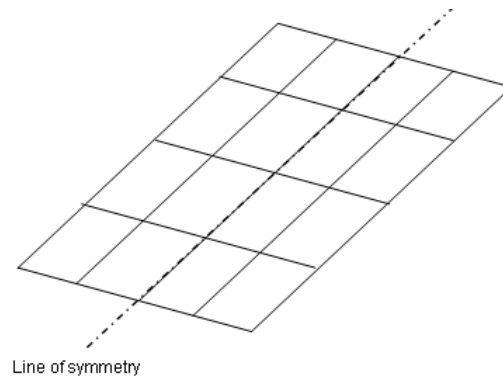


Figure 5-13 FE model symmetry

Fig. 5.13 shows the line of symmetry on the unwrapped bearing faces of the FE mesh. At present the mesh itself is symmetric in all cases but the values in the stiffness and mass matrices depend on the rest of the geometry and the constraints. If these matrices are found to be symmetric the following transformations are used to create further reduced matrices.

The matrices can be partitioned:

$$\begin{Bmatrix} F_1 \\ F_S \\ F_2 \end{Bmatrix} = \begin{bmatrix} K_{11} & K_{1S} & K_{12} \\ K_{S1} & K_{SS} & K_{S2} \\ K_{21} & K_{2S} & K_{22} \end{bmatrix} \begin{Bmatrix} \delta_1 \\ \delta_S \\ \delta_2 \end{Bmatrix} + \begin{bmatrix} M_{11} & M_{1S} & M_{12} \\ M_{S1} & M_{SS} & M_{S2} \\ M_{21} & M_{2S} & M_{22} \end{bmatrix} \begin{Bmatrix} a_1 \\ a_S \\ a_2 \end{Bmatrix} \quad 5-6$$

Where subscripts 1 = nodes to be kept, 2 = symmetric nodes to be eliminated, s = nodes on the symmetry line if any

$F_1 = F_2$ and $\delta_1 = \delta_2$ enabling use to transform the stiffness matrix to

$$\begin{Bmatrix} F_1 \\ F_S \end{Bmatrix} = \begin{bmatrix} K_{11}^* & K_{1S} \\ K_{S1}^* & K_{SS} \end{bmatrix} \begin{Bmatrix} \delta_1 \\ \delta_S \end{Bmatrix} + \begin{bmatrix} M_{11}^* & M_{1S} \\ M_{S1}^* & M_{SS} \end{bmatrix} \begin{Bmatrix} a_1 \\ a_S \end{Bmatrix} \quad 5-7$$

Where $K_{11}^* = K_{11} + K_{12}$ and similarly for $K_{S1}^*, M_{11}^*, M_{S1}^*$

5.4.3 DAMPING

Damping of the structure and Fourier smoothing of the pressure distribution were found to be highly effective at improving calculation stability.

The most obvious damping method is simple damping at each degree of freedom i.e. on the matrix diagonals only. The equations of motion are shown here.

$$\{F\} = [M]\{a\} + [D]\{v\} + [K]\{x\} \quad 5-8$$

for the nodes on the structure. The calculation that is performed in the program is to integrate the accelerations from re-arranging the equation

$$\{a\} = [M]^{-1}\{F\} - [M]^{-1}[D]\{v\} - [M]^{-1}[K]\{x\} \quad 5-9$$

Typical mass and stiffness diagonal terms are 0.1×10^{-3} kg and 0.1×10^9 Nm⁻¹, giving a critical damping value of approximately 100 Nsm⁻¹. Simple scalar damping was added to the program and values either side of the critical value tested, shown below.

Rayleigh damping is often used for structural dynamic calculations because of its ability to damp low and high frequencies more than medium frequencies. Instead of using simple scalar value for the damping, a full matrix is used based on the stiffness and mass matrices

$$[D] = \beta[K] + \alpha[M] \quad 5-10$$

leading to calculation of the acceleration

$$\{a\} = [M]^{-1}\{F\} - \alpha\{v\} - [M]^{-1}[K](\beta\{v\} + \{x\})$$

5-11

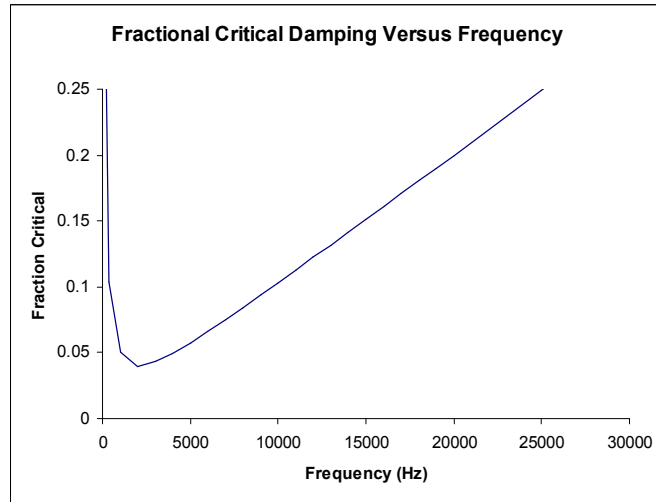


Figure 5-14 Effect of Rayleigh damping on different frequencies

Figure 5.14 shows the effect of Rayleigh damping versus frequency for a single degree of freedom using $\alpha = 503.9$ and $\beta = 3.15 \times 10^{-6}$. This corresponds to 0.05 times critical damping at 1000 Hz and 0.2 times critical damping at 20000 Hz.

The results of calculations are shown in the next chapter.

5.5 ENGINE BEARING STUDIES

The finite element models in Fig. 5.15 were used to investigate the magnitude of EHD effects.

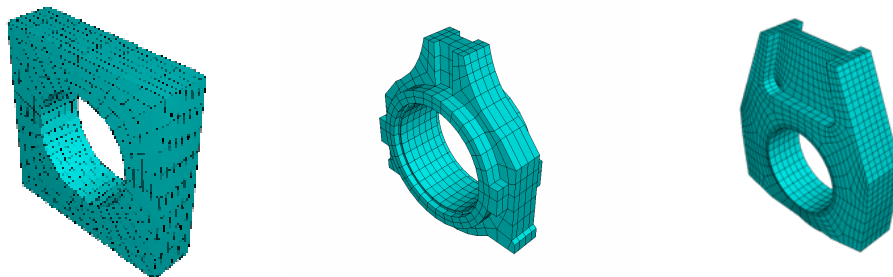


Figure 5-15 EHD Meshes

The first mesh was an approximation to a diesel engine main bearing and was chosen to run first as it was relatively stiff. The second mesh was the big end of the connecting rod from the same diesel engine.

The third mesh was an approximation of a Formula 1 racing connecting rod big end. Although obviously a very stiff structure, the much higher loads applied to this bearing could be expected to produce high deformations. In addition to simply checking the operation of the program and observing the difference between RHD and EHD calculations, this model was also used for some more studies. These included the effects of mesh density, model mechanical constraint, thermal loading and the influence of oil feed hole position.

The second mesh was also used for testing the cavitation damage parameter. The reason for choosing this engine and bearing is that it is the connecting rod big end bearing of a diesel engine as examined in Forstner and Struwe (2004), albeit a smaller engine. It had also been modelled in EHD with the mesh shown, allowing the effect of EHD deformations on the cavitation damage parameter to be examined.

The results of the calculations are shown in the next chapter.

CHAPTER 6

RESULTS OF CALCULATIONS

6.1 3 ENGINE FRICTION COMPARISON STUDY

The results of the calculations clearly showed the large effect of the cylinder gas pressure loading on friction losses for a diesel engine. They also showed the importance of low speed friction both due to the non-conforming contacts at the cam to follower contact surfaces and the Stribeck effect in the camshaft journal bearings due to camshaft drive system loads. The AIES bearing calculation programs include a contact algorithm that shares the load between the fluid film and asperities when the theoretical film thickness drops below the composite surface roughness of the bearing surfaces.

Engine friction studies are not part of the aims of the EngD project. The 3 engine study is reported here briefly because it was the first application of the Rigid Hydrodynamic solver that also solved the equations of motion of the shaft system. This program was then further developed during the year and used in the following two studies.

6.2 V8 RACING ENGINE STUDY

The results of these calculations were reported in a paper (McLuckie and Barrett, 2005b) that was presented by the author at the ASME/DETC conference in Long Beach. The results for the heavily loaded centre main bearing are summarised in the following figures and show that the planar crankshaft gives lower friction at the higher speeds but significantly higher loads on the centre main bearings. The Rigid Hydrodynamic program solved the equations of motion for the shaft using the Bulirsch-Stoer numerical integration method.

Figs. 6.1 and 6.2 show the loads on the centre main bearing versus crankshaft angle at maximum engine speed for the two crankshaft arrangements. The higher loads due to the planar crankshaft can be seen clearly.

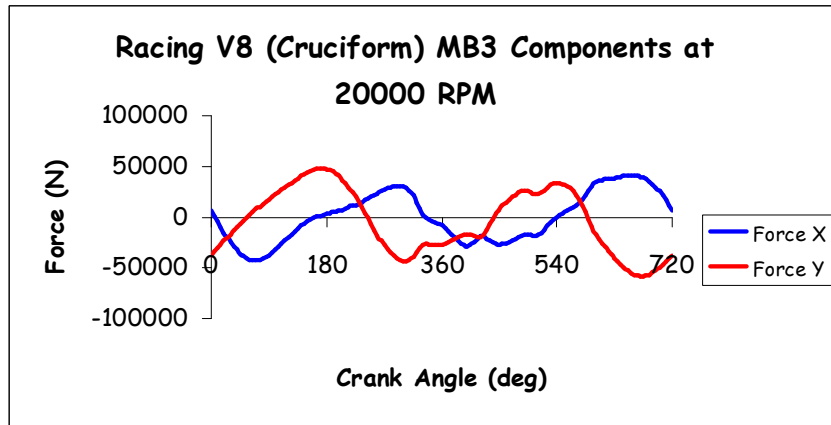


Figure 6-1 Loads on Centre Main Bearing (Two Plane Crankshaft) (Source McLuckie & Barrett 2005b)

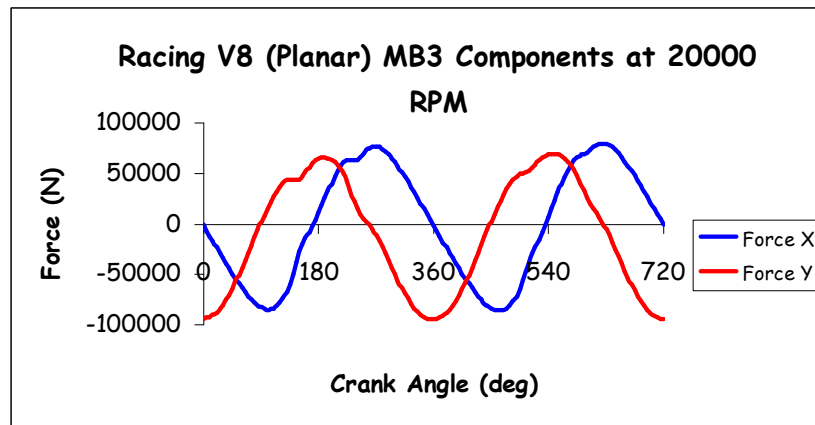


Figure 6-2 Loads on Centre Main Bearing (Single Plane Crankshaft) (Source McLuckie & Barrett 2005b)

Figs. 6.3 and 6.4 show the accelerations of the shafts within the clearance space.

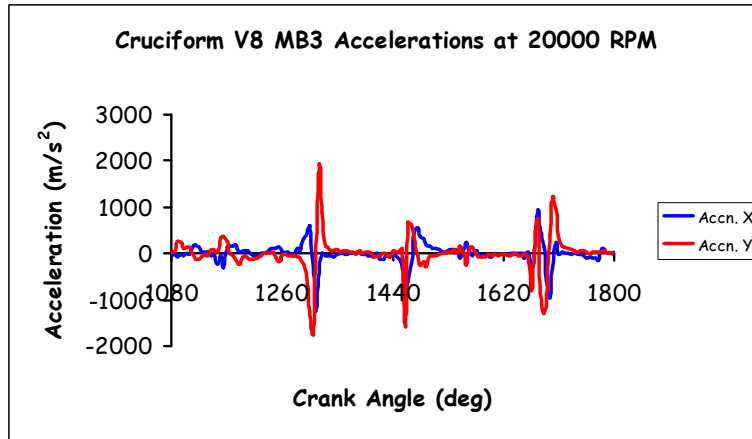


Figure 6-3 Acceleration of Centre Main Journal (Two Plane Crankshaft) (Source McLuckie & Barrett 2005b)

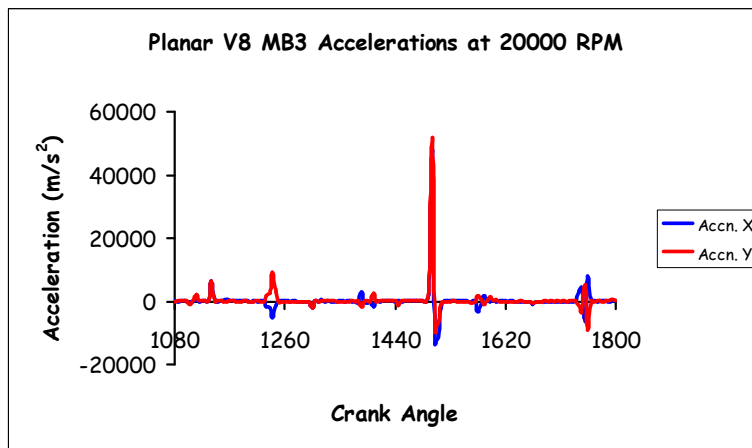


Figure 6-4 Acceleration of Centre Main Journal (Single Plane Crankshaft) (Source McLuckie & Barrett 2005b)

Figures 6.5 and 6.6 show the very large bearing orbits with small film thicknesses (below 1 μm) and high maximum oil film pressure (above 500 MPa).

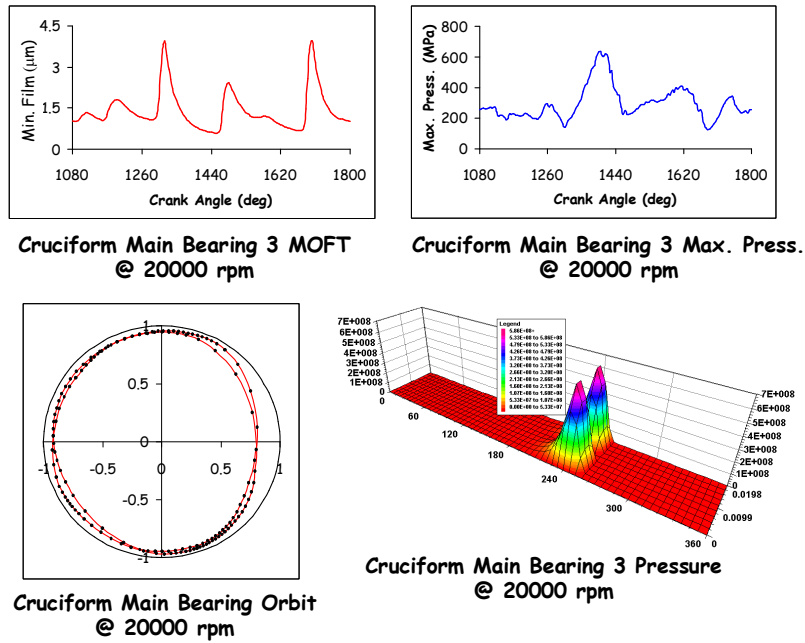


Figure 6-5 Centre Main Bearing Results (Two Plane Crankshaft) (Source McLuckie & Barrett 2005b)

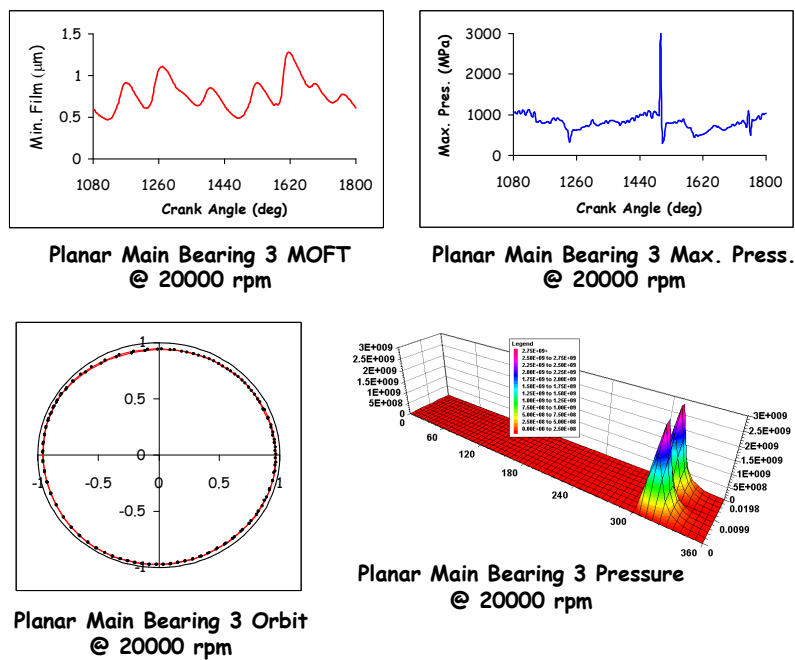


Figure 6-6 Centre Main Bearing Results (Single Plane Crankshaft) (Source McLuckie & Barrett 2005b)

Such high film pressures indicate that Elasto-Hydrodynamic solution would be more accurate. Fig. 6.7 shows that the centre main bearing is the most heavily loaded for both

crankshaft arrangements. The distribution of load is very uneven for the planar crankshaft.

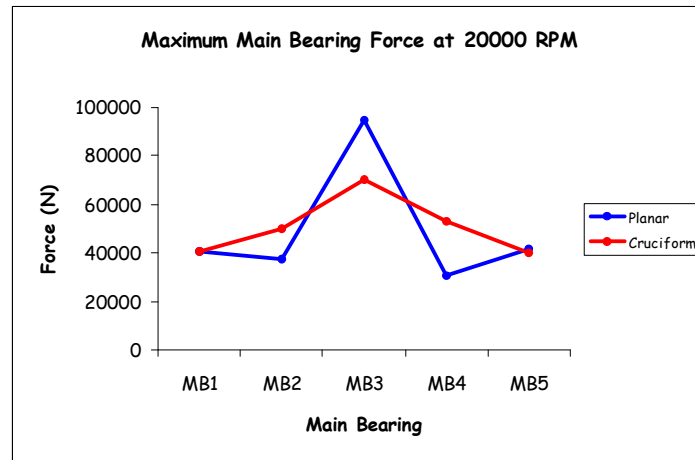


Figure 6-7 Main Bearing Loads at 20000 rev/min (Source McLuckie & Barrett 2005b)

This helps to explain how the planar crankshaft gives higher loads but slightly lower friction at high speed, shown in Fig. 6.8.

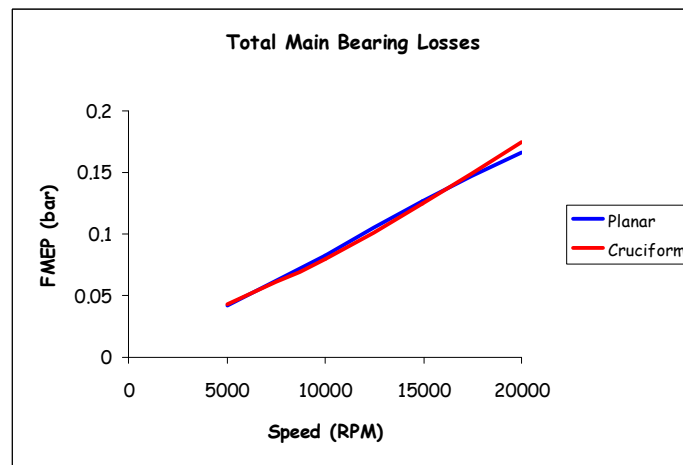


Figure 6-8 Friction Loss Comparison (Source McLuckie & Barrett 2005b)

6.3 TURBOCHARGER STUDY

The effects of bearing clearance and varying the unbalance were studied for simple plain bearings and for full floating bearings. The results were reported in McLuckie et

al. (2006). Reducing the clearance, reducing the oil feed pressure and increasing the level of unbalance increased the speed of onset of instability. However, it was not possible to obtain stable bearing operation above 30000 rev/min for plain bearings. Some of the bearing orbits are shown in the following figures and agree well with Dr. McLuckie's previous experience including his PhD project at Cranfield University (McLuckie, 1990).

Full floating bearings increased the onset speed of instability up to the required speed of 100000 rev/min provided that large unbalance factor is used.

The effect of low oil feed pressure and high unbalance in suppressing bearing instability may seem counter intuitive. It can be explained in terms of bearing oil film stiffness which increases with increasing orbit eccentricity. The results agreed qualitatively with the experimental work reported by san Andres and Kerth (2004).

The first calculations were carried out for a Plain Grooved Bearing (PGB) with diametral clearance from 4 μ m to 16 μ m for later comparison with the Full Floating Bearing (FFB). Figure 6.9 shows just one set of results at a range of speeds. Each plot is for a single revolution of the shaft. It can be seen that the journal locus starts by moving synchronously with shaft rotation at low speeds where the unbalance load is small relative to the gravity load. The locus is a small full revolution about the equilibrium position from the gravity load. At higher speed the locus becomes unstable and can be seen moving outwards and becoming sub-synchronous. At very high speeds the locus becomes larger, almost filling the clearance space, progressively closer to being centred on the bearing axis and the ratio of whirl speed to shaft speed becomes approximately 0.5. This shows classical whirl onset. Figures 6.9 to 6.16 were produced by the author's colleague Dr. BoonKai Teo using the program developed by the author. They have been published in McLuckie, Barrett and Teo (2006).

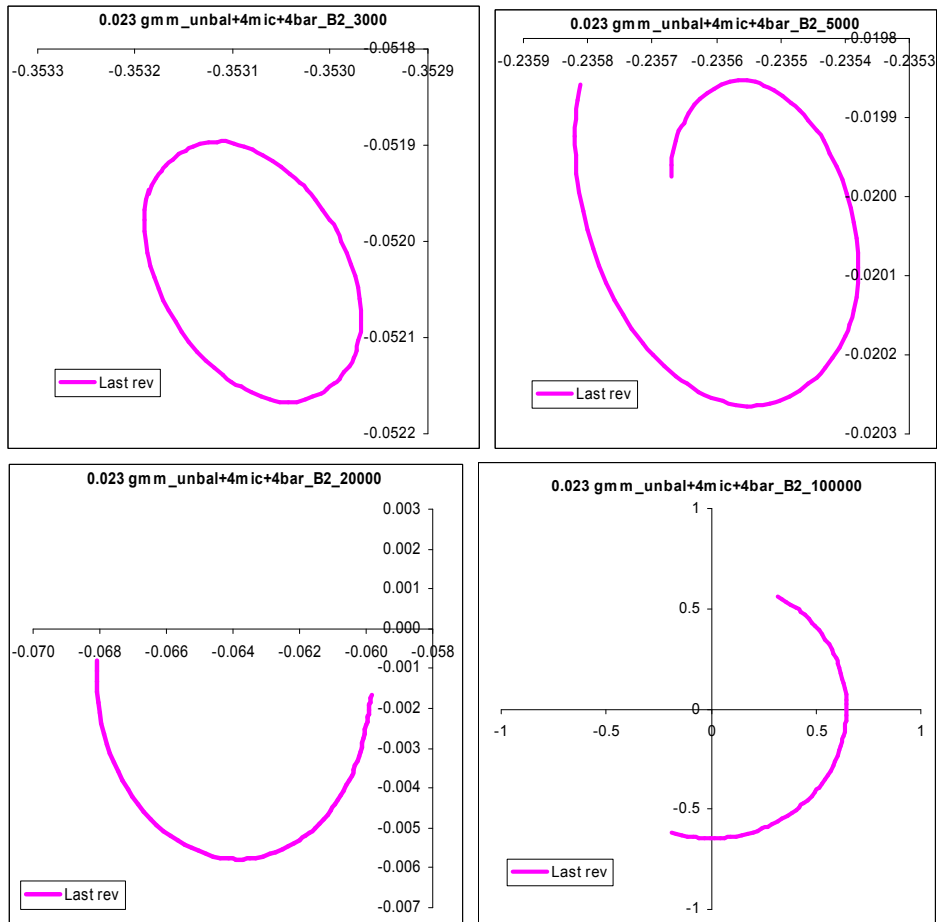


Figure 6-9 Turbine end PGB journal orbit (0.023gmm unbalance, 4 micron Clearance & 4 bar oil supply pressure) at 3000, 5000, 20000 and 100000 rev/min

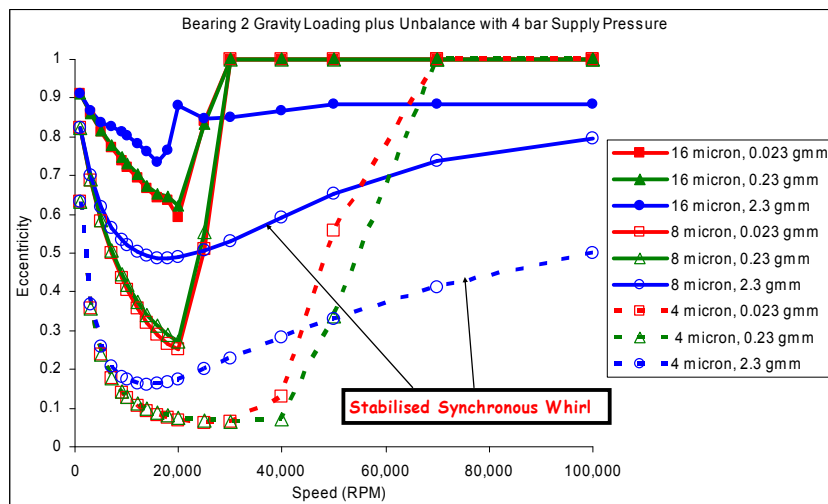


Figure 6-10 Turbine end PGB journal maximum eccentricity ratio versus speed with 4 – 16 micron clearance, 0.023 – 2.3gmm unbalance & 4 bar supply

Figure 6.10 plots the maximum eccentricity ratio of the locus at each speed for 4 bar oil supply pressure. It can be seen that the eccentricity ratio starts by reducing as the speed increases. This is to be expected as the wedge action of the oil film increases with speed. However, the unbalance load increases with the square of the speed and the oil film stiffness reduces as the film thickness increases. The onset speed for instability can be seen clearly as a sudden jump in the maximum eccentricity.

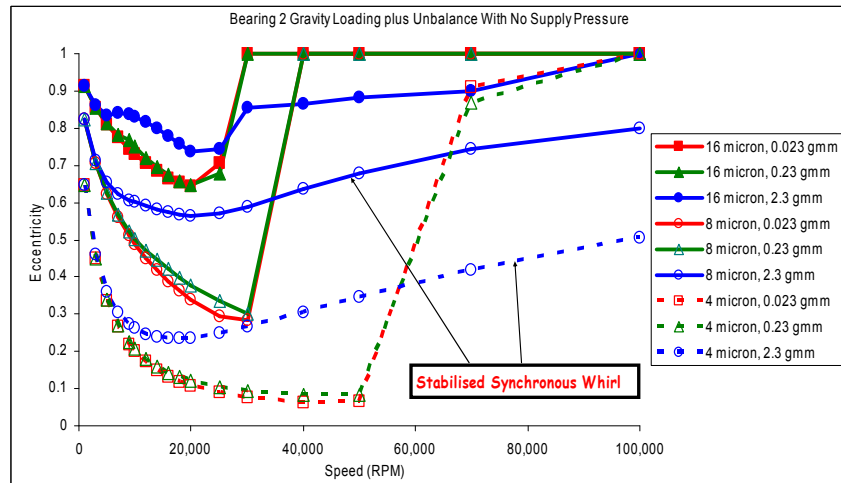


Figure 6-11 Turbine end PGB journal maximum eccentricity ratio versus speed with 4 - 16 micron clearance, 0.023gmm – 2.3gmm unbalance and 0 bar oil supply

Figure 6.11 shows the same results for zero oil supply pressure. It is interesting to note that the speed at which instability starts is increased. This can be explained by the effect of higher oil supply pressure tending to centralise the shaft in the bearing leading to lower oil film stiffness. The effect can also be seen clearly in Table 6.1

Table 6-1 Turbine end PGB sub-synchronous (half frequency) whirl onset speed

PGB Bearing Variants	Half Frequency Onset Speed (rpm)		
	4 Bar	2 Bar	0 Bar
16 micron, 0.0 gmm	7000	12000	12000
16 micron, 0.023 gmm	9000	14000	14000
16 micron, 0.23 gmm	14000	16000	16000
16 micron, 2.3 gmm	18000	20000	25000
8 micron, 0.0 gmm	12000	18000	20000
8 micron, 0.023 gmm	16000	25000	25000
8 micron, 0.23 gmm	18000	25000	30000
8 micron, 2.3 gmm	NA	NA	NA
4 micron, 0.0 gmm	5000	10000	16000
4 micron, 0.023 gmm	5000	14000	25000
4 micron, 0.23 gmm	12000	25000	35000
4 micron, 2.3 gmm	NA	NA	NA

Note that increasing the unbalance stabilises the journal orbit. This is due to the higher stiffness of the oil film. The journal orbits synchronously over the whole speed range used for the 4 μm and 8 μm diametral clearance and 2.3 gmm unbalance. Such gross unbalance would not normally be used.

Calculations were then carried out for the Full Floating Bearing (FFB) with 7 μm outer and 2.5 μm inner diametral clearances. Figure 6.12 shows remarkably similar journal loci to those shown above for the Plain Grooved Bearing (PGB).

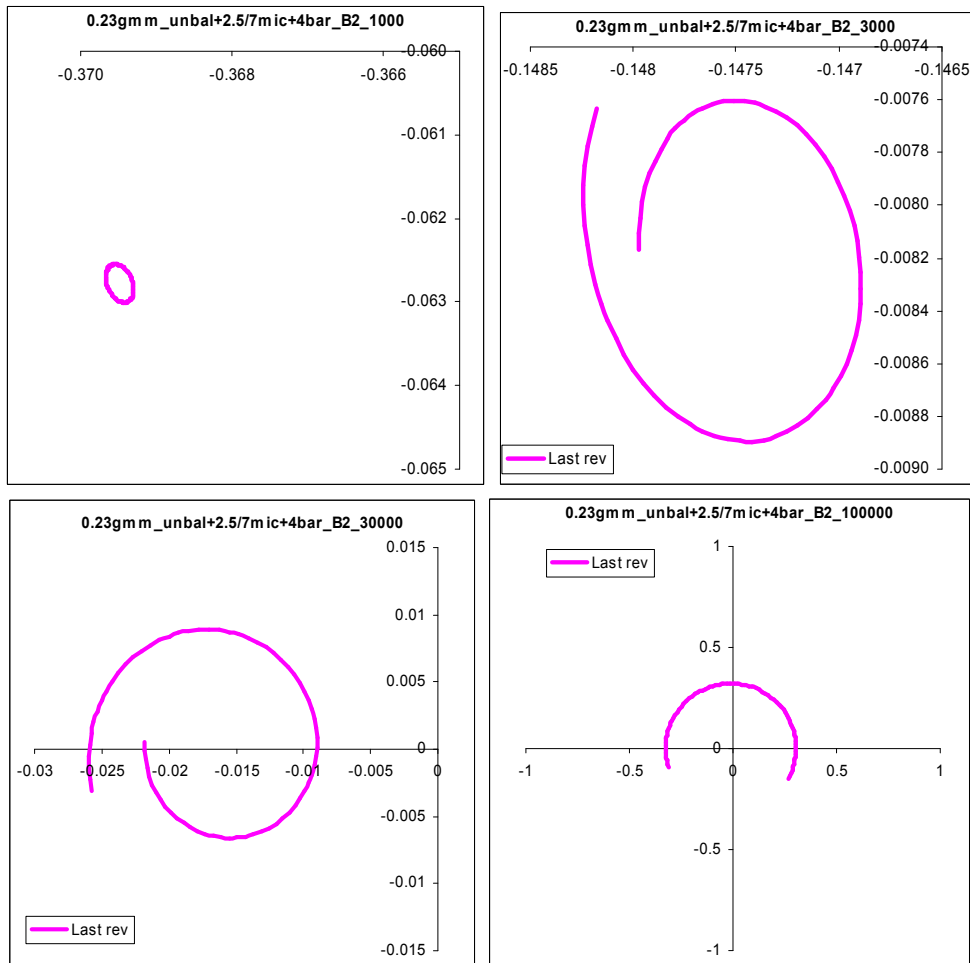


Figure 6-12 Turbine end FFB journal locus (0.23gmm, 2.5 micron inner/7 micron outer clearance, and supply pressure of 4 bar) at 1000, 3000, 30000 and 100000 rev/min

The shaft speed was varied over the same speed range as for the PGB. In these calculations the ring speed was set at 0.25 x the shaft speed. San Andres and Kerth (2004) show that this is a typical speed ratio. The program is capable of solving the system of equations including the rotary acceleration of the ring but the full set of test jobs has not yet been tried with the ring rotary speed unconstrained. It can be seen that the sub-synchronous orbit at 100000 rev/min is not at 0.5 x shaft speed but is at a slightly higher ratio, reflecting the relative speeds of shaft and ring.

Figure 6.13 shows some typical loci for the ring and these are very different. At low speeds the orbit of the ring is sub-synchronous at approximately 1/8 of the shaft speed, which is approximately half the ring speed. However, at higher speeds the motion

becomes synchronous with the shaft and the orbit becomes smaller before increasing again as the unbalance load increases with speed.

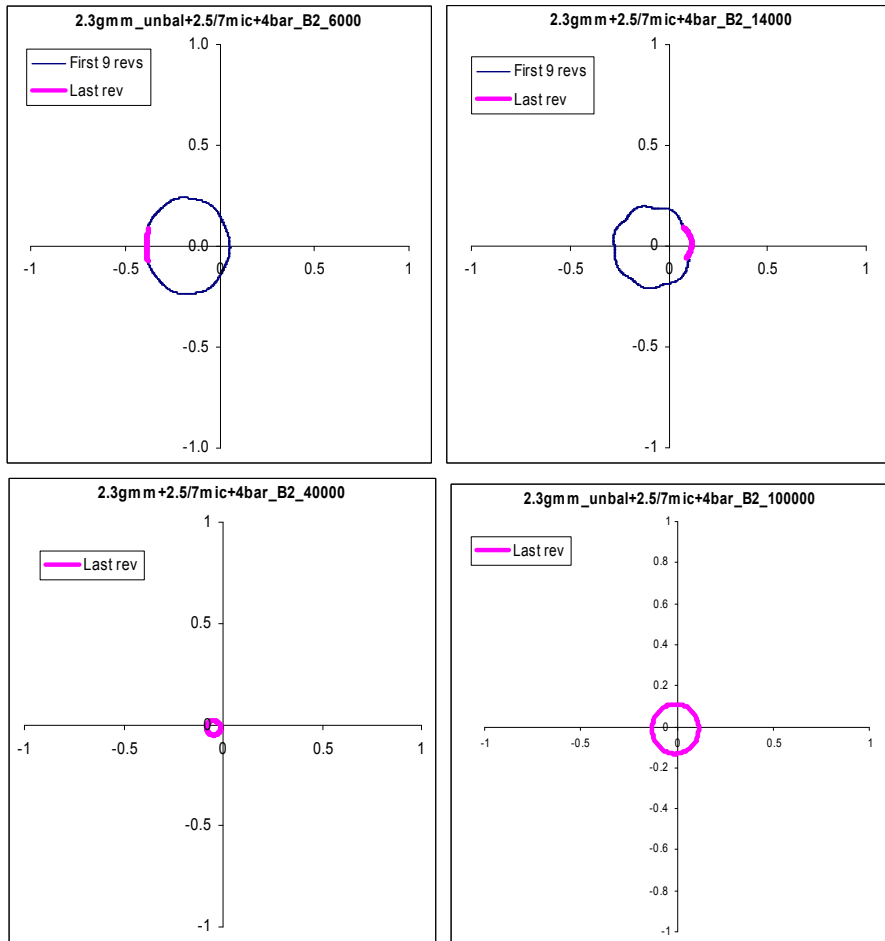


Figure 6-13 Turbine end FFB ring locus (2.3gmm, 2.5 micron inner/7 micron outer clearance, 4 bar) at 6000, 14000, 40000 and 100000 rev/min

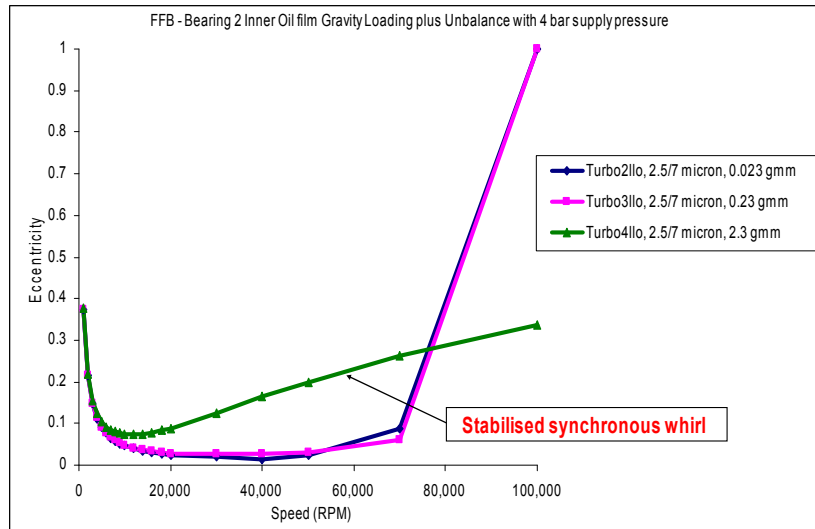


Figure 6-14 Turbine end FFB journal (2.5/7 micron clearance, 0.023gmm – 2.3gmm unbalance, 4 bar) inner bearing eccentricity vs. speed

Figure 6.14 plots the maximum eccentricity ratio at each speed for the inner oil film and, again, we see that there is a speed at which instability causes a sudden jump in the eccentricity ratio. Also, we again see the beneficial effect on bearing stability of a large unbalance load, producing synchronous whirl through the whole speed range.

Figure 6.15 shows no sudden onset of instability at high speeds for the outer oil film.

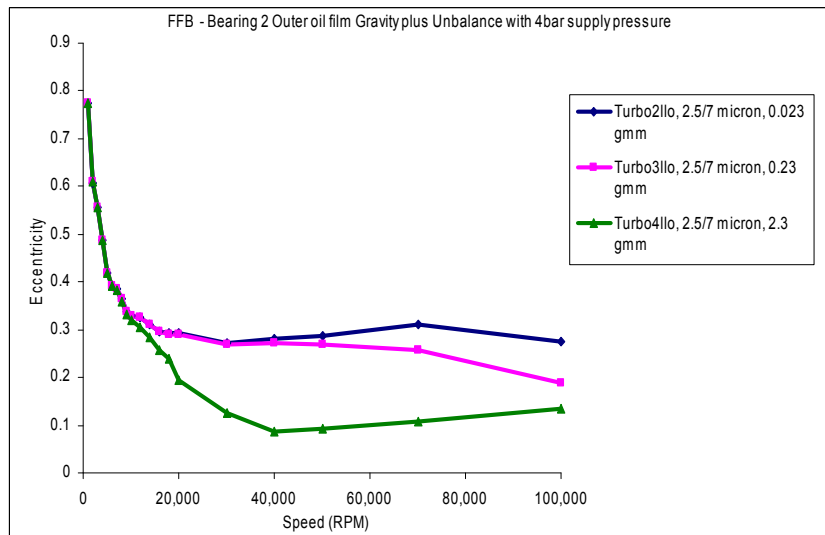


Figure 6-15 Turbine end FFB journal (2.5/7 micron clearance, 0.023gmm – 2.3gmm unbalance, 4 bar) outer bearing eccentricity vs. speed

The onset speeds for instability in the inner and outer oil films is shown in Table 6.2.

Table 6-2 Turbine end FFB sub-synchronous & synchronous whirl onset (varying unbalance, supply pressure and clearance)

FFB Bearing Variants	Onset Speed (rpm)	
	4 Bar supply	2 Bar supply
0.023gmm unbalance (inner bearing)	>1,000 (sub-synchronous)	4,000 (sub-synchronous)
0.23gmm unbalance (inner bearing)	1,000 (sub-synchronous)	6,000 (sub-synchronous)
2.3gmm unbalance (inner bearing)	Stable synchronous	Stable synchronous
0.023gmm unbalance (outer bearing)	>1,000 (sub-synchronous)	>1,000 (sub-synchronous)
0.23gmm unbalance (outer bearing)	>1,000 (sub-synchronous)	70,000 (synchronous)
2.3gmm unbalance (outer bearing)	40,000 (synchronous)	30,000 (synchronous)

Figure 6.16 compares the PGB and FFB losses for the case of 4 bar supply pressure, with unbalance varying from 0.023gmm to 2.3gmm for the lowest clearance condition for both bearing types. The highest friction is generated by the FFB bearing system. The PGB bearing system with 4 micron clearance, 4 bar supply pressure and 2.3gmm unbalance produces the lowest frictional losses.

All of these results would benefit from some more load cases and more detailed analysis.

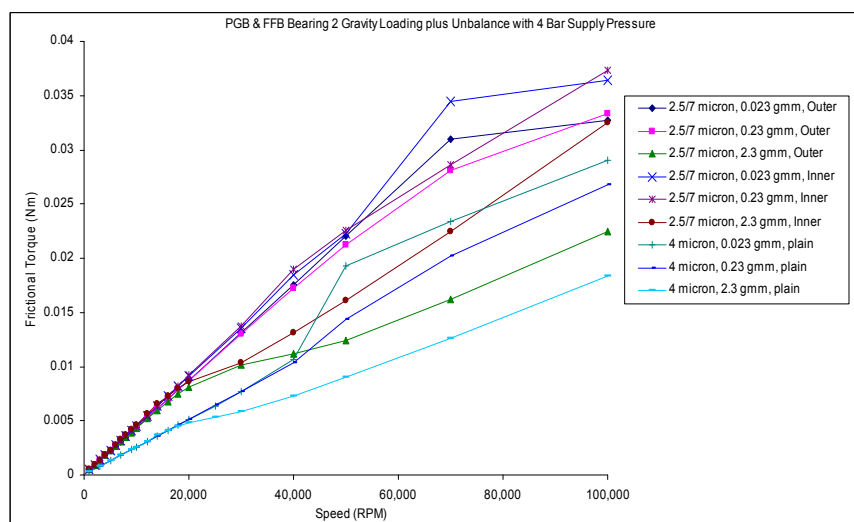


Figure 6-16 Turbine end bearing PGB and FFB friction torque versus speed (varying unbalance, supply pressure and clearance)

6.4 INVESTIGATION OF CALCULATION STABILITY

6.4.1 EFFECT OF DAMPING

Fig. 6.17 shows a typical problematic job. The eccentricity ratios in the x and y direction are plotted versus crankshaft angle. At the firing event of the engine (near to 720 degrees) the rate of change of load is sufficient to give higher forcing terms at high frequency leading to obvious oscillations. The oscillations were present at a lower amplitude until this point.

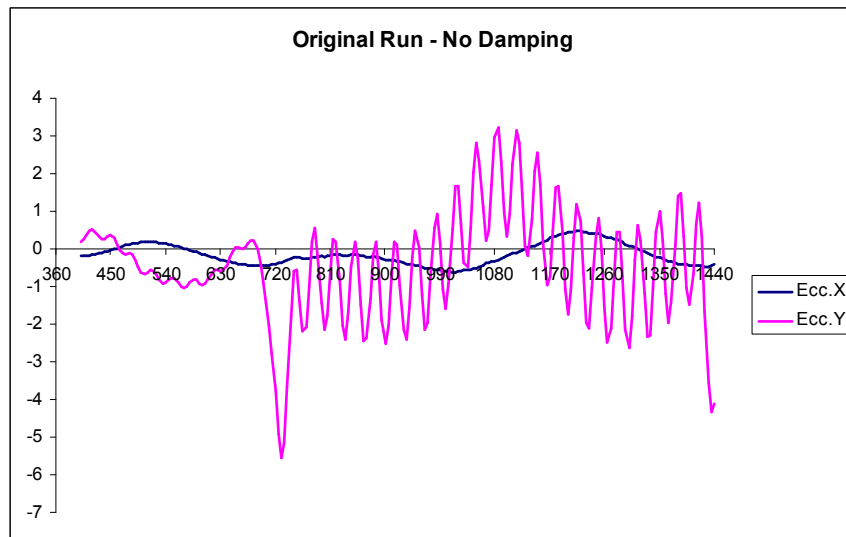


Figure 6-17 Eccentricity ratios in X and Y direction for high speed engine

Figure 6.18 tested the calculation restart capability of the program. It can be seen that the restarted calculation produces the same oscillation but runs very much quicker because of the smaller number of degrees of shaft rotation calculated.

The following curves in Fig. 6.19 show the effects of progressively increasing the diagonal damping value up to the value where there is a significant effect on the accuracy of the calculation.

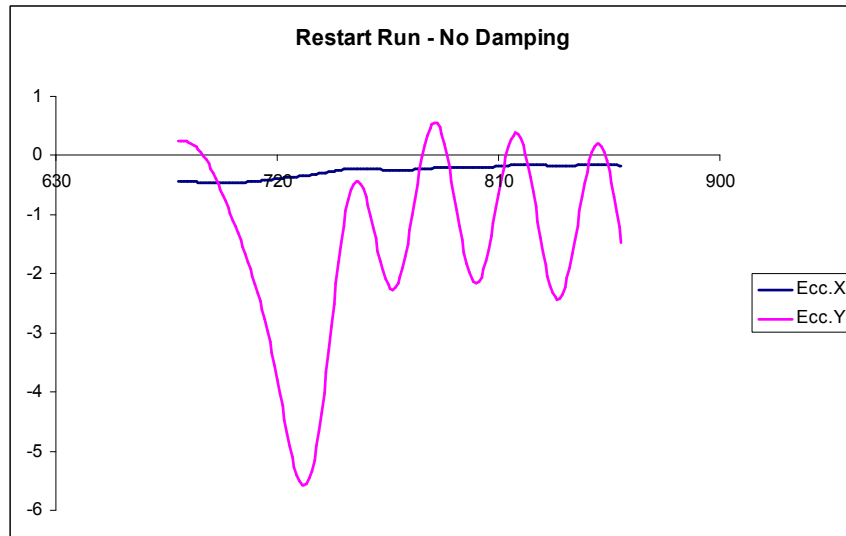


Figure 6-18 Restarted job - no damping

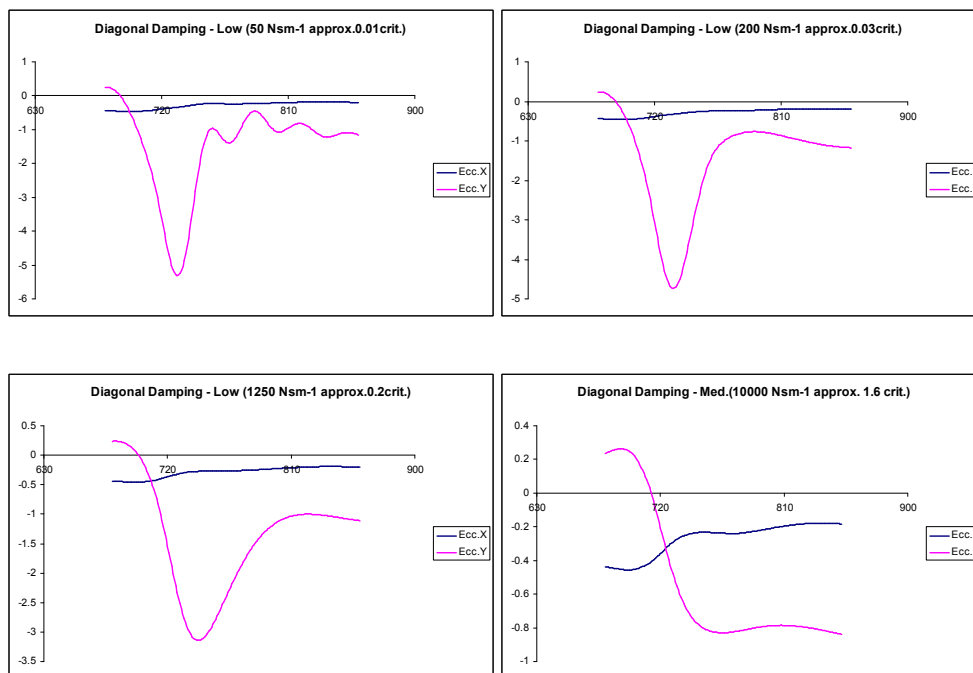


Figure 6-19 Restarted job – damping increasing from 50 to 10000 Nsm⁻¹

6.4.2 RAYLEIGH DAMPING

Figure 6.20 shows the effect of increasing Rayleigh damping on the EHD model.

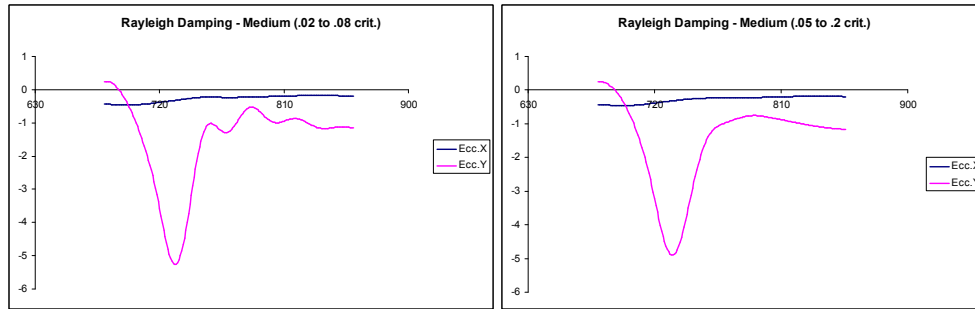


Figure 6-20 Effect of increasing damping

It was found that the diagonal damping worked slightly better than Rayleigh damping in a series of tests, giving better stability and shorter run times. Therefore, the following models used diagonal damping but both methods are available in the program.

6.4.3 FOURIER SMOOTHING OF BEARING SHAPE

In the case of relatively coarse meshes and small minimum film thickness the relative difference in oil film thickness between adjacent nodes can be large near to the minimum film thickness value. This can lead to large local variation in oil film pressure and lead to instability even when damping is applied.

The most highly loaded bearing test jobs still showed some instability in the pressure distribution although now behaving well in terms of journal orbit calculation. Fig. 6.21 shows the pressure distribution near to Top Dead Centre Non-Firing (TDC-NF) on the high speed engine big end bearing.

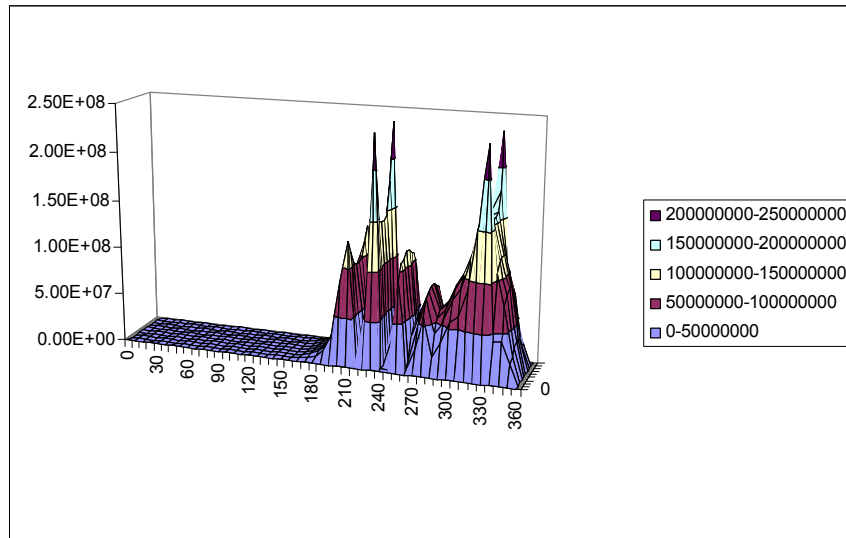


Figure 6-21 Pressure distribution without smoothing

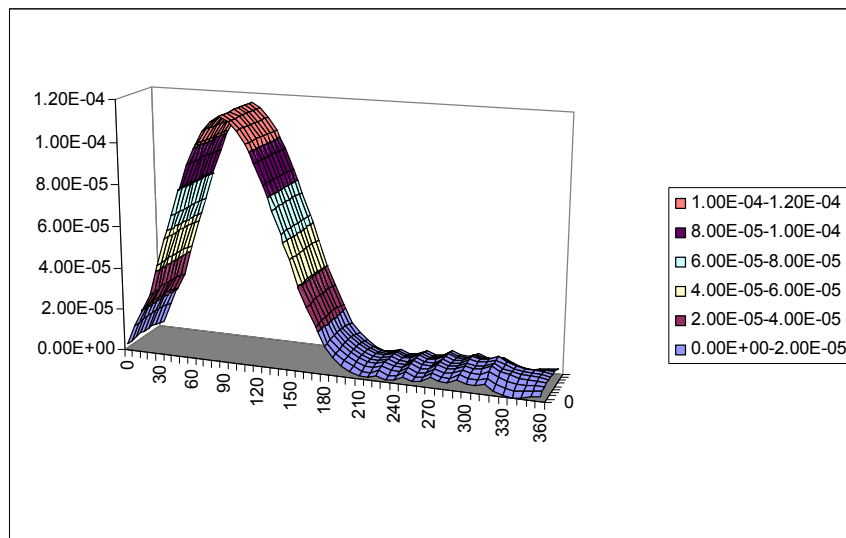


Figure 6-22 Oil film thickness distribution without smoothing

Fig. 6.22 shows the instability in the structural deformation in the region of minimum oil film thickness. The very high degree of wrap around of the bearing on the shaft journal can be seen by the extent of the low film thickness region over nearly half of the bearing circumference.

Therefore, a capability to smooth the deformed bearing shape by Fourier analysis was incorporated. The number of modes in each direction (circumferential and axial) can be

chosen by the user. The Fourier smoothing can be applied to the acceleration or the displacement

The change in the plots after applying Fourier smoothing is clear in Figs. 6.23 and 6.24.

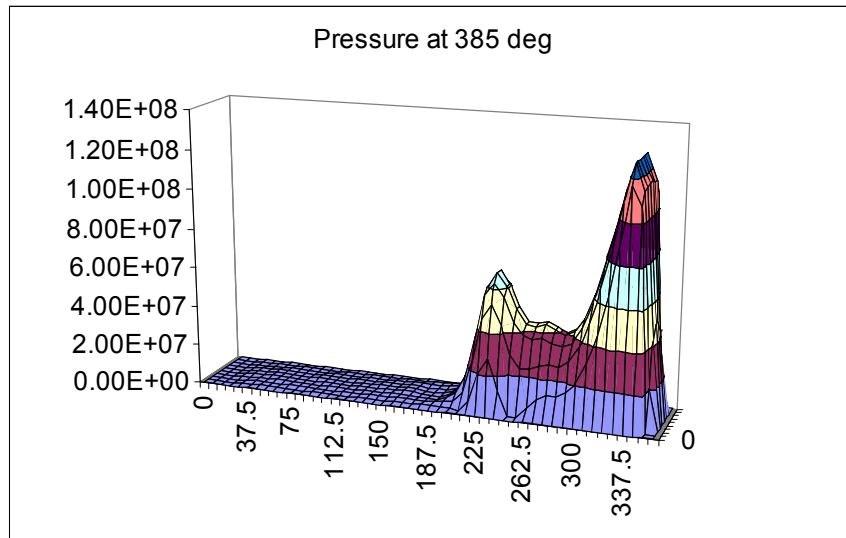


Figure 6-23 Pressure distribution - smoothed

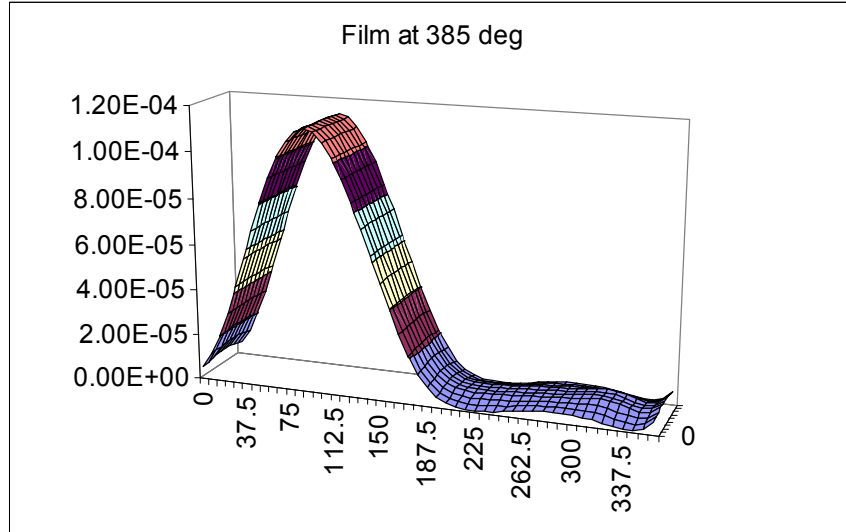


Figure 6-24 Oil film thickness - smoothed

The effect on bearing orbit and viscous power loss of Fourier smoothing was negligible and can be seen in the parameter study in the section below on ThermoElastoHydroDynamics.

6.5 DIESEL ENGINE MAIN BEARING RESULTS

The first EHD job to be attempted after the program modifications was a very simple representation of the main bearing of the test diesel engine (Fig. 6.25). This model was tested first because it was relatively stiff.

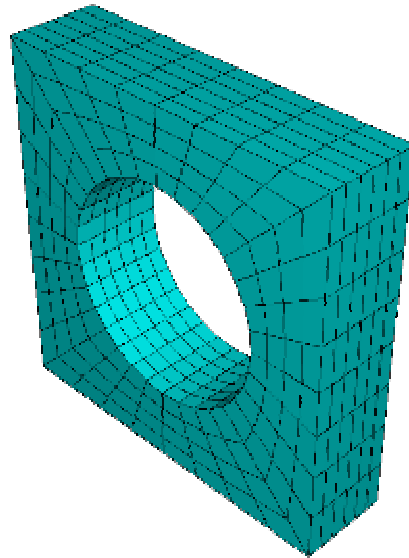


Figure 6-25 Simple test mesh for diesel engine main bearing

The comparison of the RHD and EHD journal orbits can be seen in Fig. 6.26. The maximum eccentricity for the RHD calculation was a relatively modest 0.65. Introducing structural compliance increased the maximum eccentricity to approximately 1.2. This is outside the clearance circle which would imply negative oil film thickness in an RHD calculation. The deformation of the bearing means that the film thickness remains positive.

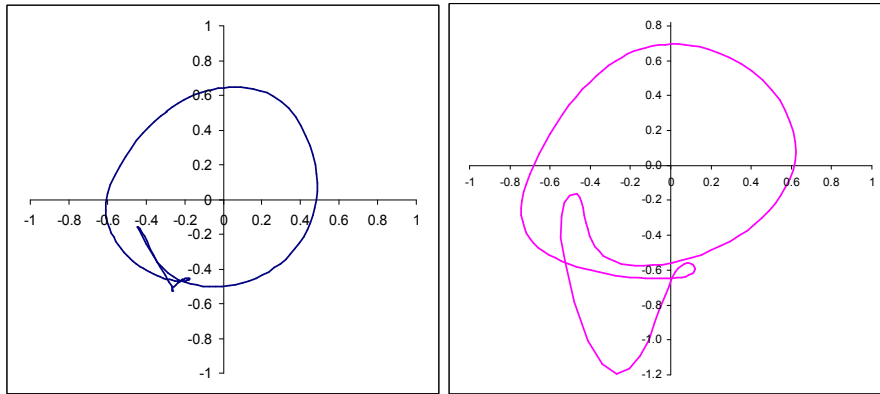


Figure 6-26 Comparison RHD and EHD journal orbits

Fig. 6.27 shows the maximum oil film pressure versus crankshaft rotation angle. The difference is small over most of the engine cycle but much larger near Top Dead Centre Firing (TDCF). This can be explained by the high force and pressure at this point in the cycle deforming the bearing sufficiently to spread the pressure distribution.

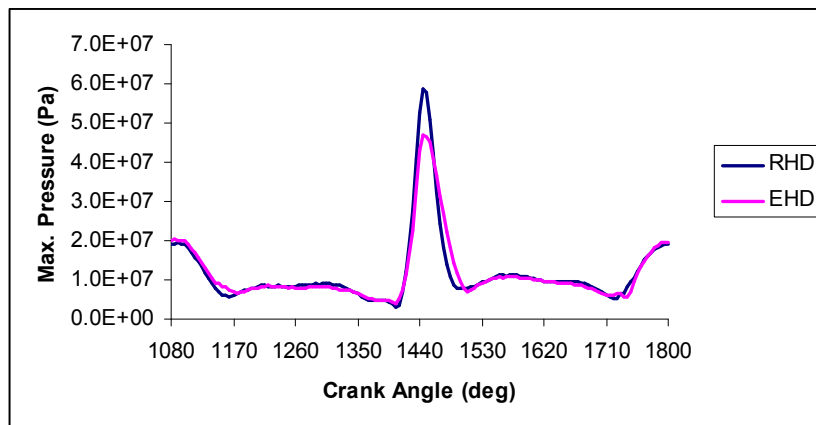


Figure 6-27 Comparison RHD and EHD Maximum Oil Film Pressure

The minimum oil film thickness in Fig. 6.28 is very similar for the two test cases. This can be explained by the high stiffness of the bearing leading to relatively small displacements. The spreading of the pressure at TDCF might be expected to produce higher minimum oil film thickness but the edges of the bearing tend to displace towards the shaft, so reducing the effect.

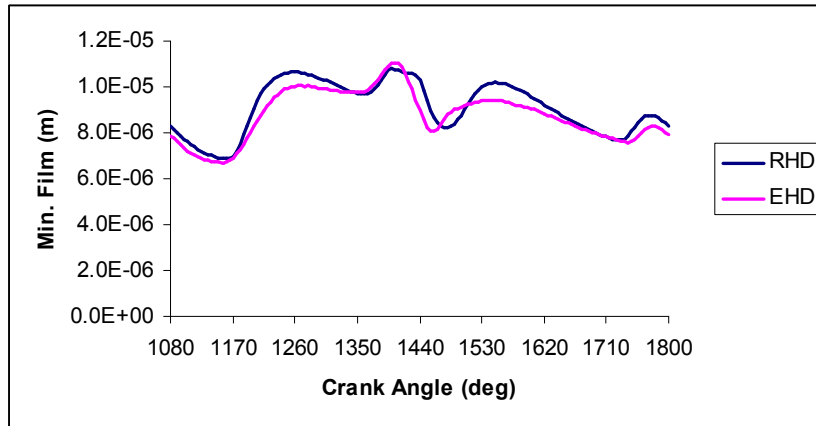


Figure 6-28 Comparison RHD and EHD Minimum Oil Film Thickness

The power loss is significantly higher for the EHD calculation over much of the cycle, Fig. 6.29.

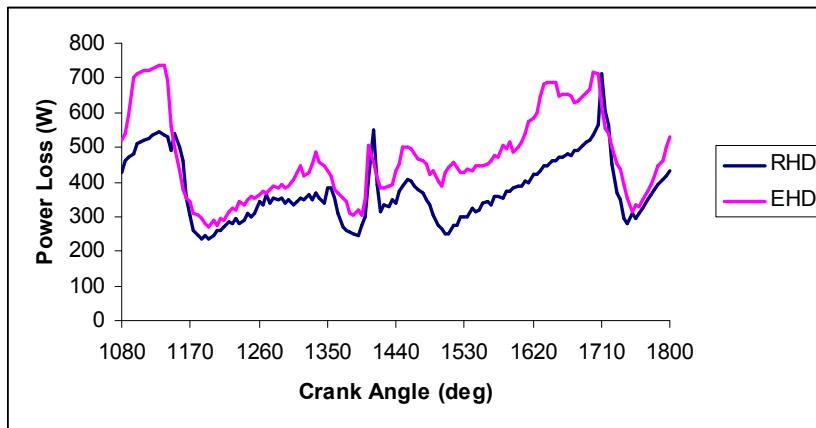


Figure 6-29 Comparison RHD and EHD power loss

The largest difference in orbits and maximum oil film pressure occurs near to Top Dead Centre Firing as would be expected for a turbo-charged diesel engine which has high combustion pressures.

6.6 DIESEL ENGINE BIG END BEARING RESULTS

The second job to be tested was the diesel engine big end bearing. The structure is clearly more flexible than the main bearing representation in the previous section (Fig. 6.30). This can be seen in the higher eccentricity ratios in Fig. 6.31, exceeding 2.5 for the EHD calculation compared to approximately 0.9 for the RHD.

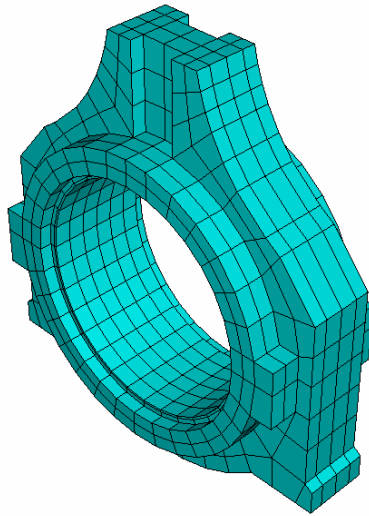


Figure 6-30 Diesel engine conrod big end bearing and housing

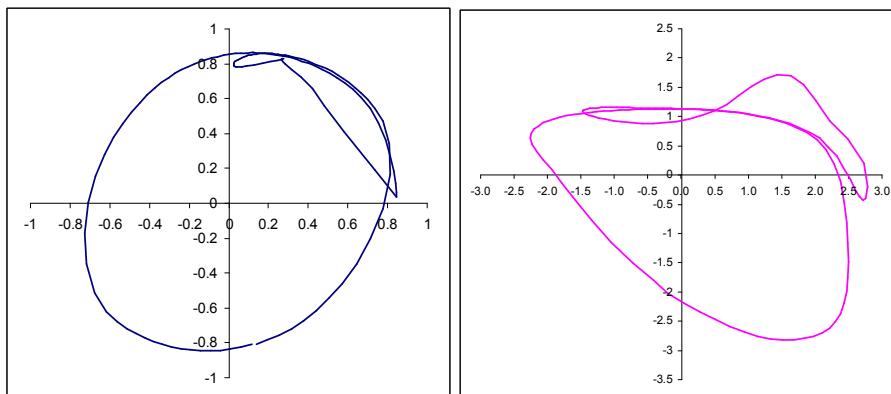


Figure 6-31 Comparison RHD and EHD journal orbits

Figs. 6.32 to 6.34 show the maximum oil film pressure, minimum oil film thickness and viscous power loss versus shaft rotation angle. The same trends can be seen as for the much stiffer main bearing calculation.

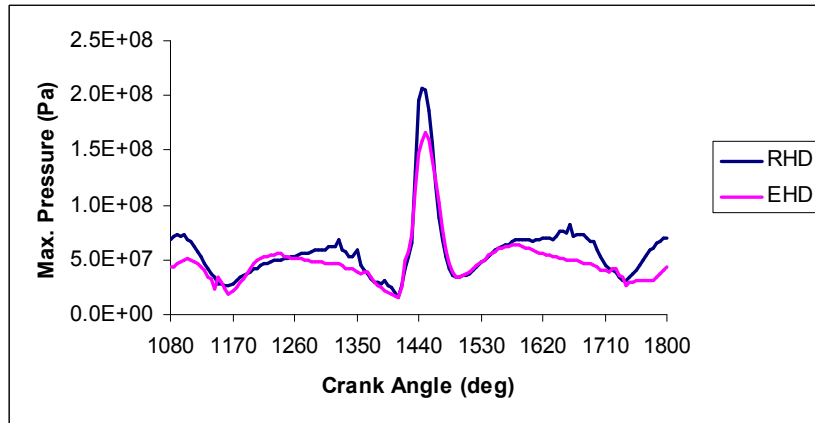


Figure 6-32 Comparison RHD and EHD Maximum Oil Film Pressure

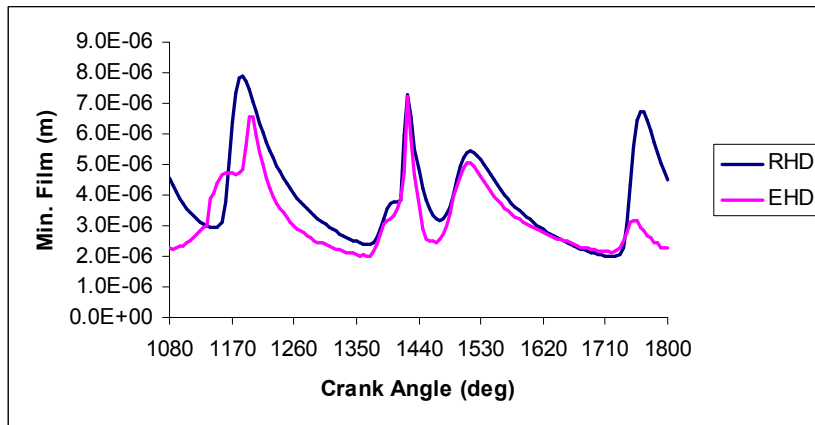


Figure 6-33 Comparison RHD and EHD Minimum Oil Film Thickness

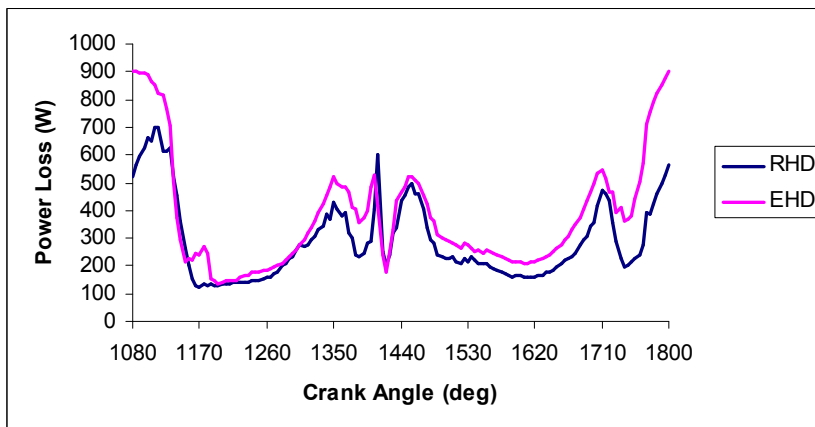


Figure 6-34 Comparison RHD and EHD

6.7 RACING CONNECTING ROD BEARING STUDY

The modifications to the calculation method shown in Section 6.4 enabled the EHD calculations for the high speed engine big end bearing to be carried out with a high degree of reliability. Fig. 6.35 shows the quite substantial structure required to withstand the forces on this engine.

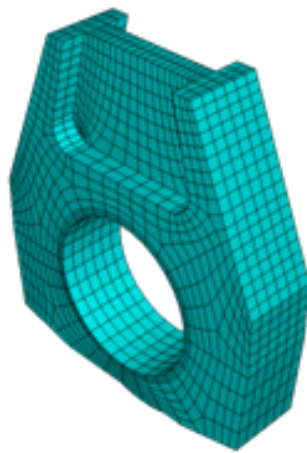


Figure 6-35 High speed engine conrod big end bearing and housing

6.7.1 CIRCULAR BEARING

Compared to the previous calculations note the much higher eccentricity ratio values on this highly loaded bearing as the housing deforms significantly, shown in Fig. 6.36. This is especially true at Top Dead Centre Non-Firing (TDCNF) when the most flexible part of the housing is heavily loaded. The different nature of the orbits compared to the diesel engine shown in the previous section is due to the much higher inertia forces on this high speed engine.

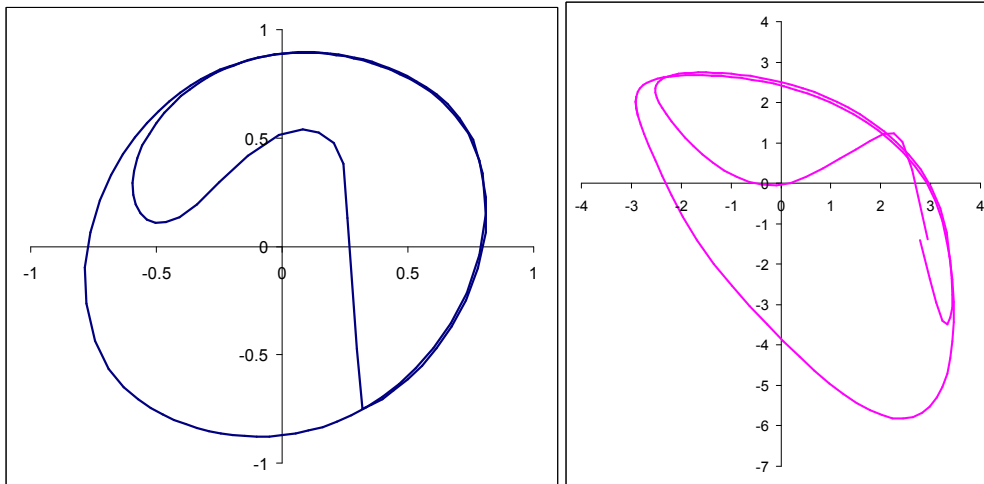


Figure 6-36 Comparison RHD (left) and EHD (right) journal orbits

Fig. 6.36 shows the shaft journal orbit eccentricity ratios for RHD and EHD calculations at a rotational speed of 16200 rpm. The deformation of the structure near to TDC-NF can be seen in exaggerated form in Fig. 6.37. The wrap around effect of the bearing on the shaft can be seen clearly. The high inertia forces acting in an upwards direction combined with the lower half of the housing being the most flexible part of the structure make this the most critical part of the engine cycle.

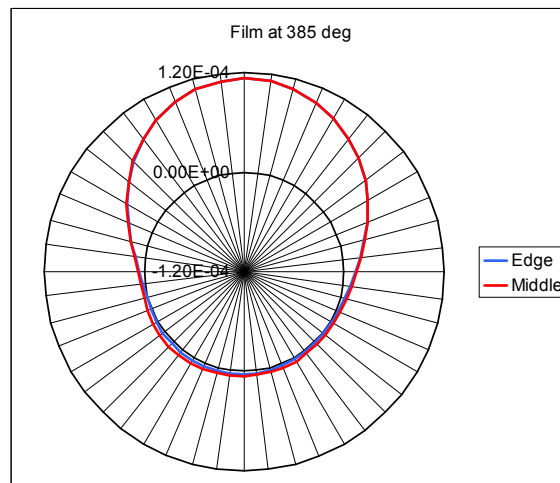


Figure 6-37 Deformed shape near to Top Dead Centre Non-Firing

The Maximum Oil Film Pressure, Minimum Oil Film Thickness and viscous power loss are shown in Figs. 6.38 to 6.40. Compared to the previous calculations, similar trends can be seen but more pronounced. In particular, note that the maximum oil film pressure is approximately halved at the Top Dead Centre and Bottom Dead Centre positions

where the high reciprocating inertia forces give the highest pressures and also highest structural deformation.

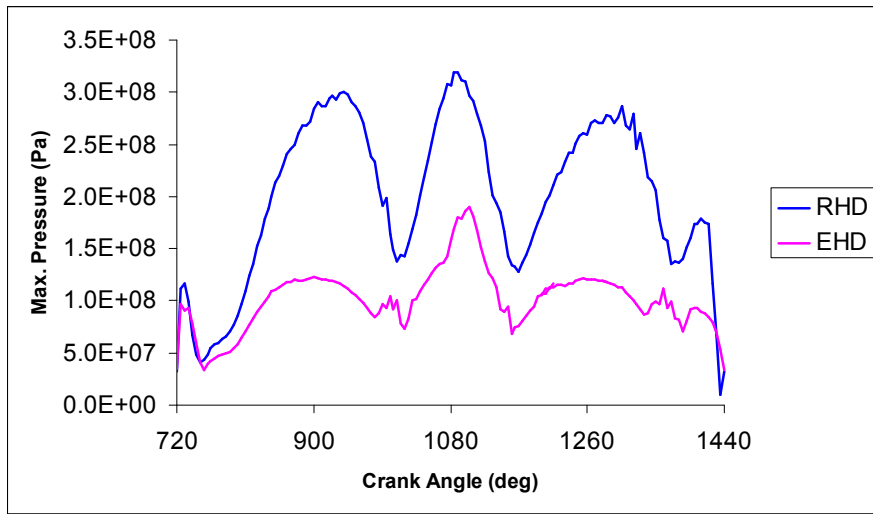


Figure 6-38 Comparison RHD and EHD Maximum Oil Film Pressure

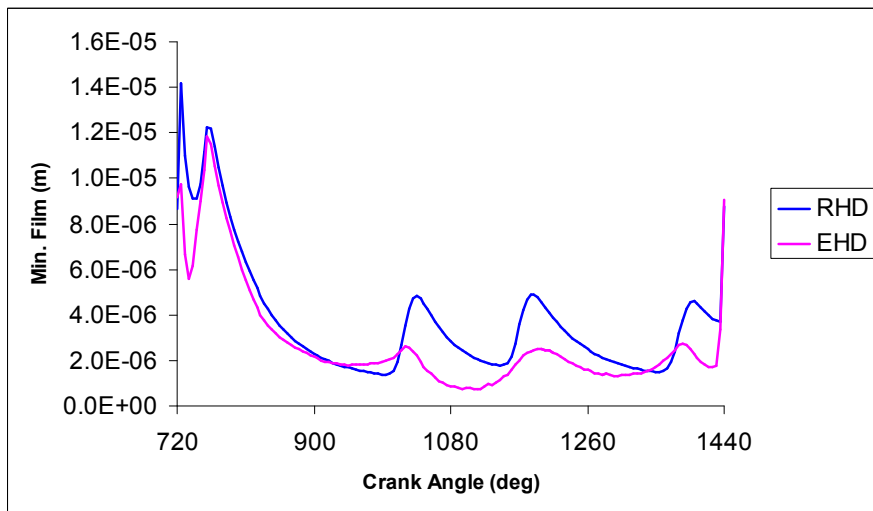


Figure 6-39 Comparison RHD and EHD Min. Oil Film Thickness

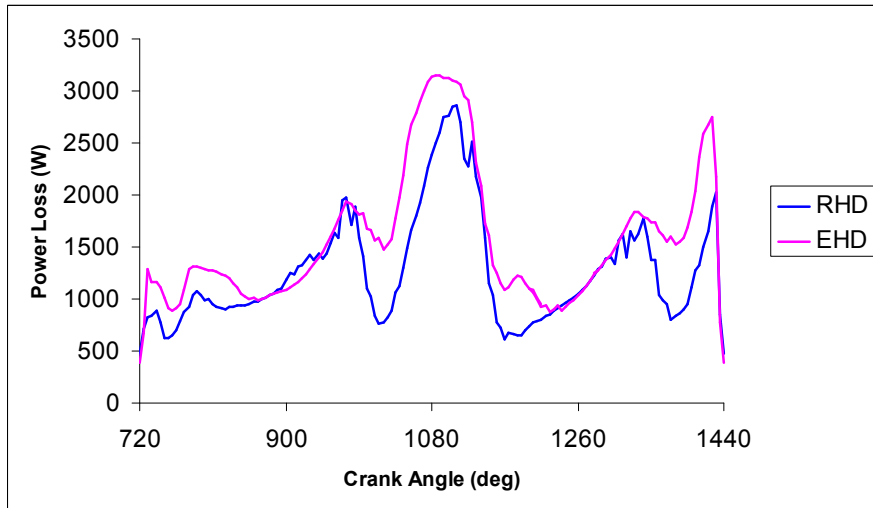


Figure 6-40 Comparison RHD and EHD power loss

6.7.2 NON-CIRCULAR BEARING FEATURES AND EFFECTS OF ASSEMBLY

Fig. 6.41 shows the measured profile (radial departure from nominal circular shape) around the big end bearing for the high speed engine. A line was fitted to the points using an 8th harmonic Fourier fit (Fig. 6.42). The bearing shape arises from a combination of non-circular shape due to crush relief features at the split line and further deformation due to assembly forces.

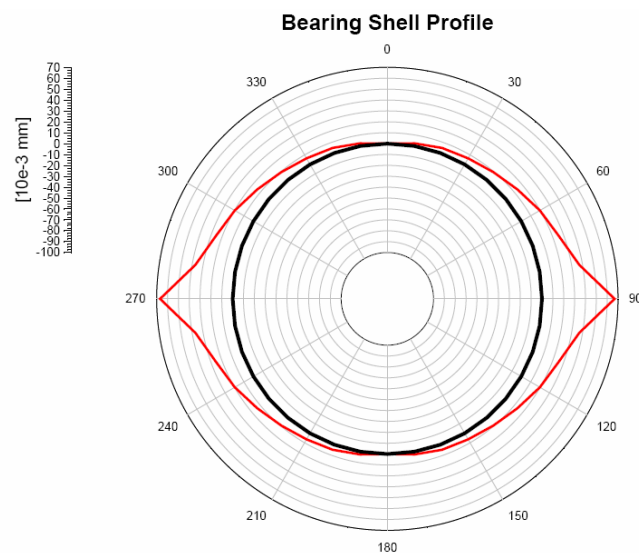


Figure 6-41 Measured assembled bearing profile

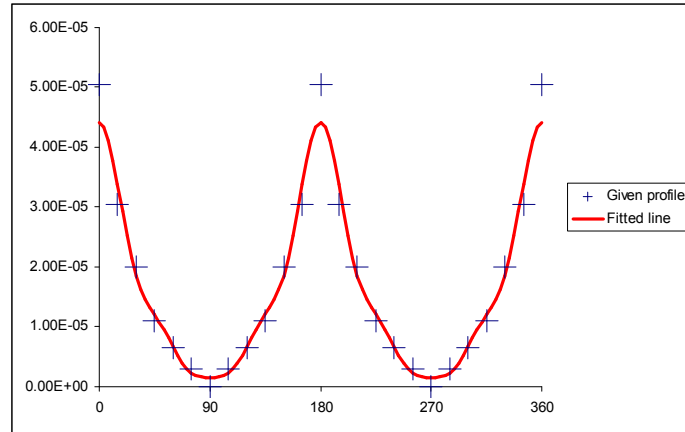


Figure 6-42 Curve fit to bearing profile

Fig. 6.43 shows the deformed shape of the bearing near to TDC-NF for the cold bearing shape. The addition of thermal deformation is shown later.

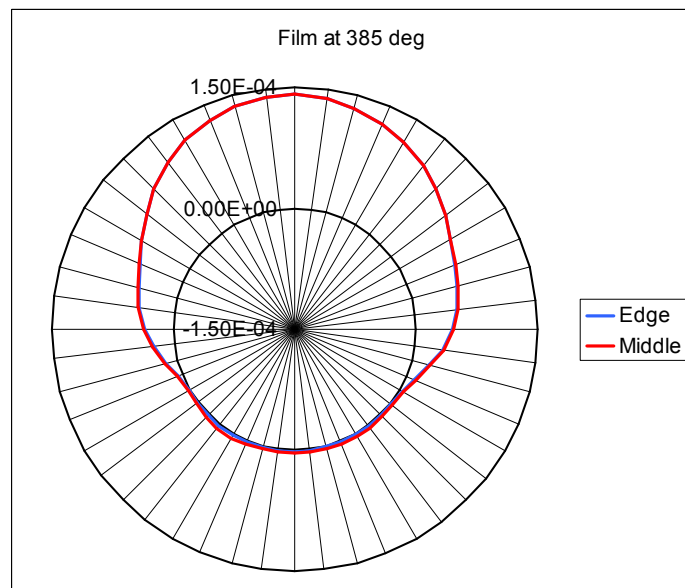


Figure 6-43 Bearing shape near TDC non-firing – EHD - non-circular bearing

6.7.3 EFFECTS OF THERMAL LOADING

The previous section showed that the elastic deformation of the bearing housing can have a significant effect on the journal orbit, maximum oil film pressure and power loss. The power loss is dissipated as heat. Typically, much of the heat is transported away by the oil flow (approximately 80% is often assumed (Bannister, 2001) and the rest flows into the surrounding components, the bearing and the shaft journal.

Thermal Loading and Deformation

Initial calculations were performed for the high speed engine big end bearing assuming 90% of the heat generated in the oil film would be carried away by the oil. This would be reduced to 80% later when performing a sensitivity study.

For the baseline EHD calculation of the previous section, the average power loss was 1590 W and average oil flow $2 \times 10^{-5} \text{ m}^3/\text{s}$. 90% of the heat going to the oil would give an oil temperature rise of 36 degC and average heat flux on bearing and journal surfaces of 40 kW/m^2 .

$$\delta T = \frac{P}{\dot{Q} \rho C} \quad 6-1$$

The finite element model of the big end bearing and housing was used to calculate the thermal deformation due to this flux (Fig. 6.44).

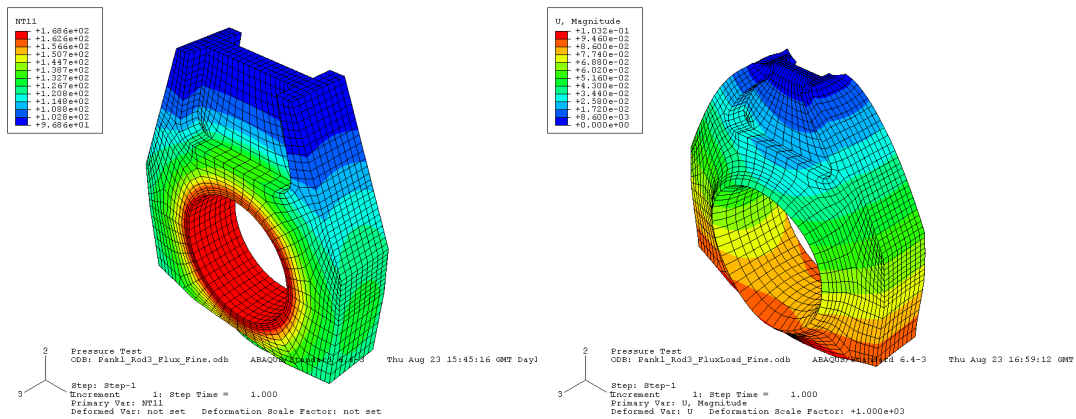


Figure 6-44 Temperatures and deformations – constant flux

For a more accurate calculation, the EHD result files were post-processed to average the viscous power loss over the cycle individually at each node point. The variation of flux over the bearing surface was large and the revised Finite Element thermal loading results are shown in Fig. 6.45. The thermal deformation on the right hand side also includes a correction to the constraints at the top of the model. The effect on the shape of the bearing was significant: see later section.

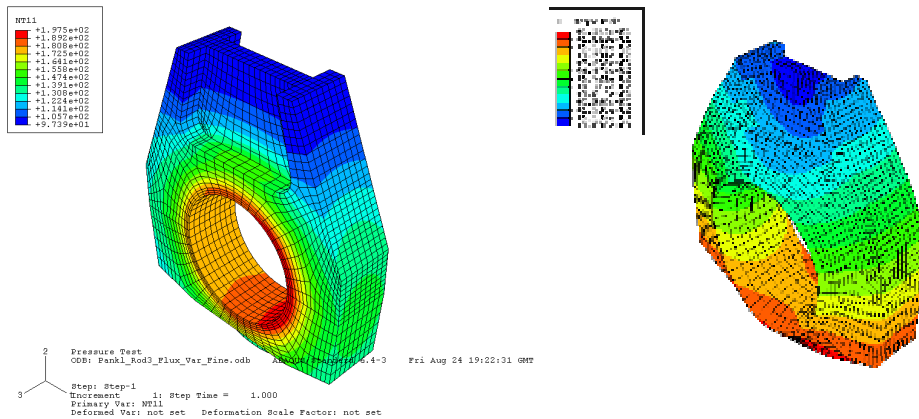


Figure 6-45 Temperatures and deformations – variable flux

The deformed shapes are compared in Fig. 6.46. The differences are large enough to make it worthwhile to calculate the variation in heat flux over the bearing surface. The following calculations all use the variable heat flux.

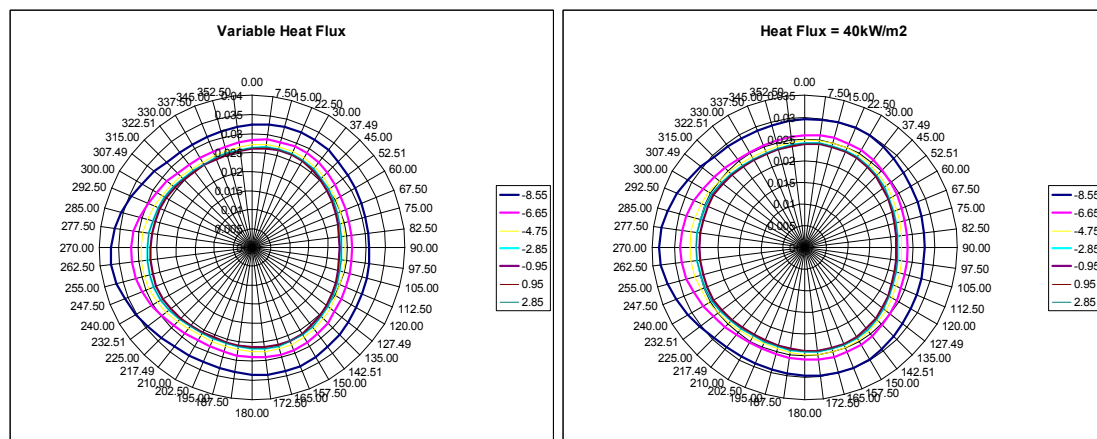


Figure 6-46 Deformations due to bearing thermal loading

Results of Sensitivity Studies

Fig. 6.47 shows the effect of carrying out an EHD calculation for the original circular profile versus the thermally deformed profile. Note how the original profile gives lowest oil film thickness at the edges of the bearing, just visible in the left hand plot. The thermally deformed profile has sufficient curvature in the axial direction to compensate and the minimum oil film occurs on the bearing centre line.

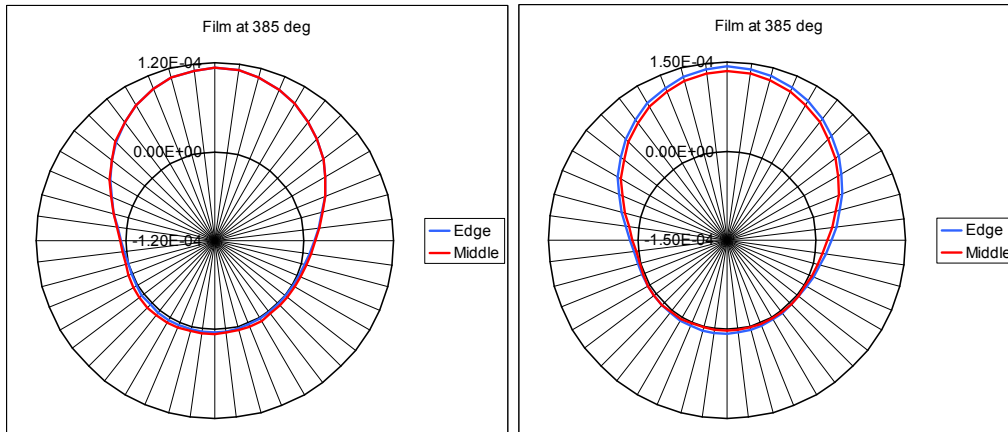


Figure 6-47 Typical bearing deformed shapes near to TDC non-firing – EHD circular bearing (left) versus thermally deformed bearing (right)

Table 6.3 shows the Finite Element runs to investigate the sensitivity of the bearing temperature and deformation to heat transfer values. Examination of the right hand side of Fig. 6.44 shows that the top of the bearing housing is over constrained. All of the degrees of freedom were constrained across the top of the model. This was almost certainly fine for EHD calculations without thermal deformation but is clearly not correct for a thermally deformed model. Therefore the second job in the table simply loosened the constraints so that the top surface of the model remained flat but able to move in its own plane apart from symmetry constraints.

Table 6-3 Heat transfer sensitivity

Job name	Percent Flow	HT Flanks	Max T	Max delta	Min delta	Description
Flux_VariableFine	5	200	197.5	0.037100926	0.022941804	Variable flux 5% to bearing, 200 kW/(m.K) heat transfer to flanks, over constrained at c of g
Flux_VariableFinex1	5	200	197.5	0.038715388	0.024219737	As above but loose constraint
Flux_VariableFinex2	5	400	167.2	0.03286447	0.019930917	As above but 400 kW/(m.K)
Flux_VariableFinex4	5	800	148.2	0.02938979	0.017588809	As above but 800 kW/(m.K)
Flux_VariableFinex4x1-5	7.5	800	174.9	0.03386698	0.018840662	As above but 7.5% to bearing
Flux_VariableFinex4x2	10	800	201.5	0.038361158	0.020097	As above but 10% to bearing

The other concern regarding the previous thermal model was that excessive bearing surface temperatures had been obtained with 10% of the viscous power loss and so those calculations had used 5% of the viscous power loss. The subsequent models in the table show the effects of increasing both the heat transfer to the crankcase gases and the heat flow to the bearing surface (back to the 10% value).

The following figures show the deformed shapes of the bearing for these runs. They should be compared to the baseline in Fig. 6.37.

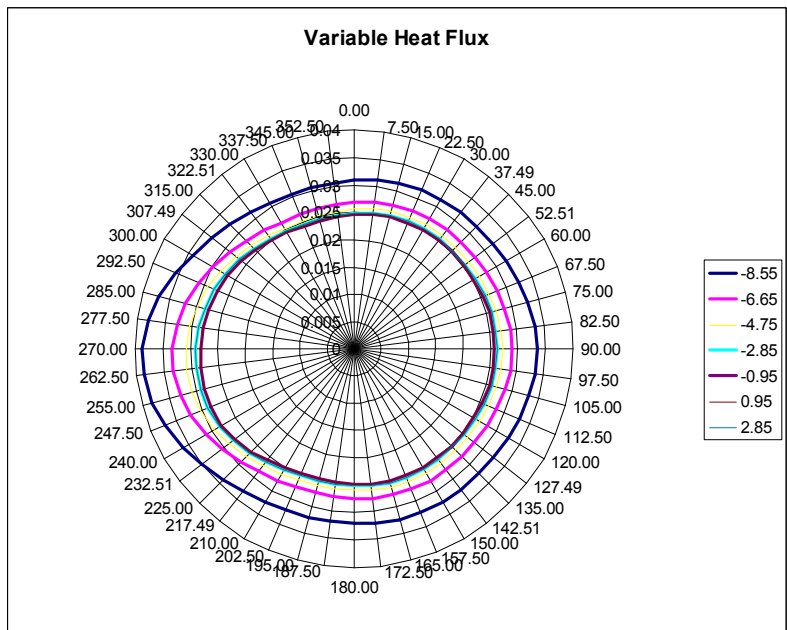


Figure 6-48 Effect of reducing constraint on conrod

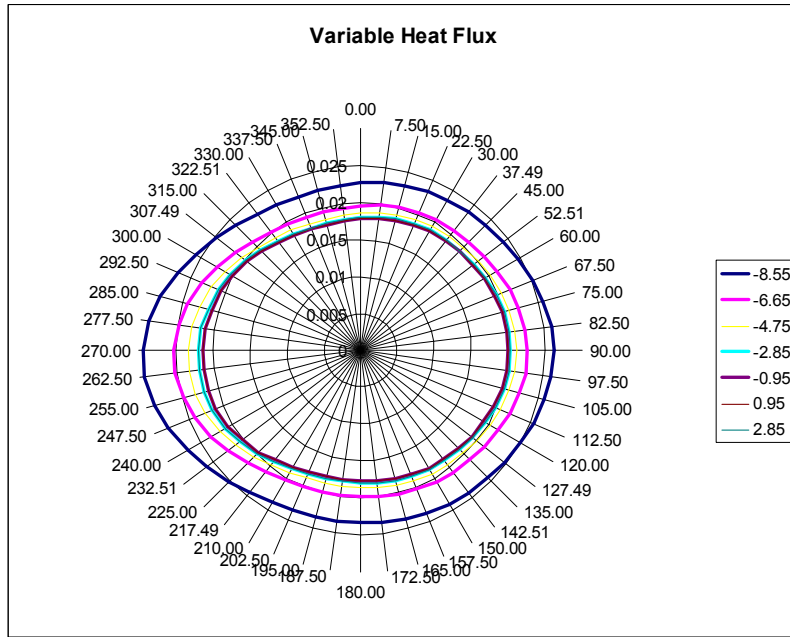


Figure 6-49 Cumulative effect of increasing heat transfer to crankcase gases x4

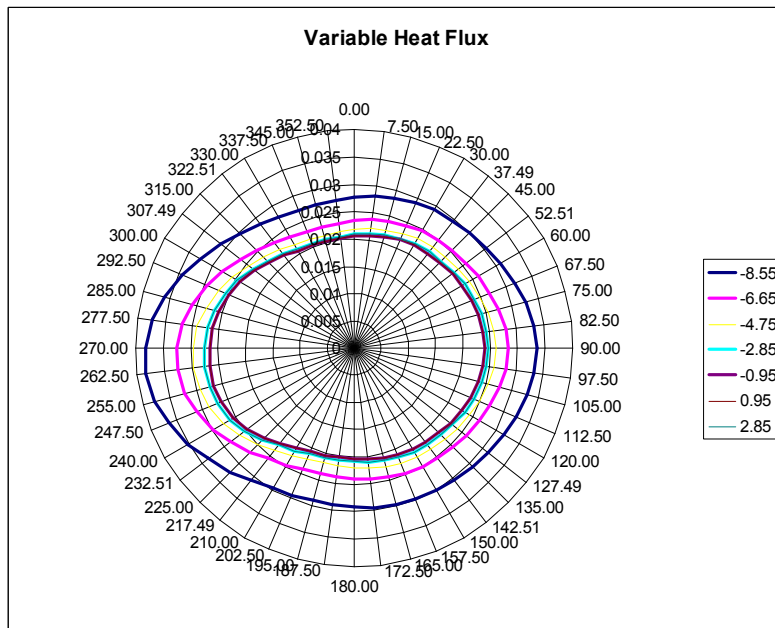


Figure 6-50 Cumulative effect of increasing heat transfer to bearing surface x2 (from 5% to 10% of viscous power loss)

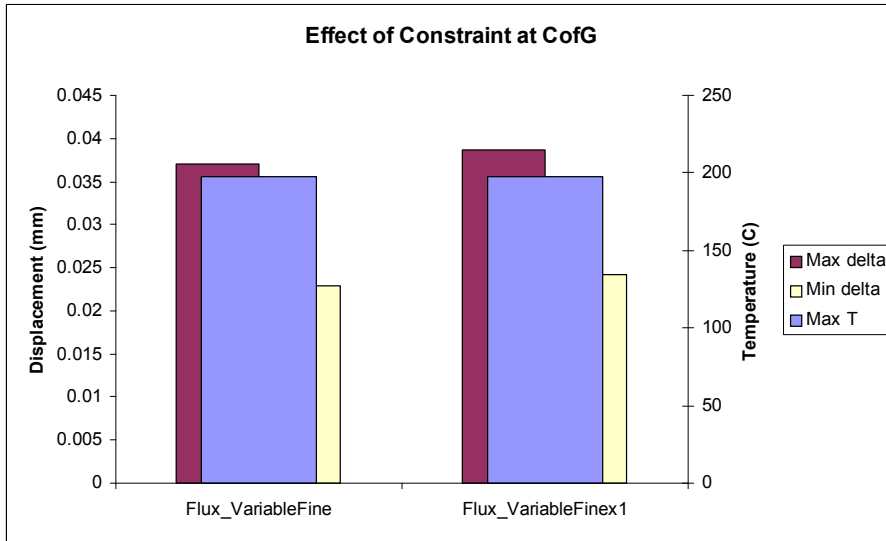


Figure 6-51 Effect of loosening constraint of the conrod model

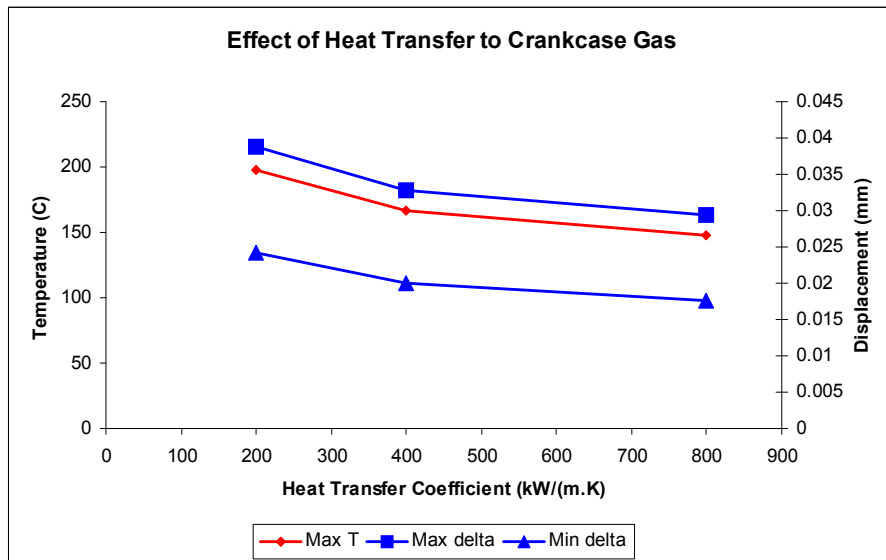


Figure 6-52 Effect of increasing the heat transfer coefficient to the crankcase gas

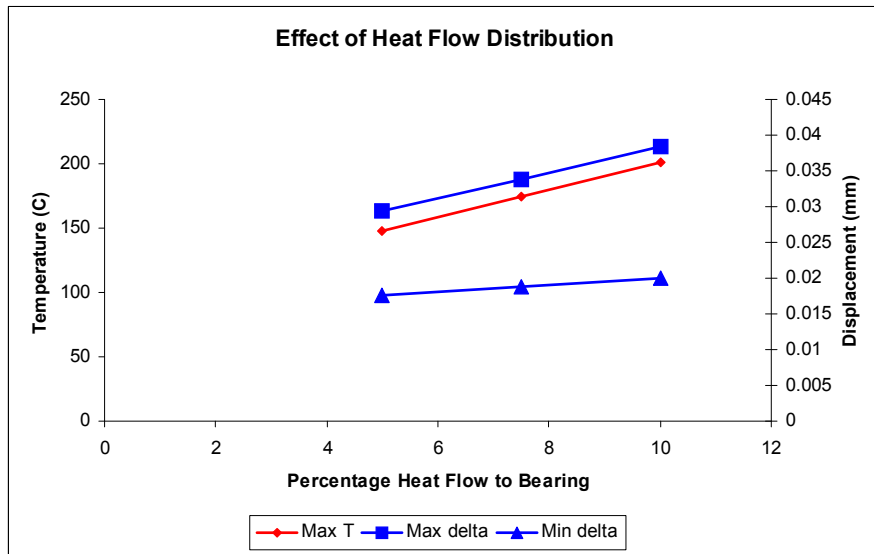


Figure 6-53 Effect of increasing the heat transfer percentage to the bearing surface

It can be seen that the effect of correcting the constraint is significant. The heat transfer is also significant. Increasing the heat transfer x4 to the crankcase gas reduces temperatures significantly. Then doubling the heat flux into the bearing surface from 5% to 10% approximately compensates for this. The original heat transfer coefficient for the crankcase gases was chosen by the author from previous experience on road going car engines at around 5000 to 6000 rpm. This would tend to suggest that, at these engine speeds (16200 rpm), the heat transfer from rod to crankcase gas is much higher than for lower speed engines and that the convention of heat flow split between oil, bearing and journal of 80%, 10%, 10% may still hold true.

Another sensitivity study looked at the effect of material properties. A particular question was whether it would be possible to cause a reduction of bearing diameter as heat was applied by a combination of stiffness, conductivity and thermal expansion values. Typical automotive engine oils have a flash temperature of 200 to 220 °C, less if contaminated by fuel. Therefore there is a real possibility of sudden increase of local heat flux where the oil film breaks down and heat is generated by boundary friction. Any tendency of the bearing surface to move towards the shaft journal would make it more liable to seizure due to positive feedback between heat generation and contact pressure leading to a runaway thermal loading. Table 6.4 shows the values tried.

Table 6-4 Material properties sensitivity study

Job name	Percent Flow	HT Flanks	Max T	Max delta	Min delta	Description
x4x2_SteelRod	10	800	201.5	0.037666436	0.02344085	Thermal properties as above but modulus changed from Titanium to Steel
x4x2_SteelRod_LowE	10	800	201.5	0.035486621	0.0229903	As above but bearing modulus halved
x4x2_SteelRod_LowEHig hAlpha	10	800	201.5	0.036517766	0.019019849	As above but bearing expansivity doubled
x4x2_Special	10	800	471.5	0.047888	-0.0129	As above but now thermal properties changed and rod stiffened further

Fig. 6.54 shows the most extreme case, which did manage to produce negative radial displacements on the bearing surface. However, the material properties were not typical of real materials. Nevertheless, it shows that such a situation is possible in theory.

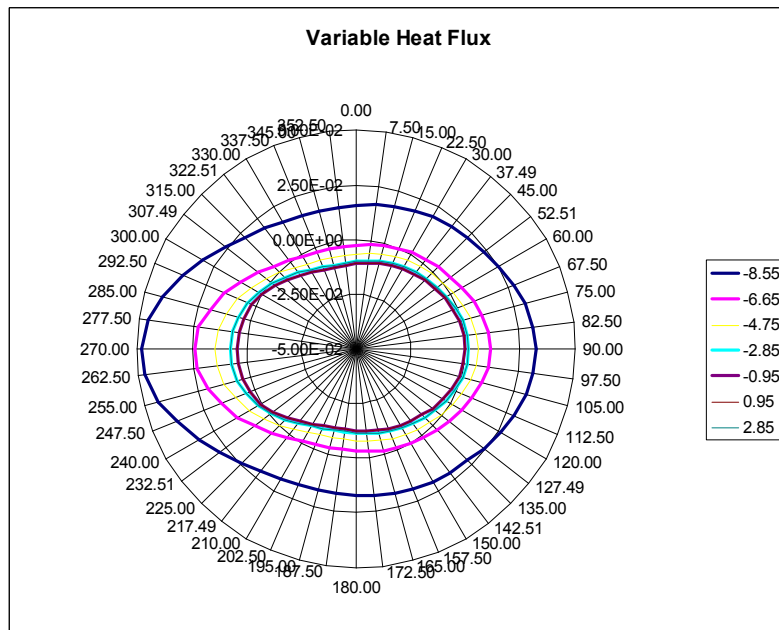


Figure 6-54 Effect of extreme variation in material properties

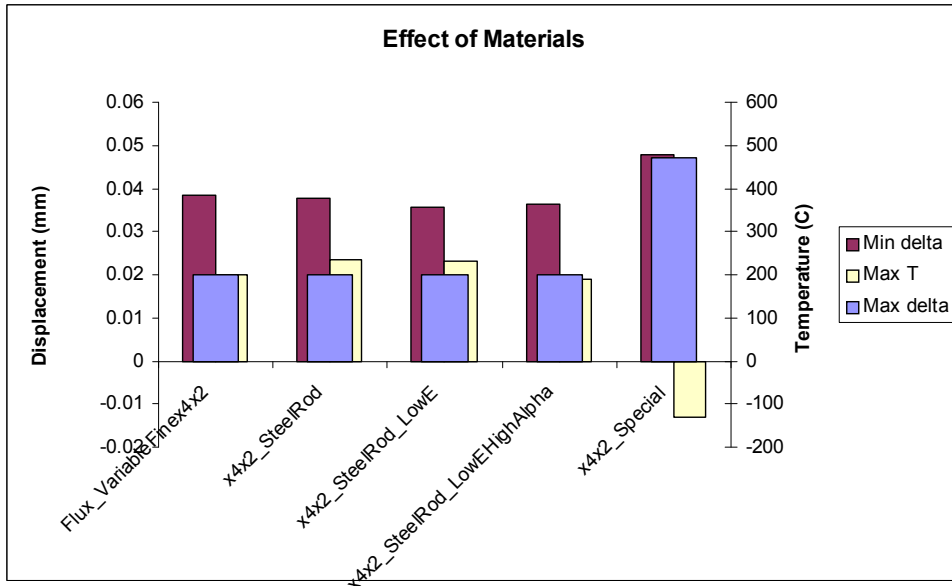


Figure 6-55 Effect of material properties on deformation and temperature at the bearing surface

Finally, there would be no point in the Finite Element studies above without looking at the effect on the EHD calculation. Three new EHD runs were performed with profiles from the constraint and heat transfer study. The main reason for the study was to judge how much difference the profiles made to the power loss in the oil film. This would give an indication of the degree of coupling between the heat generation in the oil film and thermal deformation of the structure. There is a need in future to condense the thermal stress FE model to active degrees of freedom for a fully coupled TEHD solution.

Table 6-5 EHD test jobs

Job	Profile	Oil temp. (C)	Prop. of power to oil	Torque (Nm)	%age change	Description
RD	None	95	0.9	0.915	0.0	Original circular bearing EHD job
RDF	None	95	0.9	0.916	0.1	Add Fourier smoothing
RDFProfile130	Hot Simple	130	0.9	0.657	-28.2	Add thermal deformation to circular profile and oil at 130 deg C
RDFProfile95	Hot Simple	95	0.9	0.978	6.8	As above but oil at 95 deg C
RDFProf4	Cold 2	130	0.9	0.513	-43.9	Cold profile – Fourier fit to measured profile including crush relief and deformation due to assembly loads
RDFProfileX1	Hot Simple	130	0.9	0.659	-28.0	As RDFProfile130 but with relaxed constraints
RDFProfileX4	Hot Simple	130	0.9	0.697	-23.8	As above with heat transfer coefficient to crankcase x4
RDFProfileX4X2	Hot Simple	130	0.8	0.699	-23.7	As above with heat flux to bearing surface x2

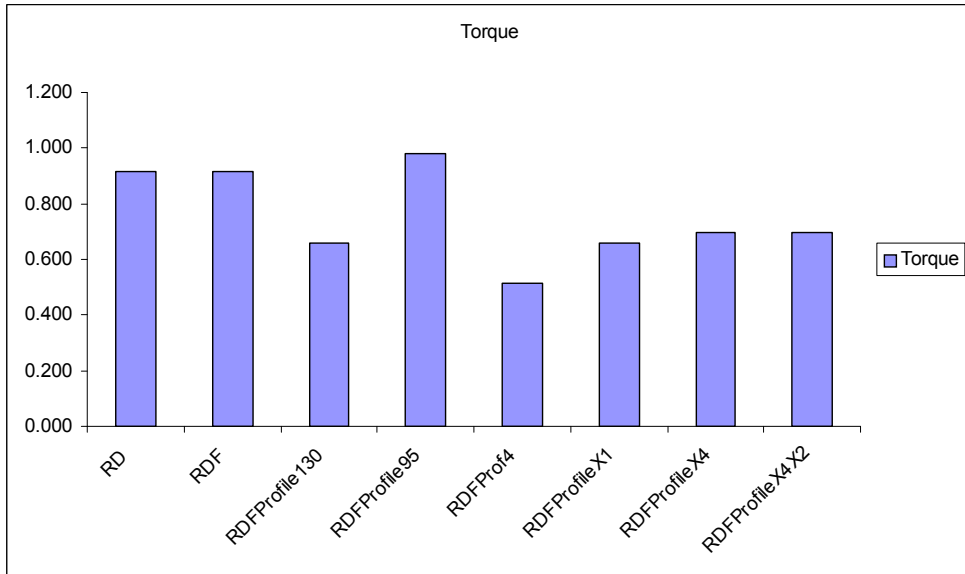


Figure 6-56 Average viscous torque

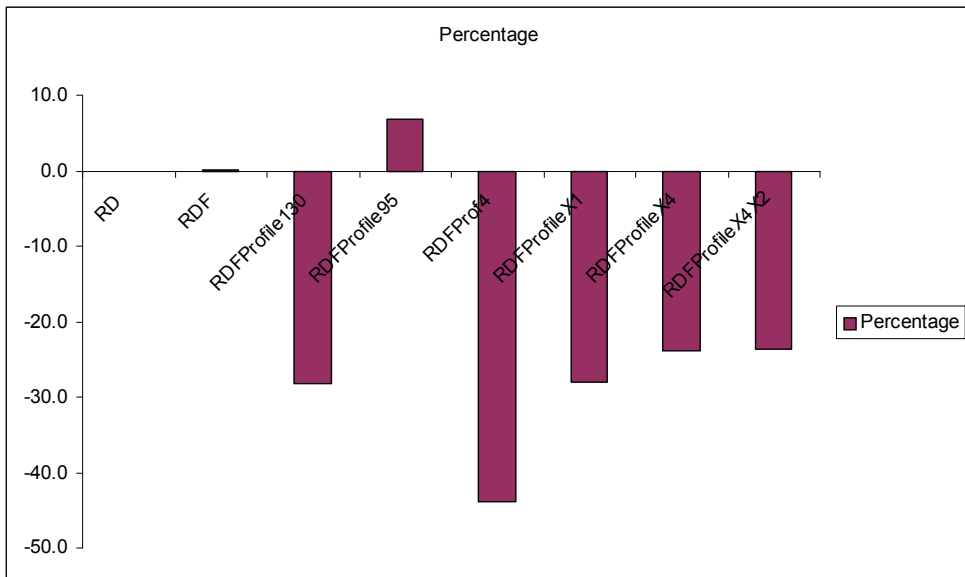


Figure 6-57 Percentage change of viscous torque

The following conclusions can be drawn from this sensitivity study

- Fourier smoothing affects the pressure distribution but has negligible effect on the viscous torque (and power loss)
- Oil temperature has a large effect on viscous torque

- Using the thermally deformed profile increases viscous torque by approximately 7%.
- Using the incorrect constraints on the model has a significant effect on bearing shape but relatively small effect on the viscous torque
- Including actual profile instead of nominal circular profile reduces viscous torque by approximately 15%
- Viscous torque increased by approx. 5% by increasing heat transfer values by amounts shown

This would indicate that taking account of the correct cold shape of the bearing complete with crush relief and assembly distortions is important along with correct knowledge of oil temperature.

Calculating heat flux from the undistorted bearing and calculating the resulting shape may be adequate for an initial ThermoElastoHydroDynamic (TEHD) analysis of journal bearings. This would be good enough for fairly reasonable results and looking at trends. However, for accurate results a more formally correct calculation would feed back the changed bearing surface heat flux and loop around the calculation until convergence.

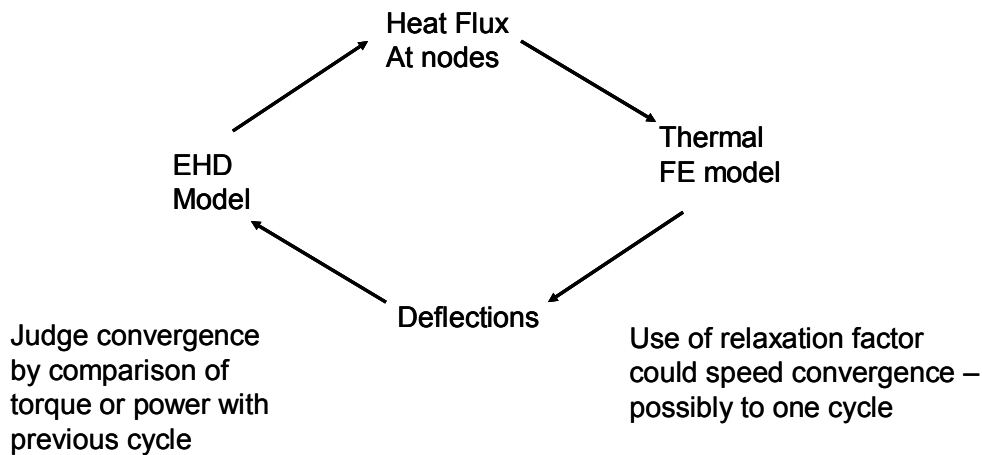


Figure 6-58 Thermo Elasto HydroDynamic calculation loop

It would not be difficult to implement such a loop in the current program. The use of a relaxation factor could well reduce the number of iterations to one or two. A potential problem is that the commercially available Finite Element program ABAQUS does not support condensation of the thermal conductivity matrix to the active degrees of freedom. It only supports this calculation for the stiffness and mass matrices of

stress/strain models. However, the calculation could be automated outside commercially available software. The condensation was implemented in Barrett (2001) for stress/strain models but that part of the problem is identical for heat flow models. A simplified form of condensation could be used that simply scales the deflections according to the average flux over the whole bearing.

Table 6-6 EHD test job results

Job name	Power (W)	Oil Flow (m ³ /s)	Temp. Rise (deg, C)	Av. Flux (W/m ²)	Description
RD	1570.4	1.969E-05	36.7	39828	Original circular bearing EHD job
RDF	1573.4	2.055E-05	35.2	39905	Add Fourier smoothing
RDFProfile130	1127.0	4.153E-05	12.5	28584	Add thermal deformation to circular profile, oil at 130 deg C
RDFProfile95	1675.5	3.069E-05	25.1	42496	As above but oil at 95 deg C
RDFProf4	873.7	2.256E-05	17.8	22159	Cold profile – Fourier fit to measured profile including crush relief and deformation due to assembly loads
RDFProfileX1	1128.7	5.007E-05	10.4	28626	As RDFProfile130 but with relaxed constraints
RDFProfileX4	1195.6	3.411E-05	16.1	30323	As above with heat transfer coefficient to crankcase x4
RDFProfileX4X2	1196.9	3.271E-05	15.0	60713	As above with heat flux to bearing surface x2

Table 6.6 and the following figures complete the information by showing power loss (simply equal to viscous loss multiplied by rotational velocity), oil flow rate and estimated temperature rise in the oil (assuming 90% of heat carried away by the oil in

this case). It can be seen that increasing the oil temperature significantly reduces the oil temperature rise!

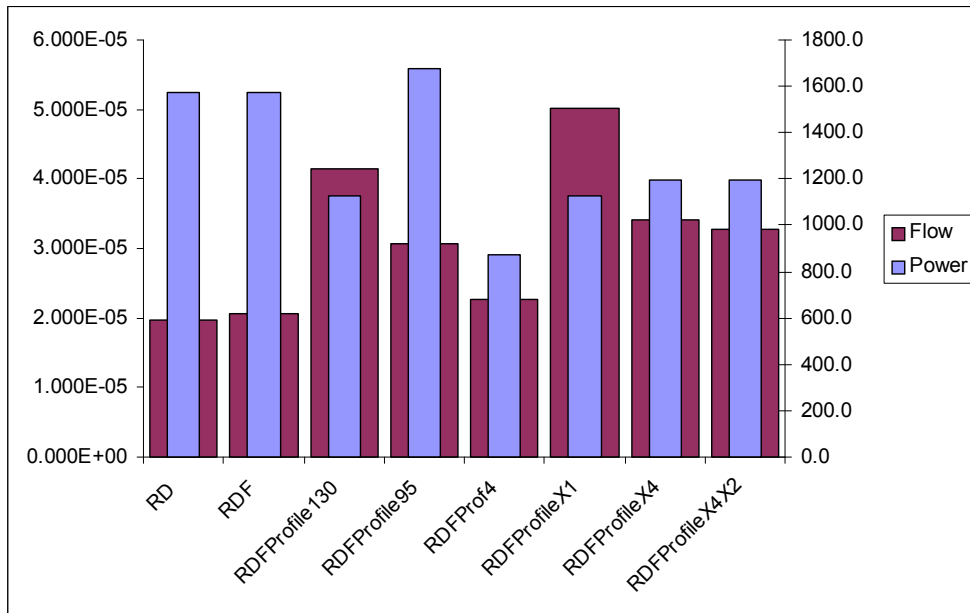


Figure 6-59 Oil flow and viscous power loss

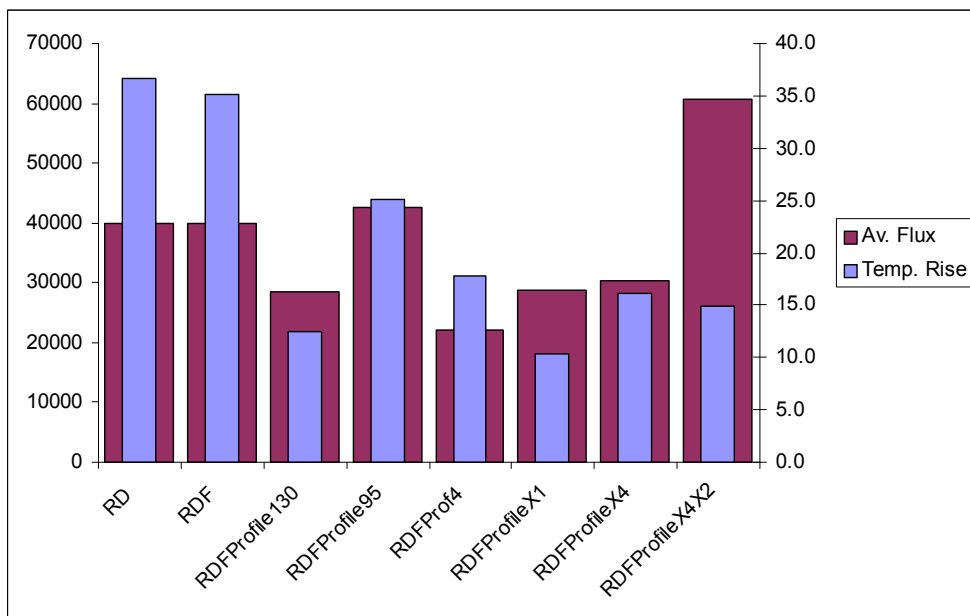


Figure 6-60 Temperature rise in the oil and average heat flux to bearing surface

6.7.4 GENERAL PARAMETER STUDIES

Two studies were performed during the year to measure the effects of parameter variations. These calculations cannot be regarded as complete.

Integration Parameters

In order to check that optimum parameters were being used for the numerical integration, a series of test jobs has been started testing the numerical integration parameters and method (Runge-Kutta-Cash-Karp, Bulirsch-Stoer and Newmark-Beta) for SBA, SALBA and RHD oil film calculation methods. Results will be shown in the thesis.

The tests will be extended to cover EHD models. At present the only methods available for EHD are the Bulirsch-Stoer numerical integration and the iterative solver. Extending the Newmark-Beta method to include EHD has been coded but not yet tested. Possible further advanced integration methods as shown in Bajer (2002) will also need to be tested to see if they provide any real advantage and coding of the Hilber-Hughes-Taylor and Bossak methods has been started.

Mesh density

So far, all completed EHD calculations have been performed for the same mesh density (48x9 elements on the FD mesh and 16x3 reduced mathematically from 32x6 on the FE mesh). It is expected that some further study will take place on this topic. However some FD mesh density variation has been completed on the RHD models. Results for the high speed engine at 16200 rpm are shown here.

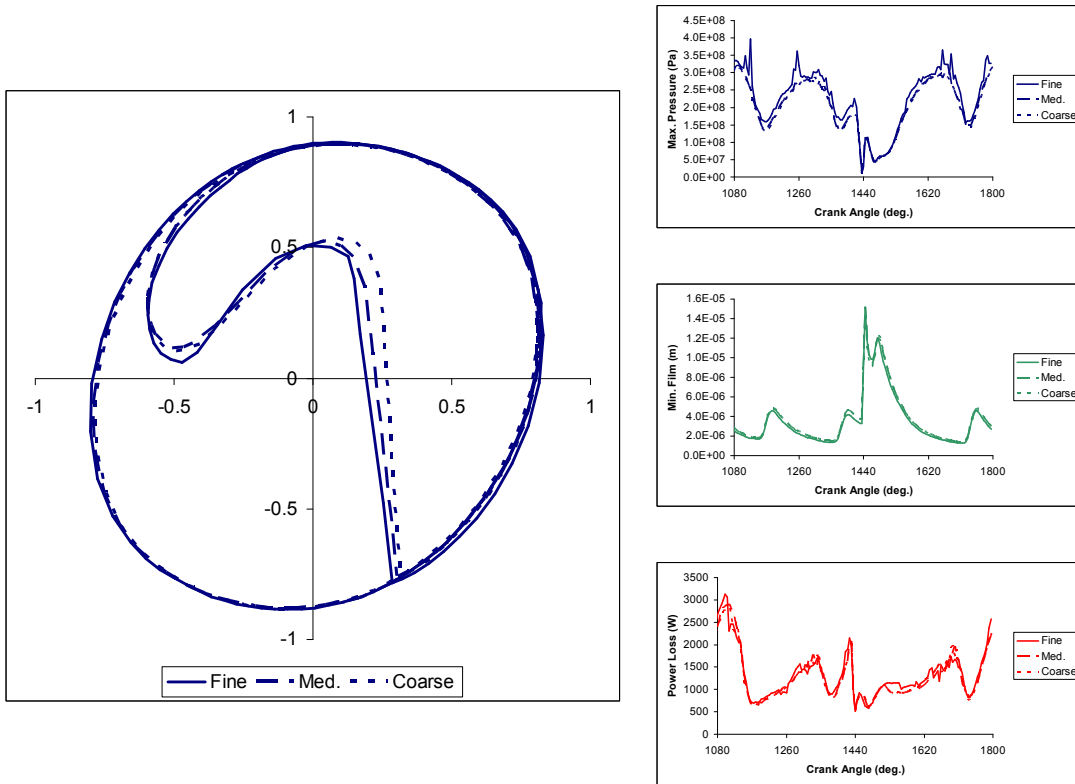


Figure 6-61 Effect of mesh density - RHD

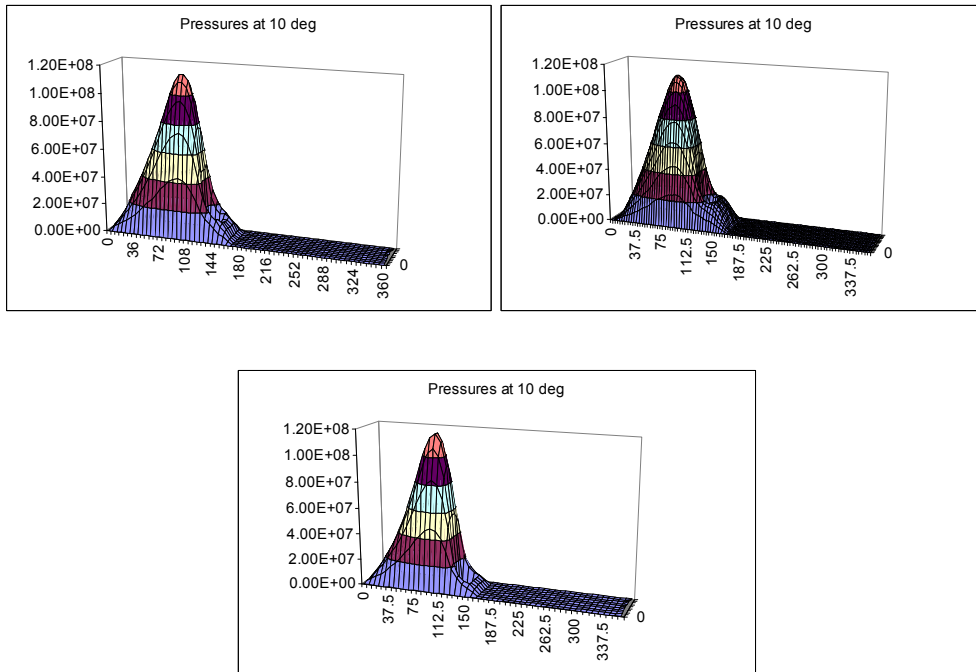


Figure 6-62 Effect of mesh density on pressure profile at 10 deg. crank angle(from top left – medium, fine, coarse)

Oil hole position

One of the reasons for carrying out calculations on the high speed engine big end bearing was to investigate experience that showed that longer bearing life could be obtained using an oil hole position 30 degrees after the Top Dead Centre position on the crankpin. That angle is regarded as the standard oil hole position by the manufacturer of the engine instead of the conventionally used 60 degrees in many other engines. In particular, it was thought that the presence of elastic deformation of the structure could influence the optimum oil hole position. This study will also be extended to investigate the influence of oil hole position on cavitation parameters once the oil film history calculation has been added to the EHD program.

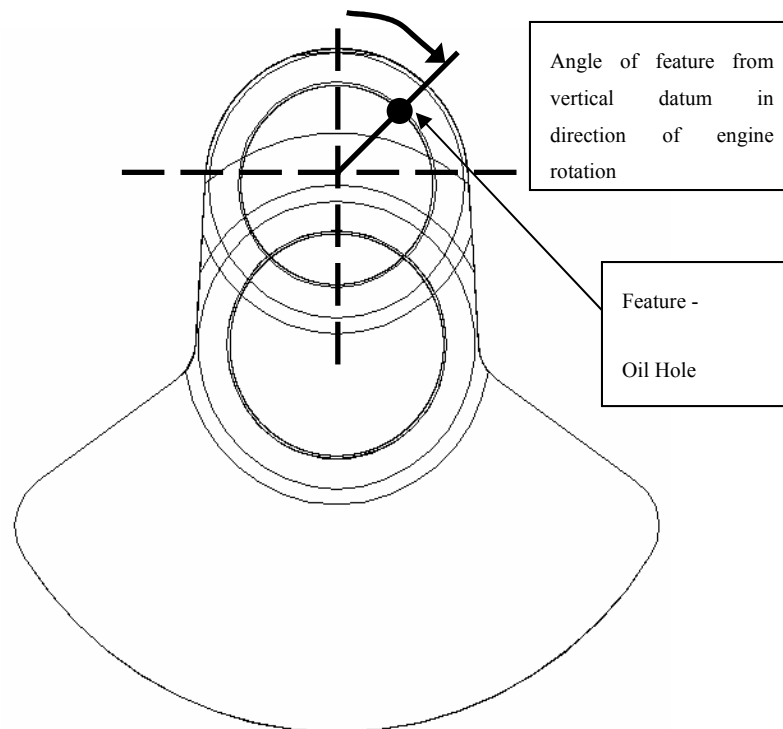


Figure 6-63 Definition of oil hole position on big end bearing journal

RHD and EHD calculations have been performed at 16200 rpm with three different oil hole positions. The EHD and TEHD results shown in a previous section were all carried out for the standard 30 degree oil hole position. The following figures expand on the previous figures and add the oil hole positions at 0 degrees and 60 degrees for comparison.

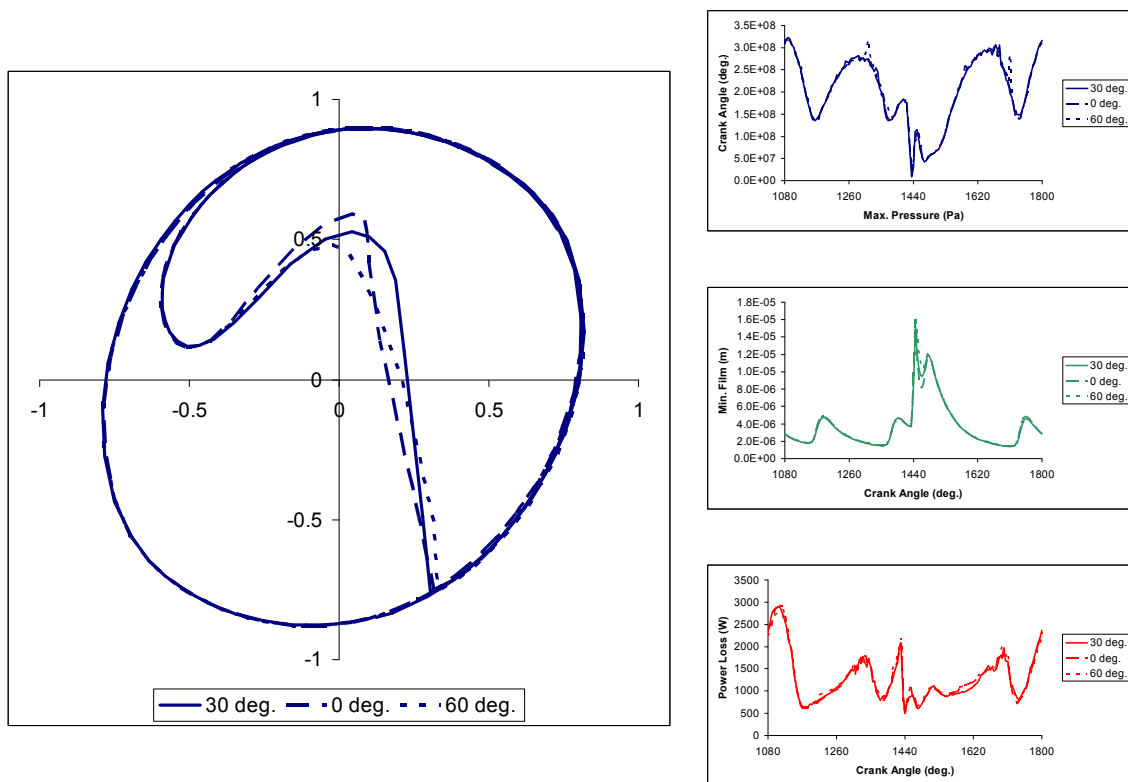


Figure 6-64 Effect of oil hole position – RHD

Fig. 6.64 shows that there is very little difference in shaft orbit, maximum pressure, minimum oil film thickness or viscous loss for the different oil hole positions. The differences in pressure distribution are much more obvious (Fig. 6.65)

Crankshaft angle of 10 degrees appeared to be the only angle at which interference of the oil hole with the pressure distribution could be seen. At this angle there is significant combustion gas pressure loading on the system despite the very high inertia loads acting in the opposite direction on this high speed engine. Fig. 6.65 shows that there is some interference of the oil hole and the pressure distribution for the standard oil hole position (first plot). This interference is at the trailing edge of the distribution so would feed oil into an expanding film. As would be expected the zero degree oil hole position produces a lot of interference (second plot) and the 60 degree position no interference at all (last plot).

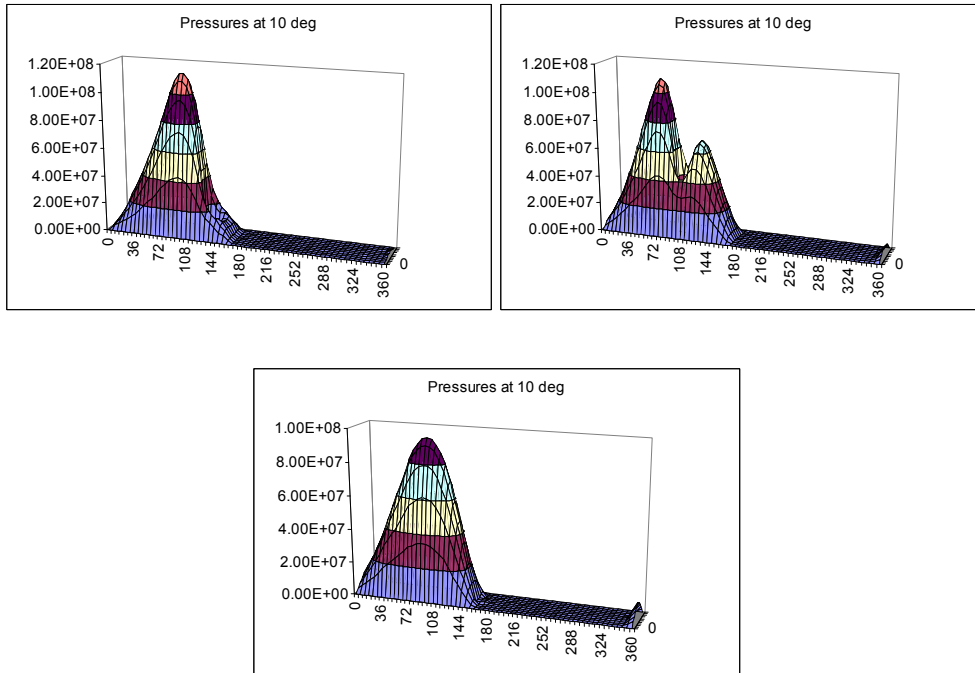


Figure 6-65 Pressure distribution at 10 deg. crank angle – RHD (oil hole positions from top left – 30, 0, 60 deg.)

The EHD calculation also shows little effect on the cycle curves for the different oil hole positions (Fig. 6.66).

It can be seen that the EHD calculation causes greater interference with the pressure distribution because it spreads the pressure compared to the RHD calculation as the connecting rod deforms (Fig. 6.67).

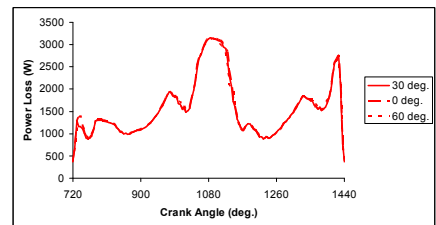
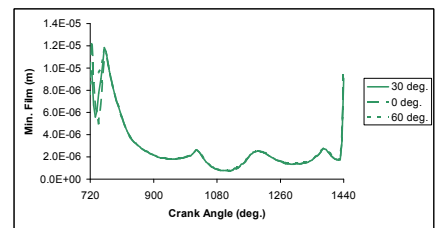
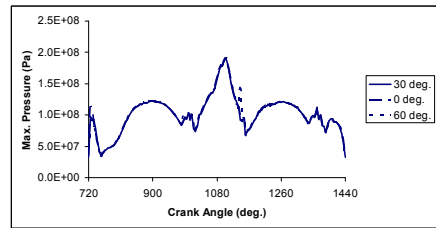
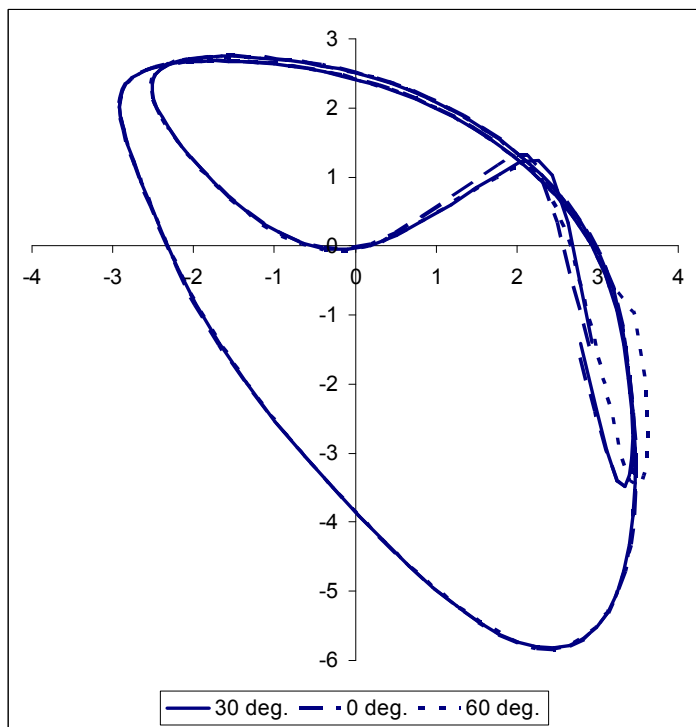


Figure 6-66 Effect of oil hole position on EHD models

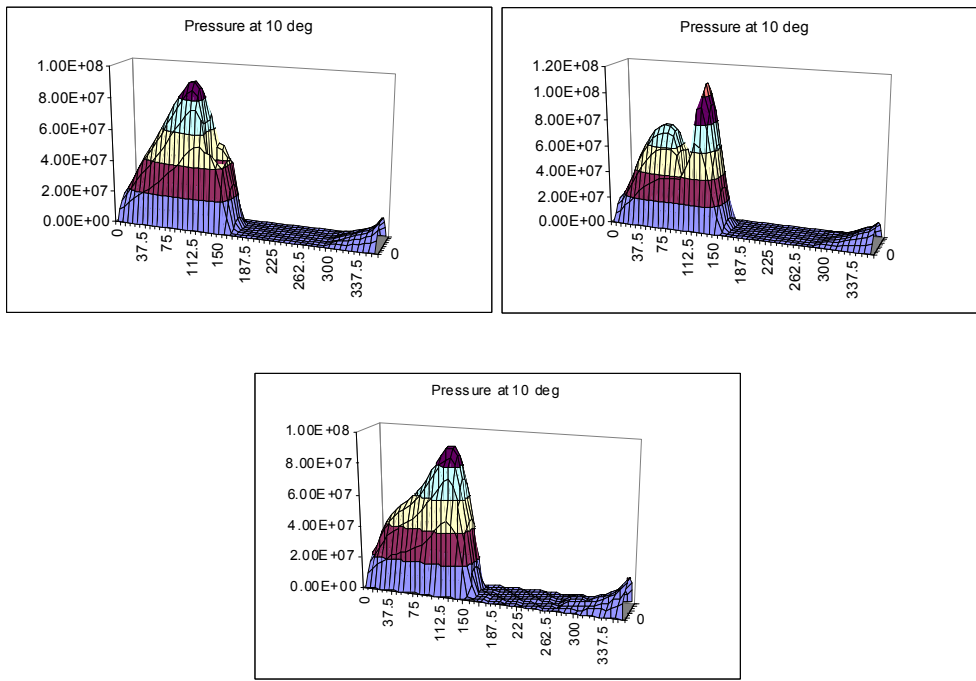


Figure 6-67 Pressure distribution for different oil hole positions at 10 deg. crank angle – EHD (oil hole positions from top left – 30, 0, 60 deg.)

The story is very similar for the thermally deformed circular bearing (Fig. 6.68 and 6.69) but note how the spreading effect of the EHD calculation has been much reduced by the crowned shape of the thermal deformation leading to pressure distributions that are much more like the RHD case (Fig. 6.65).

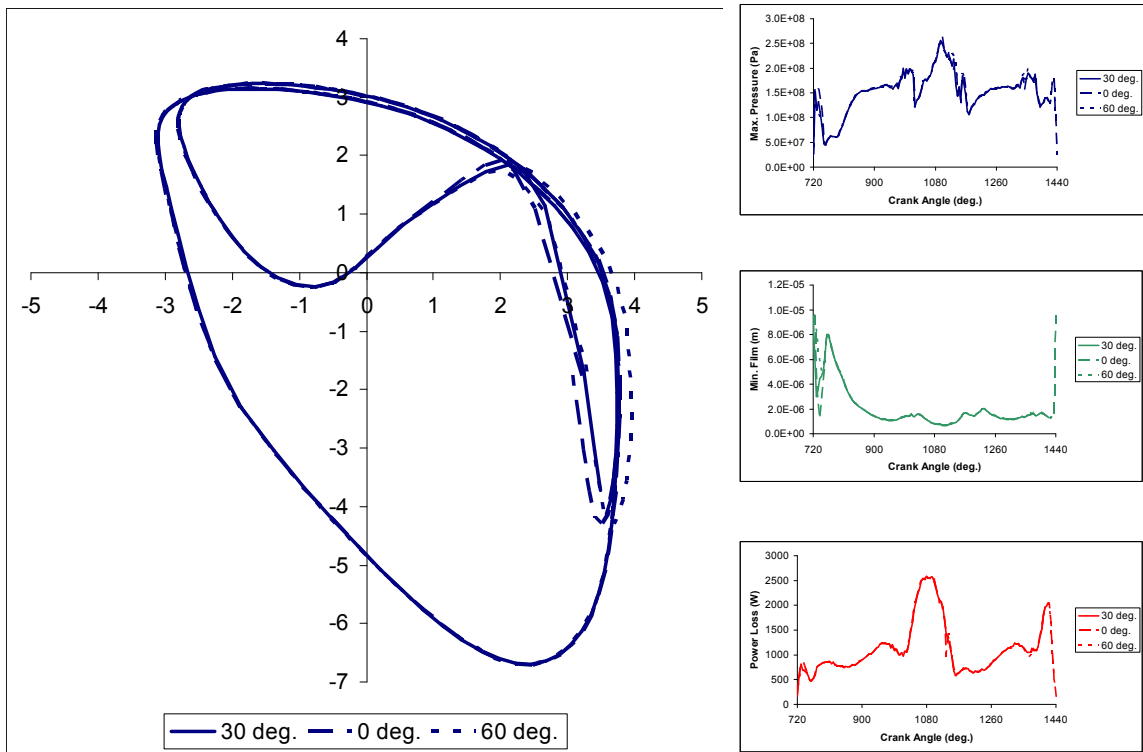


Figure 6-68 Effect of oil hole position – TEHD

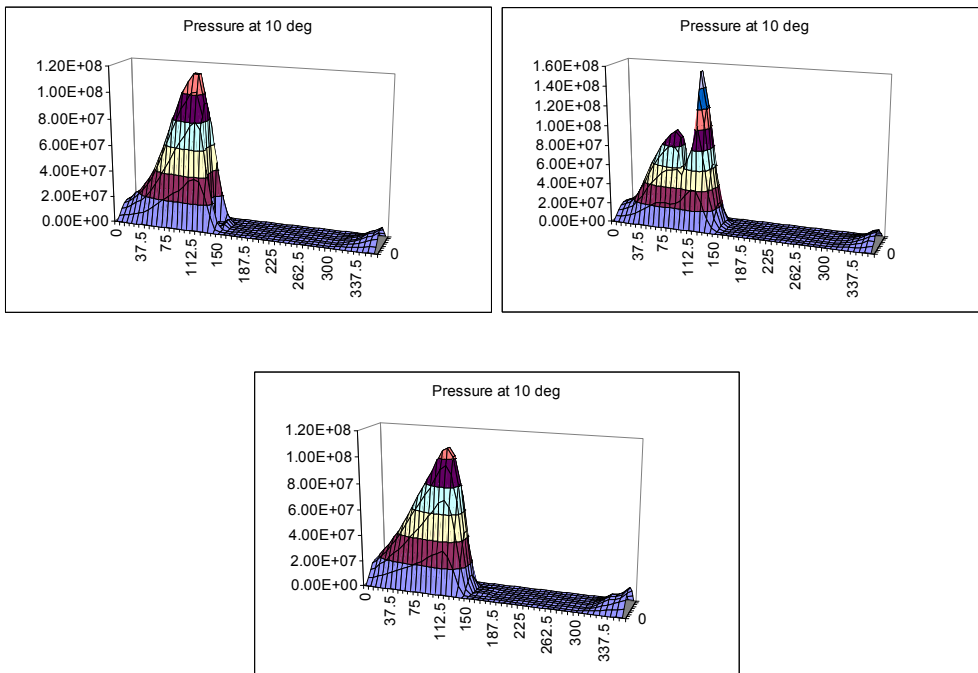


Figure 6-69 Pressure distribution at 10 deg. crank angle – TEHD (oil hole positions from top left – 30, 0, 60 deg.)

The bearing with the cold measured profile also shows little change in the cycle curves (Fig. 6.70) but goes even further than the RHD results in that the standard 30 degree oil hole position does not interfere with the pressure distribution (Fig. 6.71).

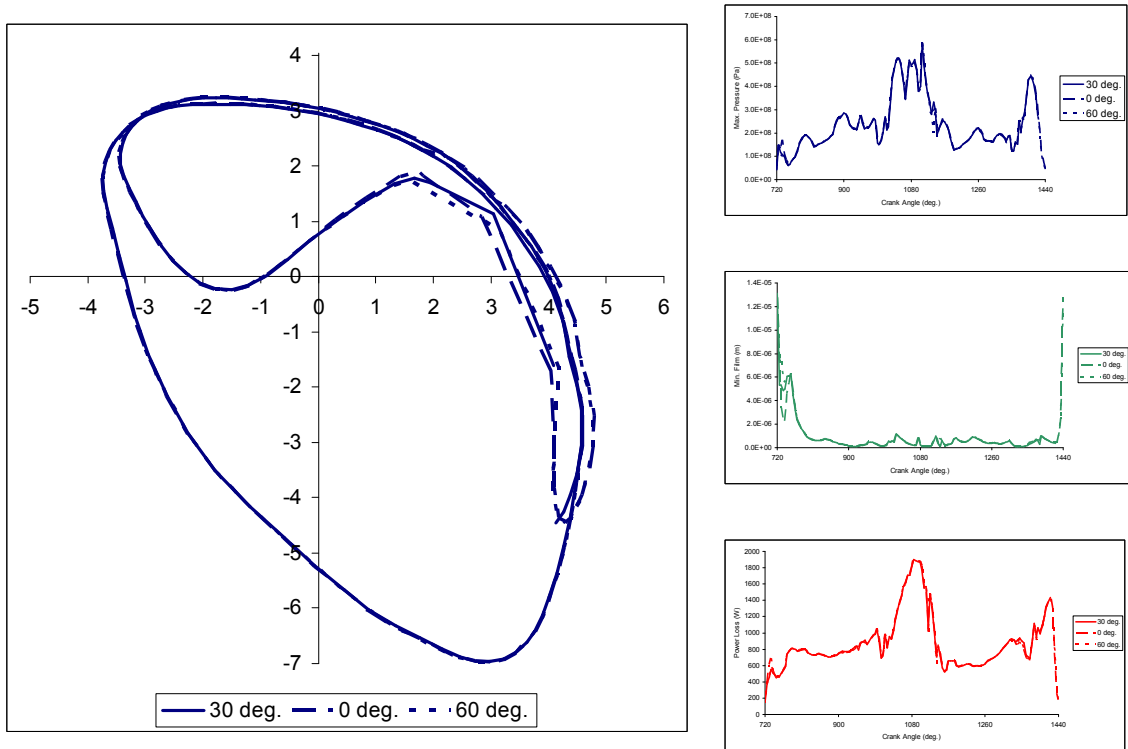


Figure 6-70 Shaped bearing comparison of effects of oil hole position

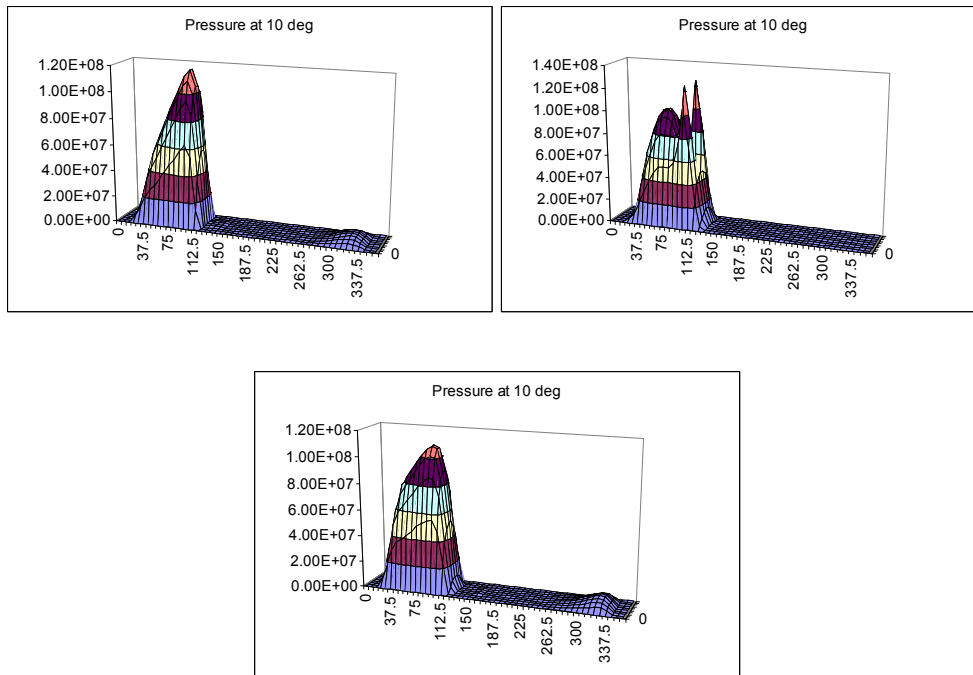


Figure 6-71 Shaped bearing – effect of oil hole on pressure distribution at 10 degrees shaft angle for oil hole at 30 deg., 0 deg., 60 deg.

These results indicate that the effects taken into account for the oil film calculation (elasticity, thermal deformation, assembly deformation) have a significant effect on the relative location of the oil hole to the trailing edge of the pressure distribution. The standard oil hole position of 30 degrees would appear to be beneficial in terms of feeding oil into the location where cavitation is starting. Therefore these test cases form the basis for looking at oil film history and cavitation. See later section and Forstner and Struwe (2004).

6.8 CAVITATION DAMAGE PARAMETER

The diesel engine connecting rod big end bearing model was used to examine the effect of the cavitation damage parameter. This bearing was chosen because the paper by Forstner and Struwe (2004) concerned the cavitation problems in a big end bearing on a diesel engine.

New calculations added to the program included the ability to record the maximum or minimum value of any of the output parameters individually at each mesh node point. The calculation of the cavitation damage parameter

$$P_C = -\min\left(\frac{dp}{d\theta}, 0\right) \times \max\left(\frac{dh}{dt}, 0\right) \times \pi DL \quad 6-2$$

was recorded at each node point and each time step. The individual terms were also recorded at each node point and time step. The parameter calculated by equation 6.2 at the end of each calculation is shown in this section.

The diesel engine big end bearing was used and the following calculations performed to see the effect on the cavitation damage parameter. Each of the calculations was changed in one respect from the baseline calculation i.e. not cumulative changes.

Table 6.7 lists the calculation cases starting with the baseline calculation, identical in every respect the diesel engine big end bearing shown earlier in the thesis. Partial grooves were examined because it is well known that these can act as a source of cavitation damage. Gasoline engine gas pressures were used to judge the effect of combustion gas pressure – gasoline engines are less likely to suffer cavitation damage. The effect of the rate of gas pressure rise was also examined because it is thought to be important, especially when changing to alternative fuels such as Compressed Natural Gas (CNG). The effect of rotational speed was looked at. The effect of elastic deformations was thought likely to be important. The elastic deformation tends to spread the oil film pressure distribution giving lower maximum oil film pressure but also leads to higher velocity of the journal in the clearance space.

Diesel, RHD, 5000 rpm	Baseline calculation, identical to the calculation shown earlier in this chapter
Diesel, RHD, partial grooves, 5000 rpm	Partial grooves added to see how those affect the distribution of the cavitation damage parameter
Gasoline, RHD, 5000 rpm	Cylinder gas pressure curve changed to that of a similarly sized gasoline engine. All other data as for original diesel engine
Diesel, RHD, fast pressure rise, 5000 rpm	Gas pressure curve changed to increase the rate of pressure rise just before Top Dead Centre Firing (TDCF)
Diesel, RHD, 3000 rpm	Slower rotation speed
Diesel, RHD, 1000 rpm	Slower again
Diesel, EHD, 5000 rpm	Include ElastoHydroDynamic (EHD) deformations of the bearing

Table 6-7 Calculation List for Cavitation Damage Parameter

6.8.1 BASELINE CASE – DIESEL, RHD, 5000 RPM

Fig. 6.72 shows the x and y eccentricity ratios versus crankshaft angle. Note that Top Dead Centre Firing is at 0, 720 and 1440 deg. And we would expect rapid movement at around this angle.

The baseline case is standard in every respect. These are typical diesel engine results – large movement at 1420 deg (700 deg), just before TDCF as the gas pressure load overcomes the inertia load. The orbit of the journal is shown in Fig. 6.73. The dots are 5 deg apart. The four colours represent the 4 strokes of the engine. Key crank angles are labelled (see later slides) – diamonds (pressure), squares (velocity), circles (rate of pressure change), triangle (velocity and rate of pressure change).

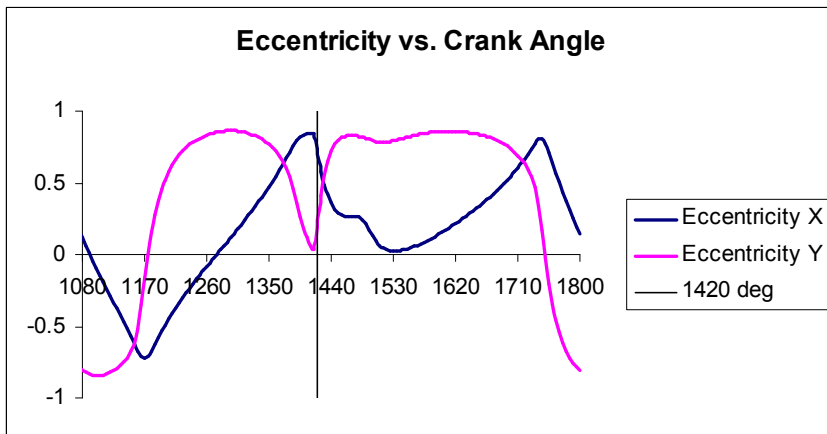


Figure 6-72 Diesel, RHD, 5000 rpm - Eccentricity

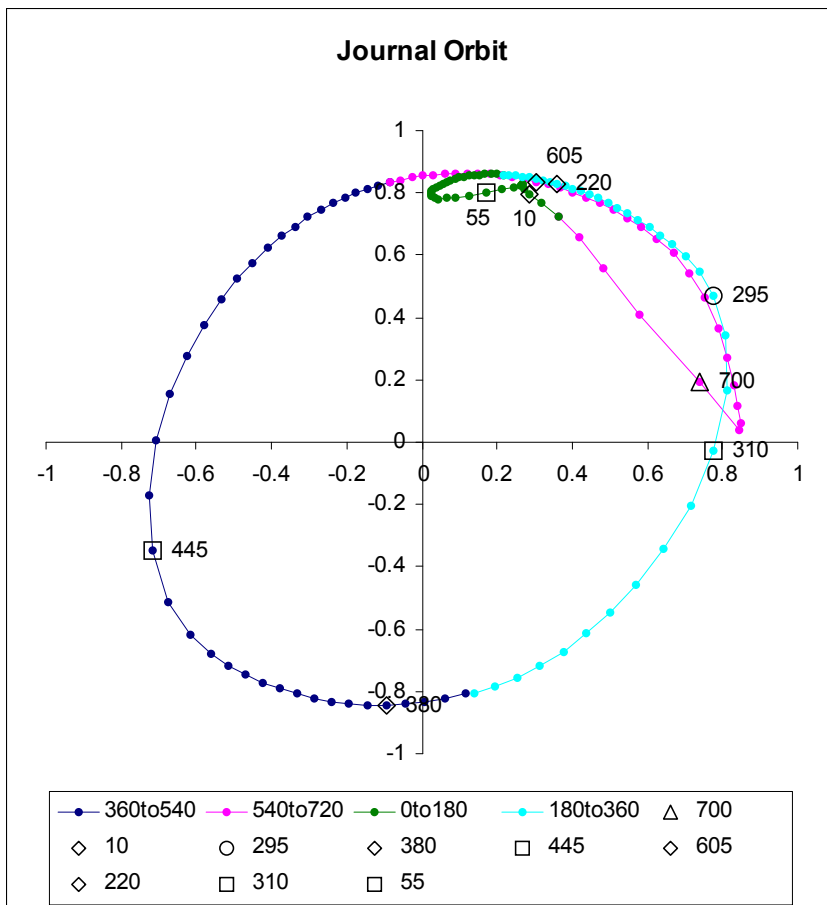


Figure 6-73 Diesel, RHD, 5000 rpm – Journal Orbit

The velocity plots show the sudden motion at 1420 (700) deg even more clearly.

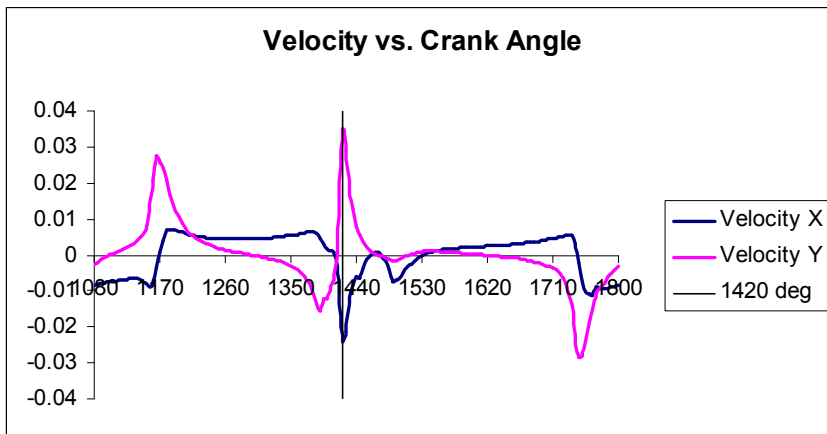


Figure 6-74 Diesel, RHD, 5000 rpm - Velocity

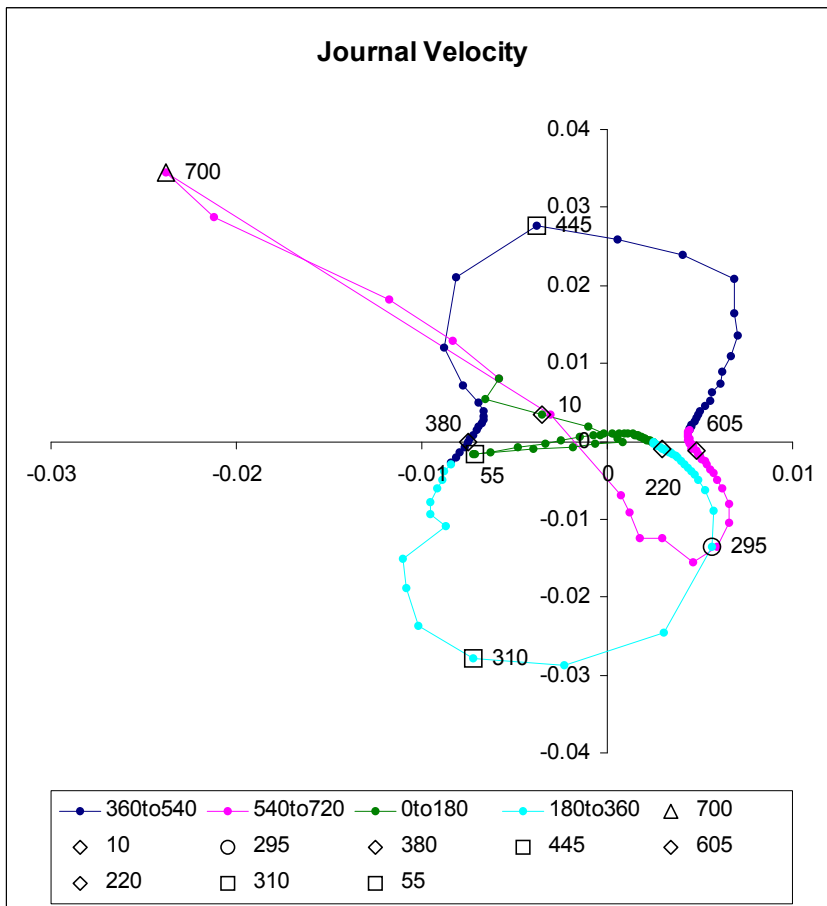


Figure 6-75 Diesel, RHD, 5000 rpm - Velocity

Peak pressures in the oil film over the cycle are shown in Fig. 6.76 with the peaks at 1100 (380), 1325 (605), 1450 (10) and 1660 (220) degrees crank angle. The journal

position in the clearance space can be checked on the earlier figures. The pressure distribution in the bearing at each of these angles is shown on the following slides.

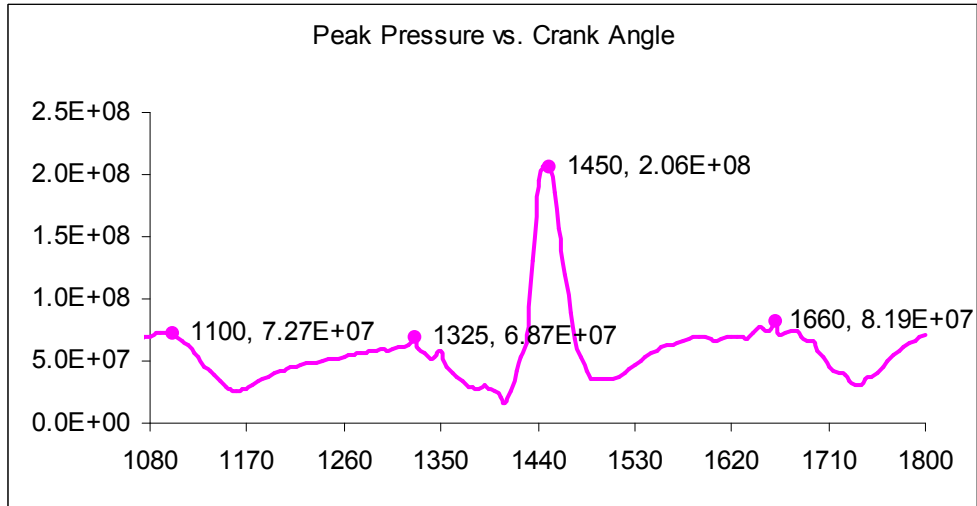


Figure 6-76 Diesel, RHD, 5000 rpm – Peak Pressures

Fig. 6.77 is a snapshot of the oil film pressure distribution at the crank angle that produces the highest pressure (10 deg ATDCF i.e. 30 deg after the start of the large movement across the clearance space). Note that, in all of the following 3D plots, the x axis is angle around the bearing and z axis is axial position on the bearing.

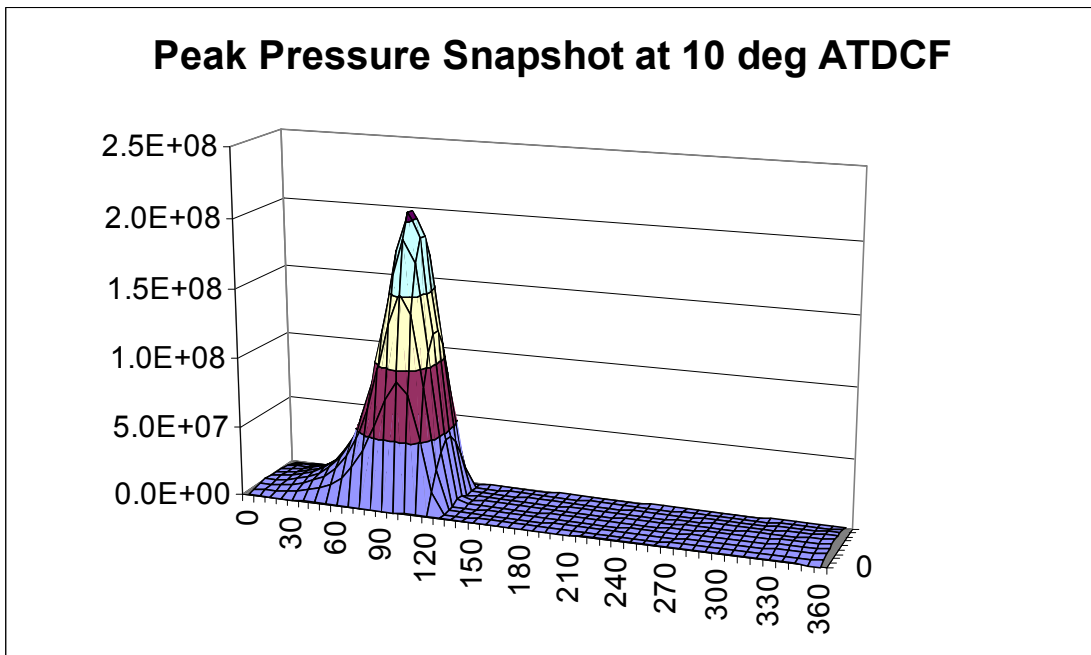


Figure 6-77 Diesel, RHD, 5000 rpm – Peak Pressure Snapshot

The pressure distributions for the minor peaks follow in Figs. 6.78 to 6.80.

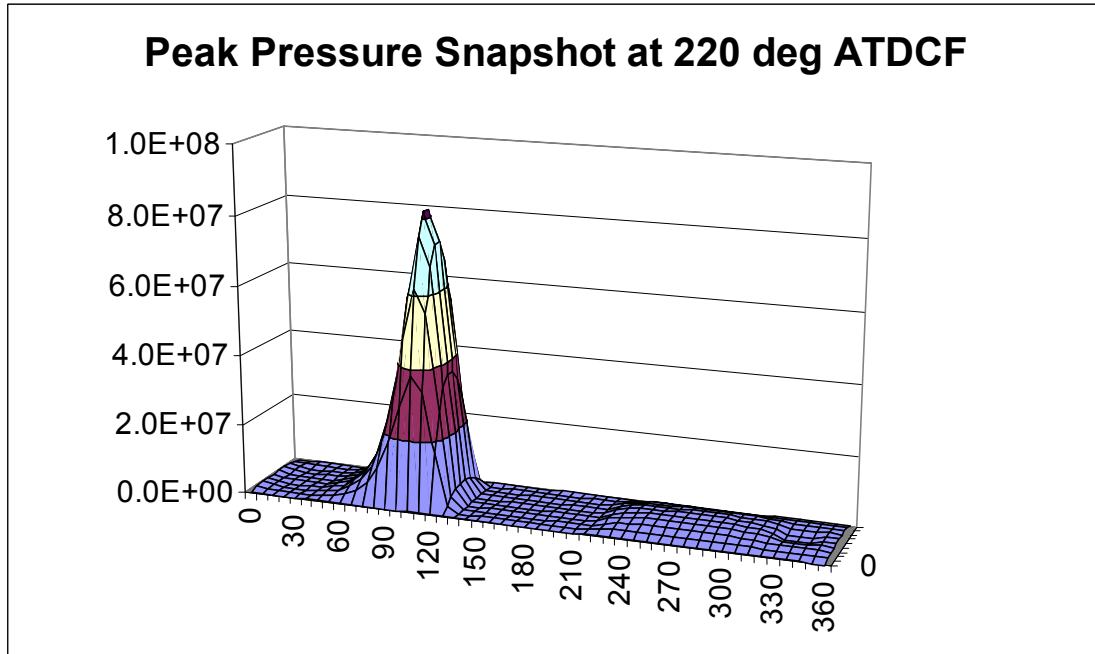


Figure 6-78 Diesel, RHD, 5000 rpm – Pressure Snapshot at 220 deg

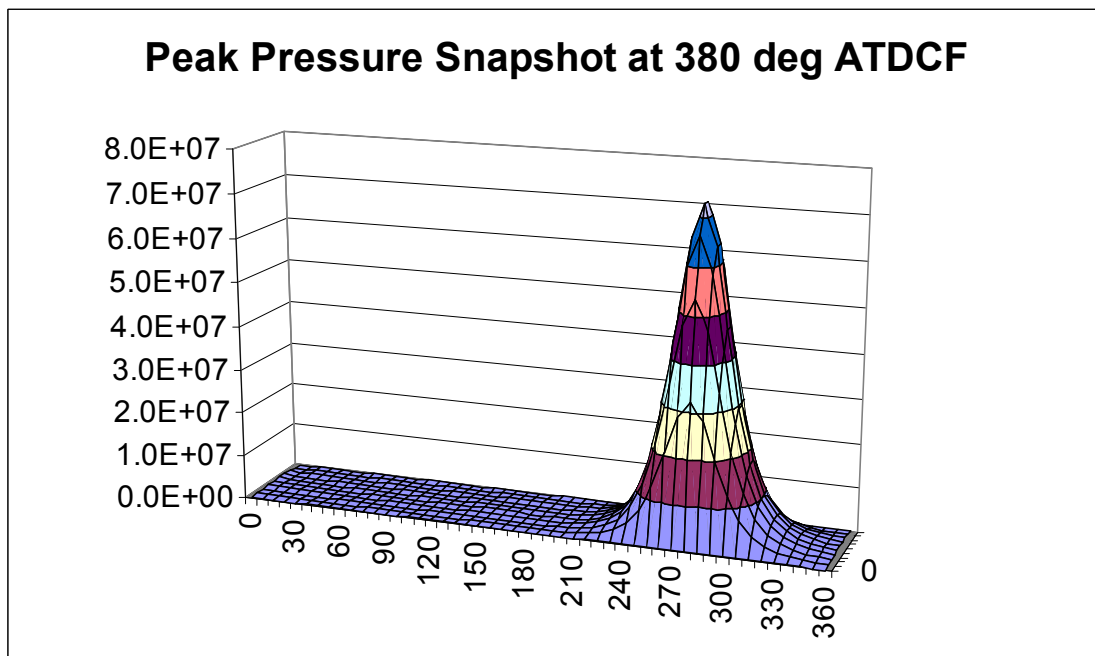


Figure 6-79 Diesel, RHD, 5000 rpm – Pressure Snapshot at 380 deg

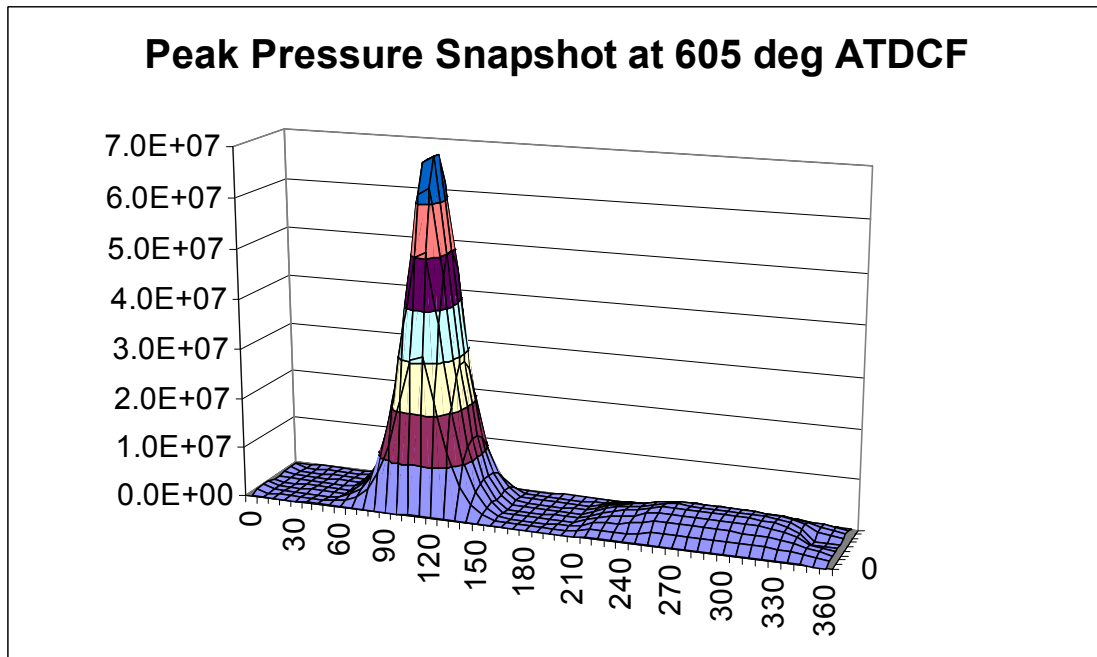


Figure 6-80 Diesel, RHD, 5000 rpm – Pressure Snapshot at 605 deg

Plotting the maximum pressure at each individual node over the whole cycle is useful for showing what is happening over the whole bearing without having to take snapshots. Fig. 6.81 shows the distribution of maximum pressure values over the cycle for all of the bearing surface.

It is possible to see that the peak value is the same as that at 10 deg. Crank angle and the minor peak is the value at 380 deg. Crank angle. Note that the minor peaks at 220 and 605 deg. have no effect because they coincide on the bearing surface with the major peak at 10 deg. Crank angle.

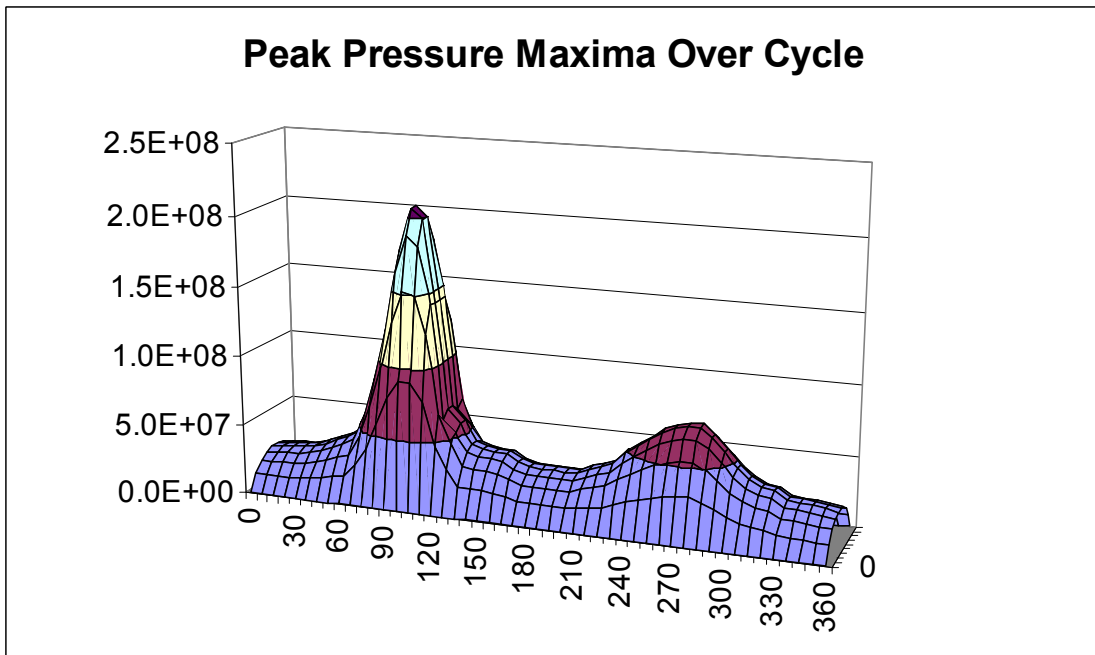


Figure 6-81 Diesel, RHD, 5000 rpm – Peak Pressure Maxima Over Cycle

The minimum film thickness over the cycle is shown in Fig. 6.82.

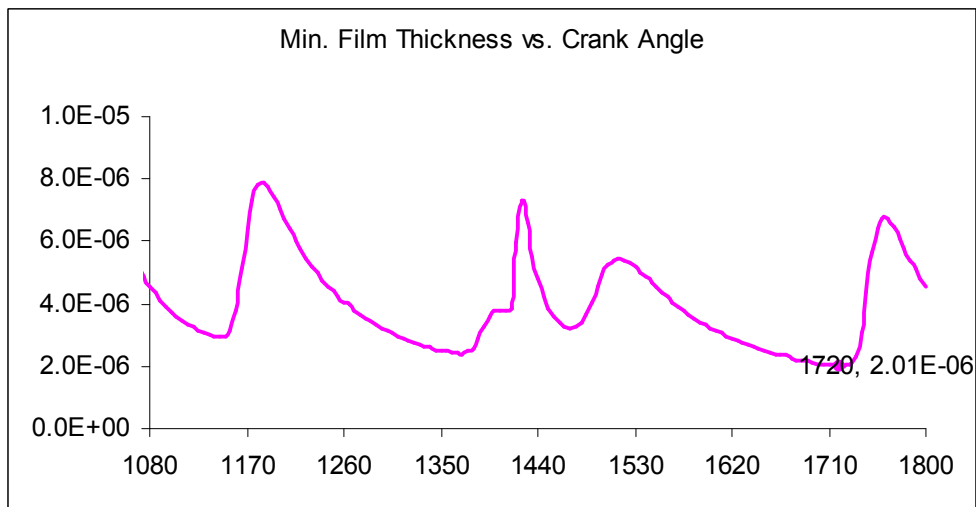


Figure 6-82 Diesel, RHD, 5000 rpm – Minimum Film Thicknesses

The snapshot of the film shape at the minimum value is shown in Fig. 6.83. This is a simple sinusoidal shape for this RHD calculation. The later EHD calculation is different. Fig. 6.84 shows a similar plot in polar coordinates. The scale is chosen so that the reader can see the journal (inner black circle) sitting in the bearing (red line).

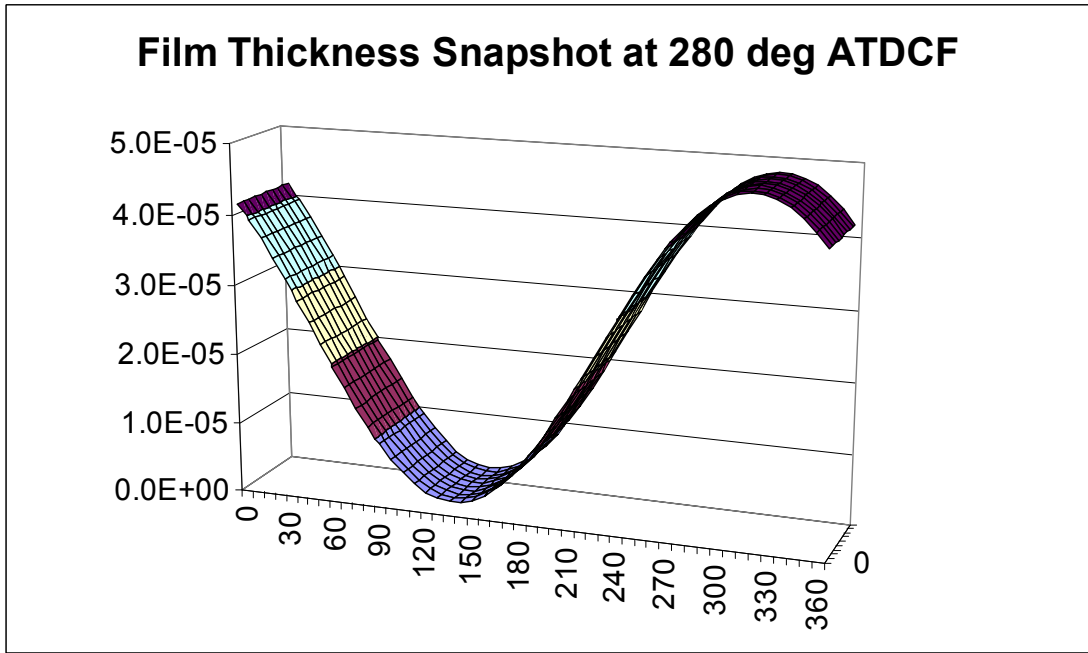


Figure 6-83 Diesel, RHD, 5000 rpm – Film Thickness Snapshot at Minimum

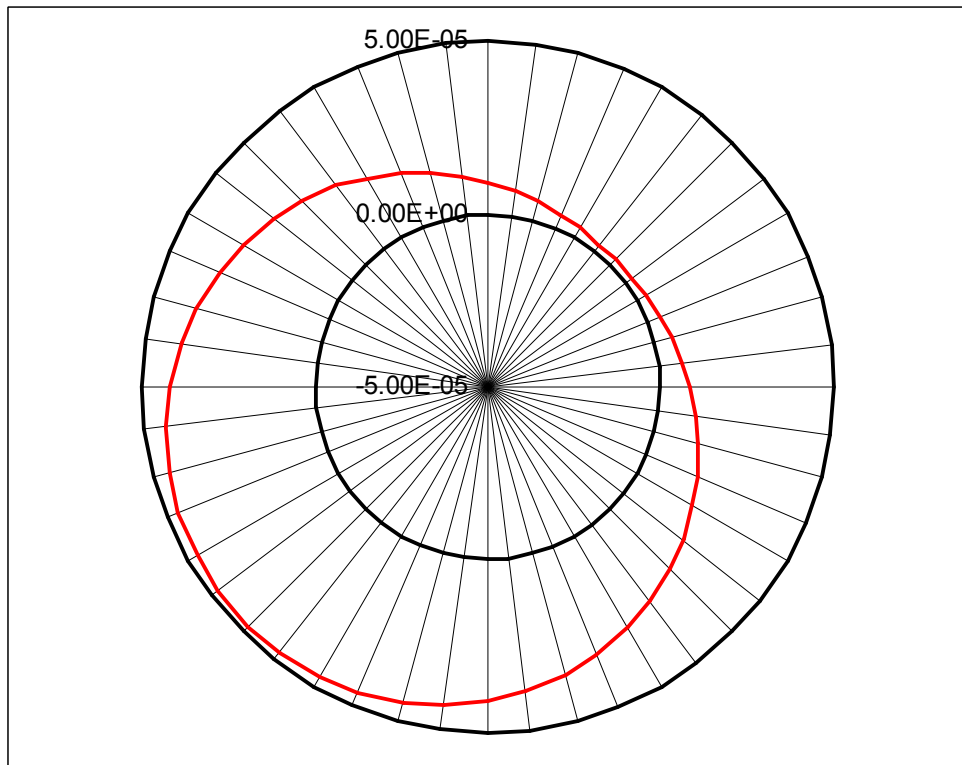


Figure 6-84 Diesel, RHD, 5000 rpm – Film Polar Plot at Minimum

Fig. 6.85 shows the minima at each node over the whole cycle. Note how this is no longer a simple sinusoid and shows where on the bearing minimum film thickness occurs.

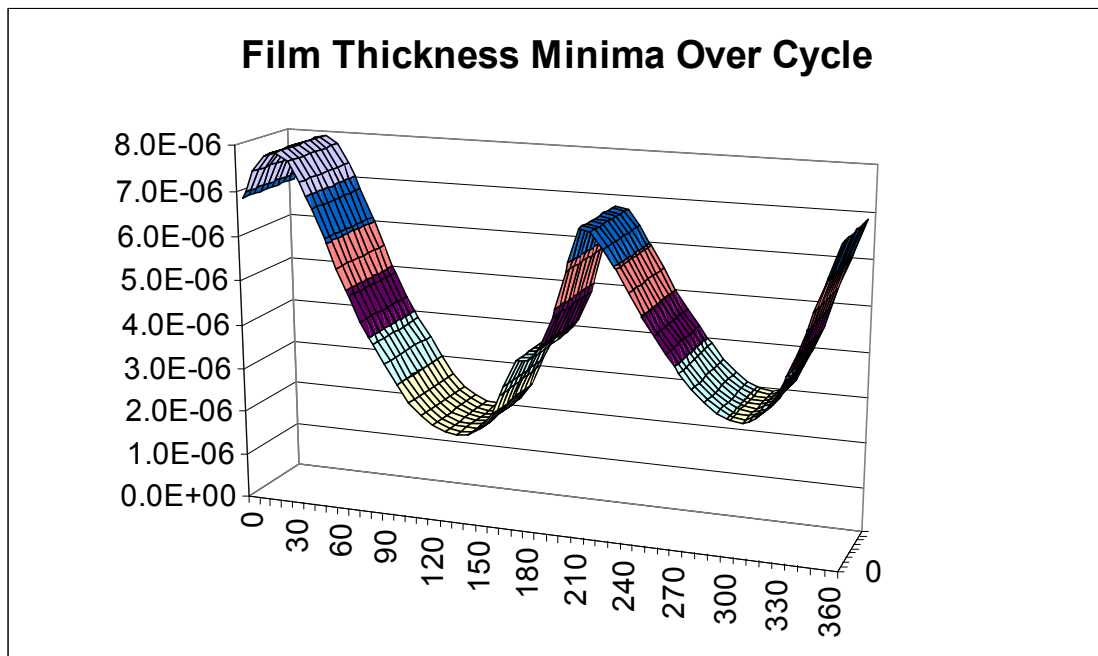


Figure 6-85 Diesel, RHD, 5000 rpm – Film Thickness Minima Over Cycle

Plotting the separation velocity (also called cavitation velocity or negative of the squeeze velocity) gives a peak value at 1420 (700) deg. Crank angle with minor peaks also labelled in Fig. 6.86.

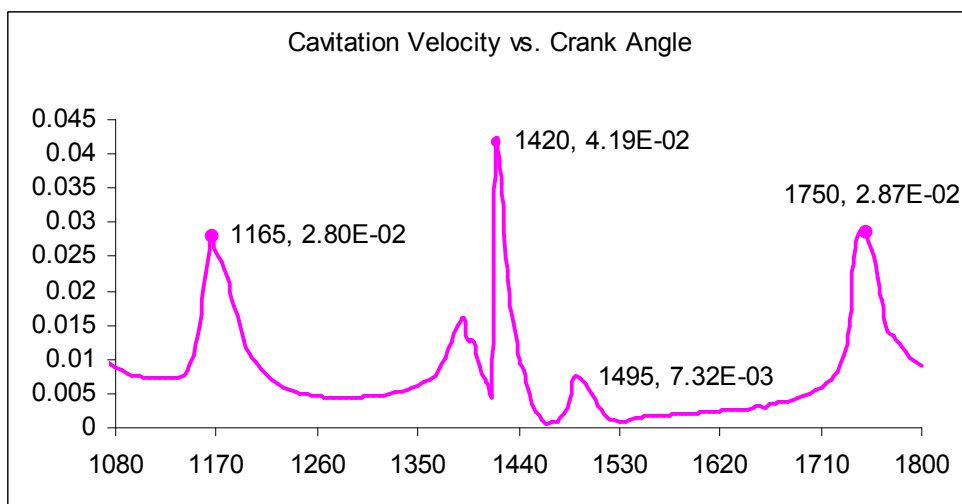


Figure 6-86 Diesel, RHD, 5000 rpm – Maximum Cavitation Velocity Over Cycle

Plotting the separation velocity (called cavitation velocity or negative of the squeeze velocity) produces a sine wave as this is RHD calculation – this is a snapshot at the maximum value in the cycle in Fig. 6.87.

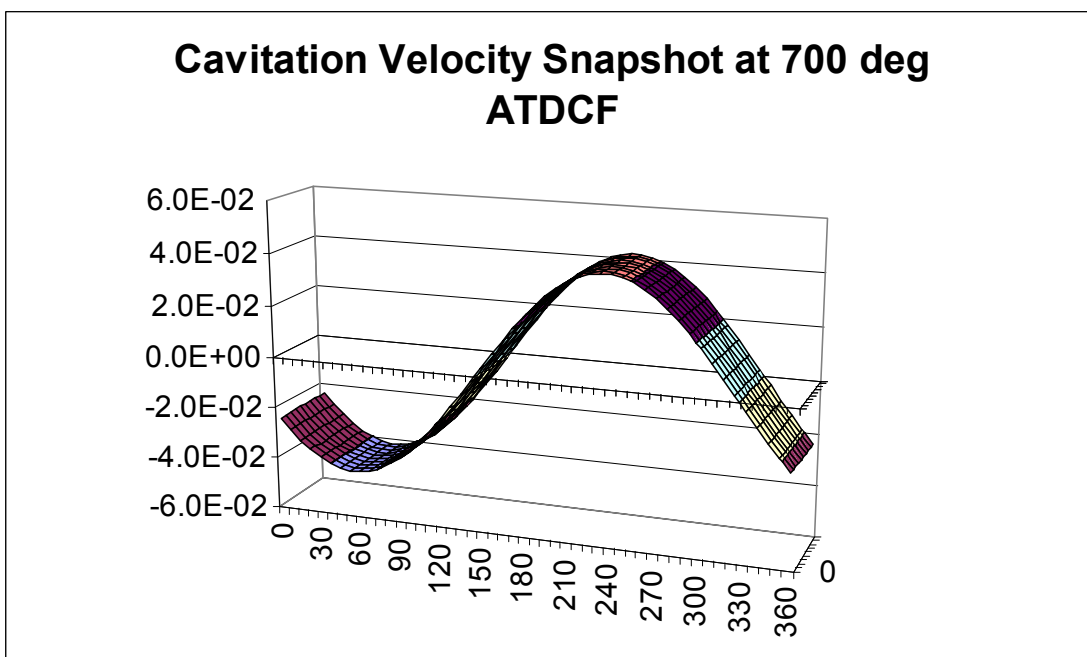


Figure 6-87 Diesel, RHD, 5000 rpm – Cavitation Velocity Snapshot at Maximum

Snapshots at minor peaks are shown in Figs. 6.88 - 6.90.

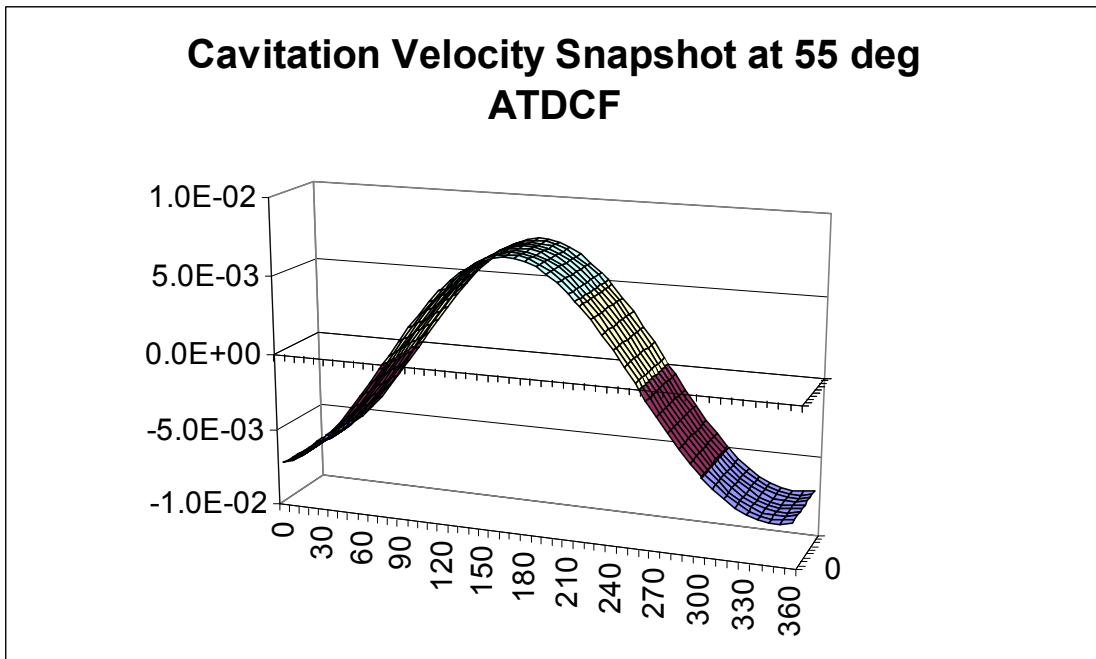


Figure 6-88 Diesel, RHD, 5000 rpm – Cavitation Velocity Snapshot at 55 deg

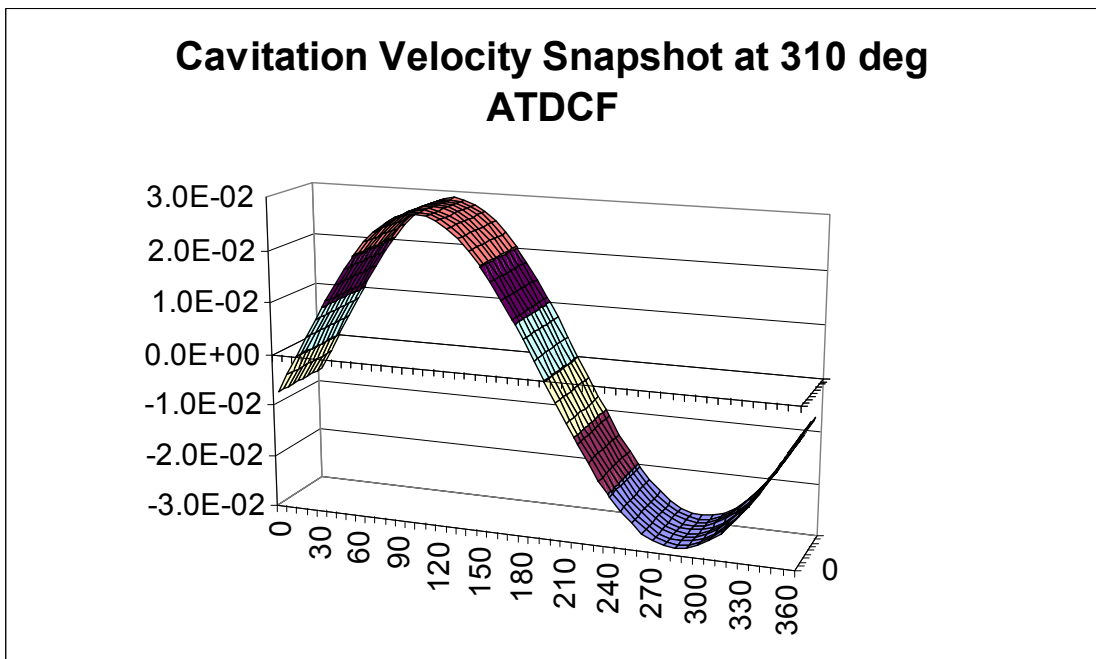


Figure 6-89 Diesel, RHD, 5000 rpm – Cavitation Velocity Snapshot at 310 deg

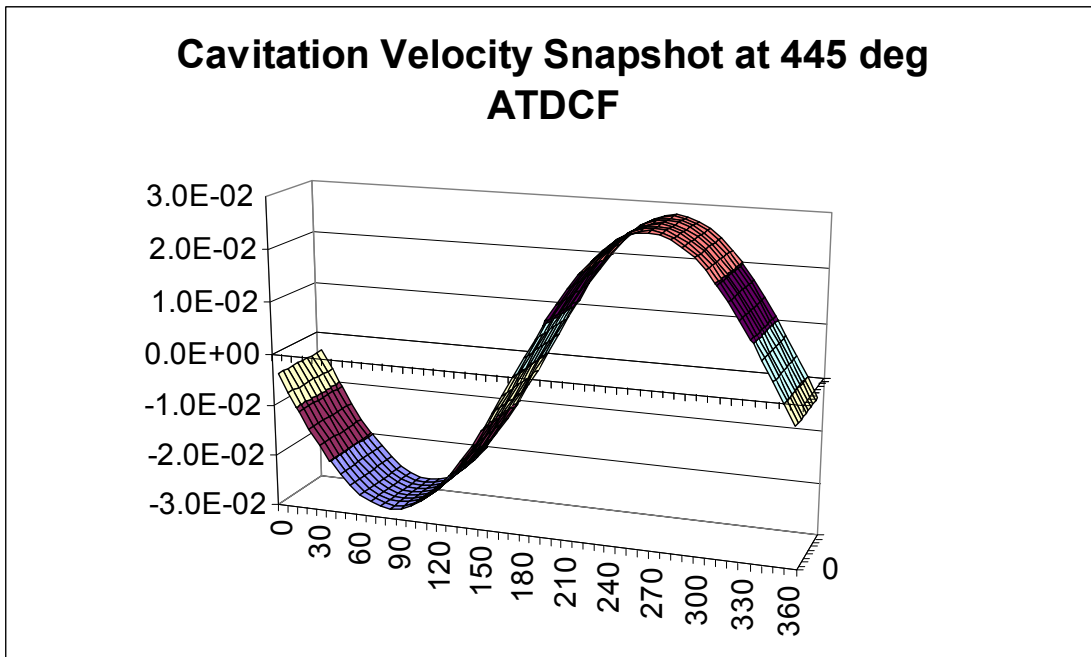


Figure 6-90 Diesel, RHD, 5000 rpm – Cavitation Velocity Snapshot at 445 deg

Again, plotting the maximum over the cycle at each node produces the same peak (from the 700 deg. Crank angle results) but a more useful view of the values over the bearing. The minor peak at 310 deg. Crankshaft angle has a significant effect, producing the small peak at about 90 deg. Bearing angle. See Fig. 6.91.

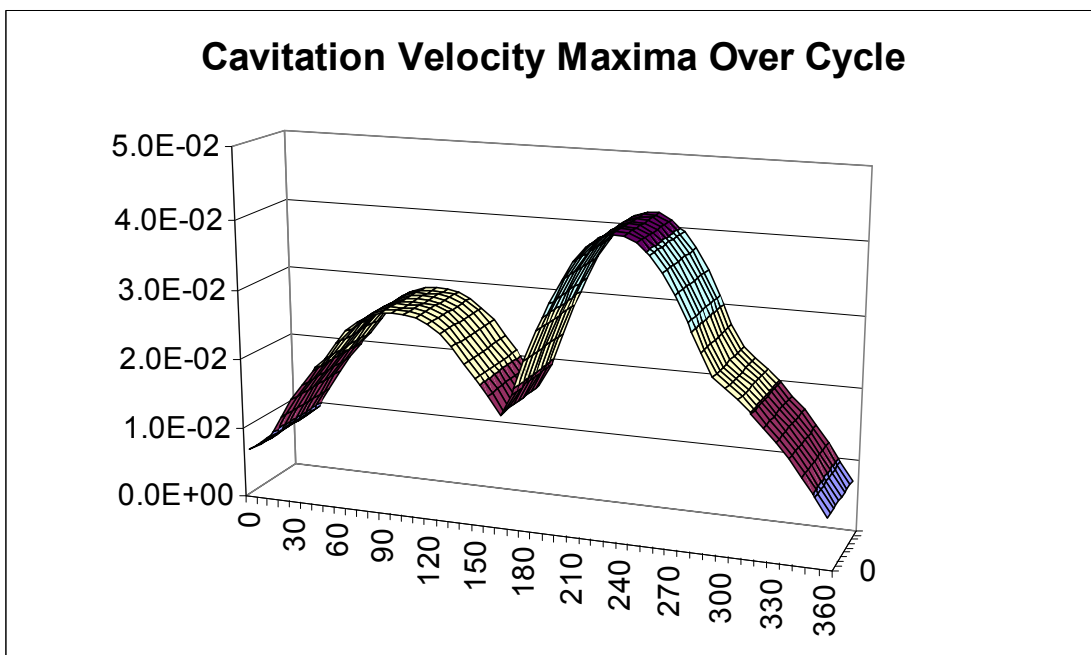


Figure 6-91 Diesel, RHD, 5000 rpm – Cavitation Velocity Maxima Over Cycle

Looking at pressure gradient dp/dq – we’re interested in the most negative values which are likely to produce cavitation. The values over the cycle are shown here in Fig. 6.92. There’s a very large negative value at 1430 (710) deg. Crank angle almost corresponding with the maximum velocity.

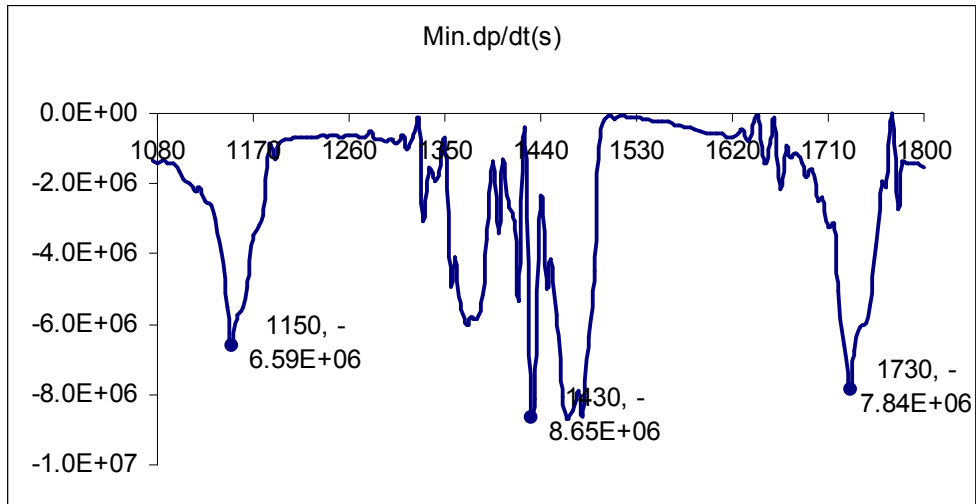


Figure 6-92 Diesel, RHD, 5000 rpm – Minimum Pressure Gradient Over Cycle

Looking at pressure gradient dp/dq – we’re interested in the most negative values which are likely to produce cavitation. Snapshots are in Figs. 6.93 – 6.95 starting with the situation at the highest negative value which occurs at 710 deg. Crank angle and 120 deg. Bearing angle.

Smoothed Pressure Gradient Snapshot at Minimum in Cycle (710 deg ATDCF)

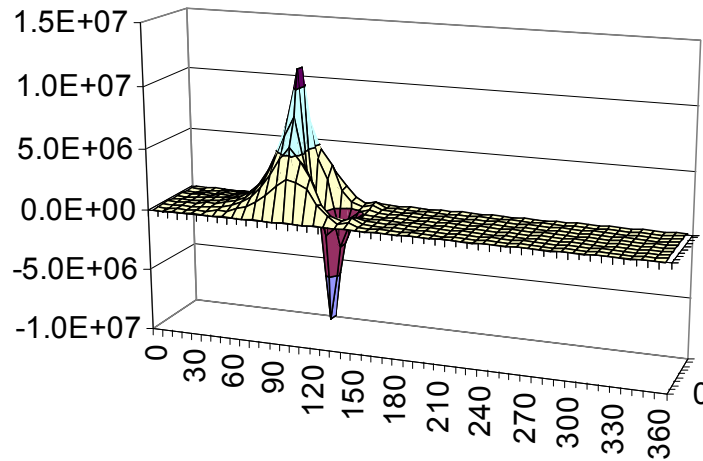


Figure 6-93 Diesel, RHD, 5000 rpm – Snapshot of Pressure Gradient at Minimum in Cycle

These are the minor peaks of negative dp/dt at 290 and 430 deg. crank angle

Smoothed Pressure Gradient Snapshot at Minimum in Cycle (290 deg ATDCF)

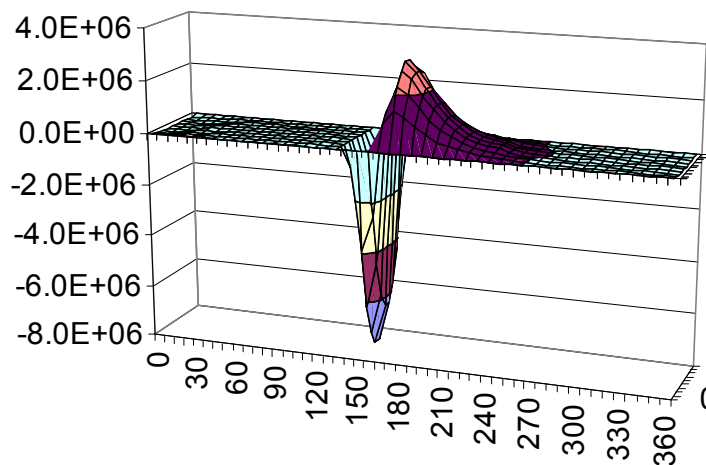


Figure 6-94 Diesel, RHD, 5000 rpm – Pressure Gradient at 290 deg

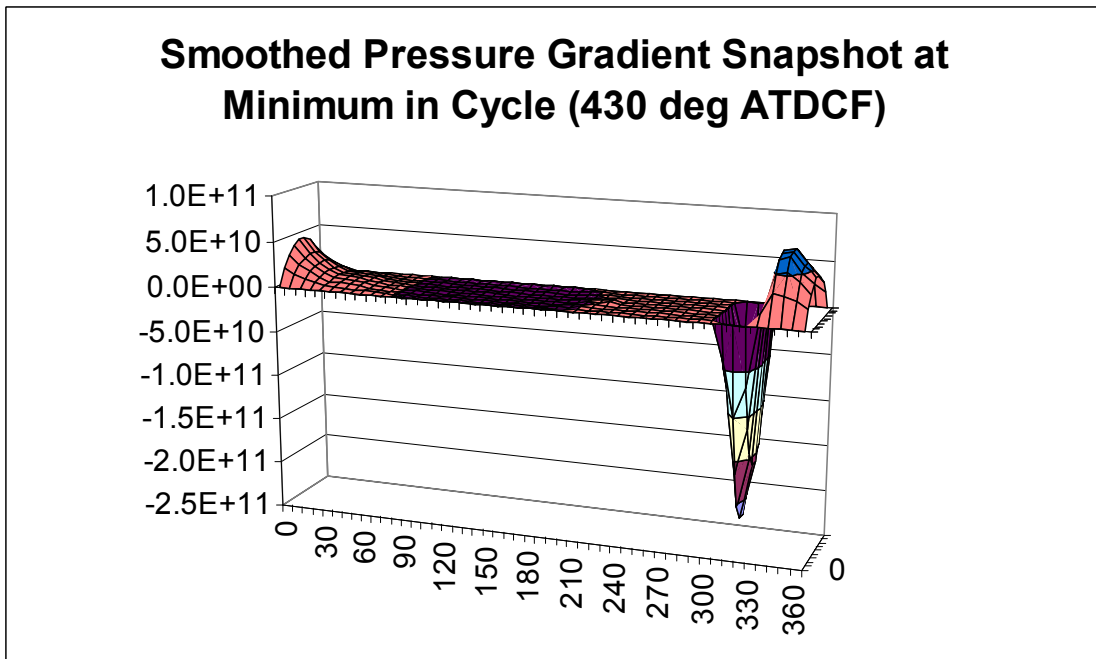


Figure 6-95 Pressure Gradient Snapshot at 430 deg

Most negative values over whole bearing over the whole cycle are shown in Fig. 6.96. The major peak at about 120 deg. Bearing angle (710 deg. Crank angle) and 320 deg. Bearing angle (430 deg. Crank angle) can be seen clearly by comparison with the previous figures.

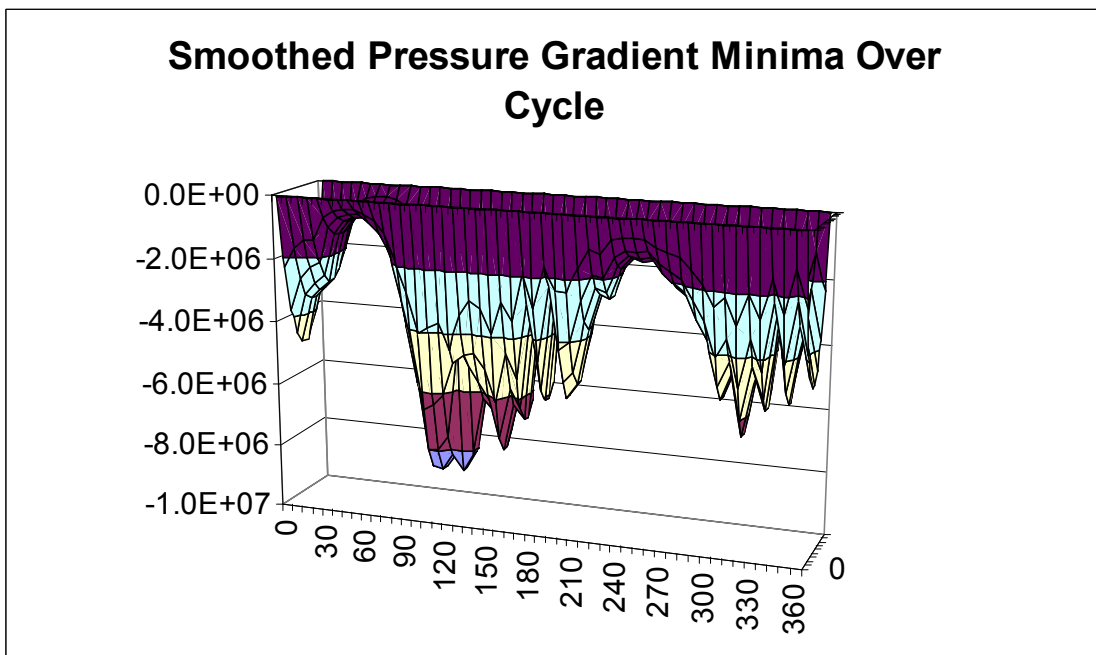


Figure 6-96 Diesel, RHD, 5000 rpm – Pressure Gradient Minima Over Cycle

Multiplying the cavitation velocity by minus the $dp/d\theta$ gives a cavitation power density plot

In Fig. 6.97, the cavitation velocities and $dp/d\theta$ values over the cycle were used but only for positive velocity and negative $dp/d\theta$ to avoid producing positive cavitation power from squeeze events. Note that the y axis is normalised. There is a discussion later about the values and units calculated.

It can be seen that the strongest effect is slightly to one side of the top of the bearing – 112.5 deg. (90 deg is top of bearing, 0 deg is on the split line). This corresponds with damage seen in the Forstner and Strewe paper. It also appears to capture the damage in the bottom shell at around 300 deg. Bearing angle.

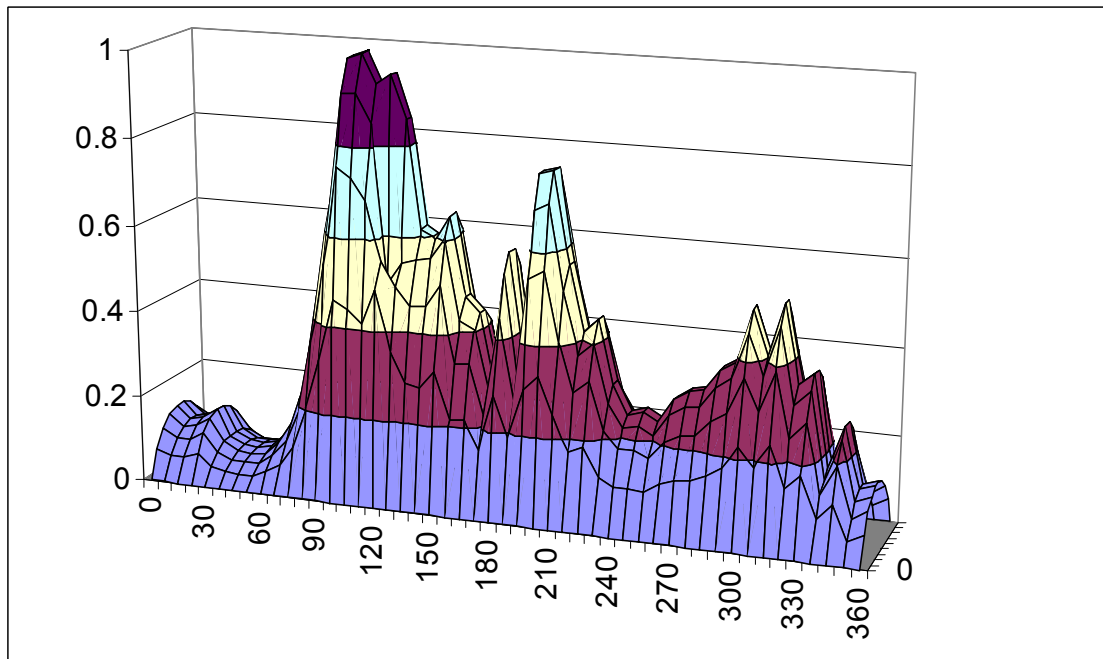


Figure 6-97 Diesel, RHD, 5000 rpm – Normalised Cavitation Damage Parameter

What would be the effect of varying basic bearing load parameters on the propensity for cavitation? The following figures should be viewed along with the previous ones which were for diesel, 5000 rpm, plain bearing.

- Diesel, 5000 rpm, partial bearing groove in bottom half

- Petrol, 5000 rpm, plain bearing
 - Note – gasoline engine cylinder pressures applied to piston with all other engine details kept as before
- Diesel, 5000 rpm with faster pressure rise
- Diesel, 3000 rpm, plain bearing
- Diesel 1000 rpm, plain bearing
- Diesel, 5000 rpm, elastic housing

Note that each calculation consists of a single change from the base case – i.e. not cumulative. The following sub-sections have figures similar to here for direct comparison but with fewer snapshots.

6.8.2 DIESEL, RHD, PARTIAL GROOVES, 5000 RPM

As might be expected, the partial grooves extending about 50 degrees into the lower half bearing from the split line do not make a large difference to the plots that follow. They should be compared to Figs. 6.72 to 6.97 as appropriate.

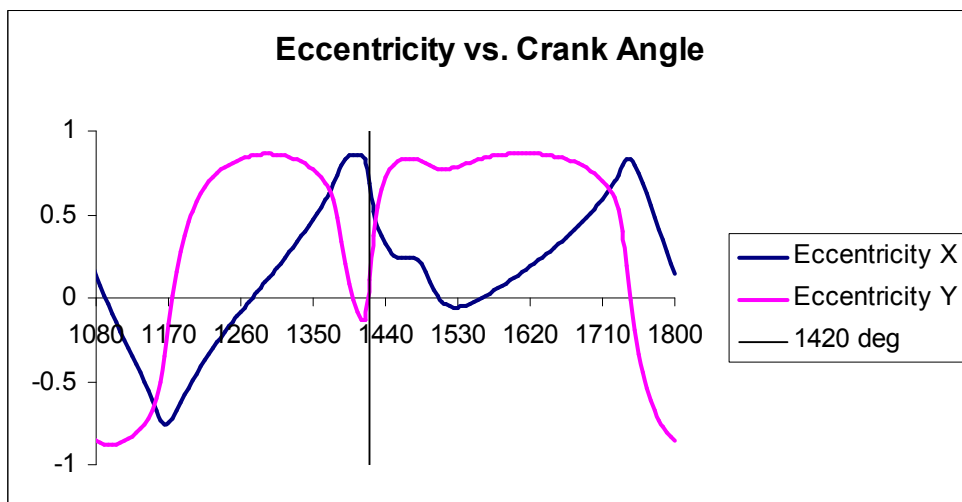


Figure 6-98 Diesel, Partial Grooves, RHD, 5000 rpm – Eccentricity

Figs. 6.98 and 6.99 show typical diesel engine eccentricity results with dominant gas pressures either side of TDCF. Very similar to the ungrooved bearing.

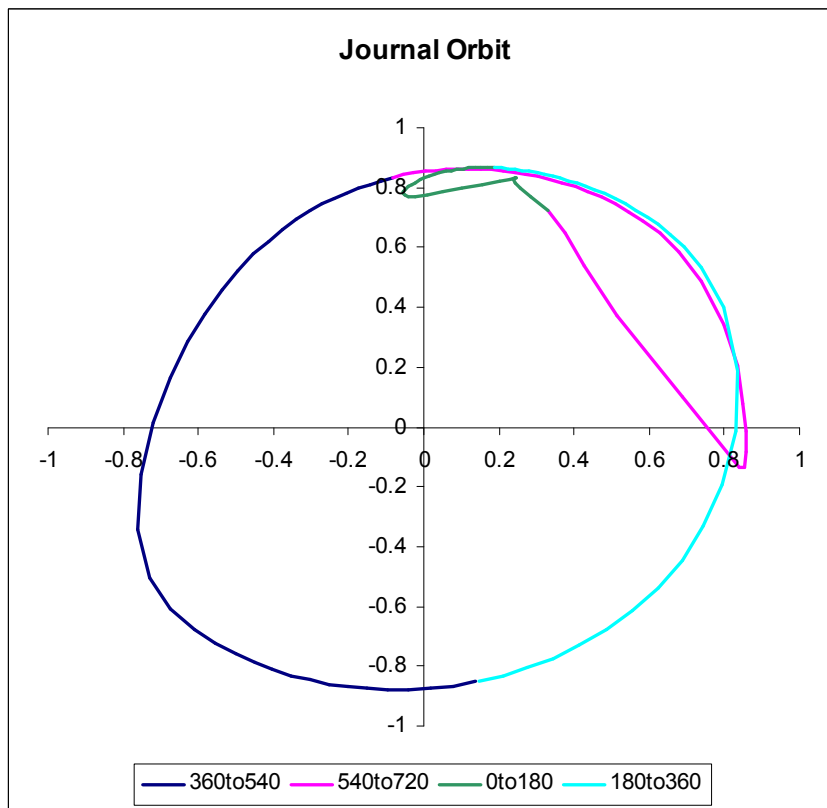


Figure 6-99 Diesel, Partial Grooves, RHD, 5000 rpm – Journal Orbit

The velocity plots show the movement just before TDCF with slightly higher velocity than the ungrooved bearing.

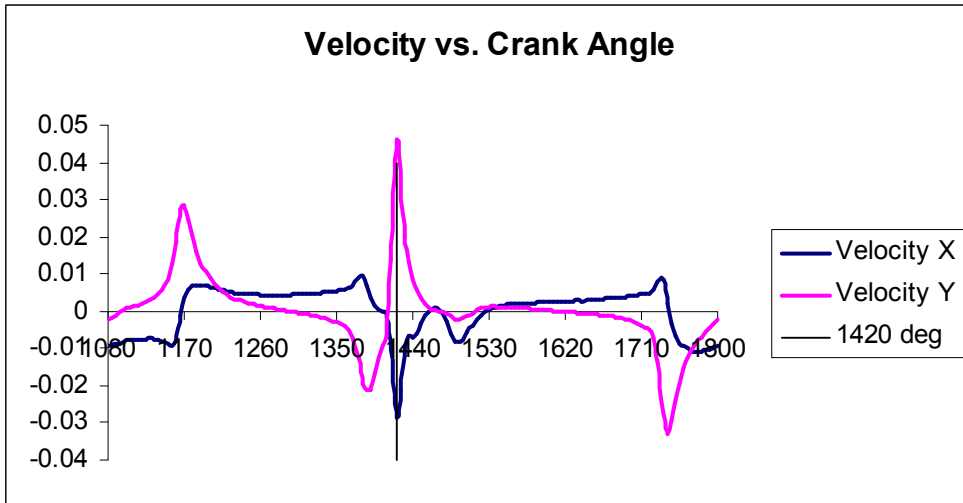


Figure 6-100 Diesel, Partial Grooves, RHD, 5000 rpm – Journal Velocity

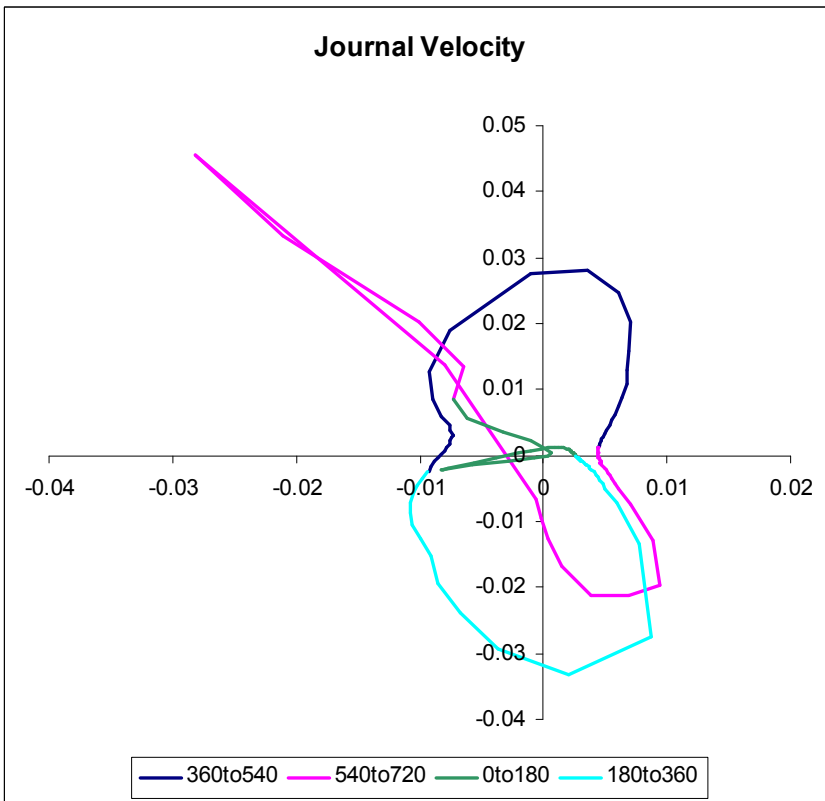


Figure 6-101 Diesel, Partial Grooves, RHD, 5000 rpm – Journal Velocity

Peak pressures over the cycle are shown with highest pressure near TDCF.

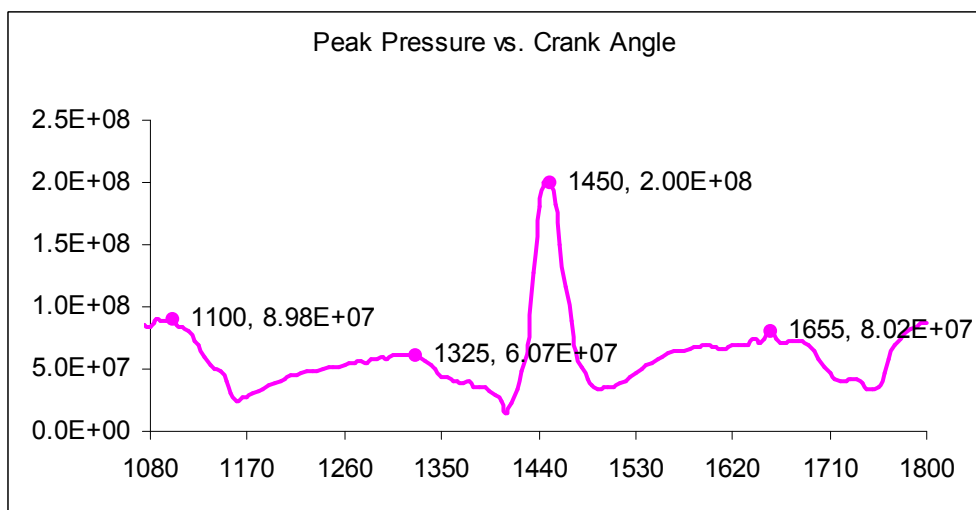


Figure 6-102 Diesel, Partial Grooves, RHD, 5000 rpm – Peak Film Pressure Over Cycle

This is a snapshot of the pressure distribution at the crank angle that produces the highest pressure (10 deg ATDCF). Note that this is near TDC firing and pressure is in the top half of the bearing.

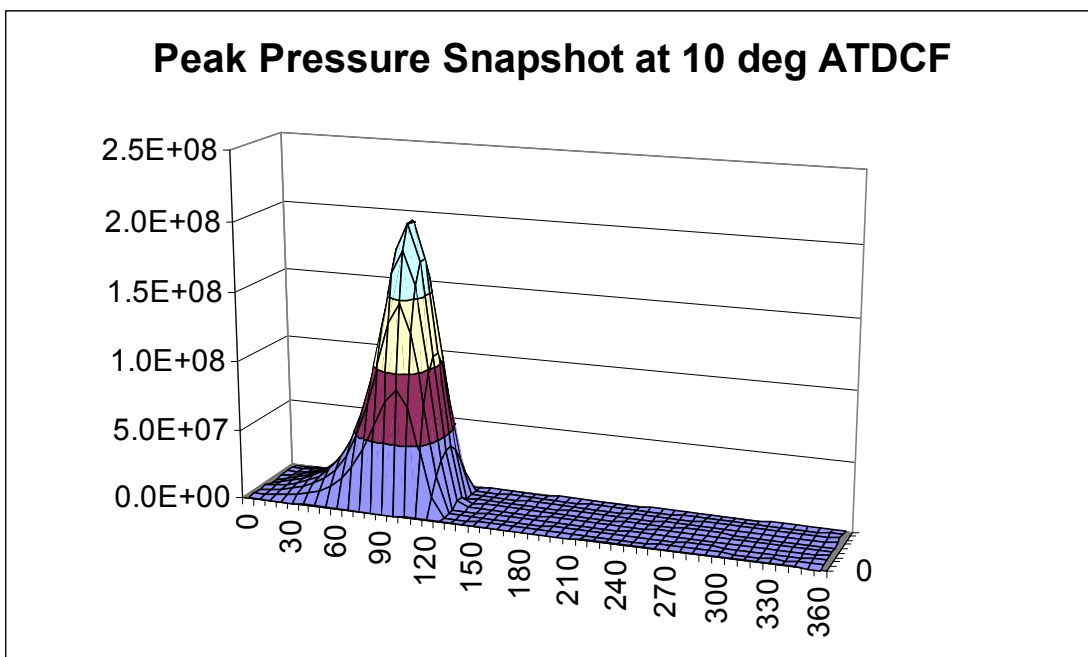


Figure 6-103 Diesel, Partial Grooves, RHD, 5000 rpm – Snapshot at Peak Pressure

Plotting the maximum pressure at each individual node over the whole cycle is useful for showing what is happening over the whole bearing. You can see that the peak value

is the same as that at 10 deg. crank angle. The secondary peak, close to TDC non-firing, in the bottom shell is smaller.

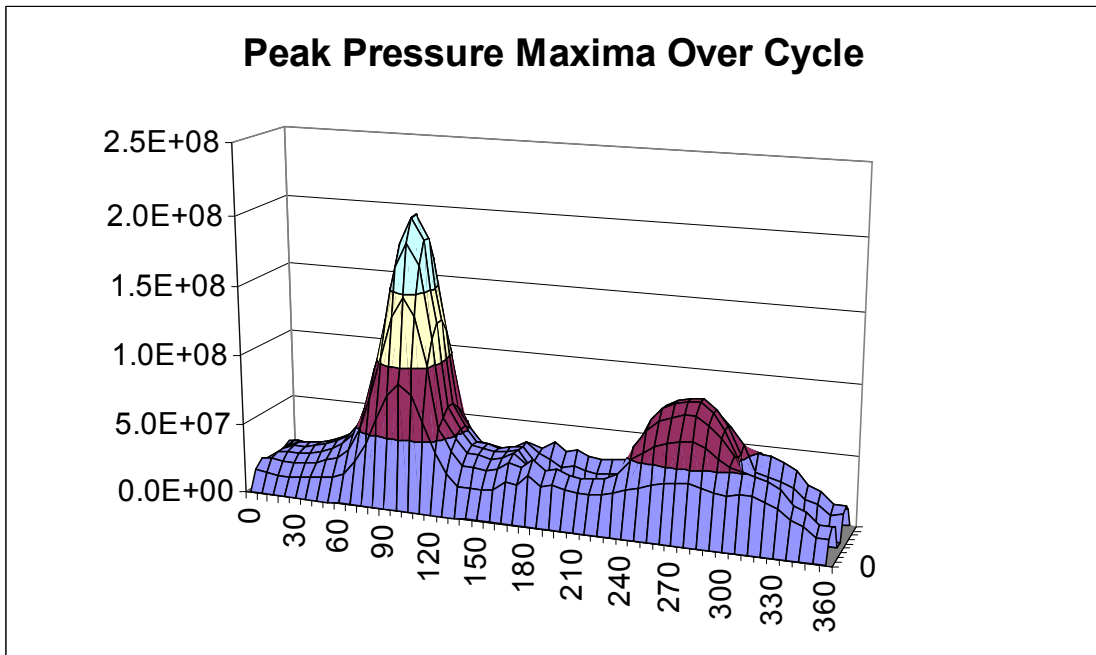


Figure 6-104 Diesel, Partial Grooves, RHD, 5000 rpm – Peak Pressure Maxima Over Cycle

Plotting the separation velocity (also called cavitation velocity or negative of the squeeze velocity) gives a peak value at 1420 (700) deg. crank angle – just before TDCF.

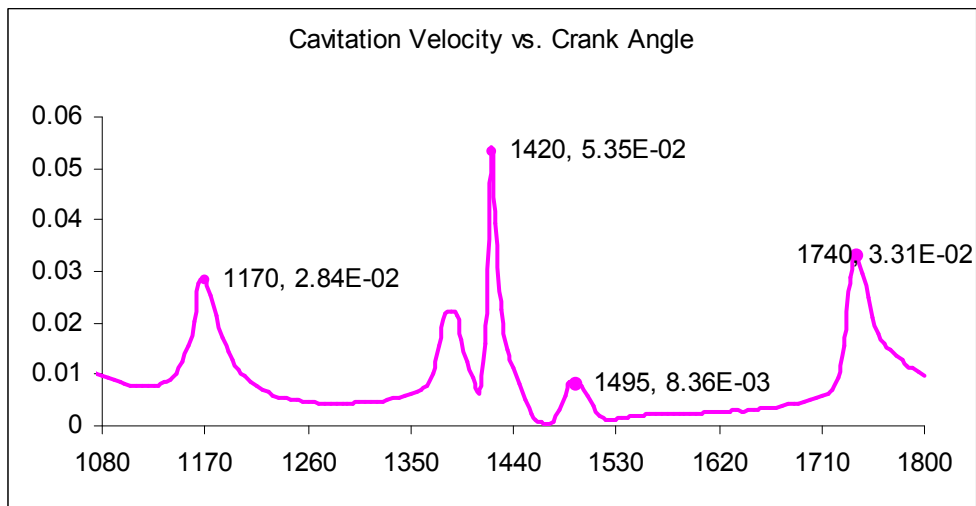


Figure 6-105 Diesel, Partial Grooves, RHD, 5000 rpm – Peak Cavitation Velocity Over Cycle

Plotting the separation velocity (called cavitation velocity or negative of the squeeze velocity) produces a sine wave as this is RHD calculation – this is a snapshot at the maximum value in the cycle

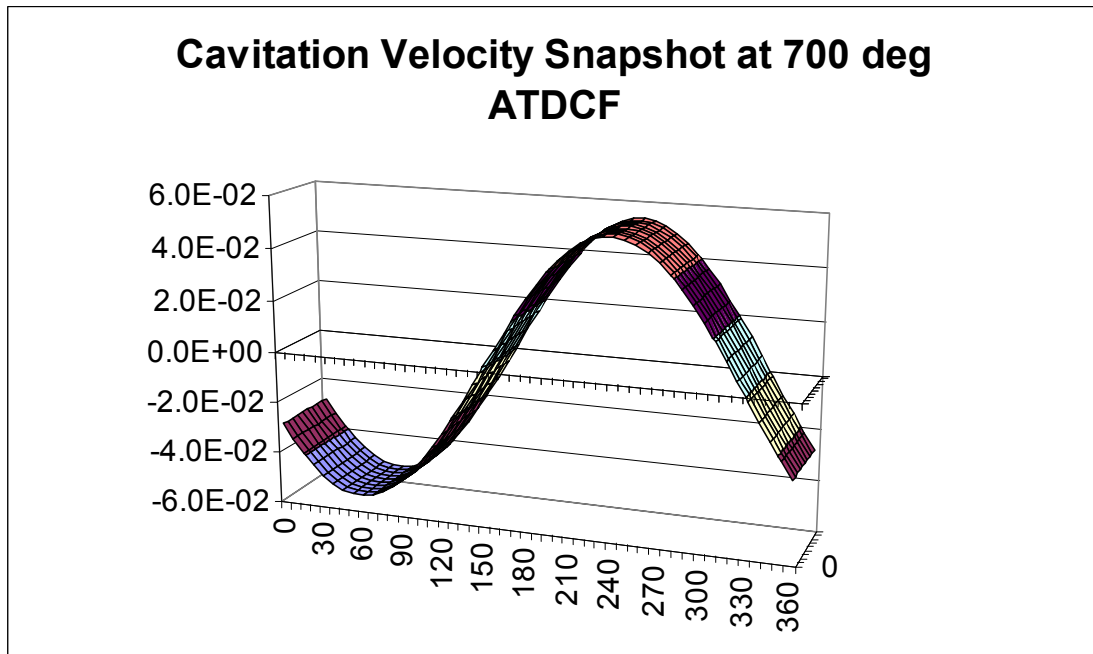


Figure 6-106 Diesel, Partial Grooves, RHD, 5000 rpm – Snapshot at Maximum Cavitation Velocity

Again, plotting the maximum over the cycle at each node produces the same peak (from the 5 deg. Crank angle results) but a more useful view of the values over the bearing. The next minor minor peak is significantly smaller.

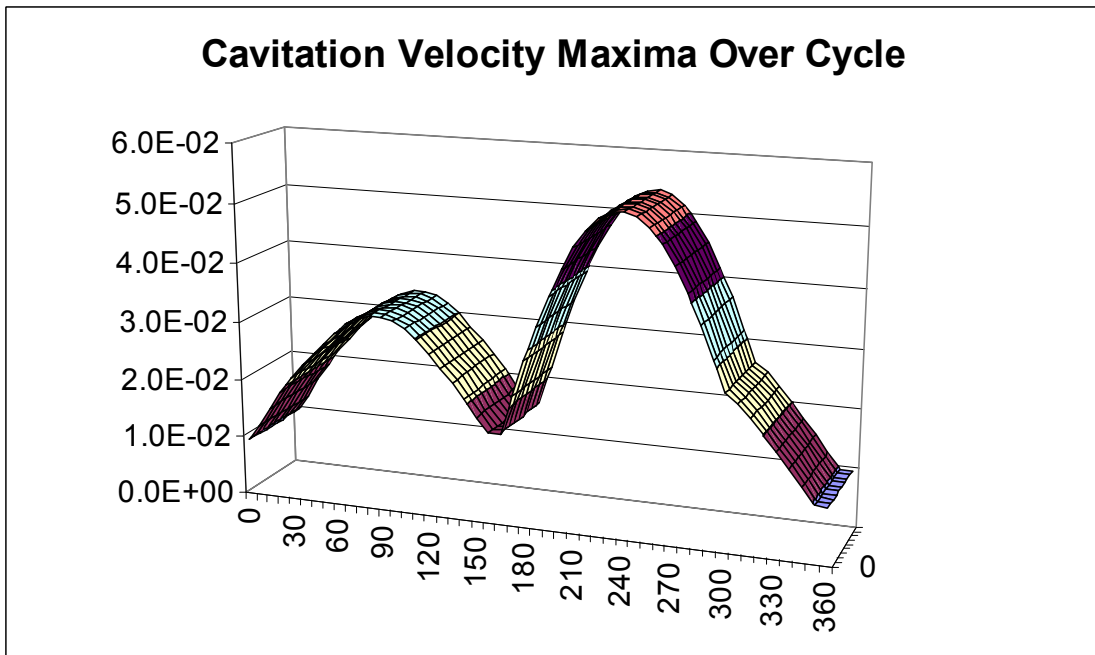


Figure 6-107 Diesel, Partial Grooves, RHD, 5000 rpm – Cavitation Velocity Maxima Over Cycle

Looking at pressure gradient $dp/d\theta$ – we're interested in the most negative values which are likely to produce cavitation. The values over the cycle are shown here. There are three main negative peaks, similar in size.

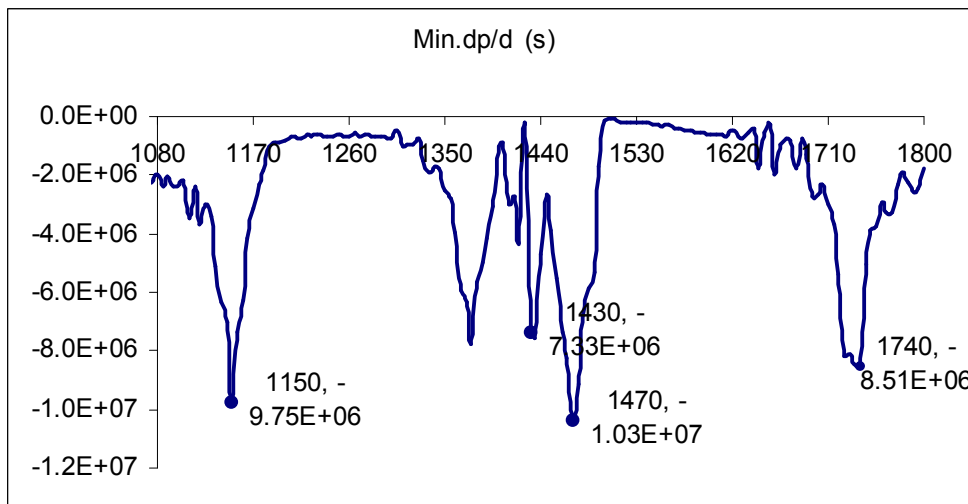


Figure 6-108 Diesel, Partial Grooves, RHD, 5000 rpm – Min. Pressure Gradient Over Cycle

Looking at pressure gradient $dp/d\theta$ – we’re interested in the most negative values which are likely to produce cavitation. Snapshot here of the situation at the highest negative value which occurs at 30 deg. crank angle although there are several other peaks nearby.

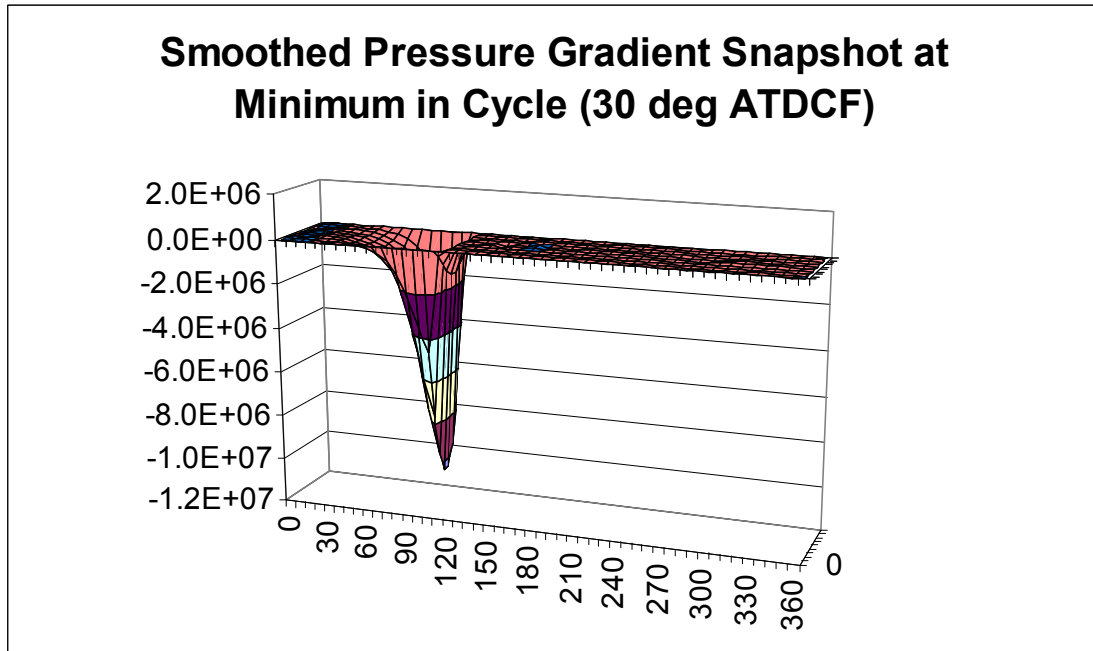


Figure 6-109 Diesel, Partial Grooves, RHD, 5000 rpm – Snapshot of Pressure Gradient at Minimum

Most negative values over whole bearing over the whole cycle are shown here.

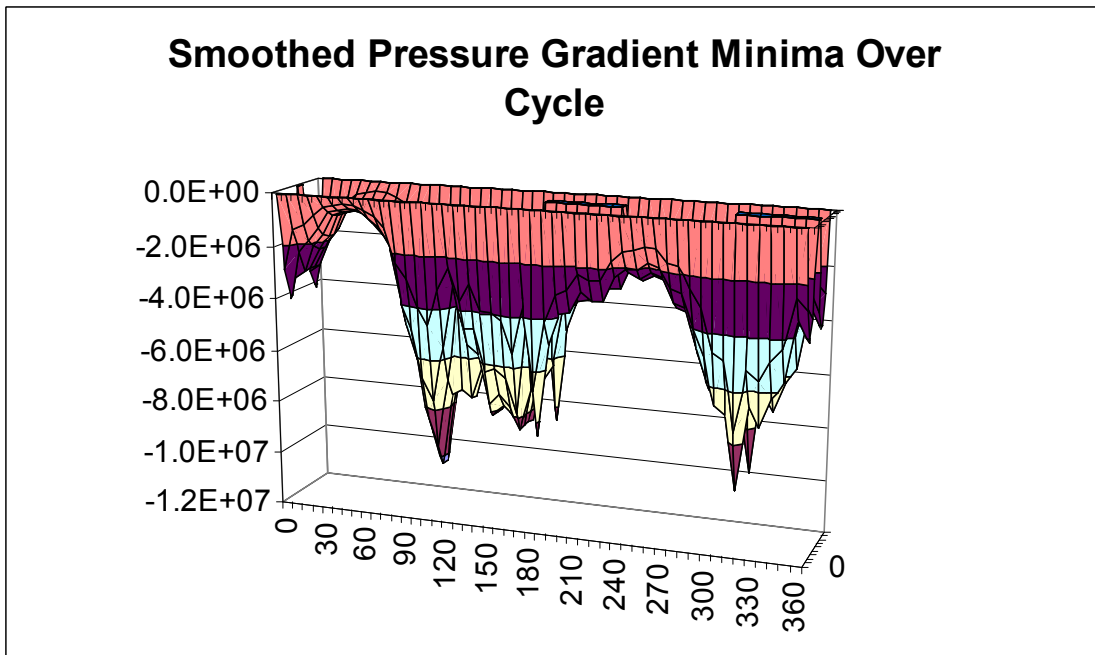


Figure 6-110 Diesel, Partial Grooves, RHD, 5000 rpm – Pressure Gradient Minima Over Cycle

It can be seen that the strongest effect is on the top of the bearing (90 deg is top of bearing, 0 deg is on the split line). Interestingly, there are peaks either side of the grooves (180 to 230 and 310 to 360 degrees). This would be expected and is discussed in Forstner and Strewé.

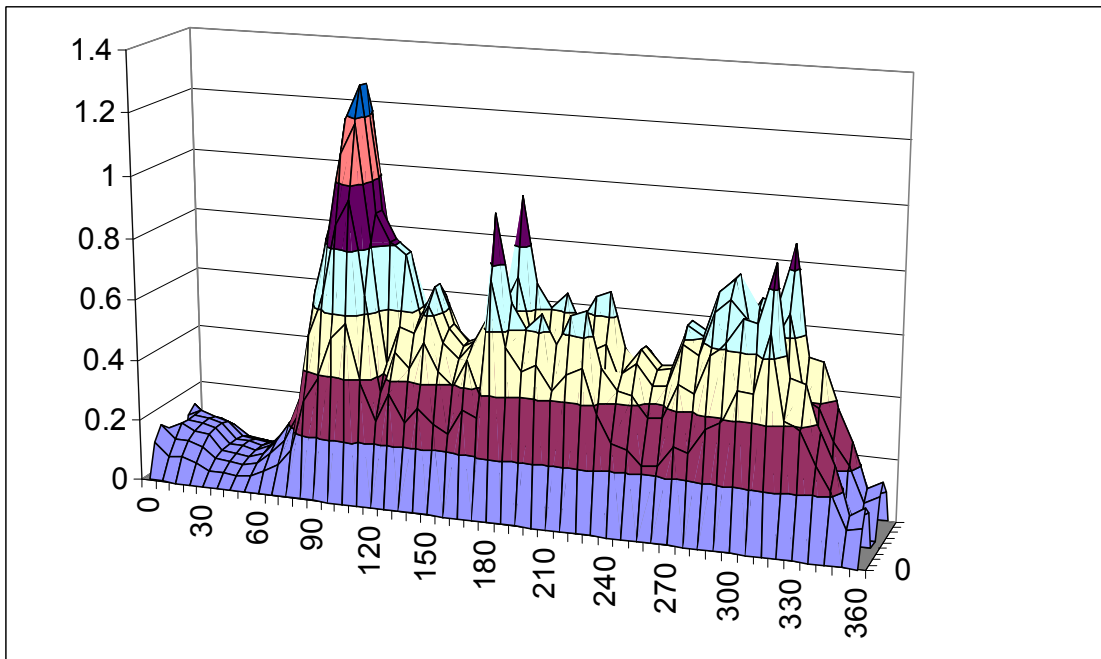


Figure 6-111 Diesel, Partial Grooves, RHD, 5000 rpm – Normalised Cavitation Damage Parameter

The gas pressure takes over from the inertia on the compression stroke and continues into the power stroke

This means that the main cavitation area is on the top shell.

The grooves do cause localised peaks in the cavitation parameter alongside them.

6.8.3 GASOLINE, RHD, 5000 RPM

The gasoline case was performed using a combustion gas pressure curve from a typical gasoline engine. The rest of the dimensions and masses were the same as the base case. In this way, the effect of gas pressure curve alone could be investigated. The following figures should be compared to Figs. 6.72 to 6.97 as appropriate.

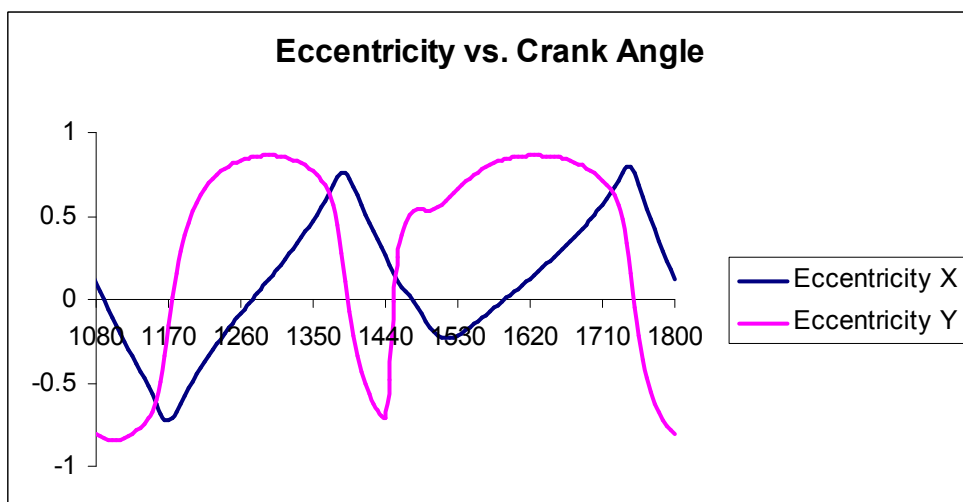


Figure 6-112 Gasoline, RHD, 5000 rpm – Eccentricity

Typical petrol engine results with dominant inertia on the compression stroke overcome by the gas pressures on the power stroke, sending the journal across the bearing clearance.

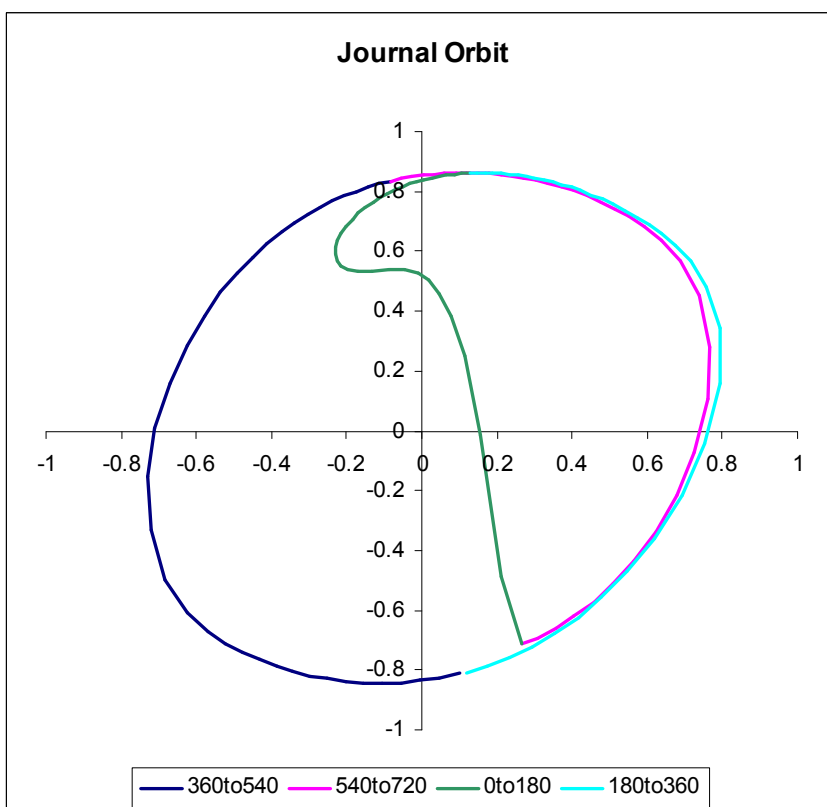


Figure 6-113 Gasoline, RHD, 5000 rpm – Journal Orbit

The velocity plots show the severe movement just after TDCF compared to the other operating conditions being investigated.

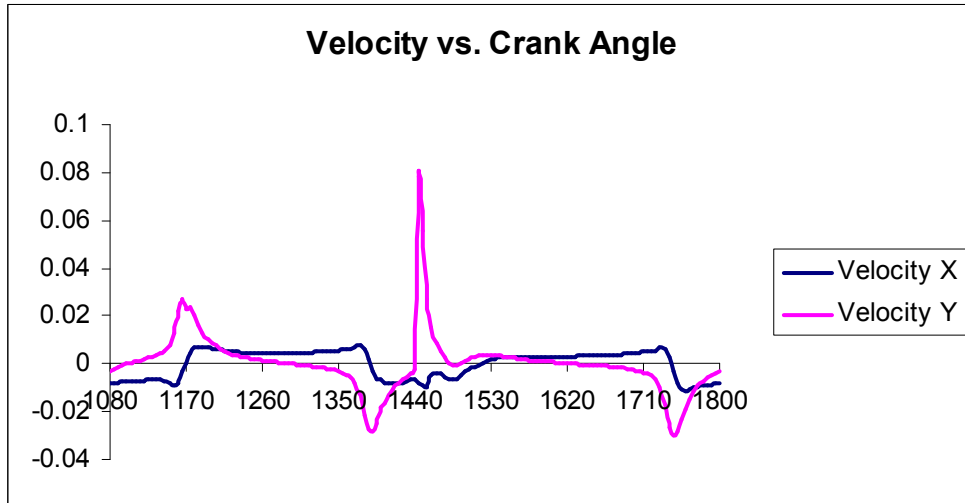


Figure 6-114 Gasoline, RHD, 5000 rpm – Journal Velocity

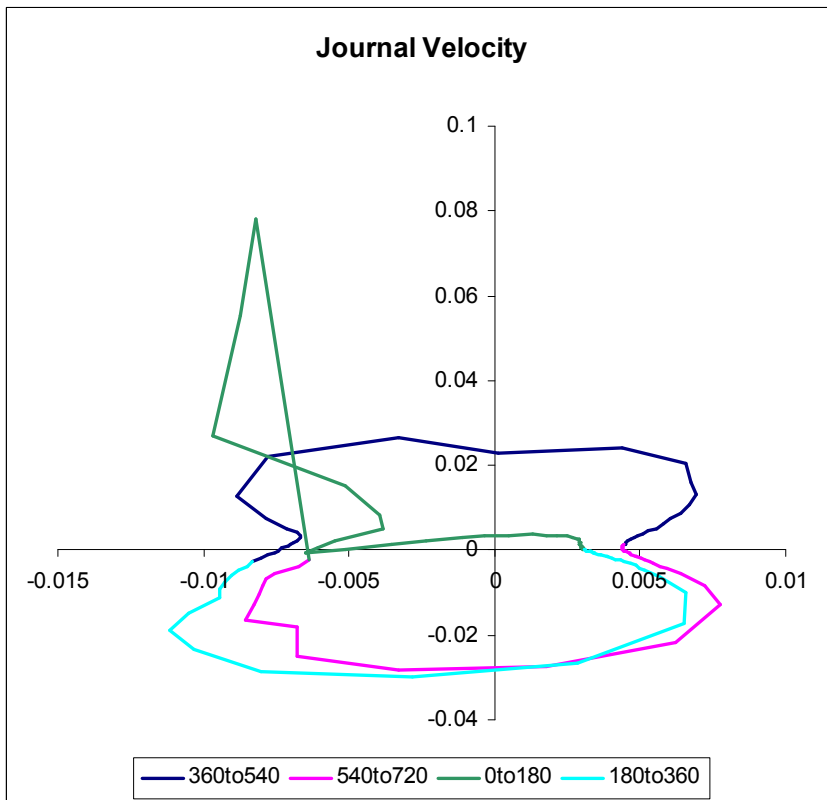


Figure 6-115 Gasoline, RHD, 5000 rpm – Journal Velocity

Peak pressures over the cycle are shown with a much reduced pressure near TDCF compared to the other conditions being investigated. This might seem paradoxical but the large movement across the clearance space is cushioned by a large oil film thickness as the gas pressure is reducing. In any case the gas pressure is approximately half the value of the diesel version.

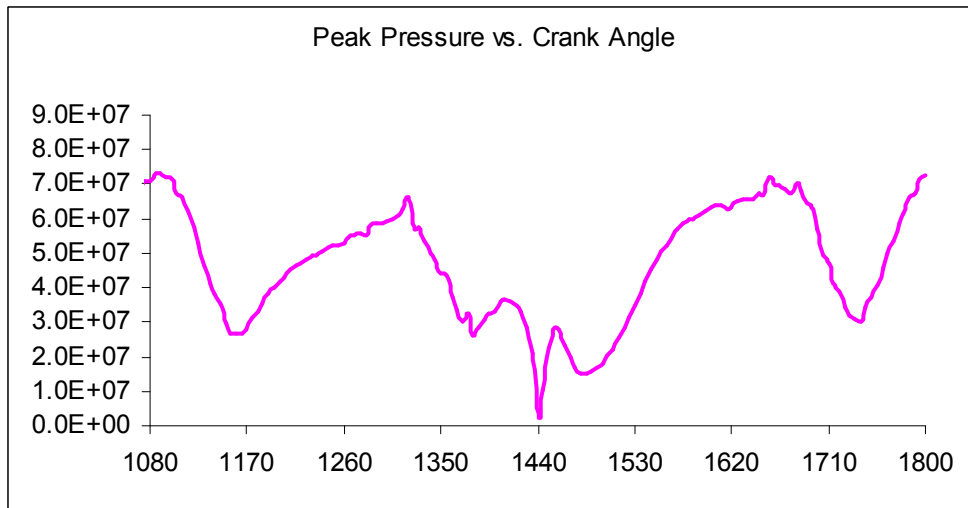


Figure 6-116 Gasoline, RHD, 5000 rpm – Peak Gas Pressure Over Cycle

This is a snapshot of the pressure distribution at the crank angle that produces the highest pressure (365 deg ATDCF). Note that this is at TDC non-firing where there is complete inertia dominance.

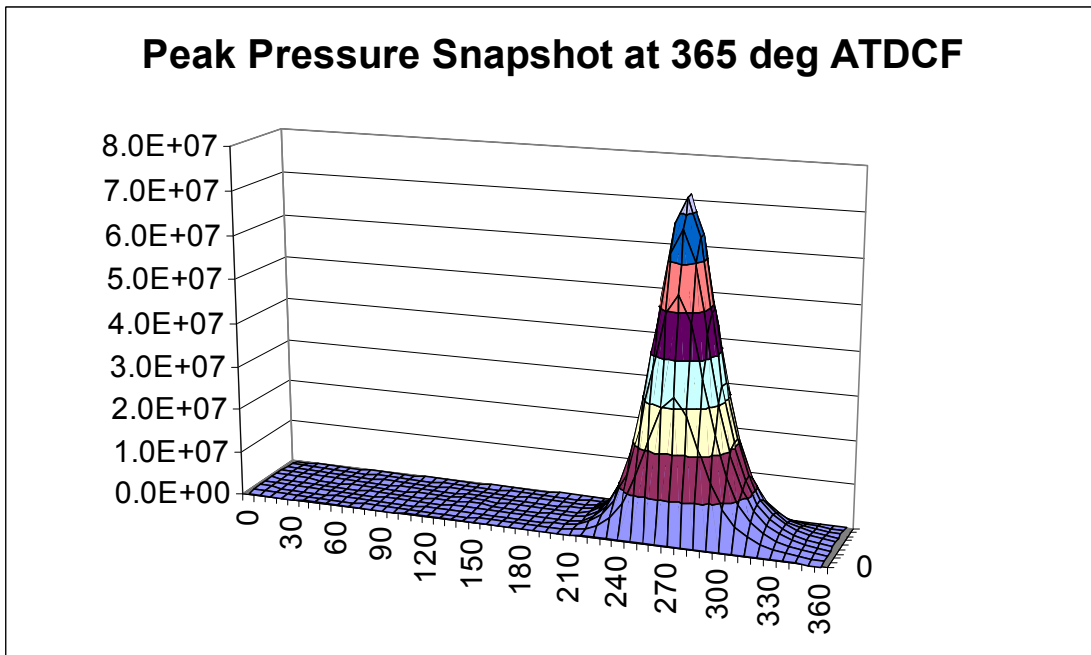


Figure 6-117 Gasoline, RHD, 5000 rpm – Peak Pressure Snapshot

Plotting the maximum pressure at each individual node over the whole cycle is useful for showing what is happening over the whole bearing. You can see that the peak value is the same as that at 365 deg. crank angle. The secondary peak, close to BDC, in the top shell is nearly as large.

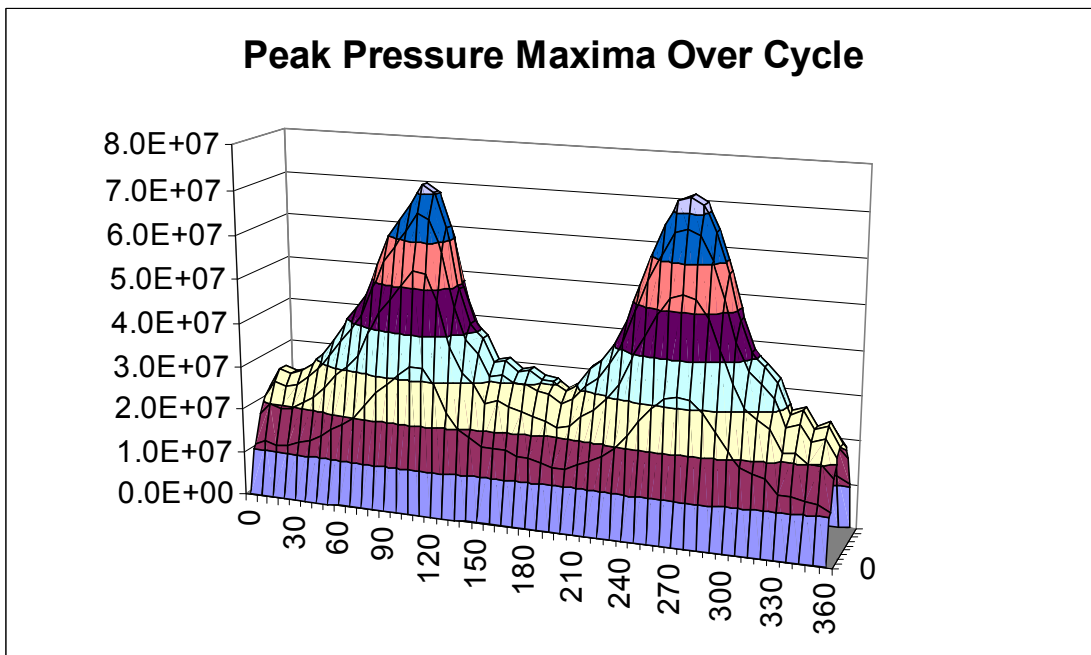


Figure 6-118 Gasoline, RHD, 5000 rpm – Peak Pressure Maxima Over Cycle

Plotting the separation velocity (also called cavitation velocity or negative of the squeeze velocity) gives a peak value at 1445 (5) deg. crank angle – just after TDCF.

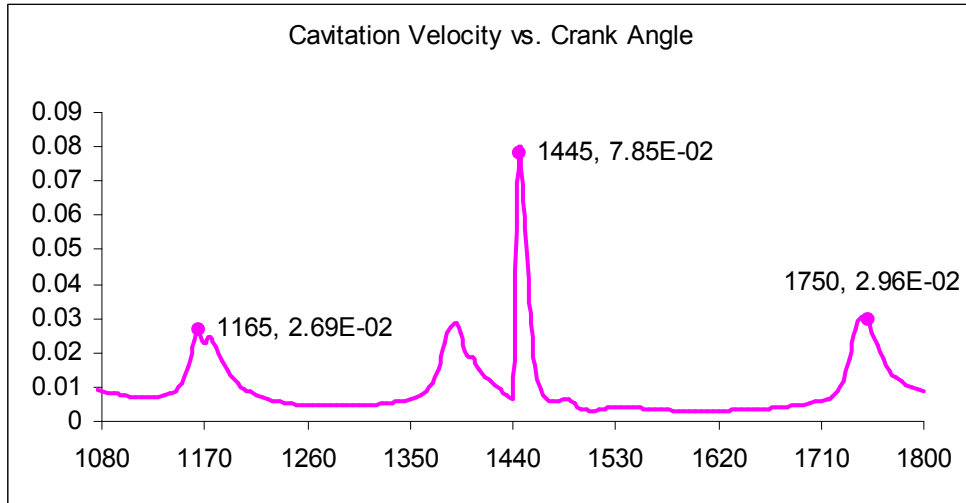


Figure 6-119 Gasoline, RHD, 5000 rpm – Maximum Cavitation Velocity Over Cycle

Plotting the separation velocity (called cavitation velocity or negative of the squeeze velocity) produces a sine wave as this is RHD calculation – this is a snapshot at the maximum value in the cycle.

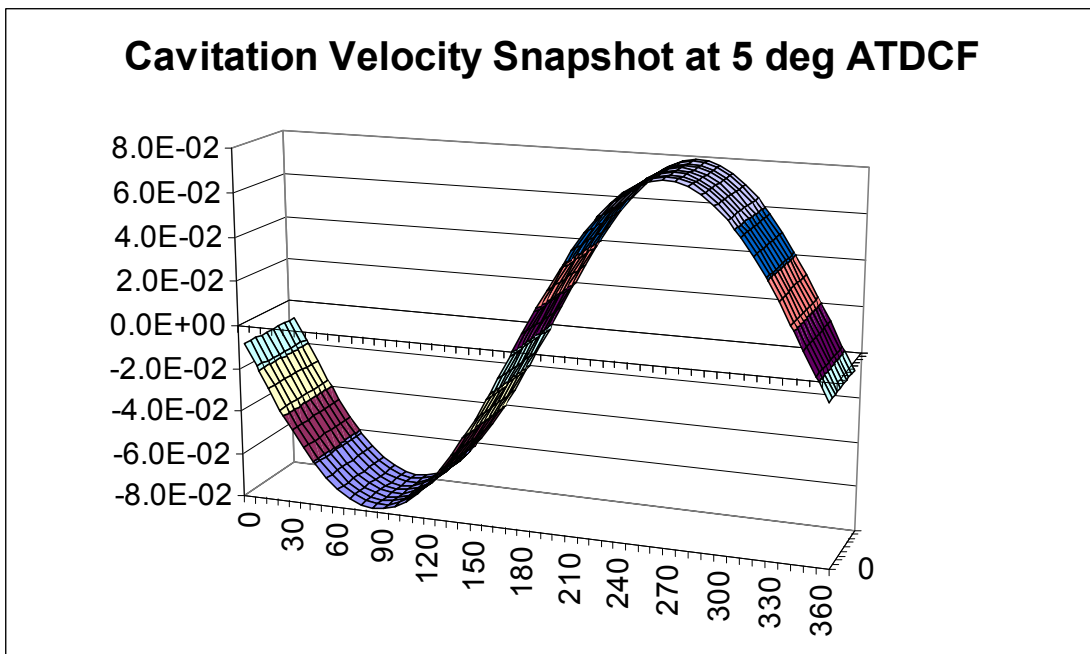


Figure 6-120 Cavitation Velocity Snapshot at Maximum

Again, plotting the maximum over the cycle at each node produces the same peak (from the 5 deg. Crank angle results) but a more useful view of the values over the bearing. The next minor minor peak is significantly smaller.

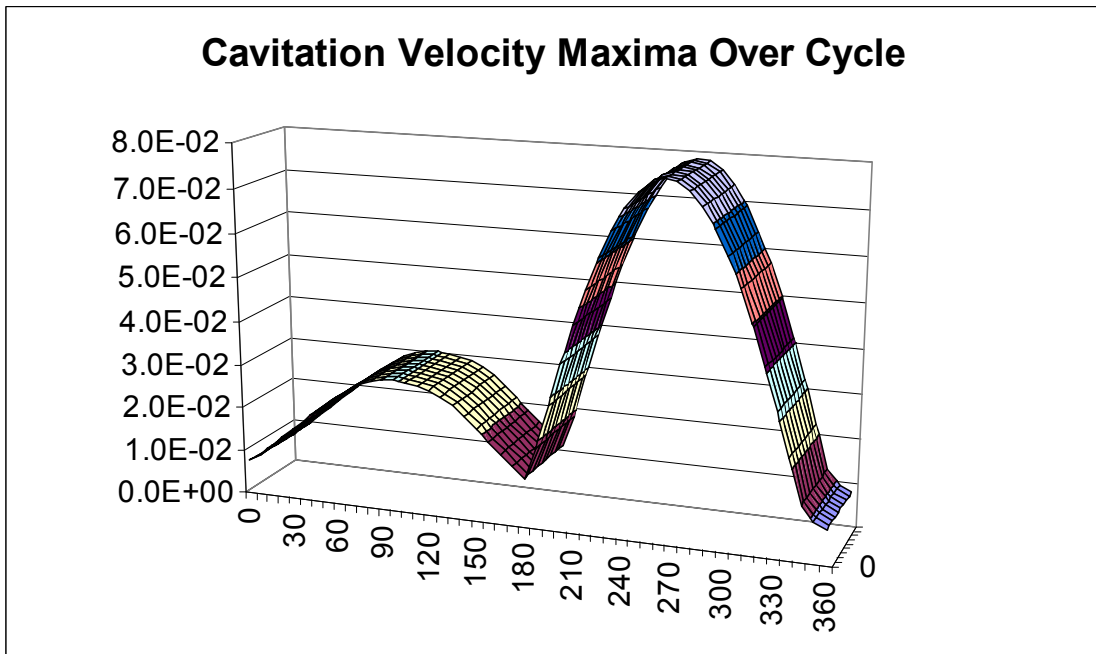


Figure 6-121 Cavitation Velocity Maxima Over Cycle

Looking at pressure gradient dp/dq – we’re interested in the most negative values which are likely to produce cavitation. The values over the cycle are shown here. There are three negative peaks, similar in size.

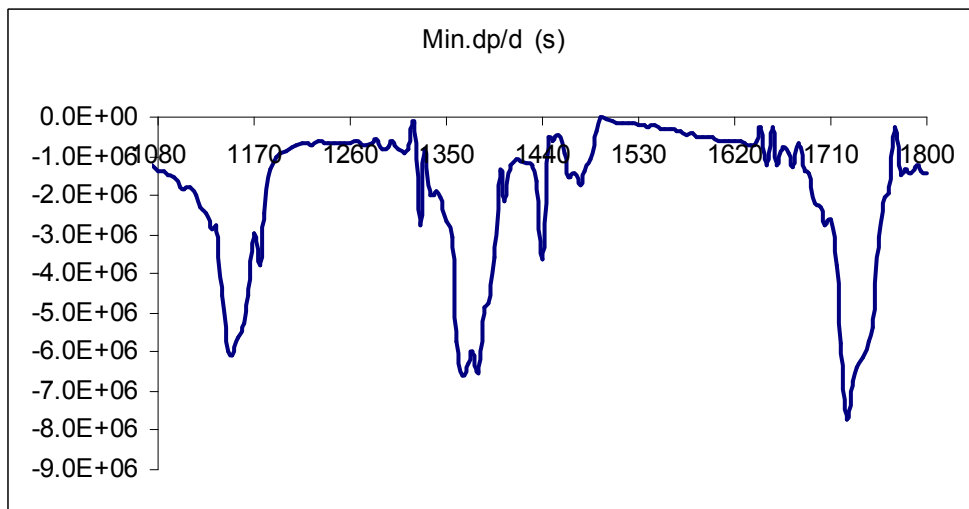


Figure 6-122 Gasoline, RHD, 5000 rpm – Minimum Pressure Gradient Over Cycle

Looking at pressure gradient $dp/d\theta$ – we’re interested in the most negative values which are likely to produce cavitation. Snapshot here of the situation at the highest negative value which occurs at 285 deg. crank angle.

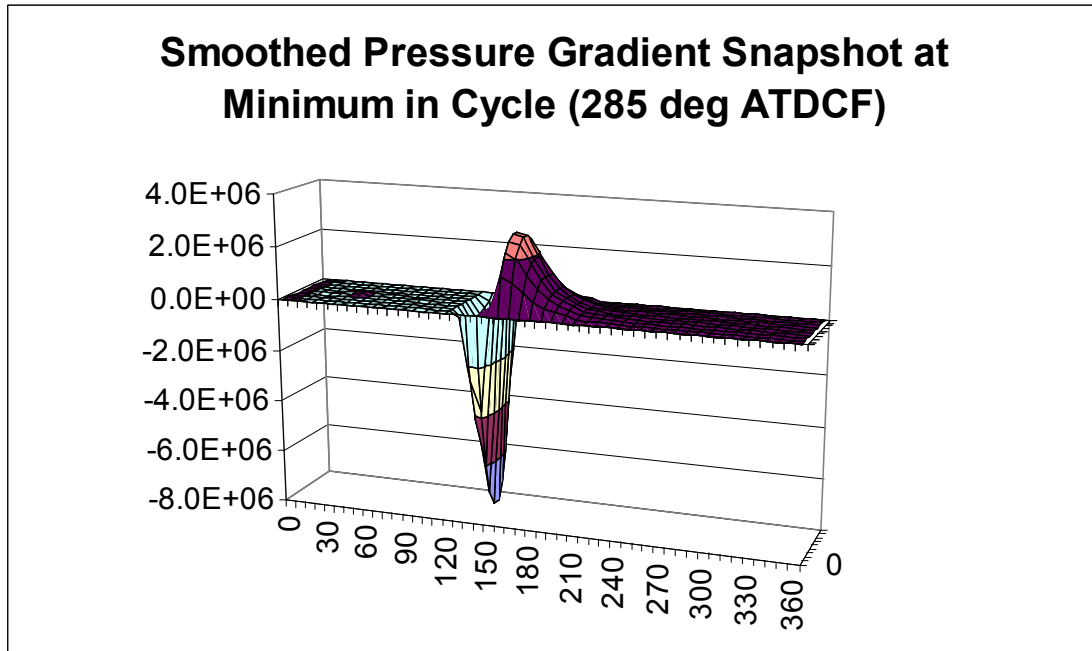


Figure 6-123 Gasoline, RHD, 5000 rpm – Pressure Gradient Snapshot at Minimum

Most negative values over whole bearing over the whole cycle are shown here.

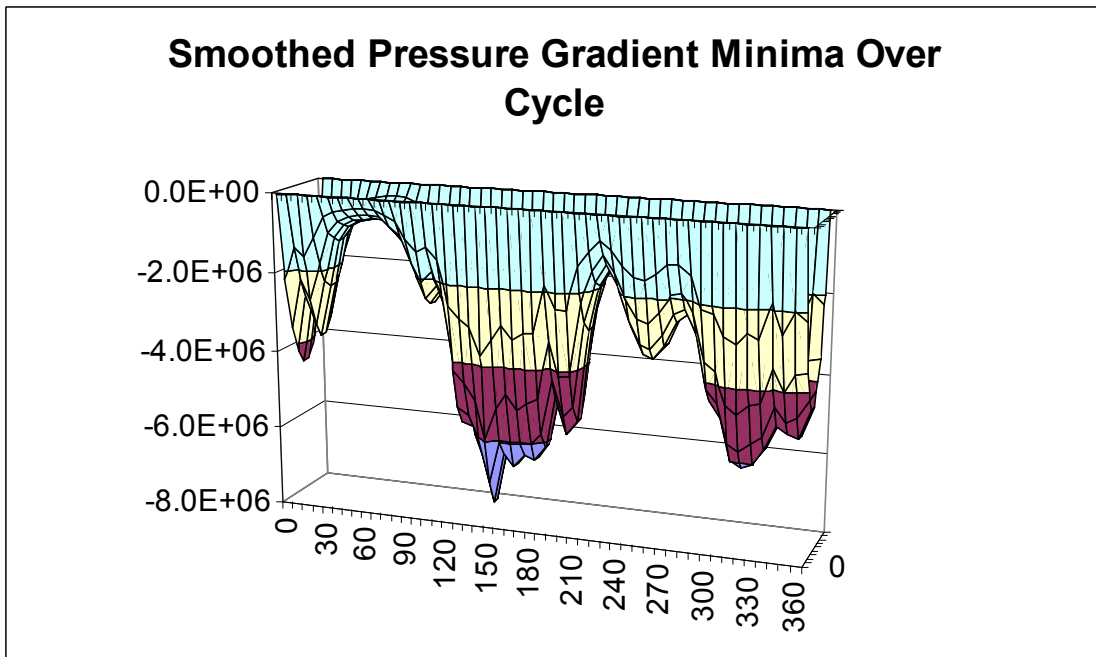


Figure 6-124 Gasoline, RHD, 5000 rpm – Pressure Gradient Minima Over Cycle

It can be seen that the strongest effect is on the bottom of the bearing (90 deg is top of bearing, 0 deg is on the split line).

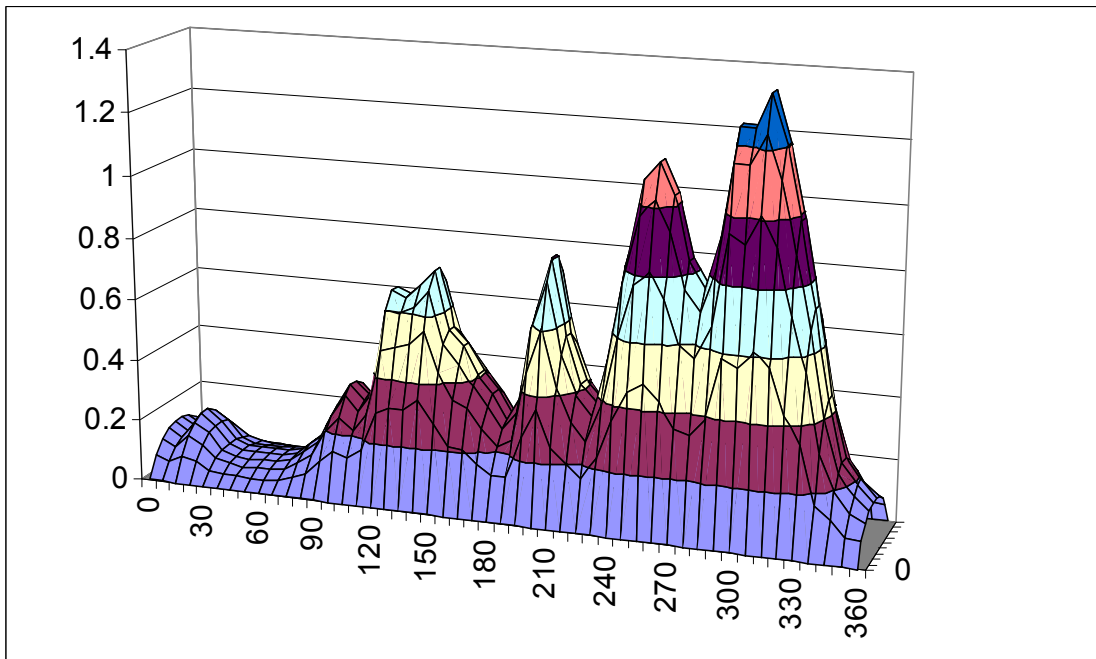


Figure 6-125 Gasoline, RHD, 5000 rpm – Normalised Cavitation Damage Parameter

The compression stroke is dominated by inertia but the power stroke is dominated by gas pressure force giving a strong initial movement just after TDCF

This means that the cavitation is likely to be concentrated in the cap half of the bearing on this occasion.

6.8.4 DIESEL, RHD, FASTER GAS PRESSURE RISE, 5000 RPM

The gas pressure curve of the base case calculation was manually adjusted to give almost twice the rate of increase at around the critical crankangle for rapid motion of the journal at 700 deg. ATDCF. The following figures should be compared to Figs. 6.72 to 6.97 as appropriate.

Figs. 6.126 to 6.129 show typical diesel engine results again – large movement at 1420 deg (700 deg), just before TDCF as the gas pressure load overcomes the inertia load.

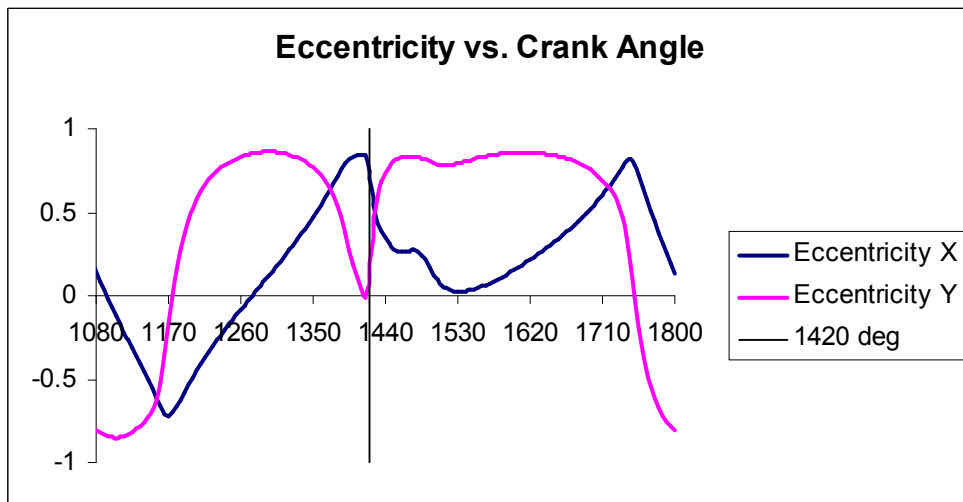


Figure 6-126 Diesel, Fast Pressure Rise, RHD, 5000 rpm – Eccentricity

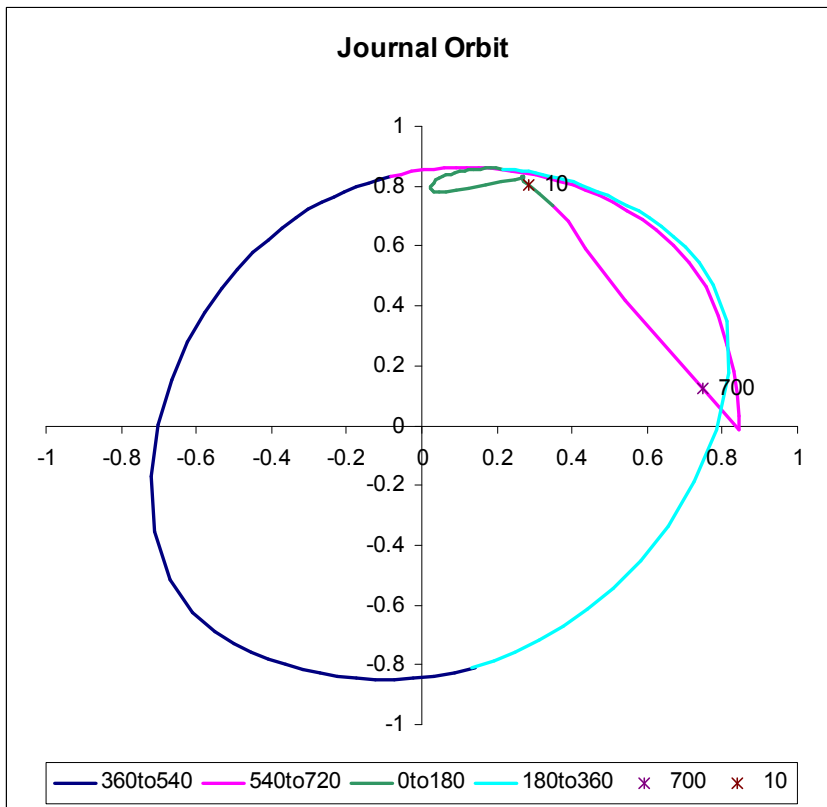


Figure 6-127 Diesel, Fast Pressure Rise, RHD, 5000 rpm – Journal Orbit

The velocity plots show the sudden motion at 1420 (700) deg. clearly and the velocity peak is larger than for the base case.

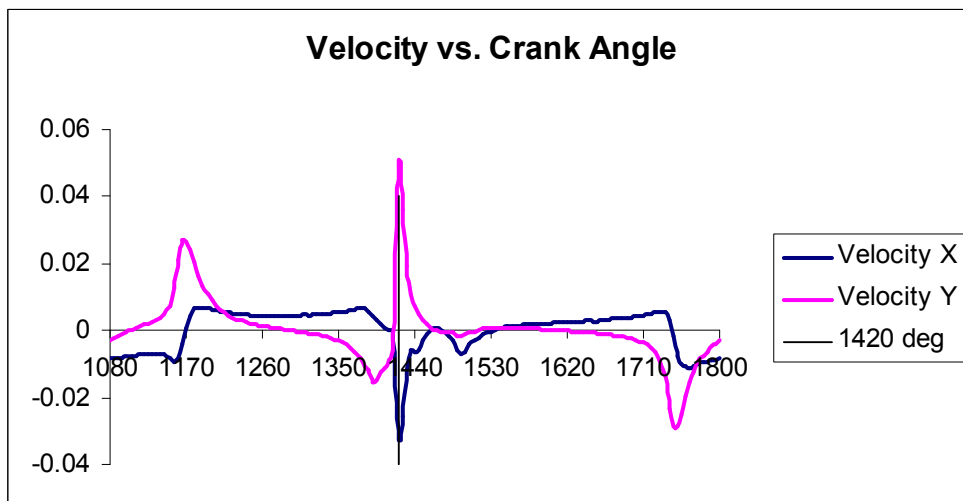


Figure 6-128 Diesel, Fast Pressure Rise, RHD, 5000 rpm – Journal Velocity

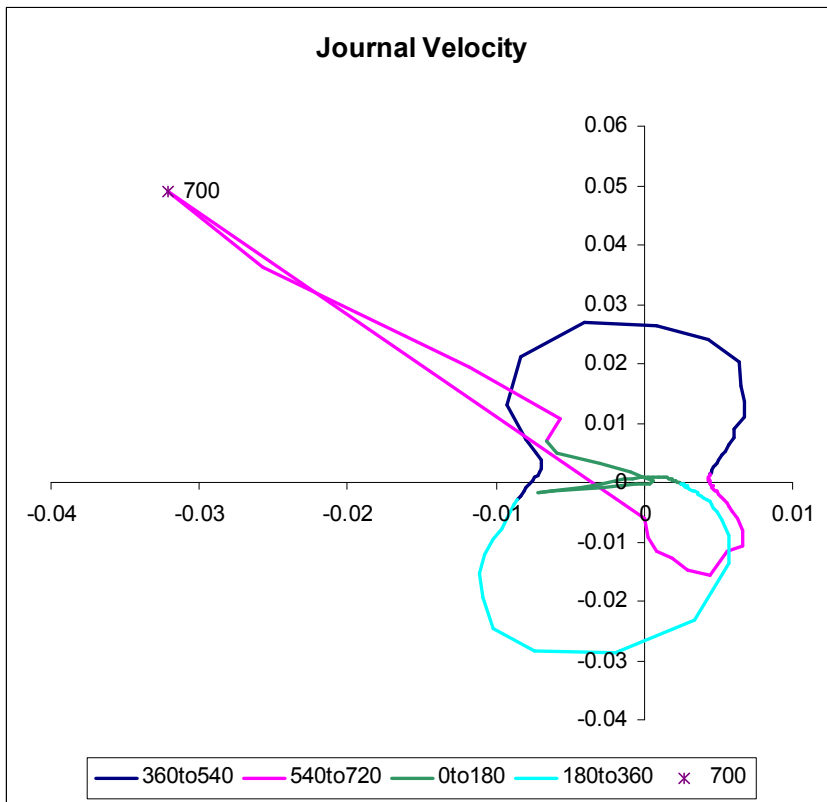


Figure 6-129 Diesel, Fast Pressure Rise, RHD, 5000 rpm – Journal Velocity

Peak pressures over the cycle are shown with the peaks at 1100 (380), 1325 (605), 1450 (10) and 1660 (220) degrees crank angle. The journal position in the clearance space can be checked on the earlier slides. The pressure distribution in the bearing at each of these angles is shown on the following slides.

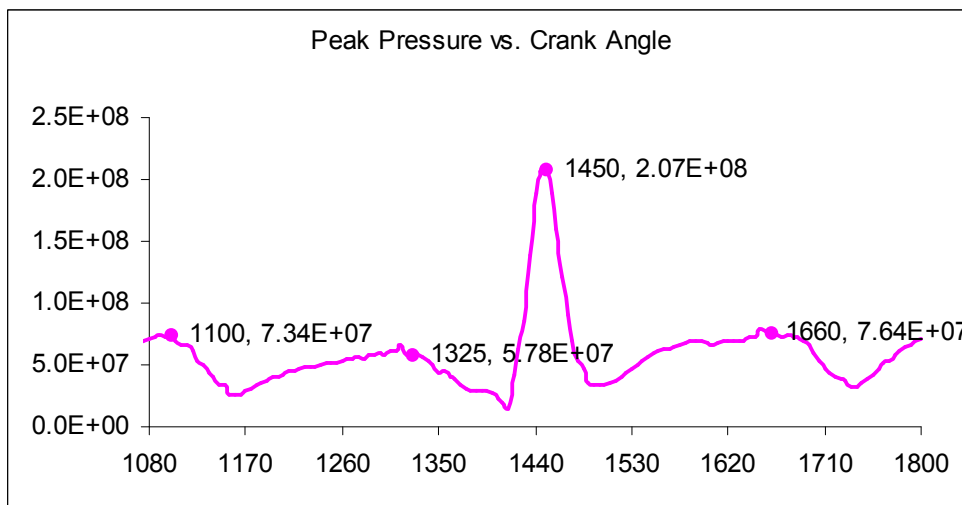


Figure 6-130 Diesel, Fast Pressure Rise, RHD, 5000 rpm – Peak Film Pressure Over Cycle

This is a snapshot of the pressure distribution at the crank angle that produces the highest pressure (10 deg ATDCF i.e. 30 deg after the start of the large movement across the clearance space).

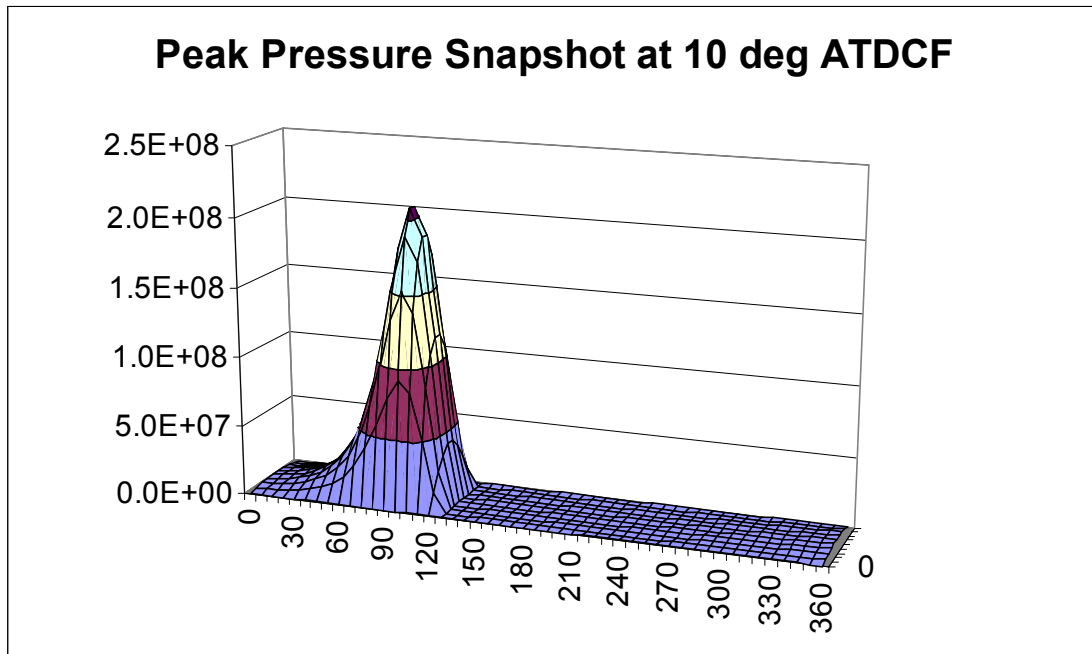


Figure 6-131 Diesel, Fast Pressure Rise, RHD, 5000 rpm – Peak Pressure Snapshot

Plotting the maximum pressure at each individual node over the whole cycle is useful for showing what is happening over the whole bearing. You can see that the peak value is the same as that at 10 deg. Crank angle and the minor peak is the value at 380 deg. Crank angle. Note that the minor peaks at 220 and 605 deg. Have no effect because they coincide on the bearing surface with the major peak at 10 deg. Crank angle.

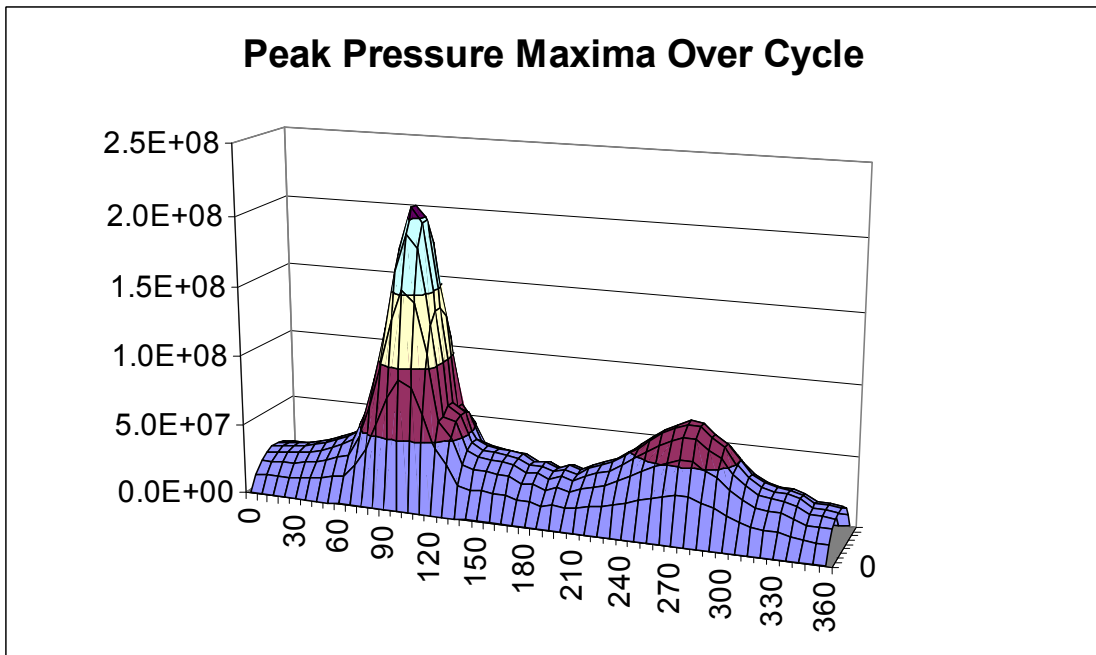


Figure 6-132 Diesel, Fast Pressure Rise, RHD, 5000 rpm – Peak Pressure Maxima Over Cycle

Plotting the separation velocity (also called cavitation velocity or negative of the squeeze velocity) gives a peak value at 1420 (700) deg. Crank angle with minor peaks also labelled above.

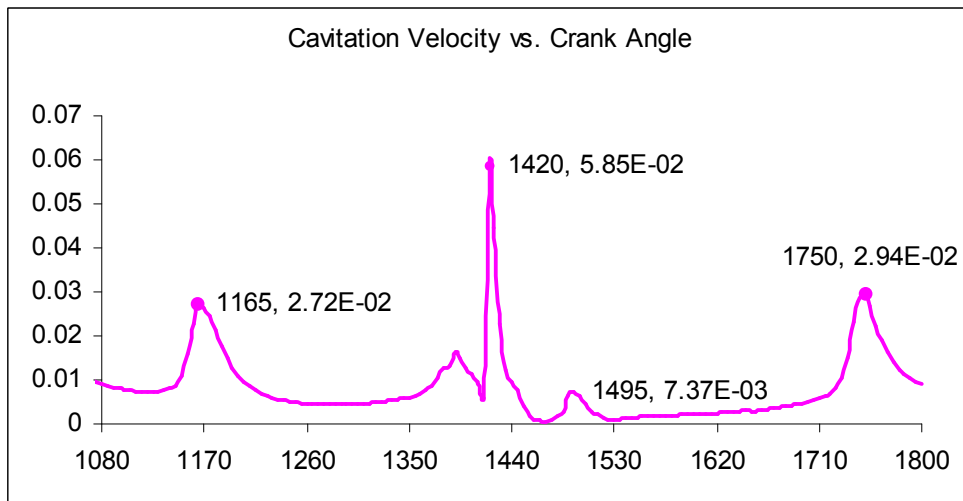


Figure 6-133 Diesel, Fast Pressure Rise, RHD, 5000 rpm – Peak Cavitation Velocity Over Cycle

Plotting the separation velocity (called cavitation velocity or negative of the squeeze velocity) produces a sine wave as this is RHD calculation – this is a snapshot at the maximum value in the cycle.

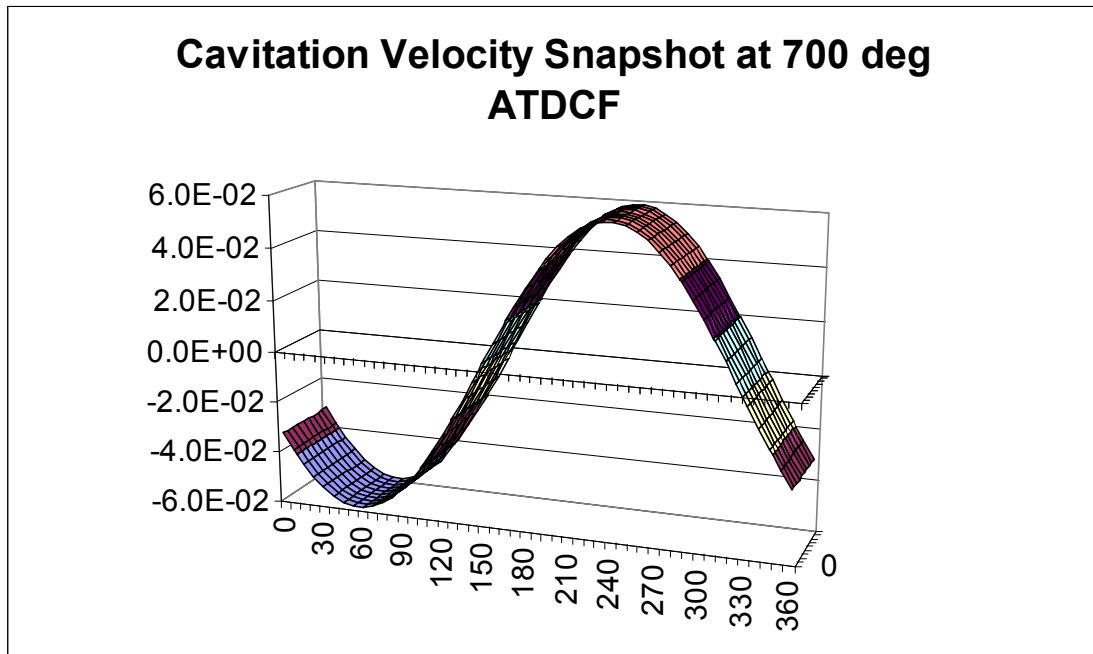


Figure 6-134 Diesel, Fast Pressure Rise, RHD, 5000 rpm – Cavitation Velocity Snapshot at Maximum

Again, plotting the maximum over the cycle at each node produces the same peak (from the 700 deg. Crank angle results) but a more useful view of the values over the bearing. The minor peak at 310 deg. has a significant effect, producing the small peak at about 90 deg. Bearing angle.

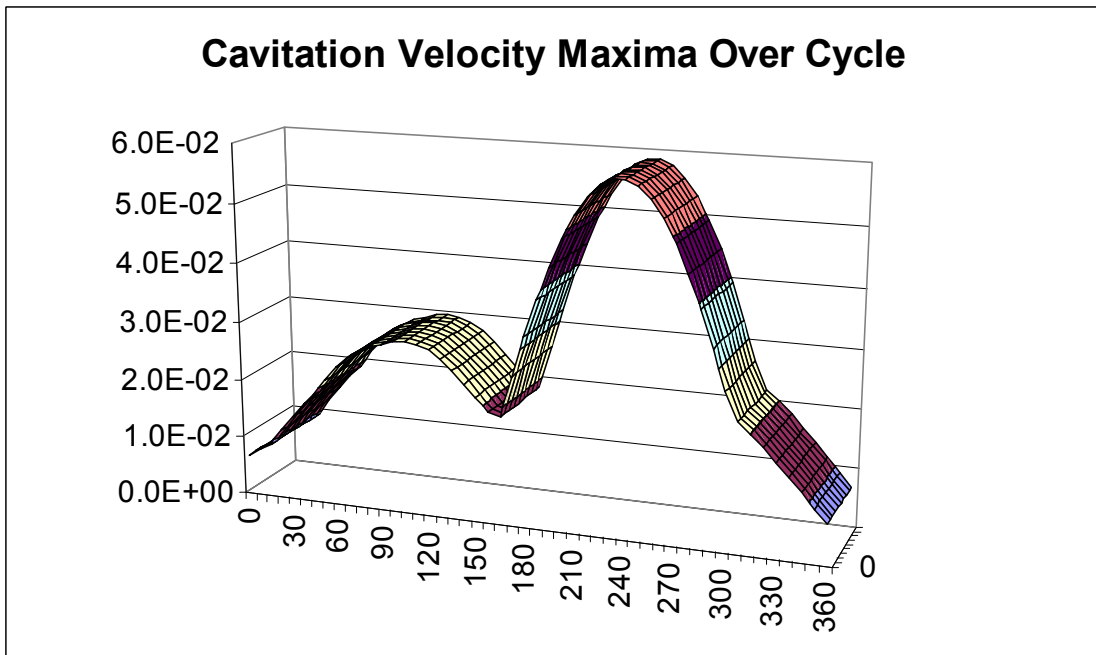


Figure 6-135 Diesel, Fast Pressure Rise, RHD, 5000 rpm – Cavitation Velocity Maxima Over Cycle

Looking at pressure gradient $dp/d\theta$ – we’re interested in the most negative values which are likely to produce cavitation. The values over the cycle are shown here. There’s a very large negative value at 1430 (710) deg. Crank angle almost corresponding with the maximum velocity.

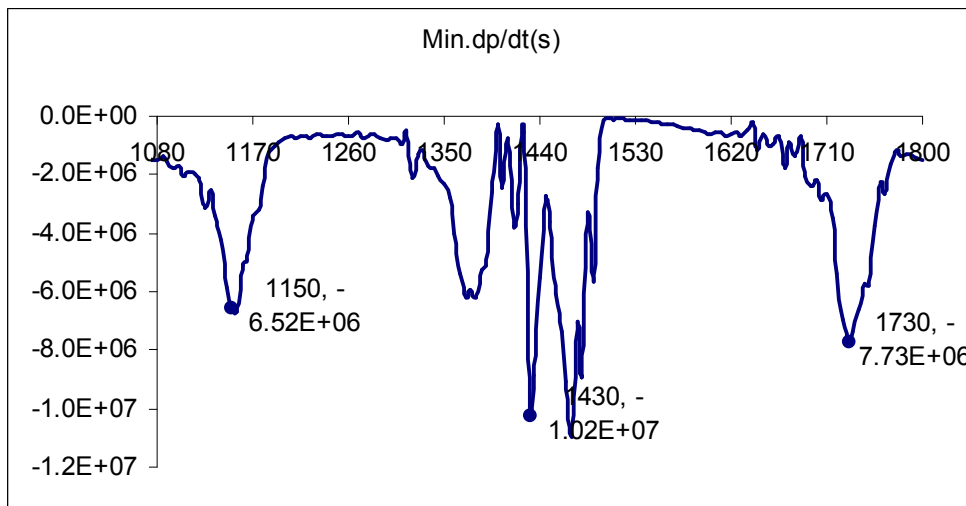


Figure 6-136 Diesel, Fast Pressure Rise, RHD, 5000 rpm – Minimum Pressure Gradient Over Cycle

Looking at pressure gradient $dp/d\theta$ – we're interested in the most negative values which are likely to produce cavitation. Snapshot here of the situation at the highest negative value which occurs at 710 deg. Crank angle.

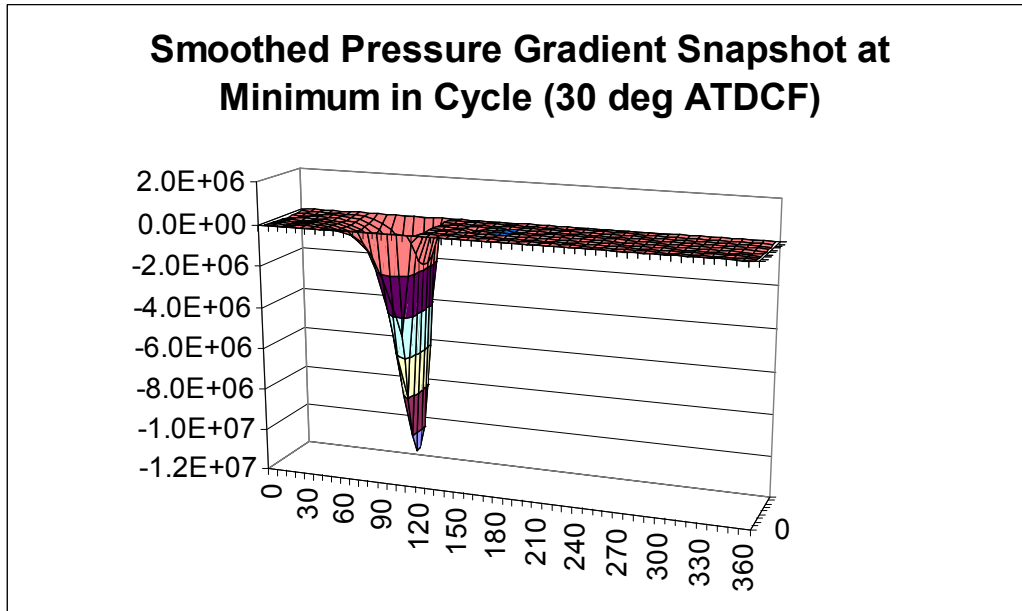


Figure 6-137 Diesel, Fast Pres. Rise, RHD, 5000 rpm – Press. Grad. Snapshot at Minimum

Most negative values over whole bearing over the whole cycle are shown in Fig. 6.138. The major peak at about 120 deg. Bearing angle (710 deg. Crank angle) and 320 deg. Bearing angle (430 deg. Crank angle) can be seen clearly.

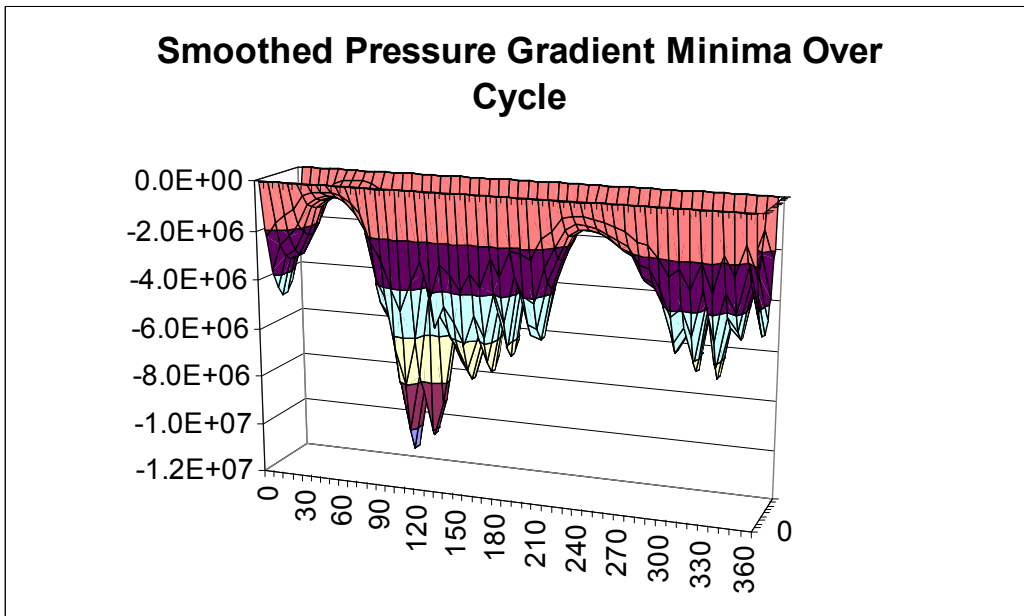


Figure 6-138 Diesel, Fast Press. Rise, RHD, 5000 rpm – Press. Grad. Minima Over Cycle

Fig. 6.139 shows the cavitation damage parameter normalised to the base case. Comparing to Fig. 6.97, it can be seen that the peak is again in the top half of the bearing and about 1.3 times the magnitude. A second peak at about 210 degrees bearing angle (just below the split line) is also above the highest value on the bas case.

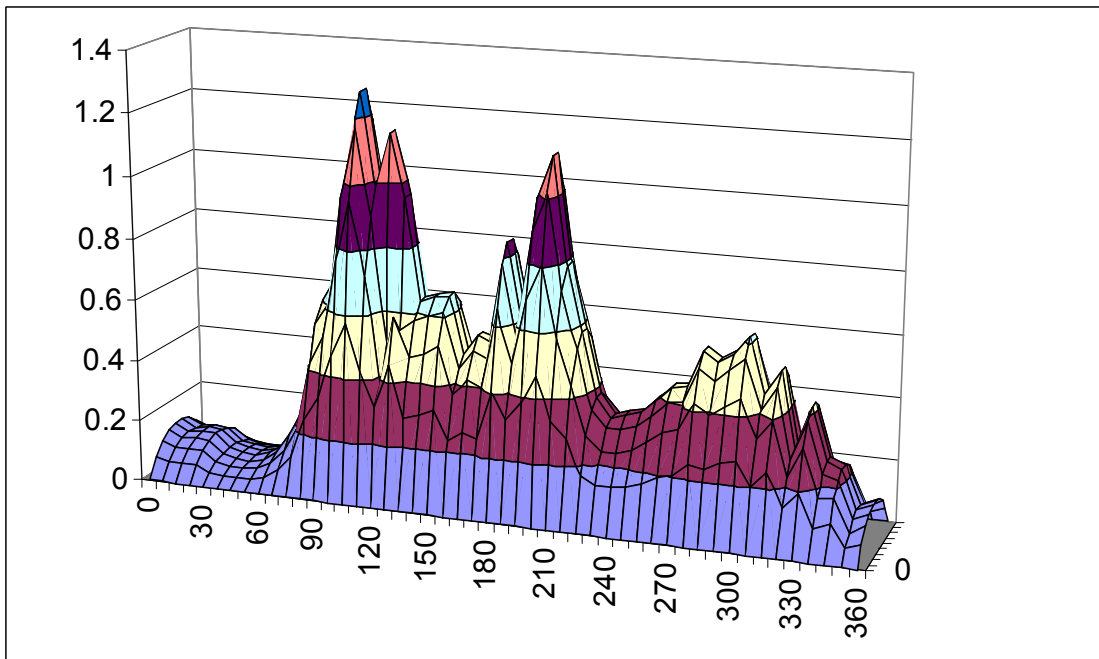


Figure 6-139 Diesel, Fast Pressure Rise, RHD, 5000 rpm – Normalised Cavitation Damage Parameter

The effect of increasing the rate of combustion gas pressure rise is

- Negligible on max. oil film pressure
- Increase rate of pressure change in the bearing
- Increase the cavitation velocity
- Increase the cavitation damage parameter

6.8.5 DIESEL, RHD, 3000 RPM

The following figures for the diesel engine running at 3000 rpm should be compared to Figs. 6.72 to 6.97 as appropriate.

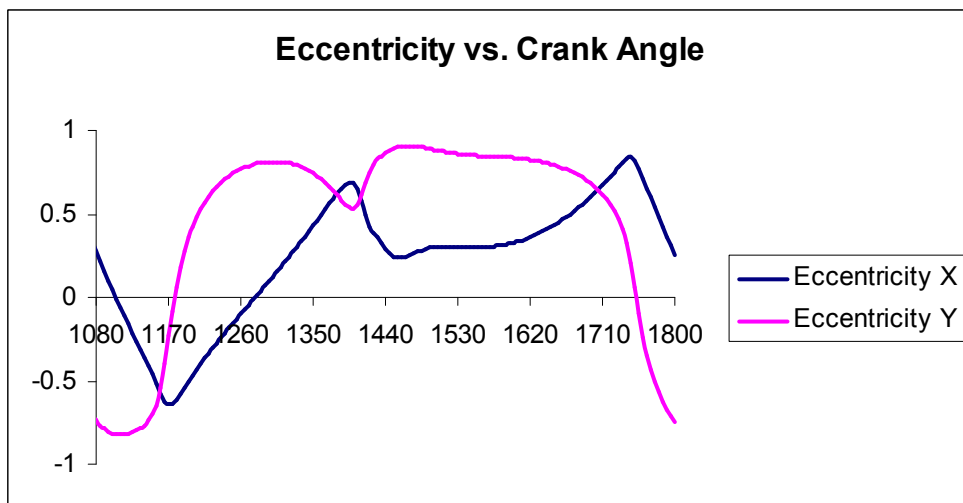


Figure 6-140 Diesel, RHD, 3000 rpm – Eccentricity

Figs. 6.140 to 6.143 show typical diesel engine results but now with very dominant gas pressures through the compression and power strokes as the inertia forces are much reduced.

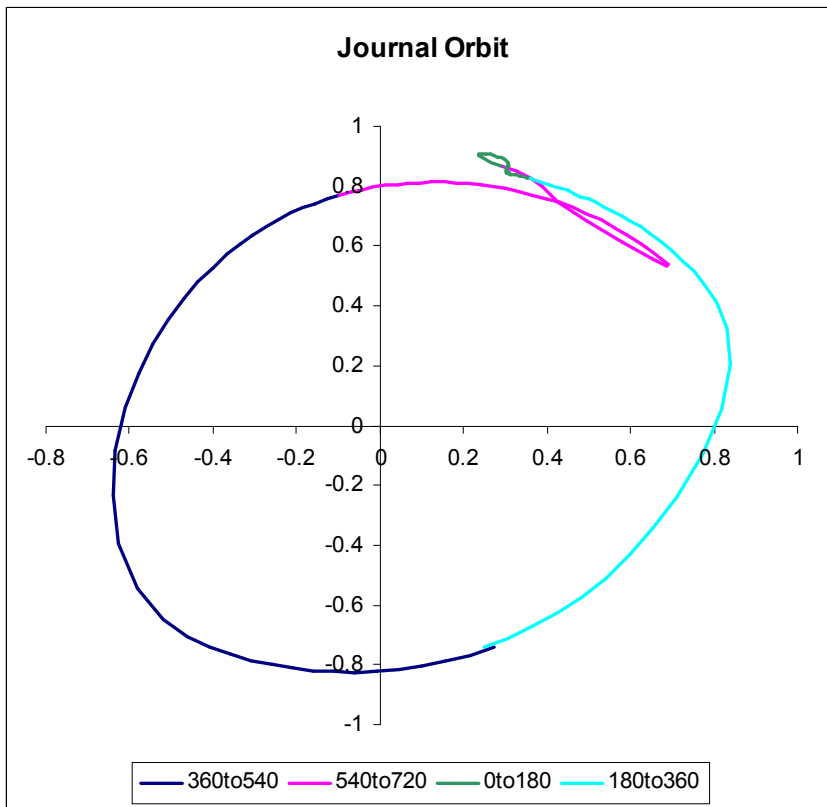


Figure 6-141 Diesel, RHD, 3000 rpm – Journal Orbit

The velocity plots show a less severe movement just before TDCF compared to 5000 rpm. Velocities significantly lower.

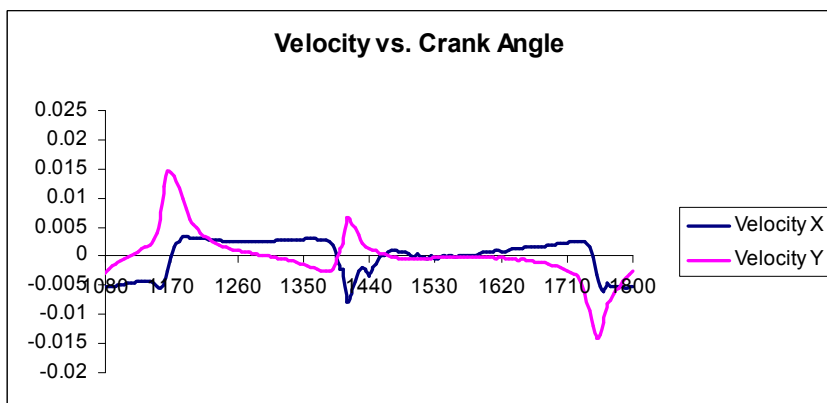


Figure 6-142 Diesel, RHD, 3000 rpm – Journal Velocity

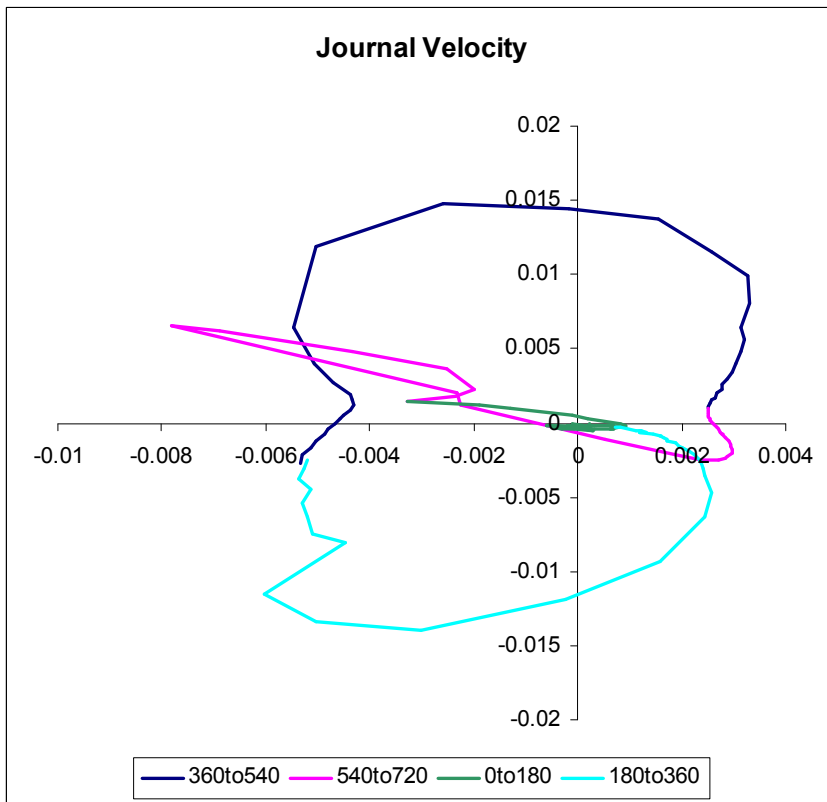


Figure 6-143 Diesel, RHD, 3000 rpm – Journal Velocity

Peak pressures over the cycle are shown with a much more dominant single peak compared to 5000 rpm. This is because there is much less inertia opposing the gas pressure force around TDCF. Note that the peak pressure is slightly later than at 5000 rpm.

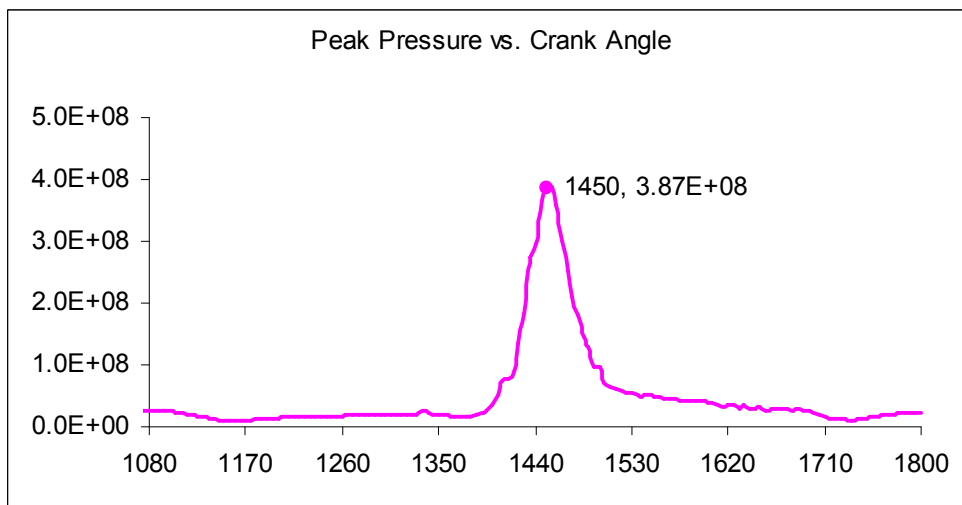


Figure 6-144 Diesel, RHD, 3000 rpm – Peak Film Pressure Over Cycle

This is a snapshot of the pressure distribution at the crank angle that produces the highest pressure (15 deg ATDCF).

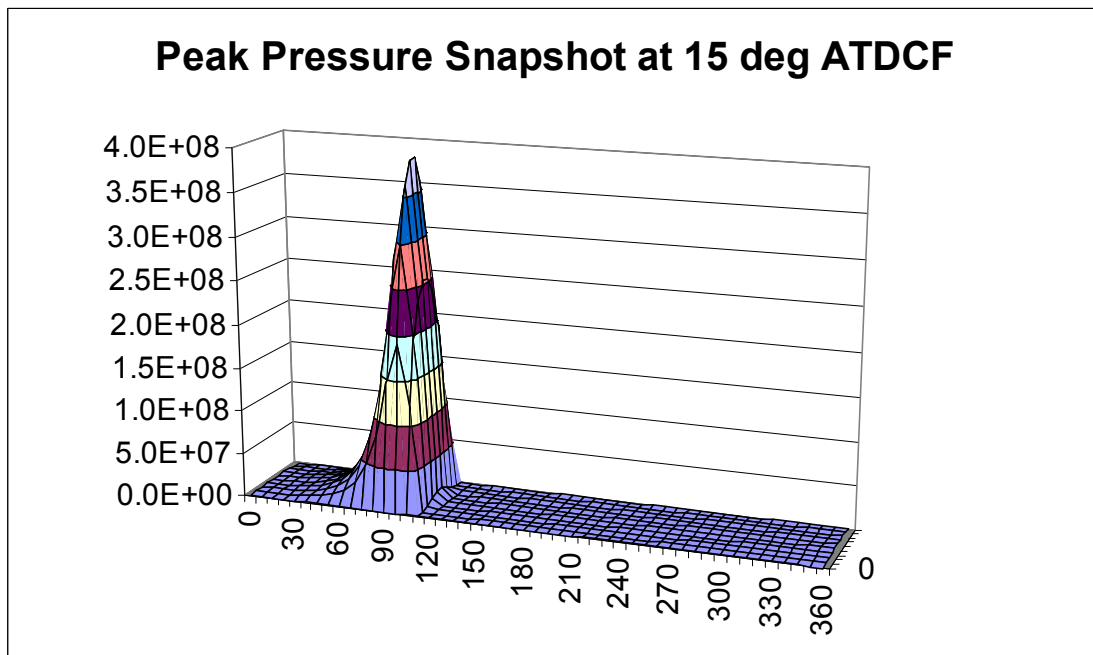


Figure 6-145 Diesel, RHD, 3000 rpm – Pressure Snapshot at Maximum

Plotting the maximum pressure at each individual node over the whole cycle is useful for showing what is happening over the whole bearing. You can see that the peak value is the same as that at 15 deg. Crank angle and the minor peaks are so small as to be almost invisible.

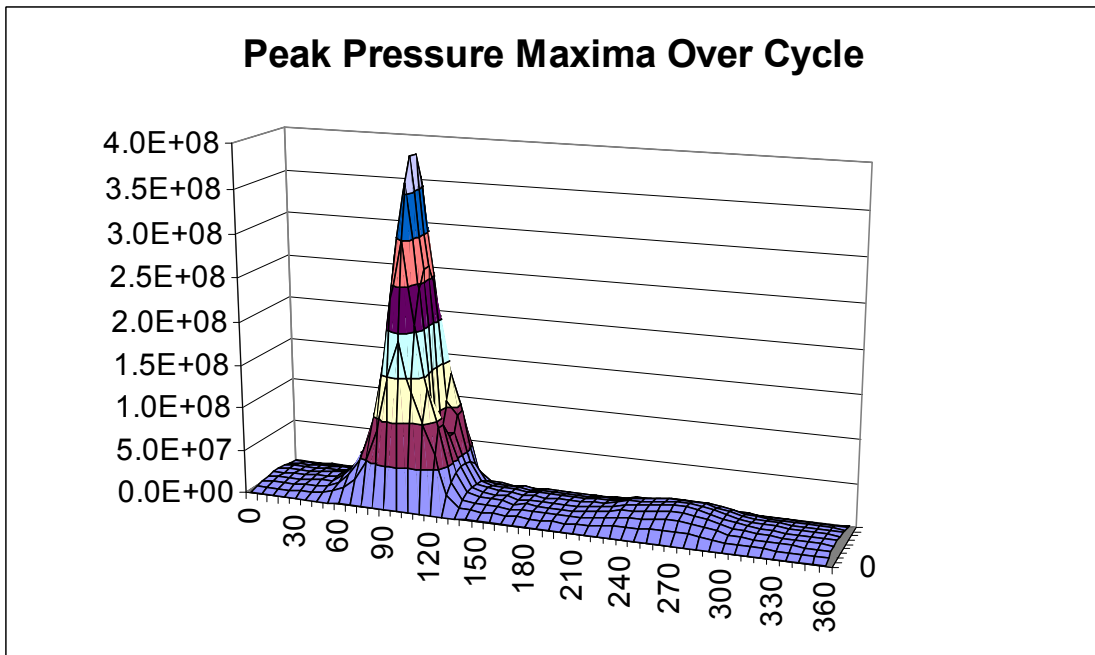


Figure 6-146 Diesel, RHD, 3000 rpm – Peak Pressure Maxima Over Cycle

Plotting the separation velocity (also called cavitation velocity or negative of the squeeze velocity) gives a peak value at 1165 (445) deg. crank angle – no longer near TDCF.

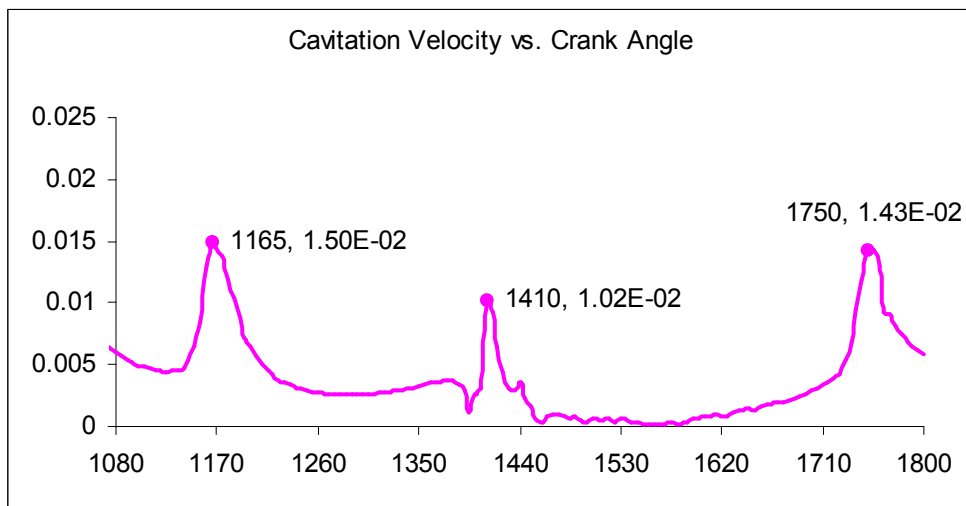


Figure 6-147 Diesel, RHD, 3000 rpm – Maximum Cavitation Velocity Over Cycle

Plotting the separation velocity (called cavitation velocity or negative of the squeeze velocity) produces a sine wave as this is RHD calculation – this is a snapshot at the maximum value in the cycle

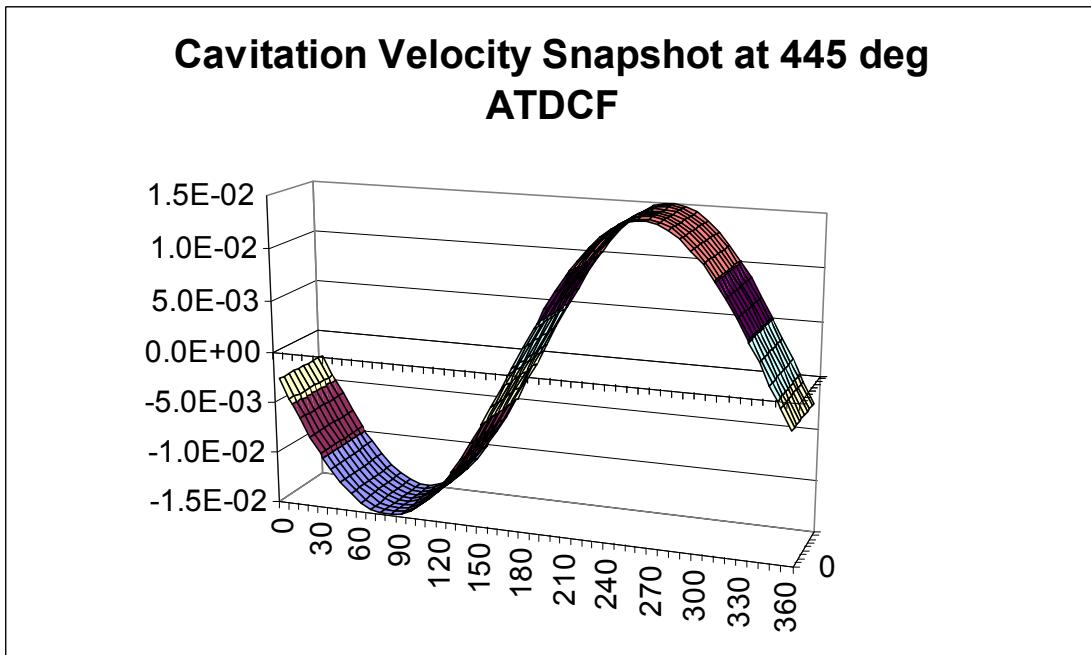


Figure 6-148 Diesel, RHD, 3000 rpm – Cavitation Velocity Snapshot at Maximum

Again, plotting the maximum over the cycle at each node produces the same peak (from the 445 deg. Crank angle results) but a more useful view of the values over the bearing. The next minor peak is nearly as large as the main peak.

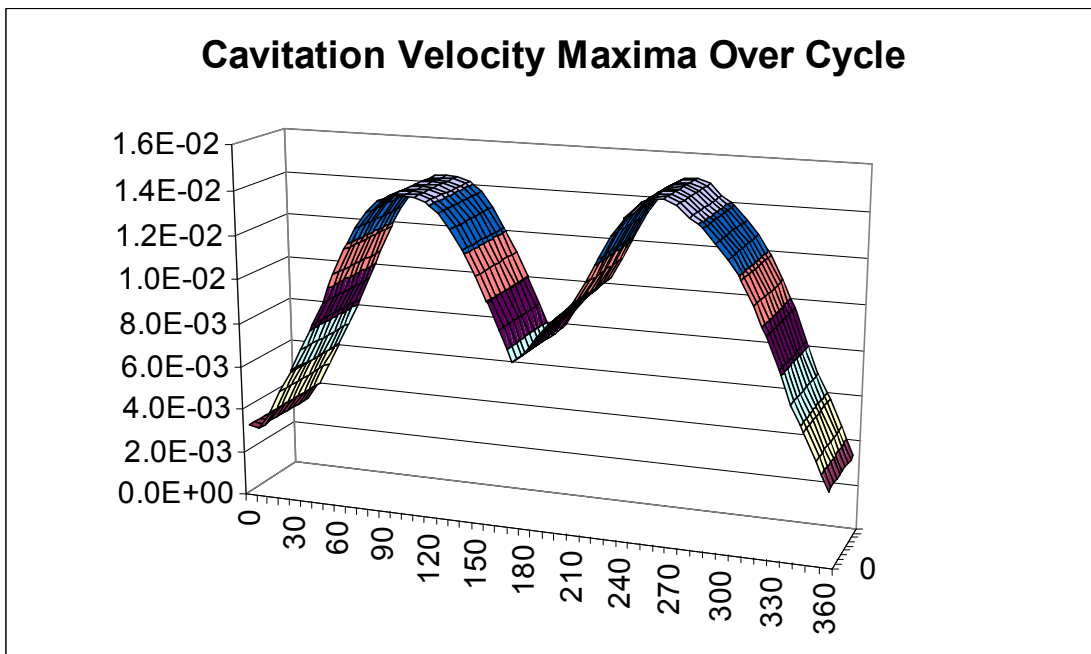


Figure 6-149 Diesel, RHD, 3000 rpm – Cavitation Velocity Maxima Over Cycle

Looking at pressure gradient $dp/d\theta$ – we’re interested in the most negative values which are likely to produce cavitation. The values over the cycle are shown here. There’s a very large negative value at 1430 (710) deg. Crank angle almost corresponding with the maximum velocity.

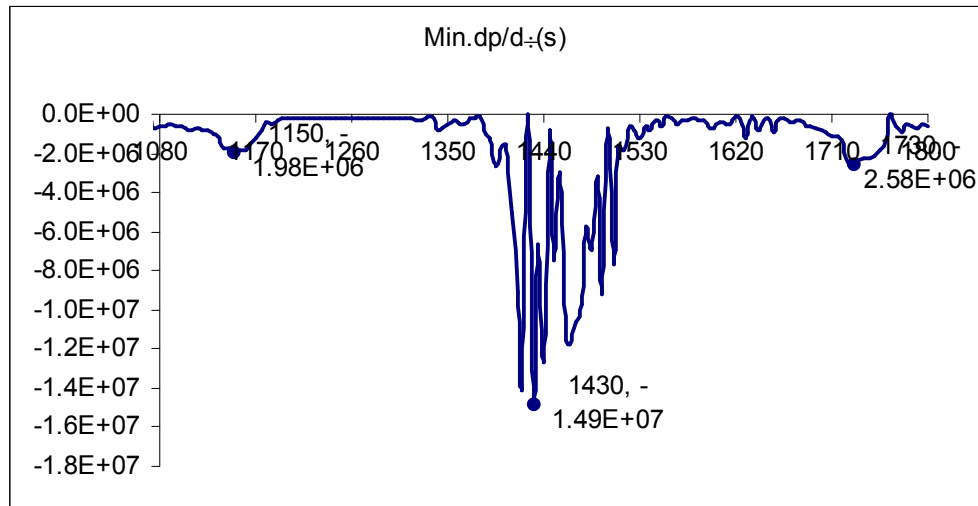


Figure 6-150 Diesel, RHD, 3000 rpm – Minimum Pressure Gradient Over Cycle

Looking at pressure gradient dp/dq – we’re interested in the most negative values which are likely to produce cavitation. Snapshot here of the situation at the highest negative value which occurs at 710 deg. Crank angle.

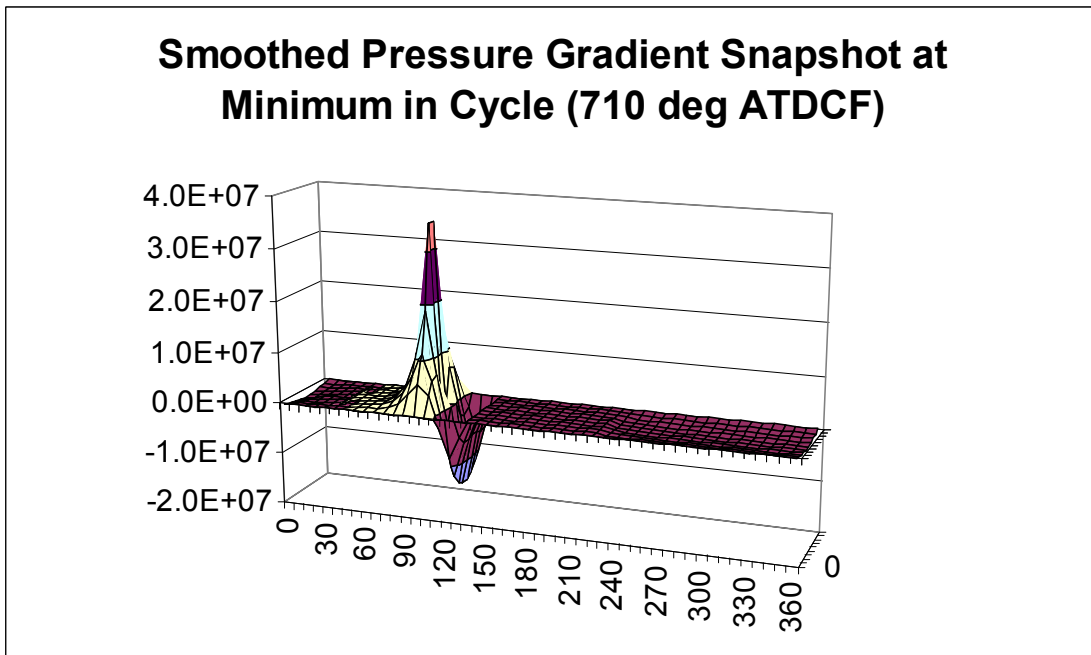


Figure 6-151 Diesel, RHD, 3000 rpm – Pressure Gradient Snapshot at Minimum

Most negative values over whole bearing over the whole cycle are shown here.

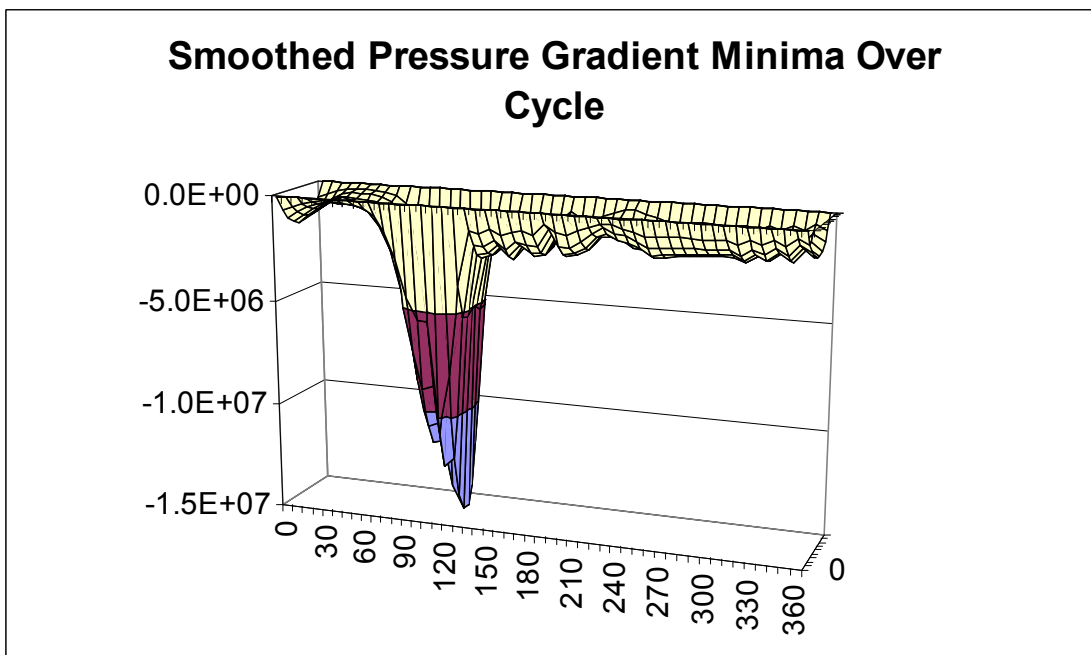


Figure 6-152 Diesel, RHD, 3000 rpm – Pressure Gradient Minima Over Cycle

It can be seen that the strongest effect is slightly to one side of the top of the bearing – 112.5 deg. (90 deg is top of bearing, 0 deg is on the split line). This corresponds with

damage seen in the Forstner and Strewe paper. There is very little effect on other parts of the bearing compared to the results at 5000 rpm.

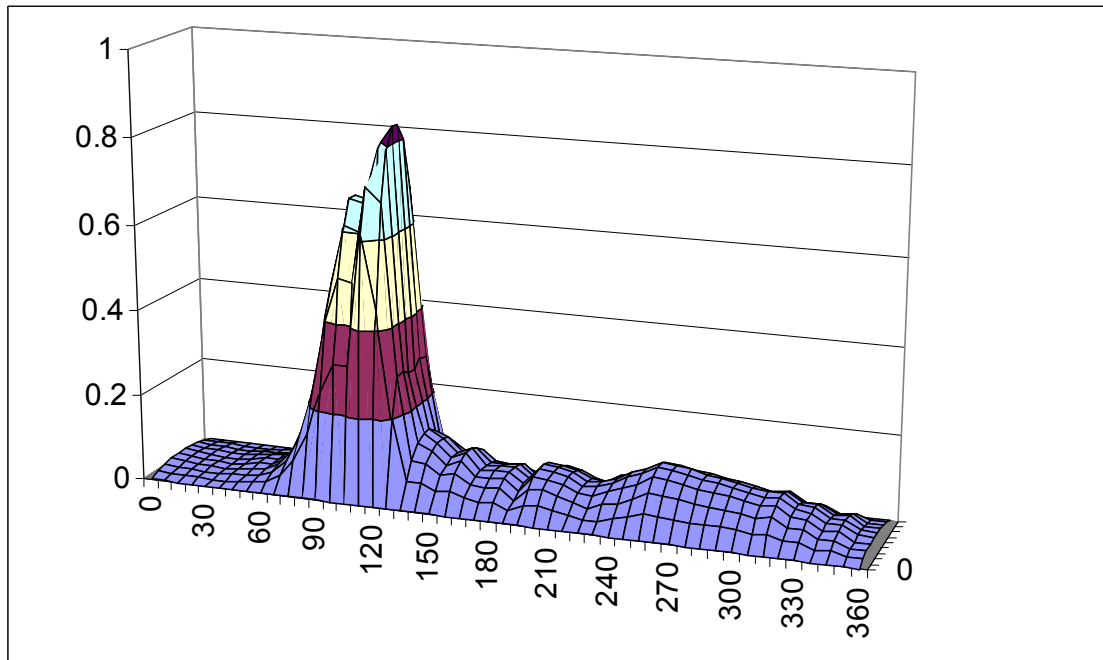


Figure 6-153 Diesel, RHD, 3000 rpm – Normalised Cavitation Damage Parameter

The domination by gas pressure force is clear from the pressure vs. time. This means that the highest pressures in the bearing on the top shell are much more dominant than at 5000 rpm. High pressure gradients are also concentrated on the top shell. This is also seen in the cavitation damage parameter distribution in Fig. 6.153. The values are now clearly concentrated very strongly in the top half of the bearing. However, the peak value is approximate 0.8 times the value at 5000 rpm.

6.8.6 DIESEL, RHD, 1000 RPM

Reducing the speed still further to 1000 rpm means that the inertia forces are insignificant compared to the gas pressure forces. The following figures should be compared to Figs. 6.72 to 6.97 as appropriate.

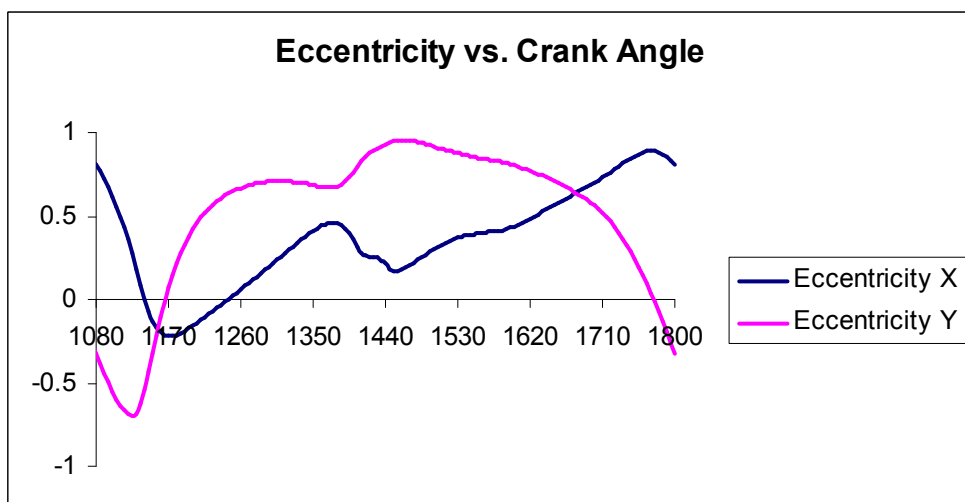


Figure 6-154 Diesel, RHD, 1000 rpm – Eccentricity

Figs. 6.154 to 6.157 are typical diesel engine results but now with very dominant gas pressures through the compression and power strokes.

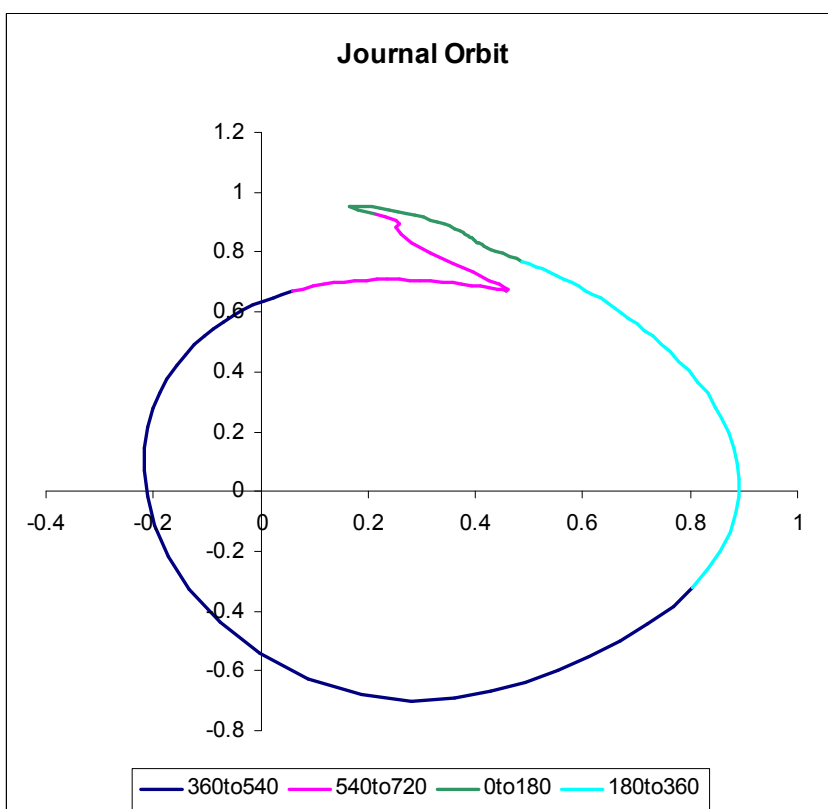


Figure 6-155 Diesel, RHD, 1000 rpm – Journal Orbit

The velocity plots show a much less severe movement just before TDCF compared to 5000 rpm. Velocities significantly lower – compare with Figs. 6.74 and 6.75.

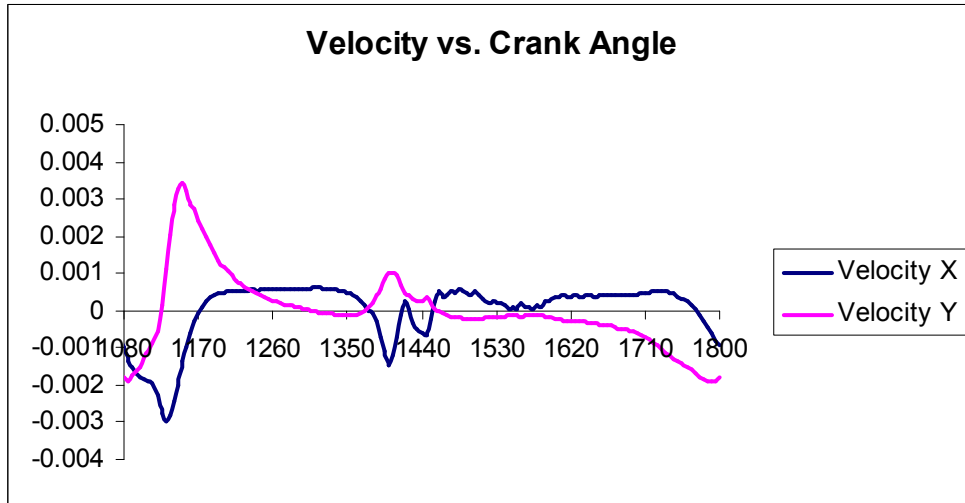


Figure 6-156 Diesel, RHD, 1000 rpm – Journal Velocity

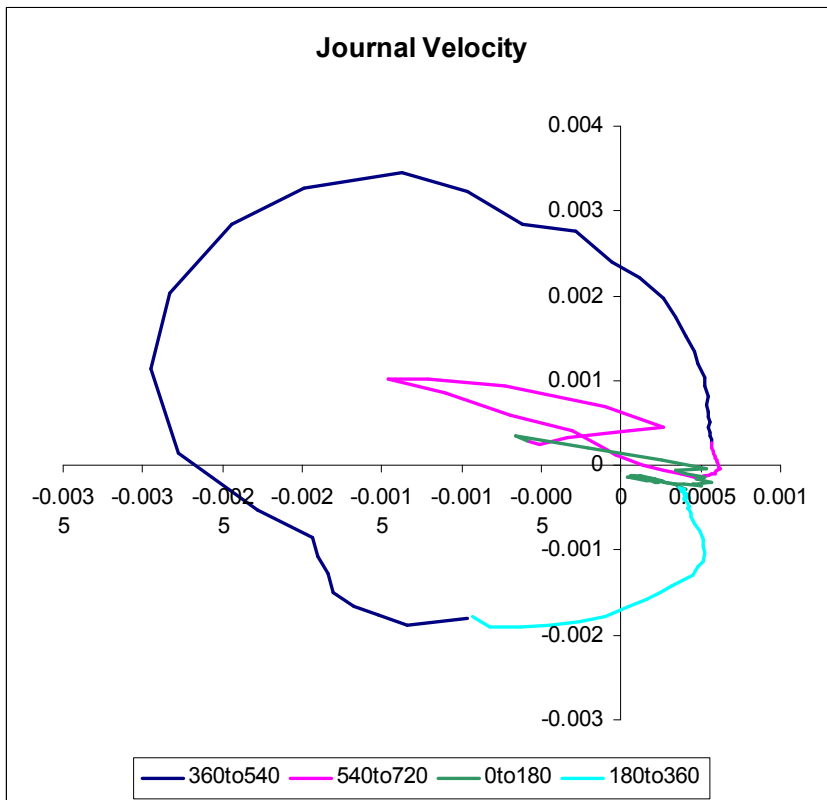


Figure 6-157 Diesel, RHD, 1000 rpm – Journal Velocity

Peak pressures over the cycle are shown with a much more dominant single peak compared to 5000 rpm. This is because there is much less inertia opposing the gas

pressure force around TDCF. Note that the peak pressure is slightly later than at 5000 rpm.

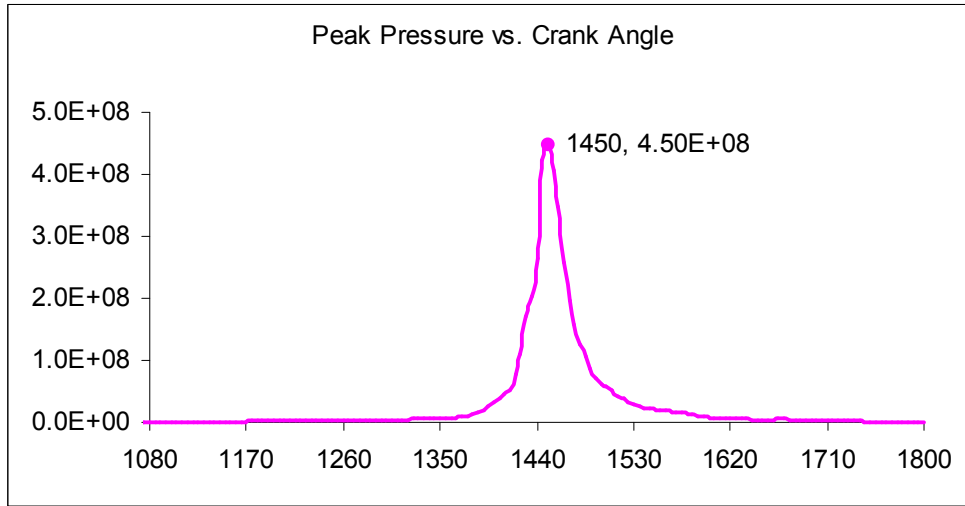


Figure 6-158 Diesel, RHD, 1000 rpm – Peak Film Pressure Over Cycle

This is a snapshot of the pressure distribution at the crank angle that produces the highest pressure (10 deg ATDCF).

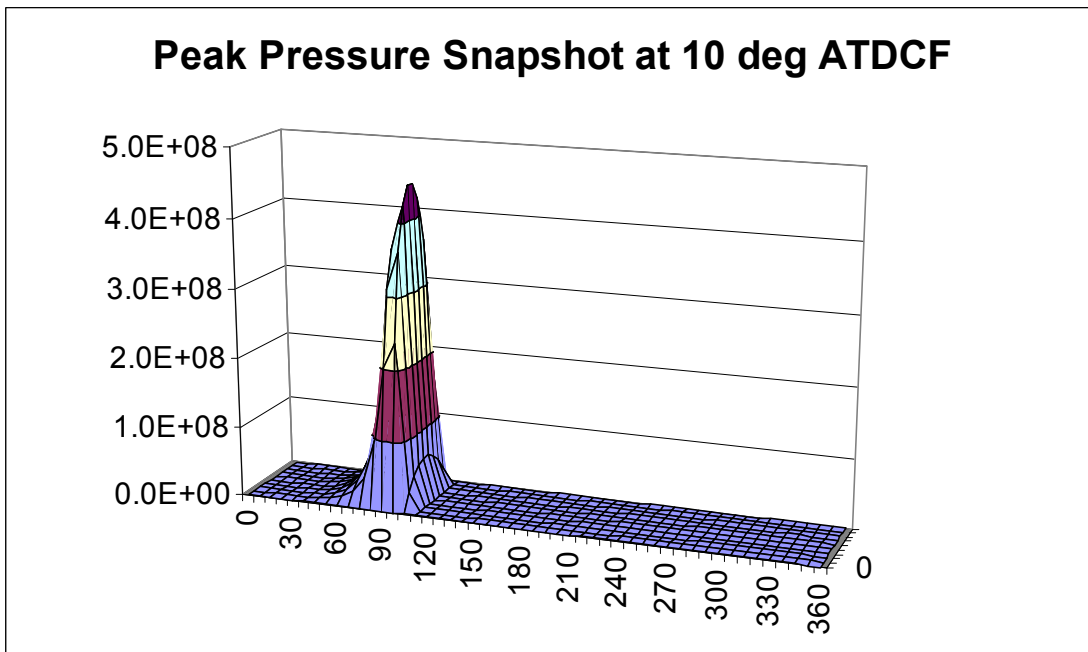


Figure 6-159 Diesel, RHD, 1000 rpm – Film Pressure Snapshot at Maximum

Plotting the maximum pressure at each individual node over the whole cycle is useful for showing what is happening over the whole bearing. You can see that the peak value

is the same as that at 10 deg. Crank angle and the minor peaks are now completely insignificant.

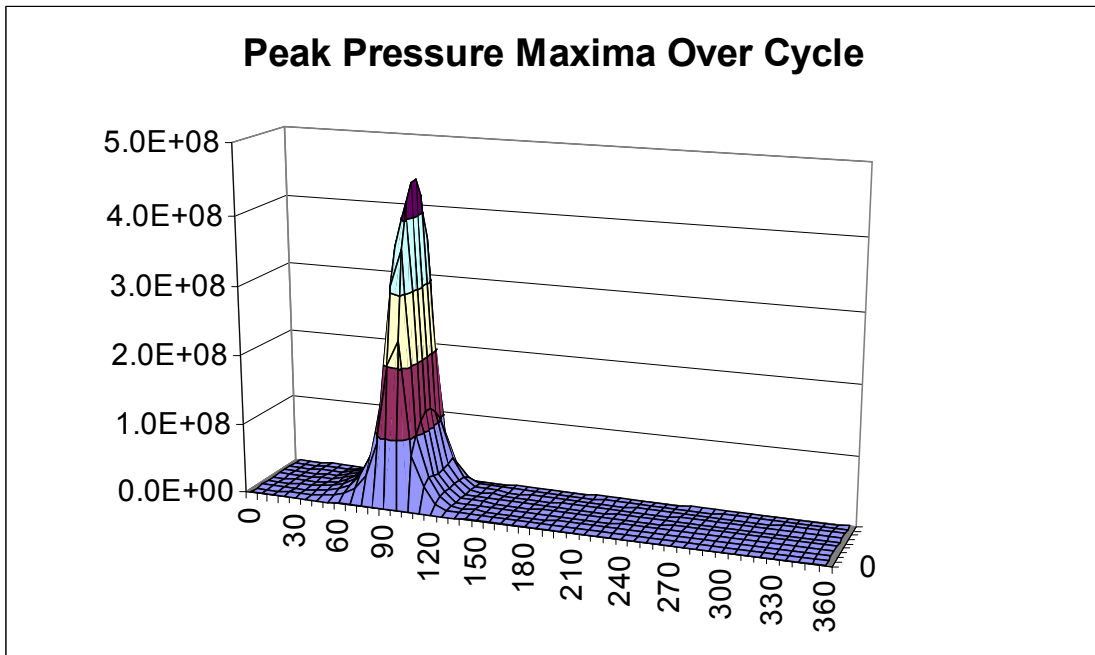


Figure 6-160 Diesel, RHD, 1000 rpm – Peak Pressure Maxima Over Cycle

Plotting the separation velocity (also called cavitation velocity or negative of the squeeze velocity) gives a peak value at 1145 (425) deg. crank angle – no longer near TDCF.

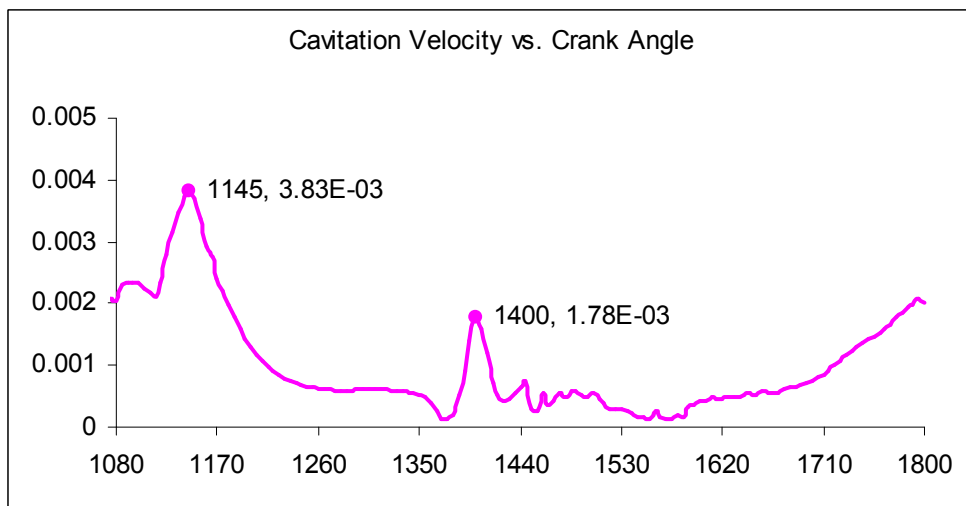


Figure 6-161 Diesel, RHD, 1000 rpm – Maximum Cavitation Velocity Over Cycle

Plotting the separation velocity (called cavitation velocity or negative of the squeeze velocity) produces a sine wave as this is RHD calculation – this is a snapshot at the maximum value in the cycle.

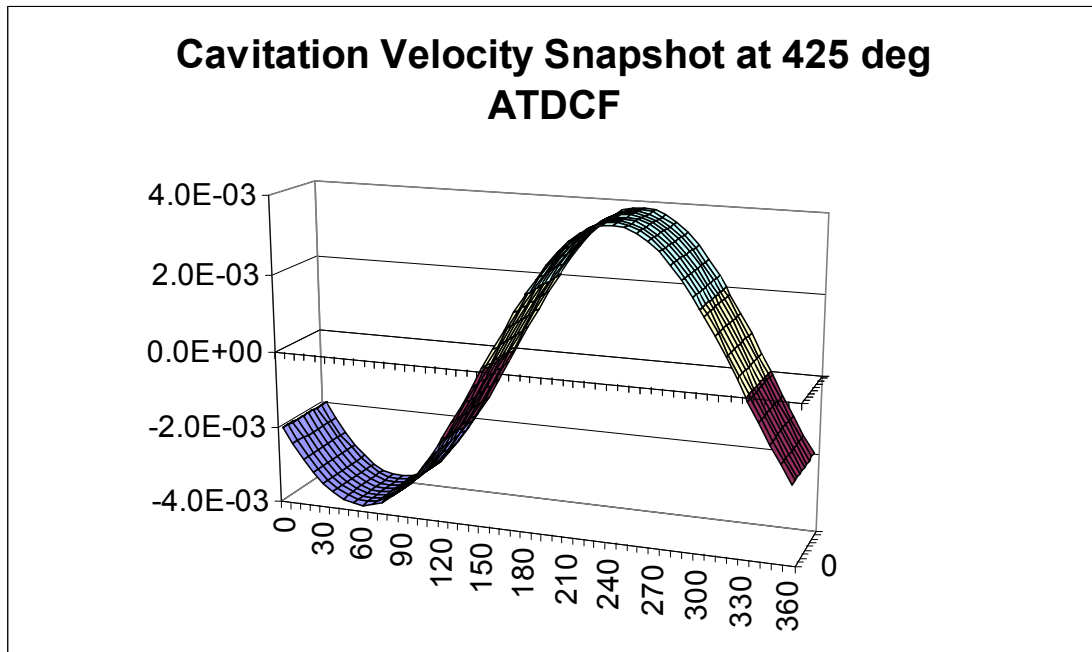


Figure 6-162 Diesel, RHD, 1000 rpm – Cavitation Velocity Snapshot at Maximum

Again, plotting the maximum over the cycle at each node produces the same peak (from the 425 deg. Crank angle results) but a more useful view of the values over the bearing. The next minor peak is small.

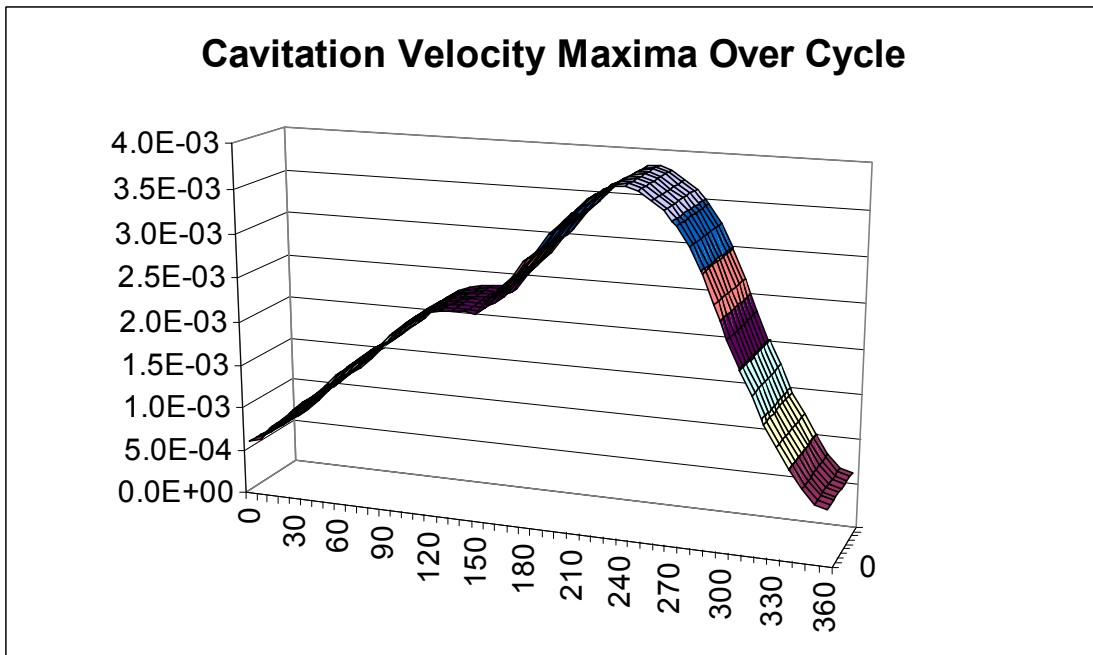


Figure 6-163 Diesel, RHD, 1000 rpm – Cavitation Velocity Maxima Over Cycle

Looking at pressure gradient $dp/d\theta$ – we’re interested in the most negative values which are likely to produce cavitation. The values over the cycle are shown here. There’s a very large negative value at 1465 (25) deg. crank angle.

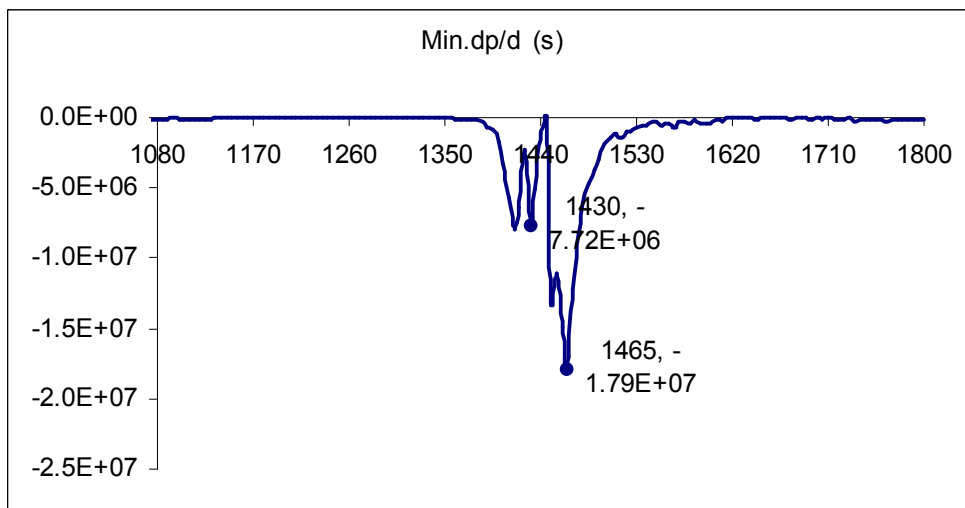


Figure 6-164 Diesel, RHD, 1000 rpm – Minimum Pressure Gradient Over Cycle

Looking at pressure gradient dp/dq – we’re interested in the most negative values which are likely to produce cavitation. Snapshot here of the situation at the highest negative value which occurs at 710 deg. Crank angle.

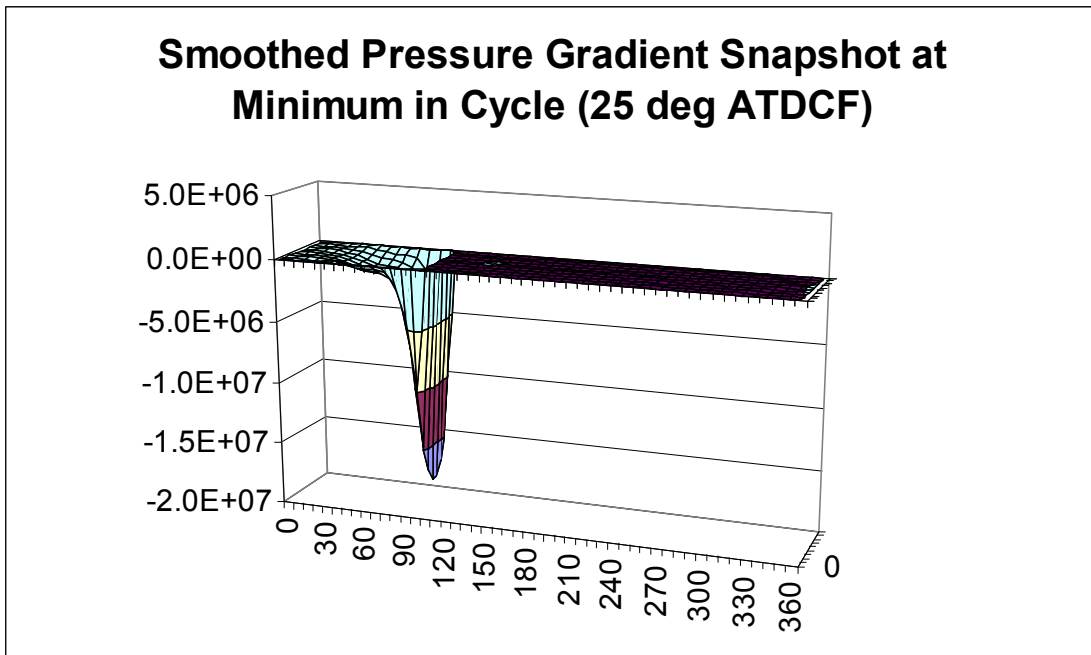


Figure 6-165 Diesel, RHD, 1000 rpm – Pressure Gradient Snapshot at Minimum

Most negative values over whole bearing over the whole cycle are shown here.

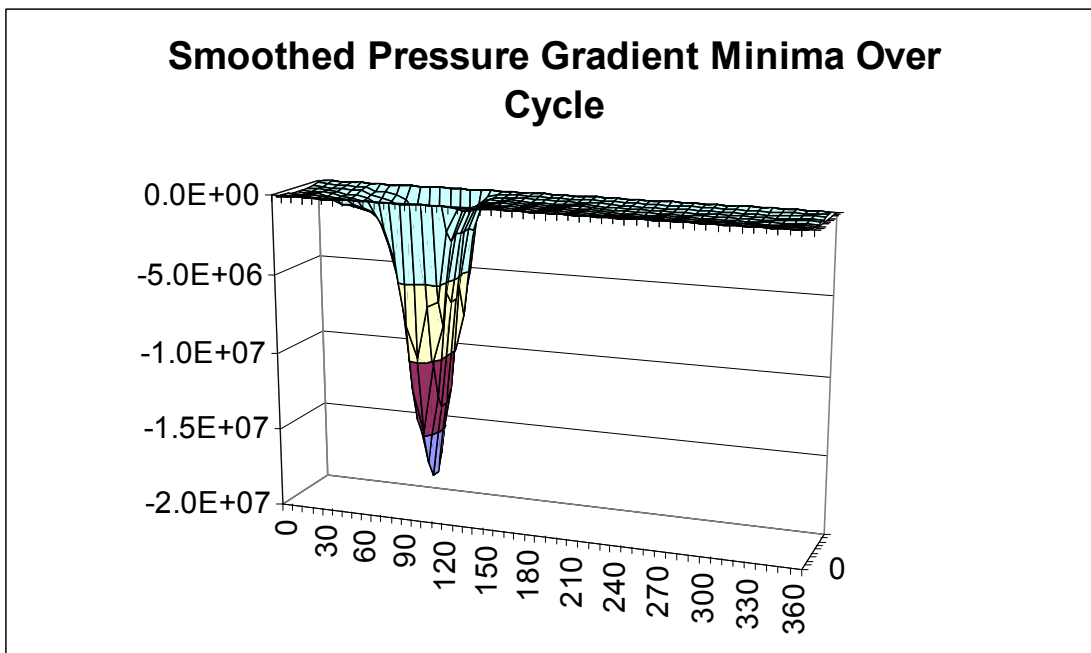


Figure 6-166 Diesel, RHD, 1000 rpm – Pressure Gradient Minima Over Cycle

It can be seen that the strongest effect is slightly to one side of the top of the bearing – 112.5 deg. (90 deg is top of bearing, 0 deg is on the split line). This corresponds with

damage seen in the Forstner and Strewe paper. There is very little effect on other parts of the bearing compared to the results at 5000 rpm.

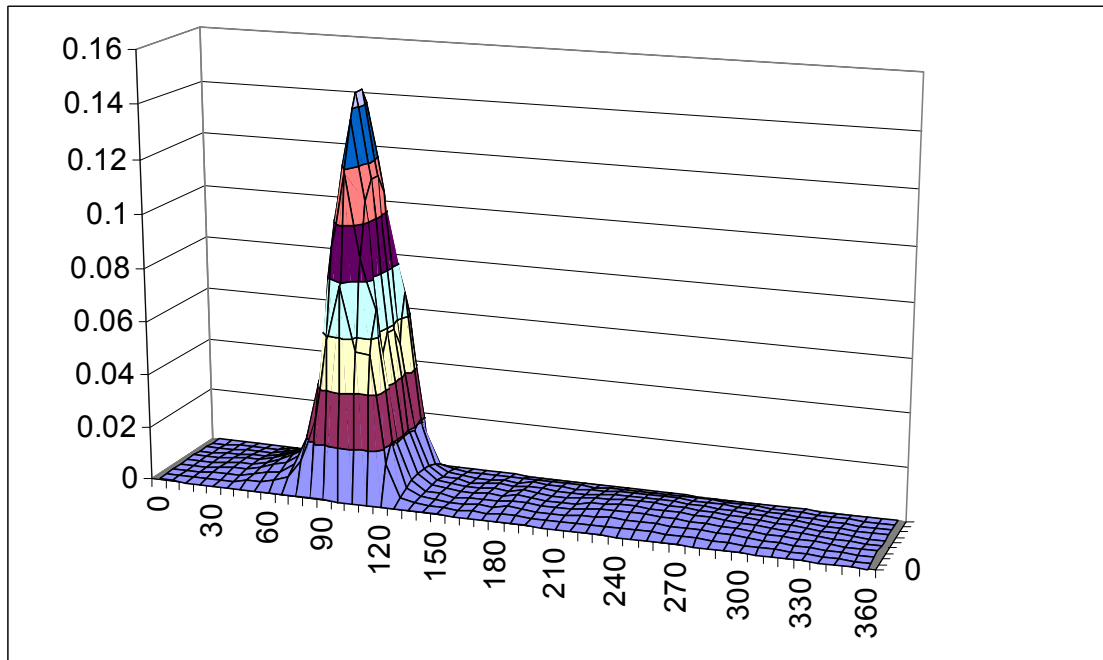


Figure 6-167 Diesel, RHD, 1000 rpm – Normalised Cavitation Damage Parameter

The domination by gas pressure force is clear from the pressure vs. time. This means that the highest pressures in the bearing on the top shell are much more dominant than at 5000 rpm. High pressure gradients are also concentrated on the top shell

This is also seen in the cavitation damage parameter in Fig. 6.167 which is now concentrated very strongly in the top half of the bearing. However, the magnitude of the peak value is now approximately 0.15 times the base case.

6.8.7 DIESEL, EHD, 5000 RPM

Taking the base case diesel calculation, 5000 rpm with RHD calculation and changing to EHD using the connecting rod big end mesh shown earlier in the thesis gives the following results which should be compared to Figs. 6.72 to 6.97 as appropriate.

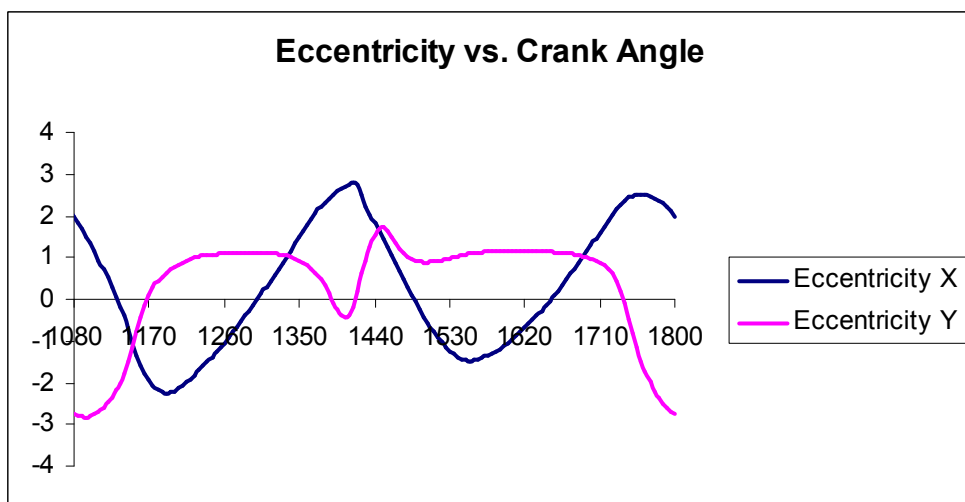


Figure 6-168 Diesel, EHD, 5000 rpm – Eccentricity

Figs. 6.168 to 6.171 are typical diesel engine results with dominant gas pressures either side of TDCF. They are very similar in appearance to the RHD results but note that the eccentricity ratios exceed unity by a considerable margin.

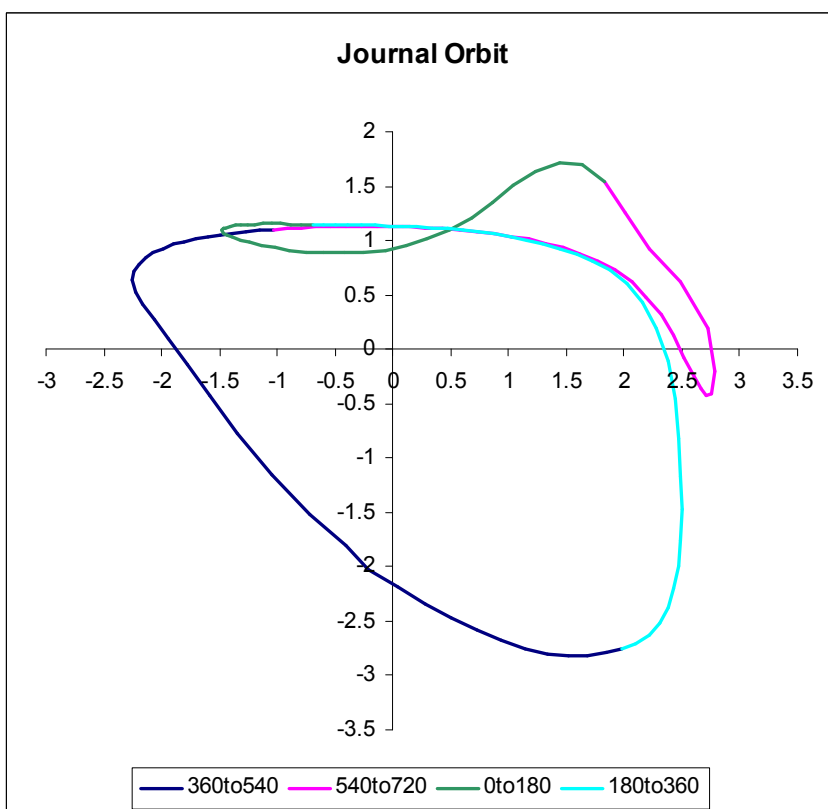


Figure 6-169 Diesel, EHD, 5000 rpm – Journal Orbit

The velocity plots show the movement just before TDCF with slightly higher velocity than the ungrooved bearing.

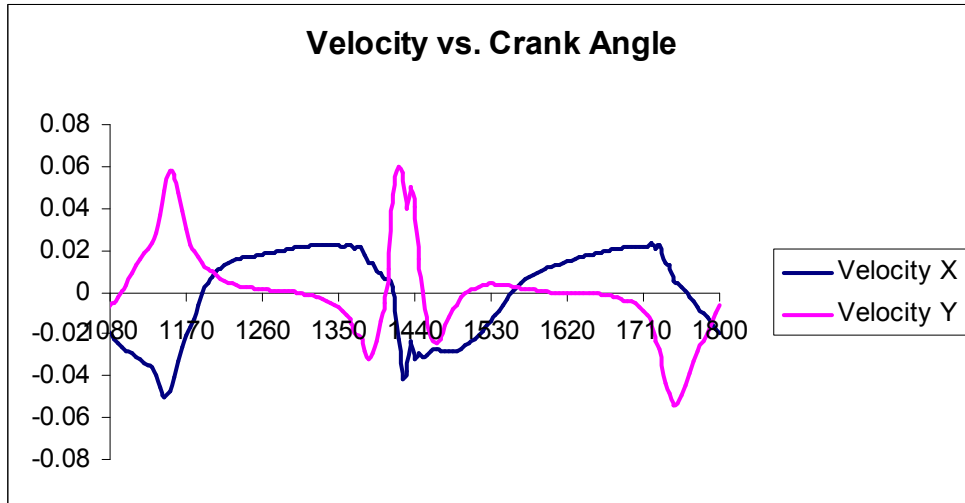


Figure 6-170 Diesel, EHD, 5000 rpm – Journal Velocity

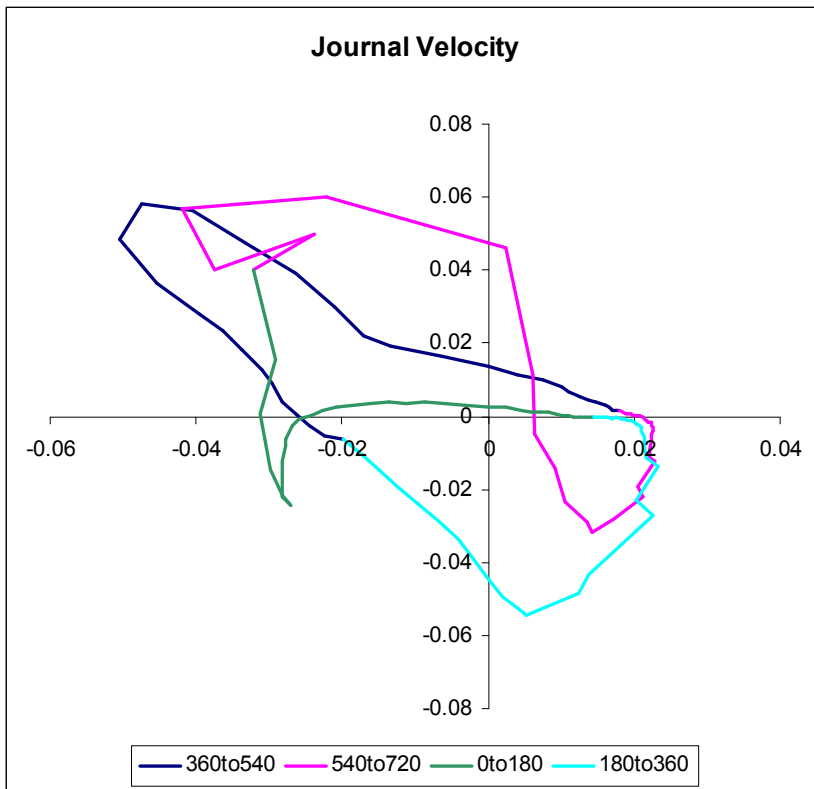


Figure 6-171 Diesel, EHD, 5000 rpm – Journal Velocity

Peak pressures over the cycle are shown with highest pressure near TDCF.

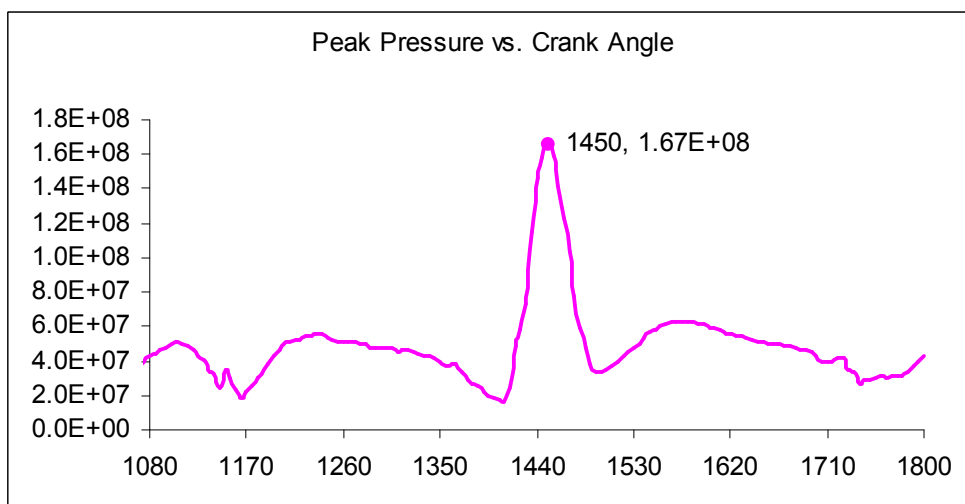


Figure 6-172 Diesel, EHD, 5000 rpm – Peak Film Pressure Over Cycle

This is a snapshot of the pressure distribution at the crank angle that produces the highest pressure (10 deg ATDCF). Note that this is near TDC firing and pressure is in the top half of the bearing.

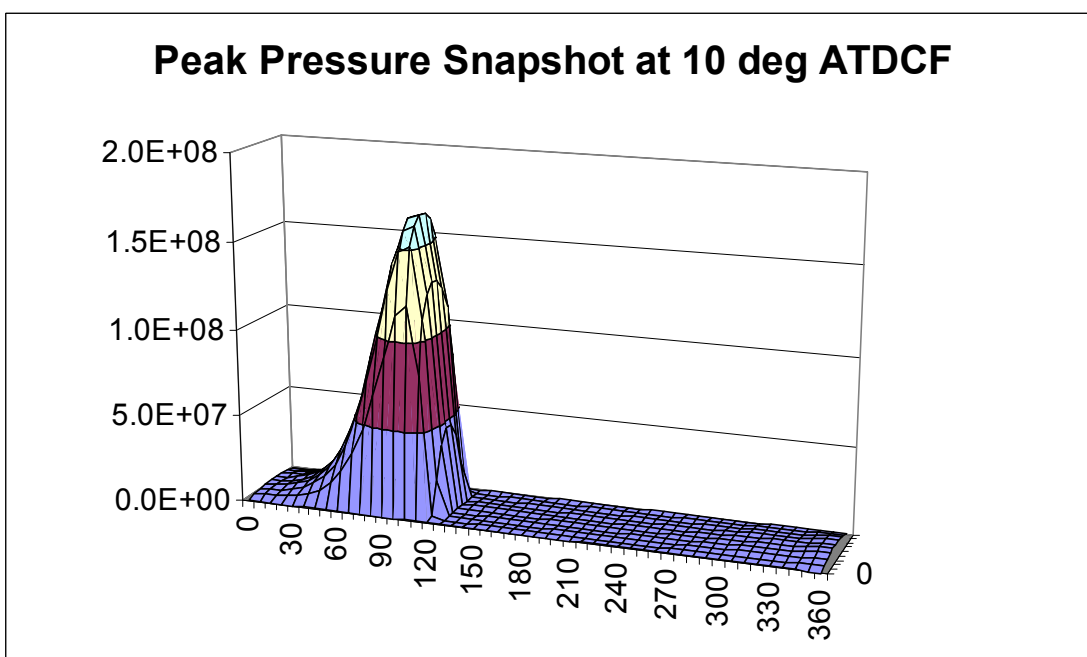


Figure 6-173 Diesel, EHD, 5000 rpm – Pressure Snapshot at Maximum

Plotting the maximum pressure at each individual node over the whole cycle is useful for showing what is happening over the whole bearing. You can see that the peak value

is the same as that at 10 deg. crank angle. The secondary peak, close to TDC non-firing, in the bottom shell is smaller.

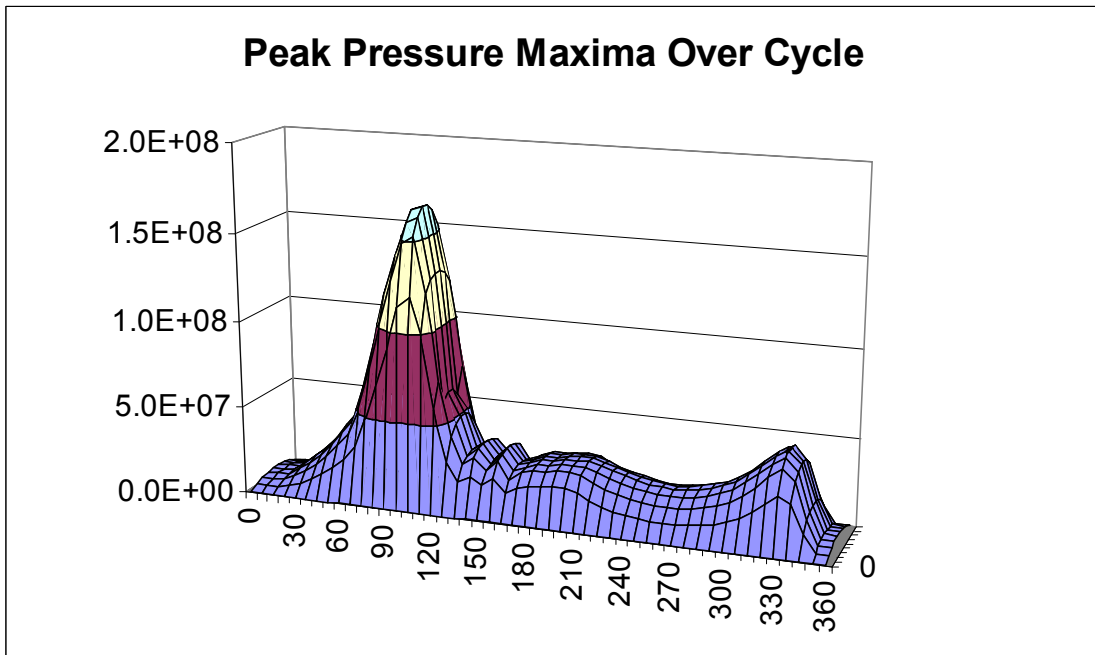


Figure 6-174 Diesel, EHD, 5000 rpm – Peak Pressure Maxima Over Cycle

Fig. 6.175 shows the minimum film thickness over the cycle. Comparing with Fig. 6.82 we can see that the minimum is slightly reduced despite the cushioning effect of the wrap around behaviour.

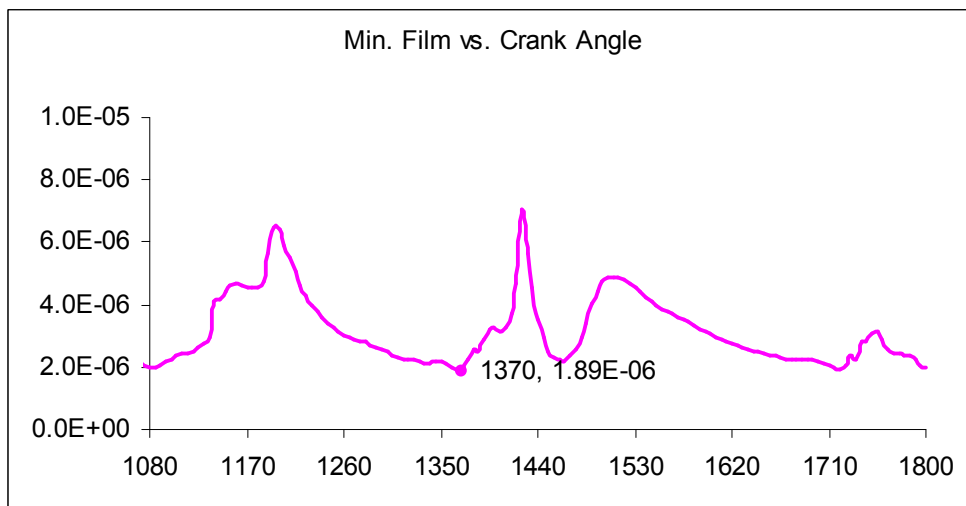


Figure 6-175 Diesel, EHD, 5000 rpm – Minimum Film Thickness Over Cycle

Figs. 6.176 to 6.179 show the film shape at two critical crank angles. One reason for lower film thickness in EHD is that the pressure distribution causes the edges of the bearing to be closer to the journal than the centre line and this can just be seen.

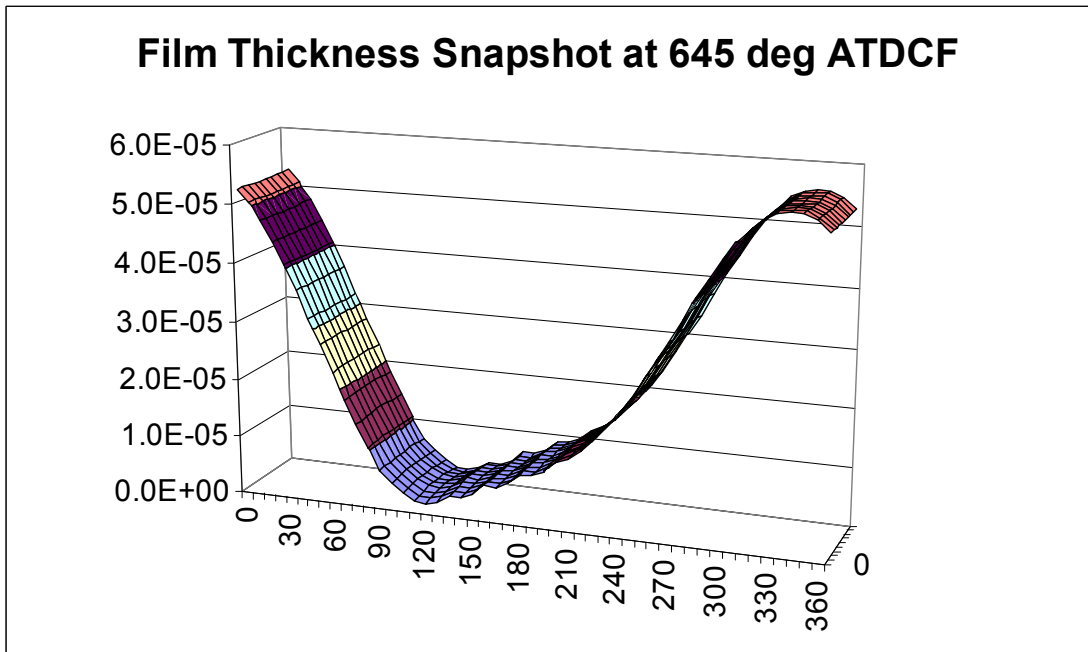


Figure 6-176 Diesel, EHD, 5000 rpm – Film Thickness Snapshot at Minimum

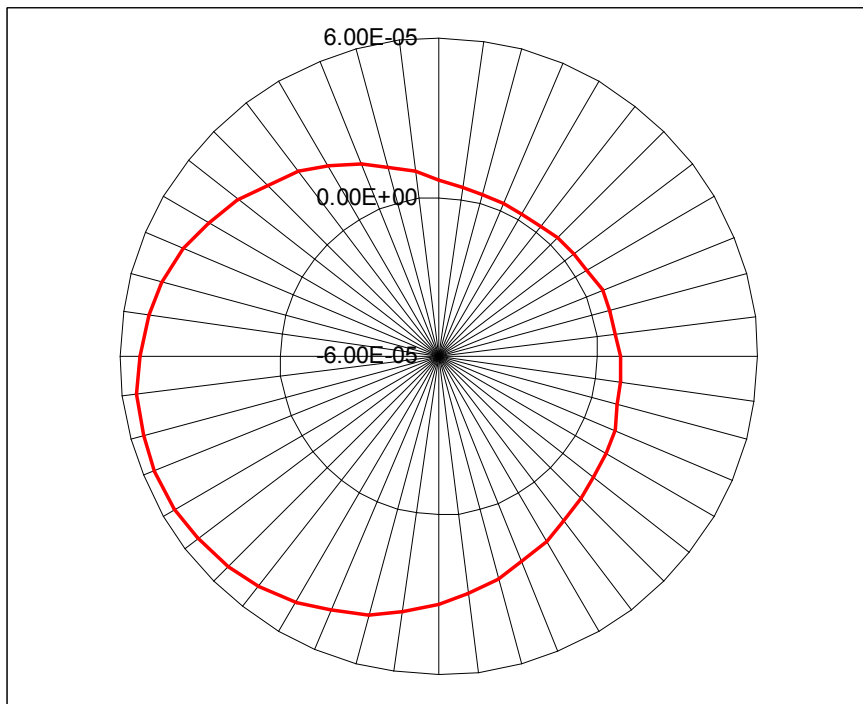


Figure 6-177 Diesel, EHD, 5000 rpm – Film Shape at Minimum Film Thickness

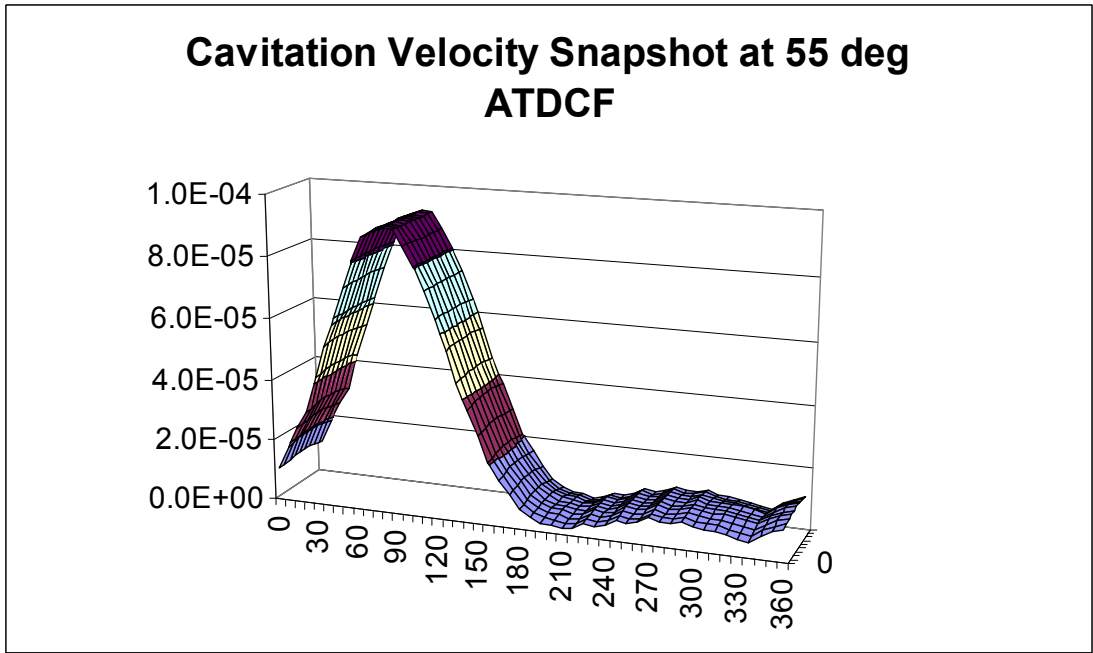


Figure 6-178 Diesel, EHD, 5000 rpm – Film Snapshot at 55 deg

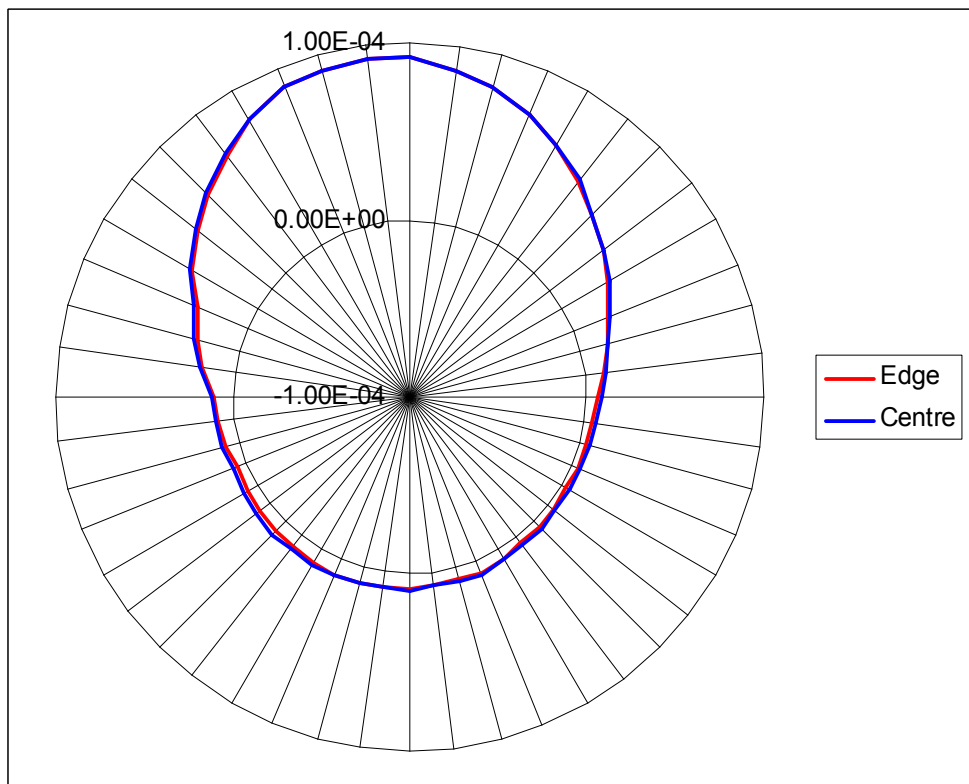


Figure 6-179 Diesel, EHD, 5000 rpm – Film Shape at 55 deg

Fig. 6.180 shows the minima over the whole bearing over the whole cycle. It is a little jagged. This particular calculation was a severe test of the stability of the EHD calculation procedure (see earlier sections on EHD program development).

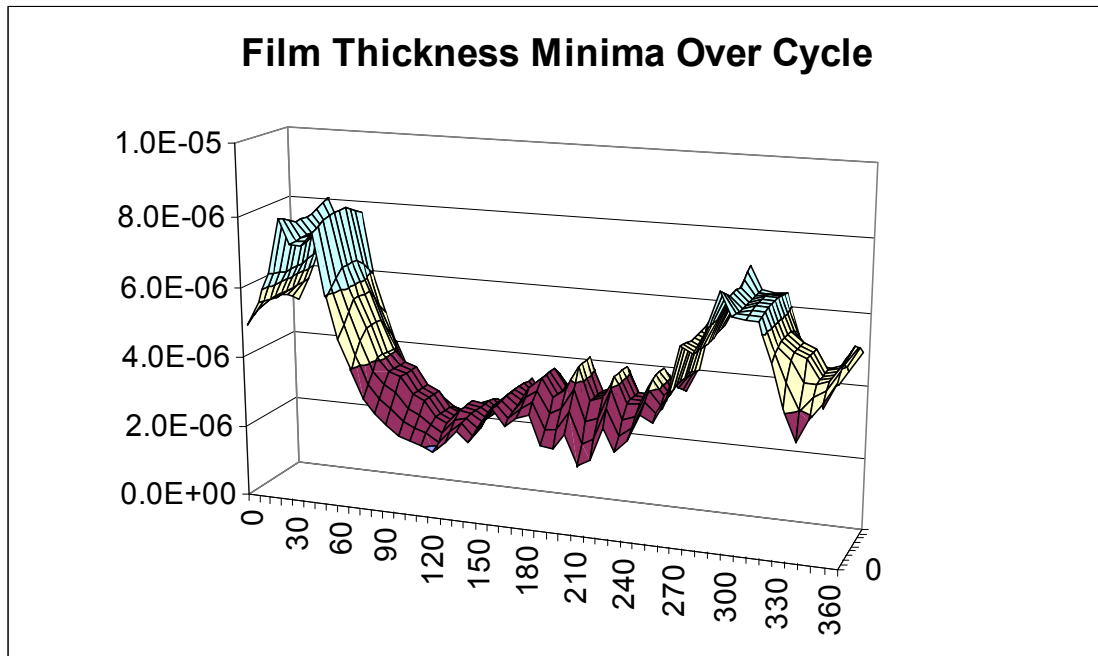


Figure 6-180 Diesel, EHD, 5000 rpm – Film Thickness Minima Over Cycle

Plotting the separation velocity (also called cavitation velocity or negative of the squeeze velocity) gives a peak value at 1425 (705) deg. crank angle – just before TDCF.

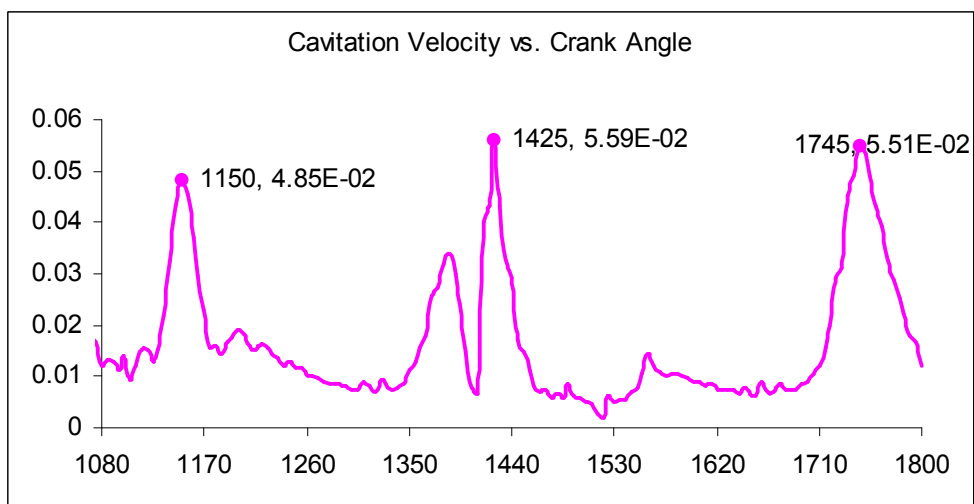


Figure 6-181 Diesel, EHD, 5000 rpm – Maximum Cavitation Velocity Over Cycle

Plotting the separation velocity (called cavitation velocity or negative of the squeeze velocity) produces a sine wave as this is RHD calculation – this is a snapshot at the maximum value in the cycle.

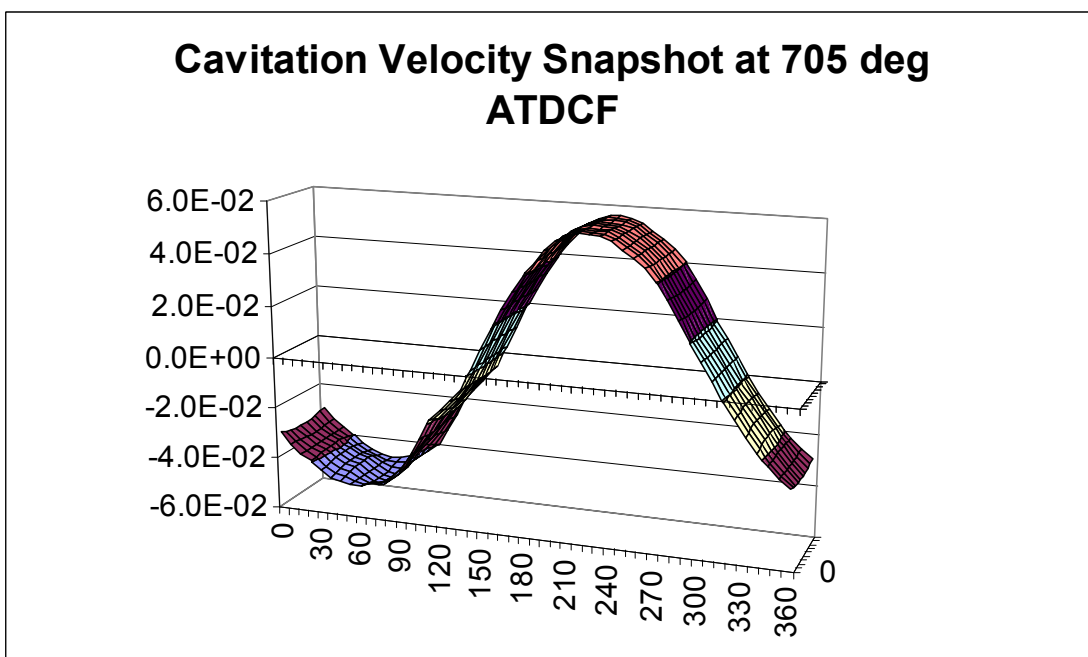


Figure 6-182 Diesel, EHD, 5000 rpm – Cavitation Velocity Snapshot at Maximum

Again, plotting the maximum over the cycle at each node produces the same peak (from the 5 deg. Crank angle results) but a more useful view of the values over the bearing.

The next minor minor peak is only a little smaller. Note the shape along the film in the axial direction, typical of EHD.

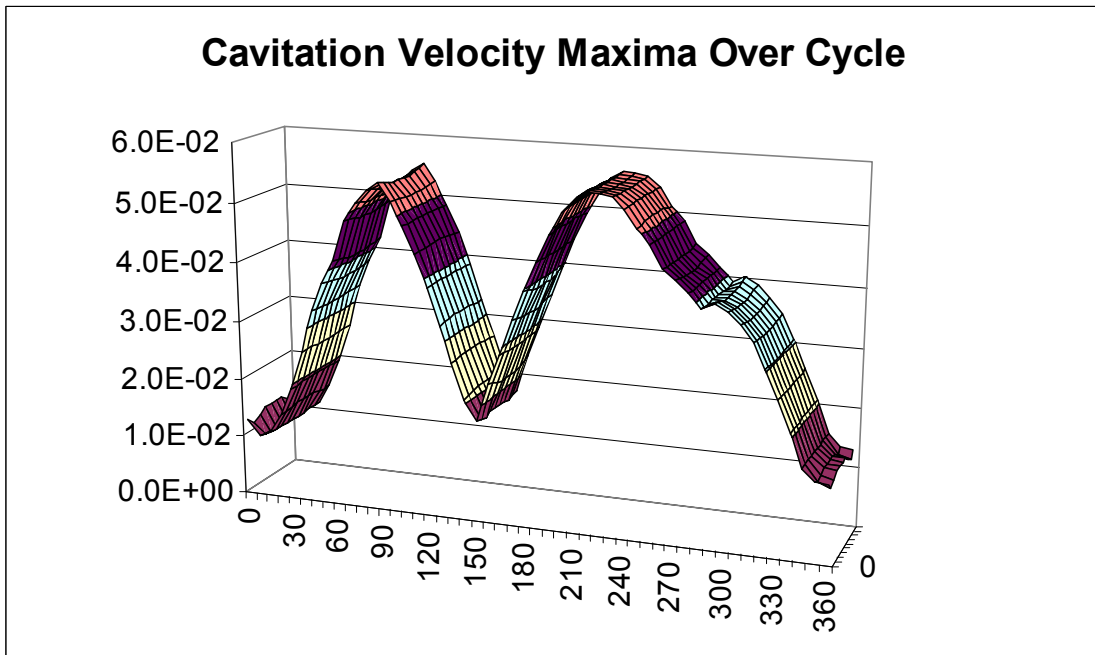


Figure 6-183 Diesel, EHD, 5000 rpm – Cavitation Velocity Maxima Over Cycle

Looking at pressure gradient $dp/d\theta$ – we’re interested in the most negative values which are likely to produce cavitation. The values over the cycle are shown here. There are three main negative peaks, similar in size.

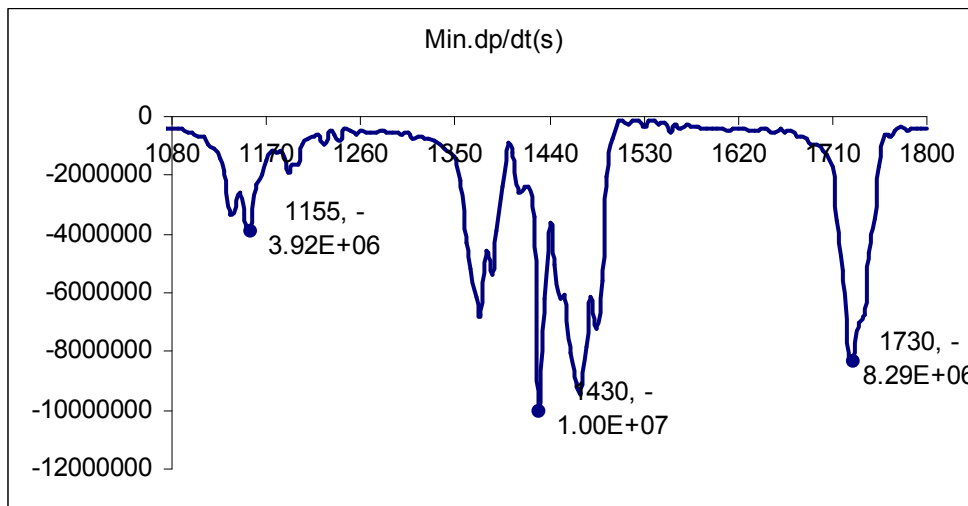


Figure 6-184 Diesel, EHD, 5000 rpm – Minimum Pressure Gradient Over Cycle

Looking at pressure gradient $dp/d\theta$ – we’re interested in the most negative values which are likely to produce cavitation. Snapshot here of the situation at the highest negative value which occurs at 30 deg. crank angle although there are several other peaks nearby.

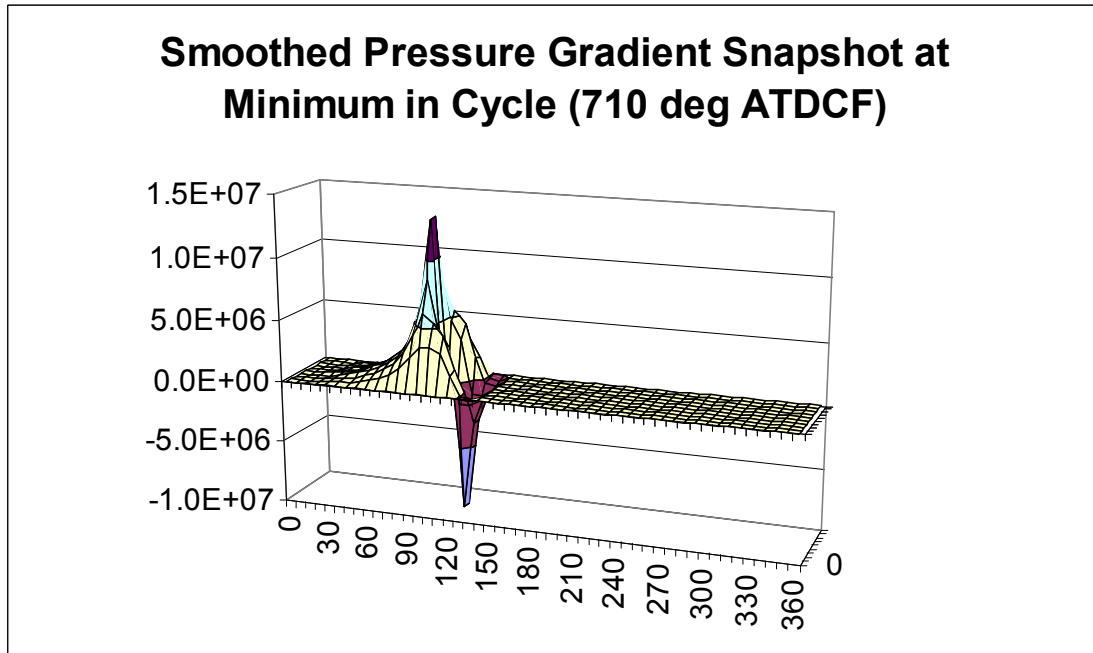


Figure 6-185 Diesel, EHD, 5000 rpm – Pressure Gradient Snapshot at Minimum

Most negative values over whole bearing over the whole cycle are shown here.

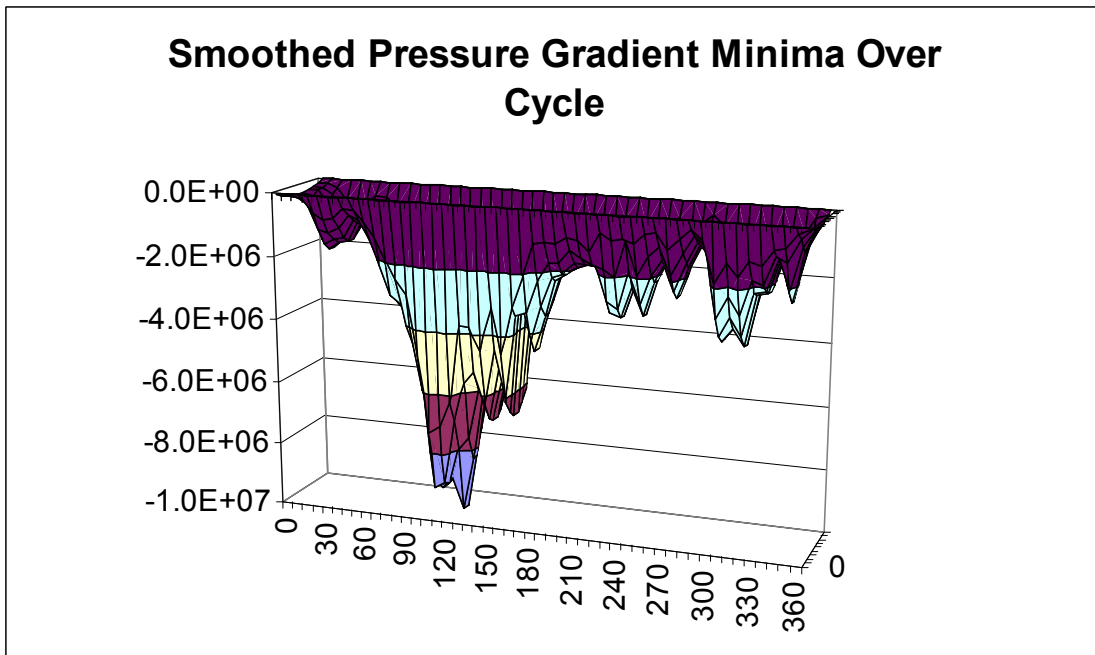


Figure 6-186 Diesel, EHD, 5000 rpm – Pressure Gradient Minima Over Cycle

It can be seen that the strongest effect is on the top of the bearing (90 deg is top of bearing, 0 deg is on the split line). Fig. 6.187 shows the cavitation damage parameter . The maximum value is significantly higher than the RHD base case – approximately 1.8 times.

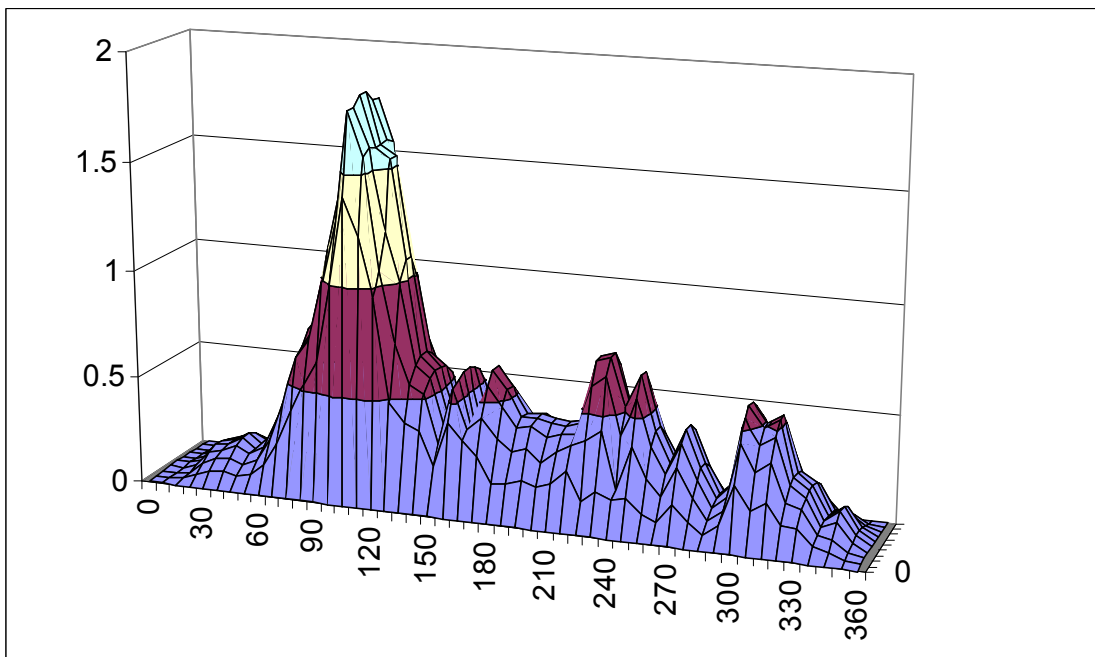


Figure 6-187 Diesel, EHD, 5000 rpm – Normalised Cavitation Damage Parameter

The gas pressure takes over from the inertia on the compression stroke and continues into the power stroke. This means that the main cavitation area is on the top shell.

The EHD deformations do not affect the general pattern of pressures, velocities and cavitation parameter. The main effect is to reduce pressures, increase velocities and pressure gradients and increase the cavitation parameter in the top half of the bearing. The increased velocities are a significant factor and imply that bearing housing flexibility may be a significant factor in causing cavitation damage.

6.8.8 DIESEL, EHD, PARTIAL GROOVES, 5000 RPM

Taking the diesel calculation, partial grooves, 5000 rpm with RHD calculation and changing to EHD using the connecting rod big end mesh shown earlier in the thesis gives the following results which should be compared to Figs. 6.72 to 6.97 as appropriate and Figs. 168 to 187 to see the effect of grooves.

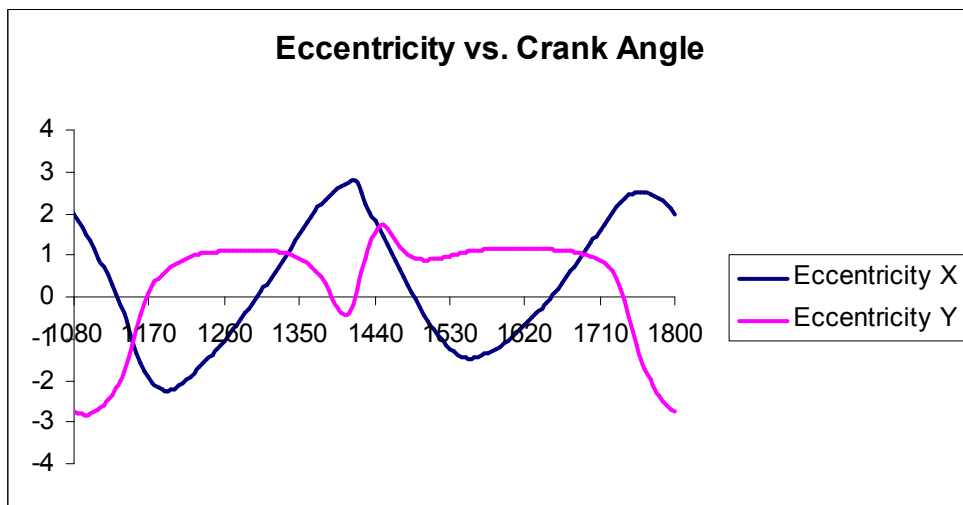


Figure 6-188 Diesel, partial grooves, EHD, 5000 rpm – Eccentricity

Figs. 6.188 to 6.191 are typical diesel engine results with dominant gas pressures either side of TDCF. They are very similar in appearance to the RHD results but note that the eccentricity ratios exceed unity by a considerable margin.

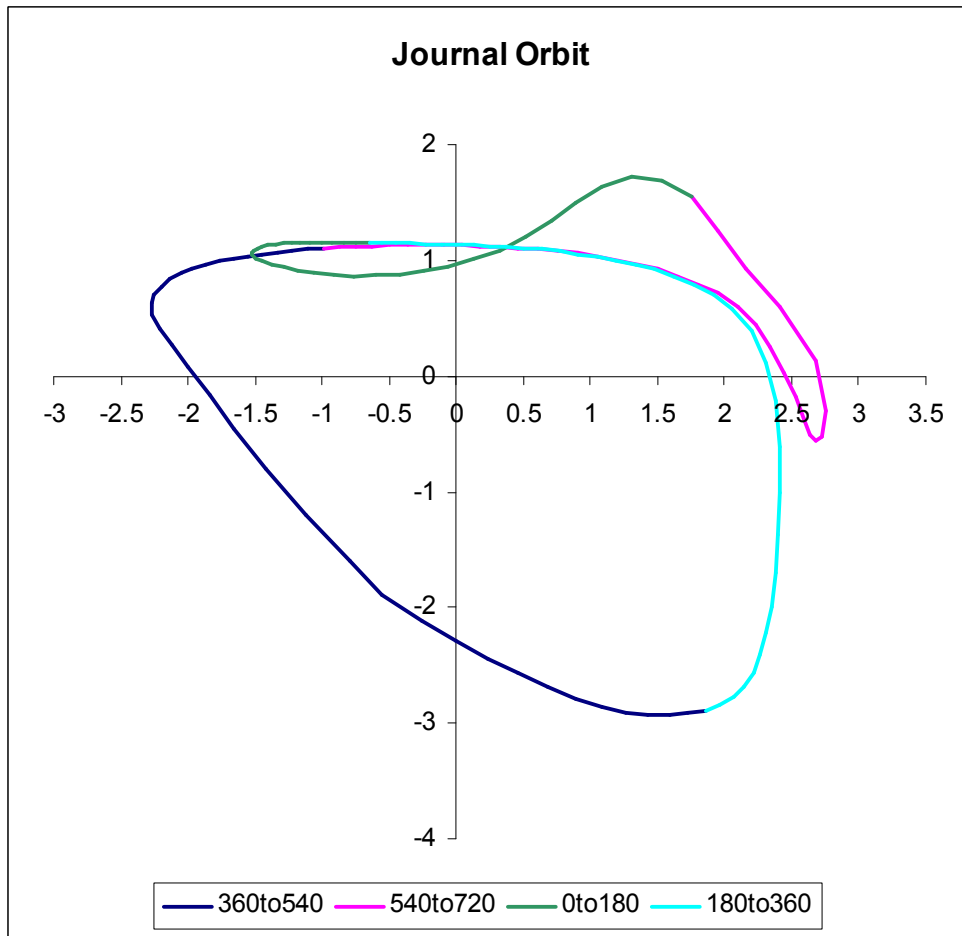


Figure 6-189 Diesel, partial grooves, EHD, 5000 rpm – Journal Orbit

The velocity plots show the movement just before TDCF with slightly higher velocity than the ungrooved bearing.

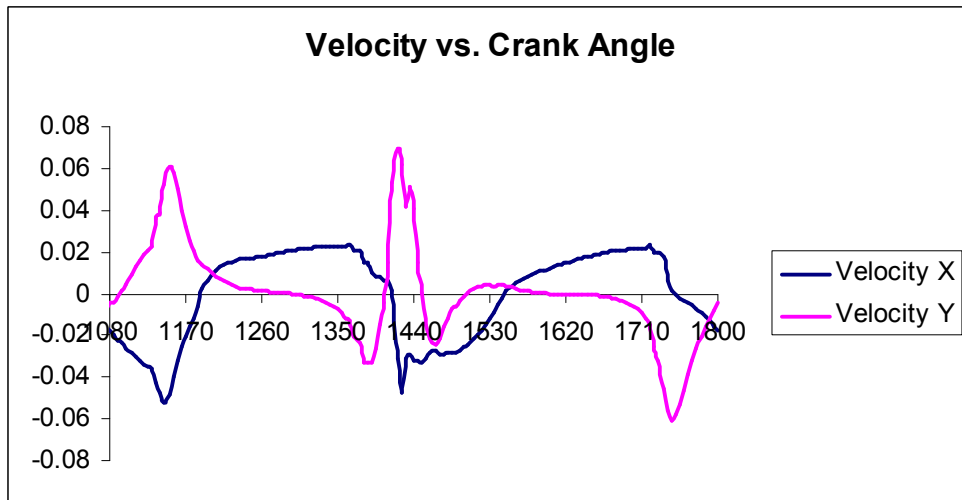


Figure 6-190 Diesel, partial grooves, EHD, 5000 rpm – Journal Velocity

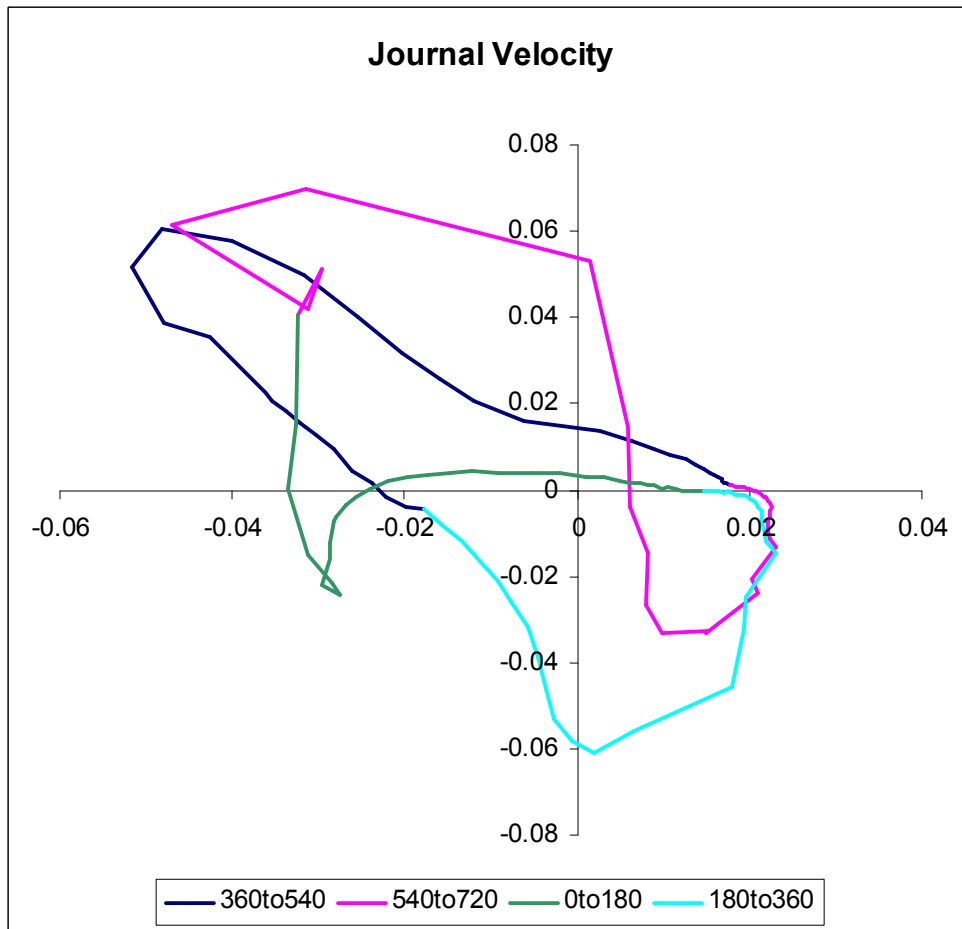


Figure 6-191 Diesel, partial grooves, EHD, 5000 rpm – Journal Velocity

Peak pressures over the cycle are shown in Fig. 6.192. with highest pressure near TDCF. Note the comparison with the ungrooved bearing in Fig. 6.172. Although the

peak pressure is changed very little, the pressures near to TDCNF are increased significantly. This is because the inertia loads at this crank angle load the bearing in the grooved region.

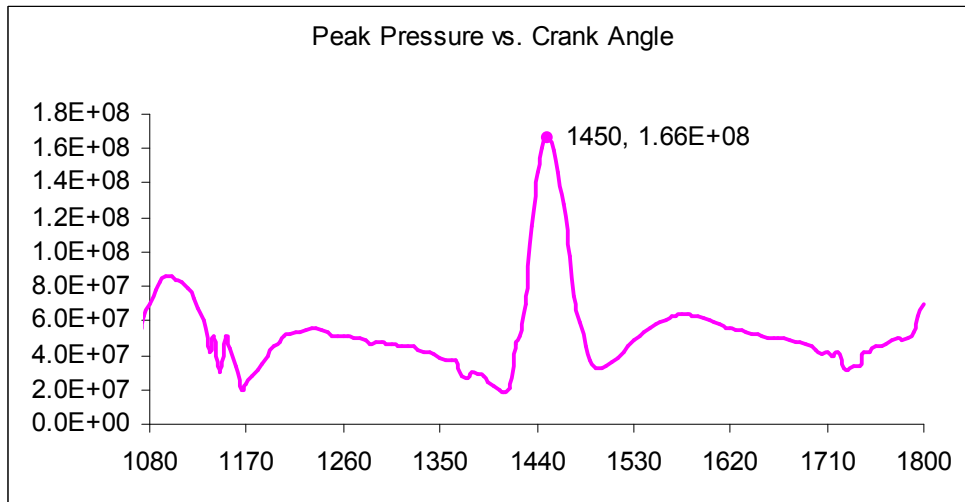


Figure 6-192 Diesel, partial grooves, EHD, 5000 rpm – Peak Film Pressure Over Cycle

This is a snapshot of the pressure distribution at the crank angle that produces the highest pressure (10 deg ATDCF). Note that this is near TDC firing and pressure is in the top half of the bearing.

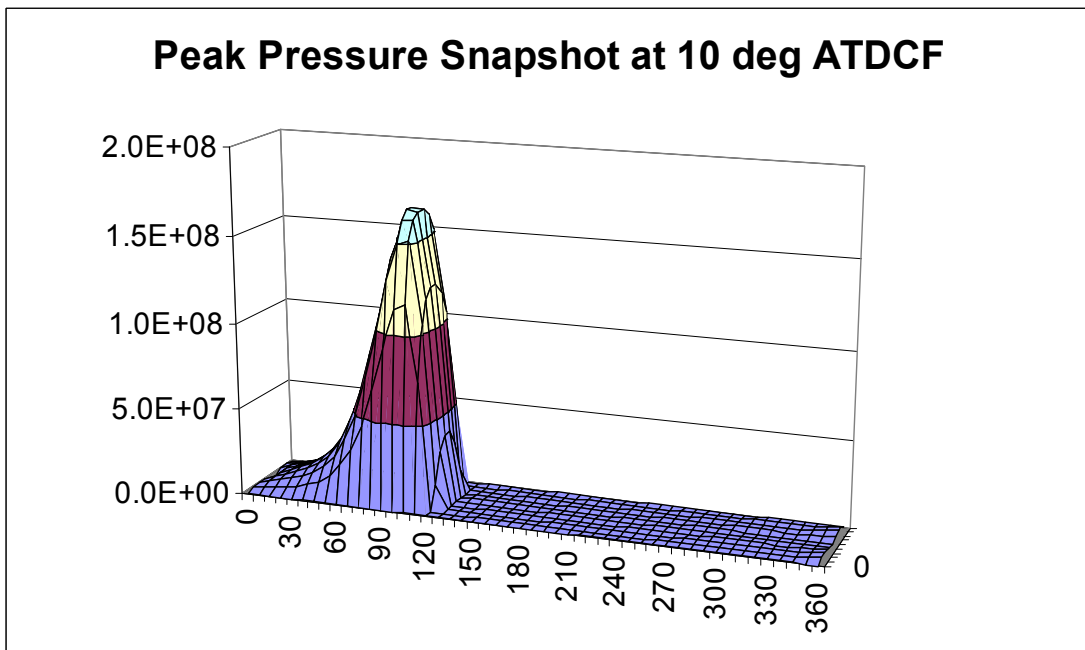


Figure 6-193 Diesel, partial grooves, EHD, 5000 rpm – Pressure Snapshot at Maximum

Plotting the maximum pressure at each individual node over the whole cycle is useful for showing what is happening over the whole bearing. You can see in Fig. 6.194 that the peak value is the same as that at 10 deg. crank angle. The secondary peak, close to TDC non-firing, in the bottom shell is smaller. Comparison with Fig. 6.174 is interesting: the effect of the partial grooves at 180 – 230 and 310 – 360 degrees on the bearing is clearly visible. The load applied to the bearing in these regions has to be carried over a smaller area, giving higher pressures.

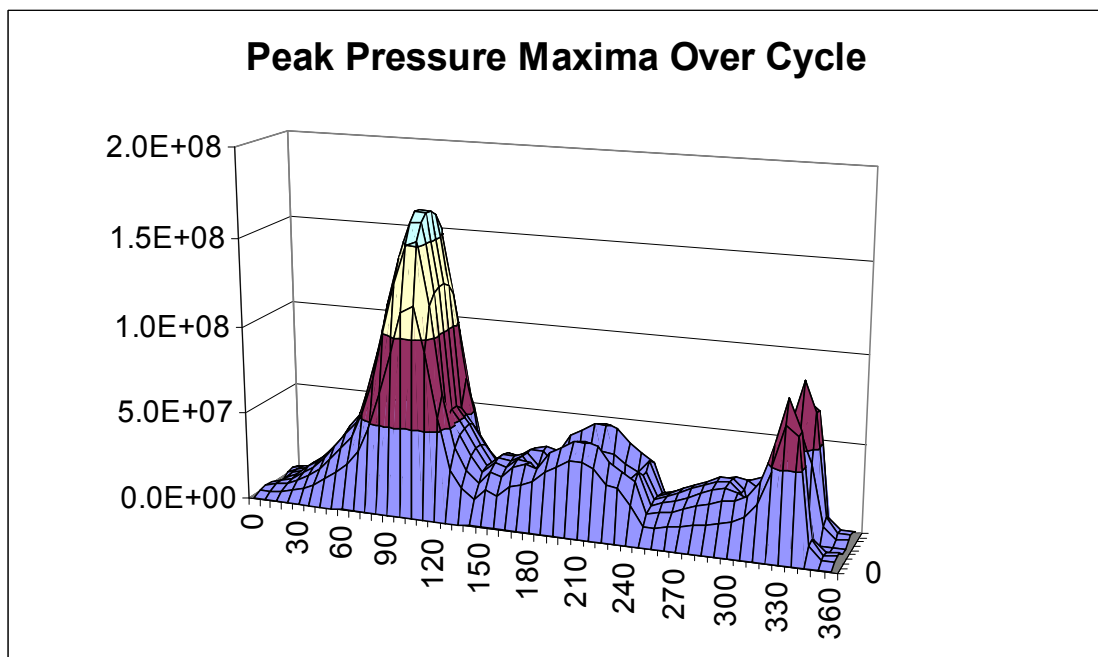


Figure 6-194 Diesel, partial grooves, EHD, 5000 rpm – Peak Pressure Maxima Over Cycle

Fig. 6.195 shows the minimum film thickness over the cycle. Comparing with Fig. 6.82 we can see that the minimum is slightly reduced despite the cushioning effect of the wrap around behaviour. Comparing to Fig. 6.175, the minimum film is now at a different part of the cycle.

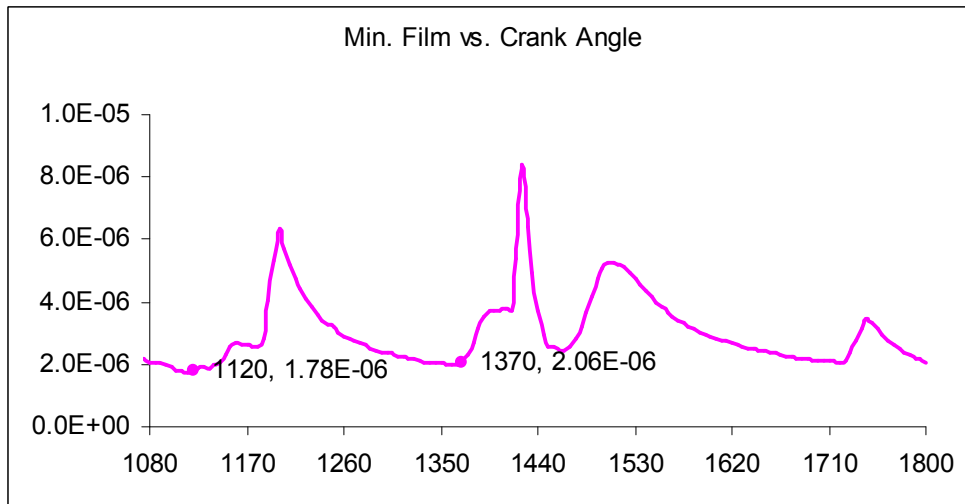


Figure 6-195 Diesel, partial grooves, EHD, 5000 rpm – Minimum Film Thickness Over Cycle

Figs. 6.196 shows the film shape at the crank angle at which the minimum occurs.

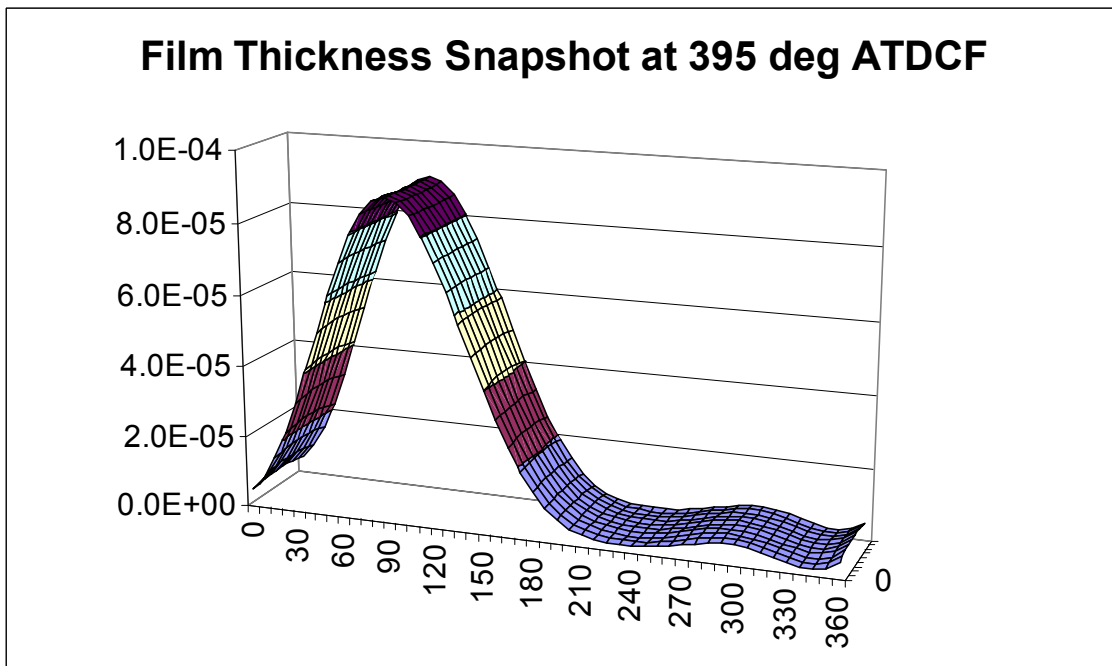


Figure 6-196 Diesel, partial grooves, EHD, 5000 rpm – Film Thickness Snapshot at Minimum

Fig. 6.197 shows the minima over the whole bearing over the whole cycle. It is a little jagged. This particular calculation was a severe test of the stability of the EHD calculation procedure (see earlier sections on EHD program development).

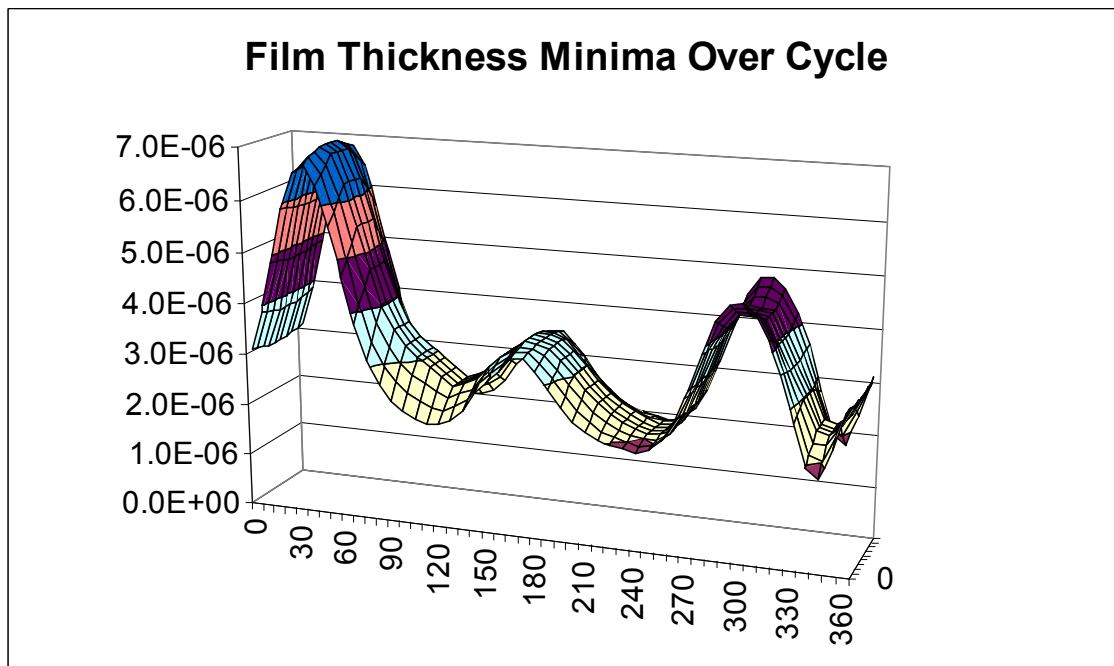


Figure 6-197 Diesel, partial grooves, EHD, 5000 rpm – Film Thickness Minima Over Cycle

Plotting the separation velocity (also called cavitation velocity or negative of the squeeze velocity) gives a peak value at 1425 (705) deg. crank angle – just before TDCF. Fig. 6.198 shows the separation velocity over the cycle. Note that the values are clearly higher than the ungrooved bearing in Fig. 6.181.

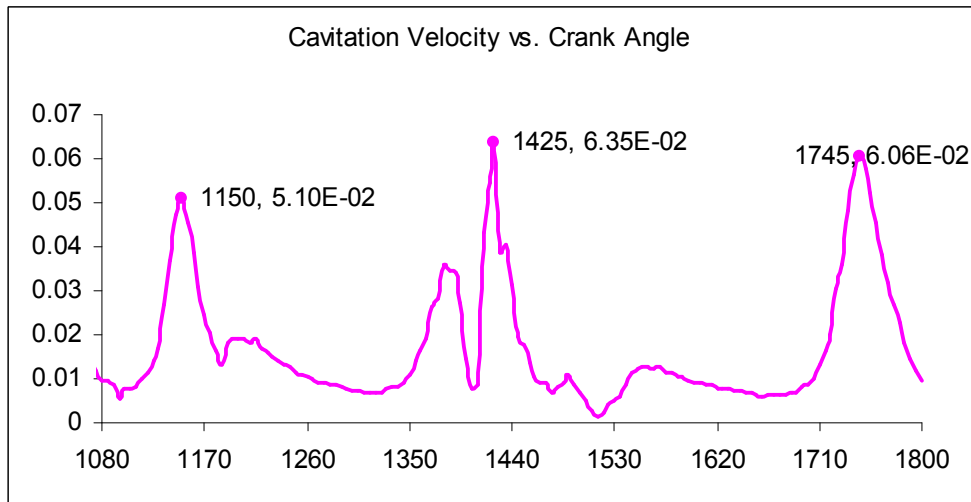


Figure 6-198 Diesel, partial grooves, EHD, 5000 rpm – Maximum Cavitation Velocity Over Cycle

Plotting the separation velocity (called cavitation velocity or negative of the squeeze velocity) no longer produces a sine wave as this is an EHD calculation – Fig. 6.199 is a snapshot at the maximum value in the cycle.

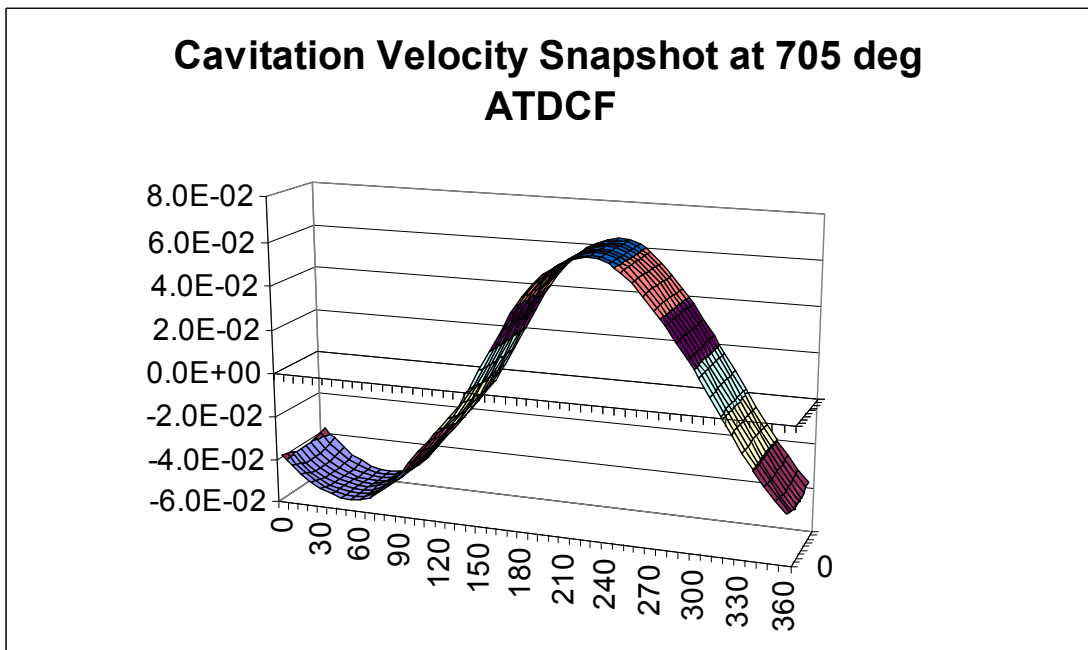


Figure 6-199 Diesel, partial grooves, EHD, 5000 rpm – Cavitation Velocity Snapshot at Maximum

Again, plotting the maximum over the cycle at each node produces the same peak (from the 5 deg. Crank angle results) but a more useful view of the values over the bearing.

The next minor peak is only a little smaller. Note the shape along the film in the axial direction, typical of EHD.

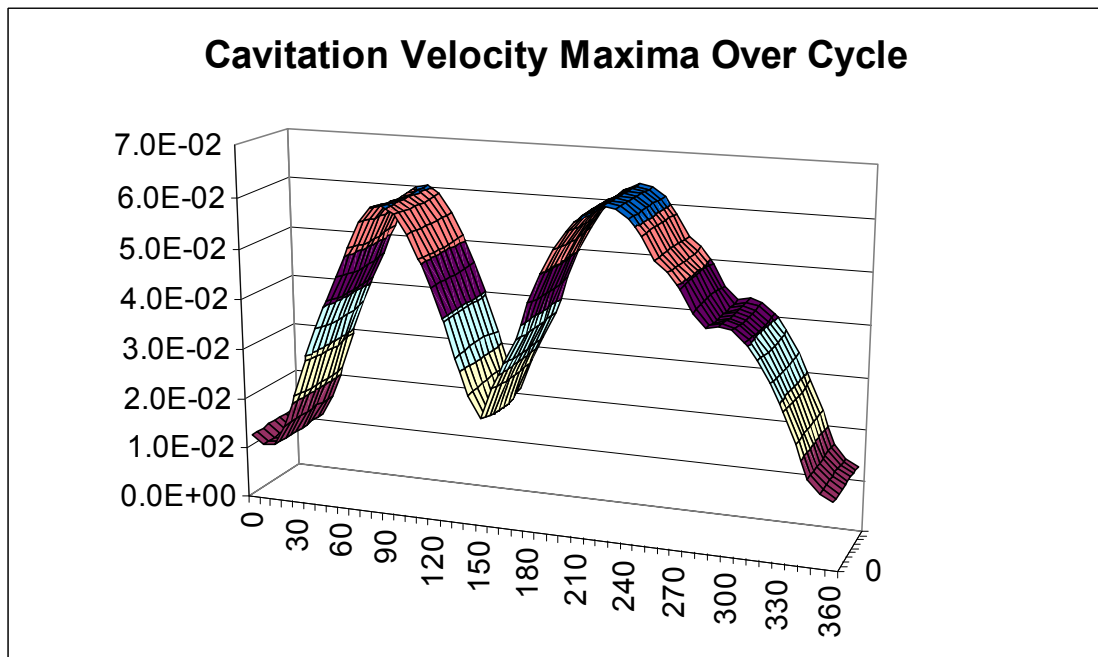


Figure 6-200 Diesel, partial grooves, EHD, 5000 rpm – Cavitation Velocity Maxima Over Cycle

Looking at pressure gradient $dp/d\theta$ – we’re interested in the most negative values which are likely to produce cavitation. The values over the cycle are shown in Fig. 6.201.

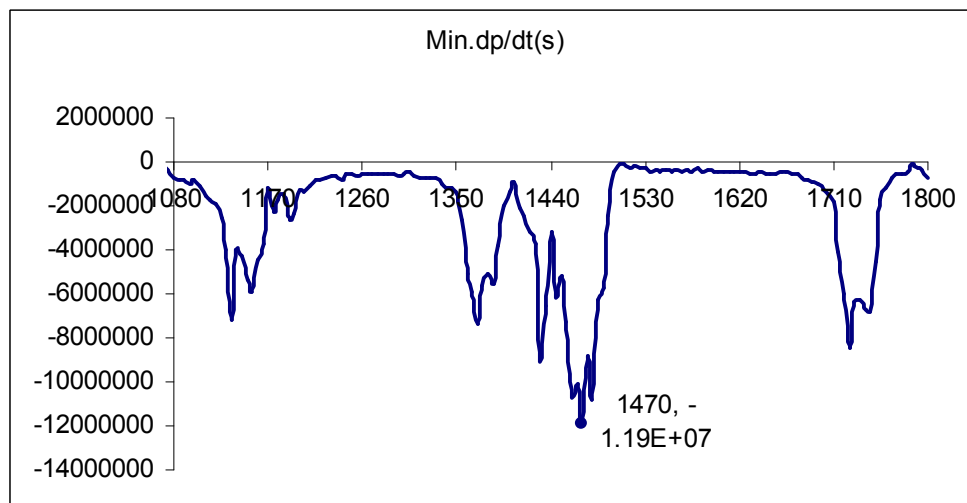


Figure 6-201 Diesel, partial grooves, EHD, 5000 rpm – Minimum Pressure Gradient Over Cycle

Looking at pressure gradient $dp/d\theta$ – we’re interested in the most negative values which are likely to produce cavitation. Snapshot here in Fig. 6.202 is of the situation at the highest negative value which occurs at 30 deg. crank angle although there are several other peaks nearby. Comparing with Fig. 6.185 shows that the magnitude of the peak minimum pressure gradient is higher.

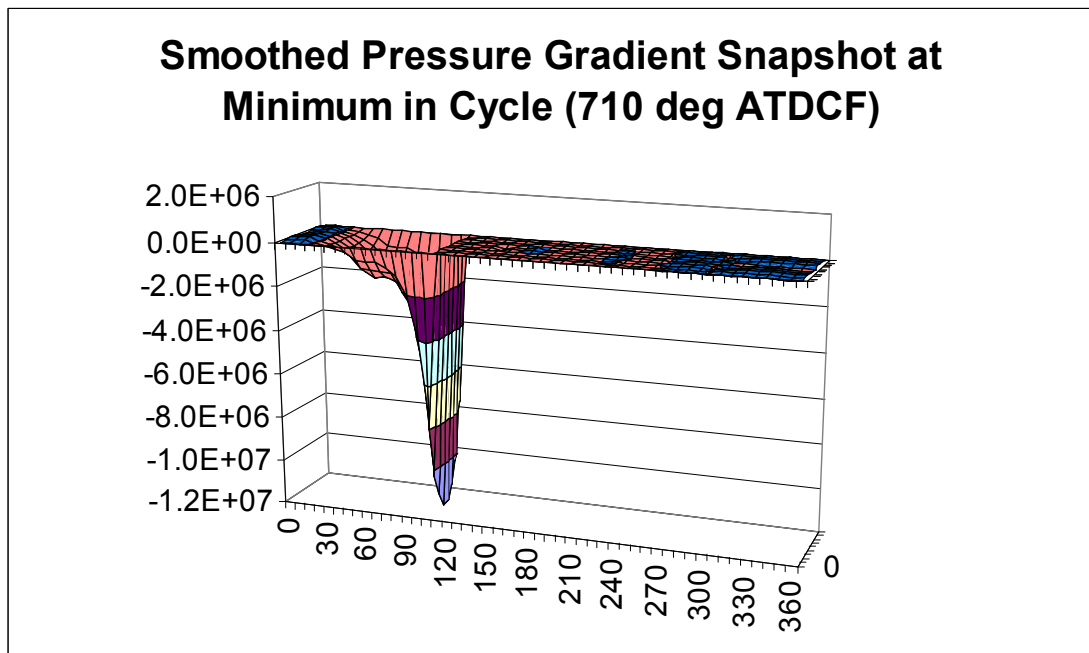


Figure 6-202 Diesel, partial grooves, EHD, 5000 rpm – Pressure Gradient Snapshot at Minimum

Most negative values over whole bearing over the whole cycle are shown here in Fig. 6.203. Comparing with Fig. 6.186, not only is the highest magnitude in the top half of the bearing (0 – 180 degrees bearing angle) increased but so too are the values in the lower half of the bearing due to the grooves.

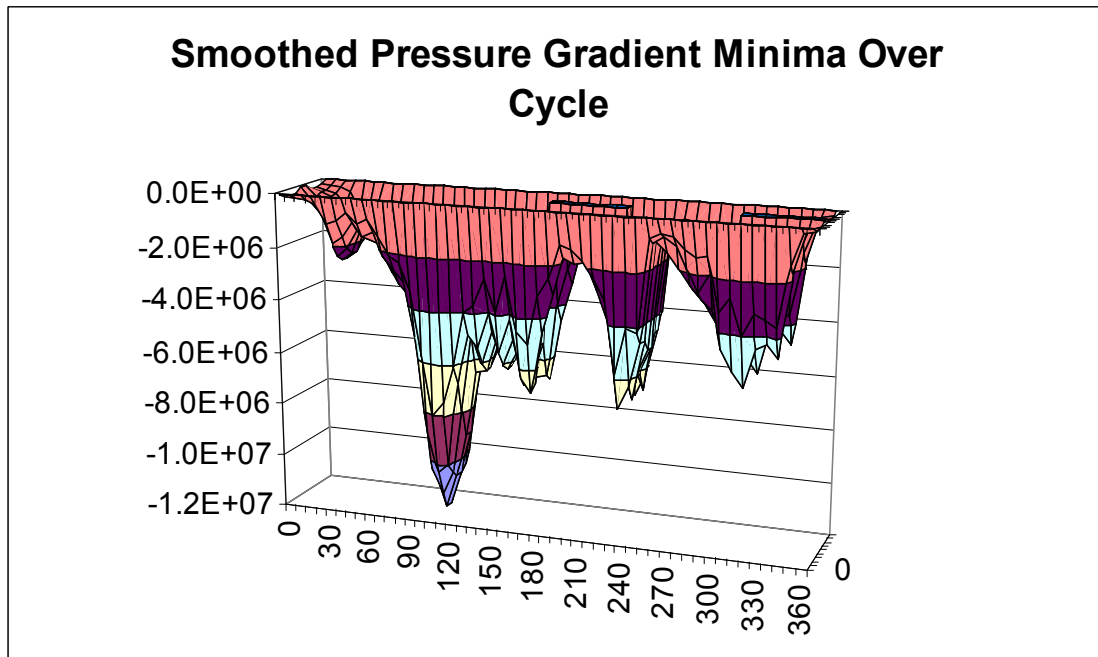


Figure 6-203 Diesel, partial grooves, EHD, 5000 rpm – Pressure Gradient Minima Over Cycle

It can be seen that the strongest effect is on the top of the bearing (90 deg is top of bearing, 0 deg is on the split line). Fig. 6.204 shows the cavitation damage parameter. The maximum value is significantly higher than the RHD base case – approximately 2.6 times. Note that it is also significantly higher than the EHD case without grooves which was approximately 1.8 times the base case – see Fig. 6.187. Also, the cavitation damage parameter in the lower half of the bearing has increased significantly alongside the grooves, although not quite enough to be higher than the values in the top half of the bearing. See the twin peaks at about 240 degrees bearing angle (the grooves are 180 – 230 and 310-360 degrees).

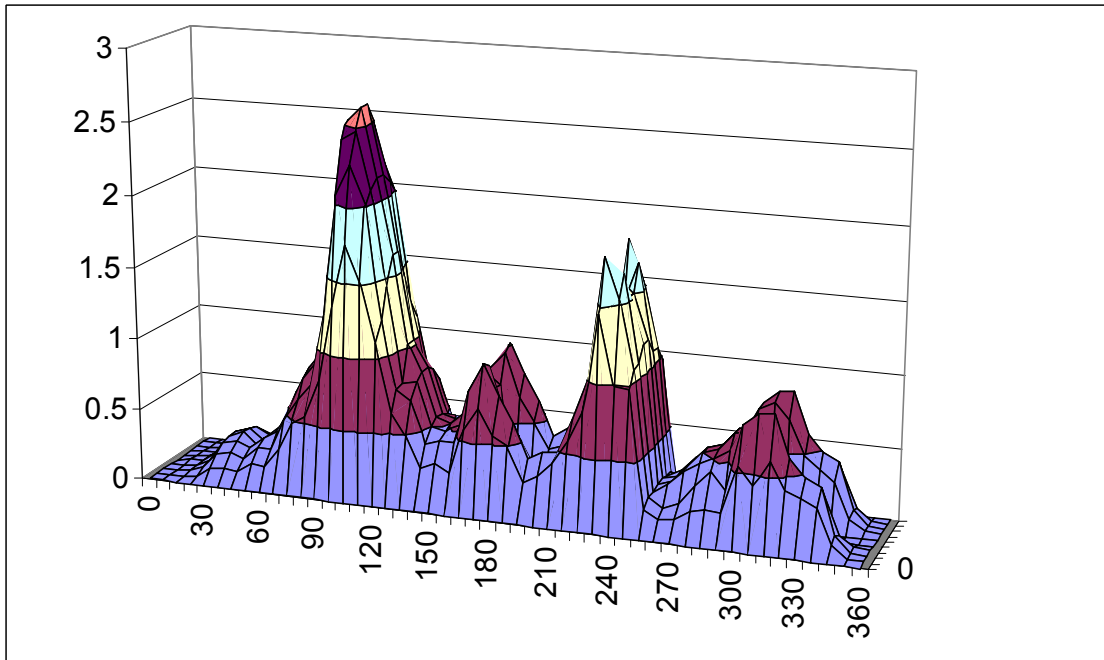


Figure 6-204 Diesel, partial grooves, EHD, 5000 rpm – Normalised Cavitation Damage Parameter

The gas pressure takes over from the inertia on the compression stroke and continues into the power stroke. This means that the main cavitation area is on the top shell.

The EHD deformations do not affect the general pattern of pressures, velocities and cavitation parameter. The main effect is to reduce pressures, increase velocities and pressure gradients and increase the cavitation parameter in the top half of the bearing. The increased velocities are a significant factor and imply that bearing housing flexibility may be a significant factor in causing cavitation damage. The presence of grooves increases the general values of the cavitation parameter. The largest increase is near to the grooves but not quite sufficient to exceed the values in the top half of the bearing in this case.

CHAPTER 7

DISCUSSION OF RESULTS

7.1 GENERAL DISCUSSION OF RESULTS

Fig. 4.1 gave some verification of the RHD model during program development as the stiffness and damping values were checked against published values.

The '3 engine study' and racing engine main bearing study were carried out with early versions of the software that could carry out only RHD calculations. Integration of the equations of motion had been implemented as well as the successive over relaxation method for the finite difference formulation of Reynold's Equation. It was found useful for studying friction losses for bearings with a defined load history and worked reliably for all of the calculations of these studies. The 3 engine study is commercially sensitive so cannot be shown in this thesis. The racing engine crankshaft study was an internal project for the purposes of using the program as part of this EngD project. The ability to use a program such as this to obtain answers to real questions is important and was demonstrated by these results. In reality the change in friction losses from a change in crankshaft layout was shown to be small and certainly small compared to the larger losses in an engine such as occur at the piston rings.

The turbocharger bearing results were especially useful. They proved that using an approach of integrating the equations of motion could be used successfully to study time marching unstable events. It may be obvious that bearing stiffness has an influence on the frequency at which a shaft and bearing system becomes unstable. Bearing stiffness increases rapidly with increasing eccentricity ratio. It was interesting to see that even gross imbalance can have the effect of increasing the frequency at which instability occurs. The behaviour of the system was able to be compared with the experimental work of san Andres and Kerth and can be seen in the next section.

Development of the EHD version of the program started well. The author and the sponsoring company AIES already used the ABAQUS finite element program and also had experience of NASTRAN. Both these programs are capable of generating reduced stiffness and mass matrices at a specified set of active nodes using a relatively simple data patch to add to the data file for any finite element model of a bearing and housing. However, it was found that getting smooth results was not always possible. The story has been told in Chapter 5. Severe excitations would cause program instability.

The diesel engine big end bearing case was severe because of the high and rapidly changing gas pressure loading. The racing engine big end bearing was severe because of the very high inertia loads at over 16000 rpm. In both these cases, getting stable program operation proved impossible simply by altering step sizes and integration accuracy parameters. This led directly to the development of new features in the program for mesh interpolation (fine FD mesh with coarse FE mesh was found to be successful), damping (Rayleigh and simple diagonal damping were found to be effective) and Fourier smoothing of the deformed shape. These options were found to work well.

Solving a set of coupled equations of motion for an EHD calculation involves a large number of arithmetic steps. The possibility that the automatic time step adjustment on the integration algorithm will select a small value has been found to be very likely. The result is that some EHD calculations can take several days on a conventional PC. In order to speed calculations the program now has an automatic procedure to detect and use symmetry. If the bearing geometry, stiffness matrix and mass matrix are all found to be symmetrical about the centre line, the program will solve for half the bearing using mirror constraints at the boundary. This occurs without user intervention but the user can force use of the symmetric or full solver using optional keyword based data input.

Despite these efforts, it is suspected that the Bulirsch-Stoer integration method may not be the best method for these calculations. Although faster program execution has been achieved certain calculations still take several days and improving the calculation speed is now an urgent consideration for commercial use of the program. This is discussed further below.

7.2 RACING ENGINE BIG-END BEARING RESULTS

The racing engine big-end study turned into a large exercise because the reason for the oil hole position in the journal being more successful than the generally accepted standard position was not understood. It was found that there are conflicting factors affecting the extent of the fluid film. Carrying out an EHD calculation alone is not a guarantee of more accurate result than RHD, depending on which result parameters are of interest.

It was found that thermal deformation of the bearing shape tends to compensate for the tendency to edge contact that occurs in EHD calculations, causing the axial profile of the bearing to arch the opposite way. However that is not the only bearing deformation that is comparable in magnitude to those caused by fluid film pressure. It was fortunate that the measured profile of a bearing after manufacture and assembly was available and this was also found to be important in determining the relationship between the continuously changing pressure profile and the position of the oil feed hole.

The method used to calculate the thermal loading and hence deformation was discussed in Chapter 6. It was based simply on calculating the energy generated by viscous loss at each node point and then assuming a proportion of that energy to be conducted into the bearing surface as a heat flux. That is a classical way of dealing with thermal loading in bearings. The deformed shape was easily calculated using the finite element model that already existed for the purpose of generating stiffness and mass matrices. The thermal deformations were transferred directly into the profile shape of the bearing. The version of the EHD program used for these calculations included the data for a bearing profile defined as a series of departures from the nominal circular profile.

Several of the papers in the literature survey relate to TEHD calculations although none using the approach used here. Adding heat generation terms into the Reynold's Equation solution could be done but would have to be investigated further. There is an issue with the capability of ABAQUS and NASTRAN to produce the matrices required to interface to a TEHD code. It would be difficult to generate the matrices for thermal deformation from separate structural and thermal elements. It would be easier from combined thermal and structural elements that exist in ABAQUS in principle but

ABAQUS does not provide the commands to create this output. Creating an integrated FE code within the EHD program would be relatively simple as linear FE theory is a standard text book subject. It may also be possible to download free software. Note that the finite element thermal deformation calculation is effectively a static calculation whereas the structural calculation is dynamic or time varying static and that would need to be taken into account in any extension to TEHD. There is a characteristic length in a dynamic heat flow calculation equal to $\sqrt{\frac{K}{\omega\rho C}}$ where

K is the thermal conductivity

ω is the frequency of input in radians / s

ρ is the density

C is the specific heat

which has a value between 0.1 and 0.4 mm for typical materials in the bearing and bearing housing at a thermal loading frequency of 5000 rpm. The variation of temperature with depth is inverse exponential but can be considered simplistically as a 'skin' within which the temperature varies and outside which the temperature is relatively constant. This means that there may be a significant effect of the time varying thermal input on the stress in the bearing material. However, the general dimensions of the bearing and housing being much more than the characteristic length means that the shape of the bearing will be effectively constant.

The method adopted for the racing big-end bearing was certainly efficient, the TEHD calculations after the Finite Element work taking a similar time to run as the EHD calculations.

7.3 VERIFICATION OF FULL FLOATING BEARING RESULTS

Calculations for a turbocharger running on two Full Floating Bearings (FFBs) were reported very briefly in Barrett (2005) and a summary of the results shown in an earlier section of this report. The general behaviour of the bearings matches that seen in

previous work such as McLuckie (1990). No experimental verification was possible at this stage but San Andres and Kerth (2004) report experimental measurements in a similar arrangement. Their paper displayed results using waterfall diagrams of the response of an accelerometer on the bearing housing. That showed similar behaviour of entering and leaving sub-synchronous instability as seen in the results shown in a previous section. Therefore, the motion in the vertical direction was Fourier analysed and the coefficients plotted on the following bubble charts, which are taken from McLuckie, Barrett and Teo (2006). Dr. BoonKai Teo and Dr. Ed Brooksbank carried out the results processing shown in this section from calculations carried out by Dr. Teo under guidance from Dr. McLuckie using the software written by this author.

Figure 7.1 is a bubble plot showing the waterfall frequency spectra for the turbine end PGB with 0.023 gmm unbalance, 4 microns bearing clearance and 4 bar oil supply pressure. The amplitude of the Fourier components are represented by the diameter of the bubble symbols on the plots. The response is almost completely sub-synchronous and the ratio to shaft speed varies from 0.5 at low speed to approximately 0.46 at 100,000 rpm.

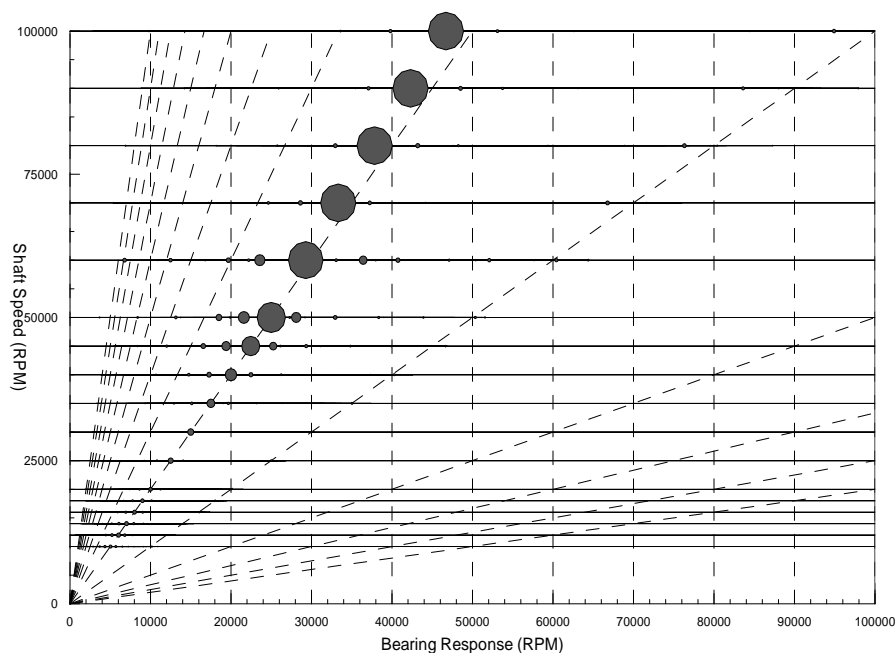


Figure 7-1 Waterfall bubble plot for turbine end PGB - 0.023 gmm unbalance, 4 microns, 4 bar supply pressure

Figure 7.2 shows response for load conditions of 2.3 gmm gross unbalance, 4 microns clearance and a 4 bar oil supply pressure. The response is synchronous over the whole speed range up to 100,000 rpm.

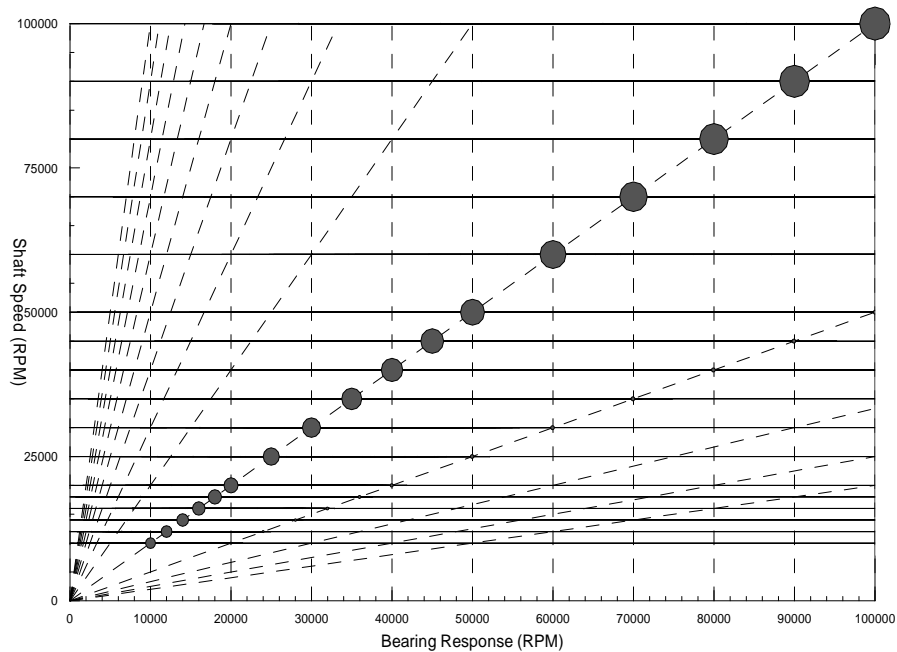


Figure 7-2 Waterfall bubble plot for turbine end PGB - 2.3 gmm gross unbalance, 4 microns clearance, 4 bar supply pressure

Figures 7.3 and 7.4 show the waterfall frequency spectra for the turbine end FFB with bearing data of 2.5/7 microns inner/outer clearance and 4 bar supply pressure. Figure 7.3 shows the response for an unbalance of 0.23gmm. San Andrés and Kerth (2004) show very similar measured results. They did not show all their bearing and rotor data so an exact comparison cannot be made.

Figure 7.3 shows an 1/8 order sub-synchronous response of the journal. This is a 1/2 order of the ring speed (0.25 times shaft speed) shown in the bubbles on the left hand side of the plot. It also shows a 5/8 order of the journal which is about 1/2 order of the combined speed of the ring and shaft. It also shows a synchronous response at the shaft rotational speed.

Figure 7.4 shows the results for a bearing with the same input data (2.5/7 microns inner/outer clearance and 4 bar oil supply pressure) but with gross unbalance of 2.3 gmm. There is a 1/8 order response up to about 40,000 to 45,000 rpm above which the

response of the ring becomes synchronous all the way to the maximum speed calculated of 100,000 rpm. The response of the shaft has 5/8 order also up to about 40,000 to 45,000 rpm and then also synchronous up to 100,000 rpm. These results are interesting and show the stabilising effect of gross unbalance.

The waterfall plots in San Andres and Kerth (2004) show very similar behaviour to that shown in Figures 7.3 and 7.4.

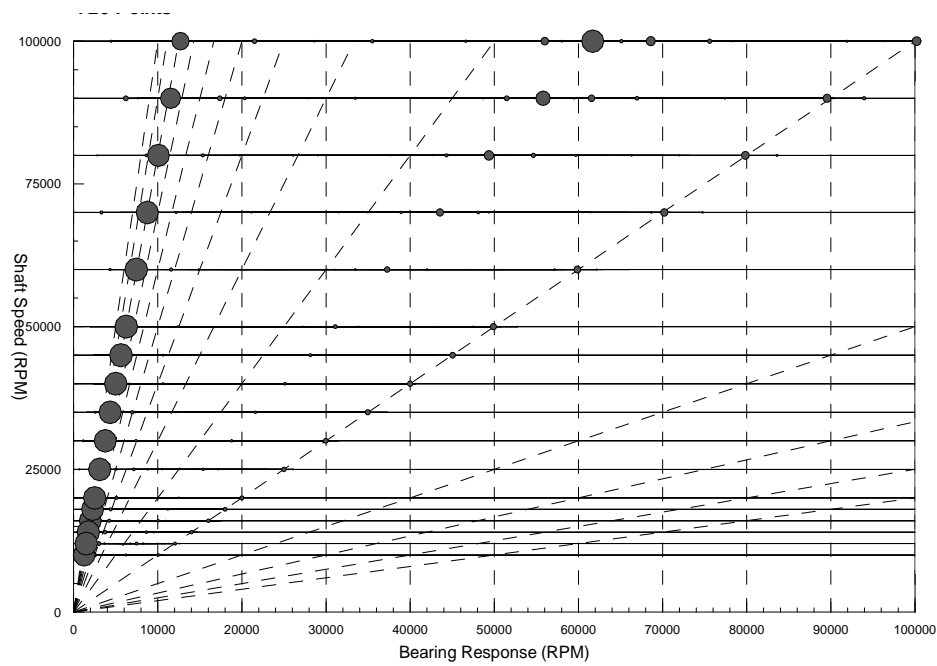


Figure 7-3 Waterfall bubble plot for turbine end FFB - 0.23 gmm unbalance, 2.5/7 microns inner/outer clearance, 4 bar supply pressure

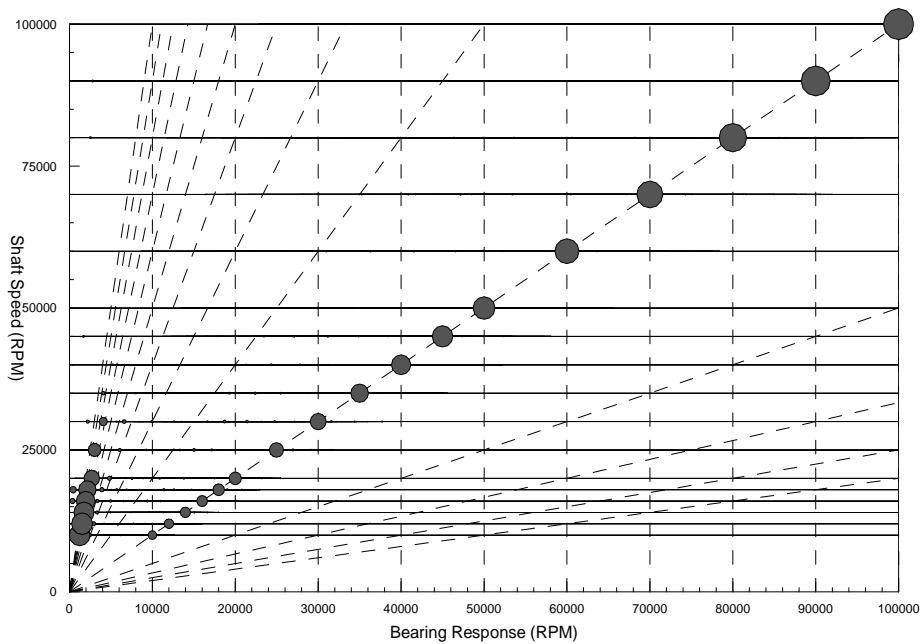


Figure 7-4 Waterfall bubble plot for turbine end FFB - 2.3 gmm gross unbalance, 2.5/7 microns inner/outer clearance, 4 bars supply pressure

7.4 CALCULATION OF CAVITATION PARAMETER

The cavitation damage parameter calculations produced a range of values that appeared to fit in with expectations. The location of the damage also fitted with the photographs of damage shown in Forstner and Struwe (2004). Table 7.1 shows the actual cavitation damage parameter values: normalised values were presented in Chapter 6.

The units of the cavitation damage parameter were in power, strictly power / angle. For easier visualisation of the effect of the changes Figs. 7.5 to 7.7.

Table 7-1 Summary of Cavitation Damage Parameter Results

Calculation	Maximum Cavitation Damage Parameter (W)	Normalised Cavitation Damage Parameter
Diesel, RHD, 5000 rpm	825	1
Diesel, RHD, partial grooves, 5000 rpm	1071	1.30
Gasoline, RHD, 5000 rpm	1123	1.36
Diesel, RHD, fast pressure rise, 5000 rpm	1056	1.28
Diesel, RHD, 3000 rpm	691	0.84
Diesel, RHD, 1000 rpm	120	0.15
Diesel, EHD, 5000 rpm	1501	1.82
Diesel, EHD, partial grooves, 5000 rpm	2165	2.62

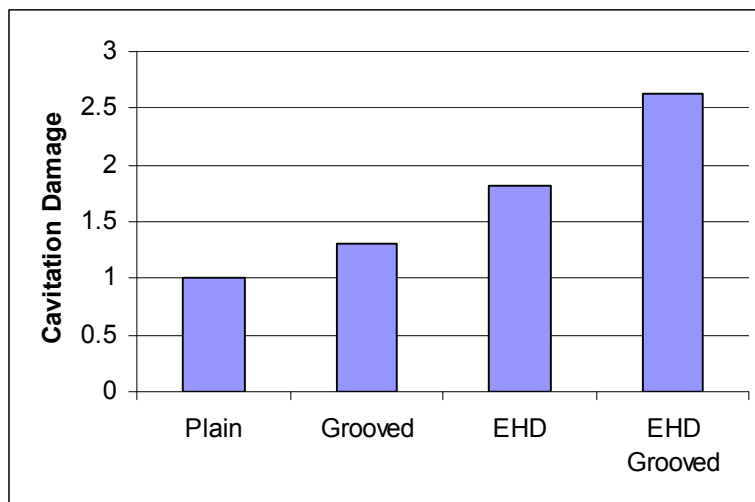


Figure 7-5 Effect of Bearing on Cavitation Damage Parameter

Fig. 7.5 shows the effect of bearing geometry and stiffness. As might be expected, partial grooves increase the tendency for cavitation and this is in agreement with Forstner and Struwe (2004). The high pressure gradients at the grooves are the cause of this behaviour. Combining flexibility and partial grooves gives a factor 2.62 increase.

The increase in cavitation damage due to bearing housing flexibility might seem a little harder to understand as bearing flexibility tends to reduce maximum pressure and spread pressure over a wider area of the bearing. In this particular case the RHD calculation gave a maximum oil film pressure of 206 MPa and the EHD calculation gave 167 MPa, a significant reduction. The main reason for the increase in the value of the cavitation damage parameter is the increase in separation velocity. This is caused by the larger clearance space created by the housing deformation. It would be interesting to look at the effect of an RHD calculation with increased clearance and EHD calculations for a range of stiffness values. The program includes a capability to multiply the stiffness and mass matrices by any value without having to re-run the Finite Element calculation.

It might also be interesting to investigate the advantages and disadvantages of using titanium for racing engine connecting rods. Titanium has approximately half the stiffness of steel as well as half the density.

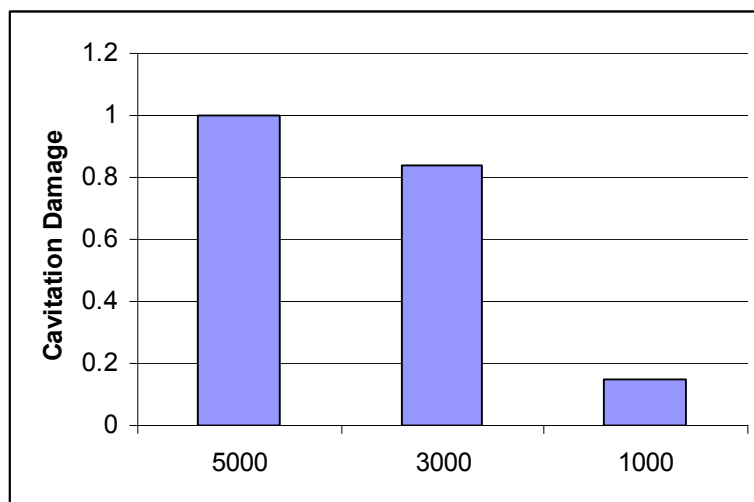


Figure 7-6 Effect of Engine Speed on Cavitation Damage Parameter

Fig. 7.6 shows the effect of rotation speed on the cavitation damage parameter. As the rotation speed decreases the loads on the bearing at and near Top Dead Centre Firing (TDCF) tend to increase as the opposing inertia forces decrease. Oil film pressures may also increase but the rate of change of load decreases as does the load in the rest of the cycle where inertia predominates. It would probably be expected that cavitation damage decrease with decreasing engine speed and that is confirmed by the results.

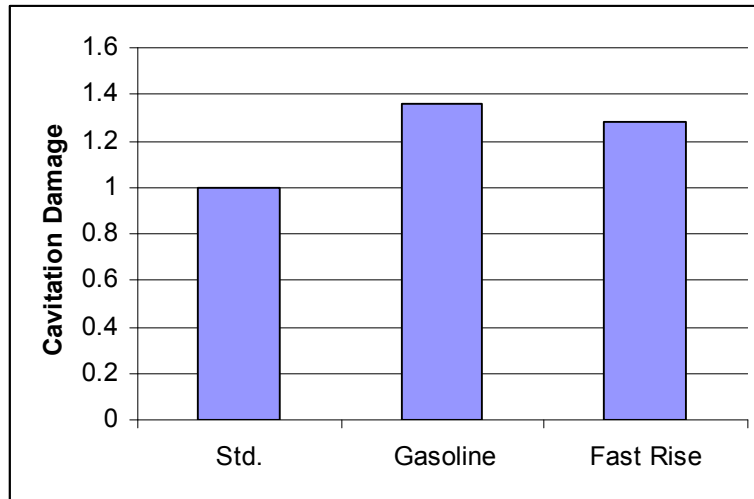


Figure 7-7 Effect of Gas Pressure Curve on Cavitation Damage Parameter

Fig. 7.7 shows the effect on the cavitation damage parameter of changing the combustion chamber gas pressure curve. In the gasoline engine case, the gas pressure curve from a gasoline engine was substituted for the diesel engine's own gas pressure curve and the loads re-calculated. The effect on the RHD calculation was to produce a finer balance between gas and inertia loads around Top Dead Centre Firing. The consequence was that the orbit within the clearance space was changed significantly and the area where the cavitation damage parameter was highest was moved to the lower cap half. The magnitude of the cavitation damage parameter was actually significantly higher.

The third bar shows the cavitation damage parameter for a calculation with the same combustion gas pressure curve as the standard engine but with the curve altered either side of 700 deg. After Top Dead Centre Firing (ATDCF). This angle is high up the compression stroke and was the point at which large journal velocity was being calculated. Approximately double the rate of gas pressure rise was put at 700 deg.

ATDCF by reducing the pressures between 680 and 697 deg. And increasing them between 703 and 720 deg. The rest of the pressure curve remained standard including the peak pressure of 13.6 MPa at 8 deg. ATDCF. The cavitation damage parameter was increased by a factor 1.28. That confirms stories that changes in engine damage (not just bearings) when changing from one fuel to another may be associated with rate of pressure change in the combustion chamber rather than magnitude of the pressures themselves. Forstner and Struwe (2004) show cavitation erosion in a diesel engine and compare with a version of the same engine converted to run on Compressed Natural gas (CNG). However they give no indication of the difference in combustion pressures or loads on the bearing. Semin et al. (2009) show combustion gas pressure curves for an engine converted from diesel fuel to Compressed Natural Gas. The results at different engine speeds seem inconsistent, but at some speeds it appears that CNG may give a very slightly higher rate of gas pressure rise but peak pressures are lower. Clearly some more investigation would be useful on this topic.

The cavitation damage parameter calculated in this program is quite simple but intended to reflect the physics of cavitation bubble formation due to rapid rate of oil film pressure reduction and rapid motion of the journal away from the bearing surface. Note that the calculation of separation velocity in the program included the effect of velocity of movement of the bearing surface in the EHD cases. This is potentially important as many cases, including this one, have deformations of the bearing surface that exceed the static radial clearance of the bearing.

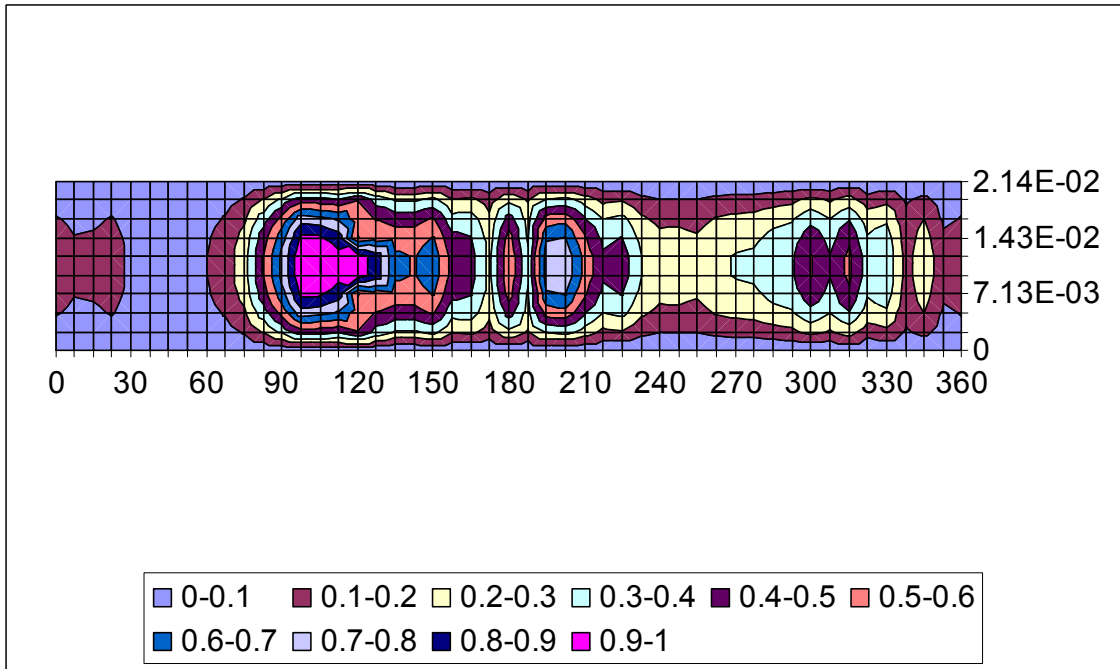


Figure 7-8 Cavitation Damage Parameter

Fig. 7.8 is simply Fig. 6.97 plotted in 2D with a larger number of colour contours. The curvature of the contours is similar to the curvature seen in the photographs in Forstner and Struwe.

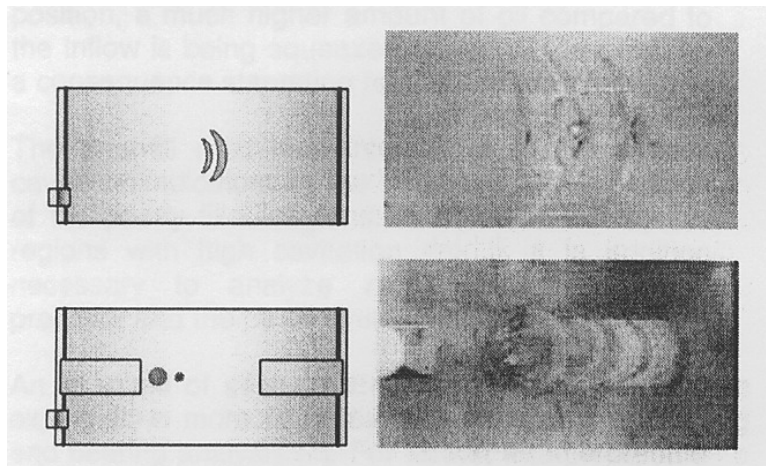


Figure 7-9 Typical Oil Flow Timing Cavitation (Forstner and Struwe, 2004)

Fig. 7.9 is taken from Forstner and Struwe (2004) and shows cavitation damage on the top half of the bearing (crescent shapes) and lower half of the bearing. Their paper did not give sufficient detail about the engine or engines involved in their study to enable a

detailed comparison. However, they did state that vibration cavitation is more likely to be seen in gas fuelled engines. Fig. 7.10 shows vibration cavitation damage.

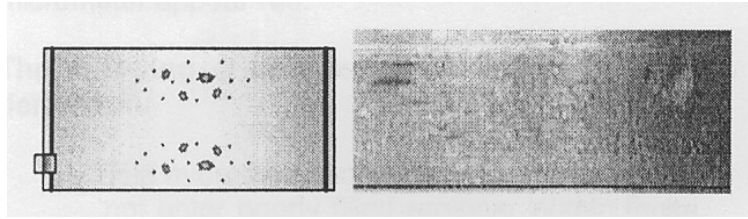


Figure 7-10 Typical Vibration Cavitation (Forstner and Struwe, 2004)

The grooves can cause disturbance of the oil film. Fig. 7.11, again from Forstner and Struwe (2004), shows damage around the groove.

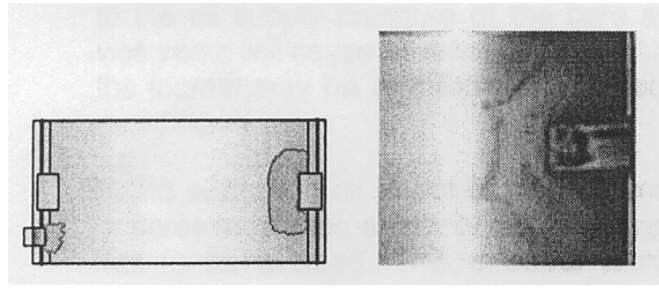


Figure 7-11 Groove Cavitation (from Forstner and Struwe, 2004)

The possibility of interaction with pressure fluctuations and the level of aeration of the oil from the feed hole is highlighted in Forstner and Struwe (2004) so there is scope to develop the cavitation damage parameter into something more sophisticated. Another factor to bear in mind for future development is that the generation of cavitation bubbles in the oil is affected by the change of pressure in the oil itself which is not quite the same as the change of pressure at a mesh node point used in this program. The oil is flowing through the mesh in the x direction at a rate that is a function of the spatial gradient $v_x = f(\partial p / \partial x)$. That implies a component of the pressure gradient with time

due to oil transport $\frac{\partial p}{\partial t} = \frac{\partial p}{\partial x} v_x + \frac{\partial p}{\partial y} v_y$ to add to the dp/dt term currently calculated at

each node. Other refinements of the cavitation damage parameter could take account of the detailed physics of bubble generation. Swales (1974) and Ettles (1974) state that cavitation damage is generally caused by vaporous cavitation rather than gaseous cavitation. Dowson and Taylor (1974) appear to disagree slightly stating that cavitation

in journal bearings is generally gaseous and that vaporous cavitation occurs in hydraulic machinery. Generally, gaseous cavitation, which involves diffusion of the dissolved gases, is relatively slow compared to the rapid pressure fluctuations that can occur. Vaporous cavitation can occur in rapidly changing pressure as it is simply a phase change of the fluid, taking heat from the liquid phase to generate gas at the saturated vapour pressure of the fluid at the temperature concerned. Vaporous cavitation requires nucleation which can be from existing micro-bubbles (including gaseous?), contaminants and surface asperities. Clearly a full and rigorous treatment of cavitation could be a substantial piece of work. Further development of the current cavitation damage parameter and correlation with some real world examples would probably be the best way to start to take the work forward to the next stage.

Bearings are not only damaged by the effect of cavitation. The stress in the bearing material is large and alternating. High compressive stress arises underneath the centre of pressure in a similar way to Hertz contact. High shear stresses arise at the ends of the pressure distribution. These effects can be analysed as a post-processing exercise by applying the time varying pressure distributions to the finite element model from which the stiffness and mass matrices were obtained. In general, a finer mesh will probably be required.

7.5 RELEVANCE OF THE PROJECT

The literature survey showed a very large variety of programs developed in university research departments and elsewhere.

For the Reynold's equation solution, the main solution methods seem to be Finite Difference with Successive Over Relaxation as used on this project or the Finite Element Method. The author's previous experience working with colleagues carrying out hydrodynamic calculations is that the Finite Difference programs seem to be more efficient than the Finite Element programs. One reason for this may be the sparse nature of the matrix making it suitable for the Successive Over Relaxation iterative solution. In the case of modelling the motion of the journal, each successive solution of Reynold's Equation can start the iteration with the results from the previous step. It was found on

this project that sometimes only a couple of iterations produced the new pressure distribution within the required accuracy. Finite Element solutions are solving a set of simultaneous equations using Gauss Elimination or derived methods which is computationally intensive, although other methods are possible.

Most EHD programs use the Finite Element Method for deformation of the structure. A few papers report use of the Boundary Element Method. The BEM has the advantage of being easier to mesh. Note that tetrahedral elements in the FEM are not sufficiently accurate for the relatively small displacements in EHD calculations.

Commercially available bearing solvers such as AVL's Excite program include mass conservation and generalised mass flow at asperities. These two features have been programmed into the solver written for this project but still require checking and testing.

The author is not aware of commercially available software including features such as oil aeration, tensile forces in the oil or choices of equations of motion solver. The software written for this project includes some choice of motion solver including quasi-static iteration, full dynamic numerical integration with choice of solver and experiments have been carried out with novel approaches. One example is the orbit envelope method shown briefly in chapter 5. The intention is to provide fast EHD solvers in the future. The reasons why speed and ease of use are important is discussed in the next chapter.

The inclusion of body forces into the software has been described earlier in the thesis and has now been implemented. It is still being tested and too late to put a study into the thesis. The body forces are considered to be important for extending the use of bearing calculation software into heavily loaded applications such as connecting rod small end bearings. These bearings often have a starved oil supply, making them more sensitive to the body forces due to acceleration.

Tensile forces may be useful to incorporate because they become relevant for lightly loaded bearings. This may not give any significant change in the results for the calculations shown in this report but the intention is that the program has a general capability. The internal Finite Difference calculation was deliberately coded to be as

general as possible and the direction of mesh wrap-around can be specified in the call to the routines. This made adaptation of the program for piston and piston ring calculations trivial. Many other hydrodynamic calculations may also be required in the future.

The development of the software shown in this thesis is not simply an exercise. It is a part of AIES's engine modelling software. The role of simulation software in engineering companies is problematic. The situation is also discussed in the introduction and in the following chapter. Many companies have bought into the vision of 3D CAD modelling of all products. The integration of simulation capability into these products is often sold as 'analysis led design'. This is not strictly true since the shape of the object being designed has to be created before it can be analysed. Genuine design activities usually involve calculation tasks before committing to the shape and dimensions. This requires a selection of calculation methods of varying complexity and fidelity. Carrying out simulation activities early in the design process is important because capital is committed through the process. Errors become more costly to put right.

Features that would be desirable in the future for the software developed for this project include

- Speed improvements probably by implementing more advanced integration methods but also by continuing the development of more radical ideas such as the envelope method referred to briefly in Chapter 5. The Newmark Beta and Hilber-Hughes-Taylor integration methods are designed specifically for second order differential equations such as these and are likely to be more stable than the Bulirsch-Stoer method. The Newmark Beta method already works successfully for RHD calculations and is being extended to the larger system of equations for EHD calculations.
- More technical features. In particular ThermoElastoHydroDynamic calculations have been shown to be important. There are detailed technical issues regarding generation of matrices to carry this out fully automatically.

- User features such as continuing the development of derived results mapped onto the bearing surface and ensuring that the interface to other software such as FEA and in the future CFD for oil feed passages is as easy as possible

CHAPTER 8

COMMERCIAL SIGNIFICANCE

8.1 INTRODUCTION

Many authors on the role of design in determining the cost of products have produced graphs showing how design decisions build in risk and cost that cannot be corrected later. Mynott (2005) provided the figures shown below. Fig. 8.1 shows the disproportionate effect that a late launch date has on profitability from a product. This is partly related to the relationship between time and price that can be obtained as competitors join the market and the early entrants reduce their costs. There is also, of course, the extra development cost incurred. One assumes that late release of a product is nearly always due to development problems. The extra development effort has to be paid for.

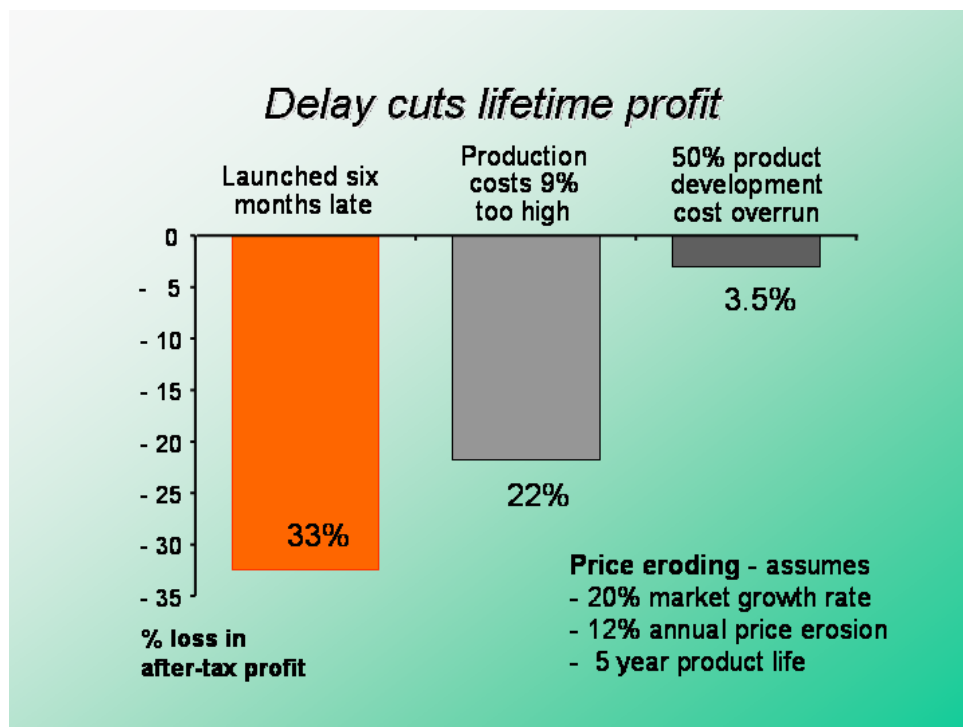


Figure 8-1 Effect of Delays (source Colin Mynott, 2005)

Generally, delayed development also implies that errors are being detected at the most costly stages of the product life cycle. Fig. 8.2 shows the catastrophic effect of errors that are detected after production has commenced.

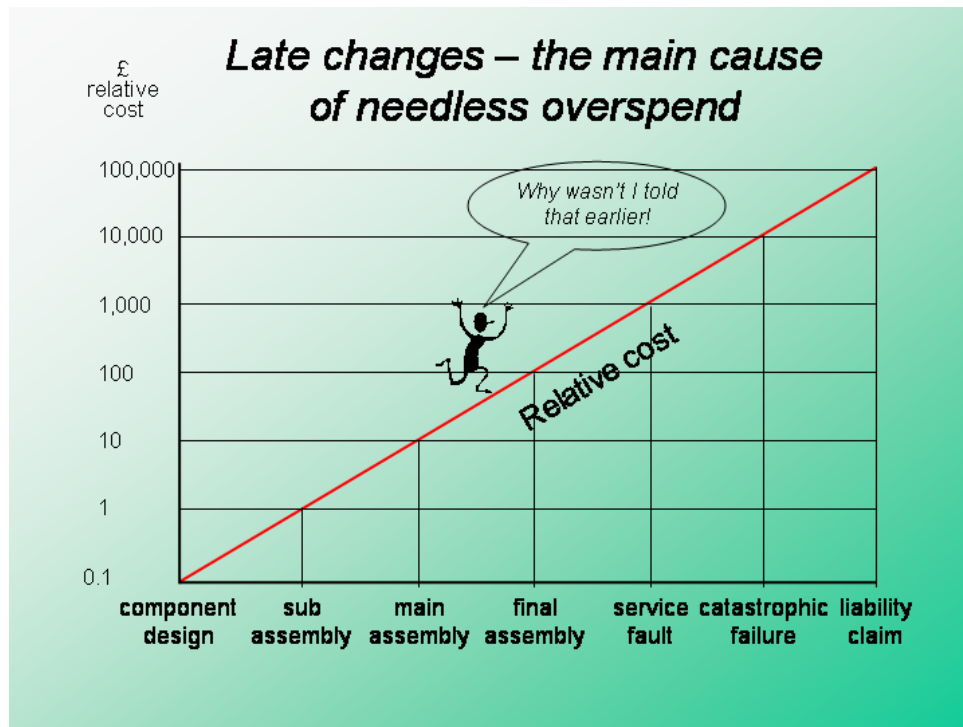


Figure 8-2 Effect of Late Changes (Source Colin Mynott, 2005)

Fig. 8.3 shows where time is wasted on typical projects. These figures show that poor design can be responsible for large losses. Therefore, accurate and reliable simulation and design analysis that can be carried out ahead of committing to design decisions is critical to business success.

Project sponsoring company AIES Ltd. is a company specialising in simulation software, design analysis and design consultancy and is the author's sponsoring company. The success of engineering and manufacturing companies is critical to AIES's success. This is the reason that AIES is focussed on the issues of bringing design analysis into the design process.



Figure 8-3 Typical Wasted Time (Source Colin Mynott, 2005)

The issues can be summarised in Fig. 8.4 showing the level of risk to project of the various stages in time.

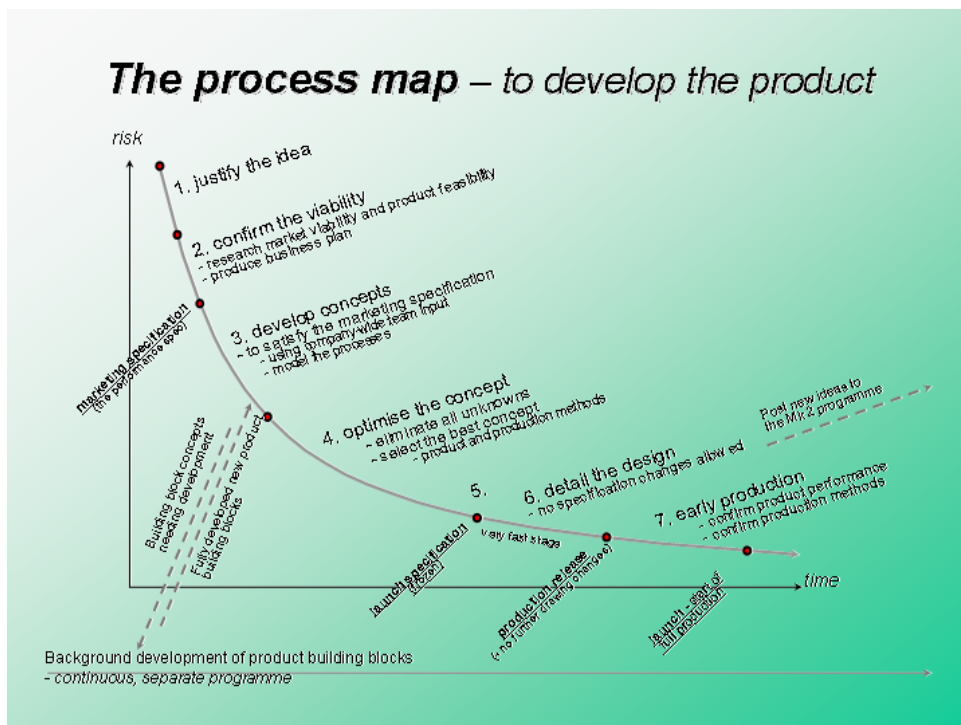


Figure 8-4 Risk vs. Time (Source Colin Mynott, 2005)

8.2 ENGINEERING PERSPECTIVE

Simulation tends to lag behind design and innovation and to be reactive. There is a need for a paradigm shift for it to become creative and proactive. There is a tendency for the same people, tools and information move around the businesses in an industry. The differentiator is the process – large gains are possible by understanding the process, capturing it and taking it forward.

It is worth considering the way in which products were designed prior to the introduction of CAD systems. Design engineers would usually carry out hand calculations prior to the definition of the geometry on a drawing board. This produced genuine analysis led design! The current CAD product vendors promote analysis led design as being the production of CAD geometry followed by analysis. Using automated generation of tetrahedral shaped elements and modern computer power shortens the process so that many iterations can be performed. This approach is failing and companies are finding it difficult to shorten product development times further. See McLuckie and Barrett (2005c).

The keynote speech at the IDETC conference in 2005 by Dennis Nagy was summarised in Chapter 1. A keynote speech by Stephen Prusha, Jet Propulsion Laboratory, on Challenges in Early-Phase Complex System Design was given in another session at the same conference. It is interesting to note that, once again, the theme concerns dissatisfaction with current design process. It was also interesting that the vast majority of papers presented at this conference went into great depth of particular aspects of the subject of the session concerned. This was very much at variance with the keynote speeches and yet not addressed in the sessions.

Mr. Prusha gave a very interesting presentation on the subject of early phase design for complex systems at JPL. These are often highly differentiated on fidelity for reasons of concept versus design sign-off etc., system level vs. component level etc. Many JPL projects are for the purposes of putting complete space missions together many years (sometimes up to 20) ahead of the event itself. Many missions are rejected after

feasibility studies but a major concern is that well over 50% end up being cancelled despite passing feasibility studies. Issues that arise include

- Requirements Creep. Need to get the customers together and operate a feature trading scheme with costs versus specification worked into models. The customers can then use models to come up with their own trade offs instead of competing with each other to up the requirements.
- Graphing Requirements Uncertainty Versus Time. ‘Infusion’ horizon is the point at which we decide we know enough with certainty whether or not to take the project further
- Science Traceability Matrix – discovering and trading key requirements – need for involvement of scientists who are only interested in their particular study not the whole mission – getting them together is very difficult
- Characterising And Trading Risk
- Importance of Context
- Collaborative Design – Concurrent engineering at JPL has changed typical project from £250k in 26 weeks in 1995 to £85k in 1 week now. 55 studies in a year
- Challenge Of Distribution – infrastructure, decision latency, sidebar interaction, design quality, speed, consistency, IPR of models when working across contractors etc.
- Model Based Design – design sensitivity required for requirements trading (trade space modelling) – more than just CAD/CAM
- Fidelity Varies With Phase – MAJOR PROBLEM of excessive model fidelity inappropriate to phase of project especially as a component of a complex system can divert resources and effectively even destroy the project. No simple link between fidelity and credibility of analysis

- Risk And Cost Lies In The Interfaces

It is interesting that the role of simulation was only a small part of the issues for JPL. With regard to model based design, it was stated that solutions are required in the areas of design infrastructure (reliability & consistency), design process, IPR issues involving contractors as well as software, technology and human infrastructure models.

CAD/CAM was not considered to be a big issue although easier transfer of models between companies would help. Technology is often ahead of the modelling capability and that was considered to be no longer acceptable. An emphasis on standards and configuration management is less important than addressing the system engineering issues. These tend to be limited by static representation, lack of sensitivities, not easily evaluated, can't assess designer performance, understanding of context, compatibility with trade processes, auditability of results.

For system models and understanding a design breadth (and evenness of models in subsystems) is more important than depth or fidelity. Understanding risk is more important than detailed cost. People issues are important rather than structure of organisation or processes for concurrent engineering to succeed. Part of the purpose of understanding risk and having breadth in the modelling is to provide options. This is preferable to simply having uncertainty and companies don't need more decimal places at the early stages of design. Flexibility is more important than standards – that's not to say that some standards are not needed

8.3 IMPORTANCE OF THE PROJECT TO THE SPONSORING COMPANY AND INDUSTRY

8.3.1 SPONSORING COMPANY

This project exists to provide strategic components for AIES Ltd.'s future range of software products. These will enable AIES's software to be distinguished from the competitor products in terms of capability.

The purpose of AIES's software is to bring design analysis and simulation into the design process. Certain functionality will be achieved through interfaces to other company's products. This is especially the case for mature technologies such as Finite Element Analysis and Computational Fluid Dynamics.

Another aspect of bringing design analysis into the design process is to provide new solvers that are more efficient than those currently available or provide capability that is not currently available. The first programs to be developed have now been released or are about to be released. These can be seen on the AIES web site at www.aiesl.co.uk.

Tribological calculation programs are additionally available commercially from companies such as AVL List, Ricardo and Gamma Technologies. Their programs are difficult to use, placing a premium on user skill and producing long delays and errors in data preparation. The technical capability of these programs are aimed very specifically at the automotive market and do not meet all of the needs of certain users. Their products also tend to be used by experts. The projects on which they are used tend to be self-contained and lead to many problems of time and relevance.

AIES has significant expertise in tribology and dynamics. Once the need for usability in the user interface has been met the customers' requirements will become faster calculations and greater confidence that those calculations are correct.

The software developed on this project will therefore play a strategic role in giving AIES's products a capability that is higher than the competitor products. It needs to answer the technical questions but also use any novel thinking to get faster and more reliable solutions.

New markets are available to companies that can provide more capable solvers in a user friendly environment. These markets include specialist internal combustion engine manufacturers, turbocharger manufacturers and others. These potential customers have generally been sceptical of the role of design analysis in the past. It has not met their requirements both technically and in terms of enabling faster and more reliable product development. They have not been willing to employ CAE specialists to carry out the calculations.

The principal aim of this project is therefore to produce improved hydrodynamic solvers that open these markets. The results of calculations will be used to demonstrate the capability to potential customers.

AIES Ltd.'s approach to reduce the time required in meshing activities is to generate the mesh and geometry together. Their patent pending method uses pre-meshed templates of hexahedral elements to generate the model geometry, by passing the CAD to FE process. Comparison of the technique with traditional approach has been shown in McLuckie and Barrett (2005c).

The requirement for this project is to develop AIES's solver technology to provide novel and competitive calculations to go into AIES's software environment. Expectation of return on this EngD project is large but difficult to estimate directly. The supply of genuinely required products into AIES software is a strategic necessity. The overall outgoings per year on this project have been relatively small. The contribution to AIES's software range is significant. The initial improvement in analysis capability for turbocharger design analysis will take AIES's software beyond the capability of current commercially available software. Therefore, the project can be expected to pay for itself with first software sale into that area. However, long term effect is the provision of rotordynamics tools into the AIES environment that are applicable in other areas such as gas turbines, camshafts, gear shafts etc.

Making CAE tools generic and easy to use enables them to fit into the design process. The significance of this for AIES's customers can be explained in terms of the risk and cost associated with time within the development process (see the graphs by Colin Mynott earlier in the chapter). Enabling customers to carry out design analysis accurately, cheaply and with confidence early in the design process can have a large effect on the cost to develop their products. This makes the approach adopted by AIES Ltd. attractive.

The ability of AIES to sustain this type of work depends on the management of strategic assets. These can be classified as

- Valuable – gives competitive parity – anyone can get to the same point by paying
- Rare – gives temporary advantage – competitors will find the secret eventually
- Imperfectly imitable – gives sustainable competitive advantage
- Non-substitutable – also gives sustainable competitive advantage

The last two categories give sustainable advantage because of their non-codifiability, complexity, specificity, causal ambiguity and/or path dependency. A competitor cannot simply go out and purchase them. However, it is also difficult to understand and hence easy to lose in Business Process Re-engineering.

Elicitation of the strategic assets of a company can be carried out by causal mapping. This will often give different results from different people. One reason is that the most important categories (imperfectly imitable and non-substitutable) depend strongly on tacit knowledge.

Perceived Use Value vs. Perceived Price diagrams (see Fig. 8.5) are useful for understanding where we are and where to go. Beware simply competing on price. PUV requires knowledge of customers.

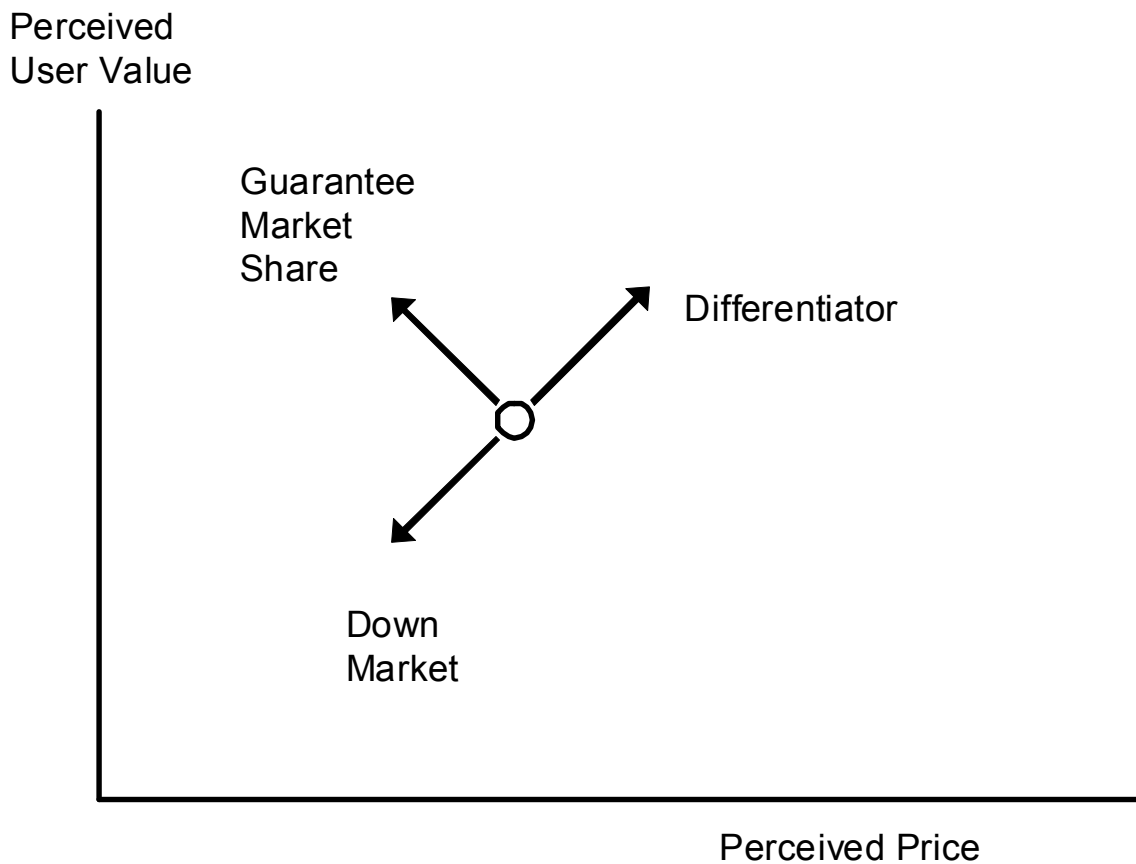


Figure 8-5 Perceived User Value vs. Perceived Price

Managing strategic assets combines the above two subjects – Valuable corresponds to PUV and/or lowering costs. Imperfectly imitable can be elicited through analysing the causal mapping, path dependency, asset configuration, first mover advantage and embeddedness. Auditing by category (Tangible, system, structural, knowledge, relational, cultural) against assessment of PUV, costs, rarity, imperfect imitability and non-substitutability can be used to highlight the strategic assets.

The following should always be kept in mind

- migration through time and the strategic fit (Systems, culture, assets).
- Porter's 5 forces – competitors, suppliers, customers, barriers to entry and substitutes
- 5 key questions – Where to compete? How to gain and sustain advantage? What assets required? How to change? What assets do we have?

- Porter's 2 generic strategies – cost leadership or differentiation
- Company culture
- Planning, SWOT, PEST

In the case of AIES, it is clear that the important strategic assets lie in the people and their combination of experience. It is a company that is able to look beyond the mathematical modelling to the practical engineering issues with a tacit knowledge of what works. The lack of connection between mathematical modelling and the real requirements of design engineers is what stands out at engineering conferences.

Porter's 5 forces and PEST analysis are dealt with below. The generic strategy for AIES must mainly be differentiation by using the strategic assets to give that usability so lacking in the competitor products. Clearly, at the early stage, it may be necessary to use competitive pricing to gain market share before making use of differentiation. For many of the customers, price of their own products is the main issue and the Perceived User Value of AIES's software can only be increased by ensuring that the customers are able to use it effectively.

The Ansoff Strategic Development Matrix in Fig. 8.6 shows that placing a new product into an existing market requires an emphasis on product development which is not exactly a surprise! Going into new markets with a new product is diversification and AIES have adopted a policy of ensuring that its software products are developed to be generic and thus inherently capable of being adapted to new markets. The adaptation of the bearing software to pistons and piston rings was shown briefly earlier in the thesis and was carried out by changing only a small amount of code.

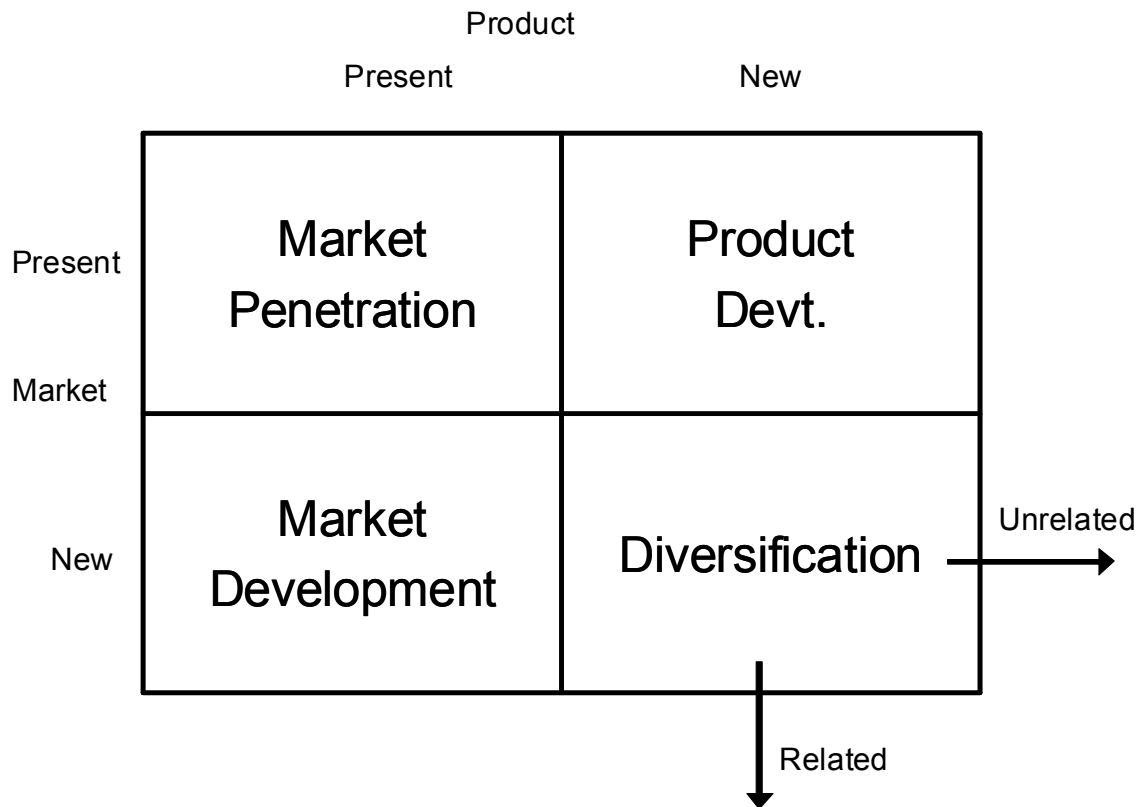


Figure 8-6 Ansoff Strategic Development Matrix

8.3.2 INDUSTRY PERSPECTIVE

The ability to get a design right is influenced strongly by the accuracy of the simulations employed. The speed of solution is also important as this enables many calculations to be carried out. It is now quite common to use techniques such as Design of Experiments to select optimised solutions automatically. Many companies have ‘Six Sigma’ programmes in operation. The aim of these is to produce products with zero defects.

Throughout most of the 20th century products were defined for manufacture by paper drawings. Products that were simple, cheap, lightly loaded and not safety critical would be designed simply from prior experience. In the case of highly loaded engineering components or systems, it would be necessary to calculate the suitability for use before creating the drawings.

Powerful computers became available for design engineers to perform calculations from the 1950s onwards with a steady increase in computing power that still shows no signs

of slowing (Moore's Law). Many engineers wrote programs to automate their calculations and used them prior to finalising designs and creation of drawings. This could be described as 'analysis-led design' long before this became a regular topic for discussion in recent years.

The introduction of powerful 3D solid modelling Computer Aided Design (CAD) programs from the 1980s onwards enabled designers to produce geometry quickly on a computer screen that could be used for several purposes. These included producing drawings, producing tool paths for computer controlled machine tools and producing discretised meshes for finite element calculations. The vendors of such programs promoted them as the core application for all other engineering processes. Much discussion in the engineering community concerns how to achieve analysis led design. The problem is that CAD systems produce geometry prior to being used for calculations, reducing the role of calculations to that of confirming or otherwise the integrity of what has already been designed.

It is important to understand the relationship between modules and systems. An emphasis on logistics and integrating sub-contractors into the manufacturing process has led to Original Equipment Manufacturers (OEMs) tending to move towards becoming assemblers of bought in modules. The role of systems integration is important because of the technical expertise required. Therefore it is becoming increasingly important to understand the difference between modules and systems. Modules consist of hardware linked by logistical convenience (generally assemblies) that can be delivered. Systems concern knowledge, especially regarding interactions between components. The following, fig. 8.7 has been adapted by the author from a diagram devised by work colleague Graham Atkin at Federal Mogul in 1999 to explain the issues to senior management.

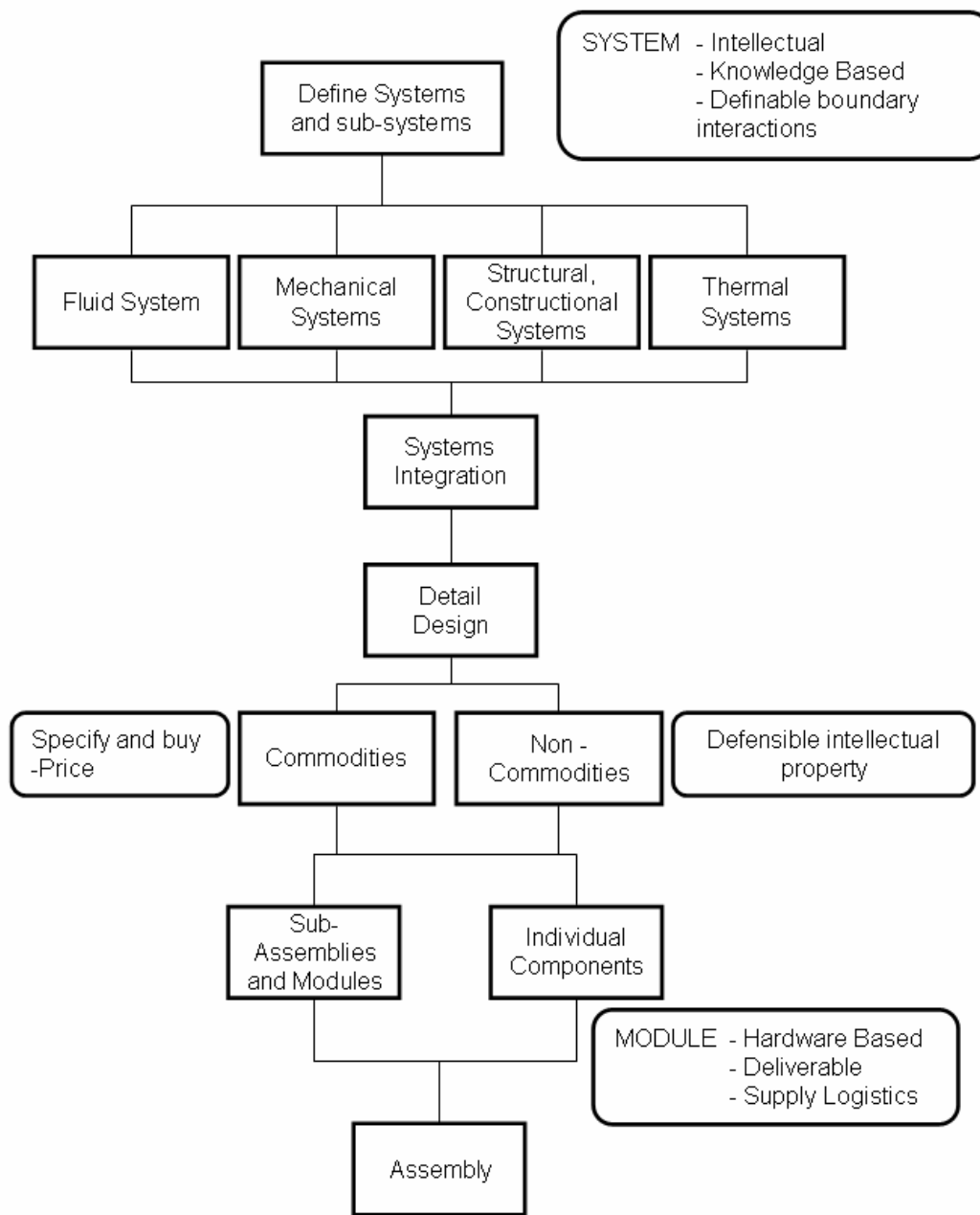


Figure 8-7 Role of Knowledge in Systems

The previous discussions, based on Mynott, Nagy and Prusha can also be put into a product development technical context by a diagram. Fig. 8.6 shows how a system might be developed in an engineering company. The feedback loops are important to

ensure that the design is satisfactory. As we go further through the process, the feedback loops become more expensive, hence the importance of effective simulation at the early stages of product design.

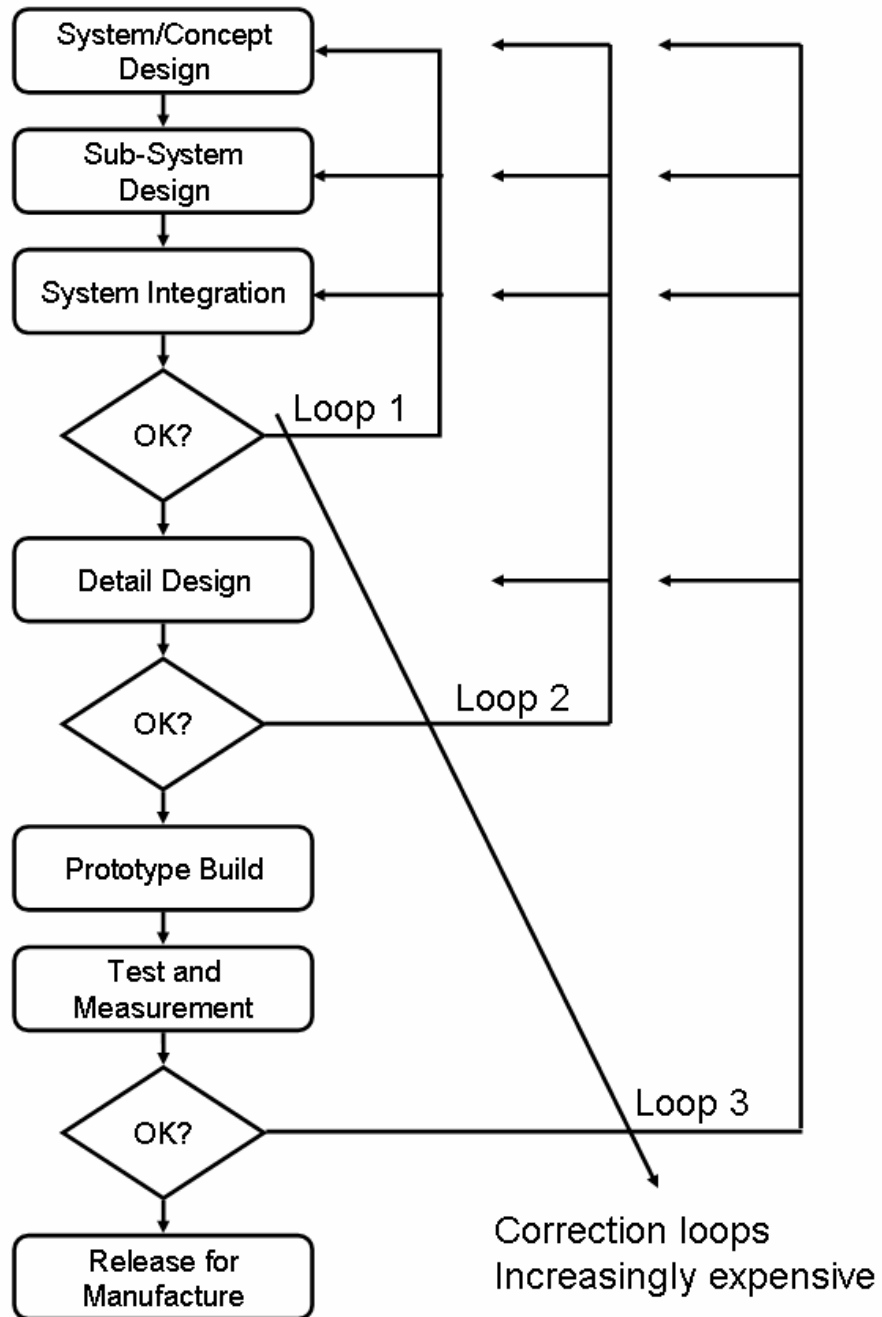


Figure 8-8 Importance of Correction Loops

The Boston Matrix (Fig. 8.9) is often used to categorise the position of businesses. Many of AIES's potential customers, especially in the automotive industry, might be thought to be mature companies in the cash cow category. Mechanical engineering, vehicle and engine production are often not regarded as advancing glamorous companies. However, most of them probably don't see it that way and do see the need for investment to meet the challenges ahead. It would not be attractive to simply attempt to compete with the established engine modelling software products without some unique selling points. The market for these was probably fairly stagnant until the opening of the Indian and Chinese markets and AIES's share of the market is bound to be small at the start.

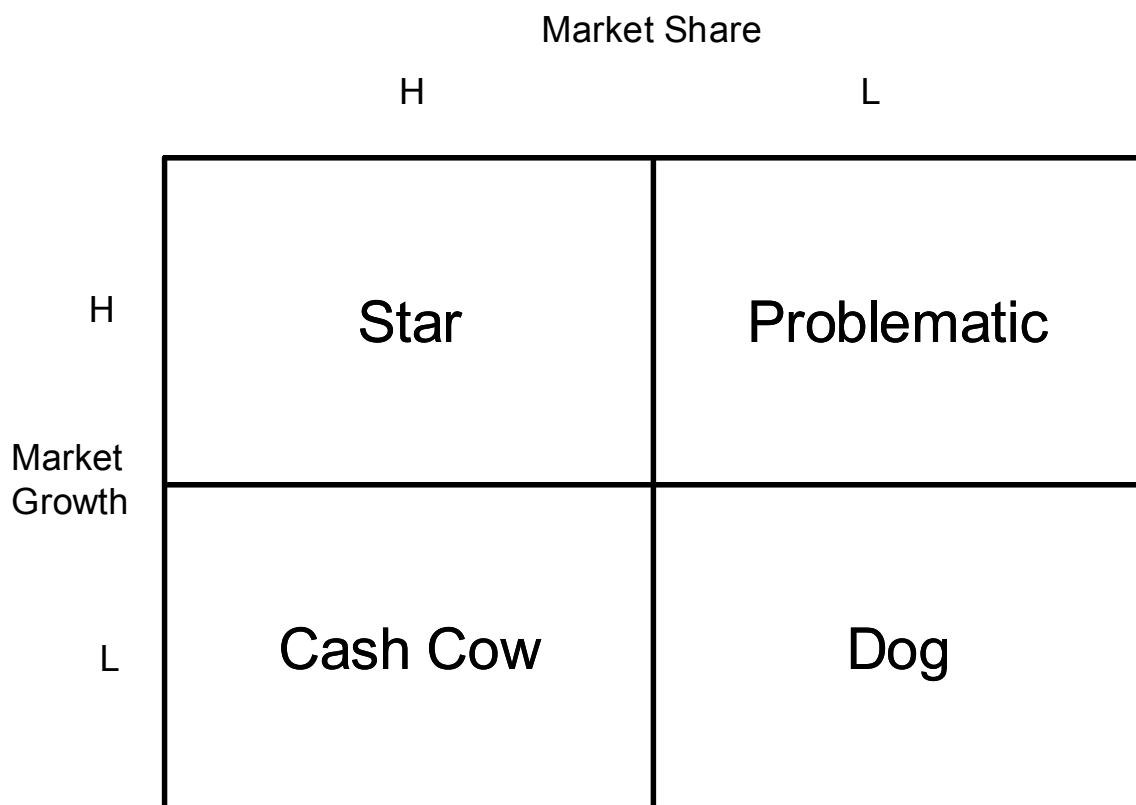


Figure 8-9 Boston Matrix

The benefits network in Fig. 8.10 shows the thinking that connects solutions to required benefits in a logical procedure that starts with the visionary purpose on the right hand side of the diagram. These can then be linked to specified quantified benefits, the process or function that needs to be changed and then the business redesign, any IT applications required and infrastructure changes required to achieve the vision. It is

intended to complete a Benefits Network from an AIES customer perspective and from AIES's perspective.

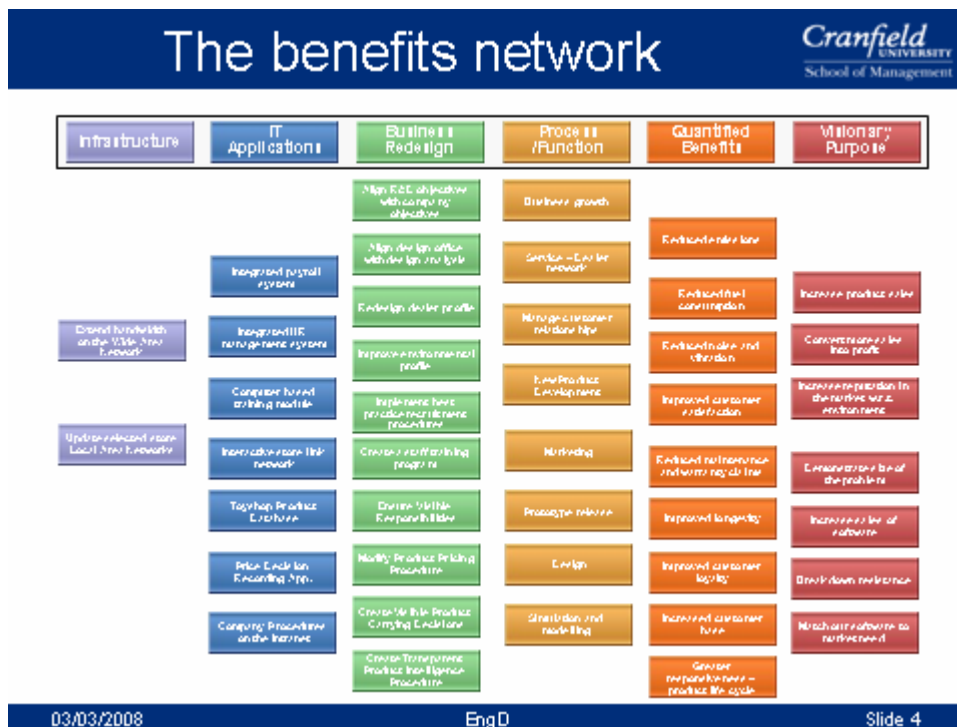


Figure 8-10 Initial Indicative Benefits Network

8.4 WORLDWIDE CONTEXT

8.4.1 POLITICAL

The advance of China and India over the last 15 years has created an opportunity for suppliers of expertise and software. Manufacturing companies in these countries are often efficient but lack expertise in product development. This makes them receptive to new ideas whereas western companies have become locked into an emphasis on standards and the use of 3D CAD.

The European Union appears to have stalled in between the desire for a single currency and the need for closer political union in order to maintain it. The situation for many international engineering companies is that they now concentrate their European headquarters and associated marketing, purchasing and crucial technical leadership

functions within the eurozone. This is largely to insure against currency fluctuations but also to have headquarters functions centrally located. These factors could be a problem for AIES as fewer potential contacts are located in the UK.

On the other hand, it was becoming obvious that all of the main political parties in the UK were responding to the aftermath of the banking crisis by talking about re-balancing the economy. There is already a small but energetic high technology manufacturing sector in the UK. This may be a springboard for recovery of mechanical engineering generally. Small high technology companies often do not have adequate analysis and simulation tools and this may present opportunities. The generic nature of AIES's software, including the software written for this project, means that adaptation to areas of technology other than internal combustion engine bearings is readily possible.

8.4.2 ECONOMIC

The recent banking crisis has affected all companies. However, India and China continue to grow. Many manufacturing companies in Europe and North America have lost people from already lean organisations. Therefore demand for external expertise is increasing. This may enable AIES to make good use of its expertise in a consultancy capacity, which brings cash in, to support the software development activities which can be slower to bring cash in while requiring investment up front.

Increasing competition in the engineering sector means that potential customers for the software produced by AIES are looking to suppliers for their competitive advantage. Any technical, cost and/or time advantages that AIES can bring them will be important.

The banking crisis is expected to have long-lasting effects on the availability of capital.

8.4.3 SOCIAL

There are problems with the image of engineering in the UK with few school leavers wishing to pursue a career. This problem may put a brake on the government's hopes of re-balancing the economy. One way to deal with this potential crisis would be immigration. However, recent political controversies suggest that this may be problematic.

Continuing shortages of hydrocarbon fuels do not appear to be able to be compensated fully by renewable energy sources in the next couple of decades. The extent to which people will be willing to abandon their use of cars and take to public transport is unclear. So far, people appear to be willing to pay high fuel prices while complaining but unwilling to change their behaviour.

8.4.4 TECHNICAL

Computer power continues to increase at an undiminished rate (Moore's Law). In addition, computer clustering to obtain parallel processing capability is now relatively easy and cheap. It can be achieved using conventional PCs and the Windows operating system. However, most academic implementations use the UNIX operating system. This is unlikely to be a major problem and AIES is already thinking in terms of this technology.

On the mechanical engineering side, it should be remembered that there have been predictions of the demise of the reciprocating internal combustion engine for many years. This has resulted in the loss of some R&D teams which have then had to be re-constituted when the predictions did not come true. The search for efficiency and low carbon emissions in transport is complex. Batteries are improving and hybrid drive systems continue to be improved within the automotive industry. This situation has continued for at least the last 15 years. It has to be remembered that the internal combustion engine has also been improved in response to the threat from other technologies. There are many improvements still to come. Diesel engines have taken the internal combustion engine forward for much of the last ten years, the big breakthroughs in efficiency having been the use of direct fuel injection and electronic control. The next big advances are expected to be in gasoline engines with improvements to variable valve control, direct fuel injection and low pressure turbocharging. Internal combustion engines are relatively cheap to produce and each improvement in battery, electric motor and fuel cell technology has still left realistic implementations of the technology significantly more expensive than current internal combustion engines. This means that increases in the severity of legislated emissions and customer demand for

lower fuel consumption can be met by implementation of technology at a lower price than the supposedly greener alternatives.

The paragraph above is probably sound for at least the next ten years. Significant breakthroughs in battery technology appear to be being made. Provided that the infrastructure issues can be resolved, it seems likely that the longer term future will see a gradual takeover of transport by electric vehicles.

In many ways these changes are not as large a threat to the internal combustion industry as they might appear to be. There may well be a demand for smaller internal combustion engines for purposes such as range extenders and other types of small genset. Different economics will apply to different types of vehicle resulting in some transport sectors continuing to use internal combustion engines for many years to come.

The changes in the detailed technology will mean that we never get to a situation where there is no demand for simulation of internal combustion engines until that technology really is near the end of its life.

The generic nature of AIES's software means that it can be applied (adapted if necessary) to other mechanical engineering areas. Rotating machinery is likely to be a growth area to the extent that the internal combustion engine contracts. This is because the alternatives involve electric motors, generators, wind and water turbines etc.

8.5 FUTURE BUSINESS MODELS

Brajdic-Mitidieri, Gosman, Ioannides and Spikes (2005) use an open source CFD program (FOAM) to examine the effect of pocket features on the performance of a slider pad bearing. The progress of this open source software within the automotive industry is interesting. It appears to have become a mainstream product (McBeath, 2010), competing head on with the well known products and causing the large CFD vendors to re-assess their own business models.

The business model relies on income from training, support, consultancy and charging customers to develop new features that they want. The software itself is free. It is coded

in the C++ language and can be modified by the user because the source code can be downloaded.

Users soon come to the conclusion that it is generally not worthwhile to modify the program exclusively for their own use as they then have problems with integration of their own code when the next version is released. It is more profitable to be a part of 'the club'. The Racecar Engineering article doesn't state if it's possible for users to write their own code and contribute it to the next release but one assumes that this is one way to make use of this business model.

Business models such as this give rise to different forms of competition. The companies involved may be said to be in co-opetition. They compete in certain areas (e.g. supply of engineered products, supply of consultancy services etc.) but cooperate in other areas (in this case being part of a club to develop the software). A characteristic of this sort of business model is also clustering in which similar businesses locate together. This concentrates expertise.

There are no immediate plans for the author's sponsoring company, AIES to adopt such a business model for its own software. However, the general approach to software development (Object Orientation) required to make such a system work certainly does fit in with the AIES approach. Tools such as FOAM and any open source FE codes may also be very useful in reducing the overhead for AIES's customers to use all of the features in the future. The modelling of lubricant supply to oil holes and thermal or structural deformation of bearings relies on external software currently. Being able to use open source software for these tasks would greatly reduce costs for both AIES and their customers.

Changing to an open source business model would almost certainly be difficult until the stage where it becomes difficult for other companies to simply copy the software and compete. There needs to be a barrier for entry of competitors – the barriers are mainly a strong user base, lack of direct competitors or product substitutes in this case. Fig. 8.11 shows Porter's 5 forces that are barriers to entry.

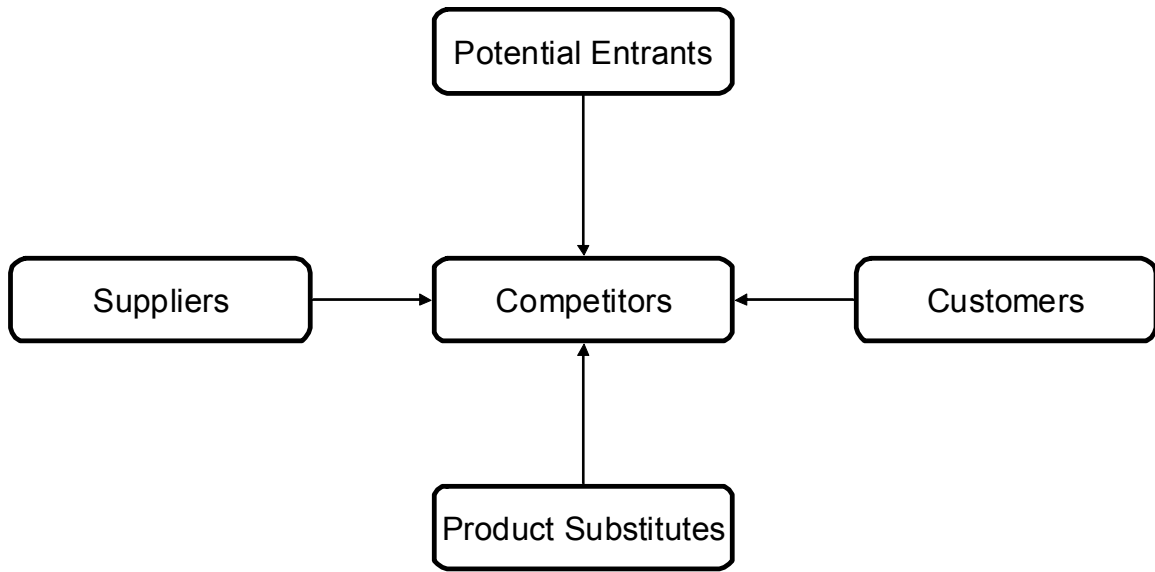


Figure 8-11 Porter's Five Forces – Barriers to Entry

The paragraphs above describe a business model that may be useful in the short term for AIES to use third party software that would be useful for its consultancy work and for interfaces to software that AIES would not wish to write itself such as FEA and CFD. However, it is far from certain that the open source model is robust and it will be interesting to see how openFOAM fares.

For the short term, AIES's own software would need to be sold in a conventional manner which means customers paying for a licence to use the executable. There are ways to maximise the profitability from this model. Software has unusually high fixed costs and low variable costs, at least when considered simply as a product, without considering support and other services such as consultancy. This makes it particularly suitable for applying third degree price discrimination.

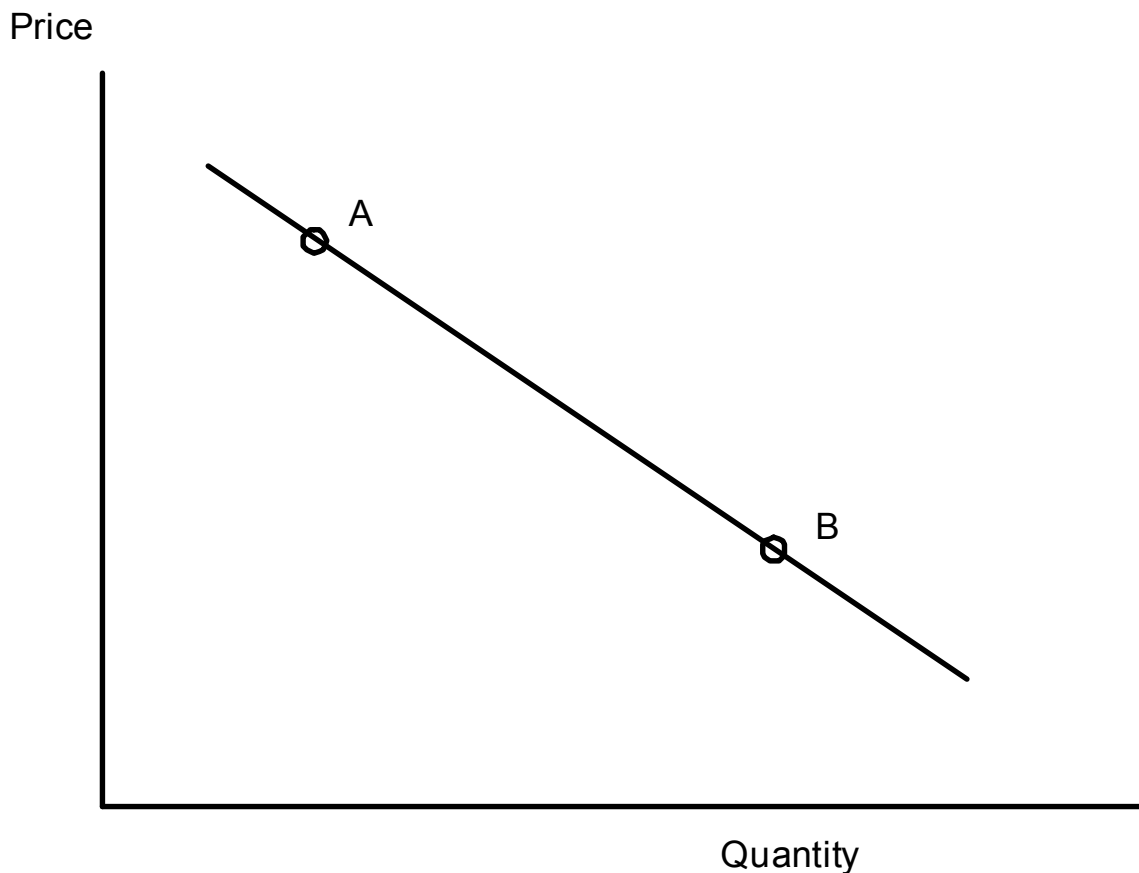


Figure 8-12 Demand Curve

Fig. 8.9 shows a simplified demand curve. There may be sufficient potential customers at point A on the graph to provide a profit. Reducing the price would increase the quantity sold, point B, but may not produce sufficient profit. A way to keep the customers willing to pay a high price and still get income from those who cannot is to discriminate by charging different customers differently. There are obvious dangers in that the customers who are paying the 'full price' will not be happy unless they are getting something for that price. Possibilities to maximise the area under the curve include charging different types of customer different amounts (e.g. different sectors such as academic may get a much lower price). Also it is possible to charge differently for different program options and features.

8.6 MBA COURSE TOPICS

Several MBA course modules were attended as part of the taught element of the EngD degree. The modules Accounting, Finance, Strategic Management, Management of Information Systems, Marketing, Microeconomics, Macroeconomics and Strategic Decision Science were relevant to the project and are summarised briefly in Appendices D to G.

CHAPTER 9

CONCLUSIONS

9.1 ACHIEVEMENTS OF THE PROJECT

The project has succeeded in developing an EHD program for journal bearings with some advanced features

- Incorporation of body forces shown to be important but needs to be demonstrated
- Inclusion of derived results parameters including mapping accumulated maximum and minimum values over the bearing surface
 - This included a new cavitation damage parameter
- The program has been used for real project work on a range of engine types from 5000 rpm diesel engines to 20000 rpm racing engines and results reported to customers and at conferences

The importance of taking care to include many influences on bearing behaviour have been demonstrated. These include thermal deformation as well as deformation due to manufacturing and assembly processes.

9.2 LESSONS FROM THE RESULTS

The results shown in the previous chapters have shown

- The importance of considering all possible influences on bearing shape for highly loaded bearings

- The usefulness of derived results parameters in reducing the need of users to apply their own post-processing to the results of calculations.

9.3 STATUS OF THE CURRENT WORK

The EHD program as it stands is capable of being used for bearing studies on a commercial basis. It has some features that are ahead of current commercially available software

- Ability to model several oil films simultaneously including Full Floating Bearings
- Ability to present novel results including
 - accumulated maximum and minimum values of result parameters over the bearing surface making understanding of results much easier
 - cavitation damage parameter
- Alternative solvers for journal position including equations of motion time marching, iterative static and novel solvers under development
- Ease of interfacing to commercial FE solvers for stiffness and mass matrix. The software shown here does not place restrictions on node numbering order and will soon also not place restrictions on spatial orientation

Other features are lacking to be fully competitive

- Mass conserving algorithm and generalised mass flow have been coded but too late for this thesis. Testing will be performed in the near future
- A speed increase is needed – probably achievable by extending the current Newmark-Beta integration routine to include EHD. This and other integration methods also in the process of being implemented now
- More sophisticated boundary conditions for EHD calculations

- Pressure-viscosity curve has been incorporated but not fully tested yet

Still more features should be considered in the future to push ahead

- Extension of cavitation damage parameter and other derived results to assist designers
- Additional features
 - Automated TEHD modelling – problems need addressing regarding ability of commercial FE codes to output the necessary matrices
 - Oil aeration, interaction with oil supply models
 - Consideration of surface tension and tensile stress in the fluid
 - Consideration of bubble formation and collapse as diffusion and thermodynamic processes within the oil film
 - Incorporate shear thinning and lubricant yield

9.4 INCORPORATION INTO AIES BUSINESS

The EHD program developed here is important to AIES's business and has already been incorporated as one of the components into its engine modelling software. The role of programs such as this in engineering companies will be important in the future. It is therefore important that the program's ease of use, reliability and ability to generate results that can be used directly by engineers are high priorities for the future.

Progress has already been made on adapting the code written for journal bearings for use in other situations. The codes for pistons, piston rings and thrust bearings have been adapted directly from the work reported here.

REFERENCES

1. Ai, X, Cheng, HS (1993) A Fast Model for Pressure Profile in Rough EHL Line Contacts. *Trans. ASME Journal of Tribology*, Vol. 115 pp 460 – 465
2. Aithen, M.B. & McCallion, H. (1991) Elastohydrodynamic lubrication of big-end bearings, part 1: theory. *Proc. IMechE.*, Part C, Vol. 205, p. 99
3. Anisimov, V.N., Anisimova, N.V. (1999) Analysis Of Complex Loaded Floating-Ringbearings For Automotive Applications, *SAE Technical Paper* 1999-01-0286. SAE International Congress and Exposition, Detroit, Michigan, March 1999
4. Aoyama, T., Suzuki, S., Atsushi, K., Takashi, N., Ozasa, T., Kato, T., Ito, T. Preventive Design and Analysis of Cavitation Noise on Diesel Engine. *R&D Review of Toyota CRDL* Vol. 40 No. 1
5. Ausas,R., Ragot,P., Leiva,J., Jai,M., Bayada,G., Buscaglia,G.C. (2007) The impact of the cavitation model in the analysis of microtextured lubricated journal bearings. *Journal of Tribology* 129 (4), pp. 868-875
6. Ausas,R.F., Jai,M., Buscaglia,G.C. (2009) A Mass-Conserving Algorithm for Dynamical Lubrication Problems With Cavitation. *Journal of Tribology* 131 i3, 031702
7. Bahai, H. and Xu, H. (1997) Three-dimensional elastoplastic finite element and elastohydrodynamic analyses of journal bearings. *Proc. Instn. Mech. Engrs.* Vol. 211 Part C pp. 143-152
8. Bair, S., Winer, W. O. (1979) Shear Strength Measurements of Lubricants at High Pressure. *Transactions of the ASME, Journal of Lubrication Technology*, Vol. 101, pp.251-257, July 1979
9. Bajer, C. (2000) *Time integration – still questions*. Institute of Fundamental Technological Research. Polish Academy of Sciences. Warsaw. Downloaded 2007.
10. Bajer, C. (2002) Time integration – still questions. *Theoretical Foundations of Civil Engineering*, v.1. pp55-66, Warsaw
11. Barrett, D.J.S. (2001) Elasto-hydrodynamic Analysis of Bearings by Coupling Finite Difference and Boundary Element Methods, Cranfield University MSc Thesis
12. Barrett, D.J.S., El-Zafrany, A. & McLuckie, I.R.W. (2002) Elasto-Hydrodynamic Analysis Of Bearings By Boundary Element And Finite Difference Methods, *Boundary Elements XXIV*, Sintra, Portugal

13. Biswas S., Snidle R.W. (1977) Calculation of Surface Deformation in Point Contact Elasto-hydrodynamics, *J.Lubrication Technol.*, 99, 313.
14. Bobach,L., Bartel,D., Deters,L. (2008) Simulation of tribological parameters of mixed friction-stressed connecting rod bearings. *Tribologie und Schmierungstechnik* 55 (2), pp. 11-20
15. Boedo, S. (1995) A Mass Conserving, Modal Based Elastohydrodynamic Lubrication Model: Effects of Structural Body Forces, Surface Roughness and Mode Stiffness Variation. PhD Dissertation, Cornell University.
16. Boedo, S., Booker, J.F. (2000) Mode-Based Elastohydrodynamic Lubrication Model With Elastic Journal And Sleeve, *Journal of Tribology, Transactions of the ASME*, v 122, n 1 (Jan 2000) p 94-102. ISSN: 0742-4787, Fairfield, NJ, USA
17. Bonneau, D., Guines, D., Frene, J. & Toplosky, J. (1995) EHD analysis, including structural inertia effects and a mass conserving cavitation model. *ASME J. Tribology*, Vol. 117, p. 540
18. Brajdic-Mitidieri, P., Gosman, A.D., Ioannides, E., Spikes, H.A. (2005), CFD analysis of a low friction pocketed pad bearing. *Transactions of the ASME. Journal of Tribology*. Vol. 127, 4, pp. 803-12, Oct. 2005
19. Braun, M.J. and Hendricks, R. (1981) An experimental investigation of the vaporous/gaseous cavity characteristics of an eccentric journal bearing. *ASLE Trans.*, Vol. 27, No. 1, pp. 1-14
20. Brewe David E. and Jacobson Bo. O. (1987) The effect of vibration amplitude on vapour cavitation in journal bearings. *Wear : (Volume 115, Issues 1-2) p. 63*
21. Brewe, D.E. (1988) Elasticity Effects on Cavitation in a Squeeze Film Damper Undergoing Noncentered Circular Whirl. *NASA Technical Memorandum* 102392
22. Brewe, D. E. (1989) Elasticity effects on cavitation in a squeeze film damper undergoing non-centered circular whirl. *Wear*, Volume 130, Issue 1, Pages 69-80
23. Brewe, D.E., Ball, J.H., Khonsari, M.M. (Editors). (1990) Current Research in Cavitating Fluid Films. *NASA Technical Memorandum* 103184
24. Brunetiere,N., Tournerie,B. (2007) Finite element solution of inertia influenced flow in thin fluid films. *Journal of Tribology* 129 (4), pp. 876-886
25. Cameron, A. (1949) The Full Journal Bearing. *Proc. Instn. Mech. Engrs.* Vol. 161, p. 73-79
26. Cameron, A., Wood, W.L. (1949) The Full Journal Bearing. *Proc. Instn. Mech. Engrs.* Vol. 161, p. 59-72

27. Castle, R.C., Bovington, C.H. The Behaviour of Friction Modifiers Under Boundary and Mixed EHD Conditions
28. Chamniprasart, K., Al-Sharif, A., Rajagopal, K. R., Szeri, A. Z. (1993) Lubrication With Binary Mixtures: Bubbly Oil. *Trans. ASME, Journal of Tribology*, Vol. 115, pp. 253-260, April 1993
29. Chow, L.S.H. and Cheng, H.S. (1976) The effect of surface roughness on average film thickness between lubricated rollers. *Journal of Lubrication Technology, Trans. ASME Series F*, Vol. 98, 1976, p.117.
30. Christensen, H., and Tonder, K. (1973) The hydrodynamic lubrication of rough journal bearings. *Journal of Lubrication Technology, Trans. ASME Series F*, Apr. 1973, p.166
31. Christopherson, D.G. (1941) A new mathematical method for the solution of film lubrication problems. *Proc. I.Mech.E.*, vol. 146, p.126
32. Christopherson, D.G. (1941) A new mathematical method for the solution of film lubrication problems. *Proc. I.Mech.E.*, vol. 146, p.126
33. Conway-Jones, J.M., Jones, G.J., Kendrick, M. (1983) Crankshaft Bearings: Advances In Predictive Techniques And Measurements In Engines, *International Congress on Combustion Engines -1983*, p 263-283 Conference: 15th International Congress on Combustion Engines, Paris
34. Cupillard,S., Glavatskih,S., Cervantes,M.J. (2008) Computational fluid dynamics analysis of a journal bearing with surface texturing. *Proceedings of the Institution of Mechanical Engineers, Part J: Journal of Engineering Tribology* 222 (2), pp. 97-107
35. Dhunput, A., Teodorescu, M., Arcoumanis, C. 2007 Investigation of cavitation development in the lubricant film of piston-ring assemblies Third International Conference on Optical and Laser Diagnostics. *Journal of Physics: Conference Series* 85 (2007) 012005, IOP Publishing.
36. Dowson, D, Taylor, CM & Miranda, AAS. (1985) The prediction of liquid film journal bearing performance with consideration of lubricant film reformation. Part 1: theoretical results. *Proc Instn Mech Engrs Vol 199 C2*, p95-102
37. Dowson, D, Taylor, CM & Miranda, AAS. (1985) The prediction of liquid film journal bearing performance with consideration of lubricant film reformation. Part 2: experimental results. *Proc Instn Mech Engrs Vol 199 C2*, p103-111
38. Dowson, D. (1998) *History of Tribology*. Professional Engineering Publishing Ltd., London, ISBN 1 86058 070 X
39. Dowson, D., Taylor, C.M. (1974) Fundamental aspects of cavitation in bearings. *Proceedings of the 1st Leeds-Lyon Symposium on Tribology (Eds.*

- Dowson, D., Godet, M., Taylor, C.M.), Leeds, Sept. 1974, Paper 1(iii), pp. 15-26
40. DuBois, G. B., Ocvirk, F.W. (1955) *Analytical Derivation and Experimental Evaluation of Short Bearing Approximation for Full Journal Bearings, Report 1157*, National Advisory Committee for Aeronautics
 41. Duffy, J.E. (1994) *Modern Automotive Technology*, Goodheart-Wilcox ISBN 0-87006-043-0, 1994
 42. Durany, J., Pereira, J., Varas, F. (2008) Numerical solution to steady and transient problems in thermohydrodynamic lubrication using a combination of finite element, finite volume and boundary element methods. *Finite Elements in Analysis and Design* 44 (11), pp. 686-695
 43. Dyson, A. (1974) Air entrainment and boundary conditions in hydrodynamic lubrication. *Proceedings of the 1st Leeds-Lyon Symposium on Tribology* (Eds. Dowson, D., Godet, M., Taylor, C.M.), Leeds, Sept. 1974, Paper 2(iii), pp. 43-51
 44. Einstein, A. (1906) Eine neue Bestimmung der Molekul-Dimension. *Ann. Physik*, Vol. 19, p.289
 45. Elrod, H.G. (1979) A General Theory for Laminar Lubrication with Reynolds Roughness. *Trans. ASME, J Lubr Tech* Vol. 101, pp 8-14
 46. Elrod, H.G. (1981) A Cavitation Algorithm, *Trans. ASME, J Lubr Tech* Vol. 103, pp 350-354, July 1981
 47. Elrod, H.G., Adams, M.L. (1974) A computer program for cavitation and starvation problems. *Proceedings of the 1st Leeds-Lyon Symposium on Tribology* (Eds. Dowson, D., Godet, M., Taylor, C.M.), Leeds, Sept. 1974, Paper 2(ii), pp. 37-41
 48. Estupiñan, E.A., Santos, I.F. (2009) Linking rigid multibody systems via controllable thin fluid films. *Tribology International* 2009: 42(10) 1478-1486
 49. Ettles, C.M.M. (1974) Contribution to the Discussion on Session 1. *Proceedings of the 1st Leeds-Lyon Symposium on Tribology* (Eds. Dowson, D., Godet, M., Taylor, C.M.), Leeds, Sept. 1974, Discussion on session 1, p. 27
 50. Evans, C. R., Johnson, K. L. (1986) The rheological properties of elastohydrodynamic lubricants. *Proc. IMechE, Vol. 200, No. C5, pp. 303-312*
 51. Evans, C. R., Johnson, K. L. (1986) Regimes of traction in elastohydrodynamic lubrication. *Proc. IMechE, Vol. 200, No. C5, pp. 313-324*
 52. Evans, H.P., Snidle, R.W. (1978) Towards a Refined Solution of the Isothermal Point Contact Elasto-hydrodynamics Problem, *Int. Conf. of Fundamentals of Tribology*, MIT, Cambridge, Mass.

53. Fantino, B., Godet, M., Frene, J. (1983) Dynamic Behaviour of an Elastic Connecting-Rod Bearing - Theoretical Study. *SAE/SP-539 Studies of Engine Bearings and Lubrication*, Paper No. 83037, 1983, pp.23-32
54. Felter, C.L. (2008) Numerical simulation of piston ring lubrication. *Tribology International* 41 (9-10), pp. 914-919
55. Feng,N., Hahn, E., Hu,W., Zhang,N. (2008) Effect of cavitation on identification of the configuration state of statically indeterminate rotor bearing system. *Institution of Mechanical Engineers - 9th International Conference on Vibrations in Rotating Machinery 2*, pp. 861-870
56. Floberg, L. (1974) Cavitation boundary conditions with regard to the number of streamers and tensile strength of the liquid. *Proceedings of the 1st Leeds-Lyon Symposium on Tribology (Eds. Dowson, D., Godet, M., Taylor, C.M.)*, Leeds, Sept. 1974, Paper 2(i), pp. 31-35
57. Forstner, C. and Struwe, F.J. (2004) Bearing Cavitation Analysis and Prevention. *CIMAC Congress 2004*, Paper 111, Kyoto
58. Frankel, A. (1946) Calculation of the Performance Characteristics of Plain Bearings. *The Engineer's Digest*, 7, pp133-138, 163-166
59. Gandjalikhan Nassab,S.A., Maneshian,B. (2007) Thermohydrodynamic analysis of cavitating journal bearings using three different cavitation models. *Proceedings of the Institution of Mechanical Engineers, Part J: Journal of Engineering Tribology* 221 (4), pp. 501-513
60. Gear, C. W., Kevrekidis, I. G. (2003) Computing in the Past with Forward Integration
61. Goenka, P.K. & Oh, K.P. (1986) An optimum connecting rod design study. *Trans ASME, J. Tribology*, Vol. 108, p. 487
62. Greenwood, J.A. & Tripp, J.H. (1971) The Contact of Two Nominally Flat Rough Surfaces, *Proc IMechE* Vol 185 48/71 pp 625 – 633
63. Gumbel, L. (1914) Monatsblatter Berlin Bezirksver. *V.D.I.*
64. Gurr,C., Lloyd,G., Rulfs,H. (2008) Influence of transient operating conditions on propeller shaft bearings. *Proceedings of the Institute of Marine Engineering, Science and Technology. Part A, Journal of Marine Engineering and Technology* , no. A12, pp. 3-11. Sept. 2008
65. Guzelby I.H. (1992) Finite and Boundary Element Analysis of Elasto-plastic Finite Strain Contact Problems, Cranfield Thesis - PhD
66. Halling J. (1989) *Principles of Tribology*, Macmillan, ISBN 0-333-24686-1, 1989

67. Halling, J. & Nuri, K. A. (1985) The elastic contact of rough surfaces and its importance in the reduction of wear. *Proc Instn Mech Engrs Vol 199 C2*, p139-144
68. Hartinger, M., Gosman, D., Ioannides, S., Spikes, H. (2008) Thermal effects in an elasto-hydrodynamic line contact using a CFD approach, 2007. *Proceedings of the ASME/STLE International Joint Tribology Conference, IJTC 2007 PART A*, pp. 179-180
69. Hayward, A.T. (1961) The viscosity of bubbly oil. *NE.L. Fluids Report No. 99*
70. Hellinger, W., Raffel, H.Ch., Rainer, G.Ph. (1997) Numerical Methods to Calculate Gear Transmission Noise. 97NV205
71. Hirani, H., Athre, K., Biswas, S. (1999) Dynamically Loaded Finite Length Journal Bearings: Analytical Method of Solution. *Trans. ASME, Journal of Tribology, Vol. 121*, pp.844-852
72. Hirata, Y., Akita, T., Arnold, S., Ohkita, A. (1992) New RH.3 Series Turbocharger For Diesel Engine With 400-2000kW Turbo Rating, *SAE Technical Paper Series*, 1992, Pages 1-6
73. Holt, C., Andrés, L.S., Sahay, S., Tang, P., Rue, G.L., Gjika, K. (2003) Test Response of a Turbocharger Supported on Floating Ring Bearings - Part I: Assessment of Subsynchronous Motions, *Proceedings of the ASME Design Engineering Technical Conference*, Volume 5 B, 2003, Pages 969-974
74. Istenes, R. R. A Comparison of Simulation and Engine Test Data for Various Skirt Profile and Cam Shapes
75. Jacobson, B.O. and Floberg, L. (1957) The Finite Journal Bearing Considering Vaporization, Chalmers University of Technology Report No. 190
76. Jacobson, B. O. and Hamrock, B. J. (1983) Vapour cavitation in dynamically loaded journal bearings. *Proc. Inst. Mech. Eng. London C206 (1983)*, pp. 133-140.
77. Jang, J.Y., Khonsari, M.M. (2008) Linear squeeze film with constant rotational speed. *Tribology Transactions* 51 (3), pp. 361-371
78. Kageyama, H. et al. (2000) Study of the Contact Pressures and Deformations of Piston Skirt in Gasoline Engine. *SAE Paper 2000-01-1784*
79. Kecskemethy, A. (2005) Application of Lie-Group, Symbolical and Object Oriented Methods to the Simulation and Design of Complex Mechanical Systems. *ASME IDETC 2005 Conference Keynote Speech*
80. Knoll, G., Schoenen, R., Wilhelm, K. (1997) Full Dynamic Analysis Of Crankshaft And Engine Block With Special Respect To Elasto-hydrodynamic Bearing Coupling, American Society of Mechanical Engineers, Internal

Combustion Engine Division (Publication) ICE, v 3 -1997 p 1-8 *Conference: Proceedings of the 1997 Spring Technical Conference of the ASME Internal Combustion Engine Division* (code 46895)Date: Apr 27-30 199

81. Kohno, K., Takahashi, S., Saki, K. (1994) Elasto-Hydrodynamic Lubrication Analysis Of Journal Bearings With Combined Use Of Boundary Elements And Finite Elements, *Engineering Analysis with Boundary Elements*, v 13, n 3 -1994, p 273-281 ISSN: 0955-7997, Elsevier Applied Science Publ Ltd., Oxford
82. Krasser, J., Laback, O., Loibnegger, B. & Priebisch, H.H. (1994) Anwendung eines elasto-hydrodynamischen Verfahrens zur Berechnung von Kurbeltriebslagern. *MTZ Motorentechnische Zeitschrift*, 55, pp. 656-663
83. Kudish, I., Kelley, F., Mikrut, D. (1999) Defects Of The Classic Formulation Of A Nonsteady EHL Problem For A Journal Bearing. New Problem Formulation, *Journal of Tribology, Transactions of the ASME*, v 121, n 4 (Oct 1999) p 995-1000 ISSN: 0742-4787, ASME, Fairfield, NJ
84. Kumar, A. (1991) Mass Conservation in Cavitating Bearings: A Finite Element Approach. PhD Dissertation, Cornell University.
85. Kumar, A. and Booker J.F. (1991) A Finite Element Cavitation Algorithm, *Trans ASME, J Lubr Techn*, Vol. 113, pp 276-286, April 1991
86. Kumar, A., Goenka, P.K. & Booker, J.F. (1990) Modal analysis of elasto-hydrodynamic lubrication: a connecting rod application. *ASME J. Tribology*, Vol. 112, p. 524
87. Lahmar, M., Haddad, A., Nicolas, D. (1998) Elasto-hydrodynamic Analysis Of One-Layered Journal Bearings, *Proceedings of the Institution of Mechanical Engineers, Part J: Journal of Engineering Tribology*, v 212, n J3 -1998, p 193-205, ISSN: 1350-6501, Prof Eng Publ Ltd., London
88. Landenberger A (1995) Finite Element versus Boundary Element for Elastic Contact Problems Using Gap Finite Elements. *Cranfield Thesis – MSc*
89. Landenberger A. (1998) The Coupling of FEM and BEM for the Solution of Elastoplasticity and Contact Problems. *Cranfield Thesis – PhD*
90. Landenberger, A, El-Zafrany, A. (1996) Coupling of Gap Finite Elements and Boundary Elements for Elastic Contact Problems. *Proceedings of the Eighteenth World Conference on the Boundary Element Method*, Braga, Portugal, 1996, p373-386
91. Lang, J.R. (1997) Kolben Zylinder Dynamik, *Fortschrittsberichte Strukturanalyse und Tribologie*, ISBN 3-88122-904-3, RWTH, Aachen.
92. Lechtape-Grueter, R. (1995) Kolbenringdynamik, *Fortschrittsberichte Strukturanalyse und Tribologie*, ISBN 3-88122-815-2, RWTH, Aachen

93. Li, C-H, Rohde, S. M. (1981) On the Steady State and Dynamic Performance Characteristics of Floating Ring Bearings. *Trans. ASME, Journal of Lubrication Technology*, Vol. 103, pp. 389-397, July 1981
94. Lin, J-R 1997 Squeeze film characteristics of long partial journal bearings lubricated with couple stress fluids *Tribology International*, Vol. 30, No. 1, pp. 53-58
95. Liu, D., Zhang, W., Zheng, T. (2008) A simplified one-dimensional thermal model for journal bearings. *Journal of Tribology* 130 (1), art. no. 011003
96. Lloyd, T., McCallion, H. (1968) Recent Developments in Fluid Film Lubrication Theory. *Proc. IMechE, Part A, Journal of Power and Energy*, Vol. 182, Part 3A, pp. 36-50
97. Ma, M-T. & McLuckie, I.R.W. (2001) An EHD Study Of A Connecting Rod Big End Bearing Including Elasticity And Inertia Effects Of The Bearing Structure, *World Tribology Conference 2001*, Vienna, Austria.
98. Ma, M-T., Taylor, C.M. (1999) A Comparative Thermal Analysis Of The Static Performance Of Different Fixed Profile Bore Plain Bearings, *Proceedings of the Institution of Mechanical Engineers J, Journal of Engineering Tribology*, V 213, J1, pp.13-30, 1999, ISSN 1350-6501
99. Ma, M-T., Offner, G., Loibnegger, B., Pribsch, H. H., McLuckie, I. R. W. (2003) A Fast Approach to Model Hydrodynamic Behaviour of Journal Bearings for Analysis of Crankshaft and Engine Dynamics , *30th Leeds-Lyon Symposium on Tribology*, Lyon, France, 2nd - 5th September 2003
100. Ma, Y-Y. (2007) Comparison of numerical methods for performances of journal bearing lubricated with couple stress fluids. *Shanghai Ligong Daxue Xuebao (Journal of University of Shanghai for Science and Technology)*. Vol. 29, no. 1, pp. 95-98. Feb. 2007
101. MacInnes, H., Johnston, A.E (1982) Comparison Of Power Loss Between Full Floating And Semi-Floating Turbocharger Bearings., *I Mech E Conference Publications* (Institution of Mechanical Engineers), 1982, Pages 157-164
102. Martin, S. (2008) Influence of multiscale roughness patterns in cavitated flows: Applications to journal bearings. *Mathematical Problems in Engineering* 2008, art. no. 439319
103. McBeath, S. (2010) The Future of CFD? *Racecar Engineering*, Vol. 20 No. 6, pp.61-64
104. McIvor, J.D.C., Fenner, D.N. (1989) Finite Element Analysis of Dynamically Loaded Flexible Journal Bearings: A Fast Newton-Raphson Method. *Trans. ASME, Journal of Tribology* Vol. 111, pp 597-604

105. McLuckie, I. & Barrett, S. (2005a) V8 Engine Bearing Dynamics - High Performance With Minimum Friction, *Proceedings of the ASME IDETC/CIE Conference*, September 24-28, 2005. Long Beach California.
106. McLUCKIE, Ian. (2003) From the engine to the vehicle and beyond. *NAFEMS world congress 2003*. May 27 - 31 Orlando, Florida, USA.
107. McLuckie, I. (1990) Instability studied of an 'O'-ring flexibly supported gas bearing mounted cool air unit. Cranfield PhD Thesis.
108. McLUCKIE, Ian & BARRETT, Scott. (2005b) Objective Faster real world solutions. *NAFEMS World Congress 2005 Malta*.
109. McLuckie I.R.W., Barrett D.J.S., Ma M-T. (2000) A valvetrain design analysis comparative study on three current diesel engines. *The First Virtual Engine Congress*, Munich. Oct. 2000.
110. McLuckie, I., Barrett, S. & Teo, B-K. (2006) Plain & Full Floating Bearing Simulations With Rigid Shaft Dynamics, Paper submitted to the *8th International Conference on Turbochargers and Turbocharging*, 17th - 18th May 2006, London
111. Mehenny, D.S., Taylor, C.M., Jones, G.J., Xu, H. (1997) The Influence Of Circumferential Waviness Of The Journal On The Lubrication Of Dynamically Loaded Journal Bearings, *SAE Transactions: Journal of Materials & Manufacturing*, vol. 106, no. 5, pp. 257-265, 1997, ISSN 0096-736X
112. Meili, S., Zhiming, Z., Xiaoyang, C., Wen, W., Kai, M., Sun, D.C. (2008) Experimental study of cavitation in an oscillatory oil squeeze film. *Tribology Transactions* 51 (3), pp. 341-350
113. Miao, J-M., Chang, B.-H., Chen, P-H. (2008) Numerical predictions of a flow field in a hydrodynamic journal bearing with herringbone microgrooves. *Progress in Computational Fluid Dynamics* 8 (7-8) pp. 486-495
114. Michell, A.G.M. (1905) *Lubrication*. London
115. Miller, D.S. (1996), *Internal Flow Systems*, BHR Group Ltd., Cranfield
116. Mokhiamer, U.M., Crosby, W.A., El-Gamal, H.A. (1999) Study Of A Journal Bearing Lubricated By Fluids With Couple Stress Considering The Elasticity Of The Liner, *Wear*, v 224, n 2 (Feb 1999) p 194-201, ISSN: 0043-1648, Elsevier Science S.A., Lausanne
117. Mokhtar, M.M.A., El-Butch, A.M.A., Ibrahim, I.M. (2005) Adoption of Floating-Ring Bearing Design in Automotive Applications, *SAE Technical Paper 2005-01-3783*, Powertrain and Fluid Systems Conference and Exhibition, San Antonio, October 2005
118. Mynott, C. (2005). NAFEMS Seminar, Business Benefits of Simulation. 1st July 2005, Salford University. Presentation available on World Wide Web at

http://nafems.org/publications/downloads/seminars/Business_Benefits_UK_July2005_02Mynott.pdf

119. NACSA, J., BUENO, R., ALZAGA, A. and KOVA, G.L.' CS. (2005) Knowledge management support for machine tool designers using expert enablers. *International Journal of Computer Integrated Manufacturing*, Vol. 18, No. 7, October - November 2005, 561 - 571
120. Nagy, D. (2005) From Hero Mountain to Payback Meadow: Pursuing the Strategic Business Benefits of CAE in Design Automation. ASME IDETC Conference Keynote Speech
121. Noda, T., Nozawa, Y., Yamamoto, M., Yamada, K. (1995) Study On The Movement Of A Piston Pin (Measurements Of Axial Movement And Load Of Piston Pin, *Transactions of the Japan Society of Mechanical Engineers*, Part C, Volume 61, Issue 592, December 1995, Pages 4744-4750
122. Offner, G., Krasser, J., Laback, O., Pribsch, H. H. (2001) Simulation of multi-body dynamics and elasto-hydrodynamic excitation in engines especially considering piston-liner contact. *Proc. IMechE, Vol. 215 Part K*, pp. 93 - 102
123. Oh, K.P., Goenka, P.K. (1985) The Elasto-hydrodynamic Solution of Journal Bearings Under Dynamic Loading. *Trans. ASME, Journal of Tribology* Vol. 107, pp 389-395
124. Okamoto, Y., Hanahashi, M., Katagiri, T. (1999) Theoretical analysis of bearing considering elastic deformation - effects of the housing stiffness and bearing length on bearing performance. *JSAE Review* v 20 n 2 p 203-209 ISSN: 0389-4304, Elsevier Science B.V.
125. Okamoto, Y., Kitahara, K., Ushijima, K., Aoyama, S., Xu, H., Jones, G.J. (2000) Study for wear and fatigue on engine bearings by using EHL analysis. *JSAE Review* v 21 n 2 p 189-196 ISSN: 0389-4304, Elsevier Science B.V. 2000.
126. Okamoto, J., Koizumi, S. (1985) Lubrication Between Ball Bearing Bore And Shaft With Clearance Fit (2) - Behavior Of Inner Ring In Full-Floating Conditions., *Journal of JSLE*, International edition, Issue 6, 1985, Pages 141-144
127. Olsson, K.O. (1965) Cavitation in Dynamically Loaded Journal Bearings, Chalmers University of Technology Report No. 308
128. Orcutt, F. K., Ng, C. W. (1968) Steady-State and Dynamic Properties of the Floating-Ring Journal Bearing. *Trans. ASME, Journal of Lubrication Technology*, pp. 243-253, January 1968
129. Ozasa, T. (2006) Mass conserving elasto-hydrodynamic lubrication model of engine bearings having regular striations. *Nippon Kikai Gakkai Ronbunshu C*

Hen (Transactions of the Japan Society of Mechanical Engineers Part C) (Japan). Vol. 18, no. 9, pp. 3030-3037. Sept. 2006

130. Ozasa, T. (2008) Surface roughness and pressure effect on viscosity in elasto-hydrodynamic lubrication model of engine bearings (Friction). *Transactions of the Japan Society of Mechanical Engineers, Part C* 74 (4), pp. 1034-1041
131. Ozasa, T., Noda, T., Konomi, T. (1997) Elasto-hydrodynamic Lubrication Model Of Connecting Rod Big-End Bearings: Application To Real Engines, *Journal of Tribology, Transactions of the ASME*, v 119, n 3 (July 1997), p 568-578 ISSN: 0742-4787, ASME, New York
132. Pan, C.H.T., Kim, T.H., Rencis, J.J. (2008) Rolling stream trails-an alternative cavitation analysis. *Proceedings of the ASME/STLE International Joint Tribology Conference, IJTC 2007 PART B*, pp. 1009-1011
133. Patir, N. (1978) Effects of Surface Roughness on Partial Film Lubrication Using an Average Flow Model Based on Numerical Simulation. PhD Dissertation, Northwestern University.
134. Patir, N. and Cheng, H.S. (1978) An Average Flow Model for Determining Effects of Three Dimensional Roughness on Partial Hydrodynamic Lubrication, *Trans. ASME, J Lubr Techn* Vol 100, pp 12 - 17, Jan 1978
135. Peklenik, J. (1968) New developments in surface characterisation and measurement by means of random process analysis. *Proc. Instn. Mech. Engrs.*, Vol. 182, Part 3K, 1967-68, p. 108
136. PISDYN helps MAHLE Metal Levy avoid Liner Cavitation (2009) http://ricardo.com/Documents/IA/Software/SCAEdocs/SoftwareCAE_Q2_2009.pdf. Accessed April 2009.
137. Pinkus, O., Lund, J. W. (1981) Centrifugal Effects in Thrust Bearings and Seals Under Laminar Conditions. *Trans. ASME, Journal of Lubrication Technology*, Vol. 103, pp. 126-136, January 1981
138. Poynton, W.A., Xu, H., Wang, D.C., Warriner, F. (1998) Effect of oil grooves on the performance of the big end bearing of a medium speed diesel engine. *American Society of Mechanical Engineers Internal Combustion Engine Division (Publication) ICE* v 31 n 2 -1998 p 1-7 Conference: Proceedings of the 1998 Fall Technical Conference of the ASME Internal Combustion Engine Division. Part 2, Clymer, NY
139. Press, W.H., Teukolsky, S.A., Vetterling, W.T., Flannery, B.P. (1992) *Numerical Recipes in FORTRAN: The Art of Scientific Computing*, 2nd Edition, Cambridge University Press. ISBN 0-521-43064-X
140. Prusha, S. (2005) Challenges in Early-Phase Complex System Design. *ASME IDETC 2005 Conference Keynote Speech*

141. Ramos, E. B., Jimenez, L., Martinez, F. J. (1999) From Concept to Practice, 4th Ricardo Software International Conference, Detroit, March 5th, 1999
142. Rao, T.V.V.L.N., Sawicki, J. T. (2005) Stability analysis of a rough journal bearing considering cavitation effects. *Transactions of the ASME. Journal of Tribology* Jan. 2005 127 1 112-119
143. Rao, T.V.V.L.N., Sawicki, J. T. (2004) Stability characteristics of herringbone grooved journal bearings incorporating cavitation effects. *Transactions of the ASME. Journal of Tribology* April 2004 126 2 281-7
144. Reason, B. R., Narang, I. P. (1982) Rapid Design and Performance Evaluation of Steady State Journal Bearings - A Technique Amenable to Programmable Hand Calculations. *ASLE Transactions*, Vol. 25, pp. 429-444
145. Reason, BR & Siew, AH. (1985) A refined numerical solution for the hydrodynamic lubrication of finite porous journal bearings. *Proc Instn Mech Engrs* Vol 199 C2 p85-93
146. Reason, R.B., Siew, A. H. (1982) A numerical solution for the design and performance evaluation of journal bearings with misalignment. *IMEchE Conference Publications*, Paper C2/82, pp. 77-81
147. Reinhardt, E., Lund, J. W. (1975) The Influence of Fluid Inertia on the Dynamic Properties of Journal Bearings. *Trans. ASME, Journal of Lubrication Technology*, pp.159-167, April 1975
148. Reynolds, O. (1886) On the Theory of Lubrication. *Phil. Trans. Roy. Soc.* Vol.177, p. 157, 1886
149. Rhow, S.K. and Elrod, H.G. (1974) The effects on bearing load carrying capacity of two-sided striated roughness. *Journal of Lubrication Technology, Trans. ASME Series F*, Vol. 96, 1974, p.554
150. Rodkiewicz, C. M., Yang, P. (1995) Proposed TEHL solution system for the thrust bearings inclusive of surface deformations. *Tribology Transactions, STLE*, Vol. 38(1995), 1, 75-85
151. Rohde, S. M., Ezzat, H. A. (1980) Analysis of Dynamically Loaded Floating-Ring Bearings for Automotive Application. *Trans. ASME, Journal of Lubrication Technology*, Vol. 102, pp. 271-277, July 1980
152. Rouleau, W.T., Steiner, L.I. (1974) Hydrodynamic Porous Journal Bearings Part 1 - Finite Full Journal Bearings. *J. Lubric. Tech., Trans. ASME*, 1974, 96, 346-353
153. Sahlin, F, Almqvist, A, Larsson, R, Glavatskih, S. (2007b) A cavitation algorithm for arbitrary lubricant compressibility . *Tribology International*, Volume 40, Issue 8, pp. 1294-1300

154. Sahlin, F., Almqvist, A., Larsson, R., Glavatskih, S. (2007a) Rough surface flow factors in full film lubrication based on a homogenization technique. *Tribology International*, Vol. 40, No. 7, pp. 1025-1034, July 2007
155. San Andrés, L., Kerth, J. (2004) Thermal Effects On The Performance Of Floating Ring Bearings For Turbochargers, *Proceedings of the Institution of Mechanical Engineers, Part J: Journal of Engineering Tribology* Volume 218, Issue 5, October 2004, Pages 437-450
156. San Andres, L., Yang, Z., Childs, D. W. (1993) Thermal effects in Cryogenic Liquid Annular Seals - Part 2: Numerical Solution and Results. *Trans. ASME, Journal of Tribology*, Vol. 115, pp. 277 - 284, April 1993
157. Savage, M.D. (1974) Cavity Instability. *Proceedings of the 1st Leeds-Lyon Symposium on Tribology (Eds. Dowson, D., Godet, M., Taylor, C.M.)*, Leeds, Sept. 1974, Paper 2(iv), pp. 53-54
158. Schweizer, B. (2008) ALE formulation of Reynolds fluid film equation. *ZAMM Zeitschrift für Angewandte Mathematik und Mechanik* 88 (9), pp. 716-728
159. Semin, A.R.I., Rosli, A.B. (2009) Effect of Diesel Engine Converted to Sequential Port Injection Compressed Natural Gas Engine on the Cylinder Pressure vs Crank Angle in Variation Engine Speeds. *American J. of Engineering and Applied Sciences* 2 (1): 154-159, 2009, ISSN 1941-7020
160. Sharda, H. B., Chandrawat, H. N., Bahl, R.C. (1993) EHD Analysis Of A Misaligned Journal Bearing, *International Journal of Mechanical Sciences*, v 35, n 5 (May 1993) p 415-423, ISSN: 0020-7403
161. Shaw, M.C. and Macks, E.F. (1949) *Analysis and Lubrication of Bearings*, 1st Ed., McGraw-Hill, NY, pp379 - 388
162. Shaw, M.C., Nussdorfer, T.J. Jr. (1947) An Analysis Of The Full-Floating Journal Bearing, NACA Report 866 Jan 1947, downloaded from <http://naca.larc.nasa.gov/reports/1947/naca-report-866/>
163. Shi, Fanghui (2002) An implicit finite element cavitation algorithm. *Computer Modeling in Engineering & Sciences* 2002 3 4 507-15
164. Shi, F., Wang, Q. (1997) Mixed-TEHD Model For Journal-Bearing Conformal Contacts - Part I: Model Formulation And Approximation Of Heat Transfer Considering Asperity Contact, *American Society of Mechanical Engineers (Paper)*, (1997)Conference: *Proceedings of the 1997 Joint ASME/STLE/IMEchE World Tribology Conference* Sep 8-12 1997, London, ISSN: 0402-1215, ASME, New York
165. Shyu, S-H., Jeng, Y-R. and Li, F. (2008) A Legendre Collocation method for thermohydrodynamic journal-bearing problems with Elrod's cavitation algorithm. *Tribology International* 41 (6), pp 493-501

166. Skjoedt, M., Butts, R., Assanis, D.N., Bohac, S.V. (2008) Effects of oil properties on spark-ignition gasoline engine friction. *Tribology International* 41 (2008) 556–563
167. Smalley, A.J., Lloyd, T., Horsnell, R., and McCallion, H. (1966) A Comparison of the Performance Predictions for Steadily Loaded Journal Bearings. *Proc. Inst. Mech. Engrs.*, 180, Pt. 3 k, pp 133-144
168. Sommerfeld, A. (1904) Zur hydrodynamischen Theorie der Schmiermittelreibung. *Z. Math. Phys.*, vol. 50, p.97
169. Southwell, R.V. (1946) *Relaxation Methods in Theoretical Physics*
170. Stieber, W. (1933) Das Schwimmlager. *V.D.I.*
171. Sun, D.C., Wen, W., Zhiming, Z., Xiaoyang, C., Meili, S. (2008) Theory of cavitation in an oscillatory oil squeeze film. *Tribology Transactions* 51 (3), pp. 332-340
172. Sun, J., Gui, C. (2007) Effect of lubrication status of bearing on crankshaft strength. *Journal of Tribology* 129 (4), pp. 887-894
173. Sun, M., Lin, X. (1992) Numerical Solution Of The Three-Dimensional Elastohydrodynamic Lubrication For Heavily-Loaded Finite Journal Bearings, *Journal of Hydrodynamics*, v 4, n 4 (Oct 1992) p 78-87, ISSN: 1001-6058
174. Suzuki, S., Noda, T., Ozasa, T., Kikuchi, T., Kanoh, T. (2008) Analysis of reducing oil flow rate in the main journal bearings of engines. *Transactions of the Japan Society of Mechanical Engineers, Part B* 2008: 74(7) 1472-1477
175. Swales, P.D. (1974) A review of cavitation phenomena in engineering situations. *Proceedings of the 1st Leeds-Lyon Symposium on Tribology* (Eds. Dowson, D., Godet, M., Taylor, C.M.), Leeds, Sept. 1974, Paper 1(i), pp. 3-9
176. Swift, H.W. (1931) The stability of lubricating films in journal bearings. *J. Inst. Engrs.* 233(Pt. 1) 267
177. Tao, H., Duan, H., Yang, J. (2004) Finite Element Analysis On The Characteristics Of Radical-Thrust Hybrid Floating Ring Bearing, *Run Hua Yu Mi Feng/Lubrication Engineering*, Issue 6, November 2004
178. Tanaka, M., Hori, Y. (1972) Stability Characteristics of Floating Bush Bearings. *Trans. ASME, Journal of Lubrication Technology*, pp. 248-259, July 1972
179. Taylor, R.I. (1999) The Inclusion of Shear Thinning in the Short Bearing Approximation, *Proc IMechE* Vol 213 Part J pp 35 – 46
180. Timperley, H.N.V. (1974) The tensile strength of liquids. *Proceedings of the 1st Leeds-Lyon Symposium on Tribology* (Eds. Dowson, D., Godet, M., Taylor, C.M.), Leeds, Sept. 1974, Paper 1(ii), pp. 11-13

181. Ting, L.L. & Mayer, J.E. (1974) Piston ring lubrication and cylinder bore wear analysis, part1 – theory. *ASME Journal of Lubrication Technology*, 1974, pp. 305-314
182. Tønder, K. (2008) Hydrodynamic pressure generation caused by surface roughness or texture. *Proceedings of the ASME/STLE International Joint Tribology Conference, IJTC 2007 PART B*, pp. 1073-1075
183. Torii, H., Nakakubo, T., Nakada, M. (1992) Elastohydrodynamic Lubrication Of A Connecting Rod Journal Bearing In Consideration Of Shapes Of The Bearing, *SAE Special Publications*, n 919 -1992, p 33-38, Paper number: 920485, Conference: International Congress and Exposition, Feb 24-28 1992, Detroit, ISSN: 0099-5908 ISBN: 1-56091-236-7
184. Tower, B. (1883) First Report on Friction Experiments. *Proc. Instn. Mech. Engrs*, Vol. 34, p.632
185. Tower, B. (1885) Second Report on Friction Experiments. *Proc. Instn. Mech. Engrs*, Vol. 36, p.58
186. Tripp, J. H. (1983). Surface Roughness Effects in Hydrodynamic Lubrication: The Flow Factor Model. *Trans. ASME, Joournal of Lubrication Technology*, Vol. 105, pp. 458-465
187. Trippett, R.J., Li, D.F. (1984) High-Speed Floating-Ring Bearing Test And Analysis, *ASLE Transactions*, Volume 27, Issue 1, January 1984, Pages 73-81
188. Trippett, R.J. (1986) Measured And Predicted Friction In Floating-Ringbearings, *SAE Technical Paper 860075*. SAE International Congress and Exposition, Detroit, Feb. 1986
189. Turaga, R., Sekhar, A.S., Majumdar, B.C. (1999) Unbalance Response and Stability Analysis of a Rotor Supported on Hydrodynamic Journal Bearings with Rough Surfaces, *Proc. IMechE* Vol.213 Part J, pp 31 - 34
190. Tzeng, S.T. and Saibel, E. (1967) Surface roughness effect on slider bearing lubrication. *ASLE Trans.*, Vol. 10, 1967, p.334
191. van der Tempel, L., Moes, H., Bosma, R. (1985) Numerical Simulation of Dynamically Loaded Flexible Short Journal Bearings. *Trans. ASME, Journal of Tribology* Vol. 107, pp 396-401
192. van Ostayen, R.A.J., van Beek, A. (2009) Thermal modelling of the lemon-bore hydrodynamic bearing. *Tribology International* 42 (1), pp. 23-32
193. Wang, Q., Shi, F., (1997) Mixed-TEHD Model For Journal-Bearing Conformal Contact - Part II: Contact, Film Thickness And Performance Analyses, *American Society of Mechanical Engineers (Paper), Proceedings of the 1997 Joint ASME/STLE/IMEchE World Tribology Conference* Sep 8-12 1997, London, ISSN: 0402-1215, ASME, New York,

194. Wang, Y., Wang, Q. J., Lin, C. (2002) Mixed lubrication of coupled journal-thrust-bearing systems. *Computer Modeling in Engineering & Sciences* 2002 3 4 517-30
195. Wang, Y., Wang, Q. J., Lin, C. (2003) Mixed lubrication of coupled journal-thrust-bearing systems including mass conserving cavitation. *Transactions of the ASME. Journal of Tribology* Oct. 2003 125 4 747-55
196. Wang, J.K., Khonsari, M.M. (2008) Effects of oil inlet pressure and inlet position of axially grooved infinitely long journal bearings. Part II: Nonlinear instability analysis. *Tribology International* 41 (2), pp. 132-140
197. Wang, J.K., Khonsari, M.M. (2008) Effects of oil inlet pressure and inlet position of axially grooved infinitely long journal bearings. Part I: Analytical solutions and static performance. *Tribology International* 41 (2), pp. 119-131
198. Wang, N., Tsai, C-M., Cha, K-C. (2009) A study of parallel efficiency of modified direct algorithm applied to thermohydrodynamic lubrication. *Journal of Mechanics*. Vol. 25, no. 2, pp. 143- 150. June 2009
199. Wang, X., Su, W-H. (2009) A numerical study of cavitating flows in high-pressure diesel injection nozzle holes using a two-fluid model. *Chinese Science Bulletin*, 2009, 54(10), 1655-1662
200. Weimar, H-J. (2002). *Entwicklung eines laser-optischen Messsystems zur kurbelwinkelaufgeloesten Bestimmung der Oelfilmdicke zwischen Kolbenring und Zylinderwand in einem Ottomotor*. Karlsruhe University, Berlin ISBN 3-8325-0203-3.
201. White, M. F., Chan, S. H. (1992) The Subsynchronous Behavior of Tilting-Pad Journal Bearings. *Transactions of the ASME, Journal of Tribology*, Vol. 114, pp. 167 - 173, January 1992
202. Wilcock, D.F. (1974) Turbulent Lubrication - Its Genesis and Role in Modern Design. *ASME Journal of Lubrication Technology*, 1974, pp. 2-6
203. Wilcock, D.F. (1980) Self-Centering Film Dividers. *ASME Journal of Lubrication Technology*, Vol. 102, 1980, pp. 490-494
204. Wilcock, D.F. (1983a) Load Carrying Efficiency Of Floating Ring Journal Bearings., *Journal Of Lubrication Technology*, Volume 105, Issue 4, October 1983, Pages 605-608
205. Wilcock, D.F. (1983b) Load Carrying Efficiency Of Floating Ring Journal Bearings., *Trans.. ASME J. Lubr. Technol.*, Volume 105, Issue 4, Oct. 1983, Pages 605-614
206. Wu, C. & Zheng, L, (1989) An Average Reynolds Equation for Partial Film Lubrication with a Contact Factor, *Trans. ASME, Journal of Tribology*, Vol 111 pp 188 – 191

207. Xia, Z., Qiao, G., Zheng, T., Zhang, W. (2009) Nonlinear modeling and dynamic analysis of the rotor-bearing system. *Nonlinear Dynamics* 57 (4), pp. 559-577
208. Xu, H. (1996a) Elastohydrodynamic Lubrication in Plain Bearings, *Elastohydrodynamics '96 (Eds. Dowson et al.), Proc. 23rd. Leeds-Lyon Symposium on Tribology*, Leeds, September 1996
209. Xu, H. (1996b) Elastohydrodynamic Analysis Of A Test Rig For Connecting Rod Bearing Simulation, *American Society of Mechanical Engineers Internal Combustion Engine Division ICE v 27-1 -1996 p 7-16, Proceedings of the 1996 18th Annual Fall Technical Conference of the ASME Internal Combustion Engine Division. Part 1*
210. Xu, H., Smith, E.H. (1990) A New Approach To The Solution Of Elastohydrodynamic Lubrication Of Crankshaft Bearings., *Proc. Inst. Mech. Eng.*, vol. 204, no. C3, pp. 187-198
211. Yang, Z., San Andres, L., Childs, D. W. (1993) Thermal effects in Cryogenic Liquid Annular Seals - Part 1: Theory and Approximate Solution. *Trans. ASME, Journal of Tribology*, Vol. 115, pp. 267 - 276, April 1993
212. Yu, Biao and Sawicki, Jerzy T. (2002) Comparison of Mobility Method and Mass Conservation in a Study of Dynamically Loaded Journal Bearings. *International Journal of Rotating Machinery*, 8(1), 71-79, 2002
213. Yuan, Y., Tao, W., Liu, E.A., Barber, G.C., Zou, Q., Guessous, L., Du, Z. (2007) Engine Lubrication System Analysis by Considering Aeration and Cavitation within the Rotating Oil Supply Passage. *Tribology Transactions*, Vol. 50, Issue 1, April 2007, pp.39-49
214. Zenggeya, M., Gadala, M., Segal, G. (2007) Hydrodynamic and thermal behavior of journal bearings using upwind Petrov-Galerkin FEM. *Tribology Transactions* 50 (2), pp. 227-247

APPENDIX A - EQUATIONS FOR SOLUTION OF REYNOLD'S EQUATION

Starting with Reynold's Equation as developed for cylindrical journal bearings:

$$\frac{\partial}{\partial x} \left(h^3 \frac{\partial p}{\partial x} \right) + \frac{\partial}{\partial y} \left(h^3 \frac{\partial p}{\partial y} \right) = 6\eta U \frac{\partial h}{\partial x} + 12\eta V$$

First, we can expand the differentials –

$$\frac{\partial}{\partial x} \left(h^3 \frac{\partial p}{\partial x} \right) = 3h^2 \frac{\partial h}{\partial x} \frac{\partial p}{\partial x} + h^3 \frac{\partial^2 p}{\partial x^2}$$

etc.

and then express the differential equations as difference equations using –

$$\left(\frac{\partial h}{\partial x} \right)_{i,j} = \frac{h_{i+1,j} - h_{i-1,j}}{2\delta x}$$

$$\left(\frac{\partial^2 p}{\partial x^2} \right)_{i,j} = \frac{p_{i+1,j} - 2p_{i,j} + p_{i-1,j}}{(\delta x)^2}$$

etc. for other terms, leading to a final equation of –

$$\begin{aligned} & 3h_{i,j}^2 \left(\frac{h_{i+1,j} - h_{i-1,j}}{2\delta x} \right) \left(\frac{p_{i+1,j} - p_{i-1,j}}{2\delta x} \right) + h_{i,j}^3 \left(\frac{p_{i+1,j} - 2p_{i,j} + p_{i-1,j}}{(\delta x)^2} \right) \\ & + 3h_{i,j}^2 \left(\frac{h_{i,j+1} - h_{i,j-1}}{2\delta y} \right) \left(\frac{p_{i,j+1} - p_{i,j-1}}{2\delta y} \right) + h_{i,j}^3 \left(\frac{p_{i,j+1} - 2p_{i,j} + p_{i,j-1}}{(\delta y)^2} \right) \\ & = 6\eta U_i \left(\frac{h_{i+1,j} - h_{i-1,j}}{2\delta x} \right) + 12\eta V_i \end{aligned}$$

As we will already have a value for $p_{i,j}$ from a previous iteration, we must regard this equation as referring to a new value $\bar{p}_{i,j}$

$$\begin{aligned}
8\bar{p}_{i,j}h_{i,j}^3(\delta x^2 + \delta y^2) &= 3h_{i,j}^2\delta y^2(h_{i+1,j} - h_{i-1,j})(p_{i+1,j} - p_{i-1,j}) + 4h_{i,j}^3\delta y^2(p_{i+1,j} + p_{i-1,j}) \\
&+ 3h_{i,j}^2\delta x^2(h_{i,j+1} - h_{i,j-1})(p_{i,j+1} - p_{i,j-1}) + 4h_{i,j}^3\delta x^2(p_{i,j+1} + p_{i,j-1}) \\
&- 12\eta U_i\delta x\delta y^2(h_{i+1,j} - h_{i-1,j}) - 48\eta V_i\delta x^2\delta y^2
\end{aligned}$$

and the residual $R_{i,j} = p_{i,j} - \bar{p}_{i,j}$.

APPENDIX B – FINITE ELEMENT STIFFNESS AND COMPLIANCE MATRIX CONDENSATION

This appendix is based on an appendix from Barrett (2001)

The commercially available finite element program ABAQUS was used to perform stiffness and mass matrix condensation. The data input patch shown in Appendix xxx caused ABAQUS to perform the condensation.

Starting with the assembled stiffness matrix for the structure, we can consider it to be partitioned into active nodes (those we want to retain), free nodes (including those with force applied) and constrained nodes (including prescribed displacements).

$$\begin{Bmatrix} F_1 \\ F_2 \\ F_3 \end{Bmatrix} = \begin{bmatrix} K_{11} & K_{12} & K_{13} \\ K_{21} & K_{22} & K_{23} \\ K_{31} & K_{32} & K_{33} \end{bmatrix} \begin{Bmatrix} \delta_1 \\ \delta_2 \\ \delta_3 \end{Bmatrix}$$

where subscripts 1 – active, 2 – free, 3 – constrained.

We want to eliminate the unknowns F_3 and δ_2 to get the relationship between F_1 and δ_1 in terms of the knowns K , F_2 and δ_3 . This is done by re-arranging the second row and substituting into the third row to give:

$$\{F_1\} = [K^*]\{\delta_1\} + [A]\{\delta_2\} + [B]\{F_3\}$$

where

$$[K^*] = [K_{11}] - [K_{12}][K_{22}]^{-1}[K_{21}]$$

$$[A] = [K_{13}] - [K_{12}][K_{22}]^{-1}[K_{23}]$$

$$[B] = [K_{12}][K_{22}]^{-1}$$

$[A]\{\delta_2\} + [B]\{F_3\}$ represents a pre-load force vector, which is zero if there is no pre-load on the structure. This information is stored by ABAQUS in a ‘.mtx’ file. For the purposes of this project it was necessary to apply further transformations to obtain a compliance matrix in terms of element local transverse and normal directions. The

following matrix transformations were coded as part of the project and based on code written by the author previously Barrett (2001).

First, the reduced stiffness matrix is inverted using Gauss Elimination. This process transforms the stiffness matrix into the identity matrix by subtracting multiples of one row from another successively:

$$K^* \delta = IF$$

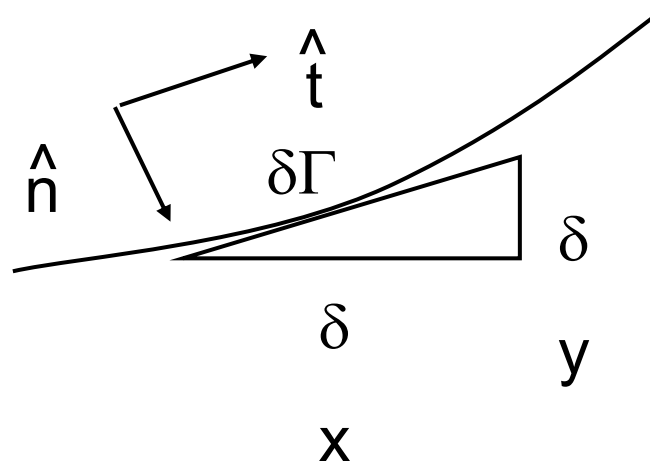
$$I \delta = C^* F$$

$$\delta = C^* F$$

where:

$$C^* = K^{*-1}$$

Conversion from x-y coordinates to local t-n requires calculation of the slope of the element side from the shape functions:



$$\delta\Gamma^2 = \delta x^2 + \delta y^2$$

$$\hat{t} = l\hat{i} + m\hat{j}$$

$$\hat{n} = m\hat{i} - l\hat{j}$$

where :

$$l = \frac{dx}{d\Gamma} = 1/\sqrt{1 + \left(\frac{dy}{d\xi}/\frac{dx}{d\xi}\right)^2}$$

$$m = \frac{dy}{d\Gamma} = 1/\sqrt{1 + \left(\frac{dx}{d\xi}/\frac{dy}{d\xi}\right)^2}$$

and

$$\frac{dx}{d\xi} = \sum_{i=1}^n \frac{dN_i}{d\xi} x_i$$

and similarly for y

The compliance matrix can then be rotated using the rotation matrix:

$$C_{t-n} = R C R^{-1}$$

where :

$$R = \begin{bmatrix} l_1 & m_1 & 0 & 0 \\ -m_1 & l_1 & 0 & 0 \\ 0 & 0 & l_2 & m_2 \\ 0 & 0 & -m_2 & l_2 \\ & & & \text{etc.} \end{bmatrix}$$

The rotated matrix is stored in an array so that it can be read by the elasto-hydrodynamic program.

APPENDIX C - EQUATIONS FOR SOLUTION OF REYNOLD'S EQUATION WITH OIL FILM HISTORY

Reynold's Equation with oil fill ratio term ($\theta = 0$ to 1) developed for cylindrical journal bearings:

$$\frac{\partial}{\partial x} \left(\theta h^3 \frac{\partial p}{\partial x} \right) + \frac{\partial}{\partial y} \left(\theta h^3 \frac{\partial p}{\partial y} \right) = 6\eta U \frac{\partial \theta h}{\partial x} + 12\eta \frac{\partial \theta h}{\partial t}$$

First, we can expand the differentials –

$$\frac{\partial}{\partial x} \left(\theta h^3 \frac{\partial p}{\partial x} \right) = 3\theta h^2 \frac{\partial h}{\partial x} \frac{\partial p}{\partial x} + \theta h^3 \frac{\partial^2 p}{\partial x^2} + h^3 \frac{\partial p}{\partial x} \frac{\partial \theta}{\partial x}$$

etc.

and then express the differential equations as difference equations using –

$$\left(\frac{\partial h}{\partial x} \right)_{i,j} = \frac{h_{i+1,j} - h_{i-1,j}}{2\delta x}$$

$$\left(\frac{\partial^2 p}{\partial x^2} \right)_{i,j} = \frac{p_{i+1,j} - 2p_{i,j} + p_{i-1,j}}{(\delta x)^2}$$

etc. for other terms, leading to a final equation of –

$$\begin{aligned}
& 3\theta_{i,j}h_{i,j}^2\left(\frac{h_{i+1,j}-h_{i-1,j}}{2\delta x}\right)\left(\frac{p_{i+1,j}-p_{i-1,j}}{2\delta x}\right) + \theta_{i,j}h_{i,j}^3\left(\frac{p_{i+1,j}-2p_{i,j}+p_{i-1,j}}{(\delta x)^2}\right) \\
& + h_{i,j}^3\left(\frac{p_{i+1,j}-p_{i-1,j}}{2\delta x}\right)\left(\frac{\theta_{i+1,j}-\theta_{i-1,j}}{2\delta x}\right) \\
& + 3\theta_{i,j}h_{i,j}^2\left(\frac{h_{i,j+1}-h_{i,j-1}}{2\delta y}\right)\left(\frac{p_{i,j+1}-p_{i,j-1}}{2\delta y}\right) + \theta_{i,j}h_{i,j}^3\left(\frac{p_{i,j+1}-2p_{i,j}+p_{i,j-1}}{(\delta y)^2}\right) \\
& + h_{i,j}^3\left(\frac{p_{i,j+1}-p_{i,j-1}}{2\delta y}\right)\left(\frac{\theta_{i,j+1}-\theta_{i,j-1}}{2\delta y}\right) \\
& = 6\eta U_i\left(\theta_{i,j}\left(\frac{h_{i+1,j}-h_{i-1,j}}{2\delta x}\right) + h_{i,j}\left(\frac{\theta_{i+1,j}-\theta_{i-1,j}}{2\delta x}\right)\right) + 12\eta\theta_{i,j}\frac{\partial h_{i,j}}{\partial t} + 12\eta h_{i,j}\frac{\partial \theta_{i,j}}{\partial t}
\end{aligned}$$

As we will already have a value for $p_{i,j}$ from a previous iteration, we must regard this equation as referring to a new value $\bar{p}_{i,j}$

$$\begin{aligned}
8\bar{p}_{i,j}h_{i,j}^3\theta_{i,j}(\delta x^2 + \delta y^2) & = 3\theta_{i,j}h_{i,j}^2\delta y^2(h_{i+1,j}-h_{i-1,j})(p_{i+1,j}-p_{i-1,j}) + 4\theta_{i,j}h_{i,j}^3\delta y^2(p_{i+1,j}+p_{i-1,j}) \\
& + 3\theta_{i,j}h_{i,j}^2\delta x^2(h_{i,j+1}-h_{i,j-1})(p_{i,j+1}-p_{i,j-1}) + 4\theta_{i,j}h_{i,j}^3\delta x^2(p_{i,j+1}+p_{i,j-1}) \\
& + h_{i,j}^3\delta y^2(p_{i+1,j}-p_{i-1,j})(\theta_{i+1,j}-\theta_{i-1,j}) \\
& + h_{i,j}^3\delta x^2(p_{i,j+1}-p_{i,j-1})(\theta_{i,j+1}-\theta_{i,j-1}) \\
& - 12\eta U_i\delta x\delta y^2\left[\theta_{i,j}(h_{i+1,j}-h_{i-1,j}) + h_{i,j}(\theta_{i+1,j}-\theta_{i-1,j})\right] \\
& - 48\eta\theta_{i,j}\delta x^2\delta y^2\frac{\partial h_{i,j}}{\partial t} - 48\eta h_{i,j}\delta x^2\delta y^2\frac{\partial \theta_{i,j}}{\partial t}
\end{aligned}$$

and the residual $R_{i,j} = p_{i,j} - \bar{p}_{i,j}$.

The equations reduce to the standard Reynold's Equation (Appendix A) if θ is set to 1.

APPENDIX D - ACCOUNTING AND FINANCE

Accounting started by walking through the elements of double entry bookkeeping. It also covered subjects such as accounting standards and consistency, management of multi-divisional organisations, reward systems for divisional managers.

Finance covered topics such as cash flow, discounted cash flow, start-up finance, risk and rate of return and dividend policy. Calculation of company value was covered and the issuing of shares and the valuing of shares during takeovers etc.

- Cost of debt needs to take account of tax, cost of equity needs to take account of risk factor – the combined rate is the Weighted Average Cost of Capital for use in Net Present Value and assessment of Internal Rate of Return for judging the viability of projects.
- Equity financing – high risk, high rate – only possibility for start-ups
- Debt financing – low risk, low rate – attractive for mature companies
- Considerations for debt – Secured/unsecured, priority ranking, committed/uncommitted, floating/fixed, currency
- Ranking in terms of risk – Debt (Secured debt, senior debt, junior debt), Hybrid (Mezzanine, warrant, convertibles) and Equity (Preference shares, ordinary shares)
- Can assess ideal mix of equity and debt in terms of Earnings Per Share versus Earnings Before Interest and Tax.
- Company valuation can be done in a number of ways that will produce very different values – important to assess in more than one way and state how done!
 - Asset based – book value or market value
 - Future based – NPV of projects, P/E ratios, multiples of sales
 - Based on WACC from costs of debt and equity
 - Bear in mind that share price will vary with the general level of the stock market (β is the ratio between the two)
 - May want to examine sensitivity of the valuation to the inputs used

Although this might seem an unlikely topic for the EngD thesis, it is clearly important for new products and new companies. Therefore, it could be a topic to take further when looking at the financial benefit from the project.

APPENDIX E - STRATEGY AND MANAGING INFORMATION SYSTEMS

The course on Strategic Management covered the following topics

- Planning, SWOT, PEST and 5 forces. Strategic thinking involves being formal and organised when considering these techniques – need to consider internal vs. external and especially now vs. future. External – Analysis – OT, PEST, 5 forces, entry and exit barriers – Industry dynamic, competitors, customers. Internal – Implementation – SW – Culture, individuals, leadership. Plan – Timescale, current dynamic, project trends forward, identify future dynamic.
- VRIN resources and tacit knowledge role in qualifying vs. competitive strategy. There is recognition that competitive advantage comes from within a firm's resources and this can be destroyed by Business Process Re-engineering. Such assets can be classified as:
 - Valuable – gives competitive parity
 - Rare – gives temporary advantage
 - Imperfectly imitable – gives sustainable competitive advantage
 - Non-substitutable – ditto
- VRIN resources can also be classified by Financial, Physical, Human and Organisational (Tangible and Intangible). The IN give sustainable advantage because of their non-codifiability, complexity, specificity, causal ambiguity and/or path dependency – can't simply go out and purchase them. However, it is also difficult for us to understand and hence easy to lose in Business Process Re-engineering.
- Perceived Use Value vs. Perceived Price diagrams are useful for understanding where we are and where to go. Beware simply competing on price. PUV requires knowledge of customers. Generate PUV with input from customers on weighted rating against important performance factors. Do this for us and our competitors.
- Managing strategic assets combines the above two subjects – V corresponds to PUV and/or lowering costs. Imperfectly imitable can be elicited through analysing the causal mapping, path dependency, asset configuration, first mover advantage and embeddedness.
 - Causal mapping important for VRIN elicitation – often very different views of the sources of company's profit from different people in the organisation
 - Auditing by category (Tangible, system, structural, knowledge, relational, cultural) against PUV, costs, R,I,N with total ranking in final column.

- Keep in mind migration through time and the strategic fit (Systems, culture, assets).
- Porter's 5 forces – competitors, suppliers, customers, barriers to entry and substitutes
- 5 key questions – Where to compete? How to gain and sustain advantage? What assets required? How to change? What assets do we have?
- Porter's 2 generic strategies – cost leadership or differentiation
- Company culture, top team harmony and change
- Corporate strategy and globalisation/national responsiveness plus parenting were mostly relevant to large global organisations. However, the topics of modes of development (internal, alliances – often successful, merger/acquisition – often unsuccessful) and the strategic option matrix (core competencies vs. market) may be relevant for us.
- Similar comment can probably be made about the implementation topic – espoused vs. realised strategy, company culture and zones of debate. Illusion of change through organisational change. Pressures to integrate vs. pressures to disintegrate, change, dynamic environments, disruptive technologies and embracing uncertainty. Complexity vs. uncertainty determines how to go about setting strategy, level of control etc.

Managing Information Systems was really about strategic analysis of company processes and their change. There was an emphasis on information flows but much of the course was much more strategic in scope. It included

- Stakeholder expectations – gap analysis
- Process analysis – see Fig. 4.1 and understanding the need to match required performance level to the category of process. This relates to IT investment decisions, whether we are trying to gain advantage or avoid disadvantage, outsourcing etc.
- Gated processes and the commitment of future spending
- Time, Cost, Quality trade off – most important to add Risk and Benefits
- Very useful and important Indicative Benefits Network method taught to connect vision to actions on business processes and IT support decisions. This technique caught the imagination of the MBA students who regarded it as one of the most useful practical techniques taught on Part 1 EMBA.

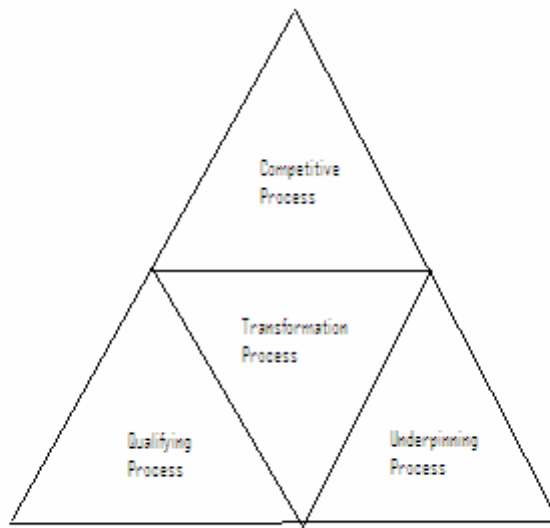


Figure 9-1 Process Triangle

APPENDIX F - MARKETING

The major topics on this course included

- Definition of customer value, evolutions from transactional to relationship marketing, the marketing mix (4Ps – Product, Price, Promotion, Place and add 2 more for relationship marketing - People and Processes)
- Tools for understanding - product life cycle, experience curve, Boston Matrix (Market growth vs. market share), Directional Policy Matrix (market attractiveness vs. rel. business strength), Product-Market Mix, SWOT with the 6Ps (existing – new), Manufacturing-Marketing Matrix, Product-Process Matrix (Volume vs. Variety)
- Formal approach to marketing planning – 10 steps in 4 phases (Goal setting, Situation review, Strategy formulation, Resource allocation and monitoring) using cross functional input leading to strategic plan taking account of company capabilities and change drivers such as competing on time, market maturity, customer power, global reach and technology
- Market segmentation has changed – no longer just social class and is a growing phenomenon. Consider customers and their grouping by identity (social, economic, demography, psychology, geography) and type of response (subjective, objective). Target and position the product considering level of focus or differentiation required. Segmentation can also be in terms of purchasing practice or by considering met and unmet needs. Buyer behaviour can be categorised differently for Business to Customer (Behaviourist/repeat purchase vs. Cognitive/desire) and Business to Business (Decision Making Unit consisting of people in various roles – user, influencer, gatekeeper, decider etc. – care over politics at customer)
- Market research must not be woolly – base on problem definition and a research plan. Various techniques possible
- Branding again must not be woolly and topics such as brand equity metrics, link to strategy, brand position maps (tradeoffs) were described
- Other topics included strategy and innovation (New Product Development process), service, marketing communication and sales management for different types of relationship

APPENDIX G - ECONOMICS AND STRATEGIC DECISION SCIENCE

These topics might appear to be lacking direct relevance. However, the situation for mechanical engineering design analysis software (outside the general purpose codes for FEA and CFD) is one of only a few players. This means that a new entrant into the market place can fundamentally affect the supply and demand curves leading to a need for competitors to respond. This makes game theory and an appreciation of the competitors' likely responses to scenarios important.

- Macroeconomic environment – the global economy and changes e.g. the emergence of India and China, increasing competition through globalisation and exchange rate movements are all relevant to the prospects for the software being developed.
- Supply and demand curves were presented in the course in a conceptual way. However it is possible to put numbers on the axes by trying different prices etc. Judging elasticity of demand could be very important for us. Can it be assumed that supply is very elastic for software simply because of the high fixed costs and low variable costs? That also leads on to the concepts of differential pricing for different customers. This is a very effective way of getting income from a variety of customers that contributes to recovering both fixed and variable costs.
- Oligopoly in special purpose design analysis software – role of new entrant – game theory. Response of competitors to a new entrant becomes very important if there are relatively few players. This can lead to a series of responses eventually leading to a new equilibrium price (Nash equilibrium – just remember that Nash was suffering from paranoid schizophrenia which was not mentioned on the course!). The role of understanding the competition, their likely responses and giving signals of intention become important.

APPENDIX H EHD PROGRAM STRUCTURE

Partial Jackson Structure Chart – Numerical Integration – Major Subroutines Only

